Scientists get serious about personality in animals *p. 644*

Defending the planet, one film at a time *p. 648*

Seafloor deformation caught in the act *pp. 654 & 701*

Science

$15
6 MAY 2016
sciencemag.org

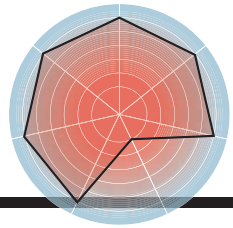
AAAS



MINIATURE RAILROAD

Close-up view of intraflagellar transport *p. 721*

CONTENTS



658
Personalized cancer immunotherapy

6 MAY 2016 • VOLUME 352 • ISSUE 6286



NEWS

IN BRIEF

632 News at a glance

IN DEPTH

635 **AMAZON RAINFOREST TO GET A GROWTH CHECK**
Ambitious experiment will test whether rising CO_2 will boost the tropical carbon sink *By D. Grossman*

636 **MORE DELAYS FOR ITER, AS PARTNERS BALK AT COSTS**
Review warns that new timeline could still be too optimistic
By D. Clery and A. Cho

637 **A REBOOT FOR WAVE ENERGY**
U.K. engineers and funders take stock of failures as they design new prototypes
By E. Stokstad

639 **WHY HUMANS ARE THE HIGH-ENERGY APES**
Our metabolism runs faster than that of other apes, likely allowing us to evolve big brains *By A. Gibbons*

640 **HUMAN EMBRYO RESEARCH CONFRONTS ETHICAL 'RULE'**
Time to revise 14-day limit for growing IVF embryos? *By P. Monahan*

FEATURES

641 **AN OASIS FOR ORCAS**
Advocates dream of flying killer whales to an ocean sanctuary, but does science support the move? *By D. Grimm*

644 **THE POWER OF PERSONALITY**
From birds to spiders, individuals exhibit consistent differences in behavior that shape the fate of their species *By E. Pennisi*
▸ PODCAST

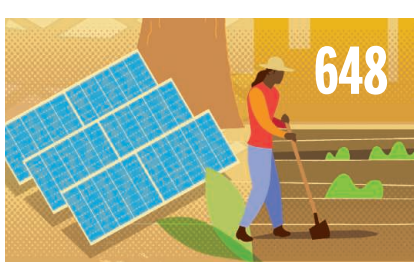
INSIGHTS

BOOKS *ET AL.*

648 **FIGHTING FOR OUR FUTURE**

PERSPECTIVES

654 **MEASURING SLOW SLIP OFFSHORE**
Monitoring changes in the seafloor might be used for earthquake and tsunami forecasting *By A. M. Tréhu*
▸ REPORT P. 701



656 **SELF-ASSEMBLY CREATES 2D MATERIALS**
Carefully chosen mixtures of polymers form rectangular platelets in solution
By M. Ballauff
▸ REPORT P. 697

657 **INSPIRED BY NATURE**
Designed proteins have structural features resembling those of natural active sites *By R. Netzer and S. J. Fleishman*
▸ RESEARCH ARTICLE P. 680; REPORT P. 687

658 **THE "CANCER IMMUNOGRAM"**
Visualizing the state of cancer–immune system interactions may spur personalized therapy
By C. U. Blank et al.



661 **HOPE FOR AMERICA'S NEXT GENERATION**
The gap in survival rates for children in the richest and poorest U.S. communities has shrunk
By M. J. Bailey and B. Timpe
▸ REPORT P. 708

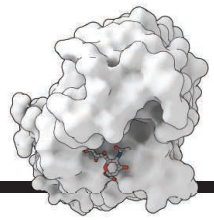
663 **WHY PURSUE THE POSTDOC PATH?**
Concise, diverse rationales require nuanced policies *By H. Sauermann and M. Roach*

Science Staff 630
New Products 730
Science Careers 731

Downloaded from http://science.sciencemag.org/ on May 5, 2016

Published by AAAS

CONTENTS



657, 680, & 687
Designer proteins

6 MAY 2016 • VOLUME 352 • ISSUE 6286



LETTERS

666 AFTER FUKUSHIMA: COLLABORATION MODEL
By N. Takamura et al.

666 AFTER FUKUSHIMA: CREATING A DIALOGUE
By M. Miyazaki et al.

666 AFTER FUKUSHIMA: ADDRESSING ANXIETY
By S. Midorikawa et al.

667 TECHNICAL COMMENT ABSTRACTS

RESEARCH

IN BRIEF

668 From *Science* and other journals

REVIEW

671 CELLULAR DYNAMICS
Nongenetic functions of the genome
M. Bustin and T. Misteli
REVIEW SUMMARY; FOR FULL TEXT:
dx.doi.org/10.1126/science.aad6933

RESEARCH ARTICLES

672 NEUROSCIENCE
Autism-associated SHANK3 haploinsufficiency causes I_h channelopathy in human neurons
F. Yi et al.
RESEARCH ARTICLE SUMMARY; FOR FULL TEXT:
dx.doi.org/10.1126/science.aaf2669

673 PRIMATE EVOLUTION
Oligocene primates from China reveal divergence between African and Asian primate evolution *X. Ni* et al.

677 ASTROPARTICLE PHYSICS
Observation of the ^{60}Fe nucleosynthesis-clock isotope in galactic cosmic rays
W. R. Binns et al.

680 PROTEIN DESIGN
De novo design of protein homo-oligomers with modular hydrogen-bond network–mediated specificity
S. E. Boyken et al.
▸ PERSPECTIVE P. 657; REPORT P. 687

REPORTS

687 PROTEIN DESIGN
Design of structurally distinct proteins using strategies inspired by evolution
T. M. Jacobs et al.
▸ PERSPECTIVE P. 657;
RESEARCH ARTICLE P. 680

691 MICROFLUIDICS
Submillisecond organic synthesis: Outpacing Fries rearrangement through microfluidic rapid mixing *H. Kim* et al.

694 GEOMORPHOLOGY
Self-organization of river channels as a critical filter on climate signals
C. B. Phillips and D. J. Jerolmack

697 POLYMER GROWTH
Uniform patchy and hollow rectangular platelet micelles from crystallizable polymer blends *H. Qiu* et al.
▸ PERSPECTIVE P. 656

701 GEOPHYSICS
Slow slip near the trench at the Hikurangi subduction zone, New Zealand *L. M. Wallace* et al.
▸ PERSPECTIVE P. 654

705 GEOBIOLOGY
Mass-dependent and -independent signature of Fe isotopes in magnetotactic bacteria *M. Amor* et al.

708 DEMOGRAPHY
Inequality in mortality decreased among the young while increasing for older adults, 1990–2010 *J. Currie and H. Schwandt*
▸ PERSPECTIVE P. 661

712 NEURODEVELOPMENT
Complement and microglia mediate early synapse loss in Alzheimer mouse models
S. Hong et al.

717 EPIGENETICS
Single-molecule decoding of combinatorially modified nucleosomes *E. Shema* et al.

721 CELL BIOLOGY
Microtubule doublets are double-track railways for intraflagellar transport trains
L. Stepanek and G. Pigino

725 PROTEIN STRUCTURE
Femtosecond structural dynamics drives the trans/cis isomerization in photoactive yellow protein *K. Pande* et al.

DEPARTMENTS

631 EDITORIAL
Don't ignore the infrastructure
By Alan I. Leshner

738 WORKING LIFE
Learning the lessons of networking
By Peter M. Grace

ON THE COVER



Intraflagellar transport (IFT) in the cilium of a eukaryotic cell. IFT trains use microtubule doublets as bidirectional railways to transport ciliary building blocks. Assigning directionality to individual microtubules ensures that trains moving forward (purple) and backward (red) do not collide. Thus, traffic jams are avoided during assembly and disassembly of the cilium. See page 721. *Illustration: C. Bickel*/Science

Downloaded from http://science.sciencemag.org/ on May 5, 2016

SCIENCE (ISSN 0036-8075) is published weekly on Friday, except the last week in December, by the American Association for the Advancement of Science, 1200 New York Avenue, NW, Washington, DC 20005. Periodicals mail postage (publication No. 484460) paid at Washington, DC, and additional mailing offices. Copyright © 2016 by the American Association for the Advancement of Science. The title SCIENCE is a registered trademark of the AAAS. Domestic individual membership and subscription (51 issues): $165 ($74 allocated to subscription). Domestic institutional subscription (51 issues): $1522; Foreign postage extra: Mexico, Caribbean (surface mail) $55; other countries (air assist delivery) $89. First class, airmail, student, and emeritus rates on request. Canadian rates with GST available upon request, GST #1254 88122. Publications Mail Agreement Number 1069624. **Printed in the U.S.A.**
Change of address: Allow 4 weeks, giving old and new addresses and 8-digit account number. **Postmaster:** Send change of address to AAAS, P.O. Box 96178, Washington, DC 20090–6178. **Single-copy sales:** $15.00 current issue, $20.00 back issue prepaid includes surface postage; bulk rates on request. **Authorization to photocopy** material for internal or personal use under circumstances not falling within the fair use provisions of the Copyright Act is granted by AAAS to libraries and other users registered with the Copyright Clearance Center (CCC) Transactional Reporting Service, provided that $35.00 per article is paid directly to CCC, 222 Rosewood Drive, Danvers, MA 01923. The identification code for *Science* is 0036-8075. *Science* is indexed in the *Reader's Guide to Periodical Literature* and in several specialized indexes.

Published by AAAS

Science
AAAS
1200 New York Avenue, NW, Washington, DC 20005
Bateman House, 82-88 Hills Road, Cambridge, UK CB2 1LQ

Editor-in-Chief Marcia McNutt
Executive Editor Monica M. Bradford **News Editor** Tim Appenzeller
Managing Editor, Research Journals Katrina L. Kelner
Deputy Editors Lisa D. Chong, Andrew M. Sugden(UK), Valda J. Vinson, Jake S. Yeston

Research and Insights

DEPUTY EDITOR, EMERITUS Barbara R. Jasny **SR. EDITORS** Caroline Ash(UK), Gilbert J. Chin, Julia Fahrenkamp-Uppenbrink(UK), Pamela J. Hines, Stella M. Hurtley(UK), Paula A. Kiberstis, Marc S. Lavine(Canada), Kristen L. Mueller, Ian S. Osborne(UK), Beverly A. Purnell, L. Bryan Ray, Guy Riddihough, H. Jesse Smith, Jelena Stajic, Peter Stern(UK), Phillip D. Szuromi, Sacha Vignieri, Brad Wible, Nicholas S. Wigginton, Laura M. Zahn **ASSOCIATE EDITORS** Brent Grocholski, Keith T. Smith **ASSOCIATE BOOK REVIEW EDITOR** Valerie B. Thompson **LETTERS EDITOR** Jennifer Sills **CHIEF CONTENT PRODUCTION EDITOR** Cara Tate **SR. CONTENT PRODUCTION EDITORS** Harry Jach, Lauren Kmec **CONTENT PRODUCTION EDITORS** Jeffrey E. Cook, Chris Filiatreau, Cynthia Howe, Barbara P. Ordway, Catherine Wolner **SR. EDITORIAL COORDINATORS** Carolyn Kyle, Beverly Shields **EDITORIAL COORDINATORS** Aneera Dobbins, Joi S. Granger, Lisa Johnson, Anita Wynn **PUBLICATIONS ASSISTANTS** Jeffrey Hearn, Dona Mathieu, Le-Toya Mayne Flood, Shannon McMahon, Scott Miller, Caitlyn Phillips, Jerry Richardson, Alice Whaley(UK), Brian White **EXECUTIVE ASSISTANT** Anna Bashkirova **ADMINISTRATIVE SUPPORT** Janet Clements(UK), Lizanne Newton(UK), Maryrose Madrid

News

NEWS MANAGING EDITOR John Travis **INTERNATIONAL EDITOR** Richard Stone **DEPUTY NEWS EDITORS** Robert Coontz, Elizabeth Culotta, David Grimm, David Malakoff, Leslie Roberts **CONTRIBUING EDITOR** Martin Enserink(Europe) **SR. CORRESPONDENTS** Daniel Clery(UK), Jeffrey Mervis, Elizabeth Pennisi **NEWS WRITERS** Adrian Cho, Jon Cohen, Jennifer Couzin-Frankel, Carolyn Gramling, Eric Hand, Jocelyn Kaiser, Catherine Matacic, Kelly Servick, Robert F. Service, Erik Stokstad(Cambridge, UK), Emily Underwood **INTERNS** Patrick Monahan **CONTRIBUTING CORRESPONDENTS** John Bohannon, Warren Cornwall, Ann Gibbons, Mara Hvistendahl, Sam Kean, Eli Kintisch, Kai Kupferschmidt(Berlin), Andrew Lawler, Christina Larson(Beijing), Mitch Leslie, Charles C. Mann, Eliot Marshall, Virginia Morell, Dennis Normile(Shanghai), Heather Pringle, Tania Rabesandratana(London), Gretchen Vogel(Berlin), Lizzie Wade(Mexico City) **CAREERS** Donisha Adams, Rachel Bernstein(Editor) **COPY EDITORS** Julia Cole, Dorie Chevlen, Jennifer Levin (Chief) **ADMINISTRATIVE SUPPORT** Jessica Adams

Executive Publisher Rush D. Holt
Interim Publisher Bill Moran **Chief Digital Media Officer** Rob Covey

BUSINESS OPERATIONS AND PORTFOLIO MANAGEMENT DIRECTOR Sarah Whalen **PRODUCT DEVELOPMENT DIRECTOR** Will Schweitzer **PRODUCT DEVELOPMENT ASSOCIATE** Hal Moore **BUSINESS SYSTEMS AND FINANCIAL ANALYSIS DIRECTOR** Randy Yi **MANAGER OF FULFILLMENT SYSTEMS** Neal Hawkins **SYSTEMS ANALYST** Nicole Mehmedovich **ASSISTANT DIRECTOR, BUSINESS OPERATIONS** Eric Knott **MANAGER, BUSINESS OPERATIONS** Jessica Tierney **SENIOR BUSINESS ANALYST** Cory Lipman **BUSINESS ANALYSTS** Sandy Kim, Meron Kebede **FINANCIAL ANALYST** Robert Clark **DIRECTOR, COPYRIGHTS LICENSING SPECIAL PROJECTS** Emilie David **PERMISSIONS ASSOCIATE** Elizabeth Sandler **RIGHTS, CONTRACTS, AND LICENSING ASSOCIATE** Lili Kiser

MARKETING DIRECTOR Elise Swinehart **ASSOCIATE MARKETING DIRECTOR** Christina Schlecht **MARKETING MANAGER** Elizabeth Sattler **MARKETING ASSOCIATE** Steven Goodman **CREATIVE DIRECTOR** Scott Rodgerson **SENIOR ART ASSOCIATES** Seil Lee, Paula Fry **ART ASSOCIATE** Kim Huynh **PROGRAM DIRECTOR, AAAS MEMBER CENTRAL** Peggy Mihelich **FULFILLMENT SYSTEMS AND OPERATIONS** membership@aaas.org **MANAGER, MEMBER SERVICES** Pat Butler **SPECIALISTS** Terrance Morrison, Latasha Russell **MANAGER, DATA ENTRY** Mickie Napoleoni **DATA ENTRY SPECIALISTS** Brenden Aquilino, Fiona Giblin

PUBLISHER RELATIONS MANAGER Catherine Holland **PUBLISHER RELATIONS, EASTERN REGION** Keith Layson **PUBLISHER RELATIONS, WESTERN REGION** Ryan Rexroth **SALES RESEARCH COORDINATOR** Aiesha Marshall **MANAGER, SITE LICENSE OPERATIONS** Iquo Edim **SENIOR OPERATIONS ANALYST** Lana Guz **FULFILLMENT ANALYST** Judy Lillibridge **ASSOCIATE DIRECTOR, MARKETING** Christina Schlecht **MARKETING ASSOCIATE** Isa Sesay-Bah

WEB TECHNOLOGIES SR. DEVELOPER Chris Coleman **DEVELOPERS** Dan Berger, Jimmy Marks, Ryan Jensen **SR. PROJECT MANAGER** Trista Smith **PROJECT MANAGER** Nick Fletcher

DIGITAL MEDIA DIRECTOR OF ANALYTICS Enrique Gonzales **DIGITAL REPORTING ANALYST** Eric Hossinger **SR. WEB PRODUCER** Sarah Crespi **WEB PRODUCER** Alison Crawford **VIDEO PRODUCER** Nguyen Nguyen **SOCIAL MEDIA PRODUCER** Brice Russ

DIRECTOR OF OPERATIONS PRINT AND ONLINE Lizabeth Harman **DIGITAL/PRINT STRATEGY MANAGER** Jason Hillman **QUALITY TECHNICAL MANAGER** Marcus Spiegler **PROJECT ACCOUNT MANAGER** Tara Kelly **DIGITAL PRODUCTION MANAGER** Lisa Stanford **ASSISTANT MANAGER DIGITAL/PRINT** Rebecca Doshi **SENIOR CONTENT SPECIALISTS** Steve Forrester, Antoinette Hodal, Lori Murphy, Anthony Rosen **CONTENT SPECIALISTS** Jacob Hedrick, Kimberley Oster

DESIGN DIRECTOR Beth Rakouskas **DESIGN EDITOR** Marcy Atarod **SENIOR DESIGNERS** Garvin Grullón, Chrystal Smith **GRAPHICS MANAGING EDITOR** Alberto Cuadra **SENIOR SCIENTIFIC ILLUSTRATORS** Chris Bickel, Katharine Sutliff **SCIENTIFIC ILLUSTRATOR** Valerie Altounian **INTERACTIVE GRAPHICS EDITOR** Jia You **SENIOR ART ASSOCIATES** Holly Bishop, Nathalie Cary, Preston Huey **PHOTOGRAPHY MANAGING EDITOR** William Douthitt **PHOTO EDITORS** Leslie Blizard, Christy Steele

DIRECTOR, GLOBAL COLLABORATION, CUSTOM PUBLICATIONS, ADVERTISING Bill Moran **EDITOR, CUSTOM PUBLISHING** Sean Sanders: 202-326-6430 **ADVERTISING MARKETING MANAGER** Justin Sawyers: 202-326-7061 science_advertising@aaas.org **ADVERTISING SUPPORT MANAGER** Karen Foote: 202-326-6740 **ADVERTISING PRODUCTION OPERATIONS MANAGER** Deborah Tompkins **SR. PRODUCTION SPECIALIST/GRAPHIC DESIGNER** Amy Hardcastle **SR. TRAFFIC ASSOCIATE** Christine Hall **SALES COORDINATOR** Shirley Young **ASSOCIATE DIRECTOR, COLLABORATION, CUSTOM PUBLICATIONS/CHINA/TAIWAN/KOREA/SINGAPORE** Ruolei Wu: +86-186 0082 9345, rwu@aaas.org **COLLABORATION/CUSTOM PUBLICATIONS/JAPAN** Adarsh Sandhu + 81532-81-5142 asandhu@aaas.org **EAST COAST/E. CANADA** Laurie Faraday: 508-747-9395, FAX 617-507-8189 **WEST COAST/W. CANADA** Lynne Stickrod: 415-931-9782, FAX 415-520-6940 **MIDWEST** Jeffrey Dembksi: 847-498-4520 x3005, Steven Loerch: 847-498-4520 x3006 **UK EUROPE/ASIA** Roger Goncalves: TEL/FAX +41 43 243 1358 **JAPAN** Katsuyoshi Fukamizu(Tokyo): +81-3-3219-5777 kfukamizu@aaas.org **CHINA/TAIWAN** Ruolei Wu: +86-186 0082 9345, rwu@aaas.org

WORLDWIDE ASSOCIATE DIRECTOR OF SCIENCE CAREERS Tracy Holmes: +44 (0) 1223 326525, FAX +44 (0) 1223 326532 tholmes@science-int.co.uk **CLASSIFIED** advertise@sciencecareers.org **U.S. SALES** Tina Burks: 202-326-6577, Nancy Toema: 202-326-6578 **EUROPE/ROW SALES** Sarah Lelarge **SALES ASSISTANT** Kelly Grace **JAPAN** Hiroyuki Mashiki(Kyoto): +81-75-823-1109 hmashiki@aaas.org **CHINA/TAIWAN** Ruolei Wu: +86-186 0082 9345 rwu@aaas.org **MARKETING MANAGER** Allison Pritchard **MARKETING ASSOCIATE** Aimee Aponte

AAAS BOARD OF DIRECTORS, CHAIR Geraldine L. Richmond **PRESIDENT** Barbara A. Schaal **PRESIDENT-ELECT** Susan Hockfield **TREASURER** David Evans Shaw **CHIEF EXECUTIVE OFFICER** Rush D. Holt **BOARD** Cynthia M. Beall, May R. Berenbaum, Carlos J. Bustamante, Stephen P.A. Fodor, Claire M. Fraser, Michael S. Gazzaniga, Laura H. Greene, Elizabeth Loftus, Mercedes Pascual

SUBSCRIPTION SERVICES For change of address, missing issues, new orders and renewals, and payment questions: 866-434-AAAS (2227) or 202-326-6417, FAX 202-842-1065. Mailing addresses: AAAS, P.O. Box 96178, Washington, DC 20090-6178 or AAAS Member Services, 1200 New York Avenue, NW, Washington, DC 20005

INSTITUTIONAL SITE LICENSES 202-326-6730 **REPRINTS:** Author Inquiries 800-635-7181 **COMMERCIAL INQUIRIES** 803-359-4578 **PERMISSIONS** 202-326-6765, permissions@aaas.org **AAAS Member Services** 202-326-6417 or http://membercentral.aaas.org/discounts

Science serves as a forum for discussion of important issues related to the advancement of science by publishing material on which a consensus has been reached as well as including the presentation of minority of conflicting points of view. Accordingly, all articles published in *Science*—including editorials, news and comment, and book reviews—are signed and reflect the individual views of the authors and not official points of view adopted by AAAS or the institutions with which the authors are affiliated.

INFORMATION FOR AUTHORS See pages 624 and 625 of the 5 February 2016 issue or access www.sciencemag.org/authors/science-information-authors

SENIOR EDITORIAL BOARD
Gary King, *Harvard University,* **Susan M. Rosenberg,** *Baylor College of Medicine,*
Ali Shilatifard, *Northwestern University Feinberg School of Medicine*

BOARD OF REVIEWING EDITORS (Statistics board members indicated with **(S)**

Adriano Aguzzi, *U. Hospital Zürich*
Takuzo Aida, *U. of Tokyo*
Leslie Aiello, *Wenner-Gren Foundation*
Judith Allen, *U. of Edinburgh*
Sonia Altizer, *U. of Georgia*
Sebastian Amigorena, *Institut Curie*
Kathryn Anderson, *Memorial Sloan-Kettering Cancer Center*
Meinrat O. Andreae, *Max-Planck Inst. Mainz*
Paola Arlotta, *Harvard U.*
Johan Auwerx, *EPFL*
David Awschalom, *U. of Chicago*
Clare Baker, *University of Cambridge*
Nenad Ban, *ETH Zurich*
Jordi Bascompte, *University of Zurich*
Franz Bauer, *Instituto de Astrofisica*
Ray H. Baughman, *U. of Texas, Dallas*
David Baum, *U. of Wisconsin*
Carlo Beenakker, *Leiden U.*
Kamran Behnia, *ESPCI-ParisTech*
Yasmine Belkaid, *NIAID, NIH*
Philip Benfey, *Duke U.*
May Berenbaum, *U. of Illinois*
Gabriele Bergers, *U. of California, San Francisco*
Bradley Bernstein, *Massachusettes General Hospital*
Peer Bork, *EMBL*
Bernard Bourdon, *Ecole Normale Supérieure de Lyon*
Chris Bowler, *École Normale Supérieure*
Ian Boyd, *U. of St. Andrews*
Emily Brodsky, *U. of California, Santa Cruz*
Ron Brookmeyer, *U. of California Los Angeles* **(S)**
Christian Büchel, *U. Hamburg-Eppendorf*
Joseph A. Burns, *Cornell U.*
Carter Tribley Butts, *U. of California, Irvine*
Gyorgy Buzsaki, *New York U. School of Medicine*
Blanche Capel, *Duke U.*
Mats Carlsson, *U. of Oslo*
Ib Chorkendorff, *U. of Denmark*
David Clapham, *Children's Hospital Boston*
Joel Cohen, *Rockefeller U., Columbia U.*
James J. Collins, *MIT*
Robert Cook-Deegan, *Duke U.*
Lisa Coussens, *Oregon Health & Science U.*
Alan Cowman, *Walter & Eliza Hall Inst.*
Robert H. Crabtree, *Yale U.*
Roberta Croce, *Vrije Universiteit*
Janet Currie, *Princeton U.*
Jeff L. Dangl, *U. of North Carolina*
Tom Daniel, *U. of Washington*
Frans de Waal, *Emory U.*
Stanislas Dehaene, *Collège de France*
Robert Desimone, *MIT*
Claude Desplan, *New York U.*
Dennis Discher, *U. of Pennsylvania*
Gerald W. Dorn II, *Washington U. School of Medicine*
Jennifer A. Doudna, *U. of California, Berkeley*
Bruce Dunn, *U. of California, Los Angeles*
William Dunphy, *Caltech*
Christopher Dye, *WHO*
Todd Ehlers, *U. of Tuebingen*
David Ehrhardt, *Carnegie Inst. of Washington*
Tim Elston, *U. of North Carolina at Chapel Hill*
Gerhard Ertl, *Fritz-Haber-Institut, Berlin*
Barry Everitt, *U. of Cambridge*
Ernst Fehr, *U. of Zurich*
Anne C. Ferguson-Smith, *U. of Cambridge*
Michael Feuer, *The George Washington U.*
Toren Finkel, *NHLBI, NIH*
Kate Fitzgerald, *U. of Massachusetts*
Peter Fratzl, *Max-Planck Inst.*
Elaine Fuchs, *Rockefeller U.*
Daniel Geschwind, *UCLA*
Karl-Heinz Glassmeier, *TU Braunschweig*
Ramon Gonzalez, *Rice U.*
Julia R. Greer, *Caltech*
Elizabeth Grove, *U. of Chicago*
Nicolas Gruber, *ETH Zurich*
Kip Guy, *St. Jude's Children's Research Hospital*
Taekjip Ha, *U. of Illinois at Urbana-Champaign*
Wolf-Dietrich Hardt, *ETH Zurich*
Christian Haass, *Ludwig Maximilians U.*
Sharon Hammes-Schiffer, *U. of Illinois at Urbana–Champaign*
Michael Hasselmo, *Boston U.*
Martin Heimann, *Max-Planck Inst. Jena*
Yka Helariutta, *U. of Cambridge*
James A. Hendler, *Rensselaer Polytechnic Inst.*
Janet G. Hering, *Swiss Fed. Inst. of Aquatic Science & Technology*
Kai-Uwe Hinrichs, *U. of Bremen*
David Hodell, *U. of Cambridge*
Lora Hooper, *UT Southwestern Medical Ctr. at Dallas*
Tamas Horvath, *Yale University*
Raymond Huey, *U. of Washington*
Fred Hughson, *Princeton U.*
Auke Ijspeert, *EPFL Lausanne*
Stephen Jackson, *USGS and U. of Arizona*
Steven Jacobsen, *U. of California, Los Angeles*
Kai Johnsson, *EPFL Lausanne*
Peter Jonas, *Inst. of Science & Technology (IST) Austria*
Matt Kaeberlein, *U. of Washington*
William Kaelin Jr., *Dana-Farber Cancer Inst.*
Daniel Kahne, *Harvard U.*
Daniel Kammen, *U. of California, Berkeley*
Abby Kavner, *U. of California, Los Angeles*
Masashi Kawasaki, *U. of Tokyo*
V. Narry Kim, *Seoul National U.*
Joel Kingsolver, *U. of North Carolina at Chapel Hill*
Robert Kingston, *Harvard Medical School*
Etienne Koechlin, *Ecole Normale Supérieure*
Alexander Kolodkin, *Johns Hopkins U.*
Thomas Langer, *U. of Cologne*
Mitchell A. Lazar, *U. of Pennsylvania*
David Lazer, *Harvard U.*
Thomas Lecuit, *IBDM*
Virginia Lee, *U. of Pennsylvania*
Stanley Lemon, *U. of North Carolina at Chapel Hill*
Ottoline Leyser, *Cambridge U.*
Wendell Lim, *U.C. San Francisco*
Marcia C. Linn, *U. of California, Berkeley*
Jianguo Liu, *Michigan State U.*
Luis Liz-Marzan, *CIC biomaGUNE*
Jonathan Losos, *Harvard U.*
Ke Lu, *Chinese Acad. of Sciences*
Christian Lüscher, *U. of Geneva*
Laura Machesky, *CRUK Beatson Inst. for Cancer Research*
Anne Magurran, *U. of St. Andrews*
Oscar Marin, *CSIC & U. Miguel Hernández*
Charles Marshall, *U. of California, Berkeley*
C. Robertson McClung, *Dartmouth College*
Graham Medley, *U. of Warwick*
Tom Misteli, *NCI*
Yasushi Miyashita, *U. of Tokyo*
Mary Ann Moran, *U. of Georgia*
Richard Morris, *U. of Edinburgh*
Alison Motsinger-Reif, *NC State U.* **(S)**
Thomas Murray, *The Hastings Center*
Daniel Neumark, *U. of California, Berkeley*
Kitty Nijmeijer, *U. of Twente*
Helga Nowotny, *European Research Advisory Board*
Ben Olken, *MIT*
Joe Orenstein, *U. of California Berkeley & Lawrence Berkeley National Lab*
Harry Orr, *U. of Minnesota*
Pilar Ossorio, *U. of Wisconsin*
Andrew Oswald, *U. of Warwick*
Margaret Palmer, *U. of Maryland*
Steve Palumbi, *Stanford U.*
Jane Parker, *Max-Planck Inst. of Plant Breeding Research*
Giovanni Parmigiani, *Dana-Farber Cancer Inst.* **(S)**
John H. J. Petrini, *Memorial Sloan-Kettering Cancer Center*
Samuel Pfaff, *Salk Institute for Biological Studies*
Joshua Plotkin, *U. of Pennsylvania*
Albert Polman, *FOM Institute AMOLF*
Philippe Poulin, *CNRS*
Jonathan Pritchard, *Stanford U.*
David Randall, *Colorado State U.*
Felix Rey, *Institut Pasteur*
Trevor Robbins, *U. of Cambridge*
Jim Roberts, *Fred Hutchinson Cancer Research Ctr.*
Barbara A. Romanowicz, *U. of California,Berkeley*
Amy Rosenzweig, *Northwestern University*
Mike Ryan, *U. of Texas, Austin*
Mitinori Saitou, *Kyoto U.*
Shimon Sakaguchi, *Kyoto U.*
Miquel Salmeron, *Lawrence Berkeley National Lab*
Jürgen Sandkühler, *Medical U. of Vienna*
Alexander Schier, *Harvard U.*
Vladimir Shalaev, *Purdue U.*
Robert Siliciano, *Johns Hopkins School of Medicine*
Denis Simon, *Arizona State U.*
Uri Simonsohn, *U. of Pennsylvania*
Alison Smith, *John Innes Centre*
Richard Smith, *U. of North Carolina* **(S)**
John Speakman, *U. of Aberdeen*
Allan C. Spradling, *Carnegie Institution of Washington*
Jonathan Sprent, *Garvan Inst. of Medical Research*
Eric Steig, *U. of Washington*
Paula Stephan, *Georgia State U. and National Bureau of Economic Research*
Molly Stevens, *Imperial College London*
V. S. Subrahmanian, *U. of Maryland*
Ira Tabas, *Columbia U.*
Sarah Teichmann, *Cambridge U.*
John Thomas, *North Carolina State U.*
Shubha Tole, *Tata Institute of Fundamental Research*
Christopher Tyler-Smith, *The Wellcome Trust Sanger Inst.*
Herbert Virgin, *Washington U.*
Bert Vogelstein, *Johns Hopkins U.*
Cynthia Volkert, *U. of Göttingen*
David Wallach, *Weizmann Inst. of Science*
Ian Walmsley, *U. of Oxford*
Jane-Ling Wang, *U. of California, Davis* **(S)**
David A. Wardle, *Swedish U. of Agric. Sciences*
David Waxman, *Fudan U.*
Jonathan Weissman, *U. of California, San Francisco*
Chris Wikle, *U. of Missouri* **(S)**
Ian A. Wilson, *The Scripps Res. Inst.* **(S)**
Timothy D. Wilson, *U. of Virginia*
Rosemary Wyse, *Johns Hopkins U.*
Jan Zaanen, *Leiden U.*
Kenneth Zaret, *U. of Pennsylvania School of Medicine*
Jonathan Zehr, *U. of California, Santa Cruz*
Len Zon, *Children's Hospital Boston*
Maria Zuber, *MIT*

BOOK REVIEW BOARD
David Bloom, *Harvard U.,* **Samuel Bowring,** *MIT,* **Angela Creager,** *Princeton U.,*
Richard Shweder, *U. of Chicago,* **Ed Wasserman,** *DuPont*

Published by AAAS

EDITORIAL

Don't ignore the infrastructure

Large-scale research facilities and new technology development have been essential to answering difficult, often intransigent scientific questions that would otherwise be inaccessible. The recent exciting discovery of gravitational waves by the Laser Interferometer Gravitational-Wave Observatory (LIGO) is but one of many startling findings that argue for major investments in large- and mid-scale instrumentation development. But such instruments and facilities are just one type of infrastructure that urgently needs investment. Routine laboratories that underpin most scientific activity are equally critical to progress, but in many cases have long been neglected and are deteriorating. A comprehensive strategy for updating these facilities and other infrastructure elements is essential for accelerating scientific momentum.

The need to repair and upgrade research infrastructure is an issue for every country. As the European Strategy Forum on Research Infrastructure argued in their March 2016 report, future prosperity depends in part on attention to the "life cycle" of scientific infrastructure. In the United States, the situation has been studied in some depth. One recent example is a plan proposed in December 2015 by the U.S. National Science Foundation (NSF) to overhaul its Antarctic Research Station at McMurdo (a cost of $300 million). This was in response to a blue-ribbon panel convened by NSF that argued that such an investment was essential for maintaining the pace of Antarctic research. The panel also called for support of a fleet of multipurpose icebreakers to ensure polar research at a world-class scale. As for more "routine" facilities, according to the latest version of NSF's biennial Survey of Science and Engineering Research Facilities, America's academic institutions invested over $3.7 billion in fiscal year (FY) 2012–2013 to revitalize science and engineering research labs, but at least another $8.3 billion is still needed. Using different survey methods, a study released in October 2015 by the Association of Public and Land Grant Universities concluded that reversing deferred but critical maintenance of U.S. agricultural research laboratories and pilot facilities alone would cost $3.2 billion. Modernizing research farm facilities would add another $1.25 billion.

Updating current core research facilities is often seen as less glamorous than funding new major equipment and shareable facilities, but it is equally critical to any strategic plan for future science. This point was made well by the Department of Energy's FY 2016 Budget Request to Congress that asked for funds to upgrade facilities at the National Laboratories (as does the FY 2017 request, now wending its way through Congress).



Icebreaker in McMurdo Sound

"...allowing research facilities to crumble will inevitably stall ... scientific momentum..."

The magnitude of the overall costs to revitalize the country's research facilities means that no single stakeholder in the scientific enterprise can meet the needs alone. What is required is an organized partnership among research universities; local, state, and federal governments; private foundations; and private industry, all of which have a substantial stake in the future of science. A first step would be for leadership from either a governmental or nongovernmental organization to convene an influential group of partners and launch a comprehensive assessment of the nation's current research infrastructure. This should be followed by an action plan that lays out how the various partners will contribute to meet those needs. An inexact but relevant example may be the sequence of efforts set in motion by the U.S. National Academies' 2007 report *Rising Above the Gathering Storm*.

The magnitude of collaborative effort needed to sustain the infrastructure is indeed daunting, and asking for major investment from the public and private sectors in the current budget climate may seem unrealistic. But allowing research facilities to crumble will inevitably stall the great scientific momentum enjoyed over the past 150 years.

– Alan I. Leshner



Alan I. Leshner is Chief Executive Officer, Emeritus, of the American Association for the Advancement of Science, and former Executive Publisher of Science. *Email: alan.i.leshner@gmail.com*

Downloaded from http://science.sciencemag.org/ on May 5, 2016

10.1126/science.aaf9719

PHOTOS: (INSET) LIN PADGHAM/FLICKR; (TOP RIGHT) DAVID SHARPE

Published by AAAS

NEWS

> “Rescuing scholars is like adopting orphan minds.”
>
> **Neuroscientist Amal Alachkar**, at a 29 April symposium in New York City on the need for support for scholars fleeing the civil war in Syria. Alachkar escaped from the University of Aleppo in 2012 and is now at the University of California, Irvine.

IN BRIEF



From this platform, researchers drilled through the sea floor to the dinosaur-killing crater.

Pay dirt! Scientists find big impact

Some 66 million years ago, a large asteroid pounded into Earth off the coast of what is now Mexico’s Yucatán Peninsula, blasted open the 180-kilometer-wide Chicxulub crater, and led to the extinction of most life on the planet. In April, a team of researchers sponsored by the International Ocean Discovery Program began drilling into the sea floor, aiming for the heart of the crater to plumb its secrets. Those include clues to the formation of a “peak ring”—a feature of the largest impact craters, spotted on other solar system bodies but erased by erosion on Earth—to hints about how life rebounded following the cataclysm (*Science*, 4 March, p. 1015). Last week, the team retrieved a 3-meter-long core from a depth of 670 meters—and it contained signs that they had found the peak ring: bits of the original granite bedrock struck by the crater, along with minerals originally deposited in hot fluid–filled cracks. By studying these rocks, the team hopes to test models of crater formation and determine whether the crater itself was one of the first habitats for microbial life after the impact. The team is funded to drill through the first week of June, and hopes to go as deep as 1500 meters. http://scim.ag/dinodrilling

AROUND THE WORLD

Pedophile drug test funding short

STOCKHOLM | Swedish researchers have fallen short of their crowdfunding target for a clinical trial of a potential drug for pedophiles. The trial, expected to be completed in 2 to 3 years, aims to assess whether a prostate cancer drug that lowers testosterone levels in the body could help prevent pedophiles from acting on their impulses (*Science*, 15 April, p. 274). As *Science* went to press, the research team had collected just 5% of the £38,000 ($55,700) it hoped to collect before 7 May. It is hard to tell to what extent the sensitivity of the research topic contributed to the disappointing campaign result, says project leader Christoffer Rahm, a psychiatric researcher at the Karolinska Institute. In hindsight, such crowdfunding campaigns “should be planned with PR [public relations] specialists,” Rahm says. “You have to change your strategy from normal grant applications.” The team is now planning to extend the crowdfunding campaign. http://scim.ag/fundingshort

Mars exploration shuffle

PARIS AND MOSCOW | Europe and Russia have delayed the launch of a Mars rover—the second prong in the ExoMars program—from 2018 until July 2020. The first ExoMars mission, the Trace Gas Orbiter, launched in March; it aims to nail down the existence and source of martian methane (*Science*, 11 March, p. 1122). The ExoMars rover will be equipped with a drill to search for life in the subsurface and will target a region called Oxia Planum, which bears signs of ancient river channels and deltas. But scientists have faced problems marrying the European-led rover to its Russian landing system. The delay puts the ExoMars rover on a parallel track with NASA’s 2020 rover, which is expected to transport rocks from the surface back to Earth. Meanwhile, Hawthorne, California–based SpaceX followed up last month’s successful ocean landing of its Falcon 9 rocket with an announcement last week of an agreement with NASA to land a craft on Mars as early as 2018. The Red Dragon mission would use a larger version of the Falcon 9 and a landing craft that has

Downloaded from http://science.sciencemag.org/ on May 5, 2016

PHOTO: © ECORD/IODP

Published by AAAS



Sentinel's first shot: the Austfonna ice cap (lower left) in Norway's Svalbard archipelago.

New Sentinel satellite snaps first images

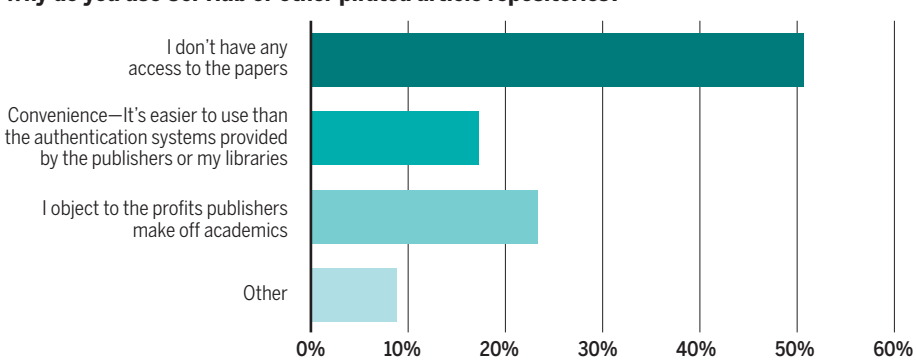
Just 2 hours after the European Space Agency (ESA) switched on its radar instrument on 28 April, the agency's newest observation satellite, Sentinel-1B, was already sending back images of an icy Norwegian archipelago. The satellite, launched on 25 April, will fly in coordination with its sister Sentinel-1A, launched in 2014: The two polar-orbiting satellites,separated by 180°, will map the planet's surface every 6 days using synthetic aperture radar imaging that can "see" through cloud cover to capture images. The Sentinel family of satellites—which so far includes two other missions launched in the last year, one to monitor vegetation, soil, water cover and coastal areas, and another to measure sea-surface topography and temperatures—form part of the European Commission-ESA's Copernicus Earth observing program.

been designed to one day carry humans. More details are expected at September's International Astronautical Congress.

Sci-Hub survey: Pirates, ahoy!

WASHINGTON, D.C. | Last week, a feature in *Science* analyzed 28 million download requests, made over 6 months, from Sci-Hub, a popular repository of pirated scientific literature. The data showed that Sci-Hub is widely used around the world. *Science*'s online survey on the topic generated more than 10,000 responses in the 4 days before this went to press. (You can take the survey here: http://bit.ly/Sci-Hub.) The sample is likely biased toward Sci-Hub fans—nearly 60% of respondents report having used it, and a quarter do so daily or weekly. Still, academic publishers may fear this dramatic result: Eighty-eight percent of respondents said it was not wrong to download pirated papers. About 50% of Sci-Hub users said their primary motive is a lack of access to the journal articles (see bar graph, below), whereas 23% said they objected to the profits publishers make, and 17% said they were motivated by simple convenience. Slightly more than 60% of survey-takers believe Sci-Hub will disrupt the traditional science publishing industry.

Why do you use Sci-Hub or other pirated article repositories?



Astro-H's death knell

TOKYO | Japan's stricken x-ray observatory ASTRO-H (renamed Hitomi after launch) cannot be recovered, the Japan Aerospace Exploration Agency (JAXA) announced on 28 April. The hopes of many astronomers were riding on the mission, which carried a soft x-ray spectrometer with 30 times the resolution of previous instruments, and was expected to revolutionize the field. Although the spacecraft's 17 February launch appeared to go flawlessly, JAXA lost contact with the craft on 26 March (*Science*, 8 April, p. 124). U.S.-based tracking radar appeared to see multiple objects at the observatory's orbital position, and ground-based satellite watchers reported seeing the craft in a slow spin. JAXA began a thorough technical investigation; they reported last week that it was likely that

IMAGES: (TOP TO BOTTOM) CONTAINS MODIFIED COPERNICUS SENTINEL DATA (2016)/PROCESSED BY ESA; C. SMITH/*SCIENCE*

Downloaded from http://science.sciencemag.org/ on May 5, 2016

Published by AAAS

both of the craft's solar arrays had broken off at their bases, where they are vulnerable to rotation.

NEWSMAKERS

Italian institute gets new boss

An outsider was named president of one of Italy's largest and most strategically important research organizations last week. Geologist **Carlo Doglioni** of the Sapienza University of Rome will take over the reins at the troubled National Institute of Geophysics and Volcanology (INGV). Outgoing President Stefano Gresta and other managers have been accused of nepotism, conflicts of interest, and misuse of funds, while two of the organization's scientists, including previous boss Enzo Boschi, were put on trial and convicted to 6 years in prison in 2012 for allegedly giving false reassurances ahead of the deadly earthquake that struck L'Aquila, Italy, in 2009. They were acquitted on appeal in 2014, a decision upheld by Italy's highest court last year. Doglioni, 59, was selected by research and education minister Stefania Giannini from a short list of five, mainly internal, candidates. He says he hopes to restore INGV's focus to its two main functions—basic research and monitoring of natural hazards.
http://scim.ag/DoglioniINGV

Primary loss is loss for science

The research community lost a key supporter last week with the defeat of Representative **Chaka Fattah** (D–PA) in a Democratic primary race in his Philadelphia, Pennsylvania–area district. Fattah, 59, had a keen interest in neuroscience, and as the top Democrat on a House of Representatives spending panel that oversees the National Science Foundation and several other science agencies, Fattah backed funding for basic research and science education. He also helped catalyze the $300 million Brain Research through Advancing Innovative Neurotechnologies project, a multiagency effort to study the brain. A representative of his west Philadelphia district for the past 22 years, Fattah will go on trial this month on bribery and fraud charges involving misuse of a $1 million campaign loan when he ran for mayor of Philadelphia in 2007. He has denied any wrongdoing, but stepped down as ranking member from the commerce, justice, science, and related agencies appropriations subcommittee when he was indicted last July, and his indictment contributed to his loss to state Representative Dwight Evans.
http://scim.ag/Fattahdefeat

'Ancient One' to get Native American burial

The 9000-year-old Kennewick Man has been the focus of 2 decades of legal battles between researchers studying early human migration and five Native American tribes. Now, he is set to receive a Native American burial. Scientists initially said that the skeleton, named for the town in Washington where he was unearthed, lacked Native American characteristics. However, a DNA study last year definitively linked the Kennewick Man to modern Native Americans (*Science*, 26 June 2015, p. 1404). After reviewing the genetic, skeletal, and statistical data, the U.S. Army Corps of Engineers last week concluded that the remains are Native American. Interested tribes may next submit a claim to acquire the skeleton for burial; until the bones are claimed, they'll remain at the Burke Museum in Seattle, Washington.



A clay facial reconstruction of Kennewick Man was sculpted around his skull.

PHOTO: BRITTNEY TATCHELL, SMITHSONIAN INSTITUTION

BY THE NUMBERS

30.7%

Fraction of overweight and obese boys in China's rural Shandong province in 2014, compared with 0.5% in 1985 (*European Journal of Preventive Cardiology*).
http://scim.ag/Chinaobesity

250 thousand

Number of deaths in the United States each year due to medical errors, making them the third leading cause of death after heart disease and cancer, and surpassing chronic respiratory disease (*The BMJ*).

41

Mean weight gain, in kilograms, of 14 people 6 years after competing on the television show *The Biggest Loser*. Mean weight loss during the show was 58 kilograms. Their metabolisms had slowed radically, researchers found (*Obesity*).

Downloaded from http://science.sciencemag.org/ on May 5, 2016

Published by AAAS



By pulling carbon dioxide out of Earth's atmosphere, the Amazon could give humanity the breathing room needed to mitigate climate change—if the numbers add up.

PHOTO: © FILIPE FRAZAO/ALAMY STOCK PHOTO

GLOBAL CHANGE

Amazon rainforest to get a growth check

Ambitious experiment will test whether rising CO_2 will boost the tropical carbon sink

By **Daniel Grossman**

David Lapola was lost. For half an hour on a steamy March day, he and his companions had tramped through virgin Amazon jungle kilometers from any paved road. They were looking for a particular site, one of eight that Lapola had marked with orange surveyor's tape about a year before. Lapola dodged a 2-meter-long tree snake. Plot 8 was nowhere in sight. Then one of the others pointed. "Just beyond the big tree," he said. "What big tree?" Lapola asked. Scores of trees loomed nearby, many with trunks that soared 30 meters into the humid air.

It was an apt reminder of the challenges facing what Richard Betts, the head of climate research at the United Kingdom's Met Office Hadley Center in Exeter, calls "one of the most exciting experiments on the planet." Lapola, a biology professor at São Paulo State University in Brazil, is a lead scientist in a project that could help answer whether the mighty photosynthetic engine of the Amazon rainforest will consume enough atmospheric carbon dioxide (CO_2) to slow global warming. The day after the forest trek, in an air-conditioned conference room 50 kilometers to the southeast in the Amazon Basin's largest city, Manaus, Brazil, Lapola and his colleagues from Brazil, the United States, and Europe discussed the daunting logistics of the experiment, known as AmazonFACE, which they hope to launch next year.

FACE (Free-Air Carbon dioxide Enrichment) experiments have been conducted at dozens of sites in more than a dozen countries. The idea is simple: Researchers spray pure CO_2 continuously into an instrumented plot, raising ambient concentrations to match levels expected as humans continue to spew the gas, and study what happens to the plants. That's a key question because through photosynthesis, land plants currently take up about a quarter of the CO_2 humans add to the atmosphere each year, sequestering it as wood and as soil carbon. This natural uptake slows the buildup of CO_2 in the air, moderating global warming. "*Nature* has done us a fantastic favor," says Scott Denning, an atmospheric scientist at Colorado State University, Fort Collins.

But many of the hypothesized carbon sinks could be winding down. Although abandoned pastures and fields in the Northern Hemisphere absorb carbon as they grow back into woodlands, for example, the uptake slows as they mature. But many scientists suspect that higher levels of CO_2 "fertilize" the rainforest, speeding its growth and creating a major carbon sink that could keep sopping up the greenhouse gas indefinitely, even as climate change makes forests such as the Amazon inhospitably warmer and drier. "It would be wonderful for humanity," Denning says.

That's the hope that AmazonFACE aims to test. For 12 years, Lapola and his collaborators plan to study 30-meter disks of forest, the elusive plot 8 among them, in the Cuieiras Biological Reserve near Manaus. Sixteen perforated tubes dangling from 35-meter towers will fumigate the plots with computer-controlled doses of CO_2, raising the concentration of the gas to 600 parts per million, or about twice the preindustrial level, which the world could reach by 2050. To conserve CO_2, the tubes will spray only in daylight, when photosynthesis takes place.

The experiment will start small, with a 2-year study of one treatment plot and one control, and then expand to four treatment plots and four controls, Lapola says. Researchers will meticulously measure the daily growth of tree trunks, the areas of leaves, and the buildup of debris on the forest floor. Instruments will collect meteorological data and monitor the composition of the air and respiration in the soil; special underground cameras will observe root growth.

Previous FACE studies have tested the responses of grasslands, deserts, temperate forests, and bogs. But nobody has undertaken one in a tropical forest, where the high canopies and remoteness pose daunting challenges. "Nothing's as hard as getting high CO_2 in a rainforest," says Patrick Meir of Australian National University in Canberra, one of Lapola's collaborators.

Downloaded from http://science.sciencemag.org/ on May 5, 2016

Published by AAAS

The discussions in Manaus underscored just how many nagging details remain to be worked out. Hardware for controlling and dispersing the CO_2 must be designed and manufactured. Researchers must decide the best way to ship CO_2 to the site. Should they buy it from Carboman, the Manaus supplier that puts the fizz in the hot city's Coca-Cola, or tap a cheaper source on the other side of the country and ship it up the Amazon River? Should they upgrade the treacherous 34-kilometer dirt road to the site, or find a special vehicle able to haul 15 tons of gas on the difficult last leg of the journey? Lapola had recently test-driven a truck that might work: a modified mobile missile launcher made in the Czech Republic.

Construction at the site should get underway by the middle of next year, Lapola says. So far, he has raised about $4 million in grants from the Inter-American Development Bank and two Brazilian agencies, nearly enough to run the two-plot startup phase of the experiment, but he will need tens of millions of dollars more to expand to eight plots for another decade, as planned. Much of the money will go to CO_2, Lapola says: With the gas constantly escaping into the sky and surrounding forest, each treatment plot will need about 3.7 metric tons of CO_2 per day, or about 1350 tons a year, at up to $1000 a ton. The 2-year startup phase of the experiment has budgeted $1.3 million for the gas alone.

Results should start coming in 6 months after AmazonFACE begins, Lapola says, but it will take years for some effects of higher CO_2 levels to become apparent. Richard Norby, a U.S. biologist from Oak Ridge National Laboratory in Tennessee and veteran FACE researcher who was at the Manaus meeting, says the results might dash hopes that the Amazon forest will provide the longed-for carbon sponge.

Norby's own experiment on a sweetgum plantation in Tennessee and studies in other forests have shown that trees exposed to elevated CO_2 initially grow faster and sequester more carbon. But sometimes the beneficial effect abates within a few years, for reasons not yet clear. Norby says he expects a similar result in the Amazon. Like many other researchers, he thinks that a lack of phosphorus—a critical plant nutrient—in most Amazon soils will limit tree growth there, no matter how much CO_2 is present in the air. In the long term, he told his colleagues on the drive from the research site to Manaus, "I don't expect the extra carbon will do didley in this system." ■

Daniel Grossman is a science journalist specializing in climate change, in collaboration with the Pulitzer Center on Crisis Reporting.



PHOTO: ITER COLLABORATIVE/EJF RICHE

FUSION ENERGY

More delays for ITER, as partners balk at costs

Review warns that new timeline could still be too optimistic

By **Daniel Clery** *and* **Adrian Cho**

It wasn't the pat on the back that ITER officials were looking for. Last week, an independent review committee delivered a report that was supposed to confirm that ITER, the troubled international fusion experiment under construction in Cadarache, France, finally has come up with a reliable construction schedule and cost estimate. But the report says only that the new date for first operations—2025, 5 years later than the previous official target—is the earliest possible date and could slip. And it underscores the challenge of ITER's ballooning budget. To start running by 2025, ITER managers have asked for an extra €4.6 billion, which they are unlikely to receive. As a result, the report says, ITER's ultimate goal—producing a "burning plasma" reaction of deuterium and tritium nuclei that sustains itself mostly with its own heat—will be delayed from 2032 until 2035 at the earliest.

ITER officials say the report confirms that the project is finally on the right track. "There is now a credible estimate of the schedule and cost envelope with respect to the financial capabilities of all the members," says ITER Director-General Bernard Bigot. "All the pieces are in place to make a decision" on enacting the plan. But others say that the new schedule is implausibly optimistic. "It's all fiction," says one expert who requested anonymity to protect his connections to the project. "As the report very carefully lays out, there are umpteen assumptions that aren't going to happen."

Dreamed up in the 1980s, ITER aims to show that deriving energy from nuclear fusion is feasible. Specifically, it aims to produce a burning plasma, trapped in an intense magnetic field, that will generate 10 times more energy than it consumes. In France, the project site is finally taking shape, as workers erect the massive facility's buildings and install the first components shipped from member states. About 40% of the work needed for first operations is done.

But delays and cost overruns have plagued ITER from the beginning. When the project partners—China, the European Union, India, Japan, Russia, South Korea, and the United States—signed the construction agreement in 2006, ITER was supposed to be finished this year for about $11 billion. The actual cost, impossible to calculate exactly because members contribute mostly parts rather than cash and use different accounting systems, could be three times as high.

ITER's woes stem from two sources, experts say. First, its design was far from complete when the agreement was signed. In fact, the report says, it's still not complete. Second, the ITER agreement established a weak central organization with little power to direct the project. Those management deficiencies were laid bare in a February 2014 review that called for 11 reforms, including the appointment of a new director-general and the completion of a realistic "baseline"

Downloaded from http://science.sciencemag.org/ on May 5, 2016

Published by AAAS

The foundations of ITER's reactor pit take shape in Cadarache, France.

construction schedule and cost estimate. Last November the ITER organization presented that new baseline—called the updated long-term schedule (ULTS)—to the ITER Council of representatives from the member states, and the council requested the independent review. The ULTS itself has never been made public, researchers say, but the panel report gives the bottom line.

The 14-member review panel, headed by Albrecht Wagner, former chief of the DESY particle physics lab in Hamburg, Germany, praised Bigot, a French nuclear physicist with extensive management experience in industry and government, for greatly improving ITER's management. The changes have "led to a substantial improvement in project performance, a high degree of motivation, and considerable progress during the past 12 months," the report says.

However, the report also suggests that the new schedule falls short of providing a true, reliable baseline. "[T]his is a success-oriented schedule with no contingency," the report says. "If any of the major risks that the [ITER organization] has identified materializes, then the [first plasma] date will almost certainly slip by some degree." The reviewers do not give a "probable" date for when ITER might actually start, notes the expert with connections to the project, who estimates it at 2028 or 2029. "The answer is so devastating that if they came out and said it in public, they might lose [the support of] the European Union," he says.

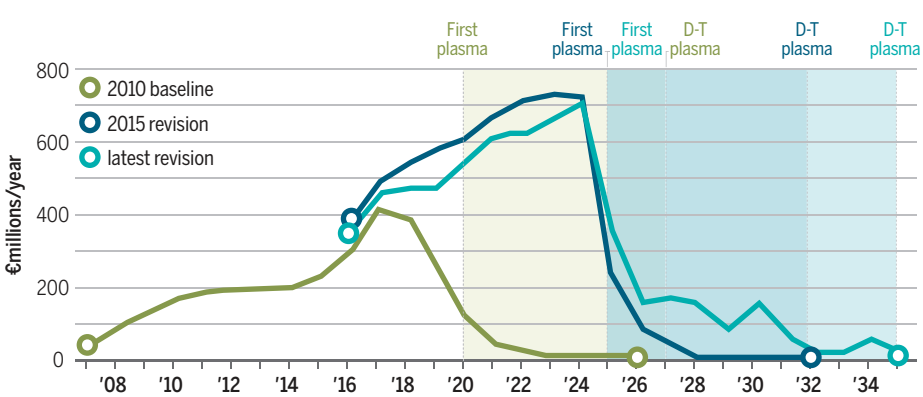
The biggest assumption behind the schedule is that members will provide an extra €4.6 billion ($5.2 billion) between now and 2025. That money would enable the ITER organization to hire many more engineers, technicians, and skilled workers to assemble the parts that the members provide. It would also enable the ITER organization to develop a reserve fund for contingencies. However, the ITER Council made it clear at its last meeting in November 2015 that the cash would not be forthcoming. In particular, representatives of the European Union—which, as host, bears 45% of the financial burden—noted that the European Parliament has fixed spending on ITER through 2020, and it cannot be increased.

Since then, the ITER organization has been trying to figure out how to keep to the schedule at a lower annual cost, adjusting it even as reviewers were analyzing it. One option would be to delay the construction of some components that won't be needed in the experiment's early years, when it will run on just hydrogen or deuterium. Neither substance can support a burning plasma, so the start of runs to achieve one would have to wait an extra 3.5 years, until 2035, the report estimates. That date "is so far off that it's more like an idea," says Stephen Dean, president of Fusion Power Associates, a nonprofit foundation in Gaithersburg, Maryland, that advocates for fusion development.

The review panel calls for the formulation of a real baseline by November. Reaching consensus on the schedule may be difficult, Dean warns, because ITER members have divergent priorities. Whereas the European Union frets over annual costs, Japan and South Korea worry about keeping the schedule for burning plasma, he says. That's because they're already planning ITER's successors, "demo" power plants that would generate electricity. To build one by 2050, they need the ITER data as soon as possible. "From the beginning of the process the Asian countries wanted to get to [deuterium-tritium] burning as fast as possible," Dean says. "They are not going to be happy to hear that the date for D-T burning is as far away as 2035." ■

ITER's evolving budget: More, later

Compared with ITER's 2010 "baseline," the schedule presented last November pushes first operations back 5 years. And to limit peak spending, ITER officials would now delay the key deuterium-tritium (D-T) runs to 2035.



DATA: ITER

RENEWABLE ENERGY

A reboot for wave energy

U.K. engineers and funders take stock of failures as they design new prototypes

By **Erik Stokstad**

In the remote Orkney archipelago off Scotland's northern coast, workers have hauled a 180-meter-long metallic sea monster onto a pier and are dismantling it. For several years, the snakelike machine floated 2 kilometers offshore, tethered to the seabed. As it undulated in the waves, fluid was forced through the sleek beast's hydraulic motors, generating up to 750 kilowatts of power, which was sent to shore via submarine cable. Now, its guts and joints are being dissected and examined for wear. "It's like an autopsy," says Tim Hurst, director of Wave Energy Scotland (WES) in Inverness, a funding program in the economic development agency that now owns the machine.

The wave energy prototype worked, but its test run ended ignominiously, amid investors' fears about its durability and slow pace of development. Fated for the scrap heap, it is a symbol of recent setbacks in the wave energy sector here. The machine's builder, Pelamis Wave Power, was the first company to feed electricity generated by a floating wave device into a national grid. But in late 2014, the Edinburgh-based company failed after investors pulled out. A year later, the other leading U.K. wave power company, Aquamarine Power in Edinburgh, went belly-up for the same reason.

Now, the Scottish government is going back to the drawing board. In December 2014, it created WES to fund cross-cutting research on wave energy and to improve technology transfer. And a new crop of companies is counting on novel, and often more-compact, designs to rescue the nascent industry. "There's quite a change going on," says Neil Kermode, managing director of the European Marine Energy Centre in Orkney, which tests wave and tidal devices. The renewed efforts, he adds, are crucial to ensuring that the United Kingdom becomes an exporter of wave energy technology.

Buffeted by strong waves and tides, the U.K. coastline is a rich resource and natural test bed for ocean energy. Efforts to harness

Downloaded from http://science.sciencemag.org/ on May 5, 2016

Published by AAAS



Workers dismantle Pelamis's prototype wave energy converter after its final test run off the Orkney archipelago.

the tides are well underway. This summer, MeyGen Limited in Edinburgh will install six underwater turbines in the Pentland Firth, near Orkney, to capture energy from tidal currents. With another 263 turbines to be installed over the next 5 years or so, the facility should generate up to 398 megawatts. Meanwhile, Tidal Lagoon Swansea Bay intends to build the world's first tidal energy lagoon. Sea walls will channel the rising tide such that water rushes into the lagoon through turbines built into the walls. When the tide subsides, the lagoon drains through the turbines. Pending a key review, the £1 billion project is slated for the Severn Estuary, where water rises up to 10.5 meters at high tide, the second-highest tidal range on the planet.

Capturing wave energy is trickier. A key challenge is that devices have to flex with everyday swells in order to generate power but be strong enough to withstand storms. Skepticism about survivability was a major factor that led investors to abandon Pelamis and Aquamarine, says Simon Cheeseman, a wave and tidal energy specialist with the Offshore Renewable Energy Catapult (OREC), a research center in Blyth, U.K. "The technology just wasn't robust enough," he says. Pelamis's prototype worked during its sheltered near-shore tests, but investors doubted that it would survive fiercer storms. It didn't help that "the sector was guilty of promising more than it could deliver," Hurst says.

WES is now trying to help the industry "climb out of the trough with a more scientific approach," Hurst says. The goal is to get companies cooperating; WES retains licensing rights to ensure broad commercialization of technologies it funds. With a £14.3 million budget over 2 years, its program mainly focuses on developing common materials and components for a range of designs. The first grants were for mechanisms that turn wave motion into electricity, called power-takeoff systems. Whereas most takeoff systems involve turbines and generators, one group is studying dielectric elastomers, which are polymers that generate electricity when flexed. In this concept, a sheet of elastomer film sandwiched between two sheetlike electrodes might capture energy in many types of wave converters. And this summer, WES will issue a call for control systems that could help devices survive rough seas. The systems might predict waves to harvest as much energy as possible or put the device into safe mode if a punishing wave looms ahead.

A separate funding round in November 2015 awarded £2.25 million for R&D on seven prototype converters (see table, below) and an enabling technology. "There are all kinds of weird, wonderful, and unfamiliar machines," says Richard Yemm, the inventor of the Pelamis converter and now with Quoceant in Edinburgh. For example, Quoceant has reworked the Pelamis blueprints to design a prototype technology with deflatable neoprene bladders that would allow wave energy devices to submerge and escape dangerous waves. Another project, the Anaconda built by Checkmate SeaEnergy in Sheerness, U.K., has an entirely new design employing a rubber tube. Waves create a bulge that ripples down the tube and spins a turbine at the far end. An approximately 9-meter-long prototype will be put through its paces in a wave tank; plans are to scale up to a 150-meter-long machine.

WES is keeping expectations in check by including technical milestones in its grants program and requiring test data before renewing funds. For its part, OREC has launched a technology assessment process to help benchmark progress. Several developers are focusing on wave energy for modest applications, such as providing power for aquaculture or desalinization for islands.

Creating a working wave energy machine is only half the battle. Converters must be economically viable to compete with wind and tidal—and that's "really ambitious," Cheeseman says. Proponents see a place for wave energy as a complement to other renewables, as the devices could generate electricity when solar panels or wind turbines are idle. "There's not one technology that can meet all the energy needs," says Henry Jeffrey, a marine energy expert at the University of Edinburgh. "We need them all." ■

The next wave

Wave Energy Scotland, a major funder of wave energy R&D, supported a variety of novel prototypes in its latest grant competition. The tank-tested models range in scale from 1:50 to 1:15.

DEVICE	COMPANY	TECHNOLOGY	KILOWATTS AT FULL SCALE
Anaconda	Checkmate SeaEnergy	Floating, water-filled rubber tube with turbine at end	1000
Waveswing	AWS Ocean Energy	Submerged, air-filled cylinder that responds to pressure fluctuations	25
WaveTrain	Joules Energy Efficiency Services	Linked floating modules with inclined pneumatic tubes and turbine	750
WaveNET Series 12	Albatern	Array of linked buoys with generators powered by hinged struts	>75
Mocean	Mocean Energy	Hinged raft with pontoon shaped to enhance flexing	500–1000
Ccell	Zyba	Oscillating wave surge converter with a curved, hinged paddle	<50
Sea Power Platform	4C Engineering	Hinged raft made of hollow concrete pontoons	1500

PHOTO: WAVE ENERGY SCOTLAND

Downloaded from http://science.sciencemag.org/ on May 5, 2016

Published by AAAS

HUMAN EVOLUTION

Why humans are the high-energy apes

Our metabolism runs faster than that of other apes, likely allowing us to evolve big brains

By **Ann Gibbons**

We may not be raring to go on a Monday morning, but humans are the Energizer Bunnies of the primate world. That's the conclusion of a new study that, for the first time, measures precisely how many calories humans and apes burn each day. Compared with chimpanzees and other apes, our revved-up internal engines burn calories 27% faster, according to a paper in *Nature* this week. This higher metabolic rate equips us to quickly fuel energy-hungry brain cells, sustaining our bigger brains. And lest we run out of gas when food is short, the study also found that humans are fatter than other primates, giving us energy stores to draw on in lean times.

"The brilliant thing here is showing for the first time that we do have a higher metabolic rate, and we do use more energy," says paleoanthropologist Leslie Aiello, president of the Wenner-Gren Foundation for Anthropological Research in New York City. "Humans during evolution have become more and more hypermetabolic," says biological anthropologist Carel van Schaik of the University of Zurich in Switzerland. "We turned up the thermostat."

For decades, researchers assumed that "there weren't any differences in the rate at which different species burned calories," says biological anthropologist Herman Pontzer of Hunter College in New York City, lead author of the new study. Comparing humans and other primates, they saw little difference in basal metabolic rate, which reflects the total calories used by our organs while we are at rest.

But in many ways, we're not like other apes: Our brains are at least three times larger, and we produce more babies in shorter intervals—both of which consume more energy. "It has been an open question—how do we do all these expensive things?" Pontzer says.

For the past 2 decades, researchers looked for an answer in tradeoffs between the energy demands of different parts of the human body. For example, Aiello and her colleagues proposed that when our brains began to expand dramatically about 1.6 million years ago, our direct ancestor *Homo erectus* evolved a smaller gut that sucked up less energy (*Science*, 15 June 2007, p. 1560). Other teams suggested that humans reduced muscle mass to save energy; walked and ran more efficiently; or got extra calories faster by eating a higher quality diet, cooking food to cut down on the energy spent in digestion, and sharing food. Indeed, there seemed to be no shortage of human adaptations that conserve energy.



Although chimps' bodies are lean compared with those of humans, new measurements show that these apes burn calories more slowly than we do.

PHOTO: STEPHEN ROBINSON/NHPA/PHOTOSHOT/NEWSCOM

Then, in 2010, researchers began to measure apes' total energy expenditures (TEEs) accurately for the first time, rather than just their resting rate. Orangutans delivered the first surprise: They have an unexpectedly low metabolic rate, Pontzer says.

So he and primatologist Stephen Ross of the Lincoln Park Zoo in Chicago, Illinois, set about measuring TEE directly in as many apes as possible at 14 zoos and two ape sanctuaries in the United States and Africa. They fed 27 chimps, eight bonobos, 10 gorillas, and 11 orangutans water labeled with certain isotopes of hydrogen and oxygen. Then they measured those two isotopes in the apes' urine to see how the ratio changed over time. The ratio reveals how much carbon dioxide the animal had generated, which reflects how many calories it had burned. The technique is the "gold standard" for metabolic studies, and the researchers did a "terrific job" using it to compare the total calories burned daily by apes and humans, says biological anthropologist William Leonard of Northwestern University in Evanston, Illinois.

The team used the same method on 141 adults from five populations around the world. After taking body size into account, they found that humans averaged about 400 more calories per day than chimps and bonobos—635 calories more than gorillas and 820 calories more than orangutans. This meant that humans burned over 27% more energy per day on average than chimps.

Although ideally all data would come from animals in the wild, other studies have shown that TEE rates in captive and wild apes are about the same, regardless of activity levels, Van Schaik notes. To be safe, the study matched relatively sedentary humans with captive apes.

The team also measured body fat in people and other primates by analyzing isotopes in the urine, finding that humans had significantly more fat than even these zoo animals. "If you're going to burn fuel faster, you better have a backup tank," Pontzer says. Once early hominins had boosted their metabolism and grown bigger brains, he says, natural selection would have favored not only fatter individuals, but also smaller guts and other energy-saving adaptations, such as cooking and efficient walking.

"What is fantastic about this paper is that Herman and his colleagues have effectively integrated all of the earlier ideas into a unified theory for energy and the evolution of human characteristics," Aiello says. Van Schaik agrees. "There has to be more energy going into our systems," he says. "Now, [Pontzer] has measured it, and it all fits together."

Next on Pontzer's agenda is to try to figure out how and when human ancestors boosted their metabolisms above the levels of our ape ancestors, for example by analyzing rates of bone growth in fossils. That's particularly intriguing to Aiello. "I'd really like to know," she says, "when did fossil hominids get fat?" ■

Downloaded from http://science.sciencemag.org/ on May 5, 2016

Published by AAAS

DEVELOPMENTAL BIOLOGY

Human embryo research confronts ethical 'rule'

Time to revise 14-day limit for growing IVF embryos?

By **Patrick Monahan**

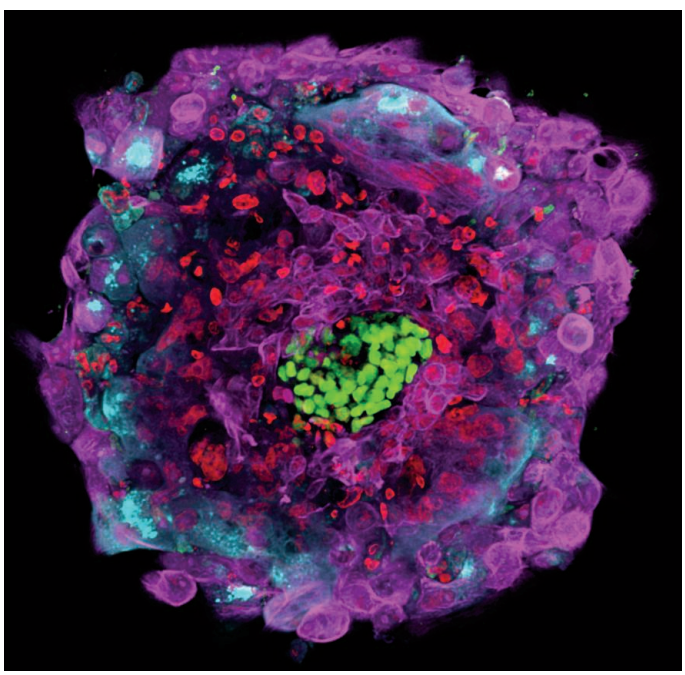
It's easy to obey a rule when you don't have the means to break it. For decades, many countries have permitted human embryos to be studied in the laboratory only up to 14 days after their creation by in vitro fertilization. But—as far as anyone knows—no researcher has ever come close to the limit. The point of implantation, when the embryo attaches to the uterus about 7 days after fertilization, has been an almost insurmountable barrier for researchers culturing human embryos.

Now, two teams report growing human embryos about a week past that point. Beyond opening a new window on human biology, such work could help explain early miscarriages caused by implantation gone awry. As a result, some scientists and bioethicists contend that it's time to revisit the so-called 14-day rule. But that won't be welcomed by those who consider the rule to have a firm moral grounding—or by those who oppose any research on human embryos.

"We're here sooner than we thought," says Insoo Hyun, a bioethicist at the School of Medicine at Case Western Reserve University in Cleveland, Ohio, and co-author of a commentary in *Nature* this week calling for a reassessment of the 14-day rule. About 4 years ago, a group led by Magdalena Zernicka-Goetz, a developmental biologist at the University of Cambridge in the United Kingdom, first reported culturing mouse embryos past the implantation stage, and it has been improving its methods ever since.

The latest tricks also work with human embryos, Zernicka-Goetz's team and a collaborating group led by Ali Brivanlou, a stem cell biologist at The Rockefeller University in New York City, report this week in *Nature* and in *Nature Cell Biology*. Both groups initially removed each embryo's outer membrane and grew the embryos in two different types of culture media, the first containing fetal bovine serum. Together, that allowed embryos to "implant" onto a plastic substrate, which was transparent, enabling the researchers to take images of what followed.

After normal implantation, part of a mammalian embryo reorganizes itself into what will become the placenta and the yolk sac. This is also the stage at which many developmental defects originate. The lab-grown human embryos hit all of the bases expected of one implanted on a uterus. They developed the right shape and generated various cell types, even though they lacked the structure and nutrition that maternal tissues would normally supply. As Harvard University stem cell researcher George Daley puts it, "The embryo is somewhat on autopilot."



A human embryo, 12 days after fertilization, has clearly begun to differentiate into multiple cell types, including those that will develop into the fetus (green).

IMAGE: GIST CROFT/ALESSIA DEGLINCERTI/ALI H. BRIVANLOU; THE ROCKEFELLER UNIVERSITY

The teams halted their studies when the embryos were 14 or 13 days past fertilization, as U.K. laws require and several U.S. guidelines recommend. But that was enough time for them to see that mouse embryos are imperfect models for human ones. For example, the cells that develop into the fetus and the yolk sac diverge later in human embryos. "You have to study the human embryo to understand the human embryo," Zernicka-Goetz says.

The 14-day rule prevents researchers from exploring the unique features of human embryos any later in development. But the rule also played a crucial part in making lab studies of embryos acceptable in the first place. Proposed in 1979 by what would later become the U.S. Department of Health and Human Services, it is now enshrined in law in 12 countries and in various guidelines in another five. The rule is pegged to the time at which human embryos develop the "primitive streak"—an easily identifiable group of cells that appears when embryos can no longer fuse or split. That, in the eyes of some religious bioethicists, marks the threshold at which an embryo is a distinct human.

Now that culture methods have finally caught up to the ethics of the 14-day rule, Hyun and his commentary co-authors say it's time to start a new conversation about whether there is scientific need, as well as a broader consensus, for lengthening the time human embryos can be grown in the lab. The 14-day rule was conceived as a policy tool to enable research, he says. "It shouldn't be thought of as a hard and fast moral pronouncement."

Others disagree. "Of course rules can always be reconsidered," says Marcy Darnovsky, executive director of the Center for Genetics and Society, an advocacy organization in Berkeley, California, that has been critical of human embryo research and modification. "But it was very much intended to be a bright line." Still others think the 14-day rule should never have been enacted at all—like Reverend Tadeusz Pacholczyk, director of education for The National Catholic Bioethics Center in Philadelphia, Pennsylvania, who calls the rule a form of "lip service to the moral status of the human embryo."

By culturing human embryos beyond 14 days, Daley says, researchers could address "deeply compelling questions," such as how the nervous system arises. But he and others who believe there may be value in revisiting the 14-day threshold stress that any alteration to it will require extensive discussion with policymakers and the public. "It was first derived and built upon trust and public dialogue," Hyun says. "If you even entertain changing it, it needs to involve a wide group of stakeholders." ■

Downloaded from http://science.sciencemag.org/ on May 5, 2016

Published by AAAS



An orca encounter at SeaWorld in San Diego, California.

PHOTO: WOLFGANG KAEHLER

AN OASIS FOR ORCAS

Advocates dream of flying killer whales to an ocean sanctuary, but experts clash over whether science supports the move

By **David Grimm**

How do you retire a 5-ton whale? That's a question some advocates and scientists have been asking themselves in the wake of SeaWorld's historic decision in March to stop breeding the 29 orcas in its care. Although the chain of theme parks says it will hold onto the animals until they die—which for many could be decades from now—a few groups want to fly them to a sanctuary in the sea, a kind of wildlife refuge for these intelligent and far-ranging creatures. The problem? No such sanctuary exists.

But the groups are laying plans. Last week, about three dozen scientists, veterinarians, and engineers announced the formation of the Whale Sanctuary Project (WSP), a Washington, D.C.–based nonprofit that has begun pressuring SeaWorld to release its orcas. The group is scouting sanctuary locations along North America's coasts—including coves and small groups of islands that could be cordoned off—with fundraising to follow. Other organizations have proposed similar ideas.

"There's enough known about how to do this that we could put up a facility in the next 3 to 5 years if we had the resources," says WSP President Lori Marino, a biopsychologist based in Kanab, Utah. "We're moving pretty quickly."

But critics say such plans are premature—and that they might not actually help the whales. Placing an orca that has spent its entire life in a sterile, concrete tank into an ocean filled with creatures and conditions it has never encountered before could be dangerous not just for the whale, but for the previously whale-free ecosystem, says Shawn Noren, a physiologist at the University of California (UC), Santa Cruz, who has studied orca biology at marine parks for nearly 20 years. And the costs are mammoth—perhaps tens or hundreds of millions of dollars. The challenges, she says, "are mind-boggling."

BOTH SIDES OF THE ORCA captivity debate agree that killer whales are remarkable animals. They can travel thousands of kilometers and dive more than 600 meters. Their large, complex brains, like those of chimps, are twice as big as would be expected for their body size. And the orca neocortex, a brain region linked to self-awareness, communication, and problem-

Downloaded from http://science.sciencemag.org/ on May 5, 2016

Published by AAAS

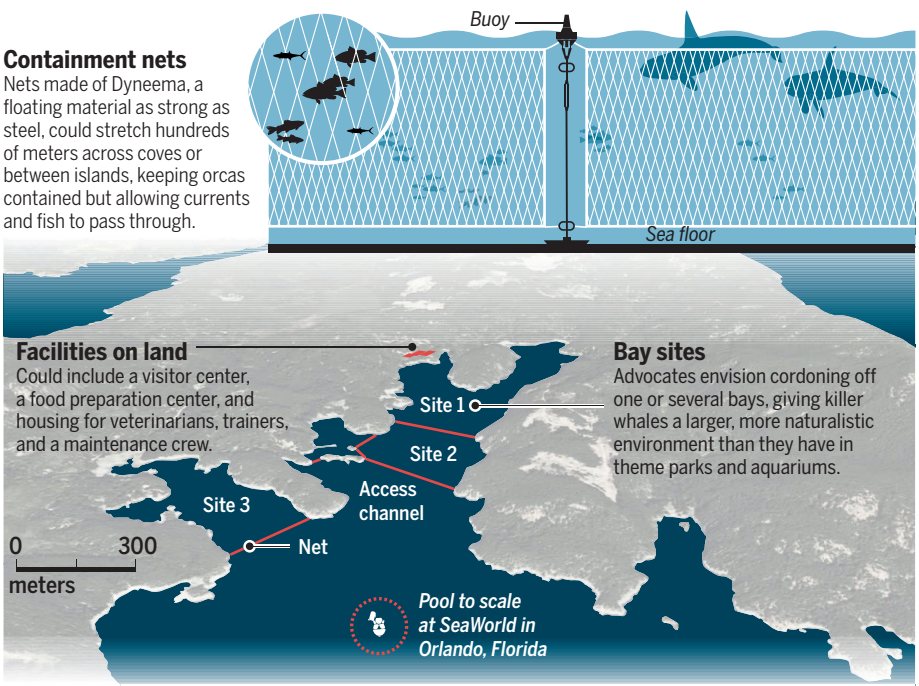
solving, is among the most highly developed in the animal kingdom. Orcas are also social creatures that live in tight-knit family units led by their mothers. They communicate in dialects of clicks and whistles that can vary by region. What's more, according to a study published last year, they're one of only three animals—besides humans and pilot whales—known to go through menopause, an adaptation that may free older females to care for their extended families.

All of this, advocates say, makes killer whales spectacularly unsuited for the relatively small, isolated tanks found in theme parks and aquariums. Marino and others have argued that such enclosures stunt the animals' physical and psychological growth, leading to stress, disease, and aggression toward other whales and even humans. Tilikum, a SeaWorld orca now in poor health, has been implicated in the deaths of three people, inspiring the 2013 documentary *Blackfish*, which played a major role in the company's decision to stop breeding its killer whales and displaying them in shows.

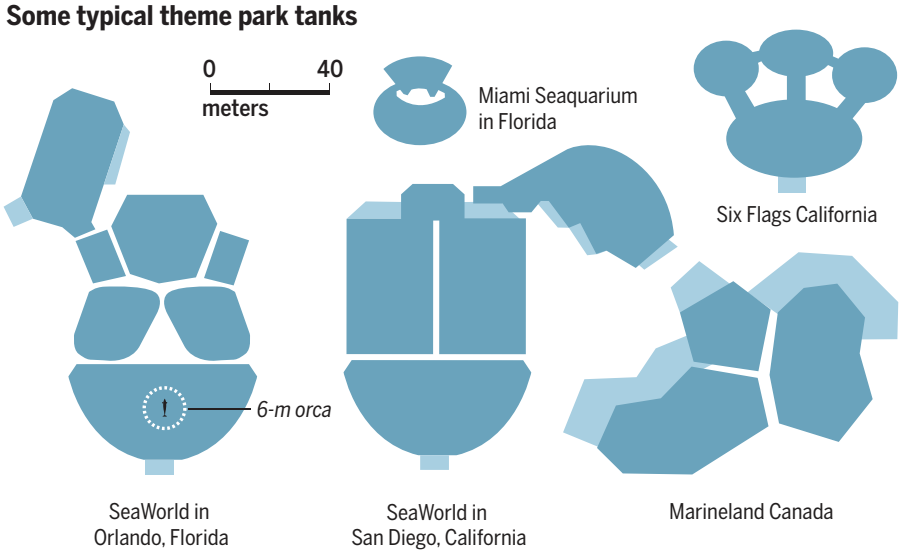
SeaWorld has countered that its orcas are healthy and well cared for, and that much of what we know about the species wouldn't have been possible without captive research. It has strongly resisted calls to release its whales to the wild, noting that they have spent most of their lives in pools, and would likely die in the open ocean. Many anticaptivity advocates actually agree. So, instead, they're pushing for a middle ground—something between a tank and the deep blue sea.

Sanctuary in the sea

Advocates hope to create an ocean refuge for captive orcas, to offer them a more natural life while protecting them from the open sea. Here's what it might look like compared with their current digs.



Some typical theme park tanks



AN ORCA SANCTUARY has been attempted once before. In 1998, advocates loaded a killer whale named Keiko (star of the 1993 film *Free Willy*) onto a giant military cargo aircraft and flew him to a remote island cove off the southwest coast of Iceland. Individuals working with the Free Willy-Keiko Foundation hoped to eventually return the 20-year-old whale to the open ocean. But first they had to build him a sea home.

It did not go smoothly. Workers fashioned a sea pen out of foam-filled plastic pipe. Encircled by a deep net, it was about two-thirds the size of a football field, anchored to the ocean bottom with more than 100 tons of chain. About a year and a half later, the foundation opened up Keiko's sea cage and gave him access to the entire cove, which had been cordoned off with a 300-meter-long net. But fierce weather and heavy currents regularly struck the cove, fraying the net and ripping bolts from the sea floor.

Then there was the herculean task of caring for the whale. At its peak, the facility employed more than 20 people, including veterinarians, security officers, and trainers who taught Keiko to hunt for himself and took him on "walks" in which he accompanied a boat in the open ocean, says Michael Parks, who was chief of marine operations for the project and is now with WSP. The cove was inaccessible by road, so everything had to be done by boat, including shipping in frozen herring by the ton to satisfy the orca's 300-fish-per-day appetite. Yearly costs were estimated at $3 million, and Keiko was there for nearly 4 years. But Parks says that while in the cove, Keiko got off the medications he had been on and grew more muscle.

In 2002, Keiko was given more access to the open ocean, and he soon joined up with a wild pod of orcas and left the cove for good. Sightings showed that he made his way to Norway, but continued to seek human contact, and never fully integrated with his wild kin. He died of pneumonia in late 2003. No orca sanctuary has been attempted since.

MARINO'S GROUP HOPES to change that. And it's not being modest with its plans. Marino, whose academic research helped show that dolphins are capable of self-awareness, became an anticaptivity advocate about 10 years ago (*Science*, 29 April 2011, p. 526). She envisions multiple sanc-

Downloaded from http://science.sciencemag.org/ on May 5, 2016

CREDITS: (DATA) GOOGLE EARTH; (ILLUSTRATION) ADAPTED BY A. CUADRA/*SCIENCE*

Published by AAAS



Keiko's temporary sea home, Klettsvik Bay off Iceland's Heimaey island, with his sea pen in the distance.

PHOTO: AP PHOTO/DON RYAN

tuaries that could hold up to several orcas, created by drawing a net between islands or cordoning off a cove like Keiko's, but in a calmer location. The enclosure would be "as open and naturalistic as possible," she says. "It will never be ideal, but it will be enormously different than a theme park." A sanctuary won't be able to replicate orca social life, Marino admits, but at least the whales could communicate acoustically with wild orcas, as Keiko did.

Roping off a stretch of water is just the beginning, however. Marino envisions a sea cage for care and feeding, a visitor education building (which could feature viewing platforms and underwater critter cams), a food preparation center, and housing for staff. "In some ways, we have to replicate what SeaWorld already has," she says. "We have to be prepared to take care of them for the rest of their lives." She estimates costs of up to $200 million per sanctuary and is counting on rich donors—and perhaps even SeaWorld itself—for help.

Howard Garrett thinks he can do it cheaper, at least for one whale. He's the cofounder and director of the Orca Network, a small nonprofit based in Freeland, Washington, that has been trying to remove an orca named Lolita from the Miami Seaquarium in Florida, where she has lived since 1970. The group has already selected a site—a calm bay in the San Juan Islands off Washington state.

Garrett envisions a simpler undertaking with no facilities for visitors. A local salmon hatchery would provide most of Lolita's food, and staff would be limited to feeders and the occasional veterinarian. He estimates about $1 million to create the enclosure and set the whale up there, and about $250,000 a year to care for her. "It's not a high-tech operation," he says. "It's a common sense operation."

For her part, Marino says Garrett's group hasn't conducted proper environmental assessments and has vastly underestimated costs. But critics say both groups have oversimplified things.

"WE ALL LIKE THE IDEA of retirement," says SeaWorld's chief zoological officer, Christopher Dold, a marine veterinarian in Orlando, Florida, who has worked with orcas for more than 20 years. But he says the park's whales already live comfortable, stimulating lives, and moving them to an ocean enclosure would be dangerous, for both them and the environment. "We're not willing to conduct that kind of experiment with the health and well-being of our killer whales."

Dold notes that the ocean can be unpredictable, citing the storm damage to Keiko's enclosure as well as pollution, ship noise, and disease—all new for captive whales. And it's not just the impact of the environment on the orca; it's the impact of the orca on the environment. "You're talking about putting killer whales in places they don't usually live," UC Santa Cruz's Noren says. What if they eat the local wildlife? "And what's the impact of all that whale poop?"

Plus, Noren says, we don't really know what these animals want. She worked with Keiko at an Oregon aquarium before he moved to Iceland, studying his diving behavior and metabolism. "He would stare at us through the window, even after our experiments were done. We were his social crew," she says. "Who knows if he really wanted to go to Iceland? You can't get inside the brain of a killer whale."

Then there's the cost. "It kind of makes me angry," says Richard Connor, an animal behaviorist at the University of Massachusetts, Dartmouth, who studies wild dolphins. He notes that threatened whales and dolphins worldwide need more resources to help save them. "I'd rather see that money spent protecting marine areas and conducting basic science." Still, Connor says that such sanctuaries might open up new research opportunities. "We've just scratched the surface of what we know about these animals."

John Ford, a marine mammal scientist at Fisheries and Oceans Canada in Vancouver, agrees. Studying orca vocalizations and feeding patterns is more accurate in an ocean setting, says Ford, who has researched killer whales in their natural environment for more than 40 years. Scientists would also have better access to the orcas in ocean sanctuaries than in the open sea. They could strap recorders to the whales and even take breath samples—things that are much easier to do with trained animals in a confined space, he says. "You could do research you can't do in captivity or the wild."

For now, however, efforts to retire the 29 orcas at SeaWorld and another 27 at aquariums and theme parks around the world remain a pipe dream. SeaWorld says it is focused on improving its captive habitats—making tanks more stimulating and naturalistic, for example with currents the orcas could turn on themselves, and perhaps even live fish.

In the meantime, anticaptivity advocates will continue to lobby SeaWorld and other facilities to retire more marine mammals, like seals and dolphins. "What we learn about retiring orcas will be used as a blueprint for others," Marino says.

Nor will the conversation stop with marine animals. Whether it's orcas, chimpanzees, or elephants, "the more cognitively advanced the creature, the more we have to think about the environment we place them in," says Stephen Ross, who oversees great ape research at the Lincoln Park Zoo in Chicago, Illinois, and also serves on the board of a chimp sanctuary. "These types of questions have always been there," he says. "They're just rising closer to the surface." ■

Downloaded from http://science.sciencemag.org/ on May 5, 2016

Published by AAAS



Downloaded from http://science.sciencemag.org/ on May 5, 2016

THE POWER OF PERSONALITY

From birds to lizards to spiders, individuals exhibit consistent differences in behavior that shape the fate of their species

By **Elizabeth Pennisi**

Type A isn't a label just for restless, aggressive people. Take the great tit, a common songbird of Europe and Asia. In a single woodlot, one tit may flit back and forth, seemingly fearless, exploring every nook and cranny of the forest floor for caterpillars and other insects. Another is an avian type B: It appears shy and skittish, rarely straying far from its nest.

To a birdwatcher or pet owner, it may be obvious that individual animals have distinct personalities. But the idea has been slow to penetrate biology. Researchers used to consider variation in individual behavior within a species as "noise" in their data and for the most part ignored it. While a Ph.D. student in human psychology at the University of California (UC), Berkeley, in the 1990s, Samuel Gosling, now a professor at the University of Texas, Austin, recalls being told that studies of animal personalities were "goofy, frivolous, and the purview of overly sentimental dog owners."

Even when researchers began taking behavior differences seriously a decade ago,

PHOTO: TIM GAINEY/ALAMY STOCK PHOTO

Published by AAAS



Field and lab studies of Europe's great tits have revealed sharp personality differences—and shown that scarce resources can favor meeker birds.

they at first had trouble with the term "personality." "When you say 'personality' to a lay person, they think of something very subjective and idiosyncratic, which is something only humans have," says Gil Rosenthal, a behavioral ecologist at Texas A&M University, College Station. But years of research have made it clear, says Renee Duckworth, an evolutionary ecologist at the University of Arizona, Tucson, that animal "personalities" are stable and quantifiable: "There are consistent differences between individuals that are not going to change no matter what the circumstances are."

Now, researchers are learning that just as human quirks and temperaments shape our lives and the world around us, the behavior patterns of individual animals affect their role in their ecosystem, their prospects for survival, and probably their evolution. "We are learning that individuals really matter," says Spencer Ingley, an evolutionary biologist at the University of North Carolina, Chapel Hill.

More than 2 decades ago, a seemingly unlikely animal, the streamside salamander (*Ambystoma barbouri*), a nondescript inhabitant of the U.S. Midwest, persuaded Andrew Sih that animal personalities are real and important. Sih, a behavioral and community ecologist from UC Davis, and one of the field's pioneers, noticed that some of the salamanders hide when fish that prey on them are around, whereas others appear unfazed. At first that seemed to make no sense—natural selection should quickly eliminate the risk-takers. But eventually Sih figured out that the bold individuals were more effective hunters, which gave them an advantage in small, fishless stream pools that were likely to dry up quickly. They could catch enough invertebrate prey to grow fast, completing their life cycle before their pools vanished, whereas the cautious individuals—better equipped for life in larger pools with predatory fish—grew too slowly to survive.

At meetings a decade ago, Sih's discussion of salamander boldness might have been a lone paper stuck in the "miscellaneous" session; now, whole symposia are devoted to animal personalities, and hundreds of papers are published each year. But some researchers aren't persuaded that animal personalities play a major role in ecology and evolution—the empirical evidence is still lacking, they argue. As Franz Weissing, a theoretical biologist at the University of Groningen in the Netherlands, puts it: "Much more is needed in order to convince the skeptics."

More is coming. Sih and others have figured out how to quantify personality along axes such as shy-bold and aggressive-nonaggressive and are applying rigorous statistics to the results. Researchers are probing the genetics that define personality and doing experiments that reveal the interplay between personality and environment. "We're right on the cusp of studies showing the ecological consequences and the evolutionary consequences," Duckworth says. "We're kind of getting into the most exciting part right now."

Why one species's personality can vary

As the existence of animal personalities becomes undeniable, researchers face a puzzle: how disparate personalities can coexist in a single species. Europe's great tits are helping explain how. At long-term field sites in Germany, the United Kingdom, and the Netherlands, Niels Dingemanse, a behavioral ecologist at the Ludwig Maximilian University of Munich in Germany, and others have manipulated the number of offspring in nests and the density of nest sites. They've found that different conditions favor opposite personalities, thereby enabling behavioral variation to persist.

When bird populations are dense, competition for territories, mates, and food sharpens, and one might expect aggressive individuals to win out. But when Dingemanse's postdoc, Marion Nicolaus, tracked 541 adults for 4 years, recording which survived and how many young they produced, she found the opposite was true. It seems that when birds have to compete for scarce resources, the aggressive ones often get into fights, which take a physical toll. Aggressive birds also strain to keep all their young fed, further taxing their health. Thus, compared with more docile individuals, these birds are more likely to wear themselves out and fail to survive to the next breeding year. Only when densities are low do type A birds outcompete gentler ones and thrive, Dingemanse says.

The findings parallel predictions made a decade ago about humans: that "in growing populations, competitive environments should favor shy, non-explorative, non-aggressive individuals," Nicolaus, Dingemanse, and colleagues write in an upcoming paper in *Ecology Letters*.

> ***"If it moves, chances are that personalities are present."***
>
> **Spencer Ingley**, University of North Carolina, Chapel Hill

The great tit studies "are at the forefront of developing new methods," the University of Arizona's Duckworth says. For example, researchers from the University of Oxford in the United Kingdom have equipped the birds at a nearby site with microchips, enabling the team to follow where the birds spend their time and with whom. That work is now dovetailing with research by Oxford's Lucy Aplin and colleagues, who have set up "puzzle box" feeding stations that allow access to food only if the bird slides a door in the correct direction. Aplin trains one bird to slide the door, then studies how this skill spreads through the population.

The result is a portrait of how personality affects learning in the great tit. The more reticent and sedentary birds tend to have just a few close associates, the micro-

Downloaded from http://science.sciencemag.org/ on May 5, 2016

Published by AAAS

chip tracking showed. New skills spread slowly through these tight-knit networks, Aplin found. Their less timid peers fly all over the place; they associate with more individuals albeit less frequently with each. And they disseminate information rapidly (see graphic, right).

The tit research impresses those trying to understand human personalities. "It epitomizes the fantasy study that we psychologists have," but could never do, Gosling says.

How personality could split species

Alison Bell has spent a decade studying personality in a small, common fish, the three-spined stickleback. At the University of Illinois, Urbana-Champaign (UIUC), her team assesses individuals' boldness by moving an artificial predator through their tank and gauging their reaction, and by measuring how quickly and thoroughly they explore a plastic kiddie pool. Some prove to be risk-takers, aggressive and extroverted—meaning that they readily intermingle with other fish. Others are the wallflowers of the aquatic world. Now, Bell and Simon Pearish of Norwich University in Northfield, Vermont, have found that those personality types drive the fish to segregate.

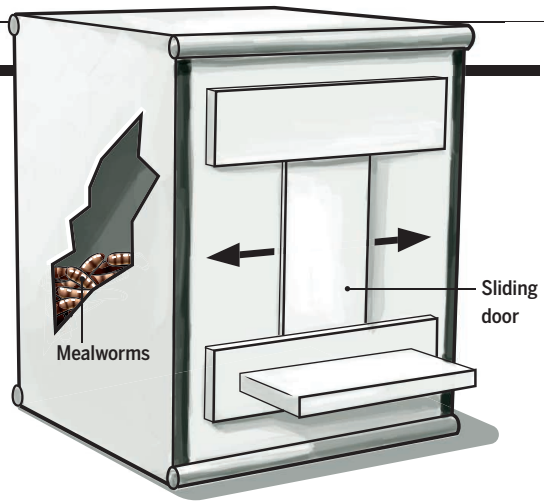
Wearing snorkels, Pearish and Bell's graduate student Miles Bensky, also at UIUC, collected more than 400 newly hatched sticklebacks from the Navarro River in northern California, noting whether each fish was found on its own or in a group. In Bell's lab, they assessed each fish's boldness and activity level, painted each one with a unique pattern, and then released them all back into the river. At first, the bold and shy fish were randomly distributed, but within 2 weeks, bold ones were in groups and shy ones were alone, Bell reported in January at the American Society of Naturalists meeting in Pacific Grove, California.

By looking for marked fish, they found that shy individuals hadn't simply moved out of the groups; they had vanished, most likely because they were not aggressive enough to compete for food in the group and had starved, or were too slow in reacting to predators that homed in on the school. On their own, however, the shy fish thrived, because remaining still is an effective antipredator defense. Bold fish, in contrast, became targets when isolated.

The finding suggests that personality types could play a role in evolution by helping divide a species into separate populations. Such segregation can lead to further differentiation and, eventually, to reproductive isolation. "That is often the first step in models of speciation," Duckworth says.

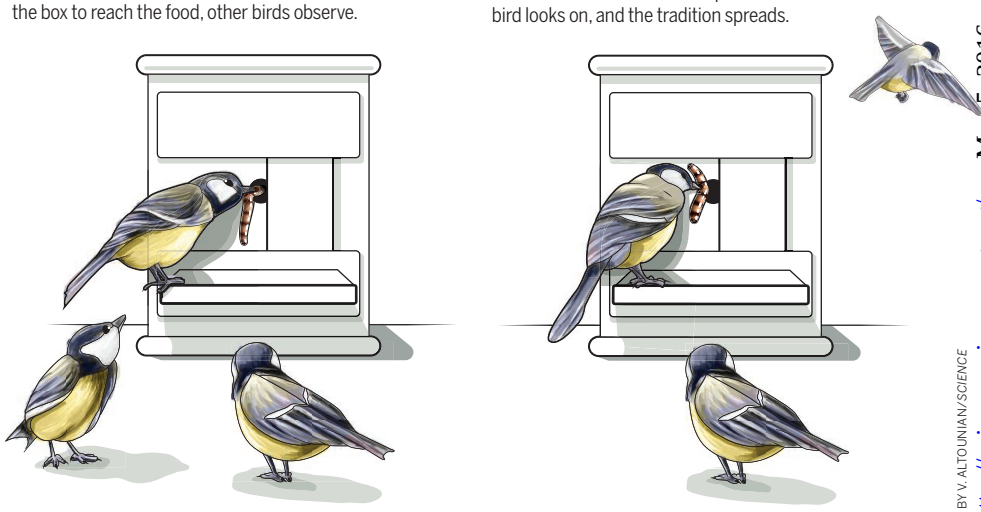
Birds solve a puzzle

Using "puzzle boxes"—feeding stations that require a bird to slide a door in a certain direction to open the box and get the food—researchers at a University of Oxford field site in the United Kingdom are exploring how traditions spread among great tits. The work is part of a larger effort to understand the birds' social networks and how they are shaped by personalities.



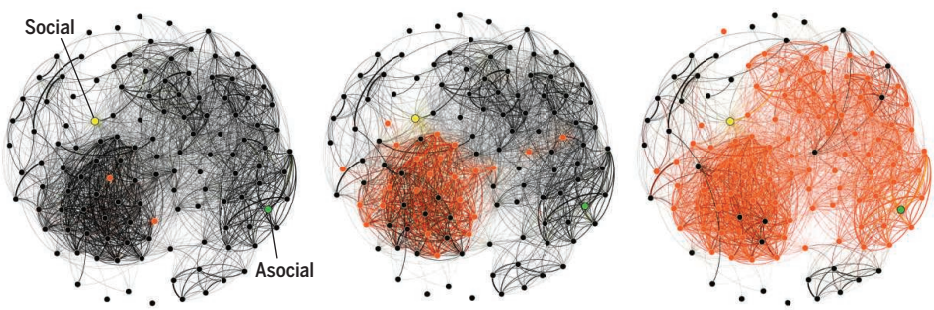
1 As a great tit trained to solve the "puzzle" opens the box to reach the food, other birds observe.

2 An observer then tries to open the box while another bird looks on, and the tradition spreads.



Social networks speed learning

Birds at the field site wear microchips that make it possible to map their social connections, which are more extensive for birds with bold personalities. The networks affect how knowledge spreads through the flock.



A social (**yellow**) and an asocial bird (**green**) are trained on the puzzle box.

The skill (**red**) spreads faster from the social than from the asocial bird.

Within 20 days, 72% of the great tits know how to work the puzzle box.

GRAPHICS: (TOP TO BOTTOM) V. ALTOUNIAN/*SCIENCE*; APLIN *ET AL*., *NATURE* (2015)

Some lizards are born to roam

At the University of Toulouse in France, a population of lizards inhabits an artificial world: 48 interconnected, 10-meter-by-10-meter enclosures containing natural habitat, covered by a net to keep birds out. Nine years ago, evolutionary ecologist Julien Cote discovered that some of the lizards there have "social" personalities, whereas others tend to avoid dense gatherings. Those loners, the team has found, sometimes stray so far that they wind up in an entirely different habitat.

In the wild, such dispersal could spur the evolution of behavioral, physiological, or even morphological changes that differentiate the wide-ranging lizards from their stay-at-home peers. It could also affect the spread

© 2016 NATURE PUBLISHING GROUP. ADAPTED BY V. ALTOUNIAN/*SCIENCE*

Downloaded from http://science.sciencemag.org/ on May 5, 2016

Published by AAAS

of disease, as work with a different lizard in Australia has shown. Sih, UC Davis's Orr Spiegel, and Michael Bull, an ecologist at Flinders University in Adelaide, Australia, put GPS tags on more than 70 sleepy lizards (*Tiliqua rugosa*) in the wild and tracked their movements and locations to see how they interacted with one another. The team then examined the lizards for tick infections and found that more docile animals—those that run away from fights—have more parasites than aggressive animals, most likely because the meek are more likely to crowd together in good hiding places or to stick so close to mates that ticks can make the jump.

In Toulouse, Cote and his team are now investigating whether the balance of lizard personalities might shift as the global climate warms. To do so, they manipulate the temperatures of their enclosures. "If some personality types are selected in a warmer climate, it could reduce this variation in personality and have some unexpected consequences," Cote says. For example, more active lizards eat a wider variety of insects; if they start to predominate in warmer climates, they could drive down the number and variety of insects, perhaps affecting other aspects of the local community. "I have no doubt that personality traits can have a cascading effect on ecosystem functioning," Cote says.

Spiders with a collective personality

Anelosimus studiosus, a small, brownish U.S. spider, lives in groups of from two to two dozen individuals and can build car-sized webs capable of snaring a small bird or mammal. Over the past decade, behavioral ecologist Jonathan Pruitt of UC Santa Barbara has determined that not only do individual spiders have personalities—bold and active or docile and inactive—but also that the mix of the two types gives each colony a distinctive "group personality." The group personality needs to fit the demands of the local environment if the colony is to survive, he and his colleagues reported in *Nature* in 2014.

For years, Pruitt has looked at spider colonies located below and above several dams in Tennessee. Though quite near each other, these colonies occupy very different environments: Plentiful insects—prey for the spiders—hatch from the stream below the dam, but far fewer emerge from the reservoir above it.

In both cases, Pruitt found, individual spiders play distinct roles in the colony. Social insects also have a division of labor, but whereas bees and ants have castes of physically different insects that specialize in different tasks, the spiders all look alike. Instead, personality defines their jobs. Pruitt assessed spider personality using a range of tests: If two spiders placed in a box together wound up on opposite sides, for example, he called them aggressive. When a spider was frightened into a ball by a puff of air that simulated a predator's approach, he measured shyness by timing how long the creature took to uncurl.

He found that the aggressive, quick-to-uncurl spiders serve the colony by killing the prey and any intruders, whereas their meeker counterparts tend the young and fix the cobwebs. "Having personality variation helps you develop [an] adaptive division of labor," Pruitt says. "That makes the whole colony better" and may have helped foster the evolution of communal living among these arachnids.

The proportions of each personality varied depending on the location of the colony. Below the dam, the spiders' prey-laden webs attracted interlopers—other spiders that preyed on food captured by the web-builders. In those colonies, at least 60% of the spiders were feisty individuals that could fend off these parasites. In colonies above the dam, where prey—and freeloaders—are scarcer, most of the spiders were sedentary and passive, devoting as much of their energy as possible to making efficient use of what little food they could capture. There, "you have a pacifist egalitarian society good at living off very little," Pruitt explains.

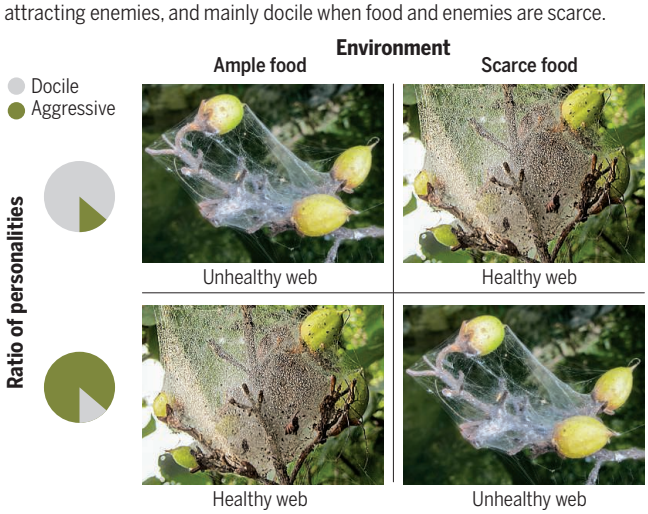
To test the importance of those group personalities, Pruitt collected spiders from the wild and redistributed them in hundreds of artificial colonies—webs built on chicken wire that could be attached to the foliage. He varied the proportion of aggressive and docile individuals and installed the colonies either above or below the dam. The right ratio in the right place was key, he found. "The mix of aggressive and unaggressive spiders has an effect on how the whole colony survives." If the experimental colony had the same ratio of personality types as natural colonies from that location, the colony thrived. But if not, the colony went extinct (see graphic, left). Somehow, Pruitt says, colonies can recognize when the balance of personalities is off and adjust accordingly, with aggressive or meek spiders reproducing at different rates.

How colonies fine-tune their collective character is one of the many mysteries in research on animal personalities. And it won't be the last as biologists scrutinize the behavior of species more and more closely. After all, Ingley says, "if it moves, chances are that personalities are present." ■



The spider's stratagem

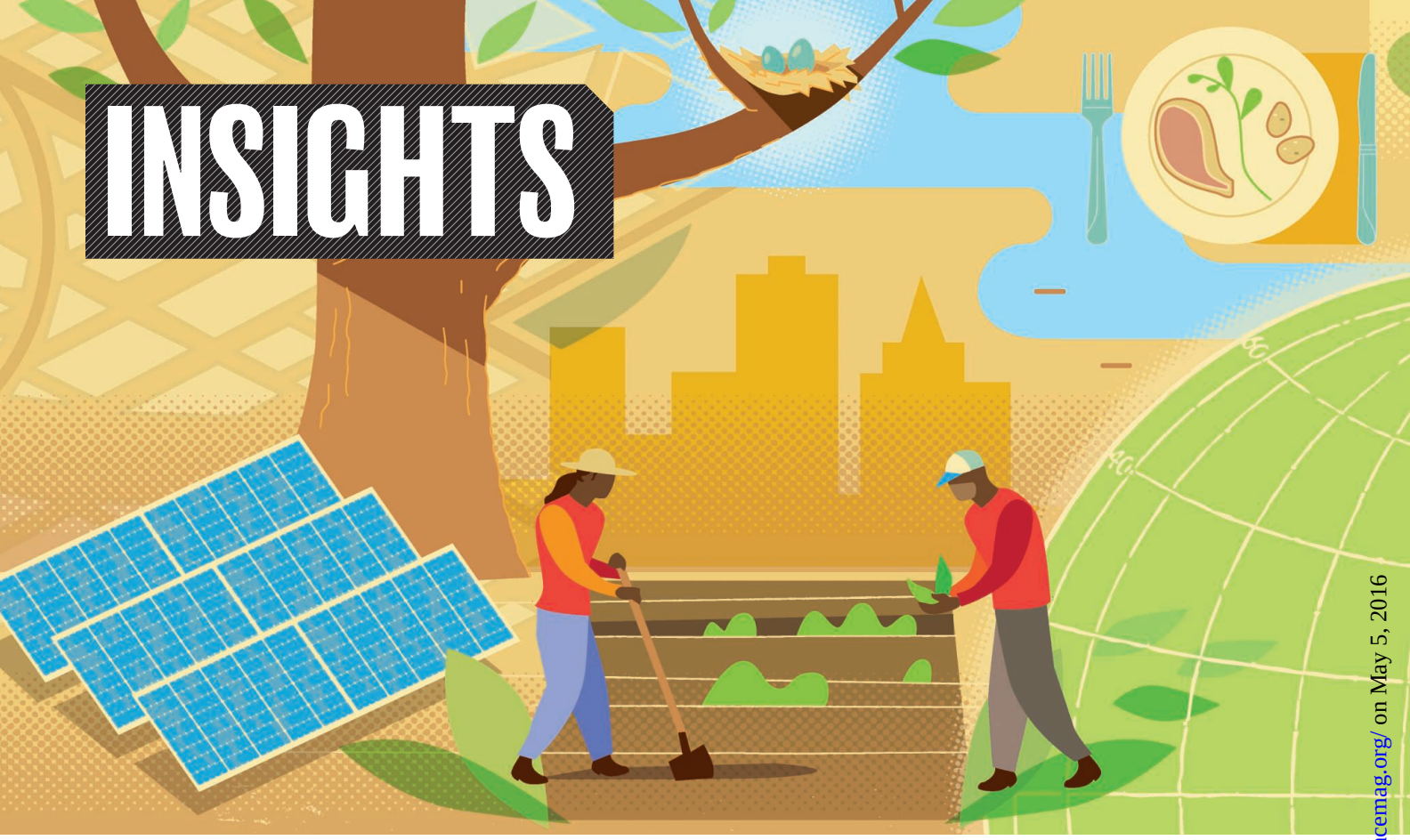
Colonies of the social spider *Anelosimus studiosus* thrive with the help of the right balance of personalities: mainly aggressive when food is plentiful, attracting enemies, and mainly docile when food and enemies are scarce.



CREDITS: (PHOTOS, TOP TO BOTTOM) JUDY GALLAGHER; JONATHAN PRUITT/UNIVERSITY OF CALIFORNIA, SANTA BARBARA; (GRAPHIC) V. ALTOUNIAN/*SCIENCE*

Downloaded from http://science.sciencemag.org/ on May 5, 2016

Published by AAAS



Downloaded from http://science.sciencemag.org/ on May 5, 2016

BOOKS *et al.*

ENVIRONMENTAL FILM FESTIVAL

Fighting for our future

IN MARCH 2016, the theaters, libraries, universities, and museums of Washington, D.C., were once again the setting for the Environmental Film Festival in the Nation's Capital, an annual event (now in its 24th year) featuring more than 140 Earth-friendly films. A number of the 2016 selections sought to celebrate the centennial of the U.S. National Park Service, highlighting how parks and protected areas play a vital role in the conservation and preservation of the Earth. Other films invited viewers to examine the powerful relationship between humans and the places we call home, probed the institutions driving climate policy, and revealed the resilience of communities confronting the early effects of global warming. Read on to learn what *Science* staff thought of 12 of this year's featured films.

The Babushkas of Chernobyl

Reviewed by **Kelly Servick**

For the past 30 years, the Ukrainian town of Pripyat has had just one official identity: a forbidden wasteland permeated with radioactive dust. The catastrophic explosion of a reactor at the Chernobyl nuclear power plant in 1986 prompted the permanent evacuation of the entire city and all other areas within a 30-kilometer radius. But within months, hundreds of residents, undeterred by the risk of carcinogenic particles, had snuck back into the so-called exclusion zone to resume their lives. Now, an aging population of roughly 100 residents, nearly all of them women, subsists by planting, foraging, and fishing in a landscape that is slowly being reclaimed by nature.

Filmmaker Holly Morris and her team spent 16 days inside the exclusion zone to document their lives, many of which were marked by the immediate threats of poverty and war long before any vague risk of radiation. Her nuanced depiction in *The Babushkas of Chernobyl* defines the dangers of the exclusion zone through many eyes: the geophysicists and government employees who are its stewards, the defiant groups of young Ukrainians who periodically sneak in for a glimpse at their generation-defining disaster, and three exuberant "babushkas," who tromp through their contaminated kingdom with wry humor and mind-boggling grit.

The women featured in the story don't show obvious health effects from the

ILLUSTRATION: ©CARL WIENS/I2IART.COM

Published by AAAS



exposure, and, in fact, the returned residents have tended to survive longer on average than those who were displaced—at great emotional cost. At one point in the film, a government scientist explains that the residents choose to stay out of "ignorance and a simple lack of knowledge." But these women's fierce attachment to their land makes it hard to dismiss their choice so easily. Theirs is an extraordinary case study for a more commonplace issue: our effort to weigh the risks of an increasingly inhospitable environment against the necessity of calling it home.

The Babushkas of Chernobyl *Holly Morris and Anne Bogart, directors. USA, 2015, 72 min.*

Ever the Land

Reviewed by **Jennifer Sills**

The Tūhoe people, or children of the mist, of the Māori tribe have suffered at the hands of the colonizing New Zealand government for more than a century. But *Ever the Land* is not a historical film. Rather, it is the story of a people who are ready to close the door on the troubles of the past and greet a new era of compromise, one that will allow them to preserve their culture and land for future generations.

The film takes place at the dawn of this new era, as a new treaty between the Tūhoe and the government goes into effect. The Tūhoe will receive a $170 million settlement, as well as an apology for past transgressions and renewed rights to the governance of the Te Urewera, the Tūhoe's native land. We join them in community meetings, where they discuss the first investment of funds: a new community center, designed to seamlessly integrate with nature in accordance with the tribe's traditions. We listen as the 83-year-old architect, who will not live to see the project completed, explains the blueprints and as his staff checks and rechecks the extensive list of local materials. We watch the community make clay bricks, one by one, from molds. Meanwhile, everyday life continues; children go to school, festivals showcase traditional dance and song, mothers tell their children bedtime stories about the god who punishes those who pollute the river, and men gather to grill meat and share stories.

The documentary is unembellished; there are no soaring strings to imbue events with emotion, no interviews to provide context, no titles to identify the people shown on the screen, and no omniscient narrator. The viewer is not so much a spectator as a witness, quietly observing the Tūhoe people as they take part in the innumerable mundane moments that cumulatively bring about change.

Finally, the official government apology is broadcast, and the community center opens with great fanfare. Yet, even as members of the tribe celebrate their reclaimed rights to the land, they maintain that they are not its owners, but rather its guardians. For the Tūhoe, "there is nothing else that brings prosperity; it's only always ever the land."

Ever the Land *Sarah Grohnert, director. New Zealand, 2015, 93 min.*

Good Things Await

Reviewed by **Dorie Chevlen**

This Danish film paints Niels Stokholm's biodynamic farm Thorshøjgaard into a picture of hyperbolic beauty: sweeping shots of verdant landscape, sensitive close-ups of leaves dripping with morning dew, and sumptuous sunsets, all accompanied by goosebump-raising vocals of an *a capella* choir. First developed by philosopher Rudolf Steiner (whose thick tome on the subject Stokholm keeps readily available for curious readers), biodynamic farming is a holistic approach to agriculture that treats soil fertility, livestock care, and vegetation growth as one self-sustaining organism.

Downloaded from http://science.sciencemag.org/ on May 5, 2016

Published by AAAS



In *Ice and the Sky*, glaciologist Claude Lorius reflects on the history of climate research and the future of the warming planet.

PHOTO: WILD TOUCH

Downloaded from http://science.sciencemag.org/ on May 5, 2016

Throughout the film, the octogenarian farmer Stokholm, who with his white beard and flannel looks like a sort of agrarian Gandolf, waxes poetic about the interconnectedness of the Earth and the importance of protecting the farm's natural rhythms. Barely alluded to is the reality that all the animals so lovingly raised on this utopian property are eventually slaughtered. The one scene that even hints at this less-than-picturesque reality—a brief shot of a bright rivulet of blood coursing through the dirt—is more painterly than PETA-provoking.

After watching Stokholm cradle baby calves and tenderly pluck carrots from his chemical-free fields, it's tempting to declare his biodynamic system the ideal agricultural model. And yet, underlying this pastoral Arcadia is the threat of both legal and financial troubles. The Danish authorities disapprove of the freedom Stokholm grants his cattle, which they argue poses a safety risk. In a telling scene toward the end of the film, Stokholm recounts an experience in which he was gored by an ox and badly injured. Speaking nonchalantly into the camera, he defends the ox and, more shockingly, forgives it. But, then again, not doing so would only prove the authorities right.

If *Good Things Await* fails in convincing viewers of the superiority of biodynamic farming, it's only because, for all its cinematographic power, it cannot undo the reality that this world is one of love and beauty, yes, but also of blood.

Good Things Await *Phie Ambo, director. Denmark, 2014, 95 min.*

Catching the Sun

Reviewed by **Marc Lavine**

Would a switch from fossil fuels to solar power create or destroy more jobs? Would the installation of solar panels on houses and businesses empower individuals and communities? Would it truly shift wealth from megacorporations to the less wealthy? Although not directly asked, these questions emerge from the stories told in *Catching the Sun* from filmmaker Shalini Kantayya. The documentary begins by detailing the health and environmental consequences of the 2012 Chevron fire and explosion in Richmond, California. The disaster became a catalyst for the environmental movement and shined a spotlight on the close relationship between Chevron and the local government, as Richmond's mayor at the time, Gayle McLaughlin, describes in the film.

Against this backdrop, Kantayya proceeds to focus on companies, entrepreneurs, activists, and nonprofits in the United States and China who are trying to advance the solar revolution. A key theme emerges through interviews with Van Jones, author of *The Green Collar Economy,* who sees solar energy as a way to be more environmentally responsible while also creating jobs, particularly in low-income communities. We see the potential for the latter in the work of Solar Richmond, a nonprofit that offers training and green business ownership opportunities for low-income and underemployed residents. One would think that this sort of win-win situation would be politically appealing, but many barriers prevent widespread adoption, particularly in the absence of a clear national policy.

In contrast, Wally Jiang is able to grow his Chinese solar business by 50% a year through the support of the government. In the film, we see his attempts to advance his business as he pursues a range of international partnerships. *Catching the Sun* is thin on numbers, from how much solar technology really costs to how well it might integrate into the electricity grid on a large scale to a proper comparison of the successes of different countries in implementing renewable energy. But it does show the personal side of solar energy and is thus an important part of the broader story.

Catching the Sun *Shalini Kantayya, director. USA, 2015, 74 min.*

Published by AAAS

Ice and the Sky

Reviewed by **Brent Grocholski**

Claude Lorius arrived in Antarctica for the first time in 1956 on a trip that lasted 16 months but hooked him into a life dedicated to returning to the bitter cold. *Ice and the Sky* is a film that traces the French glaciologist's life and discoveries. Director Luc Jacquet combines Lorius's commentary with archival footage of his scientific expeditions that range from the bare-bones three-man operation in 1956 to the much larger international deep-ice-drilling collaboration at the Vostok research base decades later. Interspersed are more recent scenes depicting the bright and brilliant landscapes of Antarctica as Lorius, now in his 80s, makes what may be his final return to the continent.

Lorius's discoveries had a profound impact on our understanding of climate change. He was the first to recognize that tiny gas bubbles trapped in ancient ice tell a story of our planet's temperature in the deep past. The film succeeds in demonstrating the strong tie between greenhouse gases like CO_2 and temperature, making the connection between humans and global warming obvious. Surprisingly, it was the discovery of radioisotopes from an atmospheric nuclear test, not the results of his own research, that eventually shocked Lorius into the realization that no place on Earth has escaped the imprint of humanity.

Despite having recognized and raised the alarm about human-induced climate change decades earlier than most, Lorius strikes an optimistic tone about the potential for humanity to avert disaster. "Man is never so sublimely in his element than when faced with adversity," he maintains near the end of the film. Perhaps we should expect nothing less from a man who knows the power of teamwork to overcome what seem to be insurmountable obstacles.

Ice and the Sky *Luc Jacquet, director. France, 2015, 89 min.*

Women and Water

Reviewed by **Carolyn Gramling**

A young Indian woman, heavy with child, carries a bright yellow plastic urn to the village well. Eight times a day, she hauls water from the well and carries it home to prepare food; wash children, floors, and pots; and tend to crops. She visits an obstetrician, who tells her she must not lift heavy things. The woman nods, expressionless.

There are few words in the film *Women and Water*; only occasional quiet narration from its subjects and the ambient sounds of their work punctuate the often stunning visuals. But Spanish filmmaker Nocem Collado still tells a powerful story of modern India's water woes: rivers choked with trash, sewage, and chemical waste; mosquito-borne diseases; and women traveling long distances to fetch water.

Four "stories," each loosely centered on a different woman, anchor the film: the expectant mother; a village woman who travels 5 hours a day to fetch water from a distant well; a rubbish collector in the slums of Mumbai; and a member of the "untouchable" caste. The film watches them unflinchingly as they go about their often-grueling daily chores and worry about their children's health and futures. It makes a strong case that the country's water-related hardships disproportionately affect women, who must find ways to channel the water to their families.

The film ends quietly; it offers no suggestions for management, little sense of the historical context in which these problems arose, and, consequently, little hope for the future. One expert interviewed in the film cites Mahatma Gandhi's famous quote, "Sanitation is more important than political independence," made nearly a century ago. In recent decades, the country has launched several campaigns—the latest in 2014—to bring clean toilets to every one of its people and end open defecation. Sanitation is only one of the many environmental challenges India faces. It will be, to say the least, an uphill climb.

Women and Water *Nocem Collado, director. Spain, 2014, 58 min.*

How to Let Go of the World

Reviewed by **Julia Fahrenkamp-Uppenbrink**

This unusually uplifting film about climate change starts and ends with a dance. At the start, filmmaker and narrator Josh Fox dances with joy because local protests have prevented oil and gas exploration in Delaware—only to realize that this local victory is not enough: The warming climate is allowing parasites to spread north, destroying hemlock forests in their wake.

Interviews with climate scientists and activists follow, painting a bleak picture, and Fox almost gives in to despair. As the camera zooms out on him lying on the snowy ground, he looks up into the sky at "all those greenhouse gases hanging there like a century of human regret."

Yet at the end of the film, he is dancing with joy again, having found hope in human courage, resilience, ingenuity, and civil disobedience around the world in the face of climate change. He has seen climate scientists lost for words at the scale of the challenge; he has watched an activist reduced to tears as his ancestral land is washed away by sea-level rise. But he has also joined local activists cleaning up oil spills from rotting pipelines in the Amazon, interviewed indigenous people in Ecuador who prevented oil exploration on their lands, blocked coal tankers from leaving port with the Pacific climate warriors, and met a tribal leader who is helping to bring solar power to one of the poorest regions in Zambia.



Access to clean, safe water sources remains out of reach for many women in India.

PHOTO: WOMEN AND WATER

Downloaded from http://science.sciencemag.org/ on May 5, 2016

Published by AAAS



Four unlikely gardeners work to change their lives and neighborhoods, one plant at a time, in *Can You Dig This.*

What unites these people is that they imagine a different world; that they believe they have a choice and are taking responsibility. Told in a highly personal and idiosyncratic style, *How to Let Go of the World* does that rare thing: inspires hope in the face of climate change.

How to Let Go of the World (And Love All the Things Climate Can't Change) *Josh Fox, director. USA, 2016, 125 min.*

Merchants of Doubt

Reviewed by **Laura M. Zahn**

"I'm not a scientist, although I do play one on TV occasionally," says Marc Morano, founder of the climate-change-denying website ClimateDepot.com. This statement summarizes the premise of *Merchants of Doubt,* a film that exposes the public relations tactics that are employed to cast doubt on science. Based on Naomi Oreskes and Erik Conway's 2010 book of the same name (reviewed in *Science*, 4 June 2010, p. 1230), the film explores the early groundwork laid by the tobacco companies to sell "doubt [as] our product" and examines how tactics to deny science have been, and continue to be, applied to flame retardants and, most prominently, climate change.

The film features interviews with players on both sides of these contentious issues. With some notable exceptions, most of those on the "science side" of the debate are scientists, whereas their counterparts appear to be people with no scientific expertise who are hired to seed uncertainty among nonexperts by those with interests contrary to scientific results. Interestingly, these individuals often function as publicists across a slew of topics, writing letters to Congress discouraging stricter cigarette laws one day and op-ed pieces questioning global warming the next.

Despite the fact that there is almost no debate in the scientific community regarding human-caused climate change, a small but well-funded group of individuals is succeeding in spreading misinformation and creating skepticism in the American public. If we as a scientific community choose to ignore this reality, we're only making their jobs easier.

Merchants of Doubt *Robert Kenner, director. USA, 2014, 96 min.*

Can You Dig This

Reviewed by **Nick Wigginton**

City residents living in "food deserts" lack easy access to grocery stores or other healthy food options. This situation disproportionately occurs in low-income communities, lowering overall public health and exacerbating inequality. Ron Finley of South Los Angeles, one of the primary subjects of *Can You Dig This,* paints an even grimmer picture. He likens the situation to a "food prison," whereby permission is often required to simply grow food in cities.

Through a series of intimate portraits, filmmaker Delila Vallot shines a light on not just the challenges of urban farming as they pertain to environmental justice but of overall urban life in Los Angeles. For her subjects, gardens represent more than just access to healthy food. An ex-con living in a halfway house finds refuge in his garden as he adjusts to life outside of prison. A school-age girl, bursting with enthusiasm, connects with her family and neighbors in public housing over her garden. In a community garden, an occasional drug dealer finds purpose and love with a fellow gardener, an ex-gangbanger struggling to achieve her dream of becoming a nurse.

As the film implies, urban farming should not simply focus on sustainability or solving the challenges of food deserts. We should recognize that urban gardens provide a chance to plant more than just food. One can plant ideas, plant hope, plant love, plant purpose. As Finley appeals to the audience during his 2013 TED talk: just #plantsomeshit.

Can You Dig This *Delila Vallot, director. USA, 2015, 80 min.*

An American Ascent

Reviewed by **Lauren Kmec**

In his famous speech, Martin Luther King Jr. declared, "I have a dream that one day every valley shall be exalted, every hill and mountain shall be made low." Flashbacks to this speech are featured in *An American Ascent,* which chronicles the journey of nine African-American mountaineers as they endeavor to climb Denali, North America's highest peak, on the 100th anniversary of its first summit. Accompanied by four guides, the men and women set out to test their personal limits and challenge people of color to rethink their relationship with the great outdoors. Most of the climbers have never attempted a trek of this magnitude, and many encounter disapproval from their peers, yet they are compelled to show that the natural world is a place for everyone.

The film deftly balances commentary from the climbers with footage of their excursion. The landscape is awe-inspiring, yet it is clear that climbing Denali will be no easy feat. Aside from challenges presented by the altitude, the mountaineers grapple with other difficulties: One man suffers a dislocated shoulder but is determined to press on. Rock slides and snow squalls materialize in minutes. More than once, the team is forced to retreat to its previous camp after several hours of climbing. But the film also features lighter moments. At one point, we see the climbers relaxing at a campsite while trading stories with others from around the world.

PHOTO: CAN YOU DIG THIS

Downloaded from http://science.sciencemag.org/ on May 5, 2016

Published by AAAS

Their camaraderie is a joy to watch.

On day 19, the climbers attempt to reach the summit, but a dangerous electrical storm foils their plans. With food and supplies running low, they must turn back without making another effort. Although their disappointment is palpable, it soon gives way to an enormous sense of pride in having proven that nature's charms are accessible to all people, regardless of race or cultural background.

An American Ascent *George Potter and Andy Adkins, directors. USA, 2015, 66 min.*

Bluespace

Reviewed by **Barbara Jasny**

Bluespace uses the possibility of terraforming Mars as a (sometimes loose) organizing principle for examining Earth's endangered ecosystems. The film is divided into three parts. In the first, "The Imagined World," the "canals" of Mars—long, straight lines observed by early astronomers that were once believed to be evidence of intelligent Martian life—are juxtaposed with images of snow-covered roads and the canals of Venice. Although no one currently expects to find little green men on Mars, the possibility that the remains of microbes might be discovered underneath or within rocks is still within the realm of reality.

In the second section, "A Gardened World," the film offers tantalizing glimpses and mentions of life in extreme environments on Earth (including the specter of new species being formed in toxic waste sites). Although there are some who believe that we should not contaminate or alter Mars, science fiction writer Kim Stanley Robinson offers a controversially different opinion in the film: "If Mars has life, we should encourage it; if not, we should share with it."

Touching briefly on people who are attempting to simulate Martian conditions here on Earth, the third section, called "A Most Liquid World," focuses mostly on footage of destroyed structures and landscapes and distressed people left in the wake of Hurricanes Sandy and Katrina. The take-home lesson is that perhaps we are not very well adjusted to our own, changing, world and that we should focus on getting things right on Earth before we consider terraforming another planet.

Bluespace, while raising some interesting ideas, needed better editing. Additionally, the affiliations of the various people who appear in the film provide some context but, unfortunately, don't appear until the closing credits. Despite its uneven presentation, the documentary offers an interesting take on an unusual topic.

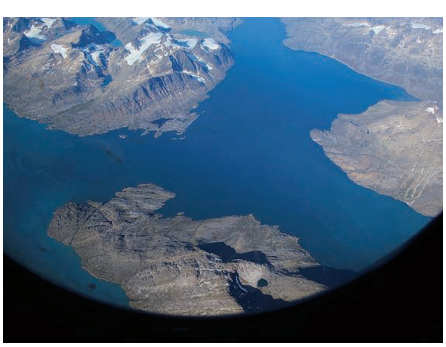


PHOTO: ©WICKED DELICATE FILMS

If rising seas ultimately imperil our existence on Earth, might Mars be made hospitable to humans?

Bluespace *Ian Cheney, director. USA, 2015, 71 min.*

Poached

Reviewed by **Caroline Ash**

Poached is a film about the obsession that drives some Englishmen to extremes to collect wild bird eggs. These men will climb trees and cliffs—several have fallen to their deaths—in pursuit of eggs. Those of rare birds of prey, including ospreys, peregrine falcons, and hen and marsh harriers, are esteemed, but most prized of all are golden and white-tailed eagles. It seems that the more inaccessible the nest and the more vigilant the protection officers, the stronger the drive to collect becomes.

The anomie and secretiveness that surround this illicit pastime are shocking. One man, encased in a rubber bird skull, is full of threats of revenge against law enforcement. He clearly fears being imprisoned, yet still boasts that he will never be caught. Many "eggers" identify as bird lovers, yet seem unable to confront the consequences of their behavior. Despite some beautiful footage of birds, ultimately, the film is unsatisfactory, and too many questions are left unanswered. What about the effect of bird collecting on bird populations? Could not the obsessives be converted into equally ardent conservationists? Although the environmentalist message might be lacking, this is nevertheless a powerful film exploring personalities gripped by obsession.

Poached *Timothy Wheeler, director. UK, 2015, 90 min.*

10.1126/science.aaf9096

Published by AAAS

Downloaded from http://science.sciencemag.org/ on May 5, 2016



Looking out to sea. Cook's Cove near Gisborne, New Zealand. Offshore, a network of seafloor sensors monitor seismic activity.

http://sciencemag.org/cgi/rights/terms

GEOPHYSICS

Measuring slow slip offshore

Monitoring changes in the seafloor might be used for earthquake and tsunami forecasting

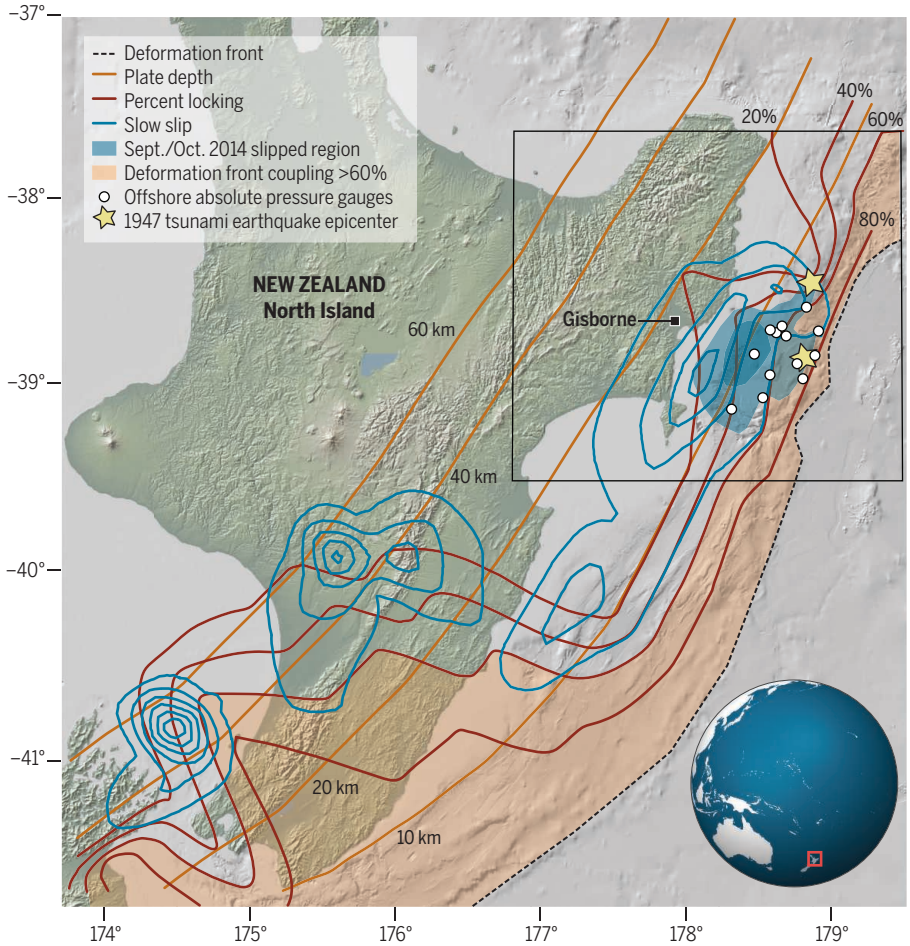
By **Anne M. Tréhu**

Tsunami earthquakes are rare events and are distinguished by an anomalously shallow source depth and slow rupture propagation speed (*1*, *2*). They can be particularly dangerous because they generate less high-frequency seismic energy than a normal earthquake; consequently, they are not preceded by the strong shaking that would warn coastal residents that a locally generated tsunami is on the way. A better understanding of the range of slip behaviors in the offshore portion of subduction zones is needed to constrain models and improve earthquake hazard forecasts. On page 701 of this issue, Wallace *et al.* (*3*) present the first offshore geodetic data from a slow-slip event on the Hikurangi subduction zone offshore from New Zealand (see the figure). This segment of the Hikurangi subduction zone is unusual in that it experienced two "tsunami" earthquakes in 1947. Continuous global positioning system (GPS) instrumentation onshore indicates that the southern part of the subduction zone is locked above a plate depth of ~40 km, with slow-slip events occurring at greater depth, similar to what is observed in many other subduction zones (*4*, *5*). In contrast, the northern part of the Hikurangi subduction zone appears to accommodate plate motion primarily through geodetically detected slow-slip events at shallow depths. The up-

College of Earth, Ocean, and Atmospheric Sciences, Oregon State University, Corvallis, OR 97331-5503, USA. Email: trehu@coas.oregonstate.edu

PHOTO: RUSSELL JAMES SMITH/FLICKR

Published by AAAS



Map of the Hikurangi subduction zone. Box shows the region discussed by Wallace *et al.* (*3*); red, blue, and yellow lines show results from previous models (*10*, *11*). The deformation front represents the seafloor position of the subduction zone fault (dashed black line). Contours show depth to the top of the subducting plate (orange). A model for total slip summed over all detected slow-slip events from 2002 to 2010 is shown as blue contours (contour interval 10 cm from an initial value of 5 cm). An elastic model for interplate coupling assumes 100% coupling at the deformation front (red); contours are shown at 20% intervals with peach shading highlighting coupling >60%. Blue shading shows the region that slipped in the September/October 2014 slow-slip event, with the position of offshore APGs shown as small white squares. The main slip patch is farther offshore than indicated by the blue contours. Although it appears that slow slip tapers off toward the deformation front, whether the slip deficit is being stored for future release in an earthquake or being dissipated through aseismic creep that is too slow to be resolved with a 1-year deployment of APGs uncalibrated for drift is unresolved.

dip extent of slow slip, however, cannot be determined from onshore data only, and offshore locking models depend strongly on model assumptions.

If the plates are assumed to be elastic and fully locked at the deformation front, an unusually shallow and narrow locked zone is expected, which implies a high risk of future tsunami earthquakes. However, it is likely that the response of the outer accretionary wedge to slow-slip events is more complex because of the rheological and frictional properties of sediments at low temperatures and pressure (*6*, *7*). Unfortunately, the outer wedge is offshore in most subduction zones. It is therefore inaccessible to GPS surveys of the kind that have shed so much light in the past two decades on the broad range of slip modes that occur on plate boundary faults. Direct measurements of offshore deformation before, during, and after major earthquakes are very limited (*8*). Seafloor geodetic measurements off Japan suggest that some earthquakes may be preceded by slow slip and that large, rapid slip in the seismogenic zone can trigger tsunamigenic slip to the trench in sediments that might usually be expected to accommodate plate motion through aseismic deformation (*8*).

The need for seafloor geodesy has been widely recognized for decades (*9*). Implementation, however, has been slow because of the large costs associated with establishing acoustic networks in the ocean to link seafloor measurements to surface ships for campaign-style surveys or with automated underwater vehicles and buoys to provide the continuous data needed to resolve slip modes in real time. This has led to development of alternative techniques for obtaining seafloor geodetic data such as differencing of swath bathymetric data, seafloor and borehole strain meters, and arrays of absolute pressure gauges (APGs), which measure changes in the mass of overlying ocean, from which seafloor uplift or subsidence can be determined (*8*). Because of their relatively low unit cost, APGs can achieve the spatial coverage needed to understand complex environments, although there are a number of challenges to be overcome, including long-term sensor drift and separation of tectonic signals from oceanographic effects.

Wallace *et al.* present an excellent test case for the use of APGs for seafloor geodesy because, based on the recent history of slow-slip events here, it was possible to anticipate a time window that would capture an event with a duration of a few weeks (short enough to be distinct from sensor drift) and because the nearby onshore GPS network was available for distinguishing likely tectonic signals from oceanographic signals of similar amplitude and wavelength. The results show that slip during the 2014 slow-slip event extended farther offshore than had been indicated by models for previous events developed using only onshore data.

Several seafloor geodetic experiments using a variety of approaches are currently under way or in the planning phase, and methods for in situ calibration of APGs are being tested (*8*). Over the next several years, these projects are sure to chip away at uncertainties in the partitioning of plate motion between seismogenic slip and aseismic slow slip or creep in subduction zones and in the role of the outer wedge in the generation of tsunamis. The results of these projects should ultimately lead to better strategies for earthquake and tsunami forecasting and early warning. ■

REFERENCES

1. H. Kanamori, *Phys. Earth Planet. Int.* **6**, 346 (1972).
2. L. Ye *et al.*, *J. Geophys. Res.* **121**, 845 (2016).
3. L. M. Wallace *et al.*, *Science* **352**, 701 (2016).
4. S. Y. Schwartz, J. M. Rokosky, *Rev. Geophys.* **45**, RG3004 (2007).
5. G. C. Beroza, S. Ide, *Ann. Rev. Earth Planet. Sci.* **39**, 271 (2011).
6. C. Marone, E. Richardson, *Geology* **38**, 767 (2010).
7. D. R. Faulkner *et al.*, *Geophys. Res. Lett.* **38**, L18303 (2011).
8. R. Bürgmann, D. Chadwell, *Ann. Rev. Earth Planet. Sci.* **42**, 509 (2014).
9. F. N. Spiess *et al.*, *Seafloor Referenced Positioning: Needs and Opportunities* (National Academy Press, 1983).
10. L. M. Wallace *et al.*, *Geochem. Geophys. Geosyst.* **10**, Q10006 (2009).
11. L. M. Wallace, J. Beavan, *J. Geophys. Res.* **115**, B12402 (2010).

10.1126/science.aaf6534

GRAPHIC: P. HUEY/SCIENCE

Downloaded from http://science.sciencemag.org/ on May 5, 2016

Published by AAAS

POLYMER GROWTH

Self-assembly creates 2D materials

Carefully chosen mixtures of polymers form rectangular platelets in solution

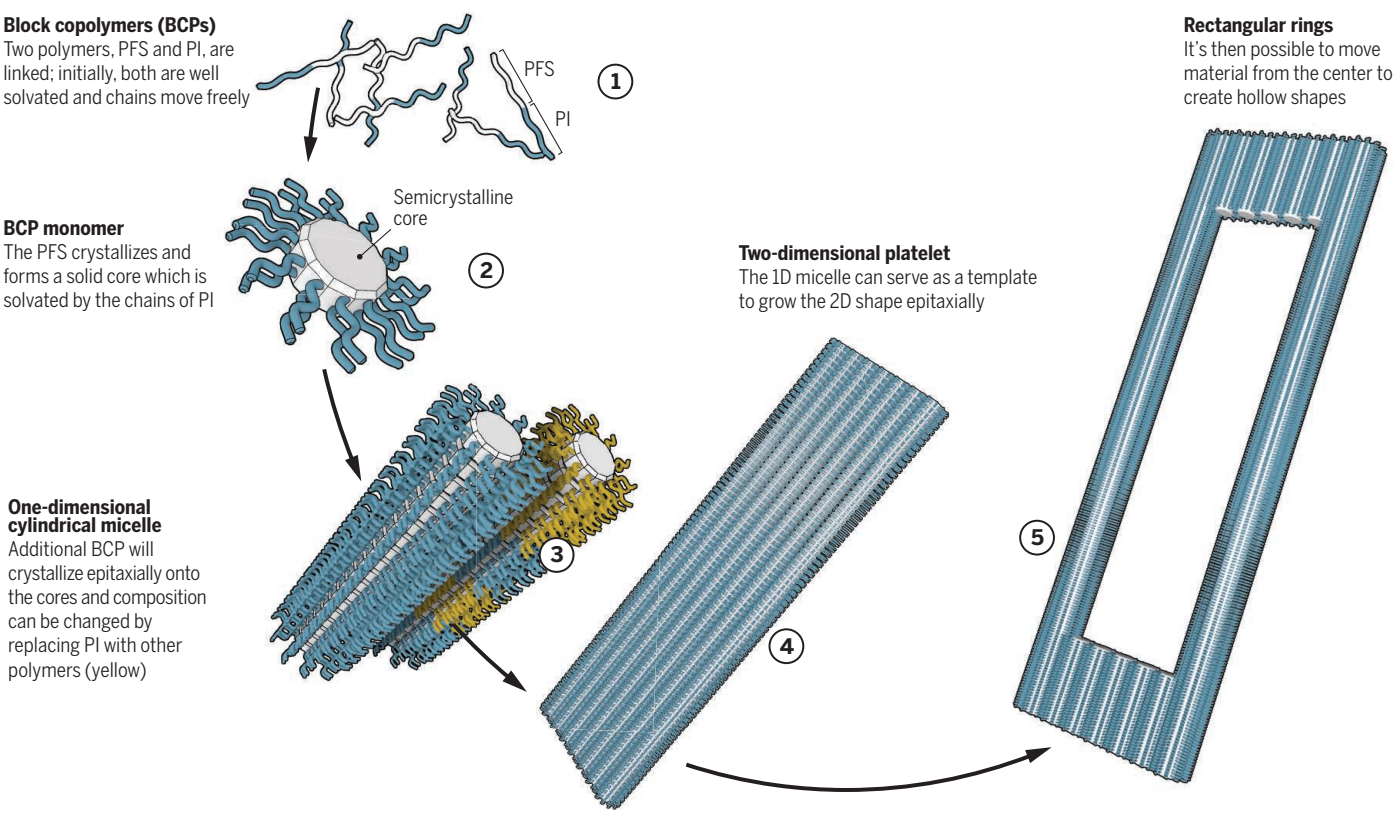
By **Matthias Ballauff**

Self-assembly (*1*) of suitable molecules and of polymers is a central issue in modern nanotechnology: Once in solution, suitable building blocks should assemble in a highly precise manner to yield much larger, supramolecular objects tailored for a particular function (*2*). Self-assembly into one-dimensional (1D) micelles with defined length and composition has been achieved (*3*, *4*), but on page 697 of this issue, Qiu *et al.* (*5*) describe a decisive step toward 2D systems: By combining the self-assembly by epitaxial crystallization of semicrystalline block copolymers (BCPs) mixed with homopolymers in judiciously chosen solvents, they created a process that leads to highly defined rectangular platelets. Manipulation of these nearly defect-free platelets gives rise to a new class of nanoscale objects that may have a wide range of applications.

Self-assembly is very common in nature. For example, lipids assemble into 2D bilayers that are the basic structures of all biological membranes and cells. In synthetic systems, surfactants assemble into micelles, which provide the basis for many household applications and technologies, and BCPs assemble into 3D structures that may be fully defined in three directions (*2*, *6*). The obvious difficulty in self-assembly, however, is that it needs to be directed—the molecules or building blocks should target the desired structure and avoid the formation of unwanted or faulty objects. Thus, intense research is directed toward processes that allow self-assembly of building blocks to be controlled in a fully defined way.

The work of Qiu *et al.* originates from the discovery that BCPs containing a block from poly(ferrocenylsilane) (PFS) may be used to generate semicrystalline micelles of equal length (*3*). The authors coupled PFS to a second, noncrystalline polymer such as polyisoprene (PI) or polysiloxane. PFS then forms a crystalline core, and the soluble block protrudes into solution and provides colloidal stability of the resulting micelles. Manners, Winnik, and co-workers have named such processes "crystallization-driven self-assembly" (CDSA), and CDSA of semicrystalline BCPs has become a very versatile process (*7*). In particular, Wang *et al.* (*3*) demonstrated that CDSA can be run as a "living" polymerization. Small micelles serve as seed particles onto which the PFS-copolymers crystallize epitaxially. All of the seeds grow with equal probability, and growth stops only when all monomers, namely the free BCP, have been used up. Hence, all micelles are nearly of

Helmholtz-Zentrum Berlin and Institut of Physics, Humboldt University, Berlin, Germany. Email: matthias.ballauff@helmholtz-berlin.de



Crystallization-driven self-assembly. One-dimensional nano-objects were generated by block copolymers (BCPs) (**1**), where one block crystallizes to form the core and the noncrystallizable block protrudes into solution (**2**). Additional BCPs will crystallize epitaxially on the cores (**3**). Qiu *et al.* extend this approach to 2D objects. A rodlike semicrystalline micelle with defined length is used as a core (**4**) onto which a mixture of homopolymers and BCP is crystallized epitaxially in solution. Material from the center can be removed to create hollow frames (**5**).

ILLUSTRATION: V. ALTOUNIAN/*SCIENCE*

Downloaded from http://science.sciencemag.org/ on May 5, 2016

Published by AAAS

equal length (*3*). Manners, Winnik, and coworkers have shown that this approach can be extended to the generation of very well-defined micellar BCPs (see the figure) (*4*). Labeling by fluorescent dyes verifies the high definition of these objects. Thus, CDSA provides the access to 1D objects with fully defined length and sequence.

Qiu *et al.* performed the next step and achieved full 2D control. In earlier work (*8*), they extended CDSA to 2D epitaxial growth of micelles with lenticular shape (*2*). The latest approach uses epitaxial crystallization on a cylindrical seed micelle. To this core, a mixture of a BCP from PFS and poly(2-vinylpyridine) (P2VP) and the homopolymer PFS is added in a solvent chosen to selectively solubilize the different blocks. Self-assembly leads to rectangular, fully defined platelets. The ratio of the BCP to the homopolymer controls the aspect ratio of these objects that can grow up to a size of 60 μm by 10 μm. Hence, a living 2D CDSA has been achieved, resulting in platelets with internal structure and nearly without defects. Qiu *et al.* explain the high definition of the platelets in terms of a simple geometric model.

"...the platelets formed by controlled 2D self-assembly add a new building block to nanotechnology."

In additional studies, one of the BCPs (P2VP) was cross-linked by addition of platinum nanoparticles. Dissolution of the non–cross-linked cores led to stable hollow nanoframes that could be manipulated by optical tweezers and laid down on a substrate. Thus, the platelets formed by controlled 2D self-assembly add a new building block to nanotechnology. These systems may open the way to a large number of applications in vastly different fields, ranging from sensors to microelectronics (*9*). At the same time, the 2D self-assembly having a precision near to crystallization presents a fundamental observation to be studied in further detail. ■

REFERENCES

1. G. M. Whitesides, B. Grzybowski, *Science* **295**, 2418 (2002).
2. A. H. Gröschel *et al.*, *Nature* **503**, 247 (2013).
3. X. Wang *et al.*, *Science* **317**, 644 (2007).
4. J. B. Gilroy *et al.*, *Nat. Chem.* **2**, 566 (2010).
5. H. Qui *et al.*, *Science* **352**, 697 (2016).
6. H. Cui, Z. Chen, S. Zhong, K. L. Wooley, D. J. Pochan, *Science* **317**, 647 (2007).
7. J. J. Crassous *et al.*, *Polymer* **62**, A1 (2015).
8. Z. M. Hudson *et al.*, *Nat. Chem.* **6**, 893 (2014).
9. F. H. Schacher, P. A. Rupar, I. Manners, *Angew. Chem. Int. Ed. Engl.* **51**, 7898 (2012).

10.1126/science.aaf4930

ILLUSTRATION: V. ALTOUNIAN/*SCIENCE*

PROTEIN DESIGN

Inspired by nature

Designed proteins have structural features resembling those of natural active sites

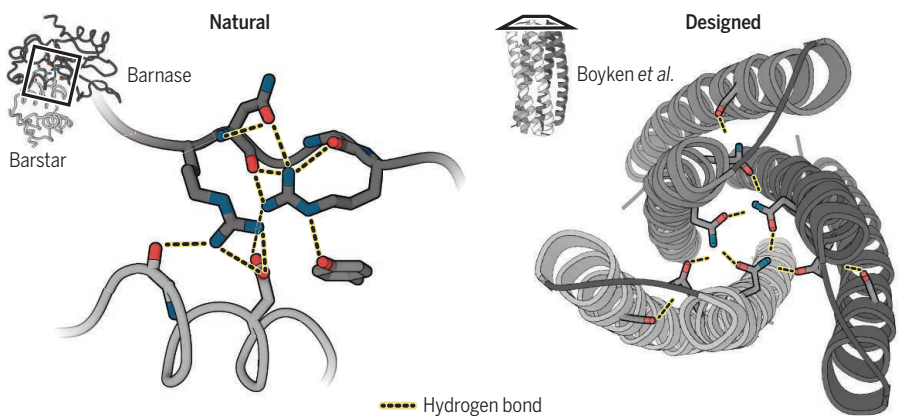
By **Ravit Netzer** *and* **Sarel J. Fleishman**

Over the past decade, scientists have made exciting progress in designing protein folds entirely on the computer and then successfully synthesizing them in the laboratory (*1*–*5*). These designer proteins had the same structure in experiment as in the model and were very stable; however, they lacked important structural features seen in protein interfaces and enzyme active sites. In two reports on pages 680 and 687 of this issue, Boyken *et al.* (*6*) and Jacobs *et al.* (*7*) use the Rosetta biomolecular modeling software to design proteins that include some of these features. Experiments show that these new designs retain high structural precision and stability.

Although understanding and control of biomolecular structure are far from complete, the high precision and stability observed in earlier design experiments (*1*–*5*) are clearly essential ingredients for designing enzymes and binding partners from scratch. But natural proteins have other features that are crucial for fulfilling their molecular function. Computer algorithms optimize surface polarity, core hydrophobicity, and backbone regularity; in a nutshell, they optimize stability. By contrast, evolution selects proteins for their ability to perform a vital molecular function, often at the expense of stability. Numerous molecular structures of natural proteins show that the active site is the protein's most energetically perturbed region, with multiple same-charge chemical groups, buried polar atoms, hydrophobic surfaces exposed to water, or broken and twisted α helices and β sheets. Can design algorithms be extended to encode such features, and if so, do the resulting proteins still show high stability and precision?

To address this question, Boyken *et al.* aimed to design buried hydrogen bonds in protein-protein interfaces starting from designed helical coiled coils. In nature, polar interactions encode high-precision binding specificity; these interactions typically require supporting networks of polar groups on both binding partners for accurate positioning (see the first figure). Because of this complexity, designed binding partners in previous work have not contained elaborate polar networks (*8*).

To overcome this limitation, Boyken *et al.* designed a large repertoire of coiled coils, including novel topologies of dimers, trimers, and tetramers. They developed an algorithm (called HBNet) to find side-chain constellations in which all polar atoms are connected through stabilizing hydrogen-bond networks (see the first figure). The authors then synthesized 114 designed oligomers and characterized the structures of various topologies. Most of them showed high precision rela-



Designed coiled-coil specificities using polar interaction networks. Natural protein-protein interactions (such as those seen between barnase and its natural inhibitor, barstar; PDB entry 1BGS) are often dominated by intricate hydrogen-bonding networks that involve both side-chain and backbone atoms for accurate preorganization. Boyken *et al.* have designed coiled coils that interact via side chain–only hydrogen-bond networks (such as design 2L6HC3_13 shown here).

Department of Biomolecular Sciences, Weizmann Institute of Science, Rehovot, Israel. Email: sarel@weizmann.ac.il

Downloaded from http://science.sciencemag.org/ on May 5, 2016

Published by AAAS

tive to the models, formed only the intended oligomers, and were stable at temperatures as high as 95°C.

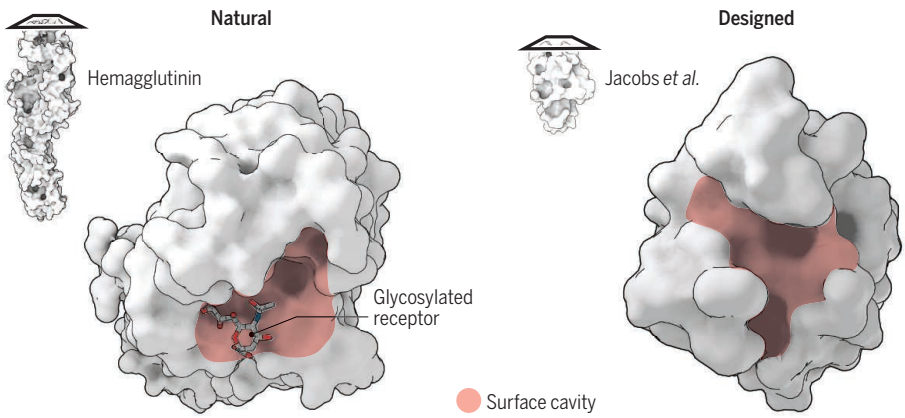
Furthermore, the hydrogen-bond networks in these oligomers were reminiscent of the simplicity and elegance of the DNA double helix, where every base on one strand is paired to a complementary base on the other through buried hydrogen bonds. Inspired by the double helix, Boyken *et al.* designed long coiled coils built from modular parts, each with its own constellation of polar side chains. These modular coiled coils may provide the basis for a new generation of protein-based molecular structures of programmable shape, similar to DNA origami. Unlike DNA, however, these assemblies could be easily interfaced with proteins of desired function.

Jacobs *et al.* address a complementary question: how to construct new proteins with features seen in protein active sites, such as cavities, long unstructured regions, and kinked helices (see the second figure). The authors first developed an algorithm (called SEWING) that generated a "parts list": thousands of backbone fragments observed in natural proteins. They then defined structural rules that determine which pairs of backbone fragments could be joined and ran computer simulations in which three or four fragments were combined and subjected to sequence optimization.

This strategy of modular design allowed Jacobs *et al.* to tap into an enormous space of potential backbones (more than 10^{16}), every fragment of which has been tested and retained by natural evolution and is therefore inherently stable. Furthermore, because each protein is built from natural fragments, the designs contain the structural idiosyncrasies observed in nature, including kinked helices and surface cavities. The authors experimentally tested 21 SEWING designs with diverse geometries, including some with cavities that could allow small-molecule binding (see the second figure). Three designs were hyperstable; moreover, the molecular structure of one of them precisely recapitulated the computational model, and another required a further round of computations to fix a design flaw.

Jacobs *et al.*'s modular design approach has natural and protein-engineering parallels; indeed, gene recombination is the main means of diversification in natural protein families and is regularly used by protein engineers (*9*). The new work extends the reach of modular design to combinations of fragments from nonhomologous proteins, for which genetic recombination is unlikely.

The remarkable selectivities and efficiencies seen in natural protein binders and enzymes require a balance between stabilizing features that specify molecular structure and functional features that are often destabilizing (*10*). Although the two studies do not attempt to design new molecular activities, they show a high level of control over biomolecular shape and interactions that brings us a step closer to realizing this goal. Future studies will show how this delicate balance between stabilizing and functional features could be leveraged to design new binding specificities and activities completely on the computer. ■



Toward designed active sites. Protein active sites often contain features such as cavities, long unstructured regions, and kinked helices. For example, a cavity on the surface of influenza hemagglutinin (wheat, PDB entry 4YY1) is used by the virus to attach to glycosylated receptors on the surface of the host cell. Jacobs *et al*. have designed novel proteins that contain features such as surface cavities (such as design CA01 shown here).

REFERENCES

1. B. Kuhlman *et al.*, *Science* **302**, 1364 (2003).
2. N. Koga *et al.*, *Nature* **491**, 222 (2012).
3. P.-S. Huang *et al.*, *Science* **346**, 481 (2014).
4. T. J. Brunette *et al.*, *Nature* **528**, 580 (2015).
5. L. Doyle *et al.*, *Nature* **528**, 585 (2015).
6. S. E. Boyken *et al.*, *Science* **352**, 680 (2016).
7. T. M. Jacobs *et al.*, *Science* **352**, 687 (2016).
8. S. J. Fleishman *et al.*, *Science* **332**, 816 (2011).
9. O. Khersonsky, S. J. Fleishman, *Protein Sci*. 10.1002/pro.2892 (2016).
10. S. Warszawski *et al.*, *J. Mol. Biol.* **426**, 4125 (2014).

10.1126/science.aaf7599

CANCER IMMUNOLOGY

The "cancer immunogram"

Visualizing the state of cancer–immune system interactions may spur personalized therapy

By **Christian U. Blank,[1,2] John B. Haanen,[1,2] Antoni Ribas,[3] Ton N. Schumacher[2]**

The impact of cancer immunotherapy on clinical cancer care is growing rapidly. However, different immunotherapies remedy distinct problems in cancer–immune system interactions. What would be the most effective therapy for an individual patient? Here, a framework is proposed for describing the different interactions between cancer and the immune system in individual cases, with the aim to focus biomarker research and to help guide treatment choice.

This "cancer immunogram" (see the figure) builds on two key observations. The outcome of cancer-immune interactions is based on a number of largely unrelated parameters such as tumor "foreignness" and T cell–inhibitory mechanisms. Furthermore, the "value" of these parameters can differ greatly between patients. For example, in some patients, intratumoral inhibition of tumor-specific T cells will be the sole defect that needs to be addressed, whereas in other patients, the tumor may simply be insufficiently foreign to elicit a clinically relevant T cell response in the first place. Because of the multifactorial nature of cancer-immune interactions, combinations of biomarker assays will by definition be required.

The proposed cancer immunogram assumes that T cell activity is the ultimate effector mechanism in human tumors. This by no means implies that inhibition of, for instance, tumor-associated macrophages, or modulation of the microbiome, is without value. Rather, the effects of such therapies are assumed to ultimately involve enhanced T cell activity. Future research will reveal whether this presumption is correct. We also acknowledge that our

[1]*Department of Medical Oncology, Netherlands Cancer Institute, Amsterdam, Netherlands.* [2]*Division of Immunology, Netherlands Cancer Institute, Amsterdam, Netherlands.* [3]*Division of Hematology/Oncology, Department of Medicine, University of California, Los Angeles, CA, USA. Email: c.blank@nki.nl; t.schumacher@nki.nl*

ILLUSTRATION: V. ALTOUNIAN/*SCIENCE*

Downloaded from http://science.sciencemag.org/ on May 5, 2016

Published by AAAS

understanding of cancer-immune interaction is still too fragmented to consider the cancer immunogram a static entity. Thus, new biomarkers are expected to be added while other biomarkers may be removed over time. Seven parameter classes may constitute a reasonable initial framework for building such an immunogram, and a brief description of these classes is provided below (*1*).

TUMOR FOREIGNNESS. The induction of T cell responses by antigen-presenting cells requires the presentation of an altered repertoire of major histocompatibility complex (MHC)–associated peptides. Such a repertoire may be formed either by tumor-derived self peptides from aberrantly expressed proteins, or by presentation of neoantigens derived from viral or mutated gene products. The outcome of a T cell–antigen encounter is modulated by T cell checkpoints such as cytotoxic T lymphocyte–associated protein 4 (CTLA-4) and programmed cell death protein 1 (PD-1).

Recent data suggest that the foreignness of human cancers may in large part be determined by their expression of neoantigens. Specifically, a correlation between mutational load—a surrogate marker for tumor neoantigen load—and outcome upon the blockage of T cell checkpoint inhibitors has been observed in melanoma and non–small cell lung cancer. The activity of PD-1 blockade in DNA mismatch repair–deficient cancers is also consistent with tumor foreignness as a determinant of anti–PD-1 immunotherapy. In addition, low intratumoral genetic heterogeneity appears associated with response to T cell checkpoint blockade, providing indirect support for a dominant role of clonal neoantigens.

Mutational load is, however, an imperfect marker for tumor foreignness, as it does not take into account a possible contribution of self antigen recognition to tumor control. Also, the formation of neoantigens from individual mutations is a probabilistic process, with each mutation representing an additional ticket in a "neoantigen lottery." Thus, although tumor foreignness can likely be guaranteed for tumors with very high mutational loads, the odds of tumor foreignness can only be inferred for tumors with an intermediate or low mutational load; more sophisticated readouts are required.

GENERAL IMMUNE STATUS. Analysis of general immune status seems mundane but will likely be of relevance in many clinical settings. A decrease in lymphocyte counts has been associated with poor outcome upon CTLA-4 blockade in melanoma patient cohorts. Furthermore, neutrophil/lymphocyte ratio has been correlated with poor patient outcome after immunotherapy, whereas elevated eosinophil counts may be associated with improved outcome in melanoma patients treated with anti–CTLA-4 antibody. In addition, myeloid-derived suppressor cell counts in circulating blood seem a negative predictor of immunotherapy outcome. Thus, simple blood analyses could characterize an immune status that is associated with poor outcome upon checkpoint modulation. Mechanistically, these correlations may reflect a reduced ability to mount or maintain a systemic tumor-specific T cell response. Alternatively, systemic immune dysfunction may simply indicate a more profound intratumoral immune inhibition. Regardless, therapies that reverse general immune dysfunction should be tested for the ability to enhance the activity of checkpoint blockade. New technologies for multidimensional measurement of immune cells and proteins are likely to yield additional parameters to gauge immune status in humans, and thereby predict capacity to respond to immunotherapeutic intervention.

"Seven parameter classes may constitute a reasonable initial framework for building such an immunogram..."

IMMUNE CELL INFILTRATION. An obvious requirement for T cell–mediated tumor control is the infiltration of tumor-reactive T cells into the tumor. Absence of such T cell infiltration into an intrinsically foreign tumor may reflect a defect at the level of T cell priming (the activation of T cells within lymphoid organs that leads to T cell proliferation), a mechanical barrier by cancer-associated fibrosis, impermeable tumor-associated vasculature, or the absence of T cell–attracting chemokines. In support of the latter, CXCL9 and CXCL10 (C-X-C motif ligands 9 and 10)—two chemokines for the receptor CXCR3—are part of a gene signature associated with improved outcome upon PD-1 blockade. More directly, a brisk preexisting $CD8^+$ T cell infiltrate is associated with improved outcome in melanoma upon anti–PD-1 immunotherapy.

The strength of the intratumoral T cell infiltrate may be a secondary consequence of other parameters of the cancer immunogram. For example, the interferon-γ (IFN-γ)–induced production of CXCL9 and CXCL10 that occurs upon recognition of tumor cells by infiltrating T cells is expected to enhance T cell recruitment in a positive feedback loop. Thus, absence of a T cell infiltrate may reflect a lack of foreignness, inefficient T cell priming, or lack of T cell attraction. Assays that can distinguish among these possibilities should be of value to guide therapy choice. In this regard, factors such as the presence of stabilized β-catenin (a transcriptional regulator) and the subset of $CD103^+$ dendritic cells deserve further attention.

ABSENCE OF CHECKPOINTS. The expression profile of both T cell checkpoints and their ligands is likely to be a valuable biomarker in many settings because it reports on the presence of specific therapeutic targets and provides information on more general aspects of the tumor-specific T cell response. In melanoma, programmed death ligand 1 (PD-L1) expression has been associated with improved outcome upon both PD-1 and CTLA-4 blockade. In the former case, the correlation may simply reflect presence of the therapeutic target. In the latter case, PD-L1 expression is likely to provide a crude measure of an ongoing tumor-specific immune response, as expression of PD-L1 can be induced by IFN-α and -γ. However, PD-L1 expression on tumor cells can also occur in an interferon-independent fashion. To further increase the value of PD-L1 as a biomarker, it will be useful to assess T cell–induced and tumor cell–intrinsic expression in clinical samples. A straightforward way to achieve this may be to combine analyses of PD-L1 expression on tumor cells with interferon expression, or with the expression of markers of the activation-exhaustion cascade in tumor-resident T cells.

ABSENCE OF SOLUBLE INHIBITORS. Tumor inflammation-associated factors can promote tumor progression. Such inflammation is characterized by the presence of subtypes of neutrophils, γδ cells, and macrophages that secrete proinflammatory factors, such as vascular endothelial growth factor A, colony-stimulating factors, the interleukins IL-1, IL-6, and IL-17, and CXCL1. IL-1 and IL-6 induce C-reactive protein (CRP), a clinical marker for tumor-associated inflammation. Mouse model data have shown that tumor-derived prostaglandin E2 can promote an inflammatory response characterized by IL-6, CXCL1, and granulocyte colony-stimulating factor secretion. Blockade of melanoma prostaglandin E2 production shifted the local environment to a type I IFN-dominated "T cell inflamed" state, resulting in improved T cell–medi-

Downloaded from http://science.sciencemag.org/ on May 5, 2016

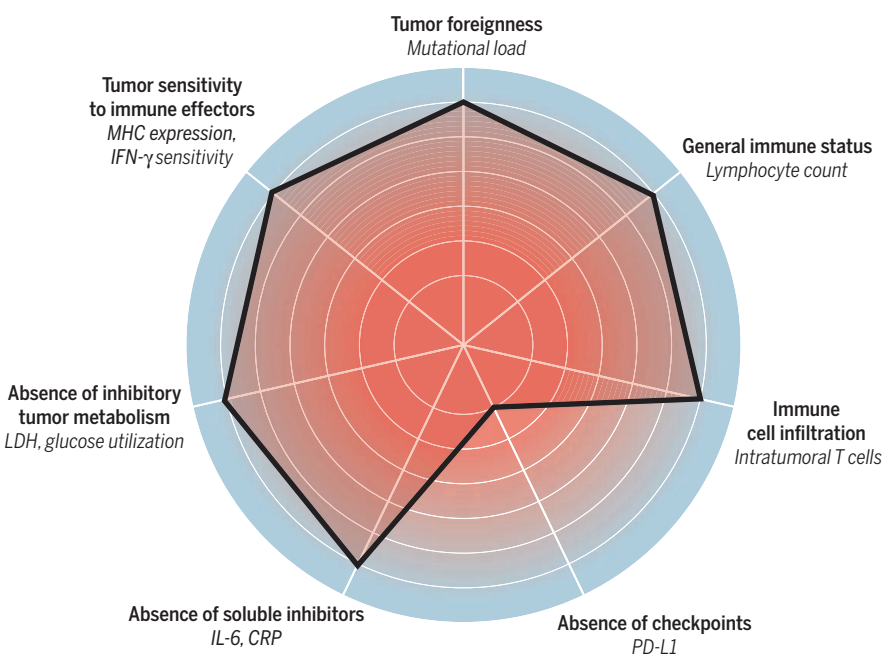
Published by AAAS

ated tumor control. These data support the notion that the tumor-promoting effects of tumor-associated inflammation can be mediated through suppression of T cell reactivity. In line with this work, increase in inflammatory markers [CRP or erythrocyte sedimentation rate (ESR)] is associated with poor outcome upon anti–CTLA-4 antibody treatment, whereas the presence of an interferon gene signature in tumors was associated with improved outcome upon PD-1 blockade. Along with many other candidates, another soluble inhibitory factor that is likely to have value as a biomarker is indoleamine 2,3-dioxygenase, which interferes with anti–CTLA-4 antibody–induced tumor control in mice.

ABSENCE OF INHIBITORY TUMOR METABOLISM. In healthy cells, glycolysis generally results in entry of pyruvate into the Krebs cycle in the mitochondria. Under conditions of hypoxia (e.g., in muscles during exercise), pyruvate is converted to lactate by lactate dehydrogenase (LDH) and pumped out of the cell. In cancer cells, however, the conversion of pyruvate into lactate takes place even in the presence of sufficient oxygen. High serum LDH concentrations correlate strongly with poor outcome upon CTLA-4 and PD-1 blockade, and phase 3 clinical trial data have corroborated these results prospectively. Lactic acid and low local pH can impair crucial T cell functions, such as cytokine production (IL-2, IFN-γ), proliferation, and lytic activity, perhaps providing a mechanistic explanation for the strength of LDH as a biomarker. On the basis of mouse model data, intratumoral hypoxia and glucose depletion also deserve attention as potential biomarkers in this class.

"...a cancer immunogram... does make it possible to... discuss treatment options in a more refined and personalized manner..."

TUMOR SENSITIVITY TO IMMUNE EFFECTORS. Reduced "visibility" for the immune system and resistance to T cell killing are accepted mechanisms of cancer immune evasion in preclinical models, and inactivation of components of the antigen presentation machinery has been observed in human cancer. Upon inactivation of antigen presentation machinery components, tumors may still be perceived as foreign through cross-presentation of tumor cell–derived antigens by antigen-presenting cells, but the final stage of tumor cell recognition will be affected. No studies have yet linked MHC expression or defects in apoptosis mechanisms to clinical outcome upon CTLA-4 or PD-1 blockade. Analysis of immunotherapy resistance at the level of tumor cell sensitivity to immune effectors will not only be useful to identify patients who are less likely to respond to T cell–activating therapies, but should also point to the T cell effector mechanisms that exert the greatest Darwinian pressure in human cancers. In particular, although tumor control by T cells is often interpreted as classical perforin- and granzyme-mediated lysis, mouse model data also suggest a role of T cell effector cytokines such as IFN-γ and tumor necrosis factor–α on either tumor stroma or cancer cells themselves.



The cancer immunogram. The radar plot depicts the seven parameters that characterize aspects of cancer-immune interactions for which biomarkers have been identified or are plausible. Potential biomarkers for the different parameters are shown in italics. Desirable states are located in blue; progressively undesirable states are shown in the red gradient. The black line connecting the data values for each parameter represents a plot for a single hypothetical patient. In the case shown, it may be argued that single-agent PD-1 blockade, rather than combined PD-1 and CTLA-4 blockade, could be a first treatment of choice. For details on this case and other hypothetical patient cases, see (*2*).

OUTLOOK. The described cancer immunogram suggests that it may be valuable to ask the following questions: Can the immune system see this tumor as foreign? Is the immune status of the patient likely to be sufficient? Is there evidence for infiltration of effector T cells into the tumor site? Are there checkpoints, soluble mediators, or metabolic factors that may hamper the activity of these cells? Would the tumor cells be sensitive to an unleashed T cell response? The information required for this analysis may be obtained from the combination of tumor genomics, immunohistochemistry, and standard assays on the peripheral blood compartment. Such measurements will be useful to determine which states of the cancer immunogram are most commonly inhabited, both during natural cancer-immune interaction and upon immunotherapy.

Certainly, a cancer immunogram should evolve, incorporating new biomarkers that reflect, for example, the capacity for T cell priming. Nonetheless, even a cancer immunogram based on present-day knowledge does make it possible to visualize the state of cancer-immune interactions in individual patients, and thereby discuss treatment options in a more refined and personalized manner (*2*). ■

REFERENCES AND NOTES

1. References for each subsection can be found in the supplementary materials.
2. Examples of hypothetical patient cases and potential treatment options can be found in the supplementary materials.

SUPPLEMENTARY MATERIALS

www.sciencemag.org/content/352/6286/658/suppl/DC1

10.1126/science.aaf2834

GRAPHIC: A. CUADRA/*SCIENCE*

Downloaded from http://science.sciencemag.org/ on May 5, 2016

Published by AAAS



Improving child health. Better access to medical care may be contributing to sizable decreases in mortality rates among children in disadvantaged counties in the United States. The photo shows 5-year-old Oscar de la Cruz getting an eye exam at the nonprofit Mary's Center in Washington, D.C., on 24 February 2014.

PHOTO: LINDA DAVIDSON/*THE WASHINGTON POST* VIA GETTY IMAGES

CHILD HEALTH

Hope for America's next generation

The gap in survival rates for children in the richest and poorest U.S. communities has shrunk

By **Martha J. Bailey** *and* **Brenden Timpe**

A deluge of recent studies has shown that poorer communities suffer worse health outcomes. Among low-income Americans, life expectancy at age 40 in the poorest areas of the U.S. is 4.5 years lower than in the highest-income areas (*1*). In 2010, infant mortality rates in the poorest U.S. communities were over 70% higher than those in the most affluent ones [see tables S3 and S4 in (*2*)]. On page 708 of this issue, Currie and Schwandt paint a more complicated but encouraging picture (*2*). They show that, despite rising inequality in almost every dimension of American life, the child mortality gap between the poorest and the richest counties has shrunk in recent decades.

Department of Economics and Population Studies Center, University of Michigan, Ann Arbor, MI, USA.
Email: baileymj@umich.edu

The authors find that between 1990 and 2010, life expectancy at birth rose for both women and men in communities across the United States. Mortality rates in all 5-year age groups of American children, from infants to late adolescents, fell dramatically. Perhaps more surprisingly, the poorest counties saw the largest absolute decreases in child mortality rates, almost twice as large as those in the richest counties. These important findings challenge the conventional wisdom that health has been uniformly worsening in more disadvantaged communities. They also challenge the idea that further increases in longevity in wealthy countries depend only on improvements among the middle-aged or elderly (*3*).

In their study, Currie and Schwandt calculate mortality rates of 5-year age groups and compare counties with different poverty rates. This method picks up nuances in U.S. health trends that are not captured by national life expectancy, a standard but relatively crude measure of health. It also allows them to zoom in on changes at different points in the age distribution and in counties across the country. Of course, the results do not imply that poverty causes shorter lives. They should be seen as demonstrating a relationship between income and health, rather than as a statement that one causes the other.

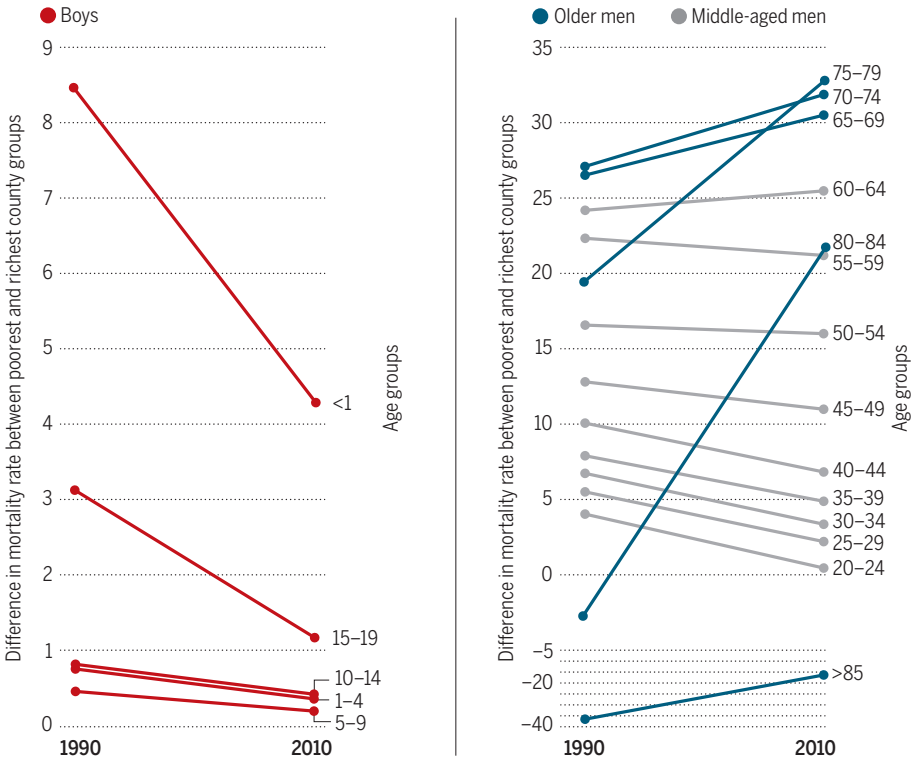
The good news is the persistent gains in life expectancy that young Americans have experienced in the last 20 years, even as economic and health inequality among their parents and grandparents has grown. Economists do not always agree on how economic conditions affect health (*4*). Still, readers may not find it surprising that child mortality rates fell sharply during the economic boom of the 1990s. It may be more surprising that child mortality rates continued to fall over the next decade, even though the U.S. economy shed 8 million jobs and the number of Americans without health insurance rose by 5.7 million between 2007 and 2010 (*5, 6*).

Downloaded from http://science.sciencemag.org/ on May 5, 2016

Published by AAAS

The Generational Divide

Between 1990 and 2010, child mortality rates fell fastest in the poorest areas of the United States, narrowing the gap between high-poverty and low-poverty counties. This trend (left) is an encouraging counterpoint to the growing mortality-rate gap among older Americans (right). Data from table S3 in (*2*).



The scale of these improvements in the most disadvantaged places in the country is impressive. Consider Genesee County, Michigan, home to the city of Flint and one of the poorest U.S. counties. Between 1990 and 2010, the county's poverty rate rose from 16 to 20%. At the same time, the 3-year moving average of infant mortality rates fell by five children per 1000 born to 7.8. In nearby Oakland County, home to more affluent Detroit suburbs with a poverty rate of ~10%, infant mortality fell by a smaller but still impressive two children per 1000 births to 5.8. This more than halved the gap from five to two deaths per 1000 births. As Currie and Schwandt show, this pattern held in almost all counties in the United States and for all groups of children under 20, resulting in much reduced disparities in child mortality (see the figure).

Not all their results are as encouraging. Corroborating recent studies (*2, 7*), the authors show that mortality trends are less favorable for Americans over age 40. Improvements in older-adult health have been much larger in more affluent areas, reflecting a growing mortality gap among older adults.

Currie and Schwandt are largely silent on the causes of these changes. Although it is unlikely that they can be attributed to a single factor, the different trends in children and adults help narrow the search. Oft-cited explanations for growing adult health disparities include the scarcity of good jobs, rising income inequality, deteriorating infrastructure, and worsening health behaviors (including lack of exercise, smoking, and opioid abuse). Some argue that this toxic cocktail is killing working-age Americans (*2, 7*). This makes the improvement in mortality among young Americans all the more impressive, because child health is adversely affected by many of the same factors (*8, 9*).

More promising explanations relate to the substantial expansions in public health programs for children over the past 25 years. The expansion of Medicaid—a program shoring up health insurance in the most disadvantaged areas—is associated with significant declines in infant mortality (*10*). Expansions of the State Children's Health Insurance Program may also have disproportionately improved health in poorer areas (*11*). Similarly, expansion of programs like Community Health Centers would have benefited poor communities most (*12*). These improvements in health care access amplified the impact of advances in medical care and health information over the same period (such as the treatment of congenital defects and prevention of sudden infant death syndrome).

Whatever the cause of the decline in health inequality among children, improved child survival has implications for the interpretation of mortality trends at older ages. The logic is simple: If the health of the children who are saved tends to be more fragile, this could result in higher death rates at older ages. For instance, the surviving children may be more likely to die in their 40s. This "selection" process—to use the language of economists—would predict modest increases in mortality rates at older ages, even though some children lived longer. Rising mortality rates for 45- to 55-year-olds may thus be at least partially attributable to gains in longevity among children 40 to 50 years ago (*13*), as well as among younger adults more recently.

Even better news is that patterns in health inequality seem to be changing for the better. Infants born in the most disadvantaged counties in 2000 were much more likely to survive than those born in 1990. Ten years later, in 2010, the mortality rates for the same cohorts were still much lower than those of the previous generation. If these declines in mortality persist, they will represent a powerful new trend with important policy implications. So far, at least, the new generation of Americans is defying the pattern of growing inequality that has defined their parents' and grandparents' generations. ■

REFERENCES AND NOTES

1. R. Chetty, M. Stepner, S. Abraham, *J. Am. Med. Assoc.* 10.1001/jama.2016.4226 (2016).
2. J. Currie, H. Schwandt, *Science* **352**, 708 (2016).
3. A. Deaton, *The Great Escape: Health, Wealth, and the Origins of Inequality* (Princeton Univ. Press, 2013), p. 123.
4. D. L. Miller, M. E. Page, A. H. Stevens, M. Filipski, *Am. Econ. Rev.* **99**, 122 (2009).
5. J. Holahan, V. Chen, *Changes in Health Insurance Coverage in the Great Recession, 2007–2010* (Kaiser Commission on Medicaid and the Uninsured, 2011).
6. Bureau of Labor Statistics, U.S. Department of Labor, *Employment, Hours, and Earnings from the Current Employment Statistics Survey*, see http://data.bls.gov/pdq/SurveyOutputServlet?request_action=wh&graph_name=CE_cesbref1.
7. A. Case, A. Deaton, *Proc. Natl. Acad. Sci. U.S.A.* **112**, 15078 (2015).
8. D. Almond, J. Currie, in *Handbook of Labor Economics*, O. Ashenfelter, D. Card, Eds. (Elsevier, Maryland Heights, MO, 2011), vol. 4B, pp. 1315–1486.
9. A. Case *et al.*, *Am. Econ. Rev.* **92**, 1308 (2002).
10. J. Currie, J. Gruber, *Q. J. Econ.* **111**, 431 (1996).
11. L. R. Wherry, S. Miller, R. Kaestner, B. D. Meyer, "Childhood Medicaid coverage and later life health care utilization," NBER Working Paper 20929 (2015).
12. M. J. Bailey, A. Goodman-Bacon, *Am. Econ. Rev.* **105**, 1067 (2015).
13. M. F. MacDorman, H. M. Rosenberg, *Trends in Infant Mortality by Cause of Death and Other Characteristics, 1960–88* (National Center for Health Statistics, Hyattsville, MD, 1993).

ACKNOWLEDGMENTS

We gratefully acknowledge the use of the services and facilities of the Population Studies Center (PSC) at the University of Michigan (R24 HD041028). During work on this project, B.T. was supported by the NIA as a PSC Trainee (T32 AG000221) and by the NICHD (R01 HD070950-02).

10.1126/science.aaf7270

GRAPHIC: C. SMITH/*SCIENCE*

Downloaded from http://science.sciencemag.org/ on May 5, 2016

Published by AAAS

SCIENTIFIC WORKFORCE

Why pursue the postdoc path?

Complex, diverse rationales require nuanced policies

By **Henry Sauermann**[1,2*] *and* **Michael Roach**[3]

POLICY

Concerns have been raised about labor market imbalances that see a growing number of postdoctoral researchers pursuing a limited number of faculty positions (*1*–*4*). Proposed demand-side solutions include capping the duration of postdoc training or hiring more permanent staff scientists (*1*, *4*, *5*). Others focus on the supply side, arguing that Ph.D.'s need better information about labor market conditions and nonacademic career options (*4*, *6*, *7*). Unfortunately, it is not clear why Ph.D. students pursue postdoc positions and how their plans depend on individual-level factors, such as career goals or labor market perceptions. We describe evidence of a "default" postdoc and of "holding patterns" that suggest a need for increased attention to career planning among students, their mentors, graduate schools, and funders.

We surveyed Ph.D. students at 39 research-intensive U.S. universities in the spring of 2010 and again in the spring of 2013. We also used online sources to hand-collect information on respondents' career outcomes. Details on survey strategy, sample characteristics, and measures are provided in the supplementary materials (SM, tables S1 to S3). We focus on 5928 respondents who, in 2010, were enrolled in Ph.D. programs in the biological and life sciences (37.47%), chemistry (11.23%), physics (14.27%), engineering (27.14%), and computer sciences (9.89%). Our featured analyses distinguish broadly between biological and life sciences and other fields; see SM for more detailed field comparisons (fig. S1 and table S3).

GOALS, INFORMATION, ABILITY. In 2010, ~79% of students in the biological and life sciences and 53% in other fields planned a postdoc. We examine how students' plans relate to three key factors: career goals, information about labor market demand, and proxies for ability. It is often assumed that Ph.D.'s do a postdoc primarily as a pathway to a research-oriented faculty position (*4*, *8*). We asked respondents to ignore job availability and rate the attractiveness of different academic and nonacademic career paths (see SM). Students planning a postdoc are more likely to have academic career goals (see the first figure). However, career goals are quite diverse even among these postdoc-planning students, with more than one-third not rating a research-oriented faculty position as their most attractive career. This may be surprising, given that the postdoc is not typically considered a stepping-stone toward nonacademic careers. However, 78% of respondents in the biological and life sciences and 42% in other fields believed that at least 1 year of postdoc training was required for a Ph.D.-level research and development (R&D) position in industry in their field (see SM). Unfortunately, there is little empirical evidence showing whether the postdoc benefits graduates pursuing nonacademic careers (*1*).

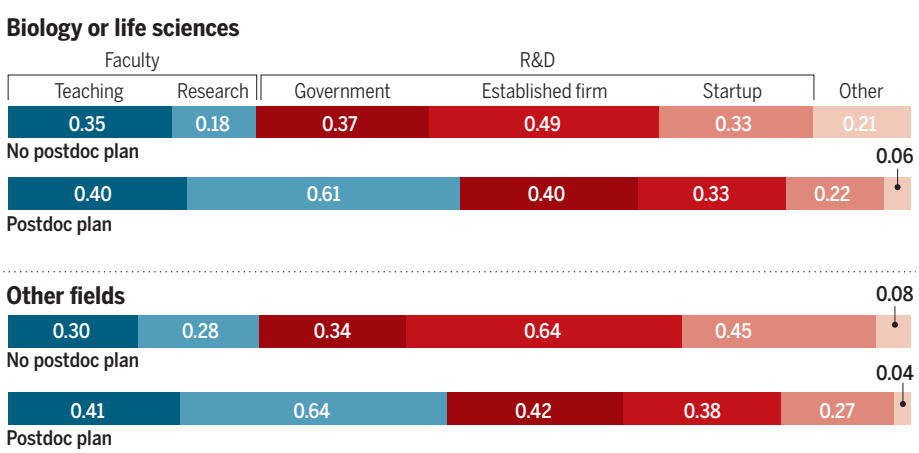
Postdoc plans may also depend on the perceived demand for full-time researchers. Limited job availability may discourage individuals from investing in low-paid postdoc training if the chances of obtaining full-time positions that reward this training are slim (*9*). On the other hand, challenging labor markets may encourage students to pursue a postdoc in order to become more competitive. We found that perceived job availability in academia and industry has no systematic relation with postdoc plans (tables S4 and S5). However, students' beliefs regarding how many years of postdoc are required to get a full-time position in their preferred sector—likely higher when the supply of graduates exceeds demand—are a strong predictor of postdoc plans.

If high-ability scientists have a greater chance of securing scarce full-time positions, they face a lower risk of "wasting" time in a postdoc and should be more likely to plan one. On the other hand, they may feel less of a need to increase their market value through postdoctoral training. To examine the role of ability, we used three objective proxies: respondents' peer-reviewed publications, fellowships from a federal agency, and their Ph.D. program's National Research Council (NRC) ranking. Respondents also subjectively assessed their research ability relative to peers. Biological and life scientists with higher scores on all measures are more likely to plan a postdoc (table S4). Fellowships, NRC ranking, and subjective ability also predict postdoc plans in other fields. This partly reflects that higher-ability students are more likely to aspire to faculty positions (see SM).

Only 62% of biological and life sciences students (56% in other fields) reported having thought about their careers to a large or great extent. Those who had thought more about their careers are less likely to plan a postdoc, especially in the biological and life sciences (table S4). This may reflect that many students see a postdoc as the "default" until they explicitly consider their long-term career paths (*4*). Advanced students are less likely to plan a postdoc, consistent with learning processes and a declining interest in faculty careers over time (*10*, *11*). Foreign students who are unsure whether to stay in the United States after graduation are more likely to plan a postdoc than those intending

Students' highest-rated careers

Share of students giving a particular career their highest attractiveness rating, putting job availability aside (careers rated independently, ties possible). *N* = 5911.



GRAPHIC: C. SMITH/*SCIENCE*

[1]*Scheller College of Business, Georgia Institute of Technology, Atlanta, GA 30308, USA.* [2]*National Bureau of Economic Research, Cambridge, MA 02138, USA.* [3]*Dyson School of Applied Economics and Management, Cornell University, Ithaca, NY 14853, USA.* **Email: henry.sauermann@scheller.gatech.edu*

Downloaded from http://science.sciencemag.org/ on May 5, 2016

Published by AAAS

to leave, perhaps because the postdoc keeps options open (table S5). Respondents who agreed to the statement "When I fail in something, I am determined to continue trying until I succeed" are more likely to plan a postdoc, which indicates that "persistence" may be important not just for scientific productivity (*12*) but also for career decisions.

CAREERS AND MARKETS. Of students who graduated by 2013, 74% took a postdoc in the biological and life sciences, compared with 46% in other fields (fig. S2). We asked postdoc respondents to the 2013 survey (N = 1006) why they did a postdoc. The most frequent reason was "A postdoc increases the chance to get my desired job." Among those without postdoc plans in 2010, the most frequent reason was "I experienced difficulty finding another job" (fig. S3). In conjunction with our earlier results, these patterns suggest that low demand for full-time researchers leads many students to plan postdoc training well before graduation, but also forces some into unplanned postdoc "holding patterns" afterwards (*13*). The observed transitions into postdocs were likely facilitated by plentiful positions (*4*), and demand for postdoc trainees may have been particularly strong because of funding from the 2009 American Recovery and Reinvestment Act.

14.75%
Respondents' estimate of the share of biological or life science Ph.D. graduates holding a tenure-track position 5 years after graduation

14.30%
Actual share reported by NSF 2012

10.60%
Actual share reported by NSF 2016

When asked whether they started the postdoc primarily to obtain a tenure-track faculty position, 60% of bio-life scientists and 51% of other scientists answered yes. When asked about their single most preferred career, 43% of respondents in the biological and life sciences and 44% in other fields chose faculty with a focus on research, but the majority preferred other career paths (fig. S4).

A common concern is that junior scientists—especially those aspiring to faculty positions—lack information about career prospects in academia (*1*, *9*, *14*). We asked respondents to estimate the share of Ph.D.'s in their field who hold a tenure-track position 5 years after graduation and compared their estimates with actual shares published in the Science and Engineering Indicators (*15*). Respondents are very accurate (see the box above and fig. S5), although more recent actual shares in the biological and life sciences have dropped below their expectations.

Given that not all Ph.D.'s aspire to faculty positions, graduates who actively pursue this path have a higher probability of becoming faculty than the population average (see SM). We asked postdocs who aspire to faculty positions to estimate the probability of their holding a tenure-track position 5 years after graduation. We see evidence of overconfidence among postdocs in the biological and life sciences but not in chemistry or physics (table S6). Overall, postdocs have a good sense of conditions in the academic labor market, although some may be overconfident regarding their own chances of securing a faculty position.

Finally, only 4% of biological and life sciences postdocs felt a "severe lack of information" regarding careers in academic research, but that share increased to 21% for research careers in government, 34% in established firms, 42% in startups, and 44% for nonresearch careers. Corresponding figures in other fields are not much lower (table S3), which suggests that a substantial share of junior scientists proceeded to the postdoc stage without sufficient information to evaluate nonacademic career options.

BETTER DATA, BETTER PLANNING. Many students plan postdocs yet do not aspire to the tenure track. A large share of postdocs prefers careers outside of academia. Thus, comparing numbers of graduates or postdocs to available faculty positions provides limited insight into labor market imbalances. Our results give urgency to the National Academies' (*4*) recommendation to collect better data on junior scientists' career aspirations, which would enable more nuanced comparisons of career goals and outcomes. Many graduates pursue a postdoc with the goal to obtain nonacademic positions, which highlights the need for data on whether and how nonacademic employers require and reward postdoctoral training (*4*, *16*).

We find that challenging labor markets encourage rather than discourage students to invest in postdoctoral training. Although this seems logical if students are strongly committed to a particular career, it provides an individual-level explanation for why the supply of postdocs does not decrease despite low demand for full-time researchers (*13*) and potentially contributes to persistent labor market imbalances (*9*, *14*). Whereas the recent National Academies report recommends that students make career plans early in the Ph.D. program, we argue that they should consider labor market conditions and career options before starting a Ph.D. program. Doing so may avoid escalating commitment to a research career and may prevent individuals from entering a postdoc holding pattern. Graduate schools could encourage career planning by requiring that applicants analyze different career options and justify why a Ph.D. is the most promising path forward. Funding agencies could implement similar requirements, especially in conjunction with moving a larger share of funding from research grants to training grants and individual fellowships (*4*, *5*).

Postdocs know that only a small share of graduates will obtain a faculty position, and warnings about limited job prospects in academia may have little impact on decisions to pursue postdocs and academic research. However, junior scientists require better information on nonacademic careers, consistent with concerns expressed by the National Academies and the National Institutes of Health (*4*, *6*). This holds in the biological sciences and in other fields. Better career information should come from advisers but also from sources such as postdoc offices, professional associations, or internships and experiential career development opportunities (e.g., as part of NIH's BEST program). Just as important, students need to actively access and process the available information and seriously consider the implications for their own careers (*4*, *7*). ■

REFERENCES AND NOTES

1. P. Stephan, *BioScience* **63**, 245 (2013).
2. K. Powell, *Nature* **520**, 144 (2015).
3. NRC, *Trends in the Early Careers of Life Scientists* (National Academy Press, Washington, DC, 1998).
4. National Academies, *The Postdoctoral Experience Revisited* (National Academy Press, Washington, DC, 2014).
5. B. Alberts, M. W. Kirschner, S. Tilghman, H. Varmus, *Proc. Natl. Acad. Sci. U.S.A.* **111**, 5773 (2014).
6. Biomedical Research Workforce Working Group, "Report of the NIH Advisory Committee to the Director" (NIH, Bethesda, MD, 2012).
7. G. S. McDowell *et al.*, *F1000Research* **3**, 291 (2014).
8. D. Cyranoski, N. Gilbert, H. Ledford, A. Nayar, M. Yahia, *Nature* **472**, 276 (2011).
9. M. S. Teitelbaum, *Science* **321**, 644 (2008).
10. H. Sauermann, M. Roach, *PLOS One* **7**, e36307 (2012).
11. K. D. Gibbs, J. McGready, K. Griffin, *CBE Life Sci. Educ.* **14**, ar44 (2015).
12. J. Hermanowicz, *Sci. Technol. Hum. Values* **31**, 135 (2006).
13. P. E. Stephan, J. Ma, *Am. Econ. Rev.* **95**, 71 (2005).
14. R. Freeman, E. Weinstein, E. Marincola, J. Rosenbaum, F. Solomon, *Science* **294**, 2293 (2001).
15. National Science Board, *Science and Engineering Indicators 2016* (National Science Foundation, Arlington, VA, 2016).
16. K. Kaplan, *Nature* **483**, 499 (2012).

ACKNOWLEDGMENTS

We are grateful for support through NSF grant SMA1262270 and from the Ewing Marion Kauffman Foundation. Any opinions, findings, and conclusions or recommendations expressed in resulting materials are those of the authors and do not necessarily reflect the view of the funding agencies. A public-use limited version of the data is available (see SM for details) at http://dx.doi.org/10.7910/DVN/DHSM1F.

SUPPLEMENTARY MATERIALS

www.sciencemag.org/content/352/6286/663/suppl/DC1

10.1126/science.aaf2061

Published by AAAS

Downloaded from http://science.sciencemag.org/ on May 5, 2016

LETTERS

Edited by **Jennifer Sills**

After Fukushima: Collaboration model

THE MARCH 2011 accident at the Fukushima Daiichi Nuclear Power Plant caused extensive human suffering and revealed the need for more effective means of communicating health risks to the public ("Epidemic of fear," D. Normile, News Feature, 4 March, p. 1022). The rehabilitation of Kawauchi, one of the villages affected by the nuclear accident, provides a model for future responses.

In March 2012, after tedious decontamination work in the village, radiation doses were found to be safe for residents of Kawauchi to return home, and schools and public offices were reopened. In 2013, the public authorities of Kawauchi village and Nagasaki University, which has helped with the reconstruction work since 2011, established a collaboration known as the "Nagasaki University–Kawauchi Village Reconstruction Promotion Base" (*1*). As part of the program, a permanent public health nurse from Nagasaki University with expertise in radiation provides health consultations to the villagers (*2*). The university also provides health radiation consultation services and monitors radiation levels in food and soil samples (*3*, *4*). Regular meetings are held in the village to foster greater dialogue between the radiation experts, physicians, radiation nurses, and community leaders of Kawauchi village and its population.

Almost 100,000 residents of Fukushima have yet to return to their hometowns, with 40,000 of them living outside the prefecture (*5*). The village-university collaboration provides a model for a multidisciplinary approach to public policy during the recovery phase of a nuclear accident.

Noboru Takamura,[1]* Makiko Orita,[1] Shunichi Yamashita,[1] Rethy Chhem[1,2]

[1]Atomic Bomb Disease Institute, Nagasaki University, Nagasaki, 852-8523 Japan. [2]Cambodia Development Resource Institute, Phnom Penh 622, Cambodia.

*Corresponding author. Email: takamura@nagasaki-u.ac.jp

REFERENCES

1. Nagasaki University, Atomic Bomb Disease Institute, Bases or Research and Education, "Nagasaki University–Kawauchi Village Reconstruction Promotion Base" (www-sdc.med.nagasaki-u.ac.jp/abdi/bases/kawauchi_e.html).
2. M. Orita *et al.*, *Radiat. Prot. Dosimetry* **156**, 383 (2013).
3. M. Orita *et al.*, *PLOS ONE* **10**, e0129227 (2015).



Holding a bonsai plant grown while evacuated, a Kawauchi resident returns to his home.

4. K. Nakashima *et al.*, *Peer J.* **3**, e2417 (2015).
5. Fukushima Prefecture, "Transition of evacuation instruction zones (updated: transition of evacuees)" (www.pref.fukushima.lg.jp/site/portal-english/en03-08.html).

After Fukushima: Creating a dialogue

FIVE YEARS HAVE passed since the accident at the Fukushima Daiichi Nuclear Power Plant. Although the additional exposure doses resulting from the accident were extremely low (*1*), it was difficult to dispel residents' fear of radiation exposure ("Epidemic of fear," D. Normile, News Feature, 4 March, p. 1022) and other health issues. To address their concerns, we and others have provided a variety of services to increase understanding between residents and medical professionals.

We have held more than 500 general health consultations, which connect Fukushima residents with health experts from universities. The experts discuss individual residents' health concerns and symptoms privately and then help coordinate integrated care to promote health and prevent disease. Through these social services, we aim to help dispel apprehensions among the evacuees and residents (*2*).

Other local medical professionals and experts have held a series of seminars to open and sustain a dialogue with residents (*3*). The municipality of Date City, which has various levels of contaminated areas, has used feedback about the experiences shared in these seminars to modify their administrative measures and policies and assign staff to explain the personal dosimeter measurement results to individual residents. They also carried out multiple projects to provide mental and physical care for small groups of residents. These activities were implemented based on advice of experts who were by the side of the residents. By putting a liaison in place, medical professionals and experts have transformed a unilateral communication about the risk of radiation into an actively bilateral communication to address the various needs for residents after the accident.

Evacuees have been gradually returning to their homes since the designation of evacuation areas was lifted in Fukushima. At this time, they feel anxious about radiation exposure and life in their new environment. Integrated health systems and community dialogues should continue to provide the returning residents with the support they need.

Makoto Miyazaki,[1] Koichi Tanigawa,[2]* Michio Murakami[3]

[1]Department of Radiation Health Management, Fukushima Medical University, Fukushima, 960-1295, Japan. [2]Fukushima Global Medical Science Center, Fukushima Medical University, Fukushima, 960-1295, Japan. [3]Department of Risk Communication, Fukushima Medical University, Fukushima, 960-1295, Japan.

*Corresponding author. Email: tanigawa@fmu.ac.jp

REFERENCES

1. S. Nagataki *et al.*, *Radiat. Res.* **180**, 439 (2013).
2. M. Miyazaki, "Yorozu health consultation project," 4th International Expert Symposium in Fukushima (2015); http://fmu-global.jp/?wpdmdl=605.
3. International Commission on Radiological Protection, ICRP and Fukushima ICRP Dialogue Initiative (www.icrp.org/page.asp?id=189).

After Fukushima: Addressing anxiety

IN HIS NEWS Feature "Epidemic of fear" (4 March, p. 1022), D. Normile described the thyroid ultrasound examination program that launched in the aftermath of the Fukushima accident. He discussed the unexpected number of positive results and the potential for overtreatment, given that the natural history of thyroid cancer in children is unclear.

Despite these uncertainties, residents from Fukushima tend to directly associate examination results to their radiation exposure (*1*). They often associate their own decisions immediately after the accident (such as whether or when to evacuate, where to permit children to play, and what to permit children to eat or drink) with the appearance of nodules on the ultrasound.

PHOTO: KYODO

Downloaded from http://science.sciencemag.org/ on May 5, 2016

Published by AAAS

In particular, mothers have developed new anxieties and feelings of self-condemnation (*2*). We highlight two strategies that could help to minimize these reactions.

First, examination results are normally provided to the examinees in written form, but we individually explained the results immediately after each examination. Our objectives were to relieve the anxieties regarding the results; to address vague concerns regarding radiation health risks; and to explain the meaning of the thyroid screening.

Second, we provided classes on thyroid examinations to the school children (from 10 to 18 years old) who were examined. We explained the associations between radiation and thyroid cancer and helped the children interpret the examination results. The decision-making about examinations often reflected the concerns of the parents rather than those of the children. Through these classes, we tried to provide the children with opportunities to think about the benefits and limitations of the screening and to prepare them for discussions with their parents about radiation health risks.

Sanae Midorikawa,[1,2]* Satoru Suzuki,[1,3] Akira Ohtsuru[1,2]

[1]Radiation Medical Science Center, Fukushima Medical University, Fukushima, 960-1295, Japan. [2]Department of Radiation Health Management, Fukushima Medical University, Fukushima, 960-1295, Japan. [3]Department of Thyroid and Endocrinology, Fukushima Medical University, Fukushima, 960-1295, Japan.

*Corresponding author. Email: hana@fmu.ac.jp

REFERENCES

1. Y. Suzuki *et al.*, *Bull. World Health Org.* **93**, 598 (2015).
2. A. Ohtsuru *et al.*, *Lancet* **386**, 489 (2015).

TECHNICAL COMMENT ABSTRACTS

Comment on "Cycling Li-O_2 batteries via LiOH formation and decomposition"

Yue Shen, Wang Zhang, Shu-Lei Chou, Shi-Xue Dou

Liu *et al.* (Research Article, 30 October 2015, p. 530) described a lithium-oxygen (Li-O_2) battery based on lithium iodide (LiI)–assisted lithium hydroxide (LiOH) formation and decomposition. We argue that LiOH cannot be oxidized by tri-iodide (I_3^-). The charge capacity is from the oxidation of I^- instead of LiOH. The limited-capacity cycling test is misleading when the electrolyte contributes considerable parasitic reaction capacity. Full text at http://dx.doi.org/10.1126/science.aaf1399

Response to Comment on "Cycling Li-O_2 batteries via LiOH formation and decomposition"

Tao Liu, Gunwoo Kim, Javier Carretero-González, Elizabeth Castillo-Martínez, Clare P. Grey

We described a lithium-oxygen (Li-O_2) battery comprising a graphene electrode, a dimethoxyethane-based electrolyte, and H_2O and lithium iodide (LiI) additives, lithium hydroxide (LiOH) being the predominant discharge product. We demonstrate, in contrast to the work of Shen et al., that the chemical reactivity between LiOH and the triiodide ion (I_3^-) to form IO_3^- indicates that LiOH can be removed on charging; the electrodes do not clog, even after multiple cycles, confirming that solid products are reversibly removed. Full text at http://dx.doi.org/10.1126/science.aaf1652

Comment on "Cycling Li-O_2 batteries via LiOH formation and decomposition"

Venkatasubramanian Viswanathan, Vikram Pande, K. M. Abraham, Alan C. Luntz, Bryan D. McCloskey, Dan Addison

Based on a simple thermodynamic analysis, we show that iodide-mediated electrochemical decomposition of lithium hydroxide (LiOH) likely occurs through a different mechanism than that proposed by Liu *et al.* (Research Article, 30 October 2015, p. 530). The mismatch in thermodynamic potentials for iodide/triiodide (I^-/I_3^-) redox and O_2 evolution from LiOH implies a different active iodine/oxygen electrochemistry on battery charge. It is therefore possible that the system described in Liu *et al.* may not form the basis for a rechargeable lithium-oxygen (Li-O_2) battery. Full text at http://dx.doi.org/10.1126/science.aad8689

Response to Comment on "Cycling Li-O_2 batteries via LiOH formation and decomposition"

Tao Liu, Gunwoo Kim, Javier Carretero-González, Elizabeth Castillo-Martínez, Paul M. Bayley, Zigeng Liu, Clare P. Grey

Lithium-oxygen (Li-O_2) batteries cycle reversibly with lithium iodide (LiI) additives in dimethoxyethane (DME) to form lithium hydroxide (LiOH). Viswanathan *et al.* argue that because the standard redox potential of the four-electron (e^-) reaction, $4OH^- \leftrightarrow 2H_2O + O_2 + 4e^-$, is at 3.34 V versus Li^+/Li, LiOH cannot be removed by the triiodide ion (I_3^-). However, under nonaqueous conditions, this reaction will occur at a different potential. LiOH also reacts chemically with I_3^- to form IO_3^-, further studies being required to determine the relative rates of the two reactions on electrochemical charge. Full text at http://dx.doi.org/10.1126/science.aad8843

Published by AAAS

Downloaded from http://science.sciencemag.org/ on May 5, 2016

TECHNICAL COMMENT

BATTERIES

Comment on "Cycling Li-O_2 batteries via LiOH formation and decomposition"

Yue Shen,[1]* Wang Zhang,[1] Shu-Lei Chou,[2]* Shi-Xue Dou[2]

Liu *et al*. (Research Article, 30 October 2015, p. 530) described a lithium-oxygen (Li-O_2) battery based on lithium iodide (LiI)–assisted lithium hydroxide (LiOH) formation and decomposition. We argue that LiOH cannot be oxidized by triiodide (I_3^-). The charge capacity is from the oxidation of I^- instead of LiOH. The limited-capacity cycling test is misleading when the electrolyte contributes considerable parasitic reaction capacity.

Liu *et al.* (*1*) reported a "breakthrough" of Li-O_2 battery. Their cathode was able to cycle 2000 times at a limited capacity of 1000 mAh g^{-1}, and the overpotential was as small as 0.2 V. In contrast to previous studies (*2*, *3*), they claim that the excellent cycling stability is based on the formation and decomposition of LiOH. Small amounts of water and LiI depress the oxidation potential of LiOH down to 3.0 V.

The major conclusion in Liu *et al.*'s Research Article was the reactions shown in Scheme 1. Adding the two charge reactions together will get the total charge reaction of

$$4LiOH \rightarrow 4Li^+ + 2H_2O + O_2 + 4e^- \quad (1)$$

This reaction is well known as the charge reaction of aqueous lithium-air batteries (*4*, *5*). The potential of this reaction is widely agreed to be 3.84 V (versus Li^+/Li) in neutral solutions or 3.42 V when pH = 12, much higher than 3.0 V in Liu *et al.*'s paper. The equilibrium potential is a thermodynamic value; it cannot be influenced by the existence of I_3^- species, which is a catalyst. The solvation effect of different solvents may bring a little difference to the charge potential, but it cannot explain a difference as large as 0.4 V. Liu *et al.* further claimed that, even with 45,000 parts per million of water, no appreciable change in the electrochemical profile was observed. The solvation situation in highly hydrated DME should be similar to the aqueous lithium-air batteries. Thus, the potential should not change very much. Therefore, LiOH cannot be oxidized at 3.0 V (versus Li^+/Li).

To determine the true charge reaction, a transparent battery was built to repeat the cycling experiment with a similar weight ratio of the reduced graphene oxide (rGO) cathode to electrolyte, as in Liu's experiment (Fig. 1A). The charge potential was indeed lower than 3.2 V (Fig. 1B), but the electrolyte became darker after every charge process, indicating that the concentration of I_3^- was increasing. This result is against Liu *et al.*'s mechanism, because they believe that the I_3^- should react with LiOH and transform back to colorless I^-. The cathode after 100 cycles of discharge and charge was measured with x-ray diffraction (XRD), and the result confirmed the LiOH accumulation (Fig. 1C).

In Liu *et al.*'s paper, the amount of electrolyte was 1 mL. The LiI concentration was 0.05 mol L^{-1}. Three I^- acquired two electrons to become I_3^-. So, the capacity of the I_3^-/I^- redox couple should be

$$\frac{0.05 \times 10^{-3}\text{mol} \times 96,485\ \text{C mol}^{-1}}{3.6\ \text{C mAh}^{-1}} \times \frac{2}{3} = 0.89\ \text{mAh} \quad (2)$$

Meanwhile, the mass loading of Liu *et al.*'s rGO cathode (active materials) was as low as 0.01 mg. When the battery was cycling at a specific capacity-limiting method of 1000 mAh g^{-1}, the capacity of the battery should be

$$1000\ \text{mAh g}^{-1} \times 0.01 \times 10^{-3}\ \text{g} = 0.01\ \text{mAh} \quad (3)$$

This value is only about 1% of the capacity of the I_3^-/I^- redox couple. Thus, during charging, the LiOH does not need to be oxidized because the oxidation of I^- could sustain the charge reaction. The charge potential is very low simply because it is the I_3^-/I^- redox reaction.

The section titled "Comparison of the Capacity Obtained with the I^-/I_3^- Couple (in Ar) with that Obtained for the Li-O_2 Cells" in Liu *et al.*'s supplementary materials does not support what they claimed, because the LiI was originally in its reduced state, so there was nothing to be further reduced and the discharge capacity was thus very small. They unfortunately did not show the

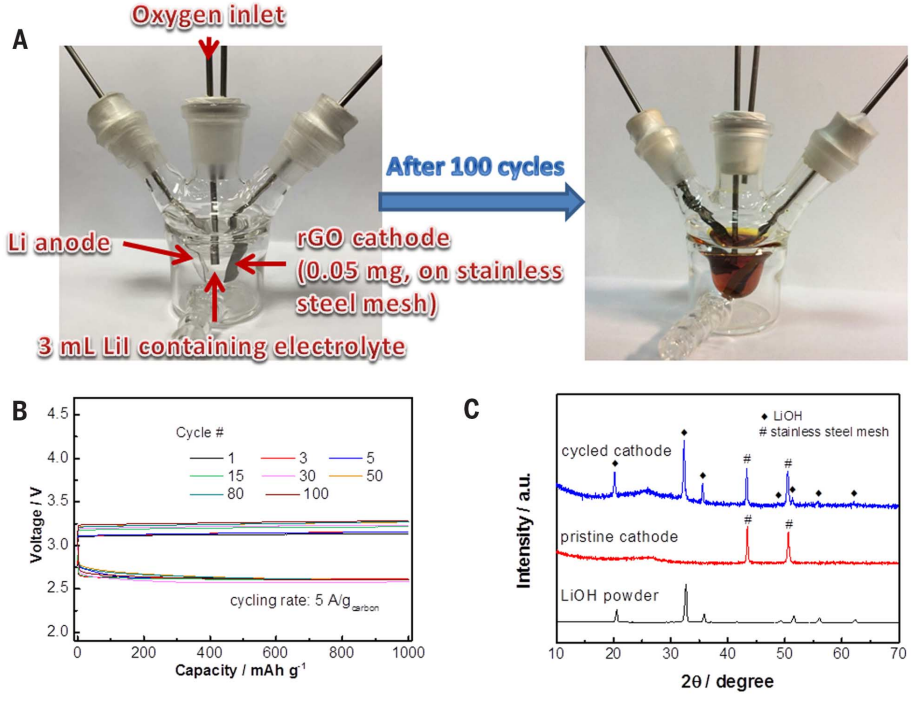
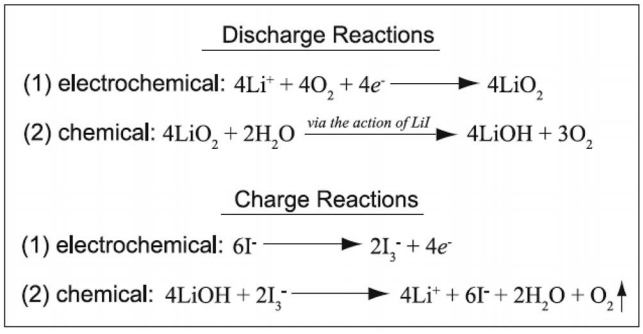


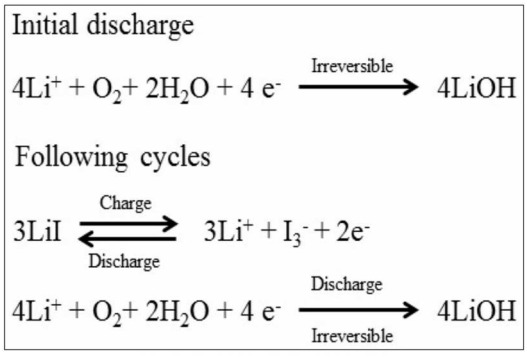
Fig. 1. Cycling test of a transparent battery. (**A**) Photograph of the battery before and after 100 cycles. (**B**) Discharge charge curves of the battery for elected cycles. (**C**) XRD pattern of the cathode after 100 cycles of discharge and charge.

[1]State Key Laboratory of Material Processing and Die and Mould Technology, School of Materials Science and Engineering, Huazhong University of Science and Technology, Wuhan, Hubei 430074, China. [2]Institute for Superconducting and Electronic Materials, Australian Institute for Innovative Materials, University of Wollongong, Innovation Campus, Squires Way, North Wollongong NSW 2522, Australia.
*Corresponding author. Email: shenyue1213@hust.edu.cn (Y.S.); shulei@uow.edu.au (S.L.C.)

Downloaded from http://science.sciencemag.org/ on May 5, 2016



Scheme 1



Scheme 2

complete charge curve with LiI electrolyte in Liu *et al.*'s figure S3 and figure 1B.

On the whole, we believe that Liu *et al.*'s proposed explanation of the reversible decomposition of LiOH is not scientifically sound. Their battery is actually a combination of an irreversible lithium-air battery and a reversible lithium-iodine battery, as shown in the reactions in Scheme 2.

For lithium-oxygen batteries, limited-capacity cycling test results can be misleading. They may conceal a large amount of parasitic reactions, especially when the weight ratio of the cathode material to the electrolyte is very small. It is necessary to use multiple techniques (*6*, *7*) to confirm whether the charge capacity is from the oxidation of the discharge product or from the side reactions.

REFERENCES AND NOTES

1. T. Liu *et al.*, *Science* **350**, 530–533 (2015).
2. M. H. Cho *et al.*, *J. Power Sources* **268**, 565–574 (2014).
3. P. G. Bruce, S. A. Freunberger, L. J. Hardwick, J. M. Tarascon, *Nat. Mater.* **11**, 19–29 (2012).
4. J. Lu *et al.*, *Chem. Rev.* **114**, 5611–5640 (2014).
5. T. Zhang, N. Imanishi, Y. Takeda, O. Yamamoto, *Chem. Lett.* **40**, 668–673 (2011).
6. Z. Peng, S. A. Freunberger, Y. Chen, P. G. Bruce, *Science* **337**, 563–566 (2012).
7. M. M. Ottakam Thotiyl *et al.*, *Nat. Mater.* **12**, 1050–1056 (2013).

ACKNOWLEDGMENTS

Funding support from Natural Science Foundation of China (51202076) and Australian Research Council linkage project (LP120200432).

22 December 2015; accepted 6 April 2016
10.1126/science.aaf1399

Downloaded from http://science.sciencemag.org/ on May 5, 2016

TECHNICAL RESPONSE

BATTERIES

Response to Comment on "Cycling Li-O_2 batteries via LiOH formation and decomposition"

Tao Liu,[1] Gunwoo Kim,[1,2] Javier Carretero-González,[1] Elizabeth Castillo-Martínez,[1] Clare P. Grey[1,2]*

We described a lithium-oxygen (Li-O_2) battery comprising a graphene electrode, a dimethoxyethane-based electrolyte, and H_2O and lithium iodide (LiI) additives, lithium hydroxide (LiOH) being the predominant discharge product. We demonstrate, in contrast to the work of Shen *et al.*, that the chemical reactivity between LiOH and the triiodide ion (I_3^-) to form IO_3^- indicates that LiOH can be removed on charging; the electrodes do not clog, even after multiple cycles, confirming that solid products are reversibly removed.

We reported on a lithium-oxygen battery that formed LiOH as the predominant discharge product, formed from a reduced graphene oxide (rGO) electrode, a dimethoxyethane (DME)–based electrolyte, and H_2O and LiI additives (*1*). On the basis of observed oxygen release, we suggested the following charge reaction.

$$4LiOH + 2I_3^- \leftrightarrow 4Li^+ + O_2 + 2H_2O + 6I^- \quad (1)$$

We also clearly stated, "We stress, however, that the equilibria that occur in the presence of oxygen, water, and iodine are complex, often involving a series of polyanions (including IO^- and its protonated form); further mechanistic studies are required to understand the role of these complex equilibria in the redox processes" (*1*). Some of these equilibria are as follows (*2*)

$$3I^- \leftrightarrow I_3^- + 2e^- \quad (2)$$

$$2OH^- + I_3^- \leftrightarrow IO^- + H_2O + 2I^- \quad (3)$$

$$\text{or } 2LiOH + I_3^- \leftrightarrow LiIO + LiI + I^- + H_2O \quad (4)$$

The IO^- ion will then disproportionate, forming IO_3^-

$$3LiIO \leftrightarrow LiIO_3 + 2LiI \quad (5)$$

Shen *et al.* (*3*) in their Comment make three major points, which we discuss below.

1) Shen *et al.* (*3*) argue that the I_3^--LiOH reaction to produce O_2 on charge is not feasible, because the OH^-/O_2 couple under standard conditions [3.84/3.42 V vs. Li^+/Li in acidic/basic standard conditions, respectively (*3*)] is higher than the I^-/I_3^- couple (reaction 2, ~3.0 V in DME). First, removal of LiOH in lithium-oxygen batteries below 3.2 V has previously been observed—e.g., with ruthenium-based catalysts and tetraglyme (*4*)/dimethyl sulfoxide (*5*)–based electrolytes and added water. Because the catalyst does not alter the equilibrium voltage, the equilibrium itself must be altered. In another Technical Response (*6*), we argued that the free-energy change of reaction 1 on moving from an aqueous to nonaqueous electrolyte system cannot be ignored and will change the equilibrium potential. Of note, we have observed that LiOH can be quantitatively removed via reactions 2 to 5, I_3^- reacting to form IO_3^- and I^- and suggesting an alternative mechanism [see figure 1 in (*6*) for details], the rate depending strongly on the amount of water and LiTFSI concentrations present in the system (Fig. 1). Reaction 1 is a four-electron process and will be strongly affected by the nature of the electrode; further studies are required to determine the relative rates of reaction 1 versus reactions 3 to 5 and the potential role that catalysts may play in determining this.

2) Shen *et al.* (*3*) observed in a transparent cell that the electrolyte color darkens on cycling due to I_3^- accumulation. They concluded that the first discharge involves the formation of LiOH via O_2 reduction at ~2.6 V [figure 1B in (*3*)] but that the subsequent charge process involves the direct oxidation of I^- to I_3^-, rather than the removal of LiOH, subsequent discharge processes, also observed at ~2.6 V, being a combination of further LiOH formation and I_3^- reduction. Because our ultraviolet (UV)–visible experiments show that the kinetics for reactions 2 to 5 are highly dependent on the water content [figure 1 in (*6*)], we suggest that the conditions used in Shen *et al.*'s experiment, 5 A/g for a charge/discharge capacity of 1 Ah/g—i.e., a 12-min charge rate—may have been too fast to allow reactions 2 to 5 to go to completion, and thus I_3^- and LiOH accumulate. By contrast, we used a charge time ranging from up to ~20 hours at 1 A/g_c for thin electrodes [e.g., figure 1 and figures S11(d) and S20 in (*1*)] to hundreds of hours for thick electrodes [e.g., figure S10 in (*1*), the amount of water content [up to ~50,000 parts per million or 5 weight % (wt %)] in our batteries also being higher than in Shen *et al.*'s. We indeed observed that I_3^- reacts with LiOH, transforming back to colorless IO_3^- and I^- after 14 hours (Fig. 1B).

The proposed mechanism by Shen *et al.* does not explain the experiment reported in figure S20 of (*1*). When the battery was fully discharged in the first cycle and then charged to the same capacity as the previous discharge, the capacity and voltage profile of the discharges in the following 11 cycles were nearly identical to that of the first cycle. We have consistently shown that the discharged product in the first cycle is quantitatively LiOH [figure 2 and figure S19 in (*1*)], the end of discharge being marked by either pore clogging or full coverage of the rGO surface by nonconductive LiOH. If during the first charge, LiOH is not effectively removed, it is difficult to propose a simple explanation for the subsequent multiple discharge processes, which show essentially the same discharge capacity, because no pore volume or bare rGO surface would be available for LiOH formation. Although we recognize that I_3^-/I^- redox chemistry must occur in subsequent cycles, it cannot be the sole discharge reaction, because the voltage is always consistent with LiOH formation (or Li_2O_2 formation, this product forming at a similar voltage in the absence of water). Finally, we note that assuming that the battery operates solely via the I^-/I_3^- couple, the maximum theoretical capacity is 0.89 mAh for our LiI concentrations. Figures S10(b) and S11(d) in (*1*) present data showing a capacity of >7000 $mAhg^{-1}$ on charge for a thick-electrode corresponding to 1.0 mAh and a thin-electrode cell that was cycled for data for 1000 cycles followed by 15 cycles at 22,000 mAh/g (0.22 mAh). Although redox shuttle mechanisms likely occur, LiOH removal must also be occurring.

3) Shen *et al.* argue that the small capacity obtained in figure S3 of our original paper "does not support what they claimed, because the LiI was originally in its reduced state, so there was nothing to be further reduced and the discharge capacity was thus very small" (*1*). Our experiments were, however, performed after a first initial charge. Thus, the discharge capacity reflects the total I_3^- concentration after this charge. Under the conditions used here, the capacity of the I_3^-/I^- couple is consistently noticeably lower than that of the total I^- content in the cell, due to the slow diffusion of the ions to the rGO electrode, the capacity reflecting both I^- diffusivity and the charge rate [see page 8 of the supplementary materials for (*1*)].

We are aware of the multiple competing reactions in this battery system, the relative kinetics of the various reactions being further complicated because (i) the two key additives, water and iodine, react with the Li metal anode, and (ii) LiOH formation consumes water, the water

[1]Department of Chemistry, University of Cambridge, Lensfield Road, Cambridge CB2 1EW, UK. [2]Cambridge Graphene Centre, University of Cambridge, Cambridge CB3 0FA, UK.
*Corresponding author. Email: cpg27@cam.ac.uk

Downloaded from http://science.sciencemag.org/ on May 5, 2016

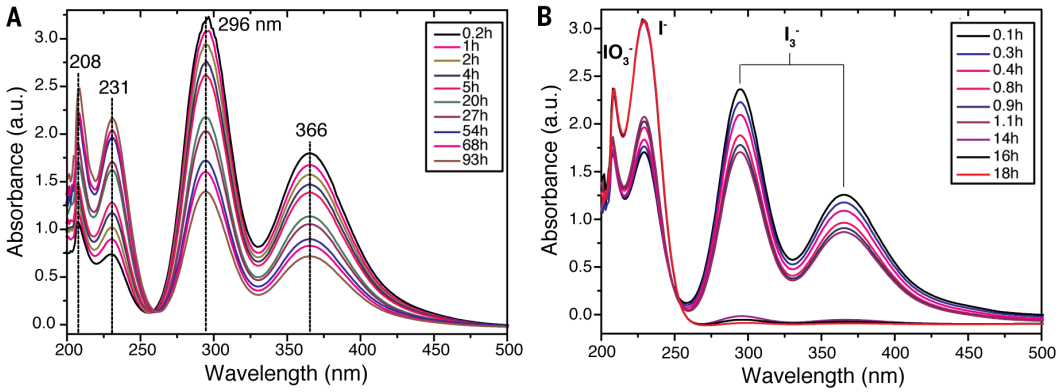


Fig. 1. UV-visible spectra after the reaction of saturated LiOH in a 3 wt % water/DME solution. (**A**) Without added 0.1 M LiTFSI. (**B**) With added 0.1 M LiTFSI. Peak intensity changes confirm the chemical reaction between LiOH and I_3^- via reactions 2 to 5, to form IO_3^- and I^- (*7*).

concentration dropping during discharge. For example, as the water concentration drops, the battery may operate via Li_2O_2 formation; I_3^- can then oxidize Li_2O_2, releasing O_2. Developing a scalable, practical device requires much further work to optimize this chemistry.

REFERENCES

1. T. Liu *et al.*, *Science* **350**, 530–533 (2015).
2. J. -L. Burgot, *Ionic Equilibria in Analytical Chemistry* (Springer-Verlag, New York, 2012).
3. Y. Shen, W. Zhang, S.-L. Chou, S.-X. Dou, *Science* **352**, 667 (2016).
4. T. Zhang, K. Liao, P. He, H. Zhou, *Energy Environ. Sci.* **9**, 1024–1030 (2016).
5. S. Wu, J. Tang, F. Li, X. Liu, H. Zhou, *Chem. Commun.* **51**, 16860–16863 (2015).
6. T. Liu *et al.*, *Science* **352**, 667 (2016).
7. J. Paquette, B. L. Ford, *Can. J. Chem.* **63**, 2444–2448 (1985).

14 January 2016; accepted 6 April 2016
10.1126/science.aaf1652

Downloaded from http://science.sciencemag.org/ on May 5, 2016

TECHNICAL COMMENT

BATTERIES

Comment on "Cycling Li-O_2 batteries via LiOH formation and decomposition"

Venkatasubramanian Viswanathan,[1]* Vikram Pande,[1] K. M. Abraham,[2] Alan C. Luntz,[3] Bryan D. McCloskey,[4] Dan Addison[5]

Based on a simple thermodynamic analysis, we show that iodide-mediated electrochemical decomposition of lithium hydroxide (LiOH) likely occurs through a different mechanism than that proposed by Liu *et al*. (Research Article, 30 October 2015, p. 530). The mismatch in thermodynamic potentials for iodide/triiodide (I^-/I_3^-) redox and O_2 evolution from LiOH implies a different active iodine/oxygen electrochemistry on battery charge. It is therefore possible that the system described in Liu *et al*. may not form the basis for a rechargeable lithium-oxygen (Li-O_2) battery.

Liu *et al*. (*1*) proposed that a highly rechargeable and electrically efficient Li-O_2 battery could be produced by using LiI and small amounts of H_2O in a nonaqueous electrolyte and a reduced graphene oxide (rGO) electrode. They suggested that LiI catalyzed oxygen reduction to LiOH when H_2O impurities were present in the otherwise nominally nonaqueous electrolyte. They conjectured that I_3^- formed during charge at ~3 V versus Li/Li^+ (all potentials herein are referenced to Li/Li^+) mediates the oxidation of LiOH to liberate O_2 without substantial parasitic reactions.

Although no thermodynamic barriers exist for the LiI-mediated formation of LiOH during discharge of water-contaminated Li-O_2 cells, the charging process warrants further analysis. We present a simple thermodynamic analysis of the triiodide-mediated LiOH oxidation mechanism proposed in their work (*1*). We consider their overall proposed charging reaction.

$$4\mathrm{LiOH} \leftrightarrow 4\mathrm{Li^+} + 4\mathrm{e^-} + 2\mathrm{H_2O} + \mathrm{O_2} \quad (1)$$

This reaction has an equilibrium potential of 3.34 V under standard conditions (*2*). The activity of water is not at standard conditions in these experiments, but even at parts per million (ppm) quantities of water, there are negligible changes to the equilibrium potential. For example, in an experiment with ~100 to 45,000 ppm, this corresponds to an equilibrium potential shift of ~0.02 to 0.009 V.

[1]Department of Mechanical Engineering, Carnegie Mellon University, Pittsburgh, PA 15213, USA. [2]Department of Chemistry and Chemical Biology, Northeastern University, Boston, MA 02115, USA. [3]SUNCAT, SLAC National Accelerator Laboratory, Menlo Park, CA 94025, USA. [4]Department of Chemical and Biomolecular Engineering, University of California, Berkeley and Energy Storage and Distributed Resources Division, Lawrence Berkeley National Laboratory, Berkeley, CA 94720, USA. [5]Liox Power Inc., 129 North Hill Avenue, Suite 103, Pasadena, CA 91106, USA.
*Corresponding author. Email: venkvis@cmu.edu.

We now consider the iodide/triiodide redox reaction, shown in figure 4 of (*1*), given by

$$6\mathrm{I^-} \leftrightarrow 2\mathrm{I_3^-} + 4\mathrm{e^-} \quad (2)$$

The redox potential for this reaction depends on the solvent (*3*). As reported in (*1*), we use the equilibrium potential—i.e., ~3.0 V—as shown in figure 1 of (*1*). Liu *et al*. point out in the caption that the crossing points of the charge/discharge curves indicate the positions of the redox potential of I^-/I_3^- in the specific electrode/electrolyte system.

The chemical reaction, shown in figure 4 of (*1*), to complete the charging cycle, is given by

$$4\mathrm{LiOH} + 2\mathrm{I_3^-} \leftrightarrow 4\mathrm{Li^+} + 6\mathrm{I^-} + 2\mathrm{H_2O} + \mathrm{O_2} \quad (3)$$

This chemical reaction is uphill in free energy by $\Delta G_{c2} = 4 \times (3.347 - 3.00) = 1.39$ eV. This corresponds to an equilibrium constant, given by $K = \exp[-(\Delta G_{c2}/k_BT)] \sim 10^{-24}$. Even if every cathode site were electrochemically active, the fraction that would transform to the product, O_2, would be exceptionally small and therefore cannot account for a reversible process regenerating O_2.

The overall free-energy diagram for the charging mechanism proposed by Liu *et al*. at $U = 3$ V is shown in Fig. 1. A simpler way to understand the inconsistency is that the minimum potential required to oxidize LiOH is 3.34 V. The iodide/triiodide redox couple has an oxidation potential of only ~3 V and hence it is not feasible to oxidize LiOH(s) with such a scheme.

In a rigorously anhydrous Li-O_2 battery that produces Li_2O_2 as the discharge product (*4*, *5*), the free-energy diagram involving an iodide/triiodide redox couple is shown in Fig. 2. In

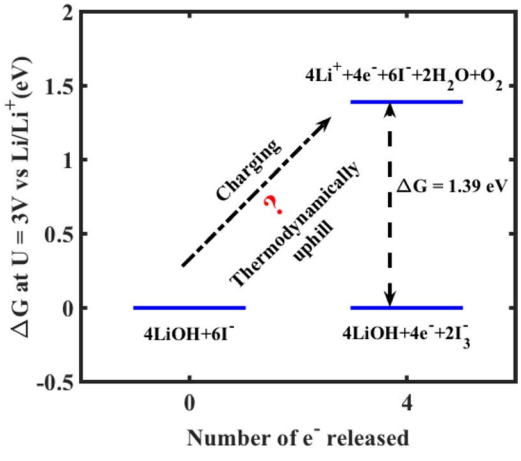


Fig. 1. Free-energy diagram for the proposed charging mechanism involving iodide/triiodide–mediated LiOH oxidation at $U = 3$ V. The chemical step associated with the oxidation of LiOH with triiodide is thermodynamically uphill by 1.39 eV.

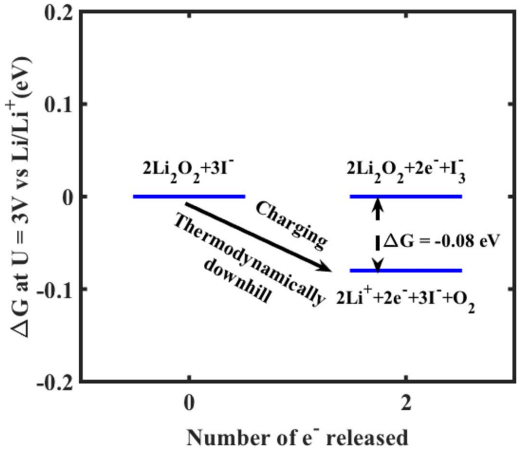


Fig. 2. Free-energy diagram for the iodide/triiodide–mediated Li_2O_2 oxidation in an anhydrous Li-O_2 battery at $U = 3$ V. The chemical step associated with the oxidation of Li_2O_2 with triiodide is thermodynamically downhill by 0.08 eV.

Downloaded from http://science.sciencemag.org/ on May 5, 2016

this case, the minimum potential required to oxidize Li_2O_2(s) is 2.96 V, and the iodide/triiodide redox couple possesses the required driving force to carry out this reaction, as shown in several experiments (*6*).

To summarize, our thermodynamic analysis shows that it is not possible to run an iodide-mediated reversible electrochemical cycle, as indicated in figure 4 of (*1*). However, given the clear evidence of LiOH disappearance during the charge process, some other electrochemical reaction or reactions involving LiOH are active. Whether these other reactions can form the basis for a rechargeable battery remains an open question. Previous reports have shown empirical evidence of parasitic reactions associated with iodide/triiodide redox couples in a Li-O_2 battery with ethereal solvents (*6*, *7*). Such irreversible routes obviously need to be avoided to allow long-term rechargeability in a Li-O_2 battery.

REFERENCES AND NOTES

1. T. Liu *et al*., *Science* **350**, 530–533 (2015).
2. D. R. Lide, Ed., *CRC Handbook of Chemistry and Physics* (CRC Press, 2004).
3. G. Boschloo, A. Hagfeldt, *Acc. Chem. Res.* **42**, 1819–1826 (2009).
4. C. Laoire, S. Mukerjee, E. J. Plichta, M. A. Hendrickson, K. M. Abraham, *J. Electrochem. Soc.* **158**, A302 (2011).
5. N. B. Aetukuri *et al*., *Nat. Chem.* **7**, 50–56 (2015).
6. W.-J. Kwak *et al*., *J. Mater. Chem. A* **3**, 8855–8864 (2015).
7. I. Landa-Medrano *et al*., *Electrochem. Commun.* **59**, 24–27 (2015).

ACKNOWLEDGMENTS

Authors acknowledge helpful discussions with G. Chase.

13 November 2015; accepted 25 March 2016
10.1126/science.aad8689

Downloaded from http://science.sciencemag.org/ on May 5, 2016

TECHNICAL RESPONSE

BATTERIES

Response to Comment on "Cycling Li-O_2 batteries via LiOH formation and decomposition"

Tao Liu,[1] Gunwoo Kim,[1,2] Javier Carretero-González,[1] Elizabeth Castillo-Martínez,[1] Paul M. Bayley,[1] Zigeng Liu,[1] Clare P. Grey[1]*

Lithium-oxygen (Li-O_2) batteries cycle reversibly with lithium iodide (LiI) additives in dimethoxyethane (DME) to form lithium hydroxide (LiOH). Viswanathan *et al.* argue that because the standard redox potential of the four-electron (e^-) reaction, $4OH^- \leftrightarrow 2H_2O + O_2 + 4e^-$, is at 3.34 V versus Li^+/Li, LiOH cannot be removed by the triiodide ion (I_3^-). However, under nonaqueous conditions, this reaction will occur at a different potential. LiOH also reacts chemically with I_3^- to form IO_3^-, further studies being required to determine the relative rates of the two reactions on electrochemical charge.

We recently reported (*1*) on a highly reversible lithium-oxygen battery composed of a reduced graphene oxide (rGO) electrode and a dimethoxyethane (DME)/LiTFSI electrolyte. The additives (H_2O and LiI) were key in controlling the nature of the battery reactions. LiOH, instead of the commonly reported Li_2O_2 phase, was the predominant product during discharge, the protons primarily coming from H_2O in the cell. On charge, LiOH was removed [as seen by x-ray diffraction and proton nuclear magnetic resonance (^{1}H NMR)], and we proposed that this occurs via a reaction with I_3^-, O_2 being observed by mass spectroscopy. In their Comment, Viswanathan *et al.* (*2*) argue that a charge mechanism involving reaction with I_3^- to produce O_2 is not feasible, because the redox potential for reaction 1

$$4Li^+ + 4e^- + O_{2,g} + 2H_2O_l \leftrightarrow 4LiOH_s \quad (1)$$

is 3.34 V versus Li^+/Li under standard conditions, whereas the redox potential for $6I^- \leftrightarrow 2I_3^- + 4e^-$, is ~3.0 V in the DME-based electrolyte used here. We discuss this issue and possible mechanisms for LiOH removal.

LiOH formation in the presence of LiI has been previously reported in lithium-oxygen batteries (*3*), and the reversible formation/decomposition of LiOH—e.g., using ruthenium catalysts and tetraglyme (*4*)/ dimethyl sulfoxide (DMSO) (*5*)–based electrolytes with added water—was observed at 3.1 to 3.2 V. It is well established that the electrolyte affects the potential of a redox couple. Indeed, even the I_3^-/I^- couple drops from 3.53 V in water under standard conditions (*6*, *7*) to 3.35, 3.1, and 3.0 V in acetonitrile (*6*), tetraglyme, and DME (*1*), respectively. The O_2/O_2^{2-} couple varies from ~3.0 V in DMSO electrolyte to ~3.5 V in acetonitrile electrolyte (*8*), and the recent "water in salt" work (*9*) showed that the redox potentials for water reduction/oxidation shift considerably due to the chemical potential changes of water and Li^+ in the electrolyte.

Changes in the redox potential of reaction 1 under nonstandard conditions arise from at least two factors. First, the concentrations of the species in the electrolyte deviate noticeably from standard conditions. Second, the different coordination environments of the species/ions differ dramatically between solvents. The standard Gibbs free-energy change, ΔG_r^o, of the overall cell reaction

$$4Li_s + O_{2,g} + 2H_2O_l \leftrightarrow 4LiOH_s \quad (2)$$

is −1282 kJ/mol (*10*) at standard conditions resulting in $E^o = -\Delta G_r^o/nF = 3.32$ V. Under nonstandard conditions, the equilibrium voltage of cell reaction 2 can be expressed as a function of the activity (α) of the reactants and products.

$$E_e = E^o + \frac{2.303RT}{nF}\lg\left(\frac{\alpha_{Li}^{v_{Li}}\alpha_{O_2}^{v_{O_2}}\alpha_{H_2O}^{v_{H_2O}}}{\alpha_{LiOH}^{v_{LiOH}}}\right) \quad (3)$$

where R is the gas constant, F is the Faraday constant, n is the number of electrons involved in the reaction, and T is the temperature.

Because Li and LiOH are solids, and gaseous O_2 is at close to ~1 bar during the cell reaction—i.e., they are in their respective standard states—the above equation can be simplified.

$$E_e = E^o + 0.01481\lg(\alpha_{H_2O}^2) \quad (4)$$

The activity, or the chemical potential, of water in the batteries is given by

$$\alpha_{H_2O} = \exp\left(\frac{\mu-\mu^o}{RT}\right) = \exp\left(\frac{\Delta H}{RT}\right)\exp\left(-\frac{\Delta S}{R}\right) \quad (5)$$

where μ is the chemical potential, and ΔH and ΔS are the enthalpy and entropy difference of water in LiI/LiTFSI/DME electrolyte compared with those in a LiI/LiTFSI aqueous electrolyte at standard conditions

$$H_2O_l \leftrightarrow H_2O_{LiI,LiTFSI,DME} \quad (6)$$

and "H_2O_l" in reaction 2 should be replaced by "$H_2O_{(LiI,LiTFSI,DME)}$". It is then relevant to ask how large a value of ΔG for reaction 6 is required to shift the potential of reaction 2 so that it drops below that of the I^-/I_3^- couple in the same electrolyte. Although this value is currently not known for DME, a relatively small value of −60.0 kJ/mol is required to reduce the couple of reaction 2 down to 3.0 V. ΔS makes only small changes to voltage (of −20 mV to −77 mV, where the entropy is approximated by the concentration of water in the system). The ΔH for reaction 6 is controlled by the loss of water-water interactions and the difference between water–Li salt and DME–Li salt interactions. Evidence for strong water–Li^+ interactions in DME comes from the hygroscopic

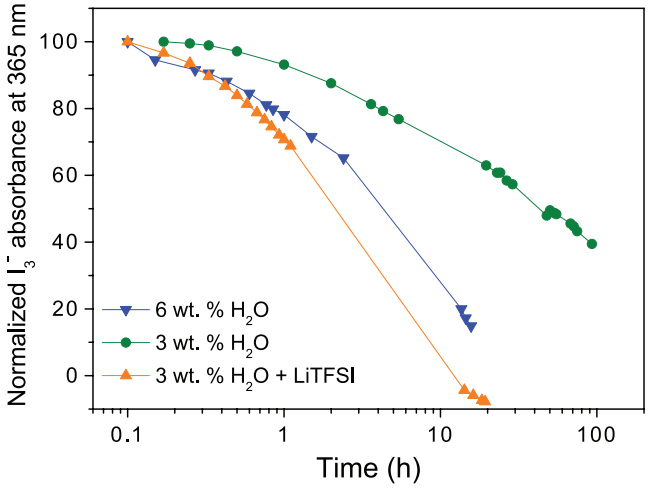


Fig. 1. Reaction kinetics of a LiOH + LiI_3 mixture in DME/water solutions followed by UV-visible spectroscopy (with LiOH in a 10^3 excess).

[1]Department of Chemistry, University of Cambridge, Lensfield Road, Cambridge CB2 1EW, UK. [2]Cambridge Graphene Centre, University of Cambridge, Cambridge CB3 0FA, UK.
*Corresponding author. Email: cpg27@cam.ac.uk

Downloaded from http://science.sciencemag.org/ on May 5, 2016

nature of LiTFSI and LiI salts and their higher solubility in water than in ethers (*7*, *9*). Theoretical calculations (*9*) also suggest a very high binding energy of water with Li^+ cations in an aqueous LiTFSI electrolyte. Hydration enthalpies for LiI and LiTFSI in water/nonaqueous solvents are an order of magnitude larger [e.g., −828 kJ/mol for LiI in water and −756 kJ/mol for LiTFSI in acetonitrile (*11*, *12*)] than the −60 kJ/mol assumed above, all suggesting that this value for ΔG_{vi} is certainly plausible, but we stress that further measurements/calculations are required.

The chemistry is, however, more complicated because I_3^- can both react with LiOH forming I^- and liberating oxygen

$$4LiOH + 2I_3^- \leftrightarrow 4Li^+ + 6I^- + 2H_2O + O_2 \quad (7)$$

and also react to form metastable IO^-, which then disproportionates forming IO_3^- and I^- (*13*, *14*).

$$6LiOH + 3I_3^- \leftrightarrow 6Li^+ + IO_3^- + 8I^- + 3H_2O \quad (8)$$

The low concentrations of water in our electrolytes help drive both reaction equilibria to the right-hand side. Our Raman and ultraviolet (UV)–visible studies of the chemical reaction of LiOH and I_3^- show that reaction 8 dominates under aqueous conditions, the rate of the reaction slowing down noticeably, but still occurring in DME solutions containing 3 to 6 weight % water (Fig. 1). Interestingly, the addition of LiTFSI speeds up the reaction. However, electrochemical studies of the oxidation of I_3^- in aqueous solutions with carbon electrodes often observe a combination of O_2 evolution and IO_3^- formation (*15*). Thus, it is clear that further studies are required to determine how much O_2 is evolved on charge versus being tied up as IO_3^-. Our $^{17}O/^1H$ NMR studies of electrodes cycled in and beyond the first cycle observe reversible LiOH formation, even when using the thick electrodes (>0.150 mg) required for the NMR experiments. Finally, Viswanathan *et al.* suggested that parasitic reactions (*3*) between I^-/I_3^- and the ether-based electrolyte represented the source of proton for LiOH and that such irreversible processes cannot form the basis of a practical Li-O_2 battery. We agree that irreversible processes must be avoided. In our work, DME electrolyte decomposition is not, however, the dominant source of the protons in LiOH, and super P carbon, rGO, and titanium carbide electrodes operate for hundreds of cycles (*1*). In our current Li-O_2 battery, the equilibria among water, oxygen, and iodide; the surface functionality of rGO; and the detailed reaction mechanism during discharge-charge all require further investigation. Nonetheless, the evidence for reversible LiOH formation, in the presence of O_2 (and LiI), is compelling.

REFERENCES

1. T. Liu *et al.*, *Science* **350**, 530–533 (2015).
2. V. Viswanathan *et al.*, *Science* **352**, 667 (2016).
3. W. J. Kwak *et al.*, *J. Mater. Chem. A* **3**, 8855–8864 (2015).
4. S. Wu, J. Tang, F. Li, X. Liu, H. Zhou, *Chem. Commun.* **51**, 16860–16863 (2015).
5. F. Li *et al.*, *Nat. Commun.* **6**, 7843 (2015).
6. G. Boschloo, A. Hagfeldt, *Acc. Chem. Res.* **42**, 1819–1826 (2009).
7. Y. Zhao, L. Wang, H. R. Byon, *Nat. Commun.* **4**, 1896 (2013).
8. L. Johnson *et al.*, *Nat. Chem.* **6**, 1091–1099 (2014).
9. L. Suo *et al.*, *Science* **350**, 938–943 (2015).
10. D. R. Lide, Ed., *CRC Handbook of Chemistry and Physics* (CRC Press, ed. 84, 2003)
11. D. F. C. Morris, *Electrochim. Acta* **27**, 1481–1486 (1982).
12. D. M. Seo, O. Borodin, S. D. Han, P. D. Boyle, W. A. Henderson, *J. Electrochem. Soc.* **159**, A1489–A1500 (2012).
13. J. Paquette, B. L. Ford, *Can. J. Chem.* **63**, 2444–2448 (1985).
14. C. H. Li, C. F. White, *J. Am. Chem. Soc.* **65**, 335–339 (1943).
15. J. E. Vitt, D. C. Johnson, *J. Appl. Electrochem.* **24**, 107 (1994).

1 December 2015; accepted 25 March 2016
10.1126/science.aad8843

Downloaded from http://science.sciencemag.org/ on May 5, 2016

REVIEW SUMMARY

CELLULAR DYNAMICS

Nongenetic functions of the genome

Michael Bustin* and Tom Misteli*

BACKGROUND: The genome is the carrier of the hereditary information that defines an organism. Most genomes consist of a linear polymer of DNA wrapped around octameric histone protein complexes to generate a chromatin structure resembling beads on a string, which further folds and organizes into domains of various sizes and degrees of compaction that are functionally relevant to the regulation of all genomic activities. A myriad of proteins, including remodeling complexes and transcription factors, bind to chromatin in a combinatorial fashion to coordinate gene expression programs. The well-accepted major functions of the genome are to store and propagate the genetic material and to control the expression of the genetic information encoded in DNA.

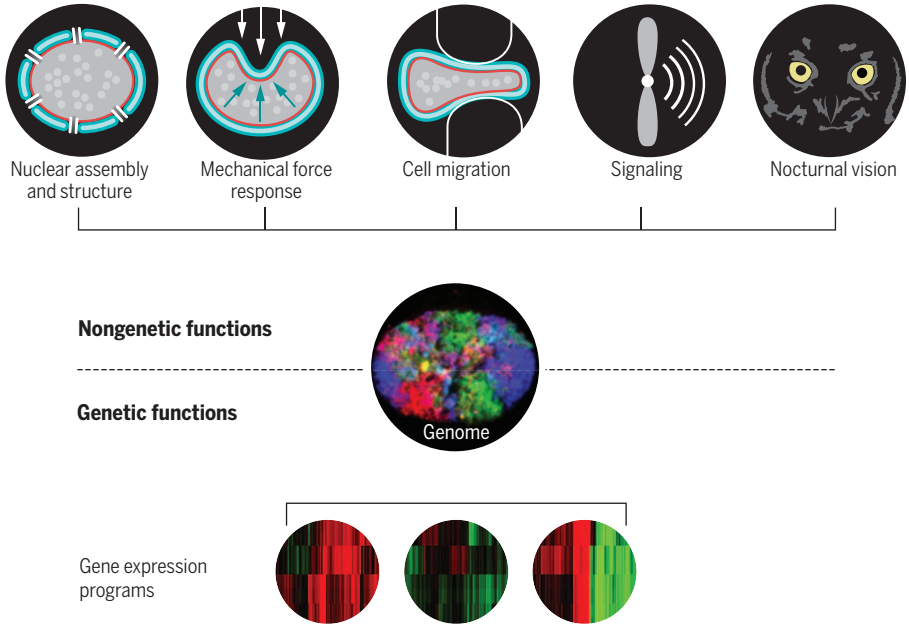
The genome is also a major physical entity of each cell; its large mass, dynamic properties, and unique structural features affect major cellular processes by nongenetic means. As a physical entity, the genome exerts mechanical forces onto its cellular environment via transmission from the nucleus to the cytoplasm, as well as within the nucleus between chromatin domains. Results from a broad range of experiments show that mechanical forces generated by the genome are critical contributors to a wide range of cellular processes and to cellular homeostasis. The chromatin fiber also serves as a physical binding scaffold both for proteins and for membranes, and it is increasingly evident that key cellular events, including faithful cell division, involve controlled interactions of large molecular protein complexes and membranes with the genetic material, independently of gene expression events.

ADVANCES: Recent findings in model systems as varied as yeast, flies, and humans reveal that genomes not only serve to control gene expression programs but also affect cellular functions by nongenetic means via their physical properties. Prominent examples of nongenetic functions of the genome include its role as a physical scaffold to support the assembly of the nuclear membrane and the nuclear pore complex, thereby facilitating the formation of a functional nuclear envelope. In addition, the physical mass of condensed chromatin at the nuclear periphery strengthens the nuclear envelope and enhances the ability of cells and nuclei to withstand mechanical forces exerted by the environment; this function is critical during cell migration or in tissues exposed to mechanical stress, such as the continuously beating heart. Furthermore, the genome serves as an anchoring platform for signaling molecules that regulate vital cellular processes, such as the controlled sequestration of cell cycle checkpoint proteins and of factors involved in licensing cells for cytokinesis. The physical organization of the genome also functions to alert and activate the DNA damage response machinery, whose proper functioning is crucial for preventing malignancies and seems necessary for the initiation of the cell cycle. At the level of tissue organization, an intriguing nongenetic function of the genome is in determining the optical properties of rod cells in the retina of nocturnal animals, thereby enhancing their night vision.

ON OUR WEBSITE

Read the full article at http://dx.doi.org/10.1126/science.aad6933

OUTLOOK: The realization that the genome acts via nongenetic mechanisms greatly expands our understanding of its biological importance. It is increasingly clear that the genome's large mass and dynamic properties play a critical role in biological processes that ultimately regulate cell function and organismal survival, such as the cellular response to mechanical forces, the propagation of the cell cycle, the ability of the cell to divide, and the ability of cells to migrate. These emerging nongenetic functions of the genome are largely unexplored, and it is likely that they affect a wider range of cellular processes than currently realized. To characterize the known nongenetic functions of the genome as well as to discover new ones, it will be essential to develop methods to measure the physical properties of genomes in intact cells. Even more important will be the establishment of techniques to specifically and precisely manipulate physical features of the genome. These lines of investigation have the potential to uncover the full spectrum of nongenetic mechanisms by which the genome affects cellular processes, and to elucidate the interplay of genetic and nongenetic genome events, ultimately leading to a more complete understanding of the complexity of genome function. ■



Genetic and nongenetic functions of the genome. In the interphase nucleus (center), the genome is organized into domains; shown is the domain organization of chromosomes in the nucleus. The well-established genetic functions of genomes (bottom) are the maintenance and transmission of genetic information and the expression of genetic programs. Nongenetic functions of the genome (top) include nuclear assembly, response to mechanical forces, cell migration, intra- and extranuclear signaling, and, at the physiological level, enhanced nocturnal vision.

National Cancer Institute, Bethesda, MD 20892, USA.
*Corresponding author. Email: mistelit@mail.nih.gov (T.M.); bustinm@mail.nih.gov (M.B.)
Cite this article as M. Bustin, T. Misteli, *Science* 352, aad6933 (2016). DOI: 10.1126/science.aad6933

Downloaded from http://science.sciencemag.org/ on May 5, 2016

REVIEW

CELLULAR DYNAMICS

Nongenetic functions of the genome

Michael Bustin and Tom Misteli

The primary function of the genome is to store, propagate, and express the genetic information that gives rise to a cell's architectural and functional machinery. However, the genome is also a major structural component of the cell. Besides its genetic roles, the genome affects cellular functions by nongenetic means through its physical and structural properties, particularly by exerting mechanical forces and by serving as a scaffold for binding of cellular components. Major cellular processes affected by nongenetic functions of the genome include establishment of nuclear structure, signal transduction, mechanoresponses, cell migration, and vision in nocturnal animals. We discuss the concept, mechanisms, and implications of nongenetic functions of the genome.

In eukaryotic cells, the genome is enclosed within the nucleus, where it is organized into chromatin fibers and separated from the cytoplasm by the nuclear membrane. The compaction of the chromatin fiber and its global organization within the confines of the nucleus play major roles in regulating the expression and propagation of the genetic information encoded in the genome (*1*, *2*). The chromatin fiber shapes and controls the cell's architectural and functional machinery by regulating gene expression. In addition to being the carrier of genetic information, the genome is also a major structural entity of the nucleus and, as such, affects cellular structure and function.

A diploid mammalian cell contains approximately 2 m of linear DNA, compressed in the form of chromatin into a nucleus of typically 10 μm in diameter. Chromatin is a linear polymer in which the DNA is wrapped around octameric histones to generate nucleosomes and form a fiber that resembles beads on a string. The chromatin fiber is further organized into several levels of higher-order structures by electrostatic, hydrostatic, and elastic interactions along the fiber and between genome regions on distinct chromosomes (*3*) (Fig. 1). Short-range interactions among nucleosomes shape the linear chromatin fiber into higher-order domains, which are maintained by forces in the piconewton range (*4*). Longer-range interactions along the fiber, facilitated by chromatin-bound proteins, promote the formation of larger domains and ultimately give rise to whole chromosomes (*5*) (Fig. 1). The polymeric properties of the chromatin fiber and their role in generating and stabilizing higher-order chromatin organization are not fully understood, and multiple polymer folding and interaction models have been proposed to explain higher-order genome architecture (*3*, *6*).

The physical features of the genome affect cellular structure and function. As a result of the mass of the genome, the inherent motion of the chromatin fiber (which undergoes fluctuations in the range of 1 to 2 μm) (*6*, *7*), and biologically mediated chromatin reorganization events (for example, during remodeling of chromatin as part of activation of a gene), the genome exerts considerable mechanical forces, both within the nucleus and onto its cellular surroundings (Fig. 1). These mechanical forces affect cellular functions by nongenetic means. Dynamic interactions between neighboring chromatin domains, either on the same or on different chromosomes, generate intranuclear mechanical forces that propagate toward the cytoplasm, particularly at sites where chromatin contacts the nuclear envelope (Fig. 1). Conversely, the genome itself is exposed to mechanical forces emanating from the cytoplasm (*8*, *9*), which may be transmitted either passively at contact points between the nuclear envelope and chromatin, or actively via the LINC (linker of nucleoskeleton and cytoskeleton) protein complex, which forms a bridge across the nuclear envelope that physically connects the genome with the cytoskeleton and transfers mechanical forces bidirectionally between the nucleus and the cytoplasm (*10*, *11*) (Fig. 1).

An additional important nongenetic means by which the genome affects cellular processes is via its ability to serve as a binding platform for cellular components. Although this property is extensively used for genetic regulation by recruiting transcription factors to their regulatory sites (*12*), other proteins and large macromolecular complexes exploit binding to chromatin to perform their functions by nongenetic mechanisms. Prominent examples include the kinetochore, the nuclear pore complex, and the DNA repair machinery. The function of these cellular machineries is critically dependent on their binding to chromatin, but it is the physical properties of

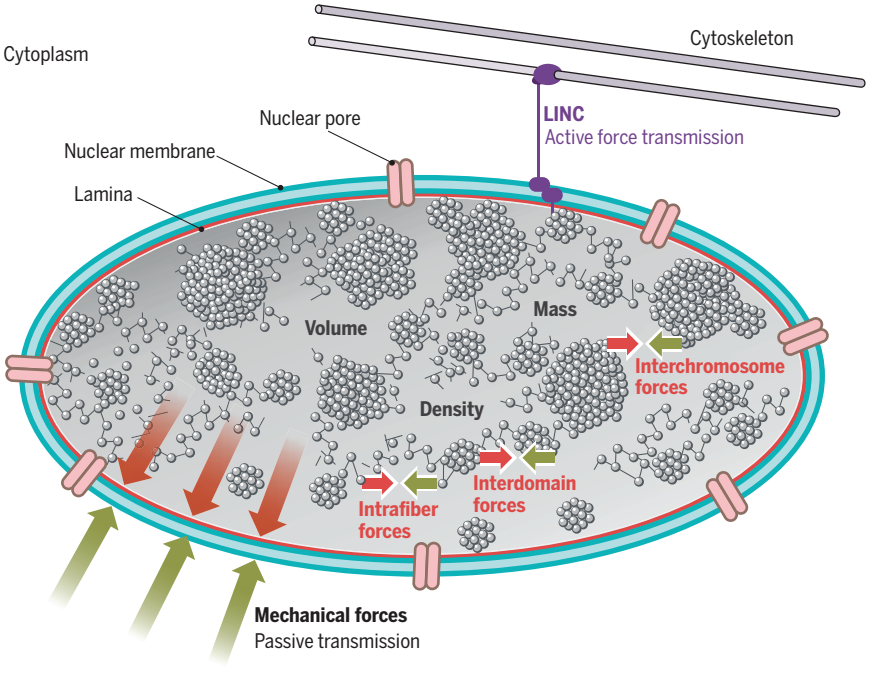


Fig. 1. The genome as a physical entity. In eukaryotes, the genome is housed in the cell nucleus, which is separated from the cytoplasm by a double membrane (blue) supported by a network of intermediate filament proteins of the lamin family (red). The genome is a prominent physical entity with considerable mass, volume, and density. Transport between the nucleus and the cytoplasm occurs via nuclear pores (pink). DNA is folded into higher-order chromatin domains and ultimately chromosomes. The genome exerts, and is exposed to, mechanical forces transmitted into and out of the nucleus, either passively (red, green arrows) or actively via the membrane-spanning LINC protein complex (purple). The genome also exerts and is exposed to intranuclear forces (red, green arrows) via intrafiber, intrachromosomal, and interchromosomal interactions.

National Cancer Institute, Bethesda, MD 20892, USA.
Email: mistelit@mail.nih.gov (T.M.); bustinm@mail.nih.gov (M.B.)

Downloaded from http://science.sciencemag.org/ on May 5, 2016

chromatin, rather than the genetic information encoded in the genome, that enables their function.

Whereas the genetic functions of the genome are well established, its nongenetic effects are poorly understood. The traditional genetic functions of the genome include storage, propagation, and transmission of the genetic material and rely on the use of the genetic information encoded in the DNA sequence. In contrast, the nongenetic functions of the genome do not use its genetic information and are mediated by the physical properties of genomes. Nongenetic functions of the genome are emerging in diverse biological processes, including nuclear assembly, response to mechanical forces, cell migration, cell cycle progression, cellular signaling, and even physiological functions such as vision in nocturnal animals. We discuss here the concept, mechanisms, and the biological implications of nongenetic functions of the genome.

The genome as a determinant of nuclear architecture

A major nongenetic function of the genome is its role in establishing and maintaining the overall structure of the eukaryotic cell nucleus (Fig. 2). This function is evident from in vivo and in vitro studies of the postmitotic assembly of the nuclear envelope, a key event in the cell cycle (*13*). During mitosis, the nuclear membrane disassembles and is absorbed by the endoplasmic reticulum (ER), and membrane fragments disperse in the dividing cell. As daughter cells are formed in telophase, the nucleus rapidly reassembles. During this stage, chromatin serves as a physical scaffold on which the nuclear membrane fragments are immobilized, facilitating their fusion into larger membrane sheets (*13*) (Fig. 2). Capture of nuclear membrane fragments, either directly by the genomic scaffold or via linker proteins, involves several inner nuclear membrane proteins including the lamin B receptor; the LEM (LAP2, emerin, MAN1) domain proteins LAP2b, emerin, and MAN1, which tether membrane fragments to chromatin via their interaction with heterochromatin protein HP1; and barrier-to-autointegration factor BAF (*14*–*17*). Direct experimental demonstration for a nongenetic scaffold function of the genome in establishing nuclear architecture comes from the finding that microinjection of bacteriophage λ DNA into *Xenopus* eggs leads to the formation of double-bilayer membranes around the injected genetic material (*18*). Similarly, nuclear membranes form in vitro around chromatin and even around purified DNA in mammalian or *Xenopus* whole-cell extracts (*19*, *20*). Nuclear membranes assemble irrespective of DNA sequence or source of the genetic material used, demonstrating the nongenetic nature of this genome function.

The genome also plays a role in a later step of nuclear reassembly, during the formation of nuclear pore complexes (NPCs) (*21*, *22*) (Fig. 2). NPCs are inserted into the reassembling nuclear membrane in telophase, as cells enter G_1. In both mouse and *Xenopus* extracts, depletion of histone H3.3 or H4 prevents the formation of NPCs during postmitotic nuclear assembly, although nuclear membrane assembly occurs normally, directly demonstrating a scaffolding role for the genome in assembly of NPCs (*21*–*23*). The mechanism for this function of nucleosomes in NPC assembly is nongenetic and involves the nuclear pore protein ELYS, which initiates the assembly process by acting as a key adaptor protein between chromatin and the NPC and in this way initiates the assembly process (*21*–*23*). An even broader role of nucleosomes and chromatin in the formation and assembly of the nuclear periphery is suggested by the finding that in *Xenopus* the assembly of the nuclear lamina is incomplete in the absence of nucleosomes (*21*). Furthermore, the lysine demethylase LSD1, implicated in chromatin compaction, is required for the in vitro assembly of the nuclear envelope and the NPC in *Xenopus* extracts (*24*). These observations suggest that chromatin globally affects the assembly and structure of the nuclear envelope by nongenetic means.

A related function of the genome is its contribution to determining nuclear size. Although one mechanism for determining nuclear size appears to be the sensing of the nuclear/cytoplasmic ratio of soluble factors (*25*), several independent lines of observations suggest a critical role for global genome architecture, and for chromatin condensation in particular, in nuclear size control. In eukaryotic cells, chromatin condensation is mediated by the ubiquitous and abundant linker histone H1 family of chromatin binding proteins (*26*). A direct role for H1-mediated chromatin condensation in nuclear size determination is evident from observations in *Tetrahymena*, which contains a large macronucleus and a small micronucleus, each with a distinct H1 isoform. Depletion of either H1 isoform results in nuclear enlargement but affects only the nucleus in which the specific isoform is normally present (*27*). Similarly, RNA interference–mediated knockdown of condensins, which play key roles in preparing chromosomes for mitosis by facilitating their compaction (*28*), increases nuclear size in both mouse embryonic stem cells and human cells (*29*, *30*). A physiological role for condensins in controlling nuclear size is also evident in mouse T cells, which fail to compact their nuclei and do not enter quiescence in the absence of condensin II (*31*). An additional architectural chromatin factor implicated in nuclear size control is the methyl-CpG binding protein MeCP2, whose loss in neurons, where it is expressed at high levels, leads to substantial nuclear shrinkage, possibly via its interplay with linker histone H1 (*32*). Taken together, these observations suggest that the global chromatin condensation status in a nucleus contributes to determining its size, evidently through nongenetic mechanisms.

The genome in the cellular response to mechanical forces

The accumulation of heterochromatin at the edge of the cell nucleus is an evolutionarily conserved feature of most eukaryotes (*2*). Targeting of compact heterochromatin to the nuclear periphery is

Downloaded from http://science.sciencemag.org/ on May 5, 2016

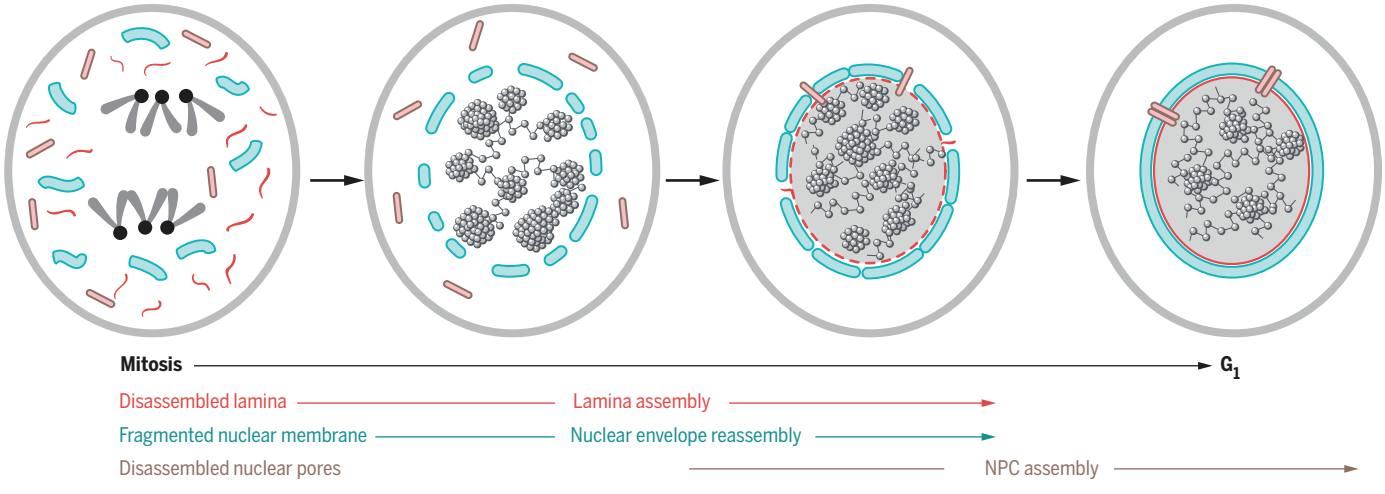


Fig. 2. The genome as a scaffold for nuclear assembly. The cell nucleus disassembles during cell division. The genome serves as a critical scaffold to organize nuclear envelope fragments (blue) and nuclear pore components (pink) during formation of the nucleus in the two daughter cells.

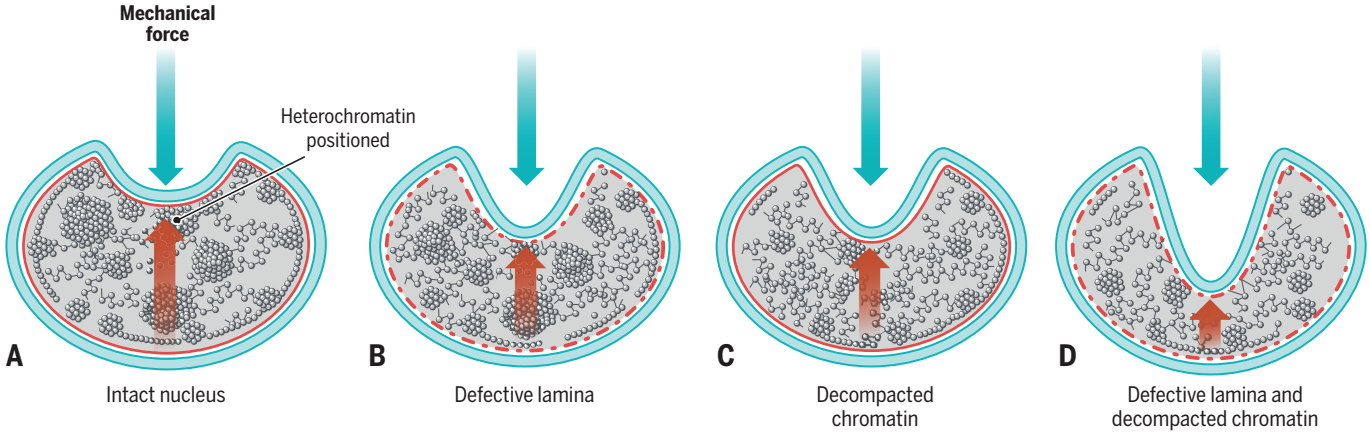


Fig. 3. Genome compactness enhances the sturdiness of the nucleus. (**A**) Mechanical forces can deform the nucleus. (**B** to **D**) Nuclear deformations are larger in cells with defective lamina or decompacted chromatin and larger still in cells that have both defective lamina and decompacted chromatin. Size of red arrow indicates the relative intranuclear opposing force.

generally thought to serve mainly as a means to facilitate gene silencing (*33*); however, several observations suggest that the peripheral sequestration of heterochromatin may also enhance the structural robustness of the nucleus and strengthen its ability to withstand physical challenges, such as mechanical forces exerted during cell migration or in mechanically active tissues (*34*, *35*) (Fig. 3).

Initial evidence for a role of chromatin in conferring nuclear robustness comes from observations in the yeast *Schizosaccharomyces pombe*, where the condensed centromeric chromatin is clustered and positioned opposite the microtubule organizing center, the region of the nucleus that is subjected to the strongest mechanical forces generated in the cytoplasm (*36*–*38*). Mutations in the nuclear proteins HEH1, HEH2, and IMA1, which tether chromatin to the inner nuclear membrane, lower the ability of nuclei to withstand mechanical forces emanating from microtubules assembled in the cytoplasm, as demonstrated by decreased nuclear stiffness when challenged by optical tweezers (*37*, *38*).

In vertebrate cells, the nucleoplasmic side of the nuclear membrane is lined by the nuclear lamina, a meshwork of intermediate filaments that supports and strengthens the nuclear membrane, thereby providing mechanical stability to the nucleus (Fig. 3). In mouse embryonic fibroblasts, down-regulation of the Prdm3 and Prdm16 methyltransferases, which facilitate heterochromatic histone H3 Lys^9 methylation and promote heterochromatinization, leads not only to decreased chromatin compaction but also to disruption of the nuclear lamina, invaginations of the nuclear envelope, and changes in nuclear shape (*39*). In addition, nuclear blebbing (deformation of the nucleus upon weakening of the nuclear lamina) and defects in the nuclear membrane have been observed in human laminopathies, diseases caused by mutations in the genes encoding the lamin proteins (*11*); similar defects are seen in tissue culture cells overexpressing HMGN5 (*35*), an architectural chromatin protein known to promote chromatin decompaction by reducing the ability of the linker histone H1 to bind to nucleosomes (*40*). In these cells, the levels of lamina components or histone modifications associated with condensed heterochromatin remain unaltered, which suggests that the defects in the nuclear membrane and lamina are directly due to changes in chromatin compaction.

An obvious interpretation of these findings is that chromatin decompaction likely alters the mechanical properties of the nucleus in a manner similar to that in cells with defective lamina components (*41*, *42*). The notion that chromatin decondensation weakens the ability of the nucleus to withstand mechanical force is also supported by the finding that in $Lmna^{-/-}$ cells, which lack nuclear lamins A and C and already have a weakened lamina, chromatin decompaction synergistically reduces nuclear robustness (*35*) (Fig. 3). Although these observations point to an interplay between chromatin and the lamina in determining the mechanical properties of nuclei, the finding that nuclear stiffness changes upon alterations in the nuclear ionic environment without apparent changes to the lamina structure suggests that chromatin by itself contributes significantly, and directly, to determining the mechanical properties of nuclei (*43*).

Evidence for a physiological, nongenetic role for heterochromatin in supporting lamina integrity and nuclear robustness comes from analyses of transgenic mice. Global overexpression of HMGN5 leads to a hypertrophic heart harboring large cells with enlarged nuclei lacking visually detectable condensed heterochromatin, and to death within a few months of birth (*35*); this phenotype is similar to that of $Lmna^{-/-}$ mice (*44*). Transgenic mice that overexpress HMGN5 only in the heart are born with cardiomyocytes lacking heterochromatin, yet their heart and cardiomyocytes appear normal, their lamina is intact, and the transcription profile of their heart tissue is indistinguishable from that of wild-type mice. However, most animals die within 3 months of birth, showing marked cardiac hypertrophy with extremely large cells and nuclei in which the lamina is disrupted (*35*). These pathologies are likely caused by loss of heterochromatin, which gradually diminishes the ability of the nucleus to withstand the mechanical forces of the continuously beating heart (*35*).

The importance of genome condensation in the physiological response to mechanical stress is also evident in mouse melanoma cells, where forces generated by microtubule reassembly after chemically induced depolymerization lead to invagination of both the nuclear envelope and the underlying lamina opposite the microtubule organizing center (MTOC) (*45*). Imaging of live cells revealed a transient accumulation of heterochromatin at the membrane invagination sites located closest to the MTOC, which suggests that the deformations in the nuclear membrane trigger genome reorganizations, perhaps aimed at counteracting and minimizing deleterious effects of physical changes in the nuclear membrane (*45*).

Taken together, these observations suggest that targeting heterochromatin to the nuclear periphery not only serves a genetic function via silencing of subset of genes, but also strengthens the nuclear lamina and the nuclear membrane by nongenetic means, thereby supporting the structural integrity of the nucleus. This function of the genome may be especially crucial in cells exposed to mechanical stress, such as cardiomyocytes and migrating cells.

Genome organization in cell migration

Cell migration is involved in a wide range of biological processes including development, tumor progression, tissue renewal, and immune responses. The nucleus is the largest and stiffest cellular organelle, and its large size and rigidity limit the ability of cells to easily move through restricted spaces. Consequently, during cell migration, the nucleus is exposed to considerable mechanical stress as it undergoes changes in shape to facilitate passage through the narrow constrictions imposed by tissues (*46*) (Fig. 4). The integrity of the nuclear lamina and its components is known to play a major role in nuclear reshaping and its ability to withstand mechanical stress during migration. Changes in the nuclear lamina that increase nuclear stiffness lower the rate of cell migration, whereas decreased nuclear stiffness can

Downloaded from http://science.sciencemag.org/ on May 5, 2016

reduce the viability of migrating cells (47, 48). Although the nuclear lamina plays a major role in affecting nuclear deformations during cell migration, additional factors, including the organization of the genome inside the nucleus, may affect this process (34, 49).

A major factor affecting genome organization is the dynamic binding of linker H1 variants to chromatin (50). H1 variant molecules continually cycle between chromatin-bound and unbound states, and the length of their chromatin residence time is related to the degree of chromatin compaction, with shorter residence times in decompacted chromatin (50). In mouse melanoma cells, migration cues result in an increase in the time that H1 variants remain bound to chromatin, leading to an increase in chromatin compaction. Migrating melanoma cells also exhibit increased levels of histone H3 Lys^{9} trimethylation, histone H3 Lys^{27} trimethylation, and histone H4 Lys^{20} methylation—histone modifications that mark transcriptionally silent or condensed heterochromatin (51)—as well as a decreased rate of nuclease digestion, an assay for chromatin compaction (52). It thus appears that cell migration is associated with chromatin compaction. Conversely, chromatin decompaction reduces the rate of cell migration. These effects are seen in the presence of transcriptional inhibitors, which suggests that the lower rate of migration is mainly due to alteration in chromatin organization rather than to transcriptional responses (53), strongly pointing to nongenetic mechanisms. A direct causal link between chromatin condensation and enhanced cell migration is also seen during migration of immune T cells and their extravasation into inflamed tissues (54). T cell migration is facilitated by integrin-induced recruitment of the histone methyltransferase G9a to the nuclear periphery, where it methylates specific residues in histone H3, thereby promoting chromatin condensation and alterations in the physical properties of the nucleus that facilitate T cell migration (54).

Changes in chromatin condensation and cell migration have also been seen in studies aimed at understanding the biological consequences of alteration in histone modifications during tumor invasion (55) and during development (56). In these processes, the effects of several histone modifications on cell migration were attributed to a genetic mechanism via their role in control of gene expression programs. However, it is also possible that some of the observed migration defects were due to epigenetically induced changes in global chromatin organization rather than to altered gene expression patterns. The decrease in nuclear size and the increase in the stability of the nuclear lamina resulting from chromatin condensation likely minimize potential damage during nuclear reshaping, thereby enhancing the migration ability of cells (34).

Chromatin-mediated signaling

The complex higher-order topology of the genome serves as an efficient binding platform for a wide range of cellular components. Although binding of chromatin remodelers and transcription factors to the genome leads to changes in gene expression patterns, other binding events occur in the genome that do not result in gene regulation but elicit downstream effects by nongenetic means. In particular, chromatin binding has been implicated in activation of cellular signaling pathways (Fig. 5).

A prominent example of chromatin-mediated signaling is the spindle checkpoint response (57). Segregation of mitotic chromosomes is mediated by the spindle microtubules, which attach to the chromosomes to align them at the metaphase plate. The attachment of microtubules occurs at the kinetochore, a complex proteinaceous structure that forms at the centromere, a specialized region of chromosomes, which is characterized by the presence of specific core histone proteins, CENP-A in mammals and Cse4 in *Saccharomyces cerevisiae* (57). The spindle checkpoint is a signaling cascade that emanates from the kinetochore and involves the recruitment of a complex set of kinetochore-associated proteins, such as BUB1-3 and MAD1-3, to chromatin (Fig. 5A). Association of these proteins with chromatin inhibits the activity of the anaphase-promoting complex (APC), which controls the destruction of mitotic cyclins and thus controls exit from mitosis. As long as the checkpoint proteins are bound to the kinetochore, APC is inhibited and cells do not proceed through mitosis. Proper attachment of microtubules to all kinetochores, most likely via sensing of microtubule tension, generates a signal to activate APC by releasing bound proteins, thus triggering progression into anaphase (Fig. 5A). In parallel, the protein phosphatase PP1-Sds22 binds to kinetochores when they reach the cortex in late anaphase, and appears to trigger subsequent cytokinesis (58). Both of these signaling pathways rely on, and are triggered by, the regulated binding of signaling components to chromatin in specialized regions of the chromosome (57, 58). Indeed, recent studies demonstrate that loss of methylation of H3 Lys^{9} at the centromere leads to defects in both sister chromatid cohesion and kinetochore attachment, ultimately causing chromosomal instability, a major driver of tumor progression (59).

A related function of chromatin-bound proteins is in defining the spatial orientation of the mitotic spindle and the cleavage furrow. Mitotic chromosomes generate from their surface a gradient of the guanosine triphosphate–bound form of Ran (Ras-related nuclear protein), which is implicated in nuclear transport during interphase and spindle assembly in mitosis (60). The gradient is generated by retention of the Ran exchange factor RCC1 on the mitotic chromosomes via binding to chromatin (61). The Ran gradient promotes spindle assembly and also influences spindle positioning via displacement of the LGN protein, which is involved in centering the spindle and maintaining its localization (62). Similarly, chromatin serves as a regulatory binding platform for a group of proteins referred to as chromosome passenger complex (CPC) proteins. These proteins are essential for accurate progression of cells through mitosis and associate with condensed chromosomes during early stages of mitosis (63). Their controlled release from chromatin at late stages of mitosis is a key regulator step in cell division, as it allows the CPC proteins to associate with the central spindle and the mid-body where they play critical roles in formation of the cleavage furrow and abscission (63).

A nongenetic signaling activity of chromatin is also evident from several findings indicating that the condensation status of chromatin can be sensed by components of the DNA damage response (DDR) machinery (64, 65) (Fig. 5B). The essential cell cycle checkpoint kinase ATR is thought to promote the detachment of chromatin from the nuclear envelope during replication and to ease the topological strain on the chromatin fiber (64, 66). Recent observations suggest that ATR is activated by changes in chromatin structure induced by mechanical and topological strain, such as unwinding during replication (64). In normally growing cells, ATR localizes in part to the nuclear envelope, but it also accumulates at the nuclear periphery in response to various stressors including osmotic stress and mechanical

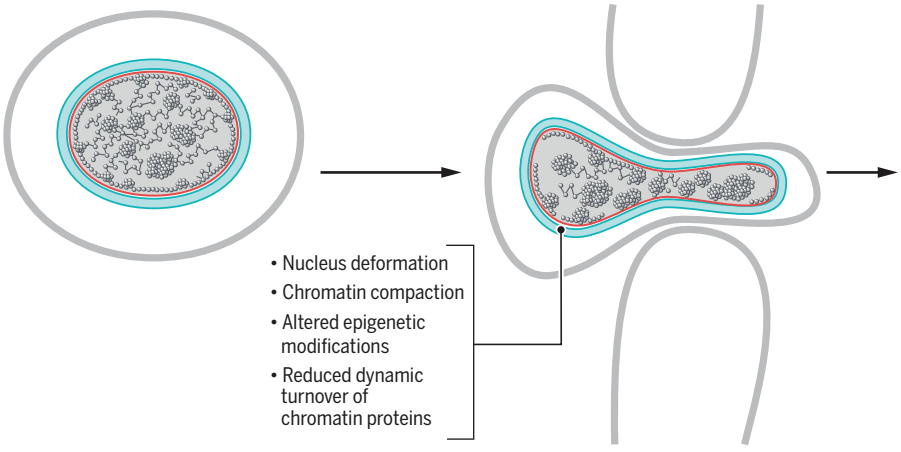


Fig. 4. Nuclear rearrangements during cellular migration. Cellular migration through narrow spaces leads to deformation of the nucleus, structural changes in the nuclear envelope (blue) and lamina (red), and genome reorganization.

Downloaded from http://science.sciencemag.org/ on May 5, 2016

force (64). ATR activation during mechanical strain is independent of DNA damage, which suggests that the kinase does not sense DNA damage but detects topological changes in chromatin or the nuclear membrane. Sensing of the chromatin condensation status may be of physiological relevance when chromosomes begin to compact during mitotic prophase, because inhibition of ATR in early mitosis delays full chromatin condensation, leading to delayed nuclear envelope breakdown and progression through mitosis (64). Independent evidence that changes in chromatin structure can trigger DDR signaling cascades comes from experiments in which highly compacted chromatin domains were generated by stably tethering heterochromatin binding factors such as heterochromatin protein HP1 to chromatin (65), which led to ATM- and ATR-dependent activation of canonical DNA damage responses, even in the absence of detectable DNA damage (65). Similarly, DDR activation without DNA damage also occurs upon global decondensation of chromatin (67).

These observations of ATR signaling and chromatin-mediated DDR induction in response to structural changes of chromatin suggest that the DDR machinery not only recognizes DNA breaks but may also be able to detect changes in chromatin structure. Sensing of chromatin structure by the DDR machinery may be an integral function of the regular DDR cascade, because recent analysis by live-cell imaging demonstrates that chromatin domains flanking the site of DNA damage undergo sequential decondensation and recondensation (68, 69). It is thus tempting to speculate that chromatin structure serves as a signal to alert the DDR machinery to damage occurring in the DNA sequence, and that the DDR machinery not only repairs damaged genome regions but also continuously surveys the physical organization of the genome.

Chromatin organization as a facilitator of nocturnal vision

A striking example of a nongenetic role of the genome that affects the biological function of a tissue rather than that of single cells is seen in the physiology of vision in nocturnal animals. Extensive comparative analysis of the global organization of the genome in rod photoreceptor cells from evolutionarily distant species revealed a remarkable correlation between heterochromatin organization and the capacity of animals for night vision (70). Whereas in most cell types and species the highly condensed heterochromatin regions of the genome are found at the nuclear periphery, in rod cells of nocturnal animals the orientation is inverted, with most heterochromatin congregated in the nuclear interior (70). The mechanism for this orientation involves the lamin A/C proteins and the inner nuclear membrane protein LBR (lamin B receptor), which appear to tether heterochromatin to the periphery (71). The likely evolutionary basis driving the inversion of heterochromatin location in nocturnal animals are the resulting beneficial changes of the optical properties of the rod cells, because the inverted pattern of heterochromatin location leads to a considerably higher refractive index at the center of the nucleus, thereby reducing light scattering and enhancing the focusing of light onto the photoreceptor plane (70). It thus appears that in the case of mammalian night vision, evolutionary pressure has selected for a physical, nongenetic, rather than a genetic, property of the genome.

Outlook

The genome has traditionally been thought to exert its function exclusively by genetic means. However, it is increasingly apparent that genomes also affect and regulate a large array of vital cellular and physiological processes through their physical properties via nongenetic means. Given that only a relatively small fraction of the genome is transcribed into protein-coding or noncoding RNAs, it is intriguing to entertain the possibility that the presence of large nontranscribed regions is not only a remnant of evolutionary genetic reshuffling events but may also serve to enhance its nongenetic functions by increasing the physical mass of the genetic material. It is notable that several of the cellular processes affected by nongenetic functions are intimately linked to mitosis, including postmitotic assembly of the nuclear membrane, chromatin-initiated spindle checkpoint signaling, and chromatin condensation, allowing for the possibility that nongenetic genome functions are particularly relevant for ensuring proper cell cycle progression. It is highly likely that additional unanticipated nongenetic functions of the genome will be discovered. For example, chromatin and chromatin binding proteins are already known to signal not only within the confines of the cell but also extracellularly, where they can function as immune triggers and are involved in the etiology of lupus erythematosus (72), enhance the sensing of cytoplasmic DNA in innate immune recognition (73, 74), and can act as cytokines in apoptosis, inflammation, and infection (75–78).

The realization that the physical properties of genomes have a substantial impact on a diverse set of cellular functions calls for several avenues of further investigation. For one, it will be critical to determine the biophysical properties of the genome in intact cells. A key step in characterizing nongenetic functions of the genome will be the development of live-cell and intravital approaches to measure the type and magnitude of forces the genome exerts on its surroundings, as well as the forces to which the genome is exposed, in intact cells under various physiological and environmental conditions. Likewise, novel experimental and computational methods need to be developed to probe, simulate, and quantify the physical properties of the nuclear environment and to determine how forces are transmitted from and to the genome. Because many of the nongenetic functions of the genome involve interaction with structural elements of the nucleus, such as the lamina or the nuclear pore complex, further investigation of these interplays should be useful in characterizing new genome functions. A particularly intriguing aspect of nongenetic genome function is its role in signaling events where the genome seems to serve as an assembly platform for signaling complexes. Characterization of chromatin-associated signaling complexes and of the physiological consequences of their interactions with the genome will be of considerable interest.

In addition to measuring the physical properties of the genome, it will be equally, if not more, important to develop methods

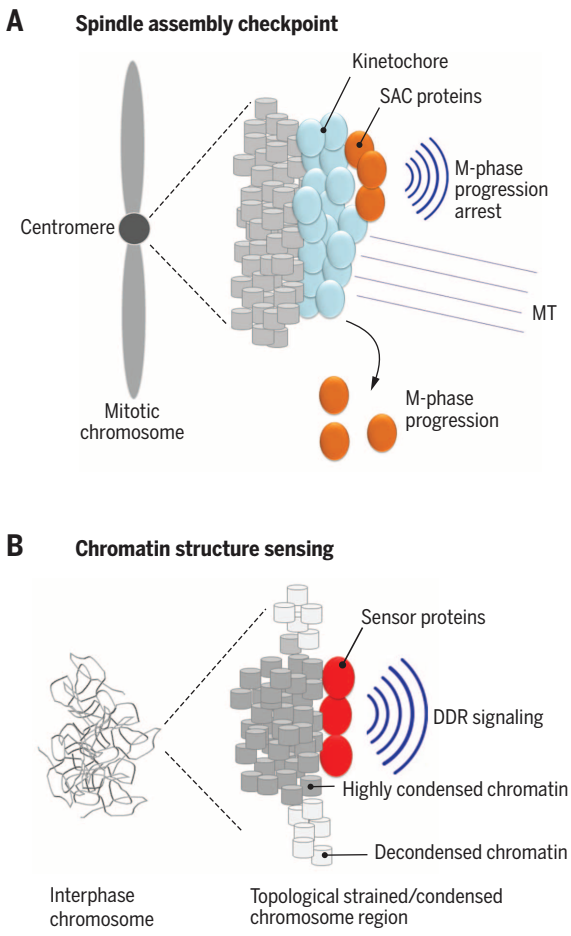


Fig. 5. The genome as a signaling platform. (**A**) Proteins of the spindle assembly checkpoint (SAC; orange) bind via the kinetochore (blue) to mitotic chromosomes at centromeres. Upon binding of microtubules (MT) to kinetochores, SAC proteins are released and promote M-phase progression. (**B**) Topologically strained or highly condensed chromosome regions can be recognized by DNA damage sensors (red) and activate DNA damage response (DDR) pathways.

Downloaded from http://science.sciencemag.org/ on May 5, 2016

to manipulate nongenetic genome features in intact cells to test their functional consequences, akin to the use of overexpression and gene inhibition to probe genetic functions of the genome. Nanomanipulation devices and light-induced optogenetic methods may be promising approaches to alter the physical properties of the genome in single cells. Ideally, these methods will be applicable to whole-animal studies so as to allow testing of nongenetic genome functions in physiological settings.

The observations discussed here highlight the emerging notion that the functions of the genome are substantially more diverse than merely the regulation of gene expression, and that the genome's physical nongenetic properties play a central role in cellular function. Although decades of studies on the regulation of gene expression have led to some of the most revolutionary advances in biology, our understanding the genome will be incomplete without elucidation of these nongenetic genome functions.

REFERENCES AND NOTES

1. G. Cavalli, T. Misteli, Functional implications of genome topology. *Nat. Struct. Mol. Biol.* **20**, 290–299 (2013). doi: 10.1038/nsmb.2474; pmid: 23463314
2. W. A. Bickmore, The spatial organization of the human genome. *Annu. Rev. Genomics Hum. Genet.* **14**, 67–84 (2013). doi: 10.1146/annurev-genom-091212-153515; pmid: 23875797
3. G. Ozer, A. Luque, T. Schlick, The chromatin fiber: Multiscale problems and approaches. *Curr. Opin. Struct. Biol.* **31**, 124–139 (2015). doi: 10.1016/j.sbi.2015.04.002; pmid: 26057099
4. Y. Cui, C. Bustamante, Pulling a single chromatin fiber reveals the forces that maintain its higher-order structure. *Proc. Natl. Acad. Sci. U.S.A.* **97**, 127–132 (2000). doi: 10.1073/pnas.97.1.127; pmid: 10618382
5. A. Rosa, Topological constraints and chromosome organization in eukaryotes: A physical point of view. *Biochem. Soc. Trans.* **41**, 612–615 (2013). doi: 10.1042/BST20120330; pmid: 23514163
6. T. Pederson, M. C. King, J. F. Marko, Forces, fluctuations, and self-organization in the nucleus. *Mol. Biol. Cell* **26**, 3915–3919 (2015). doi: 10.1091/mbc.E15-06-0357; pmid: 26543199
7. S. A. Gorski, M. Dundr, T. Misteli, The road much traveled: Trafficking in the cell nucleus. *Curr. Opin. Cell Biol.* **18**, 284–290 (2006). doi: 10.1016/j.ceb.2006.03.002; pmid: 16621498
8. J. Swift, D. E. Discher, The nuclear lamina is mechano-responsive to ECM elasticity in mature tissue. *J. Cell Sci.* **127**, 3005–3015 (2014). doi: 10.1242/jcs.149203; pmid: 24963133
9. Y. Maizels, G. Gerlitz, Shaping of interphase chromosomes by the microtubule network. *FEBS J.* **282**, 3500–3524 (2015). doi: 10.1111/febs.13334; pmid: 26040675
10. E. C. Tapley, D. A. Starr, Connecting the nucleus to the cytoskeleton by SUN-KASH bridges across the nuclear envelope. *Curr. Opin. Cell Biol.* **25**, 57–62 (2013). doi: 10.1016/j.ceb.2012.10.014; pmid: 23149102
11. Y. Gruenbaum, R. Foisner, Lamins: Nuclear intermediate filament proteins with fundamental functions in nuclear mechanics and genome regulation. *Annu. Rev. Biochem.* **84**, 131–164 (2015). doi: 10.1146/annurev-biochem-060614-034115; pmid: 25747401
12. T. C. Voss, G. L. Hager, Dynamic regulation of transcriptional states by chromatin and transcription factors. *Nat. Rev. Genet.* **15**, 69–81 (2014). doi: 10.1038/nrg3623; pmid: 24342920
13. C. Wandke, U. Kutay, Enclosing chromatin: Reassembly of the nucleus after open mitosis. *Cell* **152**, 1222–1225 (2013). doi: 10.1016/j.cell.2013.02.046; pmid: 23498932
14. M. Gorjánácz *et al*., Caenorhabditis elegans BAF-1 and its kinase VRK-1 participate directly in post-mitotic nuclear envelope assembly. *EMBO J.* **26**, 132–143 (2007). doi: 10.1038/sj.emboj.7601470; pmid: 17170708
15. M. Segura-Totten, A. K. Kowalski, R. Craigie, K. L. Wilson, Barrier-to-autointegration factor: Major roles in chromatin decondensation and nuclear assembly. *J. Cell Biol.* **158**, 475–485 (2002). doi: 10.1083/jcb.200202019; pmid: 12163470
16. S. Vlcek, B. Korbei, R. Foisner, Distinct functions of the unique C terminus of LAP2alpha in cell proliferation and nuclear assembly. *J. Biol. Chem.* **277**, 18898–18907 (2002). doi: 10.1074/jbc.M200048200; pmid: 11864981
17. S. Güttinger, E. Laurell, U. Kutay, Orchestrating nuclear envelope disassembly and reassembly during mitosis. *Nat. Rev. Mol. Cell Biol.* **10**, 178–191 (2009). doi: 10.1038/nrm2641; pmid: 19234477
18. D. J. Forbes, M. W. Kirschner, J. W. Newport, Spontaneous formation of nucleus-like structures around bacteriophage DNA microinjected into *Xenopus* eggs. *Cell* **34**, 13–23 (1983). doi: 10.1016/0092-8674(83)90132-0; pmid: 6224569
19. B. Burke, L. Gerace, A cell free system to study reassembly of the nuclear envelope at the end of mitosis. *Cell* **44**, 639–652 (1986). doi: 10.1016/0092-8674(86)90273-4; pmid: 3948244
20. P. Hartl, E. Olson, T. Dang, D. J. Forbes, Nuclear assembly with lambda DNA in fractionated *Xenopus* egg extracts: An unexpected role for glycogen in formation of a higher order chromatin intermediate. *J. Cell Biol.* **124**, 235–248 (1994). doi: 10.1083/jcb.124.3.235; pmid: 8294509
21. C. Zierhut, C. Jenness, H. Kimura, H. Funabiki, Nucleosomal regulation of chromatin composition and nuclear assembly revealed by histone depletion. *Nat. Struct. Mol. Biol.* **21**, 617–625 (2014). doi: 10.1038/nsmb.2845; pmid: 24952593
22. A. Inoue, Y. Zhang, Nucleosome assembly is required for nuclear pore complex assembly in mouse zygotes. *Nat. Struct. Mol. Biol.* **21**, 609–616 (2014). doi: 10.1038/nsmb.2839; pmid: 24908396
23. C. M. Doucet, J. A. Talamas, M. W. Hetzer, Cell cycle-dependent differences in nuclear pore complex assembly in metazoa. *Cell* **141**, 1030–1041 (2010). doi: 10.1016/j.cell.2010.04.036; pmid: 20550937
24. A. Schooley, D. Moreno-Andrés, P. De Magistris, B. Vollmer, W. Antonin, The lysine demethylase LSD1 is required for nuclear envelope formation at the end of mitosis. *J. Cell Sci.* **128**, 3466–3477 (2015). doi: 10.1242/jcs.173013; pmid: 26224877
25. P. Jevtić, L. J. Edens, L. D. Vuković, D. L. Levy, Sizing and shaping the nucleus: Mechanisms and significance. *Curr. Opin. Cell Biol.* **28**, 16–27 (2014). doi: 10.1016/j.ceb.2014.01.003; pmid: 24503411
26. S. P. Hergeth, R. Schneider, The H1 linker histones: Multifunctional proteins beyond the nucleosomal core particle. *EMBO Rep.* **16**, 1439–1453 (2015). doi: 10.15252/embr.201540749; pmid: 26474902
27. X. Shen, L. Yu, J. W. Weir, M. A. Gorovsky, Linker histones are not essential and affect chromatin condensation in vivo. *Cell* **82**, 47–56 (1995). doi: 10.1016/0092-8674(95)90051-9; pmid: 7606784
28. J. C. Bell, A. F. Straight, Condensing chromosome condensation. *Nat. Cell Biol.* **17**, 964–965 (2015). doi: 10.1038/ncb3212; pmid: 26239527
29. T. G. Fazzio, B. Panning, Condensin complexes regulate mitotic progression and interphase chromatin structure in embryonic stem cells. *J. Cell Biol.* **188**, 491–503 (2010). doi: 10.1083/jcb.200908026; pmid: 20176923
30. C. M. George, J. Bozler, H. Q. Nguyen, G. Bosco, Condensins are required for maintenance of nuclear architecture. *Cells* **3**, 865–882 (2014). doi: 10.3390/cells3030865; pmid: 25153163
31. J. S. Rawlings, M. Gatzka, P. G. Thomas, J. N. Ihle, Chromatin condensation via the condensin II complex is required for peripheral T-cell quiescence. *EMBO J.* **30**, 263–276 (2011). doi: 10.1038/emboj.2010.314; pmid: 21169989
32. M. Yazdani *et al*., Disease modeling using embryonic stem cells: MeCP2 regulates nuclear size and RNA synthesis in neurons. *Stem Cells* **30**, 2128–2139 (2012). doi: 10.1002/stem.1180; pmid: 22865604
33. W. A. Bickmore, B. van Steensel, Genome architecture: Domain organization of interphase chromosomes. *Cell* **152**, 1270–1284 (2013). doi: 10.1016/j.cell.2013.02.001; pmid: 23498936
34. G. Gerlitz, M. Bustin, The role of chromatin structure in cell migration. *Trends Cell Biol.* **21**, 6–11 (2011). doi: 10.1016/j.tcb.2010.09.002; pmid: 20951589
35. T. Furusawa *et al*., Chromatin decompaction by the nucleosomal binding protein HMGN5 impairs nuclear sturdiness. *Nat. Commun.* **6**, 6138 (2015). doi: 10.1038/ncomms7138; pmid: 25609380
36. H. Funabiki, I. Hagan, S. Uzawa, M. Yanagida, Cell cycle-dependent specific positioning and clustering of centromeres and telomeres in fission yeast. *J. Cell Biol.* **121**, 961–976 (1993). doi: 10.1083/jcb.121.5.961; pmid: 8388878
37. M. C. King, T. G. Drivas, G. Blobel, A network of nuclear envelope membrane proteins linking centromeres to microtubules. *Cell* **134**, 427–438 (2008). doi: 10.1016/j.cell.2008.06.022; pmid: 18692466
38. S. M. Schreiner, P. K. Koo, Y. Zhao, S. G. Mochrie, M. C. King, The tethering of chromatin to the nuclear envelope supports nuclear mechanics. *Nat. Commun.* **6**, 7159 (2015). doi: 10.1038/ncomms8159; pmid: 26074052
39. I. Pinheiro *et al*., Prdm3 and Prdm16 are H3K9me1 methyltransferases required for mammalian heterochromatin integrity. *Cell* **150**, 948–960 (2012). doi: 10.1016/j.cell.2012.06.048; pmid: 22939622
40. M. Rochman *et al*., The interaction of NSBP1/HMGN5 with nucleosomes in euchromatin counteracts linker histone-mediated chromatin compaction and modulates transcription. *Mol. Cell* **35**, 642–656 (2009). pmid: 19748358
41. Y. Gruenbaum, A. Margalit, R. D. Goldman, D. K. Shumaker, K. L. Wilson, The nuclear lamina comes of age. *Nat. Rev. Mol. Cell Biol.* **6**, 21–31 (2005). doi: 10.1038/nrm1550; pmid: 15688064
42. J. Lammerding *et al*., Lamin A/C deficiency causes defective nuclear mechanics and mechanotransduction. *J. Clin. Invest.* **113**, 370–378 (2004). doi: 10.1172/JCI200419670; pmid: 14755334
43. J. D. Pajerowski, K. N. Dahl, F. L. Zhong, P. J. Sammak, D. E. Discher, Physical plasticity of the nucleus in stem cell differentiation. *Proc. Natl. Acad. Sci. U.S.A.* **104**, 15619–15624 (2007). doi: 10.1073/pnas.0702576104; pmid: 17893336
44. V. Nikolova *et al*., Defects in nuclear structure and function promote dilated cardiomyopathy in lamin A/C-deficient mice. *J. Clin. Invest.* **113**, 357–369 (2004). doi: 10.1172/JCI200419448; pmid: 14755333
45. G. Gerlitz, O. Reiner, M. Bustin, Microtubule dynamics alter the interphase nucleus. *Cell. Mol. Life Sci.* **70**, 1255–1268 (2013). doi: 10.1007/s00018-012-1200-5; pmid: 23117601
46. P. Friedl, K. Wolf, J. Lammerding, Nuclear mechanics during cell migration. *Curr. Opin. Cell Biol.* **23**, 55–64 (2011). doi: 10.1016/j.ceb.2010.10.015; pmid: 21109415
47. T. Harada *et al*., Nuclear lamin stiffness is a barrier to 3D migration, but softness can limit survival. *J. Cell Biol.* **204**, 669–682 (2014). doi: 10.1083/jcb.201308029; pmid: 24567359
48. J. Swift *et al*., Nuclear lamin-A scales with tissue stiffness and enhances matrix-directed differentiation. *Science* **341**, 1240104 (2013). doi: 10.1126/science.1240104; pmid: 23990565
49. K. Wolf *et al*., Physical limits of cell migration: Control by ECM space and nuclear deformation and tuning by proteolysis and traction force. *J. Cell Biol.* **201**, 1069–1084 (2013). doi: 10.1083/jcb.201210152; pmid: 23798731
50. F. Catez, T. Ueda, M. Bustin, Determinants of histone H1 mobility and chromatin binding in living cells. *Nat. Struct. Mol. Biol.* **13**, 305–310 (2006). doi: 10.1038/nsmb1077; pmid: 16715048
51. B. D. Strahl, C. D. Allis, The language of covalent histone modifications. *Nature* **403**, 41–45 (2000). doi: 10.1038/47412; pmid: 10638745
52. H. Weintraub, M. Groudine, Chromosomal subunits in active genes have an altered conformation. *Science* **193**, 848–856 (1976). doi: 10.1126/science.948749; pmid: 948749
53. G. Gerlitz, M. Bustin, Efficient cell migration requires global chromatin condensation. *J. Cell Sci.* **123**, 2207–2217 (2010). doi: 10.1242/jcs.058271; pmid: 20530575
54. X. Zhang *et al*., Integrin α4β1 controls G9a activity that regulates epigenetic changes and nuclear properties required for lymphocyte migration. *Nucleic Acids Res.* (2015). pmid: 26657637
55. M. Hieda, N. Matsuura, H. Kimura, Histone modifications associated with cancer cell migration and invasion. *Methods Mol. Biol.* **1238**, 301–317 (2015). doi: 10.1007/978-1-4939-1804-1_16; pmid: 25421667
56. N. Hu, P. H. Strobl-Mazzulla, M. E. Bronner, Epigenetic regulation in neural crest development. *Dev. Biol.* **396**, 159–168 (2014). doi: 10.1016/j.ydbio.2014.09.034; pmid: 25446277
57. N. London, S. Biggins, Signalling dynamics in the spindle checkpoint response. *Nat. Rev. Mol. Cell Biol.* **15**, 736–747 (2014). doi: 10.1038/nrm3888; pmid: 25303117
58. N. T. Rodrigues *et al*., Kinetochore-localized PP1-Sds22 couples chromosome segregation to polar relaxation. *Nature* **524**, 489–492 (2015). doi: 10.1038/nature14496; pmid: 26168397
59. Y. Tanno *et al*., The inner centromere-shugoshin network prevents chromosomal instability. *Science* **349**, 1237–1240 (2015). doi: 10.1126/science.aaa2655; pmid: 26359403
60. P. Kalab, K. Weis, R. Heald, Visualization of a Ran-GTP gradient in interphase and mitotic *Xenopus* egg extracts.

Downloaded from http://science.sciencemag.org/ on May 5, 2016

Science **295**, 2452–2456 (2002). doi: 10.1126/science.1068798; pmid: 11923538
61. H. Y. Li, D. Wirtz, Y. Zheng, A mechanism of coupling RCC1 mobility to RanGTP production on the chromatin in vivo. *J. Cell Biol.* **160**, 635–644 (2003). doi: 10.1083/jcb.200211004; pmid: 12604592
62. T. Kiyomitsu, I. M. Cheeseman, Chromosome- and spindle-pole-derived signals generate an intrinsic code for spindle position and orientation. *Nat. Cell Biol.* **14**, 311–317 (2012). doi: 10.1038/ncb2440; pmid: 22327364
63. M. Carmena, M. Wheelock, H. Funabiki, W. C. Earnshaw, The chromosomal passenger complex (CPC): From easy rider to the godfather of mitosis. *Nat. Rev. Mol. Cell Biol.* **13**, 789–803 (2012). doi: 10.1038/nrm3474; pmid: 23175282
64. A. Kumar *et al*., ATR mediates a checkpoint at the nuclear envelope in response to mechanical stress. *Cell* **158**, 633–646 (2014). doi: 10.1016/j.cell.2014.05.046; pmid: 25083873
65. R. C. Burgess, B. Burman, M. J. Kruhlak, T. Misteli, Activation of DNA damage response signaling by condensed chromatin. *Cell Rep.* **9**, 1703–1717 (2014). doi: 10.1016/j.celrep.2014.10.060; pmid: 25464843
66. R. Bermejo *et al*., The replication checkpoint protects fork stability by releasing transcribed genes from nuclear pores. *Cell* **146**, 233–246 (2011). doi: 10.1016/j.cell.2011.06.033; pmid: 21784245
67. C. J. Bakkenist, M. B. Kastan, DNA damage activates ATM through intermolecular autophosphorylation and dimer dissociation. *Nature* **421**, 499–506 (2003). doi: 10.1038/nature01368; pmid: 12556884
68. M. K. Ayrapetov, O. Gursoy-Yuzugullu, C. Xu, Y. Xu, B. D. Price, DNA double-strand breaks promote methylation of histone H3 on lysine 9 and transient formation of repressive chromatin. *Proc. Natl. Acad. Sci. U.S.A.* **111**, 9169–9174 (2014). doi: 10.1073/pnas.1403565111; pmid: 24927542
69. S. Khurana *et al*., A macrohistone variant links dynamic chromatin compaction to BRCA1-dependent genome maintenance. *Cell Rep.* **8**, 1049–1062 (2014). doi: 10.1016/j.celrep.2014.07.024; pmid: 25131201
70. I. Solovei *et al*., Nuclear architecture of rod photoreceptor cells adapts to vision in mammalian evolution. *Cell* **137**, 356–368 (2009). doi: 10.1016/j.cell.2009.01.052; pmid: 19379699
71. I. Solovei *et al*., LBR and lamin A/C sequentially tether peripheral heterochromatin and inversely regulate differentiation. *Cell* **152**, 584–598 (2013). doi: 10.1016/j.cell.2013.01.009; pmid: 23374351
72. M. J. Podolska, M. H. Biermann, C. Maueröder, J. Hahn, M. Herrmann, Inflammatory etiopathogenesis of systemic lupus erythematosus: An update. *J. Inflamm. Res.* **8**, 161–171 (2015). pmid: 26316795
73. L. Deng *et al*., STING-dependent cytosolic DNA sensing promotes radiation-induced type I interferon-dependent antitumor immunity in immunogenic tumors. *Immunity* **41**, 843–852 (2014). doi: 10.1016/j.immuni.2014.10.019; pmid: 25517616
74. S. R. Woo, L. Corrales, T. F. Gajewski, The STING pathway and the T cell-inflamed tumor microenvironment. *Trends Immunol.* **36**, 250–256 (2015). doi: 10.1016/j.it.2015.02.003; pmid: 25758021
75. Z. Xu, Y. Huang, P. Mao, J. Zhang, Y. Li, Sepsis and ARDS: The dark side of histones. *Mediators Inflamm.* **2015**, 205054 (2015). doi: 10.1155/2015/205054; pmid: 26609197
76. M. E. Bianchi, A. Manfredi, Chromatin and cell death. *Biochim. Biophys. Acta* **1677**, 181–186 (2004). doi: 10.1016/j.bbaexp.2003.10.017; pmid: 15020058
77. D. Yang *et al*., High-mobility group nucleosome-binding protein 1 acts as an alarmin and is critical for lipopolysaccharide-induced immune responses. *J. Exp. Med.* **209**, 157–171 (2012). doi: 10.1084/jem.20101354; pmid: 22184635
78. U. Andersson, K. J. Tracey, HMGB1 is a therapeutic target for sterile inflammation and infection. *Annu. Rev. Immunol.* **29**, 139–162 (2011). doi: 10.1146/annurev-immunol-030409-101323; pmid: 21219181

ACKNOWLEDGMENTS

We thank members of the Misteli lab and P. Oberdoerffer for comments on the manuscript; G. Gerlitz (Ariel University, Israel) and members of the Bustin laboratory for informative discussions on various topics of this review; and T. Ried and R. Lefcoe for illustrations. Work in the authors' laboratories is supported by the NIH Intramural Research Program, National Cancer Institute, Center for Cancer Research.

10.1126/science.aad6933

Downloaded from http://science.sciencemag.org/ on May 5, 2016

RESEARCH ARTICLE SUMMARY

NEUROSCIENCE

Autism-associated SHANK3 haploinsufficiency causes I_h channelopathy in human neurons

Fei Yi,* Tamas Danko,* Salome Calado Botelho, Christopher Patzke, ChangHui Pak, Marius Wernig, Thomas C. Südhof†

INTRODUCTION: SHANK3 is a scaffolding protein that is enriched in postsynaptic densities of excitatory synapses but ubiquitously expressed in most cells. *SHANK3* gene mutations are significantly associated with autism spectrum disorders (ASDs), and deletion of *SHANK3* is thought to cause the major symptoms of Phelan-McDermid syndrome. Moreover, increasing evidence links *SHANK3* mutations to schizophrenia. Because SHANK3 is a synaptic protein, *SHANK3* mutations are thought to predispose to neuropsychiatric disorders by impairing synaptic function. How *SHANK3* mutations are pathogenic, however, remains unclear.

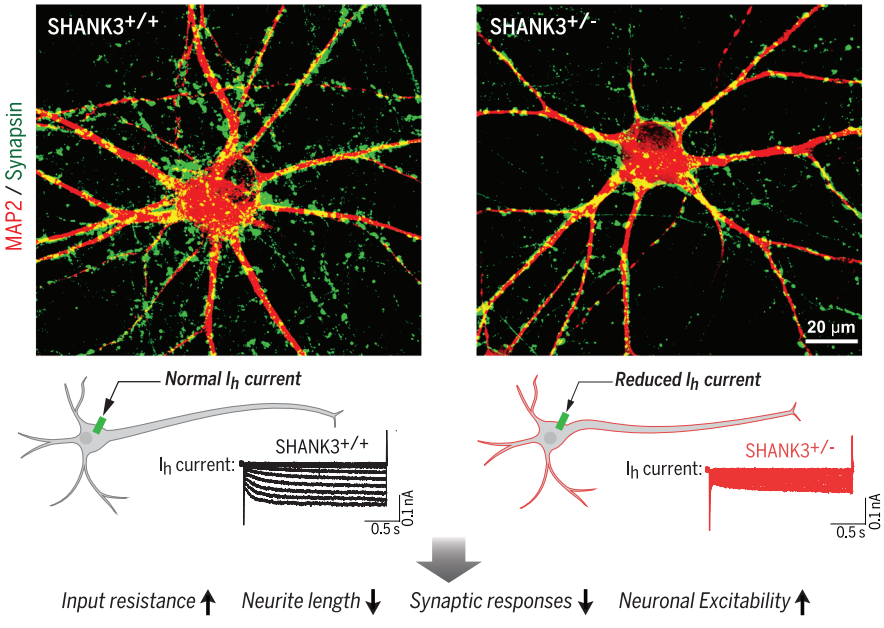
RATIONALE: Human neurons derived from Phelan-McDermid syndrome patients display complex abnormalities, including synaptic deficits and altered intrinsic electrical properties. Although some of these abnormalities are reversed by *SHANK3* reexpression, the altered electrical properties are difficult to reconcile with a primarily synaptic impairment. Moreover, in mice, *Shank3* deletions produce behavioral changes and synaptic transmission deficits, although no cellular phenotype has been identified. Here, we explored the pathogenetic mechanism of human *SHANK3* mutations with a conditional genetic approach in human neurons and correlated the results with those obtained in *Shank3*-mutant mouse neurons. We introduced conditional *SHANK3* deletions into human embryonic stem cells and examined isogenic control and heterozygous and homozygous *SHANK3*-mutant neurons derived from these conditionally mutant cells. In addition, we analyzed developing mouse *Shank3*-mutant neurons and compared their phenotype with that of human *SHANK3*-mutant neurons.

RESULTS: Heterozygous and homozygous *SHANK3*-mutant human neurons displayed diverse abnormalities, ranging from a massive increase in input resistance to increased excitability, modest impairments in dendritic arborization, and decreases in synaptic transmission. Because the increased input resistance suggested an altered channel conductance as a primary impairment, we tested various conductances. We found that the *SHANK3* mutations caused a profound impairment in hyperpolarization-activated cation (I_h) currents, which are mediated by hyperpolarization-activated cyclic nucleotide-gated (HCN) channels. This impairment produced the increased input resistance; moreover, chronic pharmacological inhibition of I_h currents in wild-type human neurons impaired dendritic arborization and synaptic transmission similar to the *SHANK3* mutations. Mechanistically, we detected a direct interaction of HCN channels with SHANK3 protein and observed a decrease in HCN-channel proteins in *SHANK3*-mutant neurons. Finally, we found that developing hippocampal neurons cultured from heterozygous and homozygous *Shank3*-mutant mice also exhibited an increased input resistance, reduced I_h currents, and an increased excitability similar to *SHANK3*-mutant human neurons.

ON OUR WEBSITE

Read the full article at http://dx.doi.org/10.1126/science.aaf2669

CONCLUSION: Using human neurons with conditional *SHANK3* mutations, we found that *SHANK3* mutations impair I_h-channel function, thereby increasing neuronal input resistance and enhancing neuronal excitability. This impairment in intrinsic electrical properties accounts, at least in part, for the decreased dendritic arborization and synaptic transmission of *SHANK3*-mutant neurons. The reduced I_h-current phenotype manifests early in neuronal development and is similarly observed in immature *Shank3*-mutant mouse neurons. We propose that, in addition to having a specifically postsynaptic function, SHANK3 protein may perform a general role during neurodevelopment by scaffolding HCN channels that mediate I_h currents in neurons and nonneuronal cells consistent with the ubiquitous expression of SHANK3. Thus, we hypothesize that *SHANK3* mutations induce an I_h channelopathy that contributes to ASD pathogenesis and may be amenable to pharmacological intervention. ■



Conditional *SHANK3* deletion in human neurons impairs I_h channel. Comparison of isogenic control and *SHANK3*-deficient human neurons reveals that heterozygous and homozygous *SHANK3* mutations dramatically decrease I_h-channel function, resulting in multifarious secondary impairments, including a decrease in dendritic arborization and synaptic responses and an increase in input resistance and neuronal excitability.

The list of author affiliations is available in the full article online.
*These authors contributed equally to this work.
†Corresponding author. Email: tcs1@stanford.edu
Cite this article as F. Yi *et al.*, *Science* 352, aaf2669 (2016).
DOI: 10.1126/science.aaf2669

Downloaded from http://science.sciencemag.org/ on May 5, 2016

RESEARCH ARTICLE

NEUROSCIENCE

Autism-associated SHANK3 haploinsufficiency causes I_h channelopathy in human neurons

Fei Yi,[1]* Tamas Danko,[1,2,3]* Salome Calado Botelho,[1] Christopher Patzke,[1] ChangHui Pak,[1] Marius Wernig,[2,3] Thomas C. Südhof [1,4]†

Heterozygous *SHANK3* mutations are associated with idiopathic autism and Phelan-McDermid syndrome. SHANK3 is a ubiquitously expressed scaffolding protein that is enriched in postsynaptic excitatory synapses. Here, we used engineered conditional mutations in human neurons and found that heterozygous and homozygous *SHANK3* mutations severely and specifically impaired hyperpolarization-activated cation (I_h) channels. *SHANK3* mutations caused alterations in neuronal morphology and synaptic connectivity; chronic pharmacological blockage of I_h channels reproduced these phenotypes, suggesting that they may be secondary to I_h-channel impairment. Moreover, mouse *Shank3*-deficient neurons also exhibited severe decreases in I_h currents. SHANK3 protein interacted with hyperpolarization-activated cyclic nucleotide-gated channel proteins (HCN proteins) that form I_h channels, indicating that SHANK3 functions to organize HCN channels. Our data suggest that *SHANK3* mutations predispose to autism, at least partially, by inducing an I_h channelopathy that may be amenable to pharmacological intervention.

Haploinsufficiency of *SHANK3* constitutes one of the more frequent single-gene mutations in autism spectrum disorders (ASDs) (*1*–*5*). Moreover, *SHANK3* is among several genes deleted in Phelan-McDermid syndrome (22q13.3 deletion syndrome), and *SHANK3* haploinsufficiency may be the most important contributing factor to Phelan-McDermid syndrome pathology (*1*–*5*). In addition, emerging evidence links *SHANK3* mutations to schizophrenia (*6*, *7*), and *SHANK3* overexpression has also been implicated in neuropsychiatric disorders (*8*). Analysis of human neurons differentiated from induced pluripotent stem cells (iPSC) from patients with Phelan-McDermid syndrome have revealed two apparently disparate phenotypes, an impairment in synaptic transmission and an increase in input resistance (*9*). The synaptic impairments of Phelan-McDermid neurons are rescued with SHANK3 (*9*), consistent with the presence of SHANK3 in postsynaptic specializations where SHANK3 is thought to function as a scaffolding protein that organizes receptor signaling (*10*–*12*). Thus, Phelan-McDermid syndrome may result from a synaptic impairment caused by *SHANK3* haploinsufficiency. The dramatically increased input resistance of Phelan-McDermid neurons, however, remains an enigma (*9*). Because human neurons with sole *SHANK3* mutations have not been analyzed, the role of *SHANK3* in the phenotypes of Phelan-McDermid neurons remains incompletely understood, as does the functional effect of a pure *SHANK3* haploinsufficiency on human neurons. In mice, heterozygous and homozygous *Shank3* mutations cause a behavioral phenotype resembling autism and/or obsessive-compulsive disorders and produce changes in synaptic transmission (*13*–*21*). However, the underlying molecular mechanisms and possible contributory nonsynaptic effects are unclear, as are the cellular effects of murine *Shank3* mutations.

To address these issues that are crucial for progress toward understanding ASDs and Phelan-McDermid syndrome, we generated human neurons with conditional heterozygous and homozygous *SHANK3* loss-of-function mutations. Unexpectedly, we found that, besides causing synaptic impairments, loss of *SHANK3* function selectively and severely impaired hyperpolarization-activated cation (I_h) currents. We observed that SHANK3 protein directly bound to hyperpolarization-activated cyclic nucleotide-gated channel (HCN) proteins mediating I_h currents and that at least some of the synaptic impairments in *SHANK3*-mutant human neurons are an indirect result of the I_h channelopathy produced by the *SHANK3* mutations during neuronal development. Finally, we observed a similar phenotype in *Shank3*-deficient mouse neurons, suggesting a general function for SHANK3 in scaffolding HCN channels.

[1]Department of Molecular and Cellular Physiology, Stanford University School of Medicine, 265 Campus Drive, Stanford, CA 94305, USA. [2]Institute for Stem Cell Biology and Regenerative Medicine, Stanford University School of Medicine, 265 Campus Drive, Stanford, CA 94305, USA. [3]Department of Pathology, Stanford University School of Medicine, 265 Campus Drive, Stanford, CA 94305, USA. [4]Howard Hughes Medical Institute, Stanford University School of Medicine, 265 Campus Drive, Stanford, CA 94305, USA.
*These authors contributed equally to this work. †Corresponding author. Email: tcs1@stanford.edu

Generation of heterozygous *SHANK3* conditional knockout (cKO) mutations

To investigate the role of *SHANK3* mutations in human neurons, we constructed conditional mutations in the *SHANK3* gene in human H1 embryonic stem cells (ES cells) using homologous recombination (Fig. 1, A and B, and fig. S1) (*22*). We chose this approach because it enables generation of matching control and mutant neurons from the same ES cell clones, thus eliminating subclone-to-subclone variability. The *SHANK3* locus expresses multiple transcripts that encode different SHANK3 isoforms with distinct protein interaction domains (Fig. 1A and fig. S2A). To conditionally delete major SHANK3 isoforms, we targeted exon 13 of the *SHANK3* gene whose deletion causes a frameshift in all major *SHANK3* mRNAs.

We converted heterozygous conditionally mutant SHANK3$^{+/cKO}$ ES cells into neurons by forced expression of the transcription factor Ngn2, which generates a homogenous population of glutamatergic excitatory neurons with abundant synapse formation (*23*). We coexpressed active (Cre) or mutant Cre-recombinase (ΔCre) with Ngn2 during neuronal differentiation to produce precisely matching wild-type [ΔCre (SHANK3$^{+/+}$)] and heterozygous mutant neurons [Cre (SHANK3$^{+/-}$)] (*24*, *25*), using two independently targeted heterozygous clones of SHANK3$^{+/cKO}$ ES cells to control for clonal variation (Fig. 1C). Immunoblotting and polymerase chain reaction (PCR) demonstrated that the heterozygous *SHANK3* KO decreased SHANK3 expression but left SHANK1 and SHANK2 expression unchanged (Fig. 1D and figs. S1, D and E, S2B, and S3). No significant changes in other synaptic proteins were observed except for a decrease in PSD95 that is known to bind to SHANKs (fig. S2, C and D) (*10*–*12*).

SHANK3 haploinsufficiency impairs dendritic arborization, intrinsic electrical properties, and synaptic transmission in human neurons

Human *SHANK3*$^{+/-}$ neurons exhibited a typical neuronal morphology with abundant synapse formation (Fig. 1E). When we quantified the morphological features of matching *SHANK3*$^{+/+}$ and *SHANK3*$^{+/-}$ neurons derived from independently derived ES cell clones, we observed that *SHANK3* haploinsufficiency significantly decreased the length and branching of neurites but had no significant effect on the density or size of synapsin-positive synapses (Fig. 1, F to I).

Next, we performed whole-cell patch-clamp recordings from matching *SHANK3*$^{+/+}$ and *SHANK3*$^{+/-}$ neurons. *SHANK3* haploinsufficiency caused a large increase (~25 to 33%) in input resistance without a change in capacitance (Fig. 2A). Moreover, *SHANK3*$^{+/-}$ neurons exhibited a major decrease in evoked excitatory postsynaptic currents (EPSCs) (~40 to 50% decrease) and in the amplitude of spontaneous miniature EPSCs (mEPSCs) (~25% decrease) but not in other mEPSC parameters (Fig. 2, B and C, and fig. S2E). Overall, these results resemble those obtained with Phelan-McDermid neurons

Downloaded from http://science.sciencemag.org/ on May 5, 2016

(9), supporting the notion that despite the large genomic deletion present in Phelan-McDermid neurons, *SHANK3* haploinsufficiency may account for most Phelan-McDermid syndrome phenotypes.

Homozygous *SHANK3* deletion aggravates *SHANK3* haploinsufficiency phenotype

To inquire whether homozygous *SHANK3* mutations produce phenotypes similar to those of heterozygous *SHANK3* mutations, we generated mutant H1 ES cells with homozygous conditional *SHANK3* mutations (22) and converted them into matching $SHANK3^{+/+}$ or $SHANK3^{-/-}$ neurons by coexpression of Ngn2 and inactive or active Cre-recombinase, respectively (Fig. 3A and fig. S4). Immunoblotting confirmed that the major SHANK3 protein isoforms were no longer expressed in $SHANK3^{-/-}$ neurons (Fig. 3B and fig. S4E). Quantitative analyses uncovered a similar, but more severe, phenotype in $SHANK3^{-/-}$ neurons than in $SHANK3^{+/-}$ neurons, with a significant decrease in dendritic arborization and in synapse density (Fig. 3, C to F, and fig. S5). Electrophysiologically, $SHANK3^{-/-}$ neurons also exhibited a large increase in input resistance, a massive decrease in evoked EPSC amplitude, and a significant decrease in mEPSC amplitude similar to $SHANK3^{+/-}$ neurons (Fig. 3, G to I). In addition, $SHANK3^{-/-}$ neurons displayed a decrease in capacitance and

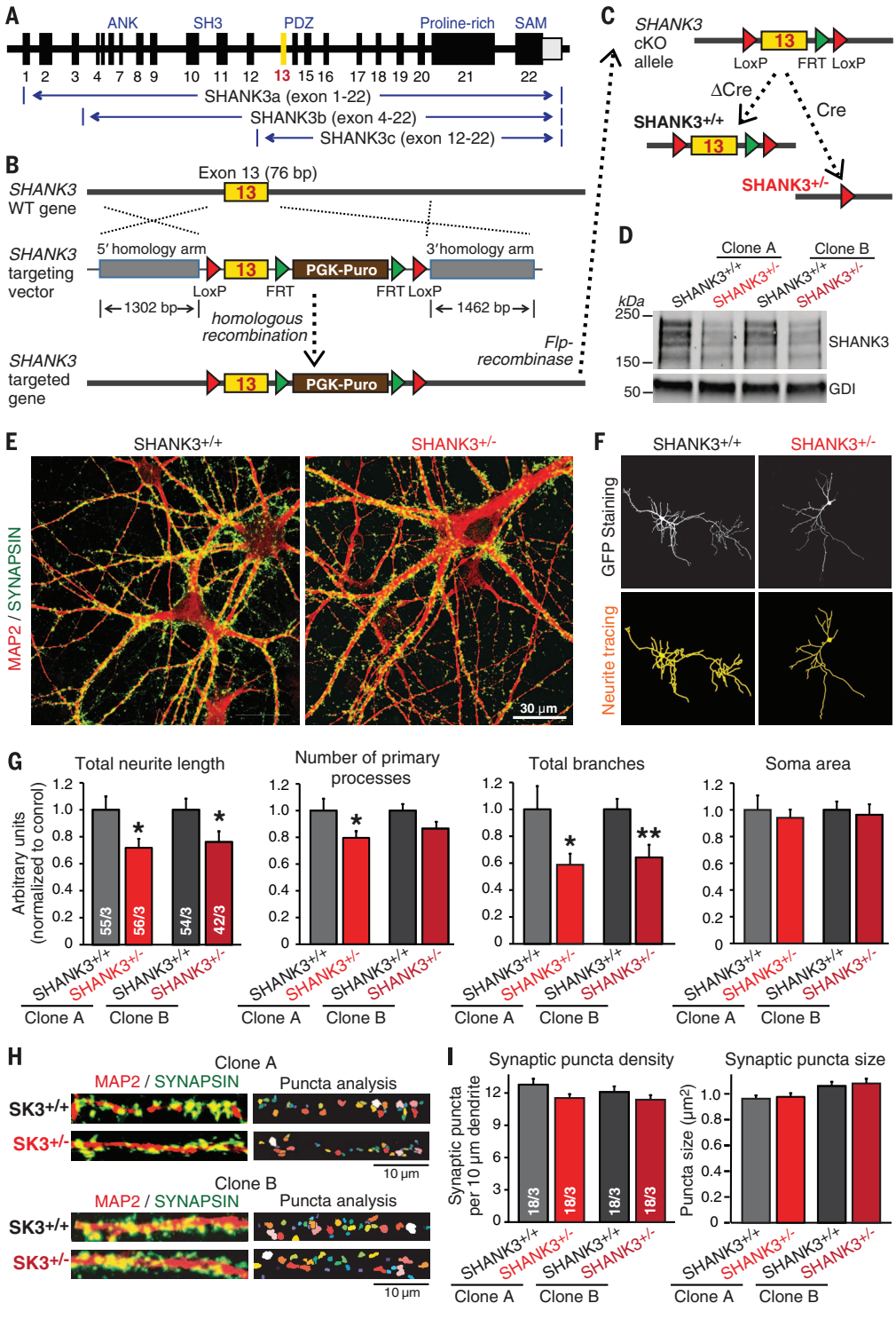


Fig. 1. *SHANK3* haploinsufficiency impairs dendritic development of human neurons. (**A**) Diagram of the *SHANK3* gene and of the three major *SHANK3* transcripts that are blocked by conditional deletion of exon 13 (yellow). (**B** and **C**) *SHANK3* targeting strategy in human ES cells. Homologous recombination was mediated using recombinant adeno-associated virus (AAV) (B) and confirmed by PCR (fig. S1B). The PGK-puromycin resistance cassette (brown box) was excised by Flp-recombinase to generate the cKO allele ($SHANK3^{+/cKO}$) (C). $SHANK3^{+/cKO}$ ES cells were converted into human $SHANK3^{+/+}$ or $SHANK3^{+/-}$ neurons by coexpression of Ngn2 with either mutant inactive Cre-recombinase (ΔCre) or active Cre-recombinase (Cre). (**D**) Reduction of SHANK3 protein levels in human $SHANK3^{+/-}$ neurons derived from two independent $SHANK3^{+/cKO}$ ES cell clones. (**E**) Representative images of $SHANK3^{+/+}$ and $SHANK3^{+/-}$ neurons (day 21) labeled by double immunofluorescence for MAP2 (red) and synapsin (green). (**F**) Representative dendritic arborization analyses by MetaMorph software of $SHANK3^{+/+}$ and $SHANK3^{+/-}$ neurons (sparsely transfected with EGFP). (**G**) *SHANK3* haploinsufficiency impairs dendritic arborization (summary graphs of indicated parameters measured in matching $SHANK3^{+/+}$ and $SHANK3^{+/-}$ neurons derived from independent $SHANK3^{+/cKO}$ ES cell clones; normalized to $SHANK3^{+/+}$ controls). (**H**) Representative images of $SHANK3^{+/+}$ and $SHANK3^{+/-}$ dendrites stained for MAP2 (red) and synapsin (green) for analysis of synaptic puncta by MetaMorph software. (**I**) Summary graphs of dendritic synaptic puncta density and size in $SHANK3^{+/+}$ and $SHANK3^{+/-}$ neurons derived from two independent $SHANK3^{+/cKO}$ ES cell clones. Data in (G) and (I) are means ± SEM. Numbers of cells/independent cultures analyzed are shown in the bars. Statistical significance was evaluated by Student's *t* test (*$P < 0.05$; **$P < 0.01$). For additional data, see figs. S1 and S2.

Downloaded from http://science.sciencemag.org/ on May 5, 2016

a notable decline in mEPSC frequency (Fig. 3, G and I).

Viewed together, our results suggest that conditional heterozygous and homozygous deletions of *SHANK3* produce similar phenotypes in human neurons. Although the *SHANK3*-mutant neurons clearly exhibit synaptic impairments, their increased input resistance and decreased dendritic arborization cannot be readily explained in terms of a synaptic change, prompting us to search for other pathogenetic mechanisms.

Heterozygous and homozygous *SHANK3* mutations impair I_h currents

The input resistance of neurons depends at least in part on their ionic conductances and ion channels. Thus, we first asked whether changes in voltage-gated Na^+ channels or K^+ channels (delayed rectifier), which generate action potentials and determine neuronal excitability, could be responsible for the increased input resistance of *SHANK3*-mutant neurons, prompted in part by binding of SHANK3 to K^+ channels (*26*). However, we detected no changes in Na^+ or K^+currents in *SHANK3*-mutant neurons (fig. S6). We next investigated whether decreased ionotropic glutamate receptor activation caused by impaired synaptic transmission in *SHANK3*-mutant neurons might be responsible. However, blocking ionotropic glutamate receptors had no effect on input resistance in $SHANK3^{+/+}$ or $SHANK3^{+/-}$ neurons (Fig. 4A).

A third candidate for an impaired membrane conductance as a cause of the increased input resistance is I_h currents that are mediated by HCN channels. In mammals, HCN channels are encoded by four genes (*HCN1* to *HCN4*) and are expressed, like SHANKs, in neuronal and non-neuronal cells (*27*–*30*) (fig. S7). HCN channels mediate hyperpolarization-activated I_h currents that depolarize membranes toward the action-potential threshold and reduce membrane resistance. I_h currents control neuronal excitability, membrane resting potentials, dendritic integration of synaptic potentials, and rhythmic oscillation of neurons (*29*, *30*). Given their multifaceted functions, impairments of I_h currents can have profound consequences for neuronal network activity [e.g., see (*31*–*33*)].

Strikingly, we found that the I_h-current inhibitor ZD7288 (*34*, *35*) increased the input resistance of wild-type neurons dramatically but had only a small effect on *SHANK3*-mutant neurons, thereby abolishing the difference in input resistance between wild-type and *SHANK3*-mutant neurons (Fig. 4B). Moreover, *SHANK3*-deficient neurons displayed an increased resting membrane potential, and the addition of ZD7288 to wild-type neurons increased their resting potential to that of *SHANK3*-deficient neurons (Fig. 4C).

Because these results suggest that the changed electrical properties of *SHANK3*-mutant neurons may be due to an impairment of I_h currents, we next directly measured I_h currents in precisely matching $SHANK3^{+/+}$ and $SHANK3^{+/-}$ or $SHANK3^{-/-}$ neurons using whole-cell recordings (Fig. 4, D and E, and fig. S8). I_h currents were readily activated by brief (2 s) hyperpolarizing voltage steps, exhibited a reversal potential of –32 mV, and were inhibited by extracellular Cs^+ and ZD7288 (fig. S8). Compared with $SHANK3^{+/+}$ neurons, both $SHANK3^{+/-}$ and $SHANK3^{-/-}$ neurons exhibited a severe decrease in I_h-current density (Fig. 4, D and E) and a

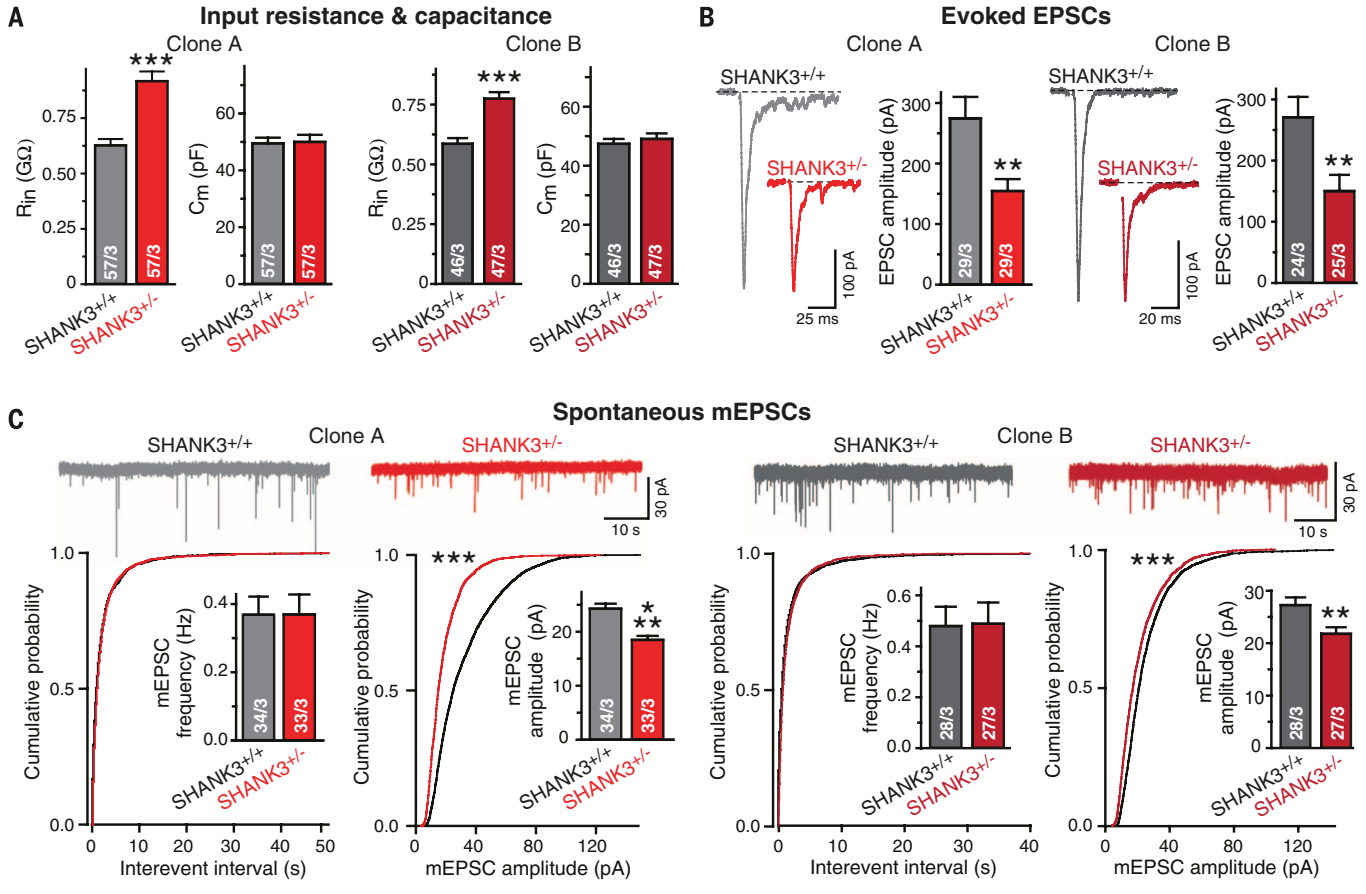
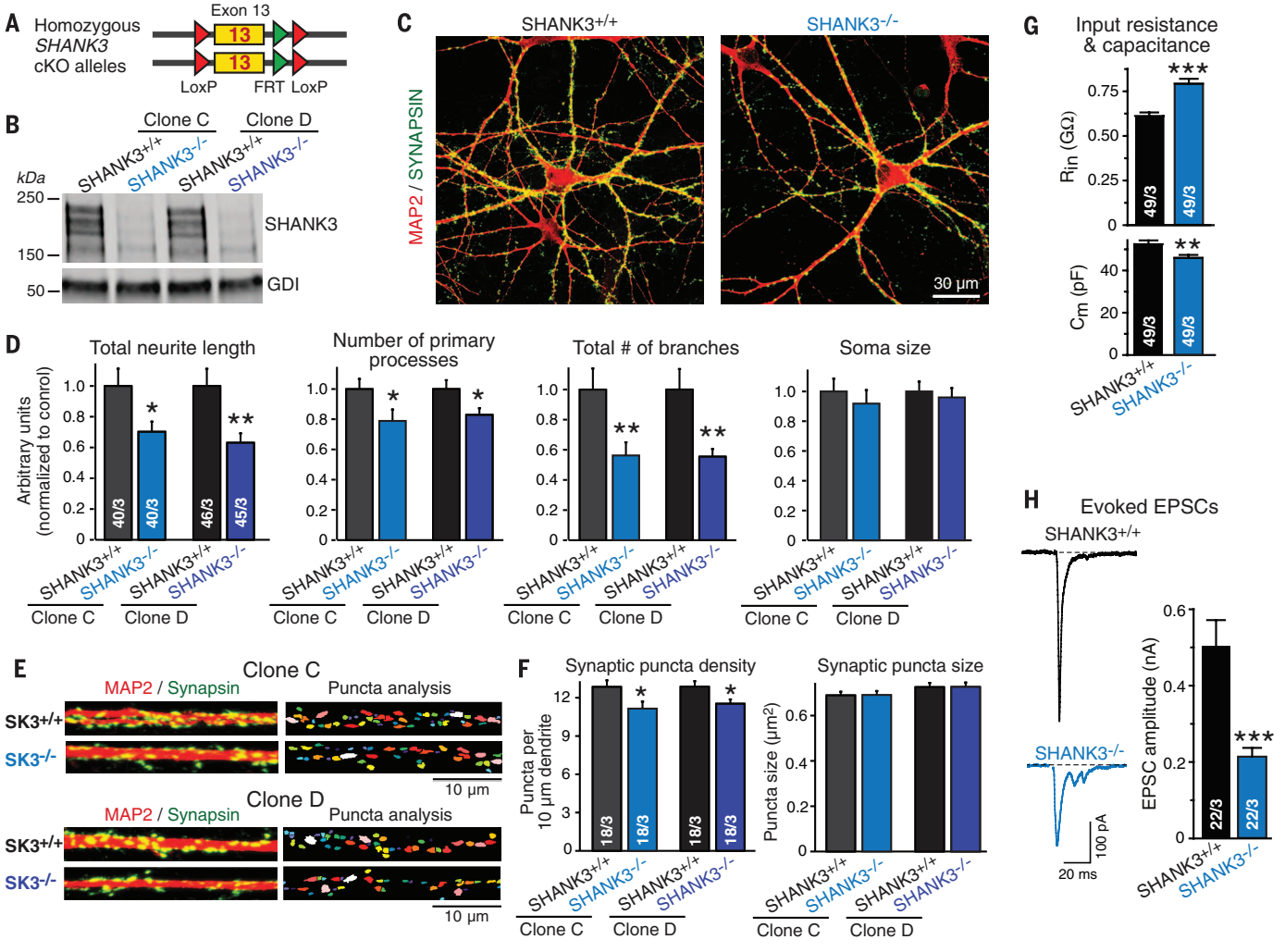


Fig. 2. *SHANK3* haploinsufficiency increases electrical input resistance of human neurons and decreases overall synaptic strength. (**A**) Input resistance (R_{in}) but not capacitance (C_m) is increased in $SHANK3^{+/-}$ neurons (summary graphs from matching human $SHANK3^{+/+}$ and $SHANK3^{+/-}$ neurons derived from two independent $SHANK3^{+/cKO}$ ES cell clones). (**B**) Evoked synaptic transmission is decreased in $SHANK3^{+/-}$ human neurons [representative EPSC traces (left) and EPSC amplitude summary graphs (right) for independent sets of neurons]. (**C**) Amplitudes but not frequencies of spontaneous mEPSCs (monitored in 1 μM tetrodotoxin) are impaired in $SHANK3^{+/-}$ neurons [top, representative traces; bottom, cumulative plots and summary graphs of the mEPSC frequency (left) and amplitude (right)]. Data are means ± SEM. Numbers of cells/cultures analyzed are shown in bars. Statistical significance was evaluated by either Student's *t* test (bar graphs) or Kolmogorov-Smirnov test (cumulative probability plots) (**$P < 0.01$; ***$P < 0.001$).

Downloaded from http://science.sciencemag.org/ on May 5, 2016

deceleration of I_h-current activation (Fig. 4F). However, other basic properties of I_h currents, such as their half-maximal activation potential (V_{50}), were not significantly altered (fig. S8). Furthermore, depolarizing voltage sag responses that are evoked by brief injections of hyperpolarizing currents in current-clamp mode (*36*, *37*) were also significantly impaired in *SHANK3*$^{+/-}$ and *SHANK3*$^{-/-}$ neurons; these impairments again were occluded by ZD7288, suggesting that these phenotypes are also due to a specific alteration in I_h-channel function (fig. S8).

Viewed together, these data suggest that *SHANK3* mutations cause I_h-channel dysfunction in human neurons. To investigate the possibility that *SHANK3*



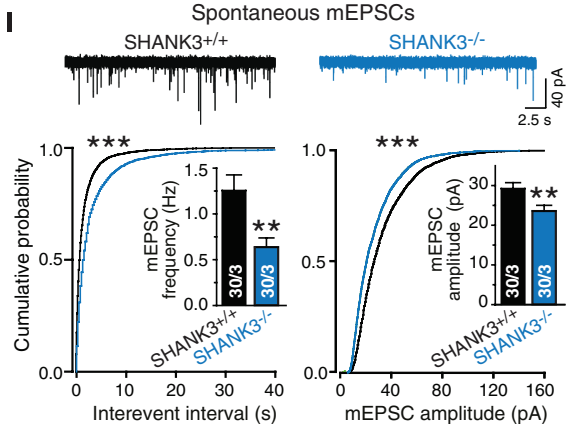


Fig. 3. Homozygous *SHANK3* deletion aggravates *SHANK3* haploinsufficiency phenotype. (**A**) Diagram of homozygous *SHANK3*$^{cKO/cKO}$ alleles (see supplementary materials for details). (**B**) *SHANK3*$^{-/-}$ neurons lack major SHANK3 proteins. Images depict immunoblots of matching *SHANK3*$^{+/+}$ and *SHANK3*$^{-/-}$ neurons derived from two independent *SHANK3*$^{cKO/cKO}$ ES cell clones. (**C**) Representative images of matching *SHANK3*$^{+/+}$ and *SHANK3*$^{-/-}$ neurons (day 21) stained by double immunofluorescence for MAP2 (red) and synapsin (green). (**D**) Homozygous *SHANK3* deletion severely impairs dendritic arborization [summary graphs of indicated parameter (normalized to *SHANK3*$^{+/+}$ controls) measured in matching *SHANK3*$^{+/+}$ and *SHANK3*$^{-/-}$ neurons derived from two independent *SHANK3*$^{cKO/cKO}$ ES cell clones]. (**E**) Representative images of dendrites stained for MAP2 (red) and synapsin (green) for analysis of synaptic puncta in *SHANK3*$^{+/+}$ and *SHANK3*$^{-/-}$ neurons. (**F**) Homozygous *SHANK3* deletion reduces synapse density (summary graphs of synaptic puncta density and size on proximal dendrites of isogenic *SHANK3*$^{+/+}$ and *SHANK3*$^{-/-}$ neurons from two independent *SHANK3*$^{cKO/cKO}$ ES cell clones). (**G**) Homozygous *SHANK3* deletion increases neuronal R_{in} (top) and decreases C_m (bottom). (**H**) Homozygous *SHANK3* deletion reduces evoked EPSC amplitudes (left, representative traces; right, summary graphs of EPSC amplitudes). (**I**) Homozygous *SHANK3* deletion decreases the frequency and amplitude of mEPSCs [top, representative traces; bottom, cumulative plots and summary graphs of mEPSC interevent intervals and frequency (bottom left) or mEPSC amplitudes (bottom right)]. Data in bar diagrams are means ± SEM. Numbers of cells/cultures analyzed are shown in bars. Statistical significance was evaluated by Student's *t* test (bar graphs) or Kolmogorov-Smirnov test (cumulative probability plots) (*P < 0.05; **P < 0.01; ***P < 0.001). For additional data, see figs. S3 to S5.

Downloaded from http://science.sciencemag.org/ on May 5, 2016

interacts with HCN channels, we coexpressed SHANK3 with HCN1, HCN2, or HCN3 channels in human embryonic kidney (HEK) 293T cells. Coimmunoprecipitations revealed that SHANK3 bound to all three isoforms of HCN channels in this assay (Fig. 4G). Mapping of the interaction domains using glutathione S-transferase (GST) pull-downs suggested that the SHANK3 ankyrin repeats directly bind to HCN channels (fig. S9). Finally, measurements of the levels of two human HCN isoforms to which antibodies were available, HCN3 and HCN4, demonstrated that the *SHANK3* deletion significantly decreased the levels of endogenous HCN proteins in human neurons, consistent with a direct interaction (Fig. 4H and fig. S10).

Because I_h currents are major determinants of neuronal excitability (*29*, *30*), we examined the effects of *SHANK3* mutations on action potential generation (Fig. 5). Consistent with the increased input resistance, *SHANK3*$^{+/-}$ and *SHANK3*$^{-/-}$ neurons fired significantly more action potentials than *SHANK3*$^{+/+}$ neurons in response to depolarizing current injections; this phenotype was abolished by the addition of ZD7288 and thus was I_h-current-dependent (Fig. 5). Moreover, because sustained rhythmic oscillations are a hallmark of neuronal circuits in various brain regions that overlap with highly enriched regions of *SHANK3* expression (*14*, *29*, *38*), we monitored the spontaneous spiking activity of *SHANK3*-mutant neurons. When neurons were held at the resting membrane potential, a large proportion of wild-type cells (~60%) fired action potentials spontaneously

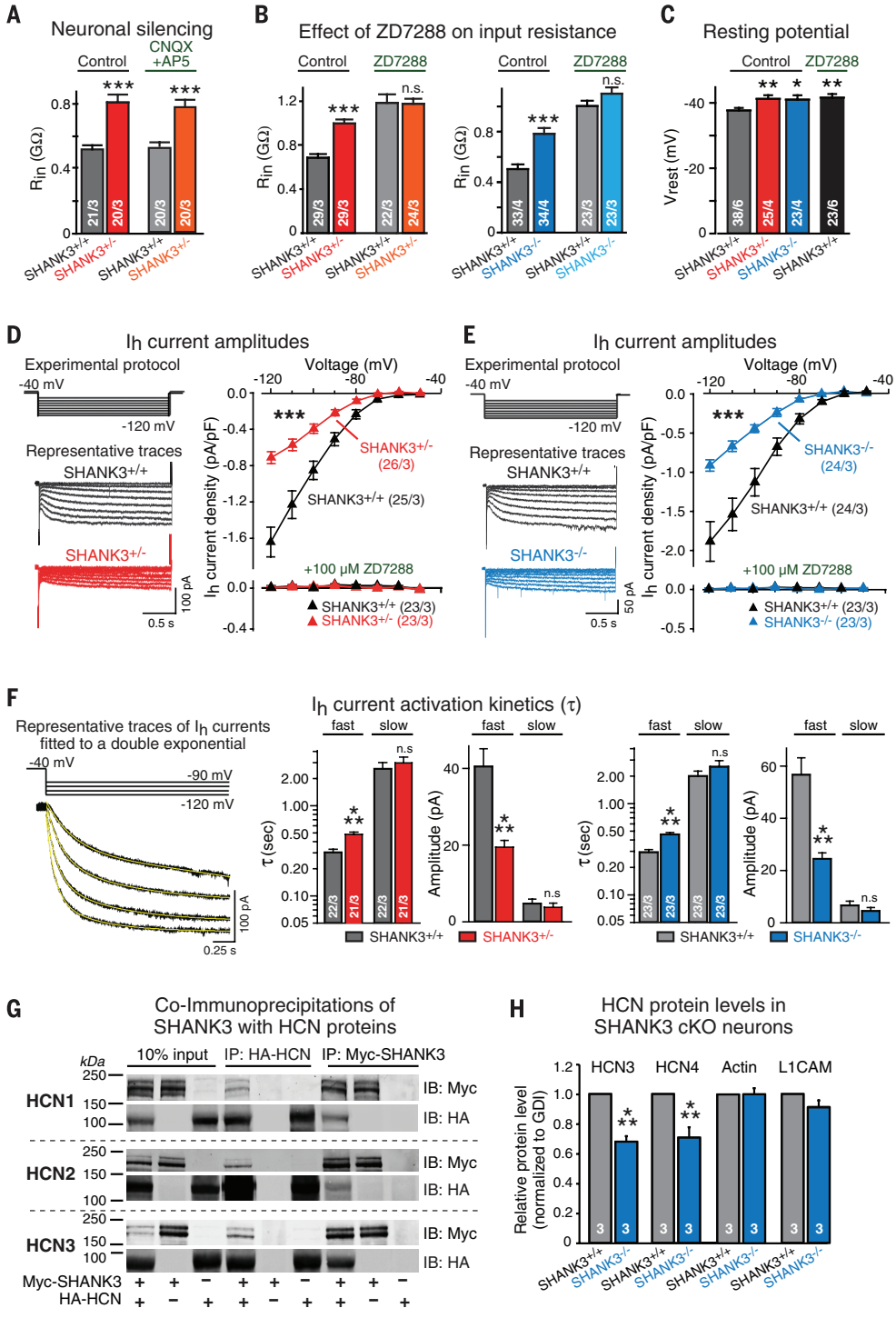


Fig. 4. *SHANK3* deletions impair I_h currents in human neurons, and SHANK3 proteins interact with HCN channels. (**A**) Neuronal silencing by blocking glutamate receptors with CNQX (20 μM) and AP5 (50 μM) does not alter neuronal R_{in}. (**B**) Blocking I_h currents with ZD7288 (100 μM) increases the R_{in} of wild-type neurons, abolishing the difference between wild-type and mutant neurons. (**C**) *SHANK3*$^{+/-}$ and *SHANK3*$^{-/-}$ neurons exhibit a more negative V_{rest} than *SHANK3*$^{+/+}$ neurons; inhibition of I_h currents in *SHANK3*$^{+/+}$ neurons with ZD7288 (5 μM) abolishes the difference. (**D** and **E**) *SHANK3*$^{+/-}$ neurons (D) and *SHANK3*$^{-/-}$ neurons (E) exhibit decreased I_h-current amplitudes compared with matching *SHANK3*$^{+/+}$ neurons (left, experimental protocol and sample traces; right, current/voltage relation of I_h currents, which are validated by inhibition with ZD7288). (**F**) Kinetics of I_h-current activation is impaired in *SHANK3*$^{+/-}$ and *SHANK3*$^{-/-}$ neurons [left, representative capacity- and leak current–subtracted I_h-current recordings fitted with a double-exponential function (yellow line superimposed on traces); center and right, summary graphs of time constants (τ) and amplitudes of fast and slow components of I_h-current activation at a test potential of –120 mV]. (**G**) SHANK3 protein binds to HCN channels mediating I_h currents. Representative immunoblots document coimmunoprecipitation of Myc-tagged SHANK3 with HA-tagged HCN1, HCN2, and HCN3 proteins coexpressed in transfected HEK293T cells; cells expressing only one or the other protein serve as negative controls. (**H**) Levels of endogenous HCN3 and HCN4 proteins are decreased in *SHANK3*$^{-/-}$ neurons, as determined by quantitative immunoblotting (for representative blots, see fig. S10). Data are means ± SEM. Numbers of cells/cultures analyzed are shown in bars or parentheses. Statistical significance was evaluated by Student's *t* test [bar graphs in (F) and (H)] or two-way analysis of variance (ANOVA) [bar graphs in (A) to (C)] and two-way repeated measure ANOVA [*I-V* plots in (D) and (E)] followed by Bonferroni's post hoc test (*$P < 0.05$; **$P < 0.01$; ***$P < 0.001$).

Downloaded from http://science.sciencemag.org/ on May 5, 2016

and regularly (fig. S11). In contrast, *SHANK3*-mutant neurons fired fewer action potentials; again, this phenotype was reversed by addition of the I_h-current inhibitor ZD7288 (fig. S11).

Shank3 deletions impair I_h currents in developing mouse neurons

To determine whether *Shank3*-mutant mice also exhibit an impairment in I_h currents, we cultured hippocampal neurons from newborn littermate *Shank3*$^{+/+}$, *Shank3*$^{+/-}$, and *Shank3*$^{-/-}$ mice. In the *Shank3*-mutant mice, exons encoding the PDZ domain of SHANK3 are deleted, similar to our conditionally *SHANK3*-mutant human neurons (*14*). We observed an overall very similar phenotype in developing mouse neurons as in human neurons (Fig. 6 and figs. S12 and S13). Specifically, quantitative imaging revealed that at 8 days in vitro (DIV8), homo- but not heterozygous *Shank3* mutations caused a significant impairment in dendritic arborization and synapse density similar to human *SHANK3* deletions (Fig. 6, A and B, and fig. S12). Electrophysiological recordings showed that although the total input resistance of mouse neurons was lower than that of human neurons, both hetero- and homozygous *Shank3* mutations produced a large increase in input resistance (Fig. 6C). Homozygous *Shank3* deletions also significantly decreased cell capacitance and increased the resting membrane potential, similar to human mutations. We then directly measured I_h currents and detected a massive impairment in both hetero- and homozygous *Shank3*-deficient mouse neurons (Fig. 6, D and E, and fig. S12). The I_h-current amplitude was decreased more than twofold by *Shank3* mutations, the I_h-current voltage sag was reduced, and the I_h-current activation kinetics was significantly decelerated. In all of these phenotypes, the homozygous mutation was more deleterious than the heterozygous mutation. These changes closely resemble those observed in human *SHANK3*-deficient neurons and also led to a markedly increased excitability in mouse *Shank3*-deficient neurons (Fig. 6F).

Chronic I_h-current inhibition impairs neuronal development similar to *SHANK3* mutations

A decrease in I_h currents by *SHANK3* mutations likely accounts for the electrophysiological changes of *SHANK3*-mutant neurons, but can it also account, at least in part, for their morphological and synaptic changes? To investigate this question, we chronically inhibited I_h channels in wild-type neurons by continuous application of low concentrations of ZD7288 (1 and 5 μM) during neuronal differentiation.

Chronic inhibition of I_h channels dramatically impaired neuronal morphology in a manner indistinguishable from that of the *SHANK3* haploinsufficiency (Fig. 7A and fig. S14). Specifically, chronic application of ZD7288 caused a dose-dependent decrease in neurite outgrowth, number of primary processes, and dendritic branching. Moreover, ZD7288 decreased the synapse density, again suggesting that major phenotypes of *SHANK3* mutations may represent indirect effects of an

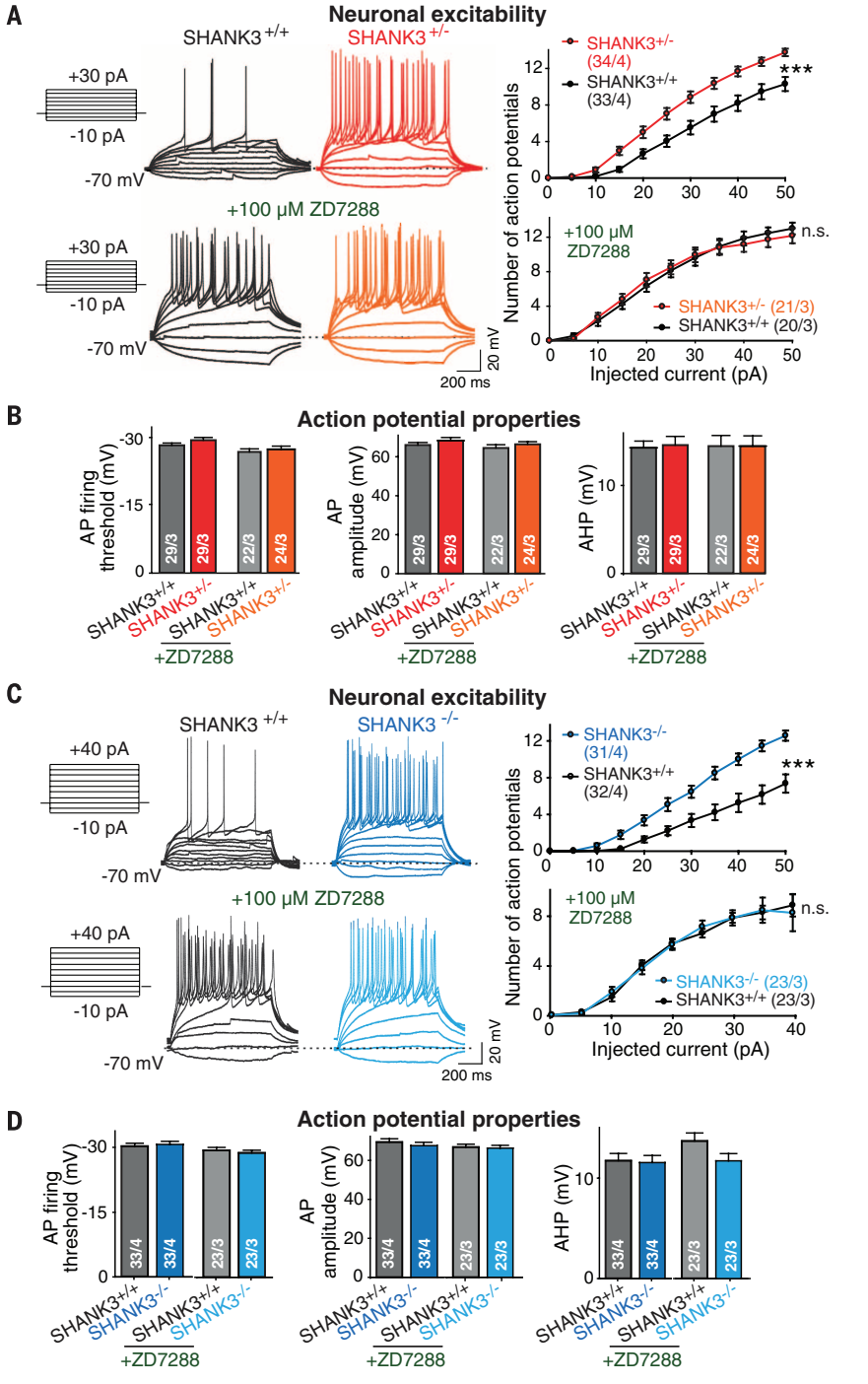


Fig. 5. *SHANK3* mutations render neurons hyperexcitable by impairing I_h currents. (**A**) *SHANK3*$^{+/-}$ mutant neurons reach action potential (AP) firing threshold earlier than matching *SHANK3*$^{+/+}$ human neurons and exhibit a steeper input-output relationship, as assessed by the number of APs elicited by increasing current injections (from −10 to +50 pA, 1-s, 5-pA increments) during current-clamp recordings. I_h-channel inhibition with ZD7288 abolishes the difference (left, experimental protocol and representative traces; right, plots of the mean AP number versus injected current). (**B**) Summary graphs of active electrical properties of matching *SHANK3*$^{+/+}$ and *SHANK3*$^{+/-}$ neurons (measured without or with ZD7288 application). From left to right: AP firing threshold, AP amplitude, and AP after-hyperpolarization amplitude (AHP). (**C**) Same as (A), but for matching *SHANK3*$^{-/-}$ and *SHANK3*$^{+/+}$ neurons. (**D**) Same as (B), but for matching *SHANK3*$^{-/-}$ and *SHANK3*$^{+/+}$ neurons. Data are means ± SEM. Numbers of cells/cultures analyzed are shown in bars or parentheses. Statistical significance was evaluated by two-way ANOVA (bar graphs) or two-way repeated measure ANOVA followed by Bonferroni's post hoc test (input-output plots) (n.s., not significant; *$P < 0.05$; **$P < 0.01$; ***$P < 0.001$).

Downloaded from http://science.sciencemag.org/ on May 5, 2016

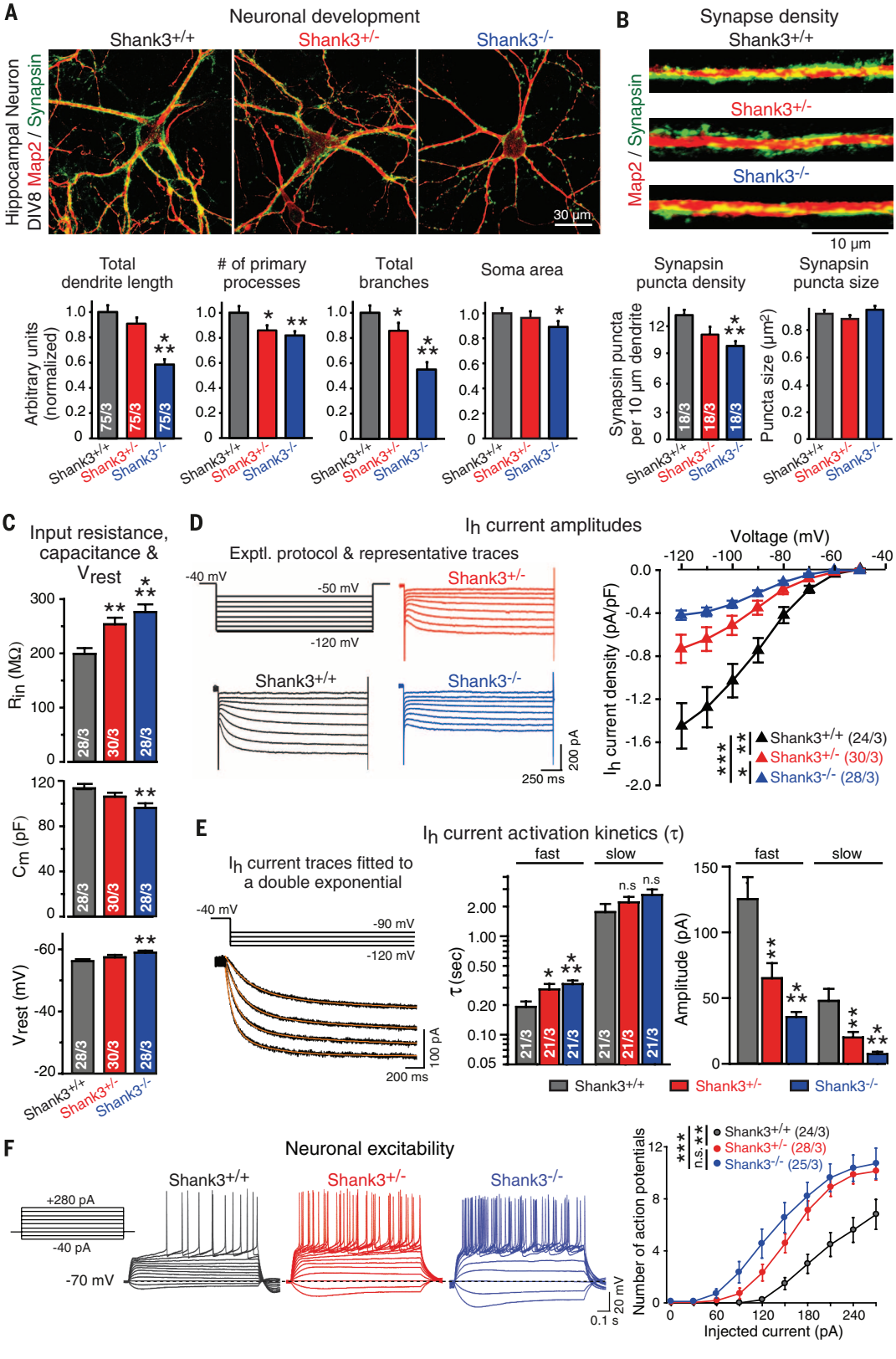


Fig. 6. Developing hippocampal neurons from *Shank3* knockout mice reproduce phenotype of human *SHANK3*-mutant neurons. (**A** and **B**) Dendritic arborization (A) and synapse formation (B) are impaired in developing *Shank3*-deficient mouse neurons [top, representative images of hippocampal neurons (A) and dendritic segments (B); bottom, summary graphs of the indicated dendritic, cellular, and synaptic parameters]. Neurons cultured from littermate $Shank3^{+/+}$, $Shank3^{+/-}$, or $Shank3^{-/-}$ mice were stained at DIV8 for MAP2 (red) and synapsin (green). (**C**) Hetero- and homozygous *Shank3* deletions increase neuronal input resistance (top), decrease cell capacitance (center), and enhance the resting membrane potential (bottom) in hippocampal neurons cultured from littermate $Shank3^{+/+}$, $Shank3^{+/-}$, and $Shank3^{-/-}$ mice and analyzed at DIV8-9. (**D**) Hetero- and homozygous *Shank3* deletions impair neuronal I_h currents in hippocampal neurons at DIV8-9 (left, experimental protocol and sample traces; right, summary graph of the current/voltage relation). (**E**) Hetero- and homozygous *Shank3* deletions decelerate I_h-current activation [left top, experimental protocol; left bottom, capacitance- and leak current-subtracted representative traces fitted with the sum of two exponential functions shown superimposed on the traces in yellow; right, summary graphs of activation time constants (τ) and component amplitudes obtained at a test potential of –120 mV]. (**F**) Hetero- and homozygous *Shank3* deletions render hippocampal neurons hyperexcitable (left, experimental protocol and representative traces of stepwise depolarizing current injections; right, summary plots of the AP number versus injected current during current-clamp recordings of neurons analyzed at DIV8-9). Data are means ± SEM. Numbers of cells/cultures analyzed are shown in bars or parentheses. Statistical significance was evaluated by one-way ANOVA followed by Tukey's post hoc test (bar graphs) or two-way repeated measure ANOVA followed by Bonferroni's post hoc test (*I-V* plot) (*$P < 0.05$; **$P < 0.01$; ***$P < 0.001$). For additional data, see figs. S12 and S13.

Downloaded from http://science.sciencemag.org/ on May 5, 2016

I_h-current impairment (Fig. 7B). In addition, chronic inhibition of I_h channels in human neurons increased the neuronal input resistance and impaired spontaneous synaptic transmission, measured after washout of the ZD7288 used to inhibit I_h currents (Fig. 7, C and D). These results suggest that long-term inhibition of I_h currents has dramatic effects on multiple facets of neuronal development.

Summary

Many mutations are thought to predispose to idiopathic ASDs by causing primary impairments in synaptic transmission (*1*–*5*). Our data show that *SHANK3* haploinsufficiency impairs synaptic function but also demonstrate that *SHANK3* haploinsufficiency decreases I_h-channel function as a primary impairment, which in turn produces major changes in intrinsic neuronal properties and secondarily affects synaptic function. Indeed, the fact that several salient phenotypes of hetero- and homozygous *SHANK3*-mutant human neurons were reproduced by pharmacologic inhibition of I_h channels suggests that I_h-channel dysfunction is a major effect of *SHANK3* haploinsufficiency. Moreover, the very similar phenotypes produced by *Shank3* mutations in developing mouse neurons, which also severely impaired I_h currents, indicates a general role for SHANK3 in scaffolding HCN channels during neuronal development at a period coinciding with the manifestation of ASDs. A role for SHANK3 as a scaffolding protein for HCN channels is plausible given the broad expression of SHANK3 in nonneuronal cells that also express HCN channels, and SHANK3 may function to enrich HCN channels at postsynaptic sites together with other proteins (*31*, *32*). Thus, we would like to suggest that an I_h-current impairment is a major pathogenetic force of *SHANK3* mutations in predisposing to ASDs and in Phelan-McDermid syndrome. Changes in I_h-channel function can conceivably be influenced pharmacologically, suggesting that pharmacological manipulation of I_h channels may be therapeutically beneficial.

HCN-channel mutations have been linked clinically with human neurological disorders, including epilepsy, sleep disorder, and impaired learning, which are commonly associated with enhanced neuron firing and/or aberrant neuronal firing patterns and are also observed in mice with HCN-channel mutations (*29*, *30*, *38*–*41*). The symptoms resulting from impaired HCN channels agree well with the hypothesized involvement of *SHANK3* deletions in ASDs and Phelan-McDermid syndrome that are also commonly associated with

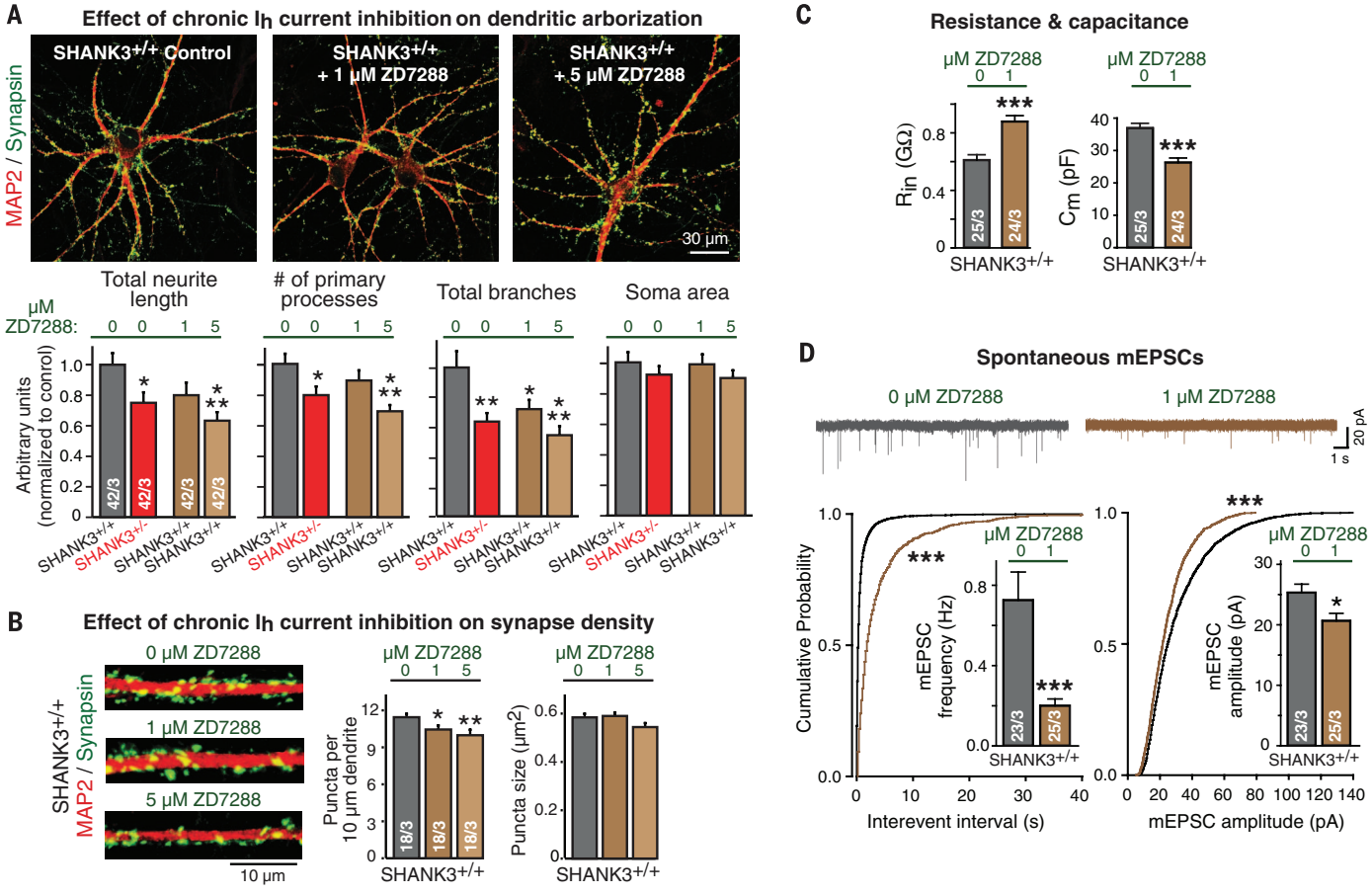


Fig. 7. Chronic inhibition of I_h currents in human neurons mimics *SHANK3* haploinsufficiency phenotype. (**A**) Chronic partial inhibition of I_h currents in wild-type *SHANK3*$^{+/+}$ neurons causes dendritic arborization defects similar to *SHANK3*$^{+/-}$ haploinsufficiency. Matching *SHANK3*$^{+/+}$ and *SHANK3*$^{+/-}$ neurons were differentiated from *SHANK3*$^{+/cKO}$ ES cells; *SHANK3*$^{+/+}$ neurons were treated with low-dose ZD7288 (1 µM or 5 µM) from days 3 to 21 of neural induction (top, representative images of neurons double-labeled for MAP2 and synapsin; bottom, summary graphs of indicated parameters normalized to the untreated *SHANK3*$^{+/+}$ control). (**B**) Chronic inhibition of I_h currents in *SHANK3*$^{+/+}$ neurons decreases synapse numbers. Experiments were performed as described for (A) (left, representative images of dendritic segments double labeled for MAP2 and synapsin; right, summary graphs of density and size of synaptic puncta). (**C**) Chronic inhibition of I_h currents in *SHANK3*$^{+/+}$ neurons significantly increases R_{in} (left) and decreases cell C_m (right). Experiments were performed as described for (A); recordings were performed after washout of ZD7288. (**D**) Chronic inhibition of I_h currents in *SHANK3*$^{+/+}$ neurons with ZD7288 (1 µM) reduces the frequency and amplitude of spontaneous mEPSCs (top, representative traces; bottom left, summary plots of the interevent interval and summary graph of the mEPSC frequency; bottom right, same for the mEPSC amplitude). Experiments were performed as described for (A); recordings were performed after washout of ZD7288. Data are means ± SEM. Numbers of cells/cultures analyzed are shown in the bars. Statistical significance was evaluated by Student's *t* test [bar graphs in (C) and (D)], one-way ANOVA followed by Tukey's post hoc test [bar graphs in (B)], or two-way ANOVA followed by Bonferroni's post hoc test [bar graphs in (A)] or Kolmogorov-Smirnov test [cumulative probability plots in (D)] (*P < 0.05; **P < 0.01; ***P < 0.001).

Downloaded from http://science.sciencemag.org/ on May 5, 2016

intellectual disability, impaired learning and memory, and epilepsy (*1*–*5*). Therefore, our data collectively suggest that impairment of HCN-channel function may contribute to the manifestations of ASDs in patients with *SHANK3* mutations and Phelan-McDermid syndrome.

Methods summary

See the supplementary materials for full details of the materials and methods (*22*).

Generation and analysis of human ES cells with heterozygous and homozygous SHANK3 cKO alleles

SHANK3-mutant ES cells were generated from H1 ES cells (passage 40; WiCell, www.wicell.org) using recombinant adenoassociated virus (AAV)–mediated homologous recombination (Fig. 1A and fig. S1A) (*24*, *25*). AAVs used for gene targeting contained a puromycin-resistance cassette surrounded by FRT sites (for Flp-recombinase mediated deletion). The cassette was inserted into the 3′ intron of exon 13 (76 base pairs) of the human *SHANK3* gene, exon 13 was flanked by LoxP sites (for Cre-recombinase mediated deletion), and 5′ and 3′ DNA homology arms were added. The same gene-targeting template was also used in the generation of homozygous SHANK3 cKO ES cells, except that a CRISPR/Cas9 targeting method was used to specifically target the second wild-type allele of the *SHANK3* gene and not the already-targeted first *SHANK3* cKO allele. Heterozygous and homozygous *SHANK3* cKO ES cell clone mutations were confirmed by PCR, and the puromycin-resistance cassette was removed by Flp-recombinase. To generate isogenic control and *SHANK3*-mutant human neurons, hetero- or homozygous *SHANK3* cKO ES cells were transdifferentiated to neurons using forced expression of Ngn2, as described (*23*). Lentiviruses encoding active (Cre) or inactive Cre-recombinase (ΔCre) were applied at 1 day before induction of neuron differentiation. Neurons were analyzed at day 21 to 23 in most experiments. For the experiments of chronic I_h-current inhibition with low-dose ZD7288 (Fig. 7), wild-type human neurons were treated with 1 μM or 5 μM ZD7288 from day 3 to day 21.

Generation and analysis of Shank3-mutant hippocampal mouse neurons

Breedings of heterozygous *Shank3*-mutant mice with deletion of the PDZ domain (exons 13 to 16) (*14*) (B6.129-Shank3tm2Gfng/J; Jackson Labs stock No. 017688) were used to produce littermate wild-type, heterozygous, and homozygous *Shank3*-mutant mice. Hippocampal neurons were cultured from newborn mice (*42*, *43*) and analyzed as immature developing neurons at DIV8-9. Mouse genotyping was performed by PCR using the Jackson Laboratory protocol.

Morphological analyses

Dendritic arborizations were analyzed in neurons that were sparsely transfected with an enhanced green fluorescent protein (EGFP) to obtain fluorescent images of individual neurons. Confocal images were analyzed unbiasedly using the "neurite outgrowth" application on MetaMorph software. For synapse morphology analyses, fixed neurons were stained by double immunofluorescence with antibodies to mitogen-activated protein kinase kinase (MAP2) (to stain for dendrites) and synapsin (to label presynaptic terminals) or HOMER1 (to label postsynaptic specializations), and images were again quantified using MetaMorph software (Molecular Devices) (*44*).

Electrophysiological recordings

Whole-cell patch-clamp recordings were performed essentially as described (*23*, *42*). EPSCs were pharmacologically isolated with 50 μM picrotoxin (PTX) and recorded at a −70 mV holding potential in voltage-clamp mode in response to extracellular stimulation with a concentric bipolar electrode (*43*). Spontaneous mEPSCs were monitored in the presence of tetrodotoxin (1 μM). Recordings of the intrinsic and active membrane properties were generally recorded in human neurons in the presence of 50 μM PTX (unless otherwise stated), and in hippocampal mouse neurons in the presence of CNQX (6-cyano-7-nitroquinoxaline-2,3-dione) (20 μM), AP5 (2-amino-5-phosphonopentanoic acid) (50 μM), and PTX (50 μM).

Input resistance (R_{in}) was calculated as the slope of linear fits of current-voltage plots generated from a series of increasing current injection steps in current-clamp mode. I_h-channel activity was measured in voltage-clamp mode as the amplitude of the slowly activating inward current component elicited by 2-s voltage steps from −50 to −120 mV in 10-mV increments from a holding potential of −40 mV with 2 mM 4-aminopyridine (4-AP) and 0.5 mM $BaCl_2$ in the bath solution. Depolarizing voltage-sag responses were evoked by brief injections of hyperpolarizing currents in current-clamp mode. Voltage-dependent Na^+ (I_{Na}) and K^+ (I_{KD}) currents were recorded in voltage-clamp mode at a holding potential of −70 mV in the presence of 2-mM 4-AP; voltage steps ranging from −90 to +40 mV were delivered at 10-mV increments. Intrinsic action potential firing properties of neurons were recorded in current-clamp mode. To assess neuronal excitability, first minimal currents were introduced to hold membrane potential around −65 to −70 mV, then increasing amounts of depolarizing currents were injected for 1 s in stepwise manner. For spontaneous AP firing, cells were held at their resting membrane potential (V_{rest}); no current was injected. The V_{rest} obtained during spontaneous firing was determined as the mean steady-state voltage recorded during interspike intervals. All experiments were performed at room temperature.

Protein-protein interaction analyses

Protein-protein interaction analyses were performed by coimmunoprecipitation of Myc-tagged full-length mouse Shank3 protein with hemagglutinin (HA)–tagged full-length human HCN proteins expressed in HEK293T cells. Coimmunoprecipitations of truncated Shank3 proteins with full-length HCN proteins were also performed to map the responsible interaction domain on Shank3. To further demonstrate the interaction between Shank3 and HCN proteins, a GST pull-down assay was performed using purified Shank3 ankyrin repeats domain and full-length HCN1 protein.

Immunoblotting

All immunoblots were visualized by fluorescently labeled secondary antibodies and quantified on Odyssey CLx Infrared Imager and Odyssey software (LI-COR Biosciences). Signals were normalized to human guanine nucleotide dissociation inhibitor (GDI) as the neuronal loading control.

REFERENCES AND NOTES

1. C. S. Leblond *et al*., Meta-analysis of SHANK mutations in autism spectrum disorders: A gradient of severity in cognitive impairments. *PLOS Genet.* **10**, e1004580 (2014). doi: 10.1371/journal.pgen.1004580; pmid: 25188300
2. C. Betancur, J. D. Buxbaum, SHANK3 haploinsufficiency: A "common" but underdiagnosed highly penetrant monogenic cause of autism spectrum disorders. *Molecular Autism* **4**, 17 (2013). doi: 10.1186/2040-2392-4-17; pmid: 23758743
3. R. O. Rosti, A. A. Sadek, K. K. Vaux, J. G. Gleeson, The genetic landscape of autism spectrum disorders. *Dev. Med. Child Neurol.* **56**, 12–18 (2014). doi: 10.1111/dmcn.12278; pmid: 24116704
4. A. M. Grabrucker, M. J. Schmeisser, M. Schoen, T. M. Boeckers, Postsynaptic ProSAP/Shank scaffolds in the cross-hair of synaptopathies. *Trends Cell Biol.* **21**, 594–603 (2011). doi: 10.1016/j.tcb.2011.07.003; pmid: 21840719
5. S. Carbonetto, A blueprint for research on Shankopathies: A view from research on autism spectrum disorder. *Dev. Neurobiol.* **74**, 85–112 (2014). doi: 10.1002/dneu.22150; pmid: 24218108
6. J. Gauthier *et al*., De novo mutations in the gene encoding the synaptic scaffolding protein SHANK3 in patients ascertained for schizophrenia. *Proc. Natl. Acad. Sci. U.S.A.* **107**, 7863–7868 (2010). doi: 10.1073/pnas.0906232107; pmid: 20385823
7. A. Guilmatre, G. Huguet, R. Delorme, T. Bourgeron, The emerging role of SHANK genes in neuropsychiatric disorders. *Dev. Neurobiol.* **74**, 113–122 (2014). doi: 10.1002/dneu.22128; pmid: 24124131
8. K. Han *et al*., SHANK3 overexpression causes manic-like behaviour with unique pharmacogenetic properties. *Nature* **503**, 72–77 (2013). doi: 10.1038/nature12630; pmid: 24153177
9. A. Shcheglovitov *et al*., SHANK3 and IGF1 restore synaptic deficits in neurons from 22q13 deletion syndrome patients. *Nature* **503**, 267–271 (2013). doi: 10.1038/nature12618; pmid: 24132240
10. S. Naisbitt *et al*., Shank, a novel family of postsynaptic density proteins that binds to the NMDA receptor/PSD-95/GKAP complex and cortactin. *Neuron* **23**, 569–582 (1999). doi: 10.1016/S0896-6273(00)80809-0; pmid: 10433268
11. J. C. Tu *et al*., Coupling of mGluR/Homer and PSD-95 complexes by the Shank family of postsynaptic density proteins. *Neuron* **23**, 583–592 (1999). doi: 10.1016/S0896-6273(00)80810-7; pmid: 10433269
12. M. Sheng, E. Kim, The Shank family of scaffold proteins. *J. Cell Sci.* **113**, 1851–1856 (2000). pmid: 10806096
13. O. Bozdagi *et al*., Haploinsufficiency of the autism-associated Shank3 gene leads to deficits in synaptic function, social interaction, and social communication. *Molecular Autism* **1**, 15 (2010). doi: 10.1186/2040-2392-1-15; pmid: 21167025
14. J. Peça *et al*., Shank3 mutant mice display autistic-like behaviours and striatal dysfunction. *Nature* **472**, 437–442 (2011). doi: 10.1038/nature09965; pmid: 21423165
15. H. E. Speed *et al*., Autism-associated insertion mutation (InsG) of Shank3 exon 21 causes impaired synaptic transmission and behavioral deficits. *J. Neurosci.* **35**, 9648–9665 (2015). doi: 10.1523/JNEUROSCI.3125-14.2015; pmid: 26134648
16. M. Kouser *et al*., Loss of predominant Shank3 isoforms results in hippocampus-dependent impairments in behavior and synaptic transmission. *J. Neurosci.* **33**, 18448–18468 (2013). doi: 10.1523/JNEUROSCI.3017-13.2013; pmid: 24259569
17. M. Yang *et al*., Reduced excitatory neurotransmission and mild autism-relevant phenotypes in adolescent Shank3 null mutant mice. *J. Neurosci.* **32**, 6525–6541 (2012). doi: 10.1523/JNEUROSCI.6107-11.2012; pmid: 22573675

Downloaded from http://science.sciencemag.org/ on May 5, 2016

18. E. Drapeau, N. P. Dorr, G. A. Elder, J. D. Buxbaum, Absence of strong strain effects in behavioral analyses of Shank3-deficient mice. *Dis. Model. Mech.* **7**, 667–681 (2014). doi: 10.1242/dmm.013821; pmid: 24652766
19. X. Wang *et al*., Synaptic dysfunction and abnormal behaviors in mice lacking major isoforms of Shank3. *Hum. Mol. Genet.* **20**, 3093–3108 (2011). doi: 10.1093/hmg/ddr212; pmid: 21558424
20. J. Lee *et al*., Shank3-mutant mice lacking exon 9 show altered excitation/inhibition balance, enhanced rearing, and spatial memory deficit. *Front. Cell. Neurosci.* **9**, 94 (2015). doi: 10.3389/fncel.2015.00094; pmid: 25852484
21. N. Uppal *et al*., Ultrastructural analyses in the hippocampus CA1 field in Shank3-deficient mice. *Molecular Autism* **6**, 41 (2015). doi: 10.1186/s13229-015-0036-x; pmid: 26137200
22. For experimental procedures, see the supplementary materials and methods on *Science* Online.
23. Y. Zhang *et al*., Rapid single-step induction of functional neurons from human pluripotent stem cells. *Neuron* **78**, 785–798 (2013). doi: 10.1016/j.neuron.2013.05.029; pmid: 23764284
24. C. Pak *et al*., Human neuropsychiatric disease modeling using conditional deletion reveals synaptic transmission defects caused by heterozygous mutations in NRXN1. *Cell Stem Cell* **17**, 316–328 (2015). doi: 10.1016/j.stem.2015.07.017; pmid: 26279266
25. C. Patzke *et al*., Analysis of conditional heterozygous STXBP1 mutations in human neurons. *J. Clin. Invest.* **125**, 3560–3571 (2015). doi: 10.1172/JCI78612; pmid: 26280581
26. C. Proepper, S. Putz, R. Russell, T. M. Boeckers, S. Liebau, The Kvβ2 subunit of voltage-gated potassium channels is interacting with ProSAP2/Shank3 in the PSD. *Neuroscience* **261**, 133–143 (2014). doi: 10.1016/j.neuroscience.2013.10.045; pmid: 24211303
27. A. Ludwig, X. Zong, M. Jeglitsch, F. Hofmann, M. Biel, A family of hyperpolarization-activated mammalian cation channels. *Nature* **393**, 587–591 (1998). doi: 10.1038/31255; pmid: 9634236
28. S. Chen, J. Wang, S. A. Siegelbaum, Properties of hyperpolarization-activated pacemaker current defined by coassembly of HCN1 and HCN2 subunits and basal modulation by cyclic nucleotide. *J. Gen. Physiol.* **117**, 491–504 (2001). doi: 10.1085/jgp.117.5.491; pmid: 11331358
29. E. E. Benarroch, HCN channels: Function and clinical implications. *Neurology* **80**, 304–310 (2013). doi: 10.1212/WNL.0b013e31827dec42; pmid: 23319474
30. O. Postea, M. Biel, Exploring HCN channels as novel drug targets. *Nat. Rev. Drug Discov.* **10**, 903–914 (2011). doi: 10.1038/nrd3576; pmid: 22094868
31. M. F. Nolan *et al*., The hyperpolarization-activated HCN1 channel is important for motor learning and neuronal integration by cerebellar Purkinje cells. *Cell* **115**, 551–564 (2003). doi: 10.1016/S0092-8674(03)00884-5; pmid: 14651847
32. M. F. Nolan *et al*., A behavioral role for dendritic integration: HCN1 channels constrain spatial memory and plasticity at inputs to distal dendrites of CA1 pyramidal neurons. *Cell* **119**, 719–732 (2004). pmid: 15550252
33. J. C. DiFrancesco, D. DiFrancesco, Dysfunctional HCN ion channels in neurological diseases. *Front. Cell. Neurosci.* **6**, 174 (2015). doi: 10.3389/fncel.2015.00071; pmid: 25805968
34. R. E. BoSmith, I. Briggs, N. C. Sturgess, Inhibitory actions of ZENECA ZD7288 on whole-cell hyperpolarization activated inward current (If) in guinea-pig dissociated sinoatrial node cells. *Br. J. Pharmacol.* **110**, 343–349 (1993). doi: 10.1111/j.1476-5381.1993.tb13815.x; pmid: 7693281
35. K. S. Shin, B. S. Rothberg, G. Yellen, Blocker state dependence and trapping in hyperpolarization-activated cation channels: Evidence for an intracellular activation gate. *J. Gen. Physiol.* **117**, 91–102 (2001). doi: 10.1085/jgp.117.2.91; pmid: 11158163
36. D. A. McCormick, H. C. Pape, Properties of a hyperpolarization-activated cation current and its role in rhythmic oscillation in thalamic relay neurones. *J. Physiol.* **431**, 291–318 (1990). doi: 10.1113/jphysiol.1990.sp018331; pmid: 1712843
37. J. S. Solomon, J. M. Nerbonne, Hyperpolarization-activated currents in isolated superior colliculus-projecting neurons from rat visual cortex. *J. Physiol.* **462**, 393–420 (1993). doi: 10.1113/jphysiol.1993.sp019561; pmid: 8331588
38. A. S. Lewis, D. M. Chetkovich, HCN channels in behavior and neurological disease: Too hyper or not active enough? *Mol. Cell. Neurosci.* **46**, 357–367 (2011). doi: 10.1016/j.mcn.2010.11.007; pmid: 21130878
39. A. M. Phillips, T. Kim, E. Vargas, S. Petrou, C. A. Reid, Spike-and-wave discharge mediated reduction in hippocampal HCN1 channel function associates with learning deficits in a genetic mouse model of epilepsy. *Neurobiol. Dis.* **64**, 30–35 (2014). doi: 10.1016/j.nbd.2013.12.007; pmid: 24368169
40. S. P. Vaidya, D. Johnston, Temporal synchrony and gamma-to-theta power conversion in the dendrites of CA1 pyramidal neurons. *Nat. Neurosci.* **16**, 1812–1820 (2013). doi: 10.1038/nn.3562; pmid: 24185428
41. M. Wang *et al*., Neuronal basis of age-related working memory decline. *Nature* **476**, 210–213 (2011). doi: 10.1038/nature10243; pmid: 21796118
42. A. Maximov, T. C. Südhof, Autonomous function of synaptotagmin 1 in triggering synchronous release independent of asynchronous release. *Neuron* **48**, 547–554 (2005). doi: 10.1016/j.neuron.2005.09.006; pmid: 16301172
43. A. Maximov, Z. P. Pang, D. G. Tervo, T. C. Südhof, Monitoring synaptic transmission in primary neuronal cultures using local extracellular stimulation. *J. Neurosci. Methods* **161**, 75–87 (2007). doi: 10.1016/j.jneumeth.2006.10.009; pmid: 17118459
44. G. R. Anderson *et al*., β-Neurexins control neural circuits by regulating synaptic endocannabinoid signaling. *Cell* **162**, 593–606 (2015). doi: 10.1016/j.cell.2015.06.056; pmid: 26213384

ACKNOWLEDGMENTS

We thank Y. Zhang, S. Maxeiner, and S. J. Lee for advice, G. Feng (MIT) for reagents, and V. Sebastiano (Stanford) for sharing instruments. This work was supported by grants from NIH (MH092931 to M.W.; NS077906 to T.C.S.; and U19MH104172 to M.W. and T.C.S.) and a postdoctoral fellowship from Vetenskapsradet, Sweden (to S.C.B.). The data are included in the main manuscript and in the supplementary materials. Author contributions: F.Y. performed the ES cell, molecular biology, expression, and cell-biology experiments, T.D. the electrophysiological experiments, S.C.B. the protein chemistry experiments, C.P. the immunoblotting experiments, and C.H.P. the gene-expression experiments. All authors planned the experiments, analyzed data, and edited the paper written by T.C.S.

SUPPLEMENTARY MATERIALS

www.sciencemag.org/content/352/6286/aaf2669/suppl/DC1
Materials and Methods
Figs. S1 to S14
References (*45*–*60*)

15 January 2016; accepted 26 February 2016
Published online 10 March 2016
10.1126/science.aaf2669

Downloaded from http://science.sciencemag.org/ on May 5, 2016

RESEARCH ARTICLES

PRIMATE EVOLUTION

Oligocene primates from China reveal divergence between African and Asian primate evolution

Xijun Ni,[1,2]* Qiang Li,[1,2] Lüzhou Li,[1] K. Christopher Beard[3,4]

Profound environmental and faunal changes are associated with climatic deterioration during the Eocene-Oligocene transition (EOT) roughly 34 million years ago. Reconstructing how Asian primates responded to the EOT has been hindered by a sparse record of Oligocene primates on that continent. Here, we report the discovery of a diverse primate fauna from the early Oligocene of southern China. In marked contrast to Afro-Arabian Oligocene primate faunas, this Asian fauna is dominated by strepsirhines. There appears to be a strong break between Paleogene and Neogene Asian anthropoid assemblages. Asian and Afro-Arabian primate faunas responded differently to EOT climatic deterioration, indicating that the EOT functioned as a critical evolutionary filter constraining the subsequent course of primate evolution across the Old World.

Primates are among the most thermophilic and hence environmentally sensitive of all mammals. As a result, both the geographic distribution and macroevolutionary patterns shown by fossil primates are strongly mediated by shifting climatic conditions during the Cenozoic. Dramatic range expansions, such as the dispersal of the earliest primates from their Asian birthplace into North America and Europe during the Paleocene-Eocene Thermal Maximum, coincided with intervals of extreme global warmth (*1*, *2*). In contrast, episodes of cooler, drier climatic conditions such as that characterizing the Eocene-Oligocene transition (EOT) resulted in continental-scale extinction of primates on landmasses that lacked direct geographic access to low-latitude refugia (*3*). Primates were extirpated at or near the EOT in North America and Europe, but Afro-Arabian primate faunas dominated by anthropoids continued to radiate during the Oligocene and Neogene (*4*–*7*). In northern China and Mongolia, mammalian faunal turnover across the EOT was pervasive enough to be compared with the European Grande Coupure, and this abrupt change in Asian mammal faunas has been designated the Mongolian Remodeling (*8*, *9*). However, assessing the impact of EOT climatic deterioration on early Asian primates has been hindered by geographic and temporal biases in the Asian fossil record. Eocene primates have been sporadically reported from northern China and Mongolia (*10*–*12*), but Eocene primates are more diverse and abundant in southern Asia, where the Oligocene record is generally absent (*13*, *14*). With the sole exception of the late early Oligocene Paali Nala locality in the Bugti Hills of Pakistan (*15*–*17*), Oligocene primates are unknown in Asia. This very limited record of Asian Oligocene primates has made it difficult to assess the impact of EOT environmental changes on Asian primate evolution. Here, we describe a diverse assemblage of fossil primates from the early Oligocene of Yunnan Province in southern China that helps to fill this gap in the record of Asian primate evolution.

We collected the primate fossils reported here via careful excavation and screen-washing at the Lijiawa fossil site in Yunnan, which has yielded more than 10 mammal taxa that indicate an early Oligocene age (supplementary materials) (*18*).

Primates Linnaeus, 1758; Strepsirhini Geoffroy, 1812; Adapiformes Hoffstetter, 1977; Sivaladapidae Thomas and Verma, 1979; *Yunnanadapis* gen. nov. **Type species**: *Yunnanadapis folivorus* sp. nov. **Included species**: The type species and *Yunnanadapis imperator* sp. nov. **Diagnosis**: Differs from *Paukkaungia*, *Hoanghonius*, and *Rencunius* in having more nearly molariform P_4 and P^4 (P^4 remains unknown in *Paukkaungia*). Lower molars further differ from those of *Paukkaungia*, *Hoanghonius*, and *Rencunius* in having less cuspidate paraconids and more angular hypoconids that are relatively mesial in position, so that the cristid obliqua is shorter than the postcristid. Upper molars further differ from those of *Hoanghonius* and (especially) *Rencunius* in lacking distinct conules. Lower molars differ from those of *Wailekia* and *Kyitchaungia* in having lingually open trigonids with protoconid and metaconid more closely approximated and talonids bearing more trenchant cristids. Upper molars differ from those of *Guangxilemur* in having more prominent parastyles and pre- and postprotocristae joining the bases of the paracone and metacone, respectively, rather than merging with the pre- and postcingula. Upper molars with weaker buccal cingulum and incomplete mesostyle, in contrast to *Guangxilemur tongi*. Lower molars differ from those of *Guangxilemur singsilai* in having lingually open trigonids and deeper, more extensive valley separating entoconid and hypoconulid. Differs from Miocene sivaladapids in lacking fully molariform P_4 and P^4 and having upper molars with distinct pericone and hypocone cusps and pre- and postprotocristae joining bases of paracone and metacone. **Etymology**: Generic name recognizes the geographic provenance of this taxon and its adapiform affinities.

Yunnanadapis folivorus sp. nov. **Holotype**: IVPP V22702, left dentary fragment preserving the crowns of C_1-M_3 (Fig. 1A and supplementary materials). **Horizon and locality**: Early Oligocene Lijiawa fossil site, upper part of Caijiachong Formation, Yuezhou Basin, Yunnan Province, China. **Diagnosis**: Smaller than *Yunnanadapis imperator*. P_3 without buccal cingulid, in contrast to *Y. imperator*. P_4 differs from that of *Y. imperator* in having much weaker buccal cingulid and hypoconid and cristid obliqua more lingual in position, yielding deeper hypoflexid and narrower talonid basin. **Etymology**: Trivial name reflects the likely dietary adaptations of this species.

Yunnanadapis imperator sp. nov. **Holotype**: IVPP V22706, right P_4 (Fig. 1B and supplementary materials). **Horizon and locality**: Early Oligocene Lijiawa fossil site, upper part of Caijiachong Formation, Yuezhou Basin, Yunnan Province, China. **Diagnosis**: Larger than *Yunnanadapis folivorus*. P_3 with strong buccal cingulid, in contrast to *Y. folivorus*. P_4 differs from that of *Y. folivorus* in having much stronger buccal cingulid and hypoconid and cristid obliqua more buccal in position, yielding shallower hypoflexid and wider talonid basin. **Etymology**: Latin "imperator" (commander), in allusion to the large size of this species.

Laomaki yunnanensis gen. et sp. nov. **Holotype**: IVPP V22708, right maxilla fragment preserving $M^{1\text{-}3}$ (Fig. 1C and supplementary materials). **Horizon and locality**: Early Oligocene Lijiawa fossil site, upper part of Caijiachong Formation, Yuezhou Basin, Yunnan Province, China. **Diagnosis**: Differs from all sivaladapids aside from *Rencunius* in having strongly developed conules on upper molars. P_4 and P^4 lack substantial molarization, in contrast to *Yunnanadapis* and Miocene sivaladapids. Upper and lower molars differ from those of *Rencunius* and *Paukkaungia* in having highly crenulated enamel, taller and more pyramidal cusps/cuspids, and more trenchant crests/cristids. Upper molars are more transverse than those of *Rencunius*, and upper molar conules are pyramidal rather than bulbous. P^4 bears

[1]Key Laboratory of Vertebrate Evolution and Human Origins, Institute of Vertebrate Paleontology and Paleoanthropology (IVPP), Chinese Academy of Sciences, 142 Xi Zhi Men Wai Street, Beijing, 100044, China. [2]Chinese Academy of Sciences (CAS) Center for Excellence in Tibetan Plateau Earth Sciences, Beijing, 100101, China. [3]Biodiversity Institute, University of Kansas, 1345 Jayhawk Boulevard, Lawrence, KS 66045-7561, USA. [4]Department of Ecology and Evolutionary Biology, University of Kansas, 1345 Jayhawk Boulevard, Lawrence, KS 66045-7561, USA.
*Corresponding author. Email: nixijun@ivpp.ac.cn

Downloaded from http://science.sciencemag.org/ on May 5, 2016

a tiny hypocone, in contrast to that of *Rencunius*. **Etymology**: Generic name derives from the Mandarin "lao" (old) and the Malagasy "maky" (lemur). Trivial name reflects the geographic provenance of this species.

Ekgmowechashalidae Szalay, 1976; *Gatanthropus micros* gen. et sp. nov. **Holotype**: IVPP V22717, isolated left M_1 (Fig. 1D and supplementary materials). **Horizon and locality**: Early Oligocene Lijiawa fossil site, upper part of Caijiachong Formation, Yuezhou Basin, Yunnan Province, China. **Diagnosis**: Differs from other ekgmowechashalid primate genera (including *Bugtilemur*, *Muangthanhinius*, and *Ekgmowechashala*) in having simpler, more nearly premolariform P_4 with hypconid and cristid obliqua located near the midline of the talonid, rather than buccally as in *Bugtilemur* and *Muangthanhinius*. P_4 without neomorphic buccal cingular cuspid, in contrast to *Ekgmowechashala*. $M_{1\text{-}2}$ lack prominent development of metastylids, in contrast to *Ekgmowechashala*. Protoconid, protocristid, and metaconid of lower molar are transversely aligned, in contrast to those of *Bugtilemur* and *Muangthanhinius*, in which these structures are obliquely oriented so that metaconid is located distolingual to protoconid. Upper molars differ from those of *Bugtilemur* in having more inflated (rather than buccolingually compressed) paracone and metacone, broader buccal cingulum, and stronger and more extensive postprotocingulum. **Etymology**: In allusion to the ekgmowechashalid affinities of this taxon, its generic name derives from the Greek "gata" (cat) and "anthropus" (man), and its trivial name derives from the Greek "micros" (small). *Ekgmowechashala* signifies "little cat man" in the Lakota language, which lacks a term for nonhuman primates.

Haplorhini Pocock, 1918; Tarsiiformes Gregory, 1915; Tarsiidae Gray, 1825; *Oligotarsius rarus* gen. et sp. nov. **Holotype**: IVPP V22727, isolated left M_1 (Fig. 1E and supplementary materials). **Horizon and locality**: Early Oligocene Lijiawa fossil site, upper part of Caijiachong Formation, Yuezhou Basin, Yunnan Province, China. **Diagnosis**: Smaller than other living and fossil tarsiers, aside from Eocene *Tarsius eocaenus* and modern *Tarsius pumilus*. Differs from extant tarsiids and Miocene *Hesperotarsius* in having well-developed conules and distobuccally oriented postmetacrista on M^1. Postprotocrista of M^1 continuous with postmetaconule crista, rather than merging with hypometacrista to form distal margin of trigon, as in extant tarsiids. M_1 differs from that of Eocene *Xanthorhysis* in being relatively shorter, broader, and higher-crowned, with entoconid located farther mesially. Lacks hypoparacrista and hypometacrista. **Etymology**: Generic name reflects the age of this taxon. Trivial name reflects the sparse documentation of Tarsiidae in the fossil record generally, as well as the meager representation of this species in the Caijiachong early Oligocene fauna.

Anthropoidea Mivart, 1864; Eosimiidae Beard *et al*., 1994; *Bahinia* Jaeger *et al*., 1999; *Bahinia banyueae* sp. nov. **Holotype**: IVPP V22730, isolated right M^1 (Fig. 1F and supplementary materials, comments regarding possible additional elements pertaining to the holotype). **Horizon**

Downloaded from http://science.sciencemag.org/ on May 5, 2016

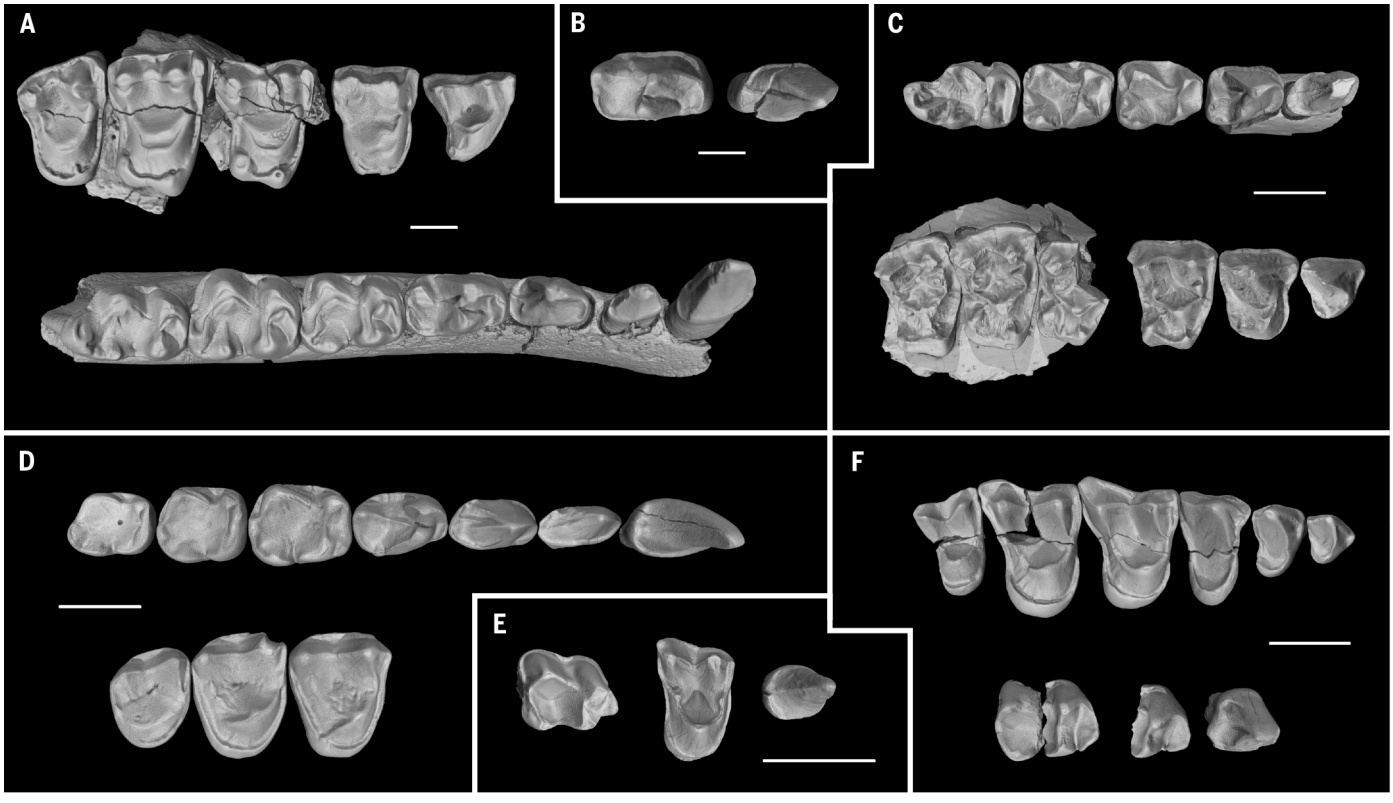


Fig. 1. Diverse primates from the early Oligocene of Yunnan Province, China. (**A**) *Yunnanadapis folivorus* gen. et sp. nov., left dentary fragment preserving C_1-M_3 (holotype, IVPP V22702), and composite upper dentition including right dP^4 (IVPP V22703), reversed left P^4 (IVPP V22704), and right maxillary fragment preserving $M^{1\text{-}3}$ (IVPP V22705). (**B**) *Yunnanadapis imperator* gen. et sp. nov., left P_3 (IVPP V22707), and reversed right P_4 (holotype, IVPP V22706). (**C**) *Laomaki yunnanensis* gen. et sp. nov., right maxillary fragment preserving $M^{1\text{-}3}$ (holotype, IVPP V22708); reversed left P^3, P^4, and M^1 (IVPP V22714, V22715, and V22716, respectively); reversed right dentary fragment preserving P_3, P_4, M_1, M_2, and M_3 (IVPP V22709, V22710, V22711, V22712, and V22713, respectively). (**D**) *Gatanthropus micros* gen. et sp. nov., left C_1 (IVPP V22718); reversed right P_2, P_3, P_4 (IVPP V22719, V22720, and V22721, respectively); left M_1 (holotype, IVPP V22717); left M_2 and M_3 (IVPP V22722 and V22723, respectively); right M^1, M^2, and M^3 (IVPP V22724, V22725, and V22726, respectively). (**E**) *Oligotarsius rarus* gen. et sp. nov., reversed left C^1 and M^1 (IVPP V22728 and V22729, respectively), and left M_1 (holotype, IVPP V22727). (**F**) *Bahinia banyueae* sp. nov., reversed left P^2 and P^3 (IVPP V22731 and V22732, respectively), right P^4 (IVPP V22733), right M^1 (holotype, IVPP V22730), right M^2 missing metacone lobe (IVPP V22734) juxtaposed with a right M^2 fragment preserving metacone lobe only (IVPP V22735), right M^3 (IVPP V22736), left P_3 and left trigonid of M_1 (IVPP V22737 and V22738, respectively), reversed right M_2 trigonid and talonid (IVPP V22739 and V22740, respectively). Scale bars, 2 mm.

and locality: Early Oligocene Lijiawa fossil site, upper part of Caijiachong Formation, Yuezhou Basin, Yunnan Province, China. **Diagnosis**: Upper molars with weaker buccal and lingual cingula than in *Bahinia pondaungensis*. Although $P^2 < P^3 < P^4$ as in *B. pondaungensis*, in *B. banyueae* P^2 is larger and P^3 is smaller in relation to P^4 than is the case in *B. pondaungensis*. **Etymology**: Trivial name honors the pioneering work on the Caijiachong mammal faunas of Yunnan Province made by our friend and colleague Banyue Wang.

Despite the dramatic faunal turnover during the EOT observed across Europe, North America, and northern Asia (*8*, *9*), the early Oligocene primate fauna from Yunnan reported here and the late early Oligocene primate fauna from Pakistan (*15*–*17*) show that multiple primate lineages successfully weathered the EOT climatic deterioration in tropical regions of Asia (Fig. 2). Indeed, most of the Asian primate clades that succeeded in traversing the EOT were able to persist there for tens of millions of years, showing that the EOT functioned as a critical filtering episode during the evolutionary history of Asian primates. Comparing the composition of the early Oligocene primate faunas from Yunnan and Pakistan with later Eocene Asian primate faunas known from China, Myanmar, and Thailand reveals that surviving this Eocene-Oligocene evolutionary filter entailed a high degree of taxonomic and ecological selectivity. Later Eocene primate assemblages in China, Myanmar, and Thailand tend to be dominated, both in terms of taxonomic richness and numerical abundance, by stem anthropoids belonging to the families Eosimiidae and Amphipithecidae (*13*, *14*, *19*, *20*). In stark contrast, only one of the six primates known from the early Oligocene of Yunnan is an anthropoid. Three of five primate species documented from the late early Oligocene of Pakistan are anthropoids, but even in this case, the anthropoid taxa known from Pakistan differ from their contemporary African relatives in being relatively small-bodied. Phylogenetic analysis (Fig. 3) shows that *Yunnanadapis folivorus*, *Y. imperator*, and *Laomaki yunnanensis* belong to the Sivaladapidae, a clade that persisted in southern and southeastern Asia until the late Miocene (*21*, *22*). Likewise, the affinities of *Gatanthropus micros* lie with *Muangthanhinius*, *Bugtilemur*, and the enigmatic North American genus *Ekgmowechashala*, which together comprise the strepsirhine clade Ekgmowechashalidae (*23*). Late Eocene–early Oligocene primates from Afro-Arabia show a very different pattern of taxonomic selectivity in response to the EOT. There, very few strepsirhines (none of which were large) survived the EOT, whereas anthropoids diversified both taxonomically and ecologically (Fig. 2) (*6*).

On the basis of the current record of early Oligocene primates from Yunnan, taxonomic selectivity across the EOT in southern Asia strongly

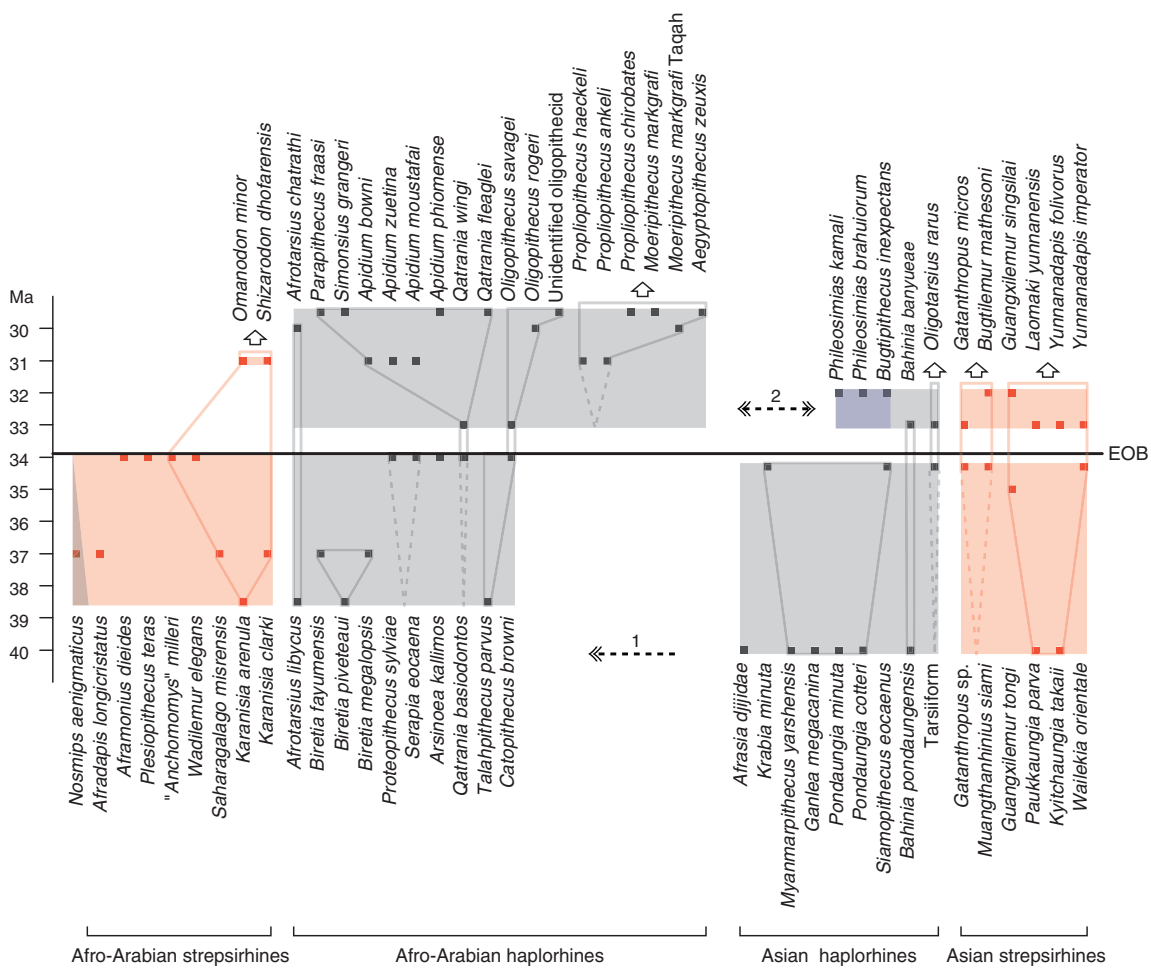


Fig. 2. Divergent taxonomic composition of fossil primates across the Eocene-Oligocene boundary (EOB) in Afro-Arabia and southern Asia. Gray area indicates haplorhines. Pale red area indicates strepsirhines. The phylogenetic affinities of *Nosmips* are uncertain (*26*). The width of the shaded areas directly reflects taxonomic diversity. Solid red and gray lines designate generally accepted monophyletic groups (Fig. 3) (*6*). Dashed lines indicate hypothetical range extensions in earlier strata. White arrows indicate that lineages persist to later intervals. Dashed line with arrowhead 1 indicates intercontinental dispersal of early anthropoids from Asia to Afro-Arabia (*6*, *27*). Dashed line with arrowhead 2 indicates a second dispersal episode of anthropoids between Afro-Arabia and Asia during the early Oligocene, as suggested by our phylogenetic analysis that *Phileosimias* and *Bugtipithecus* are more closely related to Afro-Arabian anthropoids than to Asian anthropoids (supplementary materials). Ma, million years ago.

Downloaded from http://science.sciencemag.org/ on May 5, 2016

favored strepsirhines over haplorhines. Ecologically, strepsirhines were the only Asian primates to occupy those niches available to primates of relatively large body mass because medium and large haplorhine taxa such as amphipithecids were eradicated across the EOT in Asia. This pattern of turnover across the EOT among Asian primates differs radically from that which has been observed in Afro-Arabia. There, only small strepsirhines survived the EOT, whereas anthropoid haplorhines diversified to occupy a range of body sizes that was nearly an order of magnitude larger than their previous distribution (Fig. 4). The divergent responses shown by Afro-Arabian and Asian primates across the EOT set the stage for subsequent macroevolutionary patterns within this group. Africa became the geographic nexus of anthropoid evolution, whereas Asia continued to harbor sivaladapid strepsirhines and tarsiid haplorhines. Dynamic changes to the Asian physical environment during the interval spanning the EOT included progressive retreat of the Paratethys Sea from central Asia, continued uplift of the Tibetan-Himalayan orogen, and opening of the South China Sea (*24*). Africa was not immune to global climatic changes across the EOT, but it did not experience the dramatic tectonic and paleogeographic alterations that characterized Asia at this time. It is tempting to attribute the different patterns of turnover in Asian and African primate faunas across the EOT to local changes in vegetation and paleoenvironment (*25*), but current evidence is not sufficient to rule out the possibility that stochastic processes also played a substantial role.

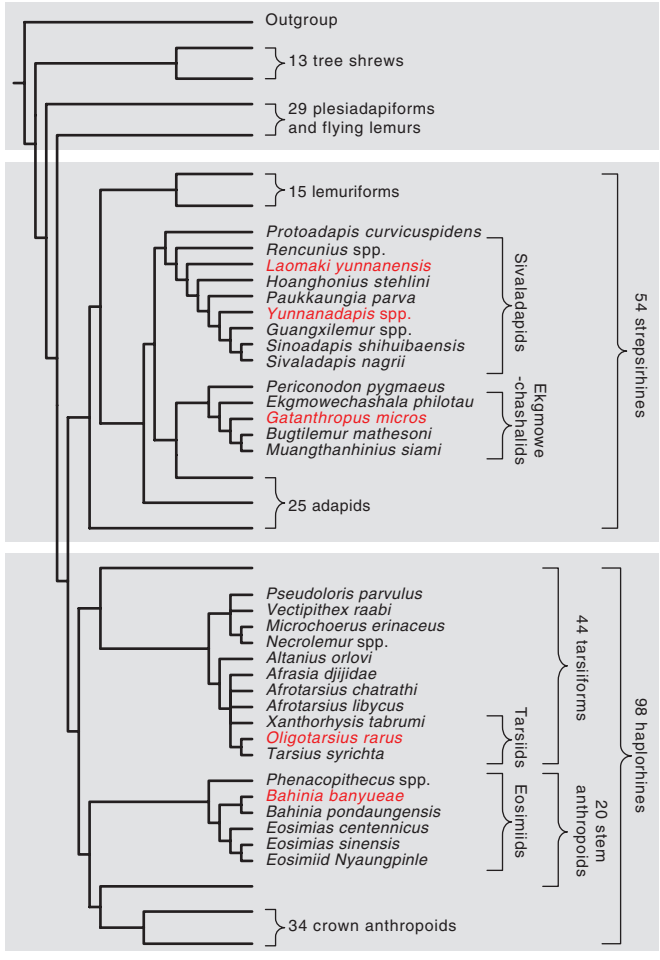


Fig. 3. Summary phylogeny of 196 mammals. Parsimony analysis is based on a data matrix that includes 1227 morphological characters and 663 molecular characters of long and short interspersed nuclear elements scored for 149 fossil and 47 living taxa. The topology of extant treeshrews, flying lemurs, and primates used as a backbone constraint or "molecular scaffold" is based on a gene supermatrix (supplementary materials).

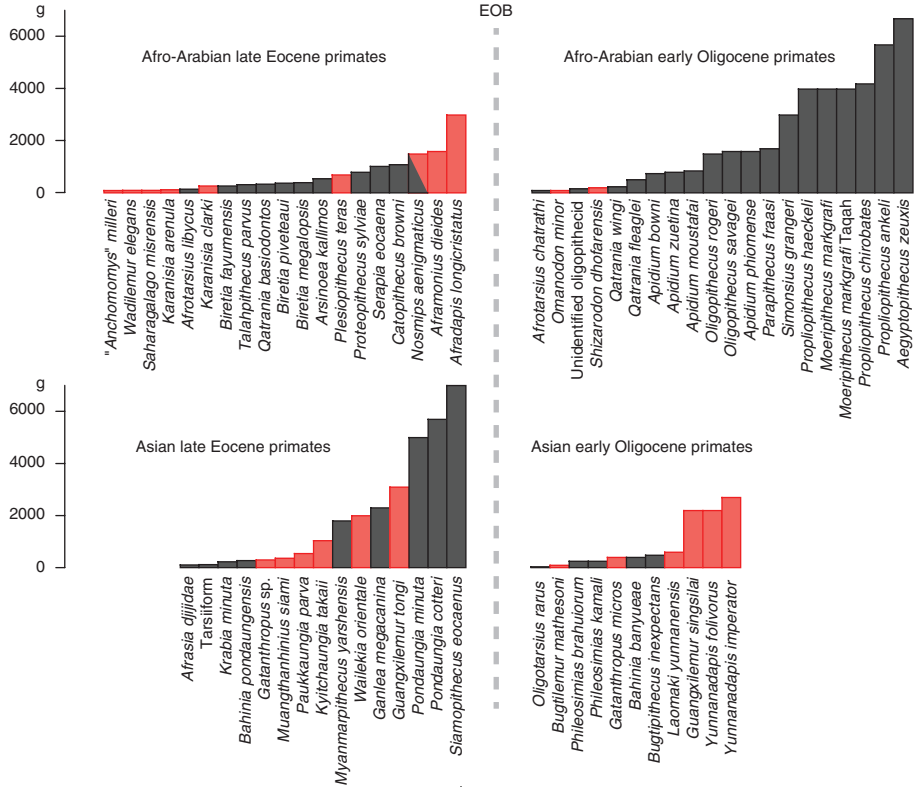


Fig. 4. Body-mass spectrum of fossil primates across the EOB in Afro-Arabia and southern Asia. Gray bars represent haplorhines. Pale red bars represent strepsirhines. *Nosmips* is uncertain (*26*). Later Eocene Afro-Arabian anthropoids occupy the middle of the spectrum. Later Eocene Afro-Arabian strepsirhines dominate the two extremes. Early Oligocene Afro-Arabian strepsirhines are restricted to the small end of the body-size distribution. Early Oligocene Afro-Arabian anthropoids span most of the body-mass range. Later Eocene Asian strepsirhines occupy the middle part of the body-mass spectrum. Later Eocene Asian anthropoids dominate the small and large body-mass areas. Early Oligocene Asian anthropoids are restricted to the small body-mass area. Early Oligocene Asian strepsirhines continue to occupy a broad range of body masses. Data are listed in table S2.

Downloaded from http://science.sciencemag.org/ on May 5, 2016

REFERENCES AND NOTES

1. X. Ni, Y. Hu, Y. Wang, C. Li, *Anthropol. Sci.* **113**, 3–9 (2005).
2. K. C. Beard, *Proc. Natl. Acad. Sci. U.S.A.* **105**, 3815–3818 (2008).
3. M. Köhler, S. Moyà-Solà, *Proc. Natl. Acad. Sci. U.S.A.* **96**, 14664–14667 (1999).
4. E. R. Seiffert, *Folia Primatol. (Basel)* **78**, 314–327 (2007).
5. I. S. Zalmout *et al.*, *Nature* **466**, 360–364 (2010).
6. E. R. Seiffert, *Evol. Anthropol.* **21**, 239–253 (2012).
7. N. J. Stevens *et al.*, *Nature* **497**, 611–614 (2013).
8. J. Meng, M. C. McKenna, *Nature* **394**, 364–367 (1998).
9. J. Sun *et al.*, *Sci. Rep.* **4**, 7463 (2014).
10. X. Ni, K. C. Beard, J. Meng, Y. Wang, D. L. Gebo, *Am. Mus. Novit.* **3571**, 1–11 (2007).
11. B. Wang, *Vertebrata PalAsiatica* **46**, 81–89 (2008).
12. X. Ni *et al.*, *Proc. R. Soc. B Biol. Sci.* **277**, 247–256 (2010).
13. K. C. Beard, T. Qi, M. R. Dawson, B. Wang, C. Li, *Nature* **368**, 604–609 (1994).
14. K. C. Beard *et al.*, *Proc. R. Soc. B Biol. Sci.* **276**, 3285–3294 (2009).
15. L. Marivaux *et al.*, *Science* **294**, 587–591 (2001).
16. L. Marivaux, J. L. Welcomme, S. Ducrocq, J. J. Jaeger, *J. Hum. Evol.* **42**, 379–388 (2002).
17. L. Marivaux *et al.*, *Proc. Natl. Acad. Sci. U.S.A.* **102**, 8436–8441 (2005).
18. O. Maridet, X. Ni, *J. Vertebr. Paleontol.* **33**, 185–194 (2013).
19. J. Jaeger *et al.*, *Science* **286**, 528–530 (1999).
20. K. C. Beard, J. Wang, *J. Hum. Evol.* **46**, 401–432 (2004).
21. P. D. Gingerich, A. Sahni, *Nature* **279**, 415–416 (1979).
22. X. Ni, in *Palaeovertebrata Sinica. Volume III. Basal Synapsids and Mammals. Fascicle 3 (Serial no. 16). Eulipotyphlans, Proteutheres, Chiropterans, Euarchontans, and Anagalids*, C. Li, Z. Qiu, Eds. (Science Press, 2015), pp. 284–389.
23. J. X. Samuels, L. B. Albright, T. J. Fremd, *Am. J. Phys. Anthropol.* **158**, 43–54 (2015).
24. A. Licht *et al.*, *Nature* **513**, 501–506 (2014).
25. R. J. Morley, in *Tropical Rainforest Responses to Climatic Change*, M. Bush, J. Flenley, W. Gosling, Eds. (Springer-Verlag, ed. 2, 2011), chap. 1, pp. 1–34.
26. E. R. Seiffert *et al.*, *Proc. Natl. Acad. Sci. U.S.A.* **107**, 9712–9717 (2010).
27. Y. Chaimanee *et al.*, *Proc. Natl. Acad. Sci. U.S.A.* **109**, 10293–10297 (2012).

ACKNOWLEDGMENTS

This project has been supported by the Strategic Priority Research Program of CAS (CAS, XDB03020501), the National Basic Research Program of China (2012CB821904), the CAS 100-talent Program, the National Natural Science Foundation of China (41472025), and the U.S. National Science Foundation (BCS 0820602, BCS 1441585, and EAR 1543684). We thank Z. Yan, G. Wang, R. Li, and G. Li for their assistance in the field. The phylogenetic data used in the paper are archived in the supplementary materials.

SUPPLEMENTARY MATERIALS

www.sciencemag.org/content/352/6286/673/suppl/DC1
Materials and Methods
Systematic Paleontology
Measurements
Body Mass Estimation
Phylogenetic Analysis
Figs. S1 to S10
Tables S1 and S2
References (*28*–*63*)
Databases S1 and S2

7 January 2016; accepted 24 March 2016
10.1126/science.aaf2107

Downloaded from http://science.sciencemag.org/ on May 5, 2016

ASTROPARTICLE PHYSICS

Observation of the ^{60}Fe nucleosynthesis-clock isotope in galactic cosmic rays

W. R. Binns,[1]* M. H. Israel,[1]* E. R. Christian,[2] A. C. Cummings,[3] G. A. de Nolfo,[2] K. A. Lave,[1] R. A. Leske,[3] R. A. Mewaldt,[3] E. C. Stone,[3] T. T. von Rosenvinge,[2] M. E. Wiedenbeck[4]

Iron-60 (^{60}Fe) is a radioactive isotope in cosmic rays that serves as a clock to infer an upper limit on the time between nucleosynthesis and acceleration. We have used the ACE-CRIS instrument to collect 3.55 × 10^5 iron nuclei, with energies ~195 to ~500 mega–electron volts per nucleon, of which we identify 15 ^{60}Fe nuclei. The ^{60}Fe/^{56}Fe source ratio is (7.5 ± 2.9) × 10^{-5}. The detection of supernova-produced ^{60}Fe in cosmic rays implies that the time required for acceleration and transport to Earth does not greatly exceed the ^{60}Fe half-life of 2.6 million years and that the ^{60}Fe source distance does not greatly exceed the distance cosmic rays can diffuse over this time, ≲1 kiloparsec. A natural place for ^{60}Fe origin is in nearby clusters of massive stars.

Signature of recent nucleosynthesis

The radioactive isotope ^{60}Fe [which decays by β^- decay with a half-life of 2.62 × 10^6 years (*1*)] is expected to be synthesized and ejected into space by supernovae, and thus could be present in galactic cosmic rays (GCRs) near Earth, depending upon the time elapsed since nucleosynthesis and the distance of the supernovae. ^{60}Fe is believed to be produced primarily in core-collapse supernovae of massive stars with mass M > ~10 solar masses ($M_\odot$), which occur mostly in associations of massive stars (OB associations). It is the only primary radioactive isotope with atomic number $Z \leq 30$ [with the exception of ^{59}Ni, for which only an upper limit is available (*2*)] produced with a half-life long enough to potentially survive the time interval between nucleosynthesis and detection at Earth. (Primary cosmic rays are those that are synthesized at the GCR source, as opposed to secondary cosmic rays, which are produced by nuclear interactions in the interstellar medium.) ^{60}Fe is difficult to measure with present-day instruments because of its expected extreme rarity, based on nucleosynthesis calculations for supernovae (*3*, *4*). The detection of ^{60}Fe in cosmic rays would be a clear sign of recent, nearby nucleosynthesis. The long period of data collection (17 years) achieved by the Cosmic Ray Isotope Spectrometer (CRIS) aboard NASA's Advanced Composition Explorer (ACE) (*5*), the excellent mass and charge resolution of the CRIS instrument, and its capability for background rejection have enabled us to detect ^{60}Fe.

^{60}Fe has been detected in other samples of matter. Measurements of diffuse γ-rays from the interstellar medium (ISM) by the spectrometer on the International Gamma-Ray Astrophysics Laboratory (INTEGRAL) spacecraft have revealed line emission at 1173 and 1333 keV from ^{60}Co, the daughter product of ^{60}Fe decay, clear evidence that "nucleosynthesis is ongoing in the galaxy" (*6*). As expected, this emission is diffuse instead of point-like, since the ^{60}Fe lifetime is sufficiently long to allow it to diffuse over distances that are large compared to the size of a supernova remnant. This is one of many strong connections between γ-ray astronomy and direct cosmic-ray studies (*7*).

Deep-sea manganese crusts from two different locations have also been found to harbor elevated ^{60}Fe levels (*8*, *9*). Analysis of crust layers using accelerator mass spectrometry showed significant increases in the ^{60}Fe/Fe ratio 2.8 million years (My) ago, "compatible with deposition of supernova ejecta at a distance of a few tens of pc" (*9*). The measurement was verified by an independent analysis (*10*), although these investigators did not find a corresponding increase in a marine-sediment sample [see (*10*, *11*) for discussion]. We note that the manganese crust studies (*8*–*10*) used outdated half-lives for ^{60}Fe and ^{10}Be—1.49 and 1.51 My , respectively—instead of the currently accepted 2.62 and 1.387 My (*1*). Using these recent lifetimes, it has been estimated that the peak in the ^{60}Fe/Fe ratio (*9*) as a function of depth corresponds to an age of 2.2 My (*11*). Lunar surface samples also show elevated ^{60}Fe/Fe ratios consistent with supernova debris arriving on the Moon ~2 My ago (*12*, *13*). These deep-sea manganese crust and lunar surface observations were compared with expectations from possible stellar sources (*11*) and found to be consistent with an origin in core-collapse supernovae, but inconsistent with Type Ia supernovae, which produce orders of magnitude less ^{60}Fe.

Cosmic-ray ^{60}Fe detection

The CRIS instrument was launched on ACE in 1997 and has operated continuously since that

[1]Washington University, St. Louis, MO 63130, USA. [2]NASA/Goddard Space Flight Center, Greenbelt, MD 20771, USA. [3]California Institute of Technology, Pasadena, CA 91125, USA. [4]Jet Propulsion Laboratory, California Institute of Technology, Pasadena, CA 91109, USA.
*Corresponding author: Email: wrb@wustl.edu (W.R.B.); mhi@wustl.edu (M.H.I.)

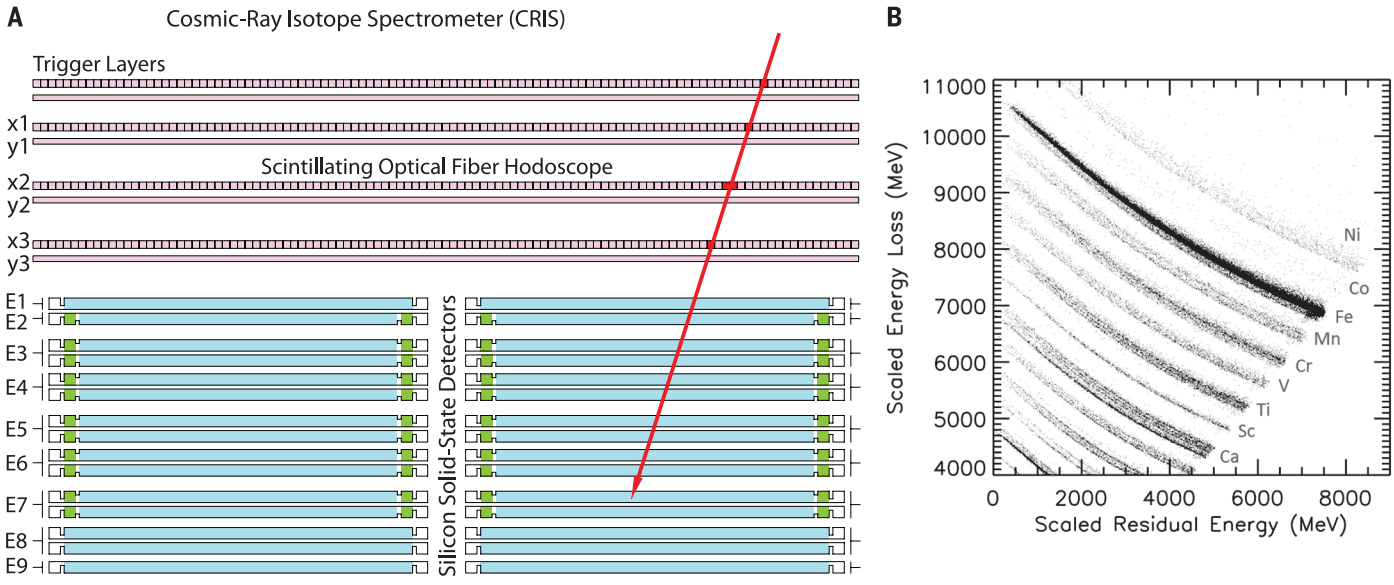


Fig. 1. CRIS instrument and data sample. (**A**) A cross-section drawing (not to scale) of the CRIS instrument is shown. There are four x,y planes of fibers; the top plane provides a trigger signal and the next three planes (x1y1,x2y2, x3y3) provide the trajectory. Beneath the fibers are four stacks of 15, 3-mm-thick silicon detectors (two stacks are visible in this side view). The central active regions of the silicon detectors are shown in blue, and guard rings used to veto side-exiting particles are in green. The detectors are grouped so that up to nine energy-loss signals (E1 to E9) are obtained for each particle entering one of the detector stacks. We use the *dE/dx* versus residual energy technique to determine the atomic number (*Z*), mass (*A*), and energy (*E*), of each cosmic ray. (**B**) Cross-plot of the sum of scaled energy losses of cosmic rays in detectors E1, E2, and E3 on the *y* axis versus the scaled energy loss in E4 on the *x* axis for a sample of particles stopping in E4, with both energies scaled by $(\sec\theta)^{-1/1.7}$, where θ is the angle of incidence through the instrument. Clear "bands" are seen for each element extending from calcium through nickel. Within some of the element bands, traces for individual isotopes of that element can be seen.

time except for intense solar-active periods, lasting for a few days each, when large fluxes of solar energetic particles exceeded the CRIS trigger rate capability. The instrument (Fig. 1A) uses a scintillating fiber hodoscope to determine particle trajectory and four stacks of silicon solid-state detectors to measure the energy loss (Δ*E*) and the total energy of cosmic-ray nuclei stopping in a detector stack. These measurements are used to identify particle charge, mass, and energy per nucleon (*5*). Data illustrating this method are shown in Fig. 1B, where we plot the energy loss (Δ*E*) versus the residual energy of nuclei stopping within a silicon detector. The elements are clearly separated into bands, and within an element band, subbands corresponding to the element's isotopes are evident.

Figure 2A is a mass histogram of the observed iron nuclei that entered the CRIS instrument through the scintillating optical fibers, penetrated the silicon detectors E1 through E3, and stopped in silicon detectors E4 through E8. These data were collected for 6142 days from 4 December 1997 to 27 September 2014. They have been selected for consistency among mass calculations using different detector combinations to reject nuclei that interacted within the instrument and other spurious events, as well as selections related to event quality (*14*).

Abundance of ^{60}Fe

Clear peaks are seen for masses from 54 to 58 amu (atomic mass units), with the exception of 57 amu, which is a shoulder on the 56 amu distribution. To the right of the 58 amu peak are 15 ^{60}Fe nuclei collected over this period, clearly separated from ^{58}Fe and located where ^{60}Fe should fall. These 15 events have a mean mass estimate of 60.04 amu and a standard deviation from the mean of 0.28 ± 0.05 amu, consistent with the 0.245 ± 0.001 amu measured for ^{56}Fe. The number of ^{56}Fe nuclei in this plot is 2.95×10^5, obtained from a Gaussian fit, and the total number of iron nuclei is 3.55×10^5. We have performed a number of tests to confirm that the 15 events are not a tail on the much more abundant ^{58}Fe distribution and have verified that in all respects tested, these events are not unusual (supplementary text and figs. S2 to S6). The strongest argument that they are ^{60}Fe

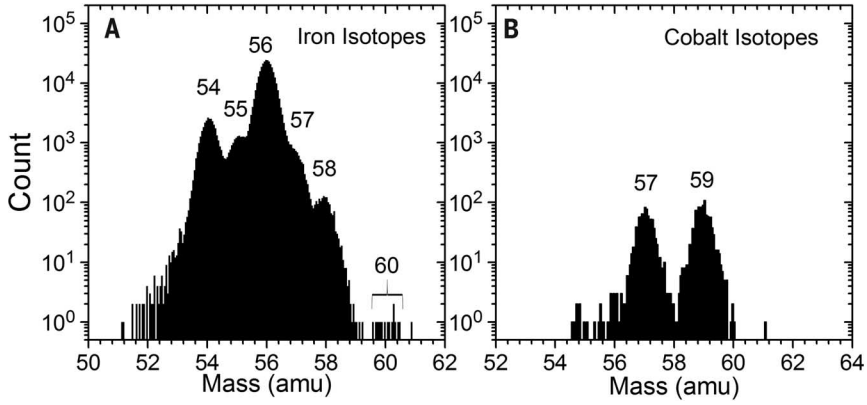


Fig. 2. Mass histograms of the observed iron and cobalt nuclei. (**A**) The mass histogram of iron nuclei detected during the first 17 years in orbit is plotted. Clear peaks are seen for masses 54, 55, 56, and 58 amu, with a shoulder at mass 57 amu. Centered at 60 amu are 15 events that we identify as the very rare radioactive ^{60}Fe nuclei. There are 2.95×10^5 events in the ^{56}Fe peak. From these data, we obtain an ^{60}Fe/^{56}Fe ratio of $(4.6 \pm 1.7) \times 10^{-5}$ near Earth and $(7.5 \pm 2.9) \times 10^{-5}$ at the acceleration source. (**B**) The mass histogram of cobalt isotopes from the same data set are plotted. Note that ^{59}Co in (B) has roughly the same number of events as are in the ^{58}Fe peak in (A). There is only a single event spaced two mass units to the right of ^{59}Co, whereas there are 15 events in the location of ^{60}Fe, which is two mass units from ^{58}Fe. This is a strong argument that most of the 15 nuclei identified as ^{60}Fe are really ^{60}Fe, and not a tail of the ^{58}Fe distribution.

Downloaded from http://science.sciencemag.org/ on May 5, 2016

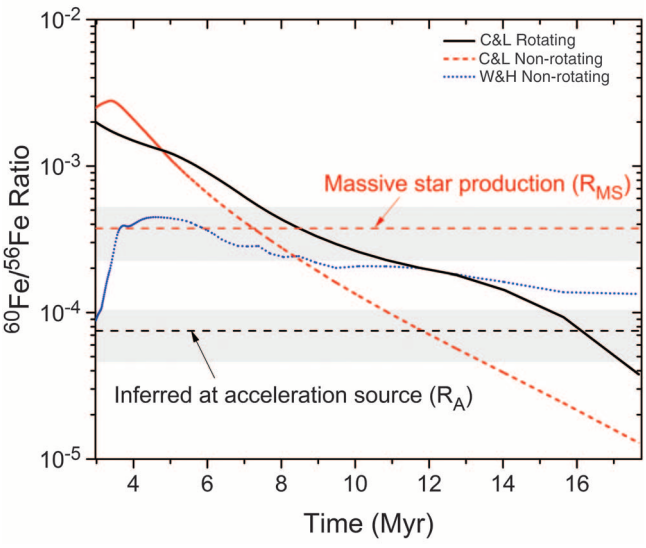


Fig. 3. Comparison of the $^{60}Fe/^{56}Fe$ ratio derived from measurements with models of supernova ejecta and stellar wind outflow in OB associations. Models of massive-star ejecta have been used to estimate the $^{60}Fe/^{56}Fe$ ratio evolution as a function of OB association age, including stellar lifetimes and radioactive decay of the ejected ^{60}Fe. The blue dotted curve shows the ratio for non-rotating stars using yields calculated by (*3*) (W&H); the red-dashed and black solid curves are for non-rotating and rotating stars, respectively, using yields calculated by (*4*) (C&L). The black dashed line is our estimated ratio (R_A) at the acceleration source derived from our measurements. Assuming that the composition at the acceleration source is 20% massive-star material and 80% normal interstellar medium material (supplementary materials), we obtain the massive-star production ratio (R_{MS}) (red dashed line). The shaded areas indicate uncertainties (not including the massive-star mix fraction uncertainty). We have compared the maximum predicted ratio (age ~3.4 My) with our measured ratio and estimate an upper limit to the time between nucleosynthesis and acceleration of several million years. Combining this with the previous measurement of ^{59}Ni (*2*), we conclude that the time between nucleosynthesis and acceleration is 10^5 years < T < several My.

nuclei and not spillover from ^{58}Fe is shown in Fig. 2B, which is a histogram of the neighboring cobalt (Z = 27) isotopes from the same data set. Note that ^{59}Co has roughly the same number of events as the ^{58}Fe peak. To the right of ^{59}Co, there is only a single event spaced by 2 amu. Similarly, we should expect only ~1 ^{58}Fe event to lie in the neighborhood of ^{60}Fe, but we see 15. It is also unlikely that these are spillover from ^{56}Fe since there is a clear separation between ^{58}Fe and the events that we identify as ^{60}Fe. Therefore, we conclude that at most, ~1 ± 1 of the 15 nuclei identified as ^{60}Fe could be spillover from lighter iron isotopes (supplementary text and fig. S1). Using the cosmic-ray propagation model described in (*15*), we have calculated the expected intensity ratio between secondary ^{60}Fe produced by fragmentation of heavier nuclei during interstellar transport and total Fe to be 2×10^{-6}, from which we conclude that only ~1 of the observed ^{60}Fe could be secondary. Thus, we have observed 13 ± 3.9 (statistical) ± 1 (systematic) = 13 ± 4.9 primary ^{60}Fe nuclei, giving measured ratios for $^{60}Fe/^{56}Fe$ and $^{60}Fe/Fe$ of $(4.4 \pm 1.7) \times 10^{-5}$ and $(3.7 \pm 1.4) \times 10^{-5}$, respectively.

These measured ratios need two small corrections. (i) Our data analysis eliminates particles that interact in the detector system. The cross-section for interaction of ^{60}Fe is slightly larger than that for ^{56}Fe, resulting in a correction factor of 1.009. (ii) Our analysis selects ^{60}Fe and ^{56}Fe with the same interval of depth of penetration in the detector. As a result, the energy interval for ^{60}Fe is smaller by a factor 0.960 than the interval for ^{56}Fe. Also, the ^{60}Fe energies per nucleon are slightly lower, although this has a very small effect because the Fe spectrum is quite flat at these energies (*15*). The resulting energy-interval correction is a factor of 1.042. Taken together, these require that the ratios be multiplied by a factor 1.051 (supplementary text). Thus, the corrected ratios near Earth are $^{60}Fe/^{56}Fe = (4.6 \pm 1.7) \times 10^{-5}$ and $^{60}Fe/Fe = (3.9 \pm 1.4) \times 10^{-5}$.

Using a leaky-box model, which accounts for radioactive decay of ^{60}Fe, nuclear interactions as the cosmic rays travel through space, and leakage out of the galaxy, these observations imply $^{60}Fe/^{56}Fe$ and $^{60}Fe/Fe$ ratios at the cosmic-ray acceleration source of $(7.5 \pm 2.9) \times 10^{-5}$ and $(6.2 \pm 2.4) \times 10^{-5}$, respectively (supplementary text).

Evidence of recent nucleosynthesis

Massive stars that undergo core-collapse exist primarily in localized groups called OB associations. The stars within these associations (or major subassociations) typically form at about the same time (within ~ 1 My), and associations have lifetimes of ~30 to 40 My (*16*). By that time, the stars with sufficient mass (>~10 $M_\odot$) have undergone core collapse. As the massive stars expel mass through high-velocity winds and supernova ejecta, superbubbles populated with the stellar wind material and ejecta are formed around the association (*16*). Calculations by Woosley and Heger (W&H) (*3*) and by Chieffi and Limongi (C&L) (*4*) estimate the production of ^{60}Fe and ^{56}Fe (outflow from stellar winds and supernova ejecta) from stars with initial masses from 12 to 120 $M_\odot$. Nearly all ^{60}Fe is in the supernova ejecta, not in the wind material. We have combined these results for a range of stellar masses with the lifetimes of the progenitor stars to determine the expected $^{60}Fe/^{56}Fe$ ratio in an OB association as a function of time. In Fig. 3, we plot the cumulative $^{60}Fe/^{56}Fe$ ratio of material injected into a superbubble as a function of time since the formation of the association at T = 0. We then derived the time that must have elapsed for this ratio to decrease to the value inferred from our cosmic-ray measurements due to the decay of the ^{60}Fe. Several different methods in which we compare our measured ratio with the modeling results lead us to conclude that an upper limit on the time between nucleosynthesis and acceleration is a few million years (supplementary text).

In previous work, on the basis of ACE-CRIS measurements of GCR ^{59}Ni and ^{59}Co, it was concluded that there is at least a 10^5-year delay between nucleosynthesis and cosmic-ray acceleration (*2*). Putting that lower limit together with this ^{60}Fe observation, we obtain a mean time (T) between nucleosynthesis and acceleration of 10^5 years < T < several My. This is quite consistent with what is expected in an OB association since a typical time between supernovae is ~1 My (*16*). In addition, the time delay between nucleosynthesis and acceleration indicates that the nuclei synthesized in a supernova are not accelerated by that supernova, but require at least one more nearby supernova to accelerate the material, on a time scale sufficiently short so that a substantial fraction of the ^{60}Fe has not decayed. The natural place for two or more nearby supernovae to occur within a few million years of each other is in OB associations. Thus, our observation of ^{60}Fe lends support to the emerging model of cosmic-ray origin in OB associations (*16*, *17*).

Using the mean lifetime of ^{60}Fe, we can also estimate the distance to the associations contributing ^{60}Fe GCRs at Earth. Assuming a diffusive propagation model, cosmic rays originate within a volume with radius $L = (D\gamma\tau)^{1/2}$ surrounding the solar system, where γ is the Lorentz factor and τ is the effective cosmic-ray lifetime. Assuming a diffusion coefficient of $D = 3.5 \times 10^{28}$ cm^2/s (*18*), and using γ and τ calculated for ^{56}Fe and ^{60}Fe (supplementary materials), we find that L_{56} = 790 pc and L_{60} = 620 pc. Because the volume scales as the cube of these diffusion lengths, the volume contributing to ^{60}Fe is only about half of that contributing to ^{56}Fe. There are >20 OB associations or major association subgroups that have been identified within 620 pc of the Sun, including the very large and nearby (<150 pc) Sco-Cen association subgroups—Upper Scorpius (with 83 OB stars), Upper Centaurus Lupus (with 134 OB stars), and Lower Centaurus Crux (with 97 OB stars) (*19*)—and the Orion OB1 association, modeled by (*20*) (with ~70 OB stars). These are very likely major contributors to the ^{60}Fe we have detected, owing to their size and proximity.

We can draw the model-independent conclusion that the detection of the radioactive supernova product ^{60}Fe surviving in cosmic rays implies

Downloaded from http://science.sciencemag.org/ on May 5, 2016

that the time required for acceleration and transport to Earth does not greatly exceed the ^{60}Fe half-life of 2.62 My. Our distance from the source of this nuclide cannot greatly exceed the distance that cosmic rays can diffuse over this time scale, which is ≲1 kpc.

Note added in proof: Additional detections of ^{60}Fe in deep-sea crusts in all major oceans of the world have recently been reported (*21*), strengthening the conclusions reached in (*9*). Also, additional detections of ^{60}Fe in lunar samples (*22*) strengthen the conclusion reached in (*12*, *13*).

REFERENCES AND NOTES

1. G. Rugel *et al.*, *Phys. Rev. Lett.* **103**, 072502 (2009).
2. M. E. Wiedenbeck *et al.*, *Astrophys. J.* **523**, L61–L64 (1999).
3. S. E. Woosley, A. Heger, *Phys. Rep.* **442**, 269–283 (2007).
4. A. Chieffi, M. Limongi, *Astrophys. J.* **764**, 21 (2013).
5. E. C. Stone *et al.*, *Space Sci. Rev.* **86**, 285–356 (1998).
6. W. Wang *et al.*, *Astron. Astrophys.* **469**, 1005–1012 (2007).
7. W. R. Binns, *Science* **334**, 1071–1072 (2011).
8. K. Knie *et al.*, *Phys. Rev. Lett.* **83**, 18–21 (1999).
9. K. Knie *et al.*, *Phys. Rev. Lett.* **93**, 171103 (2004).
10. C. Fitoussi *et al.*, *Phys. Rev. Lett.* **101**, 121101 (2008).
11. B. J. Fry, B. D. Fields, J. R. Ellis, *Astrophys. J.* **800**, 71 (2015).
12. L. Fimiani *et al.*, *43rd Lunar and Planetary Science Conference*, 1279 (2012).
13. L. Fimiani *et al.*, *45th Lunar and Planetary Science Conference*, 1778 (2014).
14. Materials and methods are available as supplementary materials on *Science* Online.
15. K. A. Lave *et al.*, *Astrophys. J.* **770**, 117 (2013).
16. J. C. Higdon, R. E. Lingenfelter, *Astrophys. J.* **590**, 822–832 (2003).
17. J. C. Higdon, R. E. Lingenfelter, *Astrophys. J.* **628**, 738–749 (2005).
18. N. E. Yanasak *et al.*, *Astrophys. J.* **563**, 768–792 (2001).
19. P. T. de Zeeuw, R. Hoogerwerf, J. H. J. de Bruijne, A. G. A. Brown, A. Blaauw, *Astron. J.* **117**, 354–399 (1999).
20. R. Voss, R. Diehl, J. S. Vink, D. H. Hartmann, *Astron. Astrophys.* **520**, A51 (2010).
21. A. Wallner *et al.*, *Nature* **532**, 69–72 (2016).
22. L. Fimiani *et al.*, *Phys. Rev. Lett.* **116**, 151104 (2016).

ACKNOWLEDGMENTS

This work was supported by NASA grants NNX08AI11G and NNX13AH66G for work performed at the California Institute of Technology, the Jet Propulsion Laboratory, and Washington University in St. Louis. Work done at Goddard Space Flight Center was funded by NASA through the ACE Project. We thank S. Woosley and J. Brown at the University of California Santa Cruz for providing modeling calculation data and for discussions about uncertainties in their calculations. We thank A. Chieffi at the Institute for Space Astrophysics and Planetology, Rome, Italy, for discussions on the uncertainties in the C&L calculations. Accelerator testing of the CRIS detectors was made possible by N. Anantaraman, R. Ronningen, and the staff at the National Superconducting Cyclotron Laboratory at Michigan State University, while H. Specht, D. Schardt, and the staff of the GSI heavy-ion accelerator in Darmstadt, Germany made possible the heavy-ion calibrations of the completed CRIS instrument. The data used are archived at NASA's Space Physics Data Facility (http://spdf.gsfc.nasa.gov) as data set ac_h2_cris and can be retrieved from this site by direct download or through the SPDF's CDAWeb data service.

SUPPLEMENTARY MATERIALS

www.sciencemag.org/content/352/6286/677/suppl/DC1
Materials and Methods
Supplementary Text
Figs. S1 to S6
References (*23*–*33*)

3 November 2015; accepted 18 March 2016
Published online 21 April 2016
10.1126/science.aad6004

PROTEIN DESIGN

De novo design of protein homo-oligomers with modular hydrogen-bond network–mediated specificity

Scott E. Boyken,[1,2,3] Zibo Chen,[1,2,4] Benjamin Groves,[5] Robert A. Langan,[1,2] Gustav Oberdorfer,[1,2,6] Alex Ford,[1,2] Jason M. Gilmore,[1,2] Chunfu Xu,[1,2] Frank DiMaio,[1,2] Jose Henrique Pereira,[7,8] Banumathi Sankaran,[9] Georg Seelig,[5,10] Peter H. Zwart,[9,11] David Baker[1,2,3]*

In nature, structural specificity in DNA and proteins is encoded differently: In DNA, specificity arises from modular hydrogen bonds in the core of the double helix, whereas in proteins, specificity arises largely from buried hydrophobic packing complemented by irregular peripheral polar interactions. Here, we describe a general approach for designing a wide range of protein homo-oligomers with specificity determined by modular arrays of central hydrogen-bond networks. We use the approach to design dimers, trimers, and tetramers consisting of two concentric rings of helices, including previously not seen triangular, square, and supercoiled topologies. X-ray crystallography confirms that the structures overall, and the hydrogen-bond networks in particular, are nearly identical to the design models, and the networks confer interaction specificity in vivo. The ability to design extensive hydrogen-bond networks with atomic accuracy enables the programming of protein interaction specificity for a broad range of synthetic biology applications; more generally, our results demonstrate that, even with the tremendous diversity observed in nature, there are fundamentally new modes of interaction to be discovered in proteins.

Hydrogen bonds play key roles in the structure, function, and interaction specificity of biomolecules. There are two main challenges facing de novo design of hydrogen-bonding interactions: First, the partially covalent nature of the hydrogen bond restricts polar hydrogen-containing donors and electronegative acceptors to narrow ranges of orientation and distance, and second, nearly all polar atoms must participate in hydrogen bonds—either with other macromolecular polar atoms, or with solvent—if not, there is a considerable energetic penalty associated with stripping away water upon folding or binding (*1*). The DNA double helix elegantly resolves both challenges; paired bases come together such that all buried polar atoms make hydrogen bonds that are self-contained between the two bases and have near-ideal geometry. In proteins, meeting these challenges is more complicated because backbone geometry is highly variable, and pairs of polar amino acids cannot generally interact as to fully satisfy their mutual hydrogen-bonding capabilities; hence, side-chain hydrogen bonding usually involves networks of multiple amino acids with variable geometry and composition, and there are generally very different networks at different sites within a single protein or interface preorganizing polar residues for binding and catalysis (*2*–*6*).

The modular and predictable nature of DNA interaction specificity is central to molecular biology manipulations and DNA nanotechnology (*7*, *8*), but without parallels in nature, it has not been evident how to achieve analogous programmable specificity with proteins. There are more polar amino acids than DNA bases, each of which can adopt numerous side-chain conformations in the context of different backbones, which allows for countless network possibilities. We hypothesized that by systematically searching through these network possibilities, it could be possible to design protein interfaces specified by regular arrays of DNA-like central hydrogen-bond networks with modular specificity analogous to Watson-Crick base pairing.

We began by developing a general computational method, HBNet, to rapidly enumerate all side-chain hydrogen-bond networks possible in an input backbone structure (Fig. 1A). Traditional protein design algorithms are not well suited for this purpose; the total system energy is generally expressed as the sum of interactions between pairs of residues for computational

[1]Department of Biochemistry, University of Washington, Seattle, WA 98195, USA. [2]Institute for Protein Design, University of Washington, Seattle, WA 98195, USA. [3]Howard Hughes Medical Institute, University of Washington, Seattle, WA 98195, USA. [4]Graduate Program in Biological Physics, Structure, and Design, University of Washington, Seattle, WA 98195, USA. [5]Department of Electrical Engineering, University of Washington, Seattle, WA 98195, USA. [6]Department of Computer Science and Engineering, University of Washington, Seattle, WA 98195, USA. [7]Institute of Molecular Biosciences, University of Graz, Humboldtstrasse 50/3, 8010-Graz, Austria. [8]Joint BioEnergy Institute, Emeryville, CA 94608, USA. [9]Molecular Biophysics and Integrated Bioimaging, Lawrence Berkeley National Laboratory, Berkeley, CA 94720, USA. [10]Berkeley Center for Structural Biology, Molecular Biophysics and Integrated Bioimaging, Lawrence Berkeley Laboratory, 1 Cyclotron Road, Berkeley, CA 94720, USA. [11]Department of Computer Science and Engineering, University of Washington, Seattle, WA 98195, USA. [12]The Center for Advanced Mathematics for Energy Research Applications, Lawrence Berkeley National Laboratories, 1 Cyclotron Road, Berkeley, CA 94720, USA.
***Corresponding author. Email: dabaker@u.washington.edu**

Downloaded from http://science.sciencemag.org/ on May 5, 2016

efficiency (*9*–*11*) and cannot clearly distinguish a connected hydrogen-bond network from a set of disconnected hydrogen bonds. HBNet starts by precomputing the hydrogen-bonding and steric repulsion interactions between all conformations (rotameric states) of all pairs of polar side chains. These energies are stored in a graph data structure in which the nodes are residue positions, positions close in three-dimensional space are connected by edges, and for each edge, there is a matrix representing the interaction energies between the different rotameric states at the two positions. HBNet then traverses this graph to identify all networks of three or more residues connected by low-energy hydrogen bonds with little steric repulsion (Fig. 1B). The most extensive and lowest-energy networks (Fig. 1C) are kept fixed in subsequent design calculations at the remaining residue positions. Networks with buried donors and acceptors not making hydrogen bonds (unsatisfied) are rejected (Fig. 1D). Details of the method, as well as scripts for carrying out the design calculations, are provided in the supplementary materials.

Inspired by the DNA double helix, we aimed to host the hydrogen-bond networks in protein oligomers with an inherent repeat structure to enable networks to be reutilized within the same scaffold. We therefore turned our attention to coiled coils, which are abundant in nature (*12*, *13*), the subject of many protein design studies (*14*–*17*), and can be generated parametrically (*18*, *19*), which results in repeating geometric cross sections. Coiled-coil packing and oligomerization state are largely determined by position-specific identities of nonpolar residues that pack between the helices (*20*–*22*); salt bridge and hydrogen-bonding interactions between residues on the periphery can provide additional specificity (*23*–*25*). In natural and designed coiled coils, buried polar interactions can also alter specificity; however, most of these cases involve, at most, one or two side-chain–side-chain hydrogen bonds with remaining polar atoms satisfied by water or ions (*26*–*30*). The relatively small cross-sectional interface area of canonical coiled coils limits the diversity and location of possible networks. To overcome these limitations, we decided to focus on oligomeric structures with two concentric rings of helices (Fig. 1E and fig. S1).

We built "two-ring" topologies from helical hairpin monomer subunits consisting of an inner and outer helix connected by a short loop by using a generalization of the Crick coiled-coil parameterization (*31*). Wide ranges of backbones were generated by systematically sampling the radii and

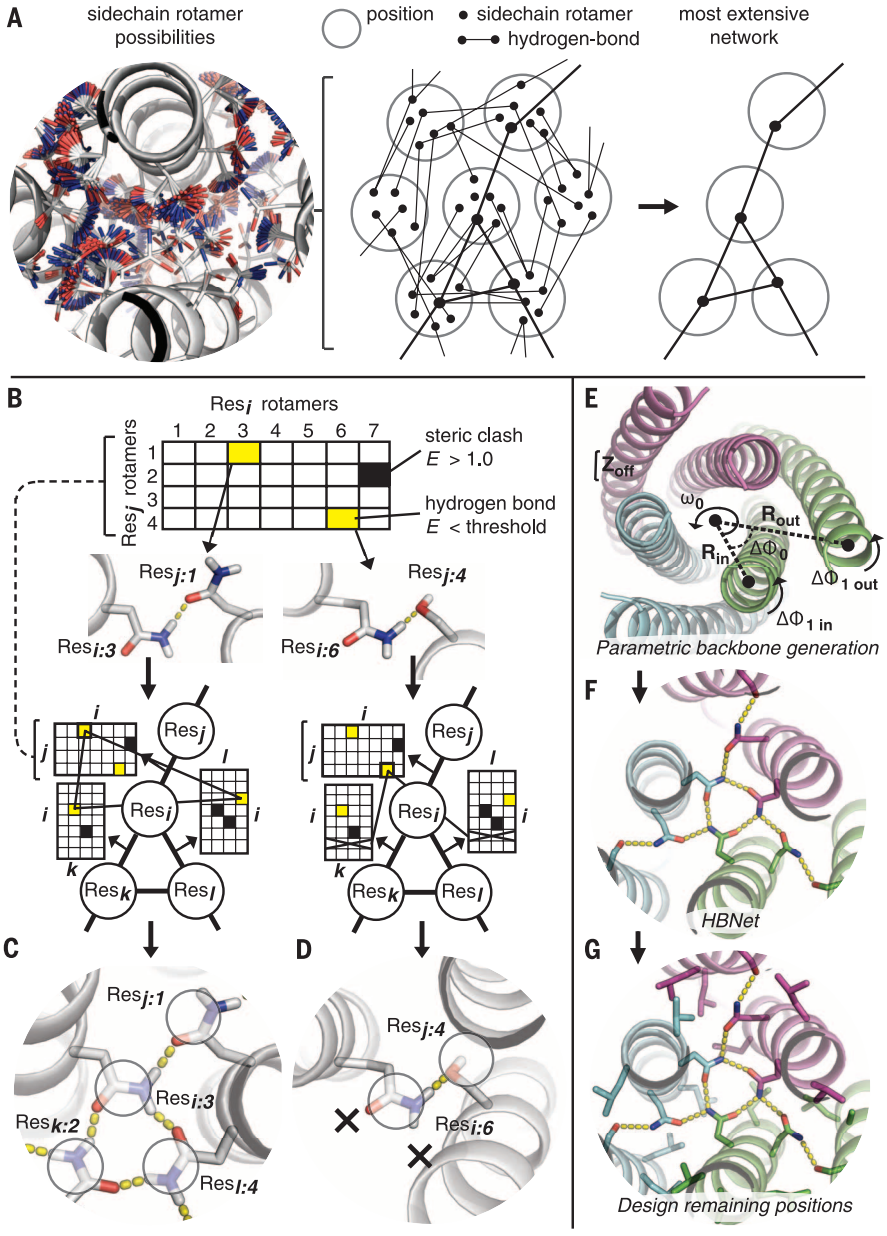


Fig. 1. Overview of the HBNet method and design strategy. (**A**) (Left) All side-chain conformations (rotamers) of polar amino acid types considered for design at each residue position (oxygen atoms colored red, nitrogen atoms blue); (middle) many combinations of hydrogen-bonding rotamers are possible, and the challenge is to traverse this space and extract (right) networks of connected hydrogen bonds. (**B** to **D**) HBNet. (B) HBNet precomputes the hydrogen bond and steric repulsive interaction energies between side-chain rotamers at all pairs of positions and stores them in a graph structure; nodes are residue positions, residue pairs close enough to interact are connected by edges, and for each edge there is an interaction energy matrix; yellow indicates rotamer pairs with energies below a specified threshold (hydrogen bonds with good geometry and little steric repulsion). Traversing the graph elucidates all possible connectivities of hydrogen-bonding rotamers (networks) that do not clash with each other. In the simple example shown, two pairs of side-chain rotamers at Res$_i$ and Res$_j$ make good-geometry hydrogen bonds, but graph traversal shows that only one of these (left) can be extended into a connected network: (C) Res$_i$ rotamer 3 (*i*:3) can hydrogen bond to both Res$_k$ rotamer 2 (*k*:2) and Res$_j$ rotamer 4 (*l*:4), yielding a "good" network of fully connected Asn residues with all heavy-atom donors and acceptors satisfied, whereas (D) would be rejected because the hydrogen-bonding rotamers *i*:6 (Gln) and *j*:4 (Ser) cannot form additional hydrogen bonds to nearby positions *k* and *l*, which leaves unsatisfied buried polar atoms. (**E** to **G**) Design strategy. (E) Parametric generation of two-ring coiled-coil backbones. For example, a *C*3 symmetric trimer (monomer subunits in different colors) is defined by the following parameters: supercoil radius of inner (R_{in}) and outer (R_{out}) helices, helical phase of the inner ($\Delta\varphi_{1in}$) and outer ($\Delta\varphi_{1out}$) helices, supercoil phase of the outer helix ($\Delta\varphi_0$), *z*-offset between the inner and outer helices (Z_{off}), and the supercoil twist (ω_0). (F) HBNet is applied to parametric backbones to identify the best hydrogen-bond networks. (G) Networks are maintained; the remaining residue positions are designed in the context of the assembled symmetric oligomer.

Downloaded from http://science.sciencemag.org/ on May 5, 2016

helical phases of the inner and outer helices, the z-offset between inner and outer helices, and the overall supercoil twist (Fig. 1E). HBNet was then used to search these backbones for networks that span the intermolecular interface, have all heavy-atom donors and acceptors satisfied, and involve at least three side chains (Fig. 1F); because of these stringent requirements, only a small fraction of backbones can support such networks—but by systematically varying the degrees of freedoms of the two-ring structures, tens of thousands of backbones can readily be generated, and the efficiency of HBNet makes searching for networks in large numbers of backbones computationally tractable. Rosetta Design (*11*, *32*) was then used to optimize rotamers at the remaining residue positions in the context of the cyclic symmetry of the oligomer (Fig. 1G). Designs were ranked based on the total oligomer energy by using the Rosetta all-atom force field (*33*) and were filtered to remove designs with large cavities or poor packing around the networks. The top-ranked designs were evaluated using Rosetta "fold-and-dock" calculations (*34*). Designs with energy landscapes shaped like funnels leading into the target-designed structure were identified, and a total of 114 dimeric, trimeric, and tetrameric designs spanning a broad range of superhelical parameters and hydrogen-bond networks were selected for experimental characterization [table S1; for design naming convention see (*35*)].

Synthetic genes encoding the selected designs were obtained and the proteins expressed in *Escherichia coli*. The ~90% (101/114) of designs that were expressed and soluble (table S2) were purified by affinity chromatography, and their oligomerization state was evaluated by size-exclusion chromatography multiangle light scattering (SEC-MALS). Of the 101 soluble designs, 66 were found to have the designed oligomerization state (table S2). The 101 soluble designs span eight different topologies (fig. S1); of these, the supercoiled tetramers have the largest buried interface area, yielded the fewest designs with all buried donors and acceptors satisfied, and had the lowest success rate (only 3 of the 13 soluble designs properly assembled). Excluding supercoiled tetramers, 72% (63/88) assembled to the designed oligomeric state, and of these, 89% (56/63) eluted as a single peak from the SEC column. The designed proteins were further characterized by circular dichroism (CD) spectroscopy; all designs tested exhibited characteristic α-helical spectra, and CD-monitored unfolding experiments showed that more than 90% of these were stable at 95°C (Fig. 2 and figs. S2 to S8).

To probe the energetic contribution of the outer ring of helices, we compared the stability of the two-ring designs to corresponding designs with only the inner ring; core interface positions of the inner helices, including hydrogen-bond network residues, were retained, and solvent-exposed surface positions were redesigned in the same manner as the surface of the two-ring designs. Design 2L4HC2_9 (Fig. 2C), a supercoiled homodimer, is folded and thermostable (Fig. 2D); Its inner helix peptide, 2L4HC2_9_inner (Fig. 2E), also forms a homodimeric coiled coil (fig. S9), but with markedly decreased thermostability (Fig. 2F). Design 2L6HC3_13 (Fig. 2G), a supercoiled homotrimer, is also folded and thermostable (Fig. 2H); however, the corresponding inner ring peptide (Fig. 2I) in isolation is unfolded (Fig. 2J) and monomeric (fig. S9D). This inner helix is internally frustrated: It has four Asn residues at canonical *a* or *d* heptad-packing positions (fig. S9E), where Asn has been found to be destabilizing (*36*, *37*), and Leu and Ile at other *a* and *d* positions, respectively, which favors homotetramers (*37*). In the presence of the outer helix and designed hydrogen-bond networks, the two-ring design assembles to the intended trimeric structure, as elucidated by x-ray crystallography (Fig. 3A). Together, these results suggest that the outer ring of helices not only increases thermostability but also can drive coiled-coil assembly, even in the context of an inner helix with low helical propensity and noncanonical helical packing (fig. S9), which permits greater sequence diversity across larger interfaces.

Structural characterization

To assess the accuracy of the designs, we determined 10 crystal structures spanning a range of oligomerization states, superhelical parameters, and hydrogen-bond networks (Fig. 3, A to F, and figs. S10 to S12). Designs for which crystals were not obtained were characterized by small-angle x-ray scattering (SAXS) (Fig. 4, figs. S13 and S14, and table S4). We solved structures for three left-handed trimers, four left-handed dimers, a left-handed tetramer, and an untwisted triangle-shaped trimer. Additional topologies characterized by SAXS include square-shaped untwisted tetramers (Fig. 4A) and dimers (Fig. 4B), as well as six-helix dimers (two inner, one outer helix) with either parallel right-handed (Fig. 4C) or antiparallel left-handed (Fig. 4D) supercoil geometry. Five of the x-ray crystallography–verified designs (Fig. 3, A and C to F) were also characterized by SAXS (fig. S14A), and the experimentally determined spectra were found to closely match those computed from the design models, which suggests that very similar structures are populated in solution.

The three left-handed trimer structures are remarkably similar to the design models with subangstrom root mean square deviation (RMSD) across all backbone *Cα* atoms and across all heavy atoms of the hydrogen-bond networks (Fig. 3, A and B, and fig. S10). These structures are constructed with supercoil phases of 0, 120, and 240 degrees for the inner helices, and 60, 180, and 300 degrees for the outer helices (fig. S1); loops connect outer N-terminal helices to inner C-terminal helices (at −60 degrees from the outer helix). Extensive 9- or 12-residue networks form the intended hydrogen bonds in the crystal structures (Fig. 3, A and B, middle, and fig. S10). Unlike previously designed single-ring trimers where three buried asparagines (Asns) resulted in substantially decreased thermostability (*38*), these two-ring trimers are stable up to 95°C and ~4.5 M

Downloaded from http://science.sciencemag.org/ on May 5, 2016

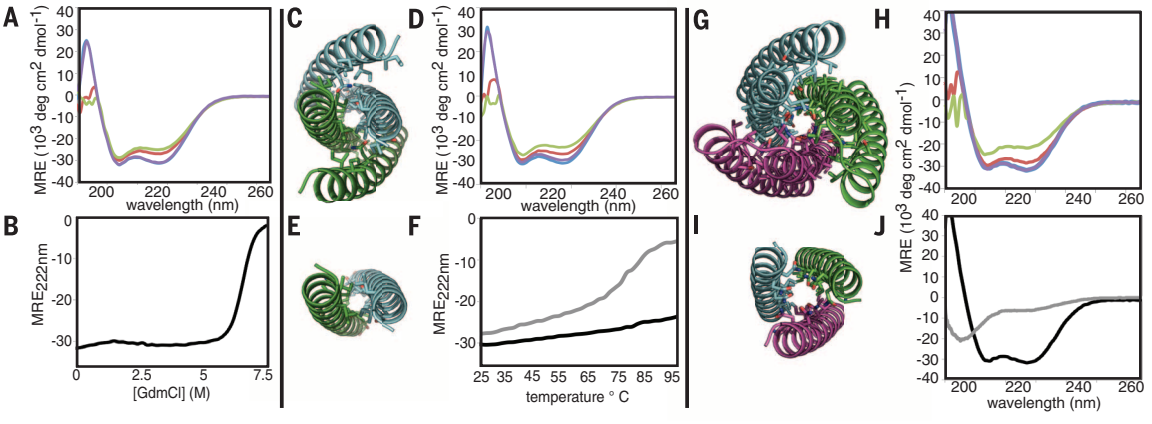


Fig. 2. The outer ring of helices increases thermostability and can overcome the poor helical propensity of the inner helices. (**A**) CD spectrum (260 to 195 nm) of design 2L4HC2_23 at 25°C (blue), 75°C (red), 95°C (green), and 25°C after cooling (purple). (**B**) Design 2L4HC2_ unfolds at 6.5 M GdmCl. (**C**) Design 2L4HC2_9, a supercoiled *C2* homodimer colored by chain, view down the supercoil axis. (**D**) CD spectrum of 2L4HC2_9 as in (A). (**E**) Inner ring design of 2L4HC2_9. (**F**) CD temperature melt monitoring absorption at 222 nm; 2L4HC2_9 (black) is considerably more stable than 2L4HC2_9_inner (gray). (**G**) Design 2L6HC3_13, a supercoiled *C3* homotrimer. (**H**) CD spectrum of 2L6HC3_13 at different temperatures as in (A). (**I**) 2L6HC3_13_inner. (**J**) CD spectra of 2L6HC3_13 (black) and 2L6HC3_13_inner (gray); in the absence of the outer helix, the inner helix is unfolded. All CD data are plotted in mean residue ellipticity (MRE) 10^3 deg cm^2 · dmol^{-1}.

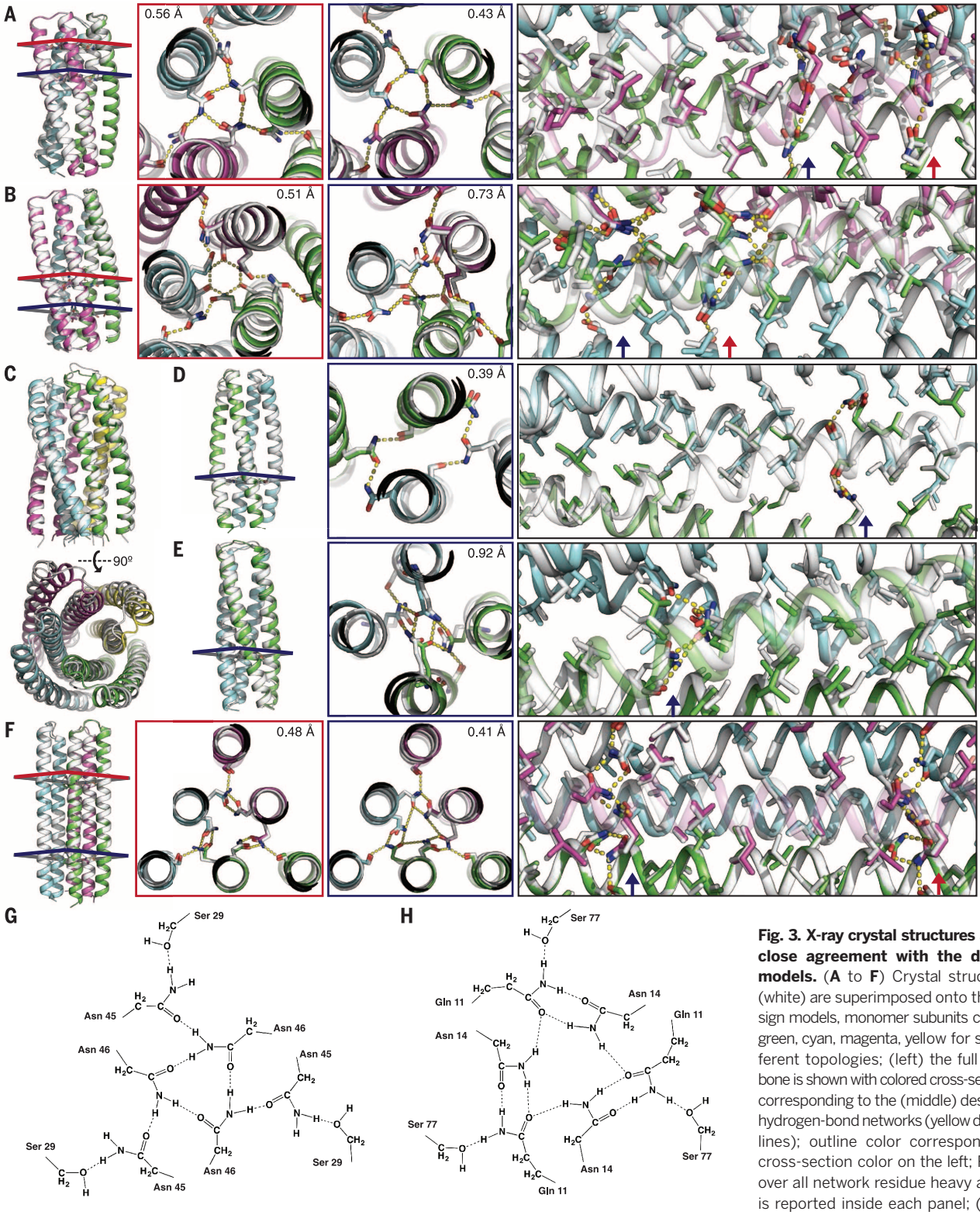


Fig. 3. X-ray crystal structures are in close agreement with the design models. (**A** to **F**) Crystal structures (white) are superimposed onto the design models, monomer subunits colored green, cyan, magenta, yellow for six different topologies; (left) the full backbone is shown with colored cross-sections corresponding to the (middle) designed hydrogen-bond networks (yellow dashed lines); outline color corresponds to cross-section color on the left; RMSD over all network residue heavy atoms is reported inside each panel; (right) hydrophobic core packing surrounding the networks, which are indicated by colored arrows. (A) 2L6HC3_13 (1.64 Å resolution; RMSD = 0.51 Å over all Cα atoms) and (B) 2L6HC3_6 (2.26 Å resolution; RMSD = 0.77 Å over all Cα atoms) are left-handed *C*3 homotrimers, each with two identical networks at different locations that span the entire interface, contacting all six helices. (C) 2L8HC4_12, a left-handed *C*4 homotetramer with two different hydrogen-bond networks (fig. S4D); the low (3.8 Å) resolution does not allow assessment of the hydrogen-bond network side chains. (D) 2L4HC2_9 (2.56 Å resolution; 0.39 Å RMSD over all Cα atoms) and (E) 2L4HC2_23 (1.54 Å resolution; RMSD = 1.16 Å over all Cα atoms) are left-handed *C*2 homodimers, each with one network. (F) 5L6HC3_1 (2.36 Å resolution; RMSD = 0.51 Å over all Cα atoms) is a *C*3 homotrimer with straight, untwisted helices and two identical networks at different cross sections. (**G** and **H**) Schematics of hydrogen-bond networks from 2L6HC3_13 (A) and 5L6HC3_1 (F). The indicated hydrogen bonds are present in both design model and crystal structure.

Downloaded from http://science.sciencemag.org/ on May 5, 2016

guanidinium chloride (fig. S3 and fig. S9) with numerous buried polar residues; 2L6HC3_13 has 12 completely buried Asns, and 2L6HC3_6 has 24 buried polar residues confined to a small region of the interface, including six Asns and six glutamines (Gln).

The four left-handed dimer crystal structures all have the designed parallel two-ring topology. Two of the dimer structures have hydrogen-bond networks in close agreement with the designs: 2L4HC2_9 (Fig. 3D) and 2L4HC2_23 (Fig. 3E) have 0.39 Å and 0.92 Å RMSD across all network residue heavy atoms, respectively, and 0.39 Å and 1.16 Å RMSD over all Cα atoms. The other two, 2L4HC2_11 (fig. S11, A and B) and 2L4HC2_24 (fig. S11, C to E), have slight structural deviations from the design models caused by water displacing designed network side chains; in the former, the interface shifts ~2 Å because of a buried water molecule bridging two network residues (fig. S11B), and in the latter, the backbone is nearly identical to the design model, but side chains of the designed network are displaced by ordered water molecules (fig. S11E). These two cases highlight the need for high connectivity and satisfaction (all polar atoms participating in hydrogen bonds) of the networks. The left-handed tetramer structure has the designed overall topology (Fig. 3C), and SAXS data are in close agreement with the design model (fig. S14), but side-chain density was uncertain because of low (3.8 Å) resolution. The amino acid sequence is unrelated to any known sequence, and the top hit in structure-based searches of the Protein Data Bank (PDB) has a different helical bundle arrangement (fig. S15D).

The five antiparallel six-helix dimers were soluble and assembled to the designed oligomeric state (table S2), with SAXS data in agreement with the design models (Fig. 4D and fig. S14). Design 2L6Hanti_3 contains a hydrogen-bond network with a buried Tyr at the dimer interface (Fig. 4D). Of the three right-handed six-helix dimers characterized by SAXS, 3L6HC2_4 (Fig. 4C) and 3L6HC2_7 (fig. S14) exhibited scattering in agreement with the design models, whereas 3L6HC2_2 did not (fig. S14). Although 3L6HC2_2 was designed to form a parallel dimer, the crystal structure revealed an antiparallel dimer interface, which highlights two design lessons (fig. S12): (i) the importance of intermolecular hydrogen bonds at the binding interface (the 3L6HC2_2 design model has only two across the interface compared with nine in 2L6HC3_6) (Fig. 3B) and (ii) the importance of favorable hydrophobic contacts complementing the networks (the 3L6HC2_2 design model has mainly Alas at the interface).

SAXS data suggest that our untwisted dimer, trimer, and tetramer designs assemble into the target triangular and square conformations (Fig. 4, A and B, and fig. S14). Guinier analysis (table S4) and fit of the low-q region of the scattering vector indicates that the seven untwisted dimers tested are in the correct oligomeric state, four of which have very close agreement between the experimental spectra and design models (Fig. 4B and fig. S14). The SAXS data on the three untwisted tetramers were all in close agreement with the corresponding design models (Fig. 4A, fig. S14, and table S4). Design 5L8HC4_6 has a distinctive network with a Trp making a buried hydrogen bond at one end of the network, which then propagates outwards toward solvent and connects to a Glu on the surface (Fig. 4A). To the best of our knowledge, oligomers with such uniformly straight helices do not exist in nature, nor have these topologies been designed previously.

The 2.36 Å crystal structure of the untwisted trimer reveals straight helices with 0.51 Å RMSD to the design model over all Cα atoms (Fig. 3F). The two hydrogen-bond networks (Fig. 3F, middle), as well as the hydrophobic packing residues surrounding the networks (Fig. 3F right), are nearly identical between the crystal structure and design model. Like the supercoiled trimers, each of these networks contains side chains from every helix, and helices were constructed to be uniformly spaced (fig. S1). The helices are nearly perfectly straight in the crystal structure, with supercoil twist values very close to the idealized design value of zero: ω_0 = −0.036 degrees per residue for the inner three helices and ω_0 = −0.137 degrees per residue for the outer three helices. Blast searches with the amino acid sequence returned no matches with E-values better than 10, and the top hit in a search for similar structures in the PDB has three supercoiled helices flanked by long extended regions (fig. S15E).

Comparison of successful versus unsuccessful network designs

Several trends emerged distinguishing successful designs. First, in successful designs, nearly all buried polar groups made hydrogen bonds. We selected designs with all heavy-atom donors and acceptors satisfied, but the networks had varying numbers of polar hydrogens unsatisfied. Networks with the largest fraction of satisfied polar groups generally had relatively high connectivity, both with respect to the total number of hydrogen bonds and number of side chains contributing to the network. The networks with the highest connectivity and structural accuracy spanned the entire cross-sectional interface, with each helix contributing at least one side chain (Fig. 3, A, B, E, and F). Design 2L6HC3_13 also has two additional smaller networks consisting of a single symmetric Asn making two hydrogen bonds, but with

Downloaded from http://science.sciencemag.org/ on May 5, 2016

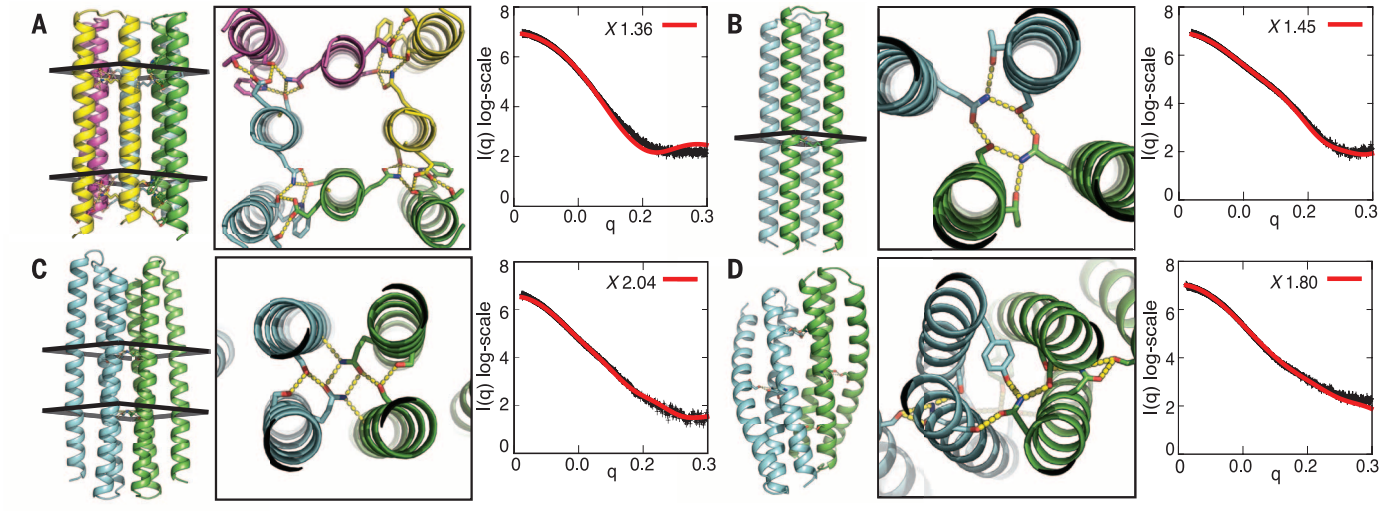


Fig. 4. Structural characterization by SAXS. (Left) backbones and (middle) hydrogen-bond networks for the design models are displayed as in Fig. 3; (right) design models (red) were fit to experimental scattering data (black) using *FoXS* (*59*, *60*); quality of fix (X) is indicated inside each panel. (**A**) Design 5L8HC4_6 (X = 1.36), an untwisted *C4* homotetramer with two identical hydrogen-bond networks. (**B**) Design 5L4HC2_12 (X = 1.45), an untwisted *C2* homodimer with a single hydrogen-bond network. (**C**) Design 3L6HC2_4 (X = 2.04), a parallel right-handed *C2* homodimer with two repeated networks, two inner helices, and one outer helix. (**D**) Design 2L6Hanti_3 (X = 1.80), a left-handed antiparallel homodimer with two inner helices and one outer helix; because of the antiparallel geometry, the same network occurs in two locations.

one polar hydrogen unsatisfied; in the crystal structure, these residues move away from the design model, displaced by water molecules (fig. S16).

The designed hydrogen-bond networks confer specificity

To test the role of the designed hydrogen-bond networks in conferring specificity for the target oligomeric state, we carried out control design calculations using the same protein backbones without HBNet, which yielded uniformly hydrophobic interfaces. In silico, despite having lower total energy in the designed oligomeric state, these designs exhibit more pronounced alternative energy-minima in fold-and-dock and asymmetric docking calculations (fig. S17), consistent with the much less restrictive geometry of nonpolar packing interactions. Experimentally, these hydrophobic designs exhibited less soluble expression than their counterparts with hydrogen-bond networks (fig. S18A) and tended to precipitate during purification; of those that remained in solution long enough to collect SEC-MALS data, all but one formed higher-molecular-weight aggregates and eluted as multiple peaks from the SEC column (fig. S18). These results suggest that the designed hydrogen-bond networks confer specificity for the target oligomeric state and resolve the degeneracy of alternative states observed with purely hydrophobic packing (this degeneracy is considerably more pronounced for our two-ring structures than traditional single-ring coiled coils, which have many fewer total hydrophobic residues and less interhelical interface area).

We used an in vivo yeast two-hybrid assay (*38*) to further probe the interaction specificity of the designed oligomers. Sequences encoding a range of dimers, trimers, and tetramers were crossed against each other in all-by-all binding assays (Fig. 5 and fig. S19): Synthetic genes for the designs were cloned in frame with both DNA binding domains and transcriptional activation domains in separate vectors, and the extent of binding between the different designs assessed by cell growth, which requires juxtaposition of the DNA binding domain with the activation domain. Even without explicit negative design, the designed homo-oligomeric interactions are stronger than the (unintended)

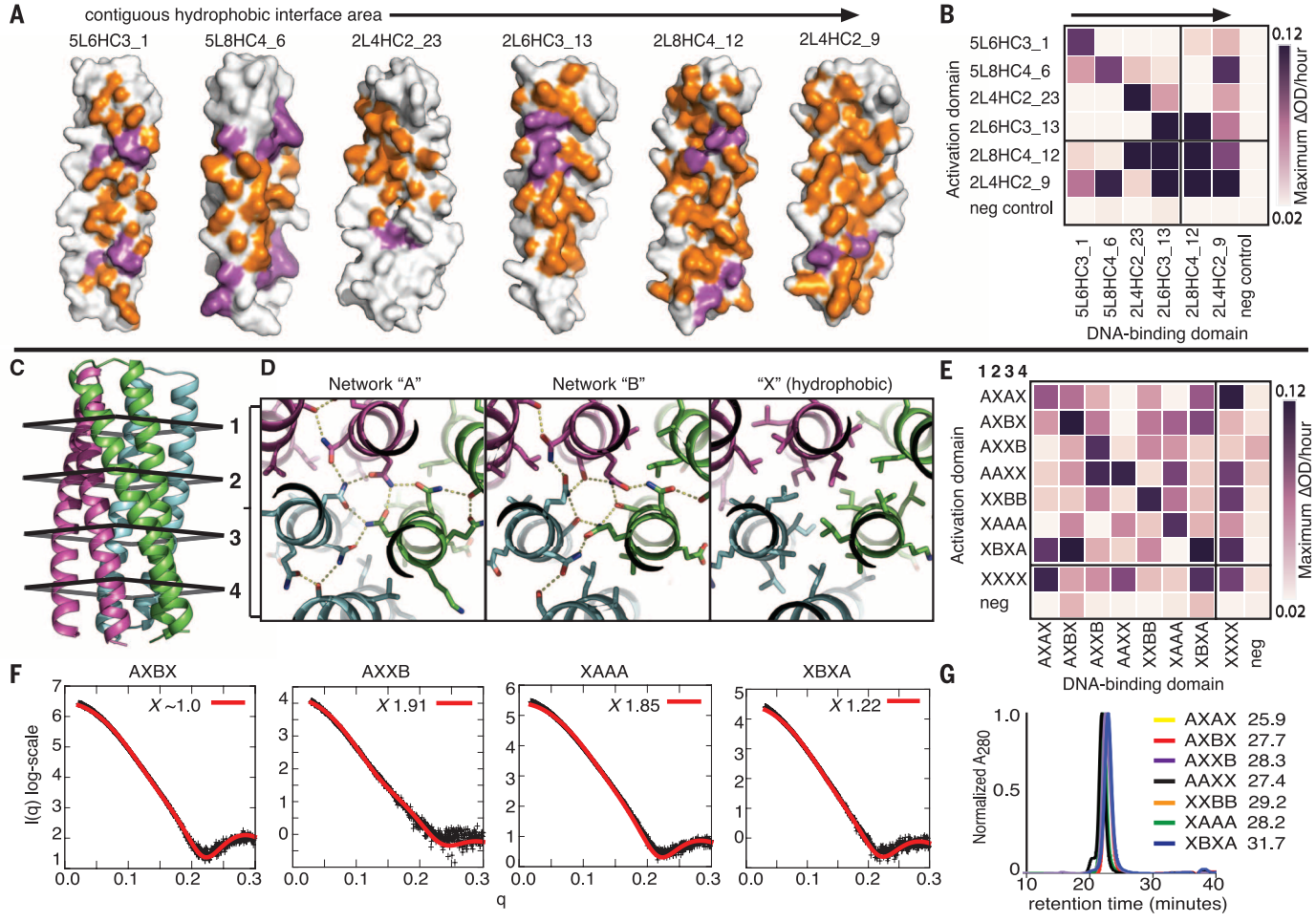


Fig. 5. The hydrogen-bond networks confer specificity. (**A**) Interaction surfaces of monomer subunits for six structurally verified designs, ordered by increasing contiguous hydrophobic interface area (orange), as calculated by hpatch (*61*); hydrogen-bond network residues are colored magenta. (**B**) Binding heat-map from yeast two-hybrid assay. Designs in (A) were fused to both DNA binding domain and the activation domain constructs and binding measured by determining the cell growth rate [maximum change in optical density (ΔOD) per hour]; darker cells indicate more rapid growth, hence stronger binding; values are the average of at least three biological replicates with standard deviations reported in fig. S19. The heat-map is ordered as in (A), and designs with more extensive networks and better-partitioned hydrophobic interface area exhibit higher interaction specificity. (**C** to **G**) Modular networks confer specificity in a programmable fashion. (C) The backbone corresponding to designs 2L6HC3_13 (Fig. 3A) and 2L6HC3_6 (Fig. 3B) can accommodate different networks at each of four repeating geometric cross sections. (D) Three possibilities for each cross section: Network "A," network "B," or hydrophobic, "X." (E) Combinatorial designs using this three-letter combination were tested for interaction specificity using the yeast two-hybrid assay as in (B). Axis labels denote the network pattern; for example, "AXBX" indicates network A at cross section 1, network B at cross section 3, and X (hydrophobic) at the two others. (F) SAXS profiles for combinatorial designs as in Fig. 4. (G) SEC chromatograms monitoring absorbance at 280 nm (A_{280}) and estimated molecular masses (from MALS); designs range from ~27 to 30 kD. AAXX, XXBB, and XXXX correspond to designs 2L6HC3_13, 2L6HC3_6, and 2L6HC3_hydrophobic_1, respectively.

Downloaded from http://science.sciencemag.org/ on May 5, 2016

competing hetero-oligomeric interactions (Fig. 5B). Designs in which the hydrogen-bond networks partition hydrophobic interface area into relatively small regions are more specific than designs with large contiguous hydrophobic patches at the helical interface (Fig. 5, A and B). The designs with the best-partitioned hydrophobic area had networks spanning the entire oligomeric interface, with each helix contributing at least one side chain. This unifying design principle can readily be enforced using HBNet.

To test if regular arrays of networks can confer specificity in a modular, programmable manner, we designed an additional set of trimers, each with identical backbones and hydrophobic packing motifs, the only difference being placement and composition of the hydrogen-bond networks. The designs are based on 2L6HC3_13 (Fig. 3A) and 2L6HC3_6 (Fig. 3B), which originated from the same superhelical parameters but have unique networks we will refer to as "A" and "B," respectively; cross sections with only nonpolar residues are labeled "X." We used this three-letter code to generate new designs in combinatorial fashion: At each of the four repeating cross sections of the supercoil (Fig. 5C), we placed the A, B, or X (Fig. 4D) followed by the same design strategy and selection process as before. The design names indicate network placement; for example, "AXAX" has network "A" at cross sections one and three and hydrophobic packing ("X") at two and four. Six of these combinatorial designs were synthesized, and five out of six were found to be folded, thermostable, and assembled to the designed trimeric oligomerization state in vitro (Fig. 5, F and G, and fig. S20). These five, along with the two parent designs (2L6HC3_13 = AAXX and 2L6HC3_6 = XXBB) and an all-hydrophobic control (XXXX), were crossed in all-by-all yeast two-hybrid binding experiments (Fig. 5E). Again, the designed self interactions were found to be the strongest. Overall, the combinatorial designs exhibit a level of specificity that is striking, given that all have identical backbones and high overall sequence similarity (fig. S20), whereas the hydrophobic control is relatively promiscuous; the central hydrogen-bond networks are clearly responsible for mediating specificity.

Conclusions

Previous de novo protein design efforts have focused on jigsaw-puzzle–like hydrophobic core packing to design new structures and interactions (*39*–*42*). Unlike the multibody problem of designing highly connected and satisfied hydrogen-bond networks, hydrophobic packing is readily captured by established pairwise-decomposable potentials; because of this and the inherent challenge of designing buried polar interactions, most protein interface designs have been predominantly hydrophobic, and attempts to design buried hydrogen bonds across interfaces have routinely failed (*43*). Polar interfaces have been designed in specialized cases (*44*–*46*) but have been difficult to generalize, with many interface design efforts requiring directed evolution to optimize polar contacts and achieve desired specificity (*47*, *48*). HBNet now provides a general computational method to accurately design hydrogen-bond networks. This ability to precisely preorganize polar contacts without buried unsatisfied polar atoms should be broadly useful in protein design challenges such as enzyme design, small molecule binding, and polar protein interface targeting.

Our two-ring structures are a new class of protein oligomers that have the potential for programmable interaction specificity analogous to that of Watson-Crick base pairing. Whereas Watson-Crick base pairing is largely limited to the antiparallel double helix, our designed protein hydrogen-bond networks allow the specification of two-ring structures with a range of oligomerization states (dimers, trimers, and tetramers) and supercoil geometries. Elegant studies have demonstrated a wide range of interaction specificity with standard single-ring coiled coils (*37*, *49*–*55*); with an outer ring of helices to enable extensive hydrogen-bond networks, it should be possible to generate a much larger range of orthogonal interactions than has been achieved previously. Our results demonstrate that a wide range of hydrogen-bond network compositions and geometries is possible in repeating two-ring topologies and multiple networks can be engineered into the same backbone at varying positions without sacrificing thermostability, and that network combination enables stable building blocks with uniform shape but orthogonal binding interfaces (Fig. 5). The DNA nanotechnology field has demonstrated that a spectacular array of shapes and interactions can be built from a relatively limited set of hydrogen-bonding interactions (*56*–*58*). It should now become possible to develop new protein-based materials with the advantages of both polymers: DNA-like programmability and tunable specificity coupled with the geometric variability, interaction diversity, and catalytic function intrinsic to proteins.

REFERENCES AND NOTES

1. P. J. Fleming, G. D. Rose, *Protein Sci.* **14**, 1911–1917 (2005).
2. R. Chakrabarti, A. M. Klibanov, R. A. Friesner, *Proc. Natl. Acad. Sci. U.S.A.* **102**, 12035–12040 (2005).
3. E. T. Judd, N. Stein, A. A. Pacheco, S. J. Elliott, *Biochemistry* **53**, 5638–5646 (2014).
4. A. Sánchez-Azqueta *et al.*, *Biochim. Biophys. Acta* **1837**, 251–263 (2014).
5. D. Xu, C. J. Tsai, R. Nussinov, *Protein Eng.* **10**, 999–1012 (1997).
6. F. B. Sheinerman, B. Honig, *J. Mol. Biol.* **318**, 161–177 (2002).
7. Y.-J. Chen, B. Groves, R. A. Muscat, G. Seelig, *Nat. Nanotechnol.* **10**, 748–760 (2015).
8. F. Zhang, J. Nangreave, Y. Liu, H. Yan, *J. Am. Chem. Soc.* **136**, 11198–11211 (2014).
9. A. G. Street, S. L. Mayo, *Structure* **7**, R105–R109 (1999).
10. B. I. Dahiyat, S. L. Mayo, *Protein Sci.* **5**, 895–903 (1996).
11. B. Kuhlman, D. Baker, *Proc. Natl. Acad. Sci. U.S.A.* **97**, 10383–10388 (2000).
12. M. Gruber, A. N. Lupas, *Trends Biochem. Sci.* **28**, 679–685 (2003).
13. P. Burkhard, J. Stetefeld, S. V. Strelkov, *Trends Cell Biol.* **11**, 82–88 (2001).
14. P.-S. Huang *et al.*, *Science* **346**, 481–485 (2014).
15. N. L. Ogihara, M. S. Weiss, W. F. Degrado, D. Eisenberg, *Protein Sci.* **6**, 80–88 (1997).
16. A. W. Reinke, R. A. Grant, A. E. Keating, *J. Am. Chem. Soc.* **132**, 6025–6031 (2010).
17. A. L. Boyle, D. N. Woolfson, *Chem. Soc. Rev.* **40**, 4295–4306 (2011).
18. G. Grigoryan, W. F. Degrado, *J. Mol. Biol.* **405**, 1079–1100 (2011).
19. P. B. Harbury, J. J. Plecs, B. Tidor, T. Alber, P. S. Kim, *Science* **282**, 1462–1467 (1998).
20. D. N. Woolfson, T. Alber, *Protein Sci.* **4**, 1596–1607 (1995).
21. P. B. Harbury, T. Zhang, P. S. Kim, T. Alber, *Science* **262**, 1401–1407 (1993).
22. A. Acharya, V. Rishi, C. Vinson, *Biochemistry* **45**, 11324–11332 (2006).
23. H. Gradišar, R. Jerala, *J. Pept. Sci.* **17**, 100–106 (2011).
24. J. B. Kaplan, A. W. Reinke, A. E. Keating, *Protein Sci.* **23**, 940–953 (2014).
25. E. G. Baker *et al.*, *Nat. Chem. Biol.* **11**, 221–228 (2015).
26. D. M. Eckert, V. N. Malashkevich, P. S. Kim, *J. Mol. Biol.* **284**, 859–865 (1998).
27. D. L. Akey, V. N. Malashkevich, P. S. Kim, *Biochemistry* **40**, 6352–6360 (2001).
28. K. J. Lumb, P. S. Kim, *Biochemistry* **34**, 8642–8648 (1995).
29. C. D. Tatko, V. Nanda, J. D. Lear, W. F. Degrado, *J. Am. Chem. Soc.* **128**, 4170–4171 (2006).
30. L. Gonzalez Jr., D. N. Woolfson, T. Alber, *Nat. Struct. Biol.* **3**, 1011–1018 (1996).
31. F. H. C. Crick, *Acta Crystallogr.* **6**, 689–697 (1953).
32. A. Leaver-Fay *et al.*, *Methods Enzymol.* **487**, 545–574 (2011).
33. M. J. O'Meara *et al.*, *J. Chem. Theory Comput.* **11**, 609–622 (2015).
34. R. Das *et al.*, *Proc. Natl. Acad. Sci. U.S.A.* **106**, 18978–18983 (2009).
35. Design nomenclature**:** The first two characters indicate supercoil geometry: "2L" refers to a two-layer heptad repeat that results in a left-handed supercoil; "3L" refers to a three-layer 11-residue repeat with a right_handed supercoil; and "5L" refers to untwisted designs with a five-layer 18-residue repeat and straight helices (no supercoiling), where "layer", in this context, is the number of unique repeating geometric slices along the supercoil axis. The middle two characters indicate the total number of helices, and last two characters indicate symmetry and oligomeric assembly. For example, "2L6HC3" denotes a left-handed, six-helix trimer with C3 symmetry.
36. A. Acharya, S. B. Ruvinov, J. Gal, J. R. Moll, C. Vinson, *Biochemistry* **41**, 14122–14131 (2002).
37. J. M. Fletcher *et al.*, *ACS Synth. Biol.* **1**, 240–250 (2012).
38. S. Fields, O. Song, *Nature* **340**, 245–246 (1989).
39. B. Kuhlman *et al.*, *Science* **302**, 1364–1368 (2003).
40. N. Koga *et al.*, *Nature* **491**, 222–227 (2012).
41. N. P. King *et al.*, *Science* **336**, 1171–1174 (2012).
42. P.-S. Huang, J. J. Love, S. L. Mayo, *Protein Sci.* **16**, 2770–2774 (2007).
43. P. B. Stranges, B. Kuhlman, *Protein Sci.* **22**, 74–82 (2013).
44. E. Procko *et al.*, *J. Mol. Biol.* **425**, 3563–3575 (2013).
45. L. A. Joachimiak, T. Kortemme, B. L. Stoddard, D. Baker, *J. Mol. Biol.* **361**, 195–208 (2006).
46. T. Kortemme *et al.*, *Nat. Struct. Mol. Biol.* **11**, 371–379 (2004).
47. J. Karanicolas *et al.*, *Mol. Cell* **42**, 250–260 (2011).
48. S. J. Fleishman *et al.*, *Science* **332**, 816–821 (2011).
49. S. F. Betz, P. A. Liebman, W. F. DeGrado, *Biochemistry* **36**, 2450–2458 (1997).
50. G. Grigoryan, A. E. Keating, *Curr. Opin. Struct. Biol.* **18**, 477–483 (2008).
51. G. Grigoryan, A. W. Reinke, A. E. Keating, *Nature* **458**, 859–864 (2009).
52. A. W. Reinke, J. Baek, O. Ashenberg, A. E. Keating, *Science* **340**, 730–734 (2013).
53. F. Thomas, A. L. Boyle, A. J. Burton, D. N. Woolfson, *J. Am. Chem. Soc.* **135**, 5161–5166 (2013).
54. A. R. Thomson *et al.*, *Science* **346**, 485–488 (2014).
55. N. H. Joh *et al.*, *Science* **346**, 1520–1524 (2014).
56. P. W. K. Rothemund, *Nature* **440**, 297–302 (2006).
57. E. Winfree, F. Liu, L. A. Wenzler, N. C. Seeman, *Nature* **394**, 539–544 (1998).
58. B. Wei, M. Dai, P. Yin, *Nature* **485**, 623–626 (2012).
59. D. Schneidman-Duhovny, M. Hammel, A. Sali, *Nucleic Acids Res.* **38** (Web Server), W540–W544 (2010).
60. D. Schneidman-Duhovny, M. Hammel, J. A. Tainer, A. Sali, *Biophys. J.* **105**, 962–974 (2013).
61. R. Jacak, A. Leaver-Fay, B. Kuhlman, *Proteins* **80**, 825–838 (2012).

ACKNOWLEDGMENTS

We thank L. Carter for assistance with SEC-MALS and protein production and Rosetta@Home volunteers for contributing computing resources to enable rigorous testing of designs by ab initio structure prediction, F. Seeger for guidance with SAXS data analysis, and M. Bick and P. Lu for assistance with crystallographic refinement. This work was supported by the Howard Hughes Medical Institute, the U.S. Department of Energy, the European Research Area (ERA)-NET BioOrigami consortium,

Downloaded from http://science.sciencemag.org/ on May 5, 2016

and NSF (MCB-1445201). Design calculations were facilitated though the use of advanced computational, storage, and networking infrastructure provided by the Hyak supercomputer system at the University of Washington. X-ray crystallography and SAXS data were collected at the Advanced Light Source (Lawrence Berkeley National Laboratory, Berkeley, California Department of Energy, contract no. DE-AC02-05CH11231); SAXS data were collected through the SIBYLS mail-in SAXS program under the aforementioned contract number, and we thank K. Burnett and G. Hura. The Berkeley Center for Structural Biology is supported in part by the National Institute of General Medical Sciences (NIH), and the Howard Hughes Medical Institute. G.O. is a Marie Curie International Outgoing Fellowship fellow (332094 ASR-CompEnzDes FP7- People-2012-IOF). B.G and J.M.G. are supported by Washington Research Foundation Innovation Postdoctoral Fellowships. Coordinates and structure files have been deposited to the Protein Data Bank with accession codes: 5J0J (2L6HC3_6), 5J0I (2L6HC3_12), 5J0H (2L6HC3_13), 5IZS (5L6HC3_1), 5J73 (2L4HC2_9), 5J2L (2L4HC2_11), 5J0L (3L6HC2_2), 5J0K (2L4HC2_23), 5J10 (2L4HC2_24). S.E.B., Z.C., and D.B. designed the research and S.E.B. and D.B. wrote the manuscript S.E.B. developed the HBNet method and wrote the program code. D.B. wrote the parametric backbone generation code with help from C.X. and G.O. A.F. wrote the loop closure program code. S.E.B., Z.C., R.A.L., and D.B. carried out design calculations. S.E.B. and Z.C. purified and biophysically characterized the designed proteins. B.G. performed yeast two-hybrid assays. J.M.G. performed mass spectrometry. J.H.P. crystallized the designed proteins. B.S. and P.H.Z. collected and analyzed crystallographic data. B.S., P.H.Z., G.O, and F.D. solved structures with help from S.E.B. and Z.C. All authors discussed results and commented on the manuscript.

SUPPLEMENTARY MATERIALS

www.sciencemag.org/content/352/6286/680/suppl/DC1
Materials and Methods
Supplementary Text
Figs. S1 to S20
Tables S1 to S5
References (*62–82*)

4 December 2015; accepted 23 March 2016
10.1126/science.aad8865

REPORTS

PROTEIN DESIGN

Design of structurally distinct proteins using strategies inspired by evolution

T. M. Jacobs,[1] B. Williams,[2] T. Williams,[2] X. Xu,[3,4]* A. Eletsky,[3,4] J. F. Federizon,[3] T. Szyperski,[3] B. Kuhlman[2,5]†

Natural recombination combines pieces of preexisting proteins to create new tertiary structures and functions. We describe a computational protocol, called SEWING, which is inspired by this process and builds new proteins from connected or disconnected pieces of existing structures. Helical proteins designed with SEWING contain structural features absent from other de novo designed proteins and, in some cases, remain folded at more than 100°C. High-resolution structures of the designed proteins CA01 and DA05R1 were solved by x-ray crystallography (2.2 angstrom resolution) and nuclear magnetic resonance, respectively, and there was excellent agreement with the design models. This method provides a new strategy to rapidly create large numbers of diverse and designable protein scaffolds.

Most efforts in de novo protein design have been focused on creating idealized proteins composed of canonical structural elements. Examples include the design of coiled coils, repeat proteins, TIM barrels, and Rossman folds (*1–6*). These studies elucidate the minimal determinants of protein structure, but they do not aggressively explore new regions of structure space. Additionally, idealized structures may not always be the most effective starting points for engineering novel protein functions. Functional sites in proteins are often created from nonideal structural elements, such as kinks, pockets, and bulges.

[1]Program in Bioinformatics and Computational Biology, University of North Carolina at Chapel Hill, Chapel Hill, NC 27599, USA. [2]Department of Biochemistry and Biophysics, University of North Carolina at Chapel Hill, Chapel Hill, NC 27599, USA. [3]Department of Chemistry, State University of New York at Buffalo, Buffalo, NY 14260, USA. [4]Northeast Structural Genomics Consortium. [5]Lineberger Comprehensive Cancer Center, University of North Carolina at Chapel Hill, Chapel Hill, NC 27599, USA.
*Present address: Department of Biochemistry and Molecular Biology, University of Georgia, Athens, GA 30602, USA.
†Corresponding author. Email: bkuhlman@email.unc.edu

The lack of nonideal structural elements from de novo designed proteins highlights a key difference between natural protein evolution and current design methods. Specifically, protein design methods universally begin with a target structure in mind. Therefore, the space of designable structures that can accommodate these nonideal protein elements is limited by the imagination of the designer. In contrast, natural evolution is based not on design but on cellular fitness provided by the evolved protein function. This lack of a predetermined target fold is a powerful feature of protein evolution that holds significant potential for the design of novel structures and functions. In an effort to tap this potential, we sought to develop a method of computational protein design inspired by mechanisms of natural protein evolution.

Gene duplication and homologous recombination mix and match elements of protein structure to give rise to new structures and functions (*7–9*). This phenomenon is most evident at the level of independently folding protein domains (*10–12*), but recent studies have shown that these same principles function at a smaller scale during the evolution of distinct, globular protein folds (*13*). Insertions, deletions, and replacement of secondary and supersecondary structural elements sample alternative tertiary structures (*14–16*). Our design strategy, called SEWING (structure extension with native-substructure graphs), is motivated by this process and builds new protein structures from pieces of naturally occurring protein domains. The process is not dictated by the need to adopt a specific target fold but rather is aimed at creating large sets of alternative structures that satisfy predefined design requirements. One of the strengths of this approach is that it ensures that all of the structural elements of the protein are inherently designable, at the same time allowing for the incorporation of structural oddities unlikely to be found in idealized proteins. Here, we apply SEWING to the design of helical proteins. We show that designed structures are diverse and contain structural features absent from alternative design strategies.

SEWING begins with the extraction of small structural motifs, or substructures, from existing protein structures. These serve as the basic building blocks for all generated models. We aimed to identify substructures that were large enough to carry information regarding structural preference yet small enough to allow combinations that can generate novel globular structures. Ultimately, we chose to extract two distinct types of substructures. The first is composed of continuous stretches of protein structure that encompass two secondary structural elements separated by a loop (Fig. 1). These substructures capture the relative orientation between adjacent secondary structure elements and maintain local packing interactions. In addition, there is evidence that substructures of this size adopt a relatively limited number of conformations that have already been sampled exhaustively in known protein structures (*14*). The second type is composed of groups of three to five secondary structural elements, where each element makes van der Waals contacts with every other element, but the elements are not necessarily continuous in primary sequence (Fig. 1, supplementary methods). Nonadjacent, or discontinuous, substructures maintain longer-range tertiary interactions that provide valuable stability and are often conserved during protein evolution (*17*).

Downloaded from http://science.sciencemag.org/ on May 5, 2016

The goal of SEWING is to combine and modify these extracted components in order to develop new tertiary structures. Naturally occurring homologous recombination, in which sequence similarity between DNA molecules leads to the combination of the genetic material, guides the formation of new protein chimeras. This process enriches for proteins that are more likely to be well folded and functional, as sequence-similarity filters for segments that are structurally compatible. In the case of SEWING, we know the three-dimensional structures of the building blocks; therefore, we can directly use structural information to probe which substructures are well suited for combination. During SEWING, continuous substructures are eligible for combination if the C-terminal region of one substructure shares high structural similarity with the N-terminal region of another substructure and if superposition of the two regions does not create any steric clashes between other regions in the two substructures. This type of superposition ensures that the three-dimensional spacing between all pairs of secondary structural elements adjacent in primary sequence is similar to that observed in the Protein Data Bank (PDB). During discontinuous SEWING, combinations are created by superimposing two elements (helices in this study) from one substructure with two elements from another substructure. For both continuous and discontinuous SEWING, structure similarity is identified by using a fast geometric hashing approach that ensures that the regions of interest can align with low root mean square deviation (RMSD) (*18*).

Once pairwise structural similarity is calculated between all substructures, these data are used to generate a large graph (Fig. 1). The nodes in this graph represent the substructures, and the edges indicate a level of structural similarity that allows recombination. Novel structures are generated from this graph by traversing a path wherein each followed edge adds new structural elements to the design model. The number of edges included in the sampled paths can control the approximate size of the generated structures. Unlike previously described methods of de novo backbone generation, no target structure is required, and output structures span a diverse set of globular folds.

Previous studies have demonstrated that protein fragments can adopt alternative structures when placed in new environments (*19*–*21*), and thus, similar to natural evolution, the next step in the design process was to further stabilize the protein through mutagenesis. This optimization step was achieved using iterative steps of side-chain packing and backbone minimization available in the Rosetta molecular-modeling suite (*22*). Preference for the amino acid sequence present in the parental substructure was used to better preserve the structural interactions inherent to the parent substructures.

To test SEWING, we designed a diverse set of helical proteins using graphs composed of continuous substructures or discontinuous substructures. Continuous and discontinuous substructures were extracted from nonredundant subsets of the PDB (*23*, *24*). In total, 33,928 continuous substructures and 4584 discontinuous substructures were extracted. Design models from the continuous graph were generated by using three-edge paths and were therefore composed of substructures extracted from four existing structures from the PDB (Fig. 1). The continuous graph contained 345 million edges, which allowed an estimated 7×10^{16} backbones that can be filtered and optimized in later designs steps (supplementary methods). Initially, 50,000 alternative tertiary structures were created and used as templates for rotamer-based sequence optimization and energy minimization. These models were filtered and sorted by using metrics that evaluate predicted energy (normalized by sequence length), side-chain packing, buried polar groups, and sequence-structure agreement (supplementary methods) (*25*). When examining the models, we noticed that the naïve SEWING procedure was biased toward creating low–contact order models, i.e., structures with few contacts between residues distant in primary sequence. To overcome this bias, we filtered for models with contact orders more representative of naturally occurring helical proteins (fig. S1). We have subsequently demonstrated that Monte Carlo sampling of the SEWING graph with a score function that favors long-range contacts can be used to build high-contact models with high frequency (fig. S1). This illustrates one way

Downloaded from http://science.sciencemag.org/ on May 5, 2016

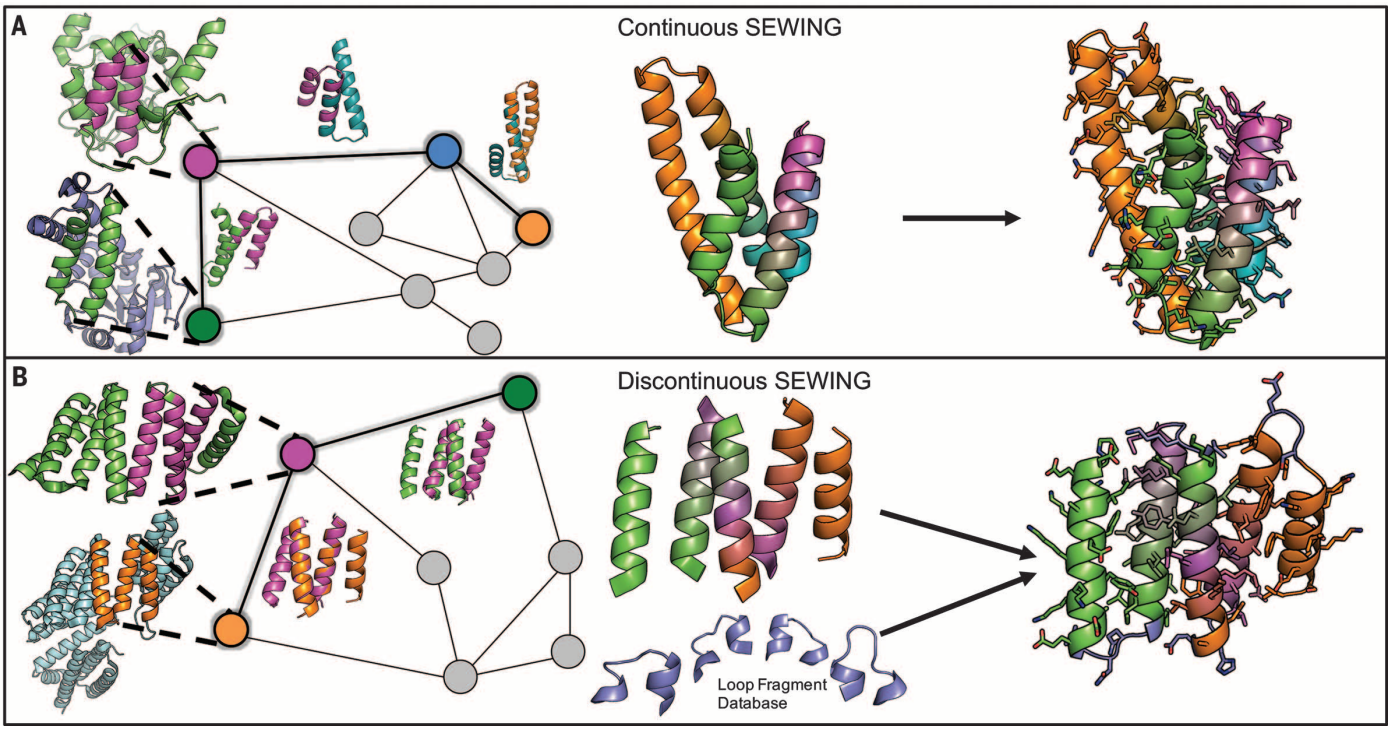


Fig. 1. Overview of the SEWING method. (**A**) Continuous SEWING workflow for CA01. (**B**) Discontinuous SEWING workflow for DA05. From left to right: Parental PDBs are shown with extracted substructures; graph schematic—colored nodes indicate substructures contained in the final design model, and superimposed structures show structural similarity indicated by adjacent edges; design model before sequence optimization and loop design; and final design models.

that directed sampling of the SEWING graph can be used to enforce design requirements.

In total, 11 designs based on continuous SEWING were selected for experimental characterization (table S1). Each region of the final designs shared between 45 and 65% sequence identity with the substructure that they were built from (figs. S2 and S3), but when performing a BLAST search with the full-length sequences, no matches were identified that aligned over the full length of the proteins. Eight designs expressed well in *Escherichia coli* and were readily purified from the soluble fraction of 1-liter cultures. Four of the eight proteins were monomeric as seen by size-exclusion chromatography–multiangle light scattering, had a circular dichroism (CD) spectrum characteristic of a helical protein, and unfolded cooperatively upon thermal denaturation (Fig. 2 and figs. S4 and S5). Two of the designed proteins are hyperthermophiles and require high concentrations of chemical denaturant in order for one to observe thermal unfolding (Fig. 2B). For one design, CA01, several thermodynamic parameters were determined by fitting a modified Gibbs-Helmholtz equation to the thermal and chemical denaturation surface (Fig. 3B and table S2) (*26*). The extrapolated melting temperature of 126°C places it among the top 0.01% of values in the ProTherm database of protein stabilities (*27*). The crystal structure of CA01 was solved to 2.2 Å and shows excellent agreement with the design model, with the RMSD of the *Cα* atomic coordinates equaling 0.8 Å. Similarly, the side-chain packing of the protein core is nearly identical for the design model and the experimental structure (Fig. 3, fig. S6, and table S3).

The structural variety in the design models for the well-folded proteins is of particular note (Fig. 2). The SEWING-generated models include kinked and curved helices (figs. S7 and S8), cavities and clefts (figs. S9 and S10), and a large range of helix-crossing angles (Fig. 2). The topologies of the SEWING models are varied when compared with previously designed α-helical proteins, which are restricted to coiled coils, repeat proteins, and up-down four-helical bundles (Fig. 2C). To compare SEWING models with naturally occurring protein structures, we searched for structurally similar domains using the Dali server (*28*). In general, large portions of the models aligned to regions of existing protein structures. However, the sequence identities across the alignments were typically below 20%, and the positions of the unaligned residues frequently diverged (fig. S11). For instance, the fifth helix of CA01 is shifted by ~9 Å relative to the fifth helix in the top Dali match. These sequences and structural differences provide unique surfaces that may serve as templates for future design goals.

To test discontinuous SEWING, models were generated from two-edge paths and, thus, were composed of structural elements from three parent structures. The variable number of helical elements in the discontinuous substructures therefore allowed design models to be composed of 5 to

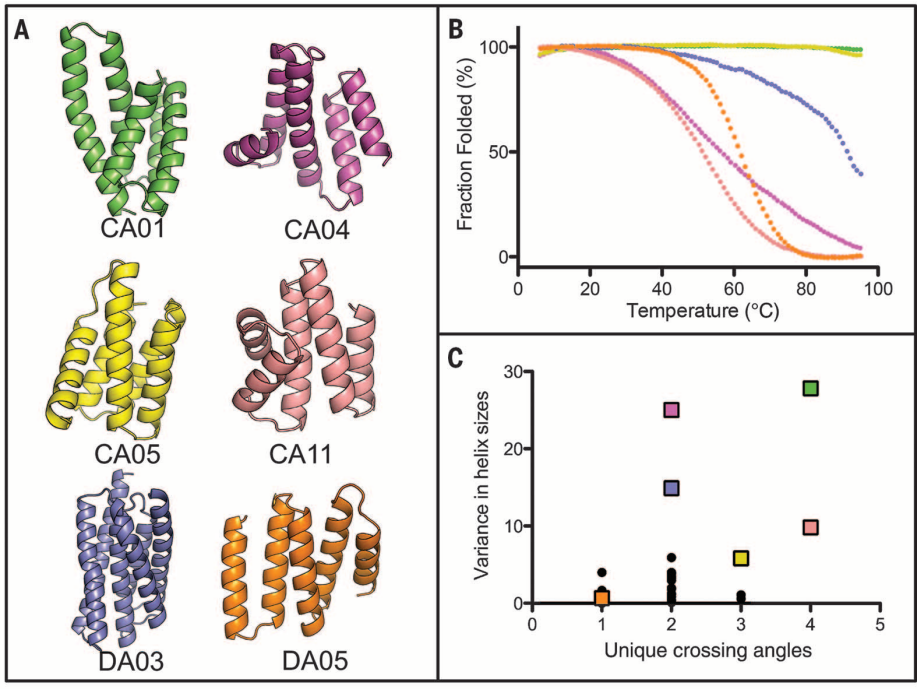


Fig. 2. Well-folded SEWING designs. (**A**) Design models obtained with continuous (CA) and discontinuous (DA) SEWING. (**B**) Temperature denaturation curves for well-folded SEWING designs, colored to match design models. (**C**) A comparison of previously designed helical structures (black dots) to SEWING models (colored squares) demonstrates the structural complexity of SEWING designs. We calculated crossing angles between all pairs of helices in each structure. Crossing angles were considered unique if they differed by >20 degrees from all other calculated angles in the same structure. Variance in helix size describes the calculated variance in the number of residues per helix for all helices in a single structure. A complete list of helix and crossing-angle definitions for de novo designs can be found in tables S5 and S6.

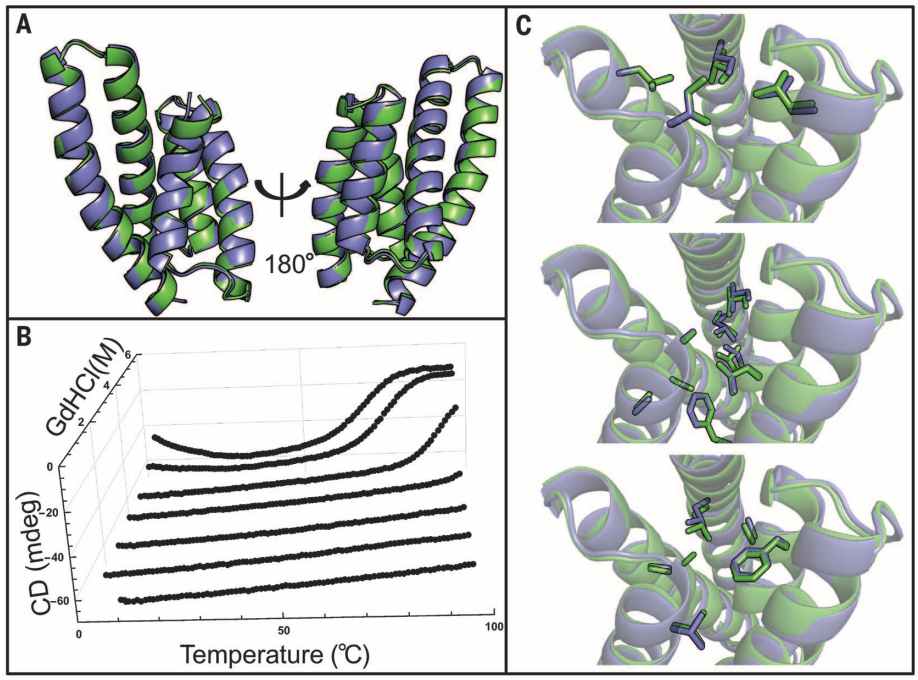


Fig. 3. Structural and biophysical characterization of CA01. (**A**) Backbone superimposition of the design model (green) and crystal structure (purple). (**B**) In the chemical and temperature denaturation experiment, a sharp unfolding transition is observed at 5 M GdHCl and 75°C. (**C**) Comparison of side-chain packing between the design model (green) and crystal structure (purple) at three different layers of the structure.

Downloaded from http://science.sciencemag.org/ on May 5, 2016

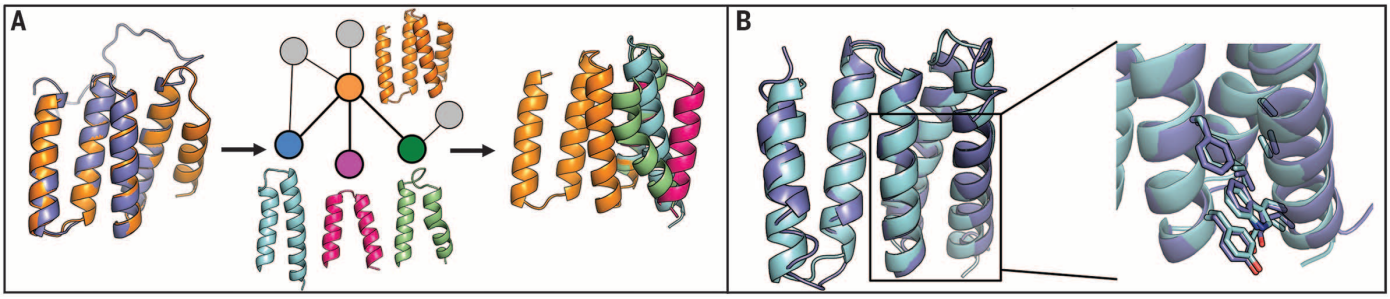


Fig. 4. Result for discontinuous assembly DA05 and DA05R1. (**A**) From left to right: Backbone superimposition of the DA05 design model (orange) with a member of the NMR ensemble (blue). An example of continuous substructure graph for the design of a new final helix onto DA05. Superimposition of three design models containing new helices. (**B**) From left to right: Backbone superimposition of the DA05R1 design model (light blue) with a member of the DA05R1 NMR ensemble (blue). A comparison of side-chain packing between the DA05R1 design model and the NMR structure for DA05R1.

11 helices. Unlike models from the continuous-substructure graph, discontinuous models require the addition of loops between consecutive helices. Loops were designed by using a database of fragments from the PDB (*29*). Each loop fragment was superimposed onto the design model and optimized using gradient-based minimization in Cartesian space. Any path that created structures for which no loop fragment could be found was eliminated from the set of designs. Design models were filtered and optimized in the same way as models from the continuous graph. In total, 10 were selected for experimental characterization (table S1).

Of these 10 designs, 2 expressed at levels sufficient for purification. Both purified proteins were helical and folded, as evidenced by CD (Fig. 2 and fig. S4). Similar to the results from the continuous designs, one discontinuous design, DA03, demonstrated high thermostability, which required high levels of denaturant to completely unfold. For this design, an 181-residue six-helix bundle, unfolding appears to follow a three-state model (fig. S12).

The structure of the other well-folded discontinuous design, DA05, was solved using nuclear magnetic resonance (NMR) spectroscopy, as the protein did not readily crystallize (figs. S13 and S14 and table S4). The first four helices of the design model match the lowest-energy member of the NMR ensemble very closely, with a Cα RMSD of 0.8 Å (Fig. 4 and fig. S6). However, the NMR data indicate that the final helix of the protein is disordered in solution. In an effort to identify the errors in the design model that led to the unstructured region, structural preference for the designed sequence was evaluated with fragment analysis as described previously (*1*). The fragments extracted for the unstructured region showed especially poor preference for the designed helical structure (fig. S15). We attempted to design a new final helix for the DA05 design using the continuous SEWING method. The final helix of the initial design model was removed, and the remainder of the model was added as a node to the continuous graph. New helices were evaluated by following a single edge from this new node (Fig. 4A). Three models designed in this way were selected for experimental testing. Two of the tested designs, DA05R1 and DA05R2, show a significant increase in melting temperature relative to the initial DA05 design (fig. S16). The NMR structure of DA05R1 shows that the newly designed helix adopts the designed conformation, which highlights the utility of combining the continuous and discontinuous graphs (Fig. 4B, figs. S17 and S18, and table S4).

The additional step of loop building is a critical difference between discontinuous and continuous SEWING. The accurate design of loops is a long-standing challenge for protein design, and this additional step may have contributed to the relatively lower success rate observed for discontinuous SEWING. In contrast, continuous SEWING maintains the relative orientation between adjacent helices, which allows many of the designed loop sequences to be taken directly from the native substructure. The power of this strategy is seen in the high structural accuracy achieved for the loops in the CA01 design (Fig. 3 and fig. S2).

Our results show that computational adaptations of basic evolutionary principles, such as recombination and mutation, can be used to design, accurately and rapidly, a diverse set of helical protein structures. The diversity of SEWING designs will further increase when alternative types of substructures are included, such as β-α motifs and β hairpins. Furthermore, discontinuous and continuous SEWING can be merged, as in the DA05R1 design, to create additional diversity. We anticipate that this structural diversity will be advantageous for functional design, as every backbone generated with SEWING has new surface and pocket features that provide potential binding sites for ligands or macromolecules. Additionally, SEWING offers an approach for stitching together functional motifs from naturally occurring proteins, an evolutionary mechanism to generate multifunctional proteins and allosteric systems.

REFERENCES AND NOTES

1. N. Koga *et al.*, *Nature* **491**, 222–227 (2012).
2. N. H. Joh *et al.*, *Science* **346**, 1520–1524 (2014).
3. P.-S. Huang *et al.*, *Science* **346**, 481–485 (2014).
4. L. Doyle *et al.*, *Nature* **528**, 585–588 (2015).
5. T. J. Brunette *et al.*, *Nature* **528**, 580–584 (2015).
6. B. Kuhlman *et al.*, *Science* **302**, 1364–1368 (2003).
7. A. L. Hughes, *Proc. Natl. Acad. Sci. U.S.A.* **102**, 8791–8792 (2005).
8. C. C. F. Blake, *Nature* **273**, 267–267 (1978).
9. M. Bashton, C. Chothia, *Structure* **15**, 85–99 (2007).
10. S. Koide, *Curr. Opin. Biotechnol.* **20**, 398–404 (2009).
11. S. Eisenbeis *et al.*, *J. Am. Chem. Soc.* **134**, 4019–4022 (2012).
12. C. Vogel, M. Bashton, N. D. Kerrison, C. Chothia, S. A. Teichmann, *Curr. Opin. Struct. Biol.* **14**, 208–216 (2004).
13. N. V. Grishin, *J. Struct. Biol.* **134**, 167–185 (2001).
14. N. Fernandez-Fuentes, J. M. Dybas, A. Fiser, *PLOS Comput. Biol.* **6**, e1000750 (2010).
15. J. Söding, A. N. Lupas, *BioEssays* **25**, 837–846 (2003).
16. G. A. Reeves, T. J. Dallman, O. C. Redfern, A. Akpor, C. A. Orengo, *J. Mol. Biol.* **360**, 725–741 (2006).
17. H. E. Aronson, W. E. Royer Jr., W. A. Hendrickson, *Protein Sci.* **3**, 1706–1711 (1994).
18. R. Nussinov, H. J. Wolfson, *Proc. Natl. Acad. Sci. U.S.A.* **88**, 10495–10499 (1991).
19. M. J. Schellenberg *et al.*, *J. Mol. Biol.* **402**, 720–730 (2010).
20. T. A. M. Bharat, S. Eisenbeis, K. Zeth, B. Höcker, *Proc. Natl. Acad. Sci. U.S.A.* **105**, 9942–9947 (2008).
21. S. de Bono, L. Riechmann, E. Girard, R. L. Williams, G. Winter, *Proc. Natl. Acad. Sci. U.S.A.* **102**, 1396–1401 (2005).
22. A. Leaver-Fay *et al.*, *Methods Enzymol.* **487**, 545–574 (2011).
23. G. Wang, R. L. Dunbrack Jr., *Bioinformatics* **19**, 1589–1591 (2003).
24. J. S. Richardson, D. C. Richardson, *Biopolymers* **99**, 170–182 (2013).
25. W. Sheffler, D. Baker, *Protein Sci.* **19**, 1991–1995 (2010).
26. B. Kuhlman, D. P. Raleigh, *Protein Sci.* **7**, 2405–2412 (1998).
27. A. Sarai *et al.*, *Biopolymers* **61**, 121–126 (2001–2002).
28. L. Holm, P. Rosenström, *Nucleic Acids Res.* **38** (Web Server), W545–W549 (2010).
29. M. D. Tyka, K. Jung, D. Baker, *J. Comput. Chem.* **33**, 2483–2491 (2012).

ACKNOWLEDGMENTS

This work was supported by NIH grants R01GM073960 and R01GM117968 (to B.K.) and GM094597 (to T.S.). Use of the Advanced Photon Source was supported by the Office of Basic Energy Sciences, Office of Science, U.S. Department of Energy, under contract no. W-31-109-Eng-38. Coordinates and structure factors have been deposited in the Protein Data Bank with the accession codes 5E6G (CA01), 2N8I (DA05), and 2N8W (DA05R1). Chemical shifts have been deposited in the Biological Magnetic Resonance Bank (BMRB) with the accession codes 25850 (DA05) and 25868 (DA05R1). T.M.J. and B.K. designed the research; T.M.J. wrote the backbone assembly code; T.M.J. and B.W. carried out the backbone assembly and design simulations; T.M.J. conducted the biophysical analysis; T.W. and T.M.J. solved the structure of CA01; and X.X., A.E., and J.F.F., with advice from T.S., solved the NMR structure of DA05 and DA05R1.

SUPPLEMENTARY MATERIALS

www.sciencemag.org/content/352/6286/687/suppl/DC1
Materials and Methods
Supplementary Text
Figs. S1 to S18
Tables S1 to S6
References (*30*–*55*)

5 November 2015; accepted 14 March 2016
10.1126/science.aad8036

Downloaded from http://science.sciencemag.org/ on May 5, 2016

MICROFLUIDICS

Submillisecond organic synthesis: Outpacing Fries rearrangement through microfluidic rapid mixing

Heejin Kim,[1]* Kyoung-Ik Min,[2]* Keita Inoue,[1] Do Jin Im,[3] Dong-Pyo Kim,[2]† Jun-ichi Yoshida[1]†

In chemical synthesis, rapid intramolecular rearrangements often foil attempts at site-selective bimolecular functionalization. We developed a microfluidic technique that outpaces the very rapid anionic Fries rearrangement to chemoselectively functionalize iodophenyl carbamates at the ortho position. Central to the technique is a chip microreactor of our design, which can deliver a reaction time in the submillisecond range even at cryogenic temperatures. The microreactor was applied to the synthesis of afesal, a bioactive molecule exhibiting anthelmintic activity, to demonstrate its potential for practical synthesis and production.

Chemical synthesis often involves competition between unimolecular and bimolecular reactivity of an intermediate. To fully explore and exploit the synthetic pathways of a given intermediate, control over its lifetime is needed along with control over its mixing time with external reagents for both its generation and trapping reactions. One efficient means of prolonging the lifetime is to lower the reaction temperature; the range from −78° to −100°C is slightly above the melting point of many organic solvents (*1*). Microfluidic devices (*2*–*9*) concomitantly deliver extremely fast mixing times unattainable by batches (*10*–*12*). However, minimizing the mixing time in the microfluidic device is quite a challenge in the low-temperature range because of the exponential rise in the viscosity of the solvent with decreasing temperature (*13*). Here, we report a microfluidic device that achieves submillisecond mixing time even at cryogenic temperatures, and we demonstrate its utility in outpacing an intramolecular rearrangement.

We initially considered modification of a stainless steel microfluidic assembly used earlier (*10*–*12*), which could deliver a residence time of a few milliseconds. However, the stainless steel was not suitable for fabricating a minuscule dead volume, although compatibility with high-pressure and low-temperature reaction conditions was ensured. To further reduce the residence time below milliseconds (*14*), it was necessary to devise a microfluidic device with a smaller internal volume that would attain a higher level of mixing efficiency within the temporal frame needed for the synthesis. Such a device had two major requirements: The reaction mixture had to be well-mixed within the lifetime of the reactive intermediate, and the device had to endure low temperature as well as high back pressure ensuing from the increased viscosity of the reaction fluid at that temperature.

On the strength of good mixing reported for a three-dimensional (3D) serpentine mixer (*15*, *16*), we designed various microchannel structures (MSs) and tested the structures for mixing efficiency on the basis of computational fluid dynamics (CFD). These structures were evaluated by monitoring the degree of mixing as a function of distance from the initial mixing point; in general, the mixing efficiency improved with increasing number of turns (see descriptions of MS-3, -4, and -5 in the supplementary materials). The turn induced chaotic advection involving rapid distortion and elongation of the fluid interface (*15*–*17*) when the side-on collision type of serpentine 3D-structured channel was used. The simulation results showed (fig. S1, B and C) that the serpentine 3D-structured channel MS-5, which has a turn before the mixing point and four turns after the mixing point in total length of 1 mm, provides mixing efficiency levels of 95% and 82% for total flow rates of 7.5 and 4.5 ml/min, respectively. These flow rates correspond to a residence time of ~0.3 ms, which confirmed the feasibility for submillisecond-scale reaction control for a respectable range of flow rates.

With the simulation results in hand, we carefully considered the choice of material for fabrication of the device. Our prior experience with polymer-based microfluidic chips pointed us to a fluoroethylene propylene–polyimide film hybrid, which offers outstanding physical toughness at high pressure and low temperature as well as chemical inertness (*18*–*20*). Figure 1 showcases the device we developed, which is a polymer-based chip microreactor (CMR) with 3D serpentine microchannel design (MS-5).

We fabricated the device in one step by thermally bonding six stacked polyimide films, each

[1]Department of Synthetic Chemistry and Biological Chemistry, Graduate School of Engineering, Kyoto University, Nishikyo-ku, Kyoto 615-8510, Japan. [2]Department of Chemical Engineering, POSTECH, Pohang 790-784, Korea. [3]Department of Chemical Engineering, Pukyong National University, Busan 608-739, Korea.
*These authors contributed equally to this work. †Corresponding author. Email: dpkim@postech.ac.kr (D.-P.K.); yoshida@sbchem.kyoto-u.ac.jp (J.Y.)

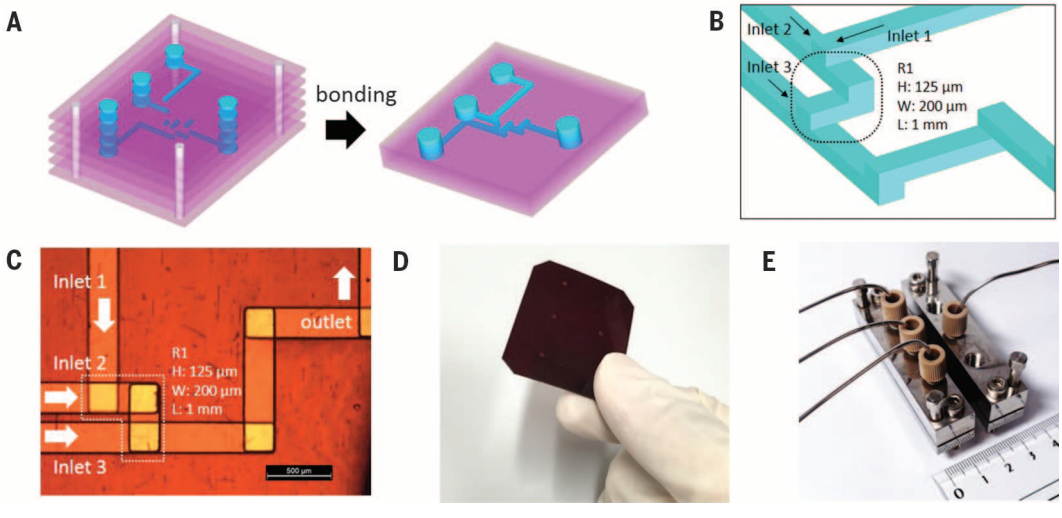


Fig. 1. Chip microreactor (CMR) fabricated with six layers of polyimide films. (**A**) Conceptual scheme for fabricating 3D serpentine microchannel structure by lamination of the patterned films and one-step thermal bonding. (**B**) Detailed scheme for a nanoliter reaction space of rectangular 3D serpentine channels (200 μm × 125 μm × 1 mm) with three inlets. (**C**) Optical image of the semitransparent CMR showing the nanoliter reaction space with three inlets and one outlet (top view; scale bar, 500 μm). (**D**) Optical image of CMR module (4.5 cm × 3.5 cm, thickness 0.7 mm). (**E**) Optical image of CMR assembly with metal holders to connect tubes.

Downloaded from http://science.sciencemag.org/ on May 5, 2016

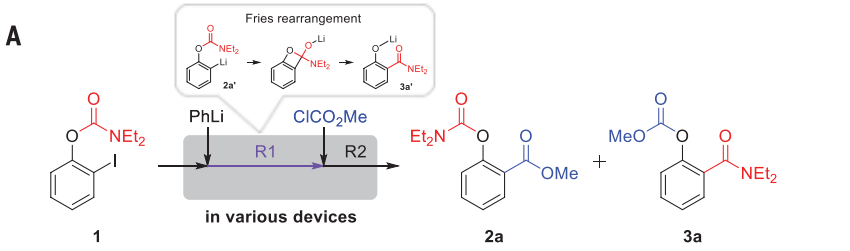
of which was patterned by ultraviolet laser ablation as previously reported (*18*–*20*). The internal volume for the reaction space, 25 nl, is provided by the rectangular serpentine channels (width 200 μm, height 125 μm, length 1 mm) within the dotted circle in Fig. 1B, as designed with the help of the simulation study (Fig. 1 and supplementary materials). We confirmed that the CMR remained chemically inert toward organolithium reagents and also robust to several hours of exposure to liquid nitrogen temperature and applied pressures of 16.2 MPa, as thoroughly verified in the previous reports (*19*, *20*).

To demonstrate the chemoselectivity attainable using the CMR, we explored the anionic Fries rearrangement (*21*, *22*), a well-known reaction that is often applied to total synthesis of natural products in organic synthesis (*23*). For example, *ortho*-lithiated *O*-aryl carbamates undergo facile intramolecular carbamoyl migration to give a constitutionally isomeric *o*-lithiated salicylamide as the temperature is raised from −78°C to room temperature. We began our investigation by conducting the reaction using *o*-iodophenyl diethylcarbamate (**1**) as a precursor (Fig. 2A). The iodine-lithium exchange of **1** followed by reaction of the resulting aryllithium intermediate **2a′** and/or rearranged **3a′** with methyl chloroformate as an electrophile was conducted at 25°C in two types of microfluidic devices: (i) a stainless steel modular microreactor (MMR) consisting of two T-shaped micromixers and microtube reactors having a circular cross-sectional channel (inner diameter 250 μm to 1000 μm; see supplementary materials) that is typically used for flash chemistry (*10*–*12*), and (ii) the polyimide-based CMR. Compound **2a** is produced from aryllithium intermediate **2a′**, whereas compound **3a** is from rearranged intermediate **3a′**.

We sought to achieve high chemoselectivity between the two isomeric products. The flow reaction using the MMR-1 microfluidic device (internal volume of R1, 79 μl) with residence time in R1 of 628 ms produced only **3a** delivering a 91% yield (Fig. 2A, entry 1); **2a** derived from unrearranged **2a′** was not detected at all. Unimolecular Fries rearrangement of **2a′** to **3a′** was evidently complete prior to the bimolecular trapping reaction with methyl chloroformate. When the internal volume of the microreactors was decreased from 39 μl (MMR-2) to 0.49 μl (MMR-6), the yield of **2a** increased with the corresponding decrease in the residence time. However, a small amount of **3a** was still produced even with the shortest residence time provided by MMR-6 (Fig. 2A, entry 6). In contrast, only **2a** was produced, with no detected **3a**, when the reaction was conducted in the CMR, where residence time was 0.33 ms for the reaction volume of 25 nl and a total flow rate of 4.5 ml/min, delivering a 74% yield (Fig. 2A, entry 7). This indicates that, by virtue of the superior mixing and residence time control of the CMR, the bimolecular reaction to generate **2a′** and the subsequent bimolecular trapping reaction with methyl chloroformate were successfully accomplished before the unimolecular Fries rearrangement could occur. The portion of the starting compound **1** remaining unreacted was 25% because of the mixing efficiency of ~80%, which is in good agreement with the simulation result (see supplementary materials). For a better yield, the number of equivalents of PhLi was increased from 1.05 to 1.2, which raised the yield of **2a** to 91% without any contamination from isomeric **3a** (Fig. 2A, entry 8), achieving >99% selectivity.

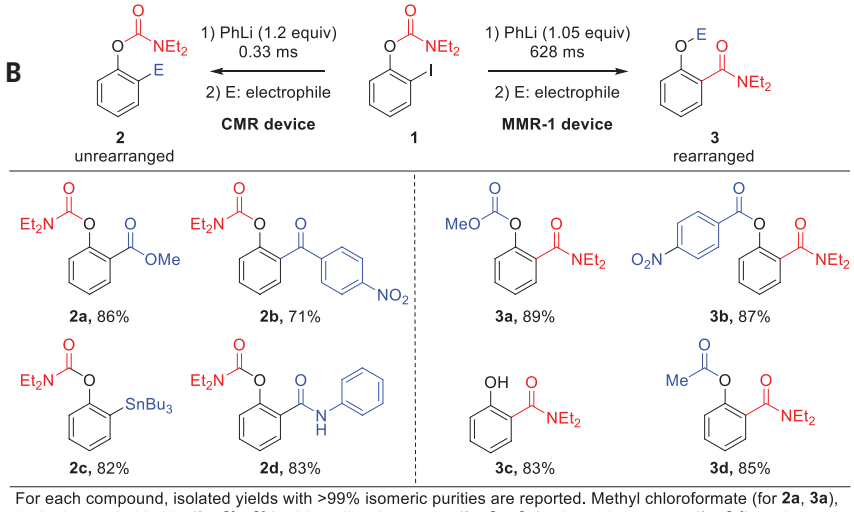
Similar chemoselectivity was attained for Fries rearrangements with various electrophiles such as methyl chloroformate, 4-nitrobenzoyl chloride, chlorotributylstannane, phenyl isocyanate, and acetyl chloride. The products derived from the unrearranged intermediate and the rearranged intermediate were selectively obtained at will using a suitable device under the optimized conditions (Fig. 2B). With the CMR, **2a** to **2d** derived from the unrearranged intermediate **2a′** were produced in good yields without any detectable formation of isomeric by-products by gas chromatography and nuclear magnetic resonance (NMR) spectroscopy, whereas **3a** to **3d** derived from the rearranged intermediate **3a′** were selectively obtained using MMR-1.

Much more challenging to outpace than the migration of the carbamoyl groups is the anionic Fries rearrangement of esters involving acyl group migration, because of the stronger reactivity of the acyl group relative to the carbamoyl group and thus the much faster nature of the reaction. We next explored these reactions using



entry	microfluidic device	inner volume of R1 (μL)	residence time in R1 (ms)	yield of **2a** (%)	yield of **3a** (%)
1	**MMR-1**	**79**	**628**	**0**	**91**
2	MMR-2	39	377	20	74
3	MMR-3	27	220	45	51
4	MMR-4	7	55	73	21
5	MMR-5	2	14	79	15
6	MMR-6	0.49	4	87	4
7*	CMR	0.025	0.33	74	0
8†	**CMR**	0.025	**0.33**	**91**	**0**

For each entry number, data are reported as ^{1}H NMR yield. See supplementary materials for experimental details. *25% of unreacted compound **1** remained. †1.2 equiv of PhLi were used.



For each compound, isolated yields with >99% isomeric purities are reported. Methyl chloroformate (for **2a**, **3a**), 4-nitrobenzoyl chloride (for **2b**, **3b**), chlorotributylstannane (for **2c**, **3c**), phenyl isocyanate (for **2d**), and acetyl chloride (for **3d**) were used as electrophiles.

Fig. 2. Control of anionic Fries rearrangement reactions of carbamates. (**A**) Effect of residence time on the product selectivity. (**B**) Exceptional chemoselectivity for anionic Fries rearrangements with various electrophiles.

Downloaded from http://science.sciencemag.org/ on May 5, 2016

various microfluidic devices (MMR-1 to -6 and CMR) in the range of reaction times from 628 ms to 0.33 ms (Fig. 3). The strong reactivity of the acyl group required lowering of the reaction temperature to –70°C. Even at this low temperature, a total flow rate of 4.5 ml/min could still be maintained, demonstrating the CMR's capability to withstand high pressure up to 160 bar (*19*, *20*).

Figure 3 shows that the yield of **5a** derived from the unrearranged intermediate increased with decreasing reaction time, but an acceptable yield was not attained until the reaction time was reduced to 4 ms, presumably because of both rearrangement and decomposition of the intermediate. The selectivity diminished for residence times longer than 4 ms (table S5). However, the use of CMR gave rise to the formation of the desired product **5a** in 86% yield with no detectable isomeric by-products derived from acyl migration. The extremely short residence (0.33 ms) achieved by CMR is responsible for the selective formation of **5a**, avoiding the rearrangement and decomposition. For a comparison, the reaction was conducted in a conventional flask. A solution of PhLi was added to a solution of 2-iodophenyl benzoate (**4a**) at –70°C, and then chlorotributylstannane was added to the resulting solution within 1 s. The reaction gave the acyl-migrated product in poor yield (12%) with no desired **5a**. A substantial quantity of by-products was confirmed by ^{1}H NMR and gas chromatography, as expected. Furthermore, using the CMR at a residence time of 0.33 ms, the aryl compounds bearing benzoyl, pentanoyl, and acetyl groups (**4**) reacted with various electrophiles to give the desired products in good yields (Fig. 4A). Even in the case of an aryl iodide bearing a sterically small acetyl group, the desired products (**5i** and **5j**) were successfully obtained in moderate yields without isomeric by-products from the acyl migration.

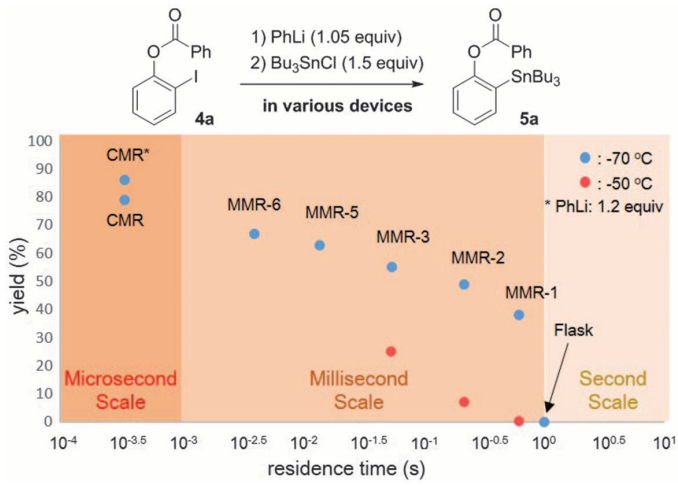


Fig. 3. Effect of residence time on the yield of the product derived from the unrearranged intermediate versus the anionic Fries rearrangement of an ester.

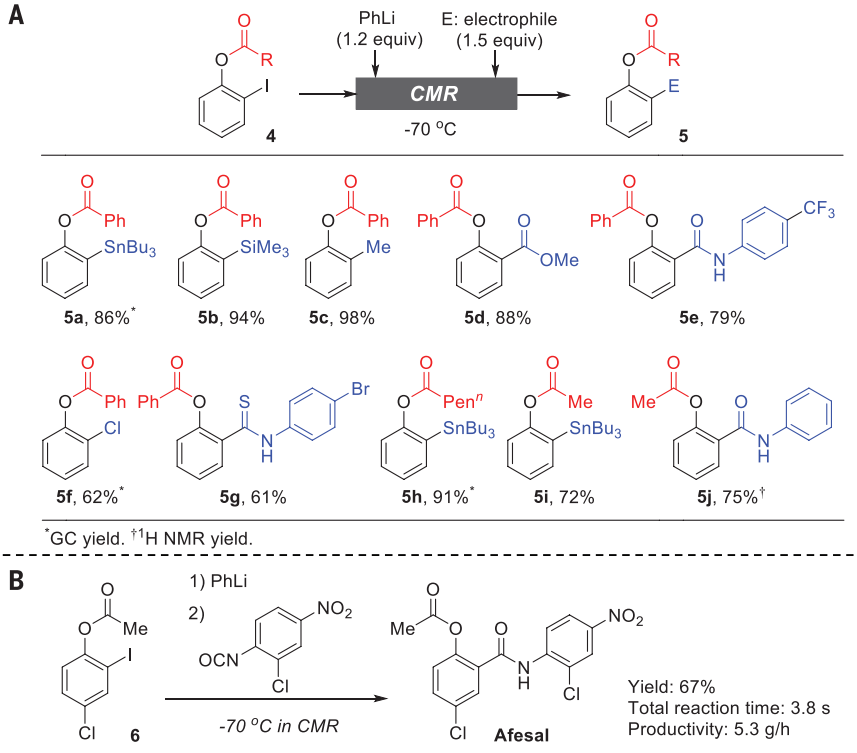


Fig. 4. Control of anionic Fries rearrangement of esters via a submillisecond-controlled CMR device. (**A**) Reaction of unrearranged intermediates with various electrophiles. Isolated yields are reported unless otherwise indicated. (**B**) Straightforward synthesis of the anthelmintic compound afesal.

The 25-nl reactor volume of the CMR may give the impression that the throughput must be very small. To demonstrate the suitability of the CMR for practical production of specialty chemicals such as drugs, we applied it to the production of a biologically active compound having anthelmintic activity, 2-(acetyloxy)-5-chloro-*N*-(2-chloro-nitrophenyl)-benzamide (afesal) (*24*), which was successfully synthesized (Fig. 4B). The sequential bimolecular reactions, including I-Li exchange of 4-chloro-2-iodophenyl acetate (**6**) to generate the corresponding aryllithium intermediate and its trapping reaction with 2-chloro-1-isocyanato-4-nitrobenzene, produced afesal in 67% isolated yield. Although the *O*-acetyl functional group has been reported to be incompatible with organolithium reactions, the *O*-acetyl function was tolerated on the submillisecond time scale of the CMR device to provide a straightforward synthetic route for afesal. The rapid continuous-flow nature of the CMR delivered a throughput of 5.3 g/hour. Thus, stacking multiple small and portable CMR systems, which individually fit in one hand, has great potential for scalable industrial chemical synthesis.

REFERENCES AND NOTES

1. I. R. Sims, *Nat. Chem.* **5**, 734–736 (2013).
2. G. M. Whitesides, *Nature* **442**, 368–373 (2006).
3. K. S. Elvira, X. Casadevall i Solvas, R. C. R. Wootton, A. J. deMello, *Nat. Chem.* **5**, 905–915 (2013).
4. K. F. Jensen, B. J. Reizman, S. G. Newman, *Lab Chip* **14**, 3206–3212 (2014).
5. S. V. Ley, D. E. Fitzpatrick, R. M. Myers, C. Battilocchio, R. J. Ingham, *Angew. Chem. Int. Ed.* **54**, 10122–10136 (2015).
6. T. Illg, P. Löb, V. Hessel, *Bioorg. Med. Chem.* **18**, 3707–3719 (2010).
7. K. Geyer, T. Gustafsson, P. H. Seeberger, *Synlett* **2009**, 2382–2391 (2009).
8. T. Tsubogo, H. Oyamada, S. Kobayashi, *Nature* **520**, 329–332 (2015).
9. V. Hessel, E. Shahbazali, T. Noel, S. Zelentsov, *ChemBioEng Rev.* **1**, 244–261 (2014).
10. J. Yoshida, A. Nagaki, T. Yamada, *Chemistry* **14**, 7450–7459 (2008).
11. H. Kim, A. Nagaki, J. Yoshida, *Nat. Commun.* **2**, 264 (2011).
12. J. Yoshida, H. Kim, A. Nagaki, *ChemSusChem* **4**, 331–340 (2011).
13. C. J. Seeton, *Tribol. Lett.* **22**, 67–78 (2006).
14. D. Bökenkamp, A. Desai, X. Yang, Y.-C. Tai, E. M. Marzluff, S. L. Mayo, *Anal. Chem.* **70**, 232–236 (1998).

Downloaded from http://science.sciencemag.org/ on May 5, 2016

15. R. H. Liu *et al.*, *J. Microelectromech. Syst.* **9**, 190–197 (2000).
16. H. Aref, *Phys. Fluids* **14**, 1315–1325 (2002).
17. Y. Z. Liu, B. J. Kim, H. J. Sung, *Int. J. Heat Fluid Flow* **25**, 986–995 (2004).
18. K.-I. Min *et al.*, *Angew. Chem. Int. Ed.* **49**, 7063–7067 (2010).
19. K.-I. Min, J. Im, H.-J. Lee, D.-P. Kim, *Lab Chip* **14**, 3987–3992 (2014).
20. K.-I. Min, J.-O. Kim, H. Kim, J. Im, D.-P. Kim, *Lab Chip* **16**, 977–983 (2016).
21. K. Fries, G. Finck, *Ber. Dtsch. Chem. Ges.* **41**, 4271–4284 (1908).
22. R. Martin, *Org. Prep. Proced. Int.* **24**, 369–435 (1992).
23. G. Bringmann *et al.*, *J. Org. Chem.* **67**, 5595–5610 (2002).
24. J. E. Semple, J.-F. Rossignol, Preparation of benzamide compounds as glutamate receptor modulators and therapeutic agents, PCT Int. Appl. WO 2012058378 (2012).

ACKNOWLEDGMENTS

Supported by National Research Foundation of Korea grants 2008-0061983, NRF-2015R1D1A3A01019112, and NRF-2014M1A8A1074940 and by Japan Society for the Promotion of Science Grant-in-Aid for Scientific Research (S) 26220804. Author contributions: H.K. and K.-I.M. conceived the concept at POSTECH; K.-I.M. fabricated the device; H.K. conducted synthetic experiments at POSETCH and Kyoto University with K.I.; D.J.I. conducted CFD simulation and analysis with K.-I.M.; and D.-P.K. and J.Y. directed the project.

SUPPLEMENTARY MATERIALS

www.sciencemag.org/content/352/6286/691/suppl/DC1
Materials and Methods
Figs. S1 to S3
Tables S1 to S6
NMR Spectra
References (*25*–*32*)

22 December 2015; accepted 28 March 2016
10.1126/science.aaf1389

GEOMORPHOLOGY

Self-organization of river channels as a critical filter on climate signals

Colin B. Phillips[1]* and Douglas J. Jerolmack[2]

Spatial and temporal variations in rainfall are hypothesized to influence landscape evolution through erosion and sediment transport by rivers. However, determining the relation between rainfall and river dynamics requires a greater understanding of the feedbacks between flooding and a river's capacity to transport sediment. We analyzed channel geometry and stream-flow records from 186 coarse-grained rivers across the United States. We found that channels adjust their shape so that floods slightly exceed the critical shear velocity needed to transport bed sediment, independently of climatic, tectonic, and bedrock controls. The distribution of fluid shear velocity associated with floods is universal, indicating that self-organization of near-critical channels filters the climate signal evident in discharge. This effect blunts the impact of extreme rainfall events on landscape evolution.

Understanding the control of climate on the geometry and erosion rate of rivers is essential for reconstructing the geologic history of landscapes and for predicting the response of rivers to human-accelerated climate change. A natural assumption is to link river erosion to climate through precipitation (*1*–*3*), yet demonstrating a clear relation is unexpectedly challenging (*4*–*7*). One reason is that bedrock river incision occurs primarily by abrasion due to the collision of particles with the stream bed (*8*) and "plucking" of loose blocks (*2*), and therefore it depends on sediment supply as well as precipitation. Another reason is that bedrock channel geometry both influences and adjusts to incision rate (*4*, *9*–*11*). The effects of climatic variability (*11*–*13*) and bedrock channel geometry (*9*, *10*) on river incision rates have been explored primarily with numerical models, but empirical observations remain limited.

In contrast to the case of bedrock systems, our understanding of the geometry of alluvial rivers (channels whose bed and banks are composed of mobile sediment) is built upon two empirically vetted theoretical principles. The first is "geomorphic work," in which the wide range of flows generated by climate—defined here as the magnitude, frequency, and phase of precipitation—is represented by a characteristic flood (*14*). This "bankfull" flood is the event whose frequency and magnitude combine to move the most sediment in the long-time limit, and it dictates channel size (Fig. 1). The second principle applies to gravel-bed rivers (median bed particle diameter, $D \geq 10$ mm), where sediment moves predominantly as bed load. Gravel-bed rivers adjust their geometry so that the width-averaged fluid shear velocity (U_*, meters per second) slightly exceeds the critical value (U_{*c}) at bankfull conditions. This is called the near-threshold channel, for which data and theory indicate that $U_*/U_{*c} \approx 1.1$ (Fig. 1) (*15*, *16*). Some studies, however, suggest that this treatment ignores details of climatic variability that may exert a substantial influence on landscape evolution (*1*, *17*, *18*). Observations reveal that the statistical distributions of discharge in many rivers possess a power-law tail (*12*, *13*, *19*), whose exponent changes with climatic setting (*17*). These observations have been interpreted to mean that channel shape may be controlled by climate and, for rivers with sufficiently heavy-tailed (log-log slope < −2) discharge distributions, that the rate of sediment transport could be dominated by extreme events due to climatic variability (*17*), which prevents rivers from achieving an equilibrium geometry over geologic timescales (*1*, *3*). Understanding the role of rivers in landscape evolution requires reconciling the proposed importance of climatic variability on channel form and dynamics with the apparent equilibrium behavior implied by near-universal hydraulic geometry scaling relations (*15*, *20*, *21*).

Climatic effects on river dynamics are typically characterized by discharge (Q, cubic meters per second), which is strongly related to precipitation (*22*), and erosion is often modeled using stream power (the product of discharge and slope, S). Bed-load motion, however, is driven by applied

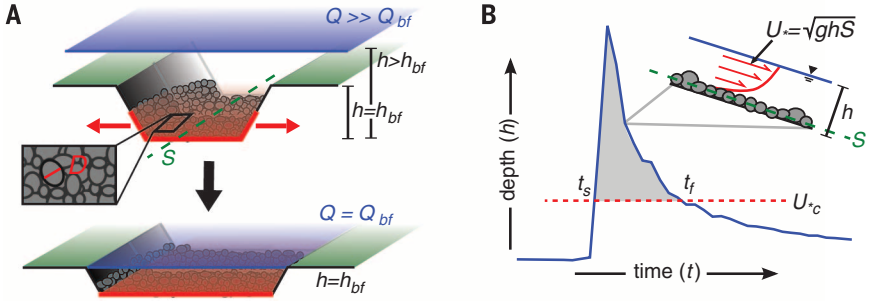


Fig. 1. Definition sketches. (**A**) Channel cross section illustrating adjustment to near-threshold bed-load transport; red regions are above the threshold of motion. The top panel shows flow exceeding bankfull conditions that induces transport on the banks, resulting in erosion and widening of the channel, which returns the system to near-threshold conditions (bottom). U_{*bf} was computed from channel surveys of S and h_{bf}. (**B**) Definition sketch of a flood, with relevant parameters shown. The gray shaded area (from the starting time t_s to the finishing time t_f) represents the part of a flood that is included in the integral for potential transport, which is calculated as $T = \int_{t_s}^{t_f} (U_*^2 - U_{*c}^2)^{3/2} dt/(gD_{50}^2)$ for $U_* \geq U_{*c}$ (*26*).

[1]St. Anthony Falls Laboratory, University of Minnesota, Minneapolis, MN 55414, USA. [2]Department of Earth and Environmental Science, University of Pennsylvania, Philadelphia, PA 19104, USA.
***Corresponding author. Email: colinbphillips@gmail.com**

Downloaded from http://science.sciencemag.org/ on May 5, 2016

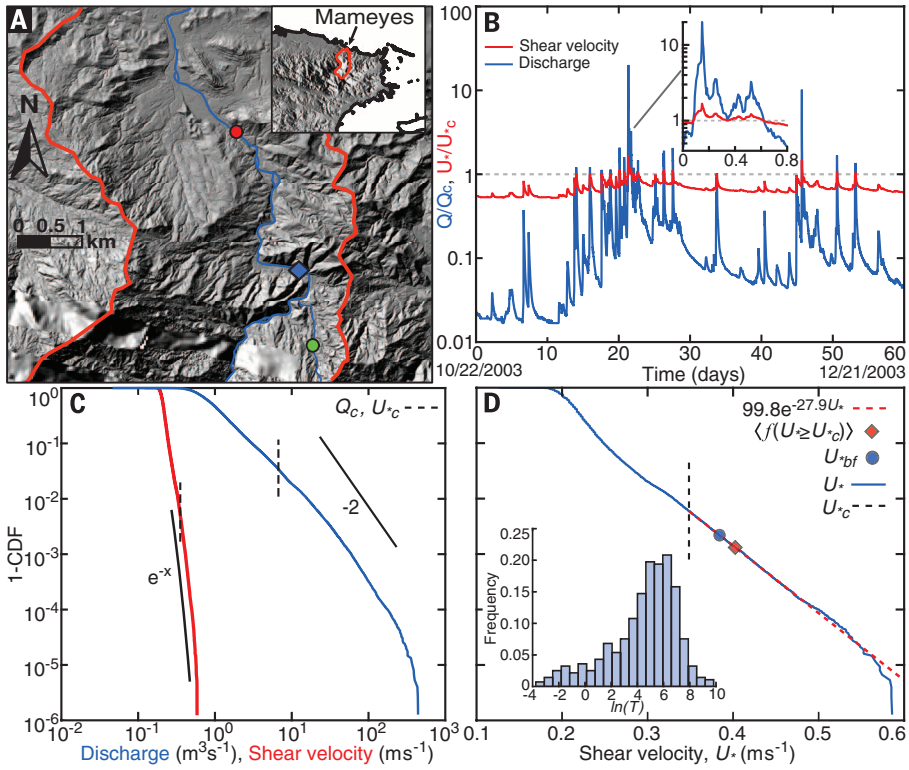


Fig. 2. The Mameyes River case study. (**A**) Lidar map of the Mameyes River catchment (red outline). The blue diamond shows the location of the USGS stream gage, and the red and green circles indicate the locations of the alluvial and the steep bedrock-alluvial tributary tracer studies, respectively. Flow is from south to north along the blue trace of the river. (**B**) Representative hydrograph from 2003 of discharge (blue) and shear velocity (red), measured every 15 min and normalized by the threshold of motion. The inset shows a single storm event. (**C**) Magnitude-frequency distribution of discharge (blue line, shown next to a slope of −2 for comparison) and of shear velocity (red line, shown next to an exponential function for comparison), indicating heavy-tail and thin-tail behavior, respectively (CDF, cumulative distribution function). A log-log slope shallower than −2 indicates infinite variance, meaning that a characteristic discharge cannot be obtained. (**D**) Magnitude-frequency distribution (semi-log scale) of U_* (blue line), which is well described by an exponential function for flows in excess of U_{*c}. The red diamond and blue circle represent bankfull shear velocity (U_{*bf}) and the average flood $\langle f(U_* \geq U_{*c}) \rangle$, respectively. The inset shows a PDF of ln(T).

fluid momentum represented by the shear velocity, $U_* = \sqrt{ghS}$, where g is gravity and h (in meters) is the width-averaged flow depth (Fig. 1B). For within-channel flows, shear velocity scales only weakly with discharge ($U_* \sim h^{1/2} \sim Q^{1/6}$) (*15*), and the relation is even weaker when flows exceed bankfull conditions and increases in Q contribute primarily to overbank flooding (*20*). We propose a set of parameters to examine the relations among hydrology, channel geometry, and bed-load transport for both bedrock and alluvial rivers, using a common framework: (i) the bankfull shear velocity, U_{*bf} (Fig. 1A); (ii) the distribution of floods, $f(U_* \geq U_{*c})$, characterized by the frequency-magnitude distribution of flows exceeding critical conditions (Fig. 2D); and (iii) the potential transport volume per unit width of bed load during a flood, T (Fig. 1B) (*23*). For bedrock-influenced rivers, the actual transport rate depends on the degree of alluvial cover and will be less than T, but T should nevertheless characterize the relative magnitude of different floods. We hypothesize that alluvial and bedrock-influenced gravel-bedded streams are near-threshold channels, and we predict that $U_{*bf}/U_{*c} \approx 1.1$ (*15*, *16*) and that peak sediment transport (T) occurs as a result of intermediate floods, not the largest floods (*14*).

We undertook a study of the Mameyes River in the Luquillo Critical Zone Observatory in northeastern Puerto Rico (Fig. 2A), which is subject to frequent large flash floods (*23*) due to orographic storms and hurricanes (*24*). We used tracer cobbles placed in a steep mixed bedrock-alluvial tributary ($S = 1.2 \times 10^{-1}$, $D = 120$ mm) and a lower-gradient alluvial reach ($S = 7.8 \times 10^{-3}$, $D = 110$ mm) to estimate U_{*c} for each site and to demonstrate that bed-load transport is proportional to T (*25*, *26*). Discharge records for the alluvial reach (Fig. 2A) show heavy-tailed (nonconvergent) scaling (Fig. 2C) (*27*). The data for the mixed bedrock-alluvial tributary are of insufficient duration for similar

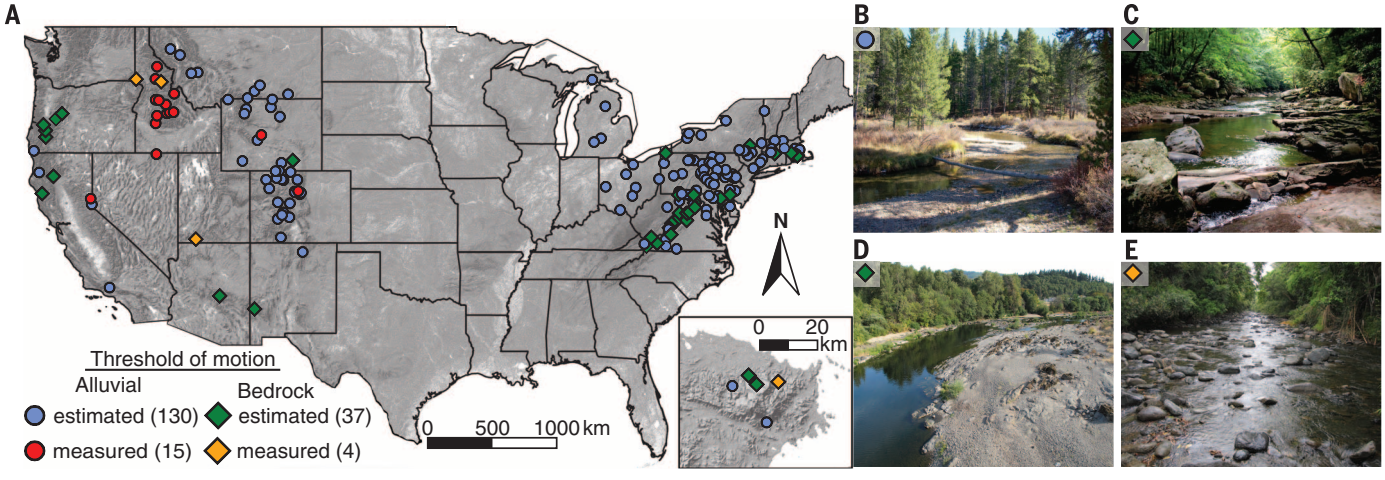


Fig. 3. Gaging stations used in this study. (**A**) Map of the continental United States and Puerto Rico (inset) with the locations of alluvial and bedrock-influenced stream gages used in this study (*26*), indicating where U_{*c} was measured or estimated. The easternmost gaging station in the map of Puerto Rico is the Mameyes River. (**B**) Halfmoon Creek ($S = 0.0084$, $D = 50$ mm), an alluvial-gravel river in the Colorado Rocky Mountains. (**C**) Bear Creek ($S = 0.021$, $D = 152$ mm), a bedrock-influenced river in Maryland. (**D**) Umpqua River ($S = 0.00067$, $D = 51$ mm), which drains a tectonically active region in the Oregon coastal and Cascade mountains. (**E**) Alluvial portion of the Mameyes River ($S = 0.013$, $D = 152$ mm). [Photo credits: D. N. Bradley (B), S. M. Baker and USGS (C), J. E. O'Connor (D)]

Downloaded from http://science.sciencemag.org/ on May 5, 2016

statistical analysis. Recorded peak discharges during flash floods can be up to 20 times the discharge associated with critical conditions (Q_c = 22 m^3 s^{-1}) (Fig. 2B). Although the threshold of motion is often exceeded more than 20 times per year (*28*, *29*), the associated shear velocity values for recorded floods are restricted to the range $U_{*c} \leq U_* \leq 2U_{*c}$ (Fig. 2B). Even the largest floods are near-threshold.

The frequency-magnitude scaling of U_* converges to an exponential function for above-critical values (Fig. 2D), and we computed $\langle f(U_* \geq U_{*c})\rangle / U_{*c}$ = 0.38 m s^{-1}/0.35 m s^{-1} = 1.1 (*23*), where the angle brackets denote the ensemble average value. The estimate for the channel-forming flood [$\langle f(U_* \geq U_{*c})\rangle$ = 0.38 m s^{-1}] is close to the bankfull shear velocity (U_{*bf} = 0.40 m s^{-1}) determined independently from morphologic surveys (*24*) of the channel (Fig. 1A); both are in agreement with near-threshold channel theory (*15*). As U_* approaches the maximum value, the tail decays faster than exponentially, indicating undersampling of the largest events (*27*, *28*). The probability density function (PDF) of T (Fig. 2D) possesses a peak, indicating the existence of a characteristic and moderate flood that transports the most sediment. Having shown that the hydrologic record of the mixed alluvial-bedrock Mameyes River displays near-critical behavior, we used measurements of channel geometry, slope, and grain size (fig. S1, A to E) (*23*) collected across bedrock and alluvial areas to test the generality of this result for the length of the river. Our calculations reveal that the ratio U_{*bf}/U_{*c} has no trend with downstream distance ($\langle U_{*bf}/U_{*c}\rangle$ = 1.3), despite substantial downstream decreases in channel slope and bedrock influence (fig. S1G), and indicates near-threshold transport throughout. Thus, an extreme distribution of discharge is not sufficient evidence to demonstrate control by infrequent, large flood events. The river's ability to adjust its width, depth, and grain size to near-critical conditions appears to decouple the distribution of U_* from the distribution of discharge imposed by climate. This critical filter confirms model predictions (*30*, *31*) that threshold sediment-transporting systems can shred external environmental signals.

We examined a wide range of gravel-bedded alluvial and bedrock-influenced streams located near U.S. Geological Survey (USGS) gages (*23*) across the United States (Fig. 3) to test the generality of the critical filter. The distributions of discharge [$f(Q \geq Q_c)$] vary widely among the rivers examined (Fig. 4A), as expected from previous research that indicates that this is predominantly an effect of spatial variation in climate (fig. S4) (*12*, *17*, *23*). In contrast, we can describe $f(U_* \geq U_{*c})$ with a global exponential function (Fig. 4B) (*23*). The average value for all streams is in agreement with near-threshold channel theory (*15*). Our data show that this characteristic flood magnitude is about equal to the morphologic U_{*bf} (Fig. 4C) (*23*), verifying the adjustment of both bedrock-influenced and alluvial rivers to the same near-critical conditions. The agreement is best for field sites where U_{*c} has been locally determined from observations (*23*), suggesting that much of the scatter in Fig. 4C is due to the notorious problem of estimation errors in determining the threshold of motion (*26*). We found a peak in T for all rivers that corresponds to moderate floods (Fig. 4C, inset), providing additional evidence that extreme events do not dominate channel form (fig. S7).

The rivers that we examined act as a filter, converting the wide range of climatically driven discharge distributions into a universal distribution of excess shear velocity. Flows greatly exceeding critical conditions cannot occur for long without leading to bank erosion, channel widening, and the restoration of flow conditions to near-critical (Fig. 1). This filtering is a logical consequence of the self-organization of rivers to a near-threshold channel geometry. We extend this reasoning beyond alluvial gravel-bedded rivers to bedrock-influenced rivers. The apparent generality of the critical filter calls into question the proposed links between extreme precipitation events, climate variability, and long-term river incision (*1*, *3*, *17*). Although large floods occur, they do not appear to control channel geometry for the rivers that we studied. An important caveat, however, is that we lack data for the steepest-slope rivers, where stream gages are rare, and for rapidly uplifting landscapes, where steep-walled gorges may violate our reported relations. The time scale of channel adjustment to external forcing is an important parameter, because this represents the time necessary to decouple $f(U_* \geq U_{*c})$ from discharge. Our results suggest that channel geometry has adjusted to the current hydrologic regime in almost all the rivers that we examined, even though some of these are influenced by bedrock. How, and for how long, this adjustment plays out is not well understood. Other studies have shown that alluvial (*29*) and bedrock (*32*) channels may respond to hydrologic perturbations on decadal time scales. Laboratory experiments (*33*, *34*) have demonstrated that coarse-grained bedrock channels may ultimately evolve their geometry and slope toward near-threshold transport conditions under an imposed sediment load. Although adjustments in the slope of natural rivers may take centuries to millions of years (*9*, *35*), our analysis indicates that channel geometry adjusts rapidly to accommodate bed-load transport under an imposed slope and grain size. Another possibility is that rivers with more resistant banks may sort sediment rapidly under an imposed channel geometry, so that the grain sizes remaining on the channel bottom are near-threshold for the bankfull flood. Both mechanisms of adjustment may be present within a single catchment (*32*). We suggest that landscape evolution models could

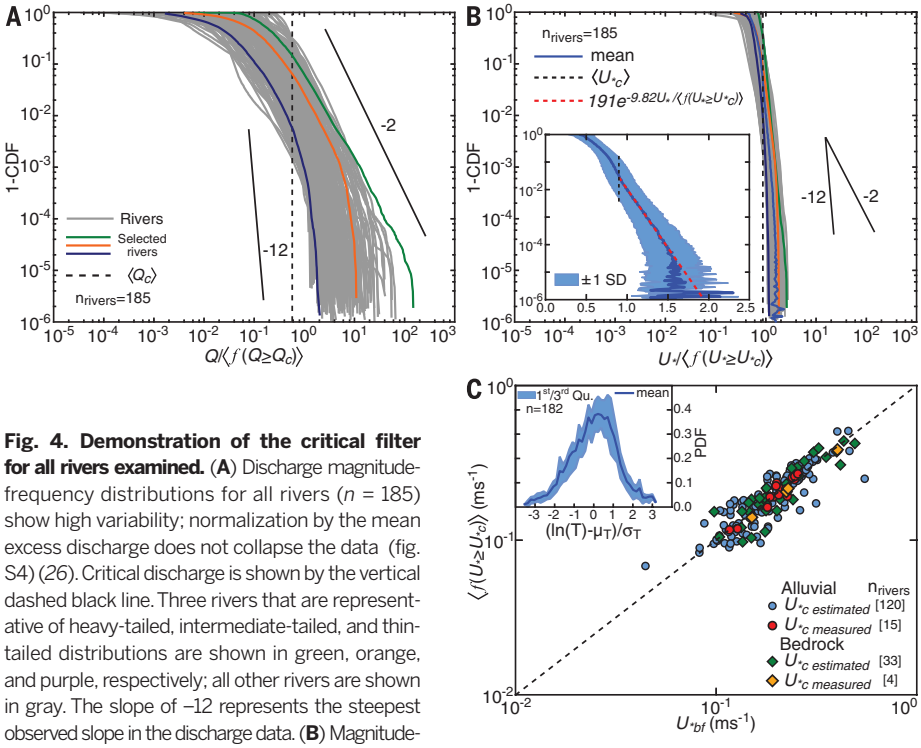


Fig. 4. Demonstration of the critical filter for all rivers examined. (**A**) Discharge magnitude-frequency distributions for all rivers (n = 185) show high variability; normalization by the mean excess discharge does not collapse the data (fig. S4) (*26*). Critical discharge is shown by the vertical dashed black line. Three rivers that are representative of heavy-tailed, intermediate-tailed, and thin-tailed distributions are shown in green, orange, and purple, respectively; all other rivers are shown in gray. The slope of –12 represents the steepest observed slope in the discharge data. (**B**) Magnitude-frequency distribution for $U_*/\langle f(U_* \geq U_{*c})\rangle$ for all stream gages, with same colors as (A); normalization by the mean reasonably collapses the data onto a single curve. The mean is indicated by the bold blue line. The inset shows the data on a semi-log plot, with light blue indicating ±1 SD. The dashed red line is an exponential fit to the mean for values of U_* greater than U_{*c} (dashed vertical black line). The tail decays faster than exponentially, indicating undersampling of the largest events (*27*, *28*). (**C**) Relation between $\langle f(U_* \geq U_{*c})\rangle$ and U_{*bf}, determined from independent surveys. The relation is strongest for rivers in which U_{*c} was measured. The inset shows the averaged distribution of T from all rivers, with light blue indicating the first and third quartiles (each river was standardized by using its mean μ and SD σ) (fig. S6). The peak indicates that moderate floods, and not extreme events, have sculpted the channels (fig. S7) (*26*).

Downloaded from http://science.sciencemag.org/ on May 5, 2016

implement a channel closure scheme by assuming $U_{*bf}/U_{*c} = 1.1$. In addition, a fixed-magnitude flood event with an intermittency factor (*36*) may be adequate for modeling the influence of climate on erosion over long time scales. Our results lend support to empirical studies that found that modest transport events perform the bulk of incision in bedrock-influenced rivers (*37*, *38*).

The critical filter that we have described here eliminates a substantial portion of the spectrum of environmental forcing, helping to explain how landscape patterns such as rivers remain stable in the face of highly stochastic driving. Channel adjustment decouples the sediment transport rate within a river from climatic influence. The delivery and removal of coarse sediment may determine the speed limit for river incision and landscape evolution (*8*), because bed-load transport remains near-threshold regardless of climate in bedrock-influenced and alluvial rivers.

REFERENCES AND NOTES

1. P. Molnar, *Annu. Rev. Earth Planet. Sci.* **32**, 67–89 (2004).
2. K. X. Whipple, *Annu. Rev. Earth Planet. Sci.* **32**, 151–185 (2004).
3. Z. Peizhen, P. Molnar, W. R. Downs, *Nature* **410**, 891–897 (2001).
4. D. W. Burbank *et al*., *Nature* **426**, 652–655 (2003).
5. K. X. Whipple, *Nat. Geosci.* **2**, 97–104 (2009).
6. K. L. Ferrier, K. L. Huppert, J. T. Perron, *Nature* **496**, 206–209 (2013).
7. B. J. Yanites, S. E. Kesler, *Nat. Geosci.* **8**, 462–465 (2015).
8. L. S. Sklar, W. E. Dietrich, *Geology* **29**, 1087–1090 (2001).
9. M. Attal, G. E. Tucker, A. C. Whittaker, P. A. Cowie, G. P. Roberts, *J. Geophys. Res.* **113**, F03013 (2008).
10. B. J. Yanites, G. E. Tucker, *J. Geophys. Res.* **115**, F04019 (2010).
11. G. E. Tucker, G. R. Hancock, *Earth Surf. Process. Landf.* **35**, 28–50 (2010).
12. D. Lague, N. Hovius, P. Davy, *J. Geophys. Res. Earth Surf.* **110**, (2005).
13. D. Lague, *Earth Surf. Process. Landf.* **39**, 38–61 (2014).
14. M. G. Wolman, J. P. Miller, *J. Geol.* **68**, 54–74 (1960).
15. G. Parker, P. R. Wilcock, C. Paola, W. E. Dietrich, J. Pitlick, *J. Geophys. Res.* **112**, F04005 (2007).
16. G. Parker, *J. Fluid Mech.* **89**, 127–146 (1978).
17. P. Molnar, R. S. Anderson, G. Kier, J. Rose, *J. Geophys. Res.* **111**, F02001 (2006).
18. R. A. DiBiase, K. X. Whipple, *J. Geophys. Res.* **116**, F04036 (2011).
19. D. L. Turcotte, L. Greene, *Stoch. Hydrol. Hydraul.* **7**, 33–40 (1993).
20. L. B. Leopold, M. G. Wolman, J. P. Miller, *Fluvial Processes in Geomorphology* (WH Freeman and Company, 1964).
21. D. R. Montgomery, K. B. Gran, *Water Resour. Res.* **37**, 1841–1846 (2001).
22. J. W. Kirchner, *Water Resour. Res.* **45**, W02429 (2009).
23. Materials and methods are available as supplementary materials on *Science* Online.
24. A. S. Pike, F. N. Scatena, E. E. Wohl, *Earth Surf. Process. Landf.* **35**, 1402–1417 (2010).
25. C. B. Phillips, R. L. Martin, D. J. Jerolmack, *Geophys. Res. Lett.* **40**, 1328–1333 (2013).
26. C. B. Phillips, D. J. Jerolmack, *Earth Surf. Dynam.* **2**, 513–530 (2014).
27. D. Sornette, *Critical Phenomena in Natural Sciences: Chaos, Fractals, Selforganization and Disorder: Concepts and Tools* (Springer, ed. 2, 2006).
28. D. J. Furbish, M. W. Schmeeckle, *Water Resour. Res.* **49**, 1537–1551 (2013).
29. L. J. Slater, M. B. Singer, *Geology* **41**, 595–598 (2013).
30. D. J. Jerolmack, C. Paola, *Geophys. Res. Lett.* **37**, L19401 (2010).
31. M. J. Van de Wiel, T. J. Coulthard, *Geology* **38**, 87–90 (2010).
32. J. P. L. Johnson, K. X. Whipple, L. S. Sklar, T. C. Hanks, *J. Geophys. Res.* **114**, F02014 (2009).
33. N. J. Finnegan, L. S. Sklar, T. K. Fuller, *J. Geophys. Res.* **112**, F03S11 (2007).
34. J. P. L. Johnson, K. X. Whipple, *J. Geophys. Res. Earth Surf.* **115**, (2010).
35. D. L. Egholm, M. F. Knudsen, M. Sandiford, *Nature* **498**, 475–478 (2013).
36. C. Paola, P. L. Heller, C. L. Angevine, *Basin Res.* **4**, 73–90 (1992).
37. K. Hartshorn, N. Hovius, W. B. Dade, R. L. Slingerland, *Science* **297**, 2036–2038 (2002).
38. J. R. Barbour *et al*., *Geophys. Res. Lett.* **36**, L04401 (2009).

ACKNOWLEDGMENTS

Research was supported by the NSF Luquillo Critical Zone Observatory (LCZO) (grant EAR-1331841 to D.J.J.), the NSF INSPIRE program (Integrated NSF Support Promoting Interdisciplinary Research and Education; grant EAR-1344280 to D.J.J.), and an NSF Postdoctoral Fellowship (grant EAR-1349776 to C.B.P.). We thank M. Brandon for encouraging this study; J. Willenbring, P. Wilcock, C. Paola, J. Kirchner, D. Furbish, and three anonymous reviewers for comments that improved this manuscript; and J. Buffington, W. Dietrich, G. Grant, J. O'Connor, A. Pike, J. Scheingross, M. Singer, L. Sklar, and J. Warrick for assistance in acquiring additional stream data. The authors declare that they have no competing financial interests. The data in this study are available from multiple sources: Field site data are compiled in table S1; all unprocessed stream gage data are freely available from the USGS National Water Information System; and lidar data are available from the LCZO. The Mameyes stream morphology and derived hydrograph data are available at https://figshare.com/authors/Colin_Phillips/644773.

SUPPLEMENTARY MATERIALS

www.sciencemag.org/content/352/6286/694/suppl/DC1
Materials and Methods
Figs. S1 to S7
Table S1
References (*39*–*91*)

29 August 2015; accepted 24 March 2016
10.1126/science.aad3348

POLYMER GROWTH

Uniform patchy and hollow rectangular platelet micelles from crystallizable polymer blends

Huibin Qiu,[1]*† Yang Gao,[1]* Charlotte E. Boott,[1]‡ Oliver E. C. Gould,[1]‡ Robert L. Harniman,[1]‡ Mervyn J. Miles,[2] Stephen E. D. Webb,[3] Mitchell A. Winnik,[4] Ian Manners[1]§

The preparation of colloidally stable, self-assembled materials with tailorable solid or hollow two-dimensional (2D) structures represents a major challenge. We describe the formation of uniform, monodisperse rectangular platelet micelles of controlled size by means of seeded-growth methods that involve the addition of blends of crystalline-coil block copolymers and the corresponding crystalline homopolymer to cylindrical micelle seeds. Sequential addition of different blends yields solid platelet block comicelles with concentric rectangular patches with distinct coronal chemistries. These complex nano-objects can be subject to spatially selective processing that allows their disassembly to form perforated platelets, such as well-defined hollow rectangular rings. The solid and hollow 2D micelles provide a tunable platform for further functionalization and potential for a variety of applications.

Nanoscale two-dimensional (2D) materials, typified by graphene and metal chalcogenide or clay nanosheets, are of broad utility. In principle, the solution self-assembly of block copolymers (BCPs) provides a convenient route to analogous planar nanostructures derived from soft matter (*1*, *2*). However, the formation of 2D platelet micelles is generally uncommon relative to other morphologies (*3*, *4*). Moreover, although considerable control has recently been achieved over the structures of 1D BCP micelles—in which fibers of tunable length and low dispersity (*5*, *6*) with periodic patches (*7*, *8*), block architectures (*9*), and amphiphilicity (*10*) are now accessible—progress with 2D assemblies is much more limited. Thus, the preparation of solid and hollow colloidally stable 2D micelles with similar fidelity and complexity remains a key challenge.

Self-assembly of BCPs with amorphous core-forming blocks in selective solvents provides a route to a diverse array of core-shell nanoparticles (micelles) with equilibrium or nonequilibrium morphologies of widespread utility (*3*, *4*). The most common morphologies formed are spheres, cylinders, and vesicles, and colloidal stability is provided by the presence of the solvent-swollen corona-forming block. The co-assembly or "blending" of different BCPs has recently been shown to provide a useful route to targeted conventional morphologies and also more complex nanostructures, such as disk-sphere or disk-cylinder hybrid micelles (*11*, *12*). As a result of their preference for the formation of rigid assemblies characterized by a core-corona interface with low mean curvature, BCPs with crystallizable core-forming blocks offer a promising route to planar

[1]School of Chemistry, University of Bristol, Bristol BS8 1TS, UK. [2]School of Physics, University of Bristol, Bristol BS8 1TL, UK. [3]Central Laser Facility, Science and Technology Facilities Council, Research Complex at Harwell, Rutherford Appleton Laboratory, Didcot OX11 0QX, UK. [4]Department of Chemistry, University of Toronto, Toronto, Ontario, M5S 3H6, Canada. *These authors contributed equally to this work. †Present address: School of Physical Science and Technology, ShanghaiTech University, Shanghai, 201210, China. ‡These authors contributed equally to this work. §Corresponding author. Email: ian.manners@bristol.ac.uk

Downloaded from http://science.sciencemag.org/ on May 5, 2016

micellar architectures (platelets) containing a core analogous to the well-studied but colloidally unstable 2D lamellar single crystals formed by the solution crystallization of homopolymers (*2*, *13*). Although platelet BCP micelles offer much promise as functional, colloidally stable 2D nano-objects, synthetic approaches that allow access to low dispersities, dimensional control, and spatial control of functionality are limited. Recent advances include the formation of platelets from end-functionalized, crystallizable linear polymers (*14*, *15*) or hyperbranched analogs (*16*), which permits programmed nanoparticle attachment and patterning, and the creation of 2D assemblies from homopolymer crystals consisting of alternate rings of BCP and homopolymer (*17*, *18*).

Lenticular platelet micelles can be formed via the growth of platelet-forming BCPs with a crystallizable poly(ferrocenyldimethylsilane) (PFS) core-forming block and a relatively short complementary corona-forming block (core:corona block ratio > 1:1) upon addition to a solution containing cylindrical micelle seeds (*19*). Quantitative experiments demonstrated that the area of the resulting lenticular platelet micelles showed a linear dependence on the unimer-to-seed ratio. The living nature of this crystallization-driven self-assembly (CDSA) process enabled the preparation of concentric lenticular platelet block comicelles with spatially segregated coronas through the sequential addition of PFS BCPs with different corona functionalities. However, the platelet formation was governed by a growth mechanism that gave the micelles a lenticular shape with irregular edges rather than a well-defined rectangular morphology (*19*). Moreover, as a direct result of the short coronal chain lengths for the BCPs used, the resulting platelets possess a low propensity for further processing. For example, poor colloidal stability above a size of ~1 μm leads to aggregation, and effective corona cross-linking (*20*) has not been possible.

In order to resolve these issues, we have explored the analogous seeded growth of blends of PFS BCPs possessing much longer solubilizing corona-forming blocks together with the corresponding crystalline PFS homopolymer. We studied the seeded growth of the blends of PFS-*b*-PDMS with a long corona-forming PDMS block (PDMS, polydimethylsiloxane) and PFS homopolymer in which the degrees of polymerization for the PFS block and homopolymer were relatively large (fig. S1A). Nonpolar hexane was chosen as a selective solvent for the hydrophobic PDMS block but also as an only moderately poor solvent for PFS, which would therefore be expected to prevent the rapid precipitation of the PFS homopolymer. A mixture of PFS_{49}-*b*-$PDMS_{504}$ (core:corona block ratio ~1:10; the subscripts refer to the number-average degree of polymerization) and PFS_{43} unimers in tetrahydrofuran (THF) was added to colloidal solutions of the PFS_{28}-*b*-$PDMS_{560}$ cylindrical micelle seeds [number-average length (L_n) = 50 nm – 5.00 μm; number-average core width (W_n) = 13 nm, by means of transmission electron microscopy (TEM)]. This led to growth only from the seed termini to yield dumbbell-like micelles with a cylindrical central segment derived from the original seed and two platelet-like or platelet-cylinder–like end segments arising from the blends for the cases of the 1:1 and 10:1 BCP:homopolymer mass ratios (mole ratio ~1:5 and ~2:1), respectively (fig. S2). In contrast, the use of blends with significantly shorter PFS blocks led to rectangular platelets that result from substantial growth from the seeds in both the terminal and lateral directions (figs. S3 and S4). Thus, when blends of PFS_{28}-*b*-$PDMS_{560}$ (block ratio 1:20) and PFS_{20} (1:1 mass ratio, mole ratio ~1:10) were added to the cylindrical PFS_{28}-*b*-$PDMS_{560}$ seeds, high–aspect ratio ribbon-like platelet micelles were formed with uniform but broadened PFS cores (W_n = ~50 nm versus 13 nm in the seed) (fig. S3). Moreover, the resulting micelles were of uniform size (A_w/A_n = 1.02 – 1.08; A_w and A_n are weight- and number-average area, respectively) and showed a linear dependence of area on the unimer-to-seed ratio consistent with a living CDSA process (fig. S3E).

To expand the generality of our approach to rectangular platelets that are dispersible in hydrophilic media, we also explored the self-assembly of the blends derived from PFS_{36}-*b*-$P2VP_{502}$ [block ratio 1:14; P2VP, poly(2-vinylpyridine)], a BCP with a polar corona-forming P2VP block, and PFS_{20} homopolymer. A mixture of hexane and isopropanol (iPrOH) was used to overcome the solubility issues (*10*, *21*), and living CDSA could therefore be achieved for cylindrical micelle seeds with either a hydrophobic-corona (derived from PFS-*b*-PDMS) or a polar-corona (from PFS-*b*-P2VP). With a PFS_{36}-*b*-$P2VP_{502}$–to-PFS_{20} mass ratio of ~1:1 (mole ratio ~1:13) (fig. S5), the living CDSA by using the same cylindrical PFS_{28}-*b*-$PDMS_{560}$ seeds in 1:3 (v/v) hexane/iPrOH (fig. S6) gave rise to low-dispersity platelet micelles (A_w/A_n < 1.01) with regular rectangular morphologies (Fig. 1). These rectangular platelets were formed rapidly (~5 min) (fig. S7) and were characterized by a dual-trapezoid sectorized texture emanating from the central seed, with a differential in contrast observed with TEM and of height with atomic force microscopy (AFM) analyses (~18 nm for the higher, more electron-dense

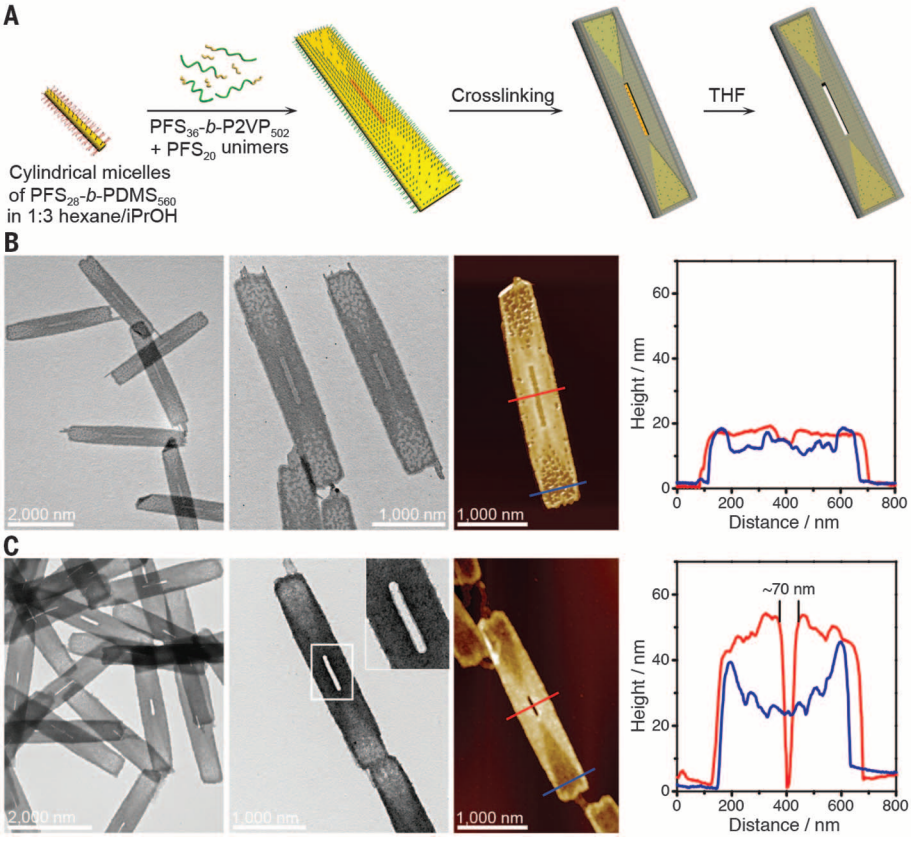


Fig. 1. Rectangular platelet micelles by living CDSA of PFS_{36}-*b*-$P2VP_{502}$/PFS_{20} blends. Low-dispersity rectangular platelet micelles can be formed by living CDSA of the PFS_{36}-*b*-$P2VP_{502}$/PFS_{20} blends initiated by the cylindrical micelle seeds of PFS_{28}-*b*-$PDMS_{560}$ in a mixture of hexane and iPrOH. (**A**) Schematic diagram illustrating this process. (**B**) TEM images and AFM height images and profiles of a representative sample of the rectangular platelet micelles formed by the addition of a mixture of the PFS_{36}-*b*-$P2VP_{502}$ and PFS_{20} unimers (1:1 mass ratio) in a small amount of THF to a solution of the PFS_{28}-*b*-$PDMS_{560}$ cylindrical micelle seeds (L_n = 590 nm) in a mixture of hexane and iPrOH (1:3, v/v) at 45°C. (**C**) Analogous images for perforated rectangular platelets formed after cross-linking the P2VP coronas via coordination of the pyridyl groups on P2VP to small Pt nanoparticles and subsequent redispersal in THF so as to remove the PFS_{28}-*b*-$PDMS_{560}$ cylindrical micelle seeds.

Downloaded from http://science.sciencemag.org/ on May 5, 2016

regions versus ~12 nm for the lower regions) (Fig. 1B). The TEM and AFM data suggest that the growth process leads to a higher density of BCP with P2VP coronal chains lateral to the seed and for homopolymer in the terminal regions. The length, width, area, and aspect ratio of these platelets could be precisely controlled by the unimer-to-seed ratio and the length of the cylindrical micelle seeds (fig. S8). Giant rectangular platelets with dimensions of 60 by 10 μm (fig. S9) could be created without any obvious defects by using a slow-growth process in a mixture of hexane and methanol (1:3, v/v) and nevertheless retained their high colloidal stability. We attributed this to the relatively high-volume fraction of the corona-forming block [core:corona ratio ~3:5 versus >1:1 for the lenticular platelet-forming PFS BCPs used in (*19*)]

To explore the location of the P2VP corona-forming block in the rectangular platelets, corona cross-linking was achieved via coordination of the pyridyl groups on P2VP with small (diameter ~2 nm) platinum (Pt) nanoparticles (NPs) (*22*). After redispersal for 24 hours in THF (a good solvent for both PFS and P2VP), the rectangular platelets retained their integrity, except for a perforated channel in the center that corresponded to the previous location of the uncross-linked seed (Fig. 1C and fig. S10). The dual-trapezoid sectorized texture became more apparent through TEM after corona cross-linking as a result of the increase in electron density contrast owing to the presence of Pt NPs [identified by means of energy-dispersive x-ray (EDX) spectroscopy] (fig. S11). Moreover, AFM demonstrated that relative to the corresponding values before cross-linking (Fig. 1B), the height of the central region at the side of the channel and also the platelet edges was increased by ~30 nm, compared with ~5 nm near the platelet ends (Fig. 1C). This is consistent with the presence of a higher density of incorporated Pt NPs in the former regions owing to a higher concentration of P2VP corona chains. These results therefore also indicate that although P2VP corona chains are distributed over the whole rectangular platelet, their concentration is significantly higher in the central regions lateral to the seed. The seeded assembly of the BCP-homopolymer blend to form uniform rectangular platelets therefore appears to be a cooperative growth process because, in the absence of seeds, irregular platelets or other morphologies were formed (fig. S5). Moreover, monitoring of the growth process demonstrated that the mechanism of formation differs from that for lenticular platelet micelles for which only a BCP is added to the seed. Thus, the rectangular platelets form through simultaneous growth in both the terminal and lateral directions relative to the seed (fig. S7), whereas in the lenticular case, growth proceeds initially from the ends of the cylindrical micelle seed termini followed by a gradual enveloping process (*19*).

The difference in micellar morphology formed by the seeded growth of PFS_{28}-*b*-$PDMS_{560}$/PFS_{20} blends in hexane (higher aspect ratio, ribbon-like) and the PFS_{36}-*b*-$P2VP_{502}$/PFS_{20} blends in 1:3 hexane/iPrOH (lower aspect ratio, rectangular) indicated a substantial influence of the coronal chemistry and/or solvent composition on the living CDSA process. Indeed, the formation of rectangular platelets by the PFS_{36}-*b*-$P2VP_{502}$/PFS_{20} blends was favored in iPrOH-dominated hexane/iPrOH mixtures but not in hexane-dominated systems (fig. S6A). For the PFS_{28}-*b*-$PDMS_{560}$/PFS_{20} blends, the resulting micellar morphology changed from ribbon-like platelets for hexane:iPrOH > 1:1 (v/v) to rectangular platelets at hexane:iPrOH < 1:2 (v/v) (fig. S6B). These studies indicate that the use of relatively short crystallizable segments in the BCP/homopolymer blends and a careful choice of solvent composition should permit the formation of rectangular platelets from BCPs with a broad range of corona chemistries.

We targeted patchy rectangular platelet multiblock comicelles by the seeded growth of sequentially added PFS_{28}-*b*-$PDMS_{560}$/PFS_{20} and PFS_{36}-*b*-$P2VP_{502}$/PFS_{20} blends (fig. S1B). For example, concentric rectangular platelet triblock comicelles were prepared by the addition of the PFS_{28}-*b*-$PDMS_{560}$/PFS_{20} (1:1 mass ratio) blend unimers in THF to a solution of the rectangular platelets derived from the PFS_{36}-*b*-$P2VP_{502}$/PFS_{20} blends, followed by a further addition of the PFS_{36}-*b*-$P2VP_{502}$/PFS_{20} (1:1 mass ratio) blend unimers in THF after 10 min (Fig. 2A). TEM and AFM analyses indicated that the P2VP corona regions were darker (more electron-rich) and of greater height than the PDMS corona regions (Fig. 2B), favoring an easy identification of the segmented structures. The dimensions of the P2VP- and PDMS-corona

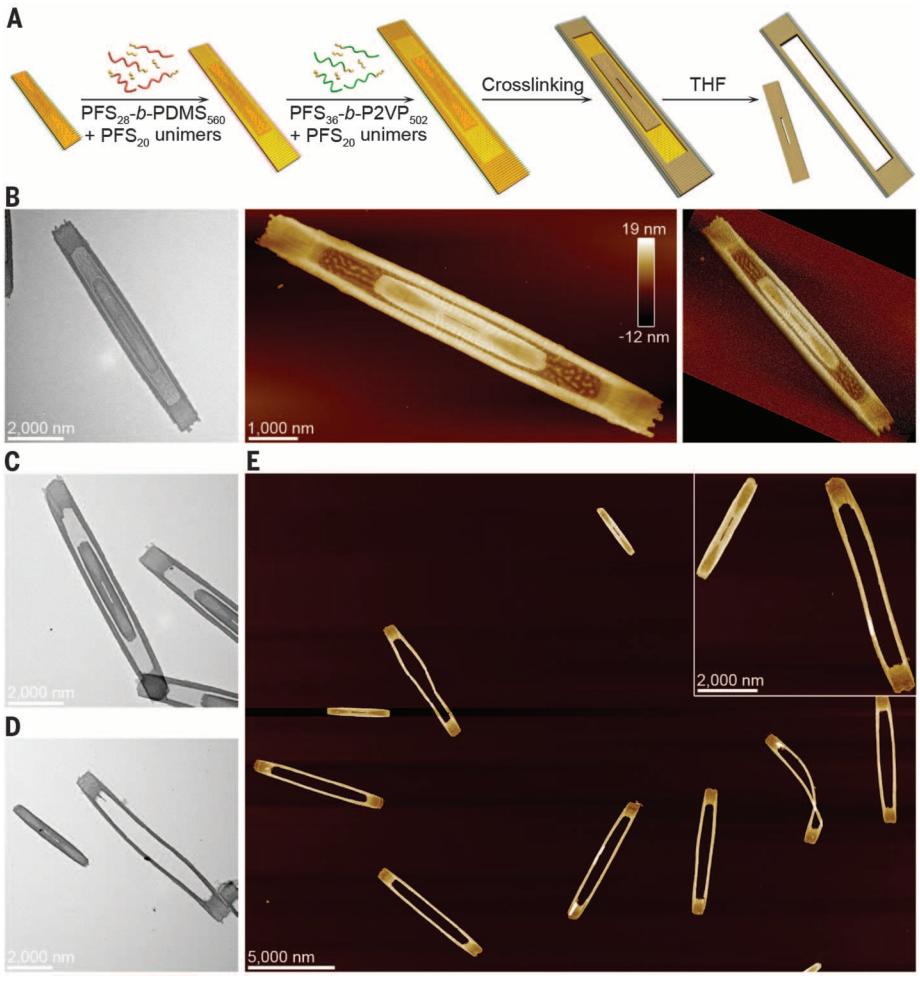


Fig. 2. Patchy and hollow rectangular platelet micelles. Concentric rectangular platelet block comicelles can be prepared through the sequential, alternate addition of PFS_{36}-*b*-$P2VP_{502}$/PFS_{20} and PFS_{28}-*b*-$PDMS_{560}$/PFS_{20} blend unimers. (**A**) Schematic diagram illustrating this process. (**B**) TEM, AFM height, and AFM 3D images of triblock comicelles formed through the sequential addition of the PFS_{36}-*b*-$P2VP_{502}$/PFS_{20}, PFS_{28}-*b*-$PDMS_{560}$/PFS_{20}, and PFS_{36}-*b*-$P2VP_{502}$/PFS_{20} blend unimers (BCP:homopolymer = 1:1 mass ratio) to a solution of the PFS_{28}-*b*-$PDMS_{560}$ cylindrical micelle seeds (L_n = 810 nm) in a mixture of hexane and iPrOH (1:3, v/v) at 45°C. Because P2VP has a higher glass transition temperature (T_g) and a larger volume repeat unit than that of PDMS, for similar degrees of polymerization the P2VP regions are higher in AFM height images and, because the path length is longer for electrons, darker with TEM. (**C**) TEM image of rectangular platelets after cross-linking of the P2VP coronas. (**D** and **E**) TEM and AFM height images of a mixture of perforated rectangular platelets and well-defined hollow rectangular rings formed after redispersal in THF.

Downloaded from http://science.sciencemag.org/ on May 5, 2016

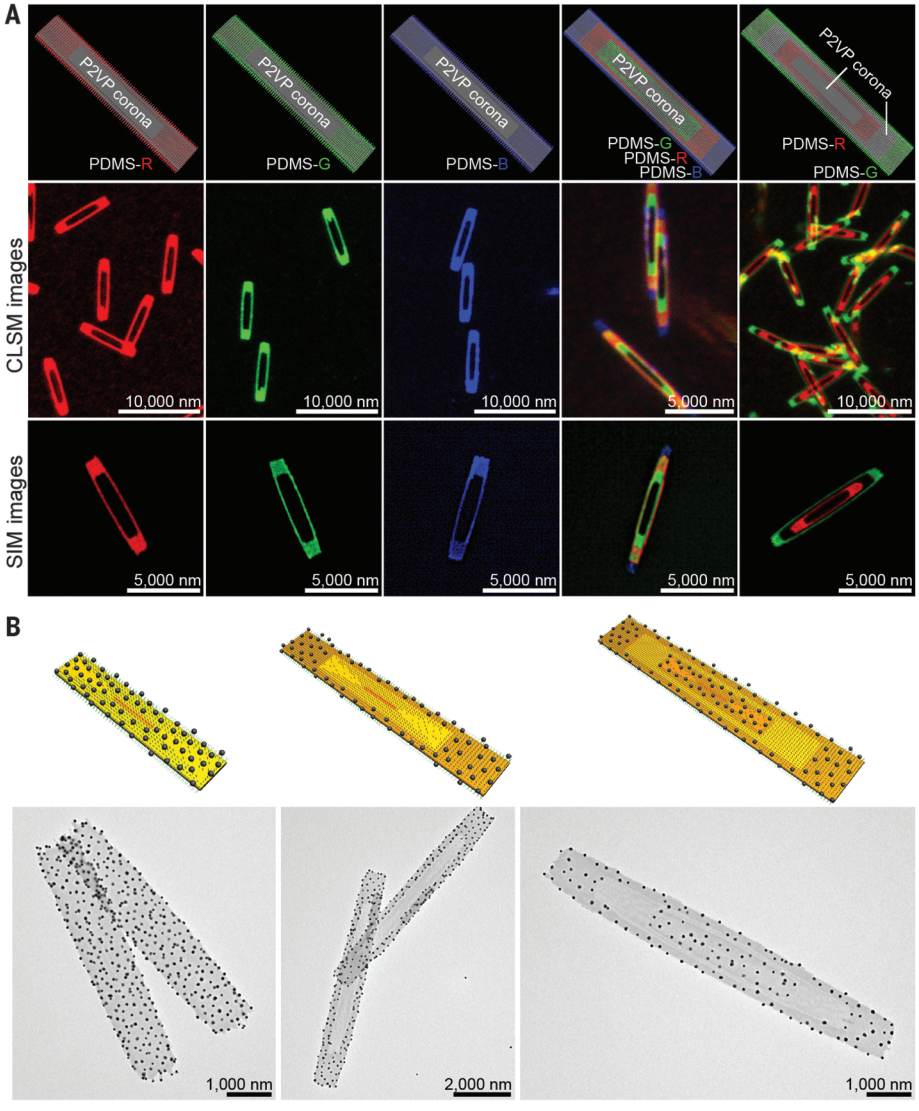


Fig. 3. Spatially selective functionalization of rectangular platelets. The coronas of the rectangular platelet micelles and block comicelles can be selectively functionalized by using a series of fluorescent PFS BCPs or via association with nanoparticles. (**A**) Schematic representations and CLSM and SIM images of typical rectangular platelet block comicelles, with segregated regions composed of nonfluorescent P2VP coronas and multiple dye-functionalized fluorescent PDMS coronas. The PDMS coronas with red, green, and blue fluorescence are denoted as PDMS-R, PDMS-G, and PDMS-B, respectively. For the images in column 4, the rapid photobleaching of the blue dye required the use of low-excitation laser power and rapid scans that substantially limited resolution. (**B**) Schematic representations and TEM images of rectangular platelet micelles and block comicelles, with silica nanoparticles selectively deposited on the P2VP coronas.

regions were precisely controllable by the amount of the respective blend added.

Although self-assembled hollow structures such as nanotubes (*23*), toroids (*24*), dynamic tubules (*25*), and nanocapsules (*26*) are of intense interest, well-defined and monodisperse rectangular 2D structures are unknown. On the basis of the triblock platelet comicelle structure, we envisaged that cross-linking of the P2VP coronas followed by the addition of a good solvent for the PFS core and coronas should lead to disassembly in order to generate a perforated architecture. The P2VP coronas were once again heavily cross-linked via coordination with Pt nanoparticles (Fig. 2C) (*22*), and subsequent redispersal in THF led to the formation of a mixture of perforated rectangular platelets and well-defined hollow rectangular rings with relatively broader ends and narrower rims along the long axis (Fig. 2, D and E, and fig. S11). Similarly, the concentric rectangular platelet diblock comicelle precursors were prepared via the sequential addition of the PFS_{28}-*b*-$PDMS_{560}$/PFS_{20} and PFS_{36}-*b*-$P2VP_{502}$/PFS_{20} blends in THF to a solution of the PFS_{28}-*b*-$PDMS_{560}$ cylindrical micelle seeds, and pure ring-like structures were obtained after shell cross-linking and redispersal in THF (fig. S12). The size, aspect ratio, and rim thickness of the rectangular rings can be readily tailored by the seed length and the unimer-to-seed ratio applied to each unimer addition (fig. S12C). The excellent dimensional stability and sharp edges of the hollow rectangular rings are attributed to the high cross-linking density present. The living nature of this CDSA process also allowed the formation of more complex multiblock comicelles (for example, heptablock comicelles) (fig. S13A) by use of further steps involving dissolved blends. Moreover, with the additional use of the PFS_{36}-*b*-$PnBMA_{756}$/PFS_{20} [PnBMA, poly(*n*-butylmethacrylate)] blends, rectangular platelet block comicelles with even more complex and tunable segmented 2D structures were also fabricated (fig. S13B).

The rectangular platelet micelles and block comicelles offer a tunable 2D platform for the fabrication of functional materials. For a proof-of-concept demonstration, we synthesized a series of fluorescent PFS-*b*-PDMS BCPs—namely, PFS_{29}-*b*-($PDMS_{652}$-*r*-R_{19}), PFS_{29}-*b*-($PDMS_{652}$-*r*-G_{19}), and PFS_{29}-*b*-($PDMS_{652}$-*r*-B_{19})—in which the PDMS block was functionalized with red (R), green (G), and blue (B) dyes, respectively (*27*). Living CDSA of their blends with PFS_{20} homopolymer, together with the nonfluorescent PFS_{36}-*b*-$P2VP_{502}$/PFS_{20} blends, yielded fluorescent concentric rectangular platelet block comicelles with multiple and variable fluorescence for the selected segments, as confirmed with confocal laser scanning microscopy (CLSM) and structured illumination microscopy (SIM) analyses (Fig. 3A). Further functionalization was also feasible by using the spatially defined coronal chemistries. For example, silica nanoparticles (average diameter 70 nm) could be selectively deposited onto the P2VP coronas as a result of the hydrogen bonding (*28*), allowing the controlled patterning in the form of solid rectangles and/or rings (Fig. 3B).

We demonstrate a versatile method for the formation of well-defined, low-dispersity rectangular platelet micelles with tunable dimensions based on a new conceptual approach that involves seeded growth of crystallizable polymer blends of BCPs and homopolymers. Multiblock platelet comicelles are accessible with the sequential addition of different blends, and cross-linking/dissolution strategies allow the formation of well-defined hollow rectangular micelles. The resulting solid and hollow platelets exhibit excellent colloidal stability, owing to the substantial volume fraction of coronal chains, and are sufficiently robust to be manipulated in solution, including with optical tweezers (fig. S14). The introduction of diverse functions can be envisaged by the use of various other polymers, such as π-conjugated materials as the crystallizable component (*29*–*31*), and also by means of facile coronal functionalization. Moreover, the segmented planar solid and hollow 2D structures open possible avenues to customizable platforms for future applications in fluorescent imaging, sensing, electronics, and catalysis and as liquid crystals, motile nano/micro machines, or therapeutic carriers.

Downloaded from http://science.sciencemag.org/ on May 5, 2016

REFERENCES AND NOTES

1. X. Zhuang, Y. Mai, D. Wu, F. Zhang, X. Feng, *Adv. Mater.* **27**, 403–427 (2015).
2. C. E. Boott, A. Nazemi, I. Manners, *Angew. Chem. Int. Ed. Engl.* **54**, 13876–13894 (2015).
3. Y. Mai, A. Eisenberg, *Chem. Soc. Rev.* **41**, 5969–5985 (2012).
4. F. H. Schacher, P. A. Rupar, I. Manners, *Angew. Chem. Int. Ed. Engl.* **51**, 7898–7921 (2012).
5. X. Wang *et al.*, *Science* **317**, 644–647 (2007).
6. J. B. Gilroy *et al.*, *Nat. Chem.* **2**, 566–570 (2010).
7. H. Cui, Z. Chen, S. Zhong, K. L. Wooley, D. J. Pochan, *Science* **317**, 647–650 (2007).
8. A. H. Gröschel *et al.*, *Nature* **503**, 247–251 (2013).
9. T. Gädt, N. S. Ieong, G. Cambridge, M. A. Winnik, I. Manners, *Nat. Mater.* **8**, 144–150 (2009).
10. H. Qiu, Z. M. Hudson, M. A. Winnik, I. Manners, *Science* **347**, 1329–1332 (2015).
11. J. Zhu *et al.*, *Nat. Commun.* **4**, 2297 (2013).
12. D. B. Wright *et al.*, *Macromolecules* **48**, 6516–6522 (2015).
13. G. Rizis, T. G. M. van de Ven, A. Eisenberg, *Angew. Chem. Int. Ed. Engl.* **53**, 9000–9003 (2014).
14. B. Li, C. Y. Li, *J. Am. Chem. Soc.* **129**, 12–13 (2007).
15. B. Dong, T. Zhou, H. Zhang, C. Y. Li, *ACS Nano* **7**, 5192–5198 (2013).
16. B. Yu, X. Jiang, J. Yin, *Macromolecules* **47**, 4761–4768 (2014).
17. W. Y. Chen *et al.*, *Macromolecules* **37**, 5292–5299 (2004).
18. J. X. Zheng *et al.*, *Macromolecules* **39**, 641–650 (2006).
19. Z. M. Hudson *et al.*, *Nat. Chem.* **6**, 893–898 (2014).
20. R. K. O'Reilly, C. J. Hawker, K. L. Wooley, *Chem. Soc. Rev.* **35**, 1068–1083 (2006).
21. P. A. Rupar, L. Chabanne, M. A. Winnik, I. Manners, *Science* **337**, 559–562 (2012).
22. H. Qiu, V. A. Du, M. A. Winnik, I. Manners, *J. Am. Chem. Soc.* **135**, 17739–17742 (2013).
23. J. P. Hill *et al.*, *Science* **304**, 1481–1483 (2004).
24. D. J. Pochan *et al.*, *Science* **306**, 94–97 (2004).
25. Z. Huang *et al.*, *Science* **337**, 1521–1526 (2012).
26. K. Baek, I. Hwang, I. Roy, D. Shetty, K. Kim, *Acc. Chem. Res.* **48**, 2221–2229 (2015).
27. Z. M. Hudson, D. J. Lunn, M. A. Winnik, I. Manners, *Nat. Commun.* **5**, 3372 (2014).
28. L. Jia *et al.*, *Nat. Commun.* **5**, 3882 (2014).
29. J. Qian *et al.*, *J. Am. Chem. Soc.* **136**, 4121–4124 (2014).
30. J. Schmelz, A. E. Schedl, C. Steinlein, I. Manners, H. Schmalz, *J. Am. Chem. Soc.* **134**, 14217–14225 (2012).
31. L. Sun *et al.*, *Nat. Commun.* **5**, 5746 (2014).

ACKNOWLEDGMENTS

H.Q. acknowledges a European Union Marie Curie Postdoctoral Fellowship. H.Q and Y.G. thank the European Research Council for support, and I.M. acknowledges an Advanced Investigator Grant. C.E.B. thanks the Engineering and Physical Sciences Research Council (EPSRC)–funded Bristol Chemical Synthesis Centre for Doctoral Training, O.E.C.G. thanks the EPSRC-funded Bristol Center for Functional Nanomaterials, and M.A.W. thanks the Natural Sciences and Engineering Research Council of Canada. For assistance, the authors thank V. A. Du (polymer synthesis) and J. A. Jones of the Electron Microscopy Unit (School of Chemistry, TEM) and Wolfson Bioimaging Facility (CLSM) at Bristol. PeakForce AFM was carried out in the Chemical Imaging Facility at Bristol, and SIM imaging was performed at Harwell, using equipment funded by EPSRC and the Medical Research Council, respectively. H.Q. and I.M. conceived the project. H.Q. and Y.G. performed the self-assembly experiments. C.E.B. synthesized the fluorescent polymers. H.Q., C.E.B., and S.E.D.W. performed the CLSM and SIM imaging, and H.Q. and R.L.H. performed the AFM analysis. O.E.C.G. performed the manipulation experiments using optical tweezers and the corresponding analyses. H.Q. and I.M. prepared the manuscript with input from all the other authors. The project was supervised by I.M.

SUPPLEMENTARY MATERIALS

www.sciencemag.org/content/352/6286/697/suppl/DC1
Materials and Methods
Figs. S1 to S14
References (*32*–*39*)

26 November 2015; accepted 17 March 2016
10.1126/science.aad9521

GEOPHYSICS

Slow slip near the trench at the Hikurangi subduction zone, New Zealand

Laura M. Wallace,[1]* Spahr C. Webb,[2] Yoshihiro Ito,[3] Kimihiro Mochizuki,[4] Ryota Hino,[5] Stuart Henrys,[6] Susan Y. Schwartz,[7] Anne F. Sheehan[8]

The range of fault slip behaviors near the trench at subduction plate boundaries is critical to know, as this is where the world's largest, most damaging tsunamis are generated. Our knowledge of these behaviors has remained largely incomplete, partially due to the challenging nature of crustal deformation measurements at offshore plate boundaries. Here we present detailed seafloor deformation observations made during an offshore slow-slip event (SSE) in September and October 2014, using a network of absolute pressure gauges deployed at the Hikurangi subduction margin offshore New Zealand. These data show the distribution of vertical seafloor deformation during the SSE and reveal direct evidence for SSEs occurring close to the trench (within 2 kilometers of the seafloor), where very low temperatures and pressures exist.

Over the past 10 to 15 years, the increased availability of continuously operating Global Positioning System (cGPS) networks has revolutionized our ability to investigate spatiotemporal variations in tectonic deformation processes. These networks have enabled the discovery of slow-slip events (SSEs) at many of the world's subduction plate boundaries. SSEs are similar to earthquakes, as they involve rapid slip along a fault at rates faster than typical plate motion. However, unlike an earthquake, slip in a SSE takes place over weeks to years rather than seconds. The discovery of SSEs has revealed a much richer diversity of fault slip behavior at subduction zones than was originally thought to occur (*1*–*4*). In some cases, SSEs are observed to have a close temporal and spatial relation to damaging megathrust earthquakes (*5*–*9*).

To date, most detailed studies of crustal deformation in SSEs have focused on events occurring at 20 to 40 km depth, where they are typically observed by land-based geodetic networks (*1*, *2*, *10*–*12*). Although recent studies suggest that SSEs occur on the shallow portion of many offshore plate boundaries (<15 km depth) (*13*–*19*), detailed investigation of deformation during these shallow SSEs has been hampered by a lack of suitable seafloor geodetic methods (*20*). Delineating the trenchward extent and spatial distribution of SSEs on the shallow megathrust is critical for understanding the range of physical conditions that are conducive to slow-slip behavior. Moreover, the unexpectedly large (>50 m) coseismic slip observed near the trench in the 2011 moment magnitude (M_w) 9.0 Tohoku-Oki earthquake and tsunami (*21*, *22*) underscores the need to comprehend the spectrum of fault slip behavior occurring on the shallowest portion of the subduction megathrust, where tsunamigenic earthquakes occur.

One promising tool that can be used to investigate vertical deformation of the seafloor during transient deformation events is the absolute pressure gauge (APG) (*6*, *20*, *23*–*25*). APGs can be deployed on the seafloor and will continuously record changes in pressure exerted on the seafloor by the overlying water column. If the seafloor rises vertically during a SSE, this will be recorded as a pressure decrease (decreasing water depth); downward movement of the seafloor will be recorded as a pressure increase (increasing water depth). APGs have documented large vertical deformation (tens of centimeters to meters) during volcanic unrest events at Axial Seamount (*24*). Two previous studies have shown likely vertical deformation due to slow slip at subduction zones offshore Costa Rica (*25*) and Japan (*6*), although these studies were based on data from only a few (two to four) APGs, making it impossible to define the spatial distribution of offshore deformation and slow slip. The Costa Rica study (*25*) shows the first convincing evidence for slow slip near the trench, based on formation and seafloor pressure-change data from two Integrated Ocean Drilling Program borehole observatories near the Middle America Trench just after periods of tremor and slow slip observed at onshore cGPS sites. Here, we present the first-ever detailed investigation of seafloor deformation above a shallow subduction interface SSE, using a network of APGs at the Hikurangi subduction zone offshore New Zealand (Fig. 1).

The Pacific Plate subducts westward beneath the eastern North Island of New Zealand along

[1]University of Texas Institute for Geophysics (UTIG), Austin, TX 78758, USA. [2]Lamont-Doherty Earth Observatory (LDEO), Columbia University, Palisades, NY 10964, USA. [3]Disaster Prevention Research Institute, Kyoto University, Kyoto, Japan. [4]Earthquake Research Institute, University of Tokyo, Tokyo, Japan. [5]Department of Geophysics, Tohoku University, Sendai, Japan. [6]GNS Science, Lower Hutt, New Zealand. [7]Department of Earth and Planetary Sciences, University of California–Santa Cruz, Santa Cruz, CA 95064, USA. [8]Cooperative Institute for Research in Environmental Sciences, University of Colorado–Boulder, Boulder, CO 80309, USA.
***Corresponding author. Email: lwallace@utexas.edu**

Downloaded from http://science.sciencemag.org/ on May 5, 2016

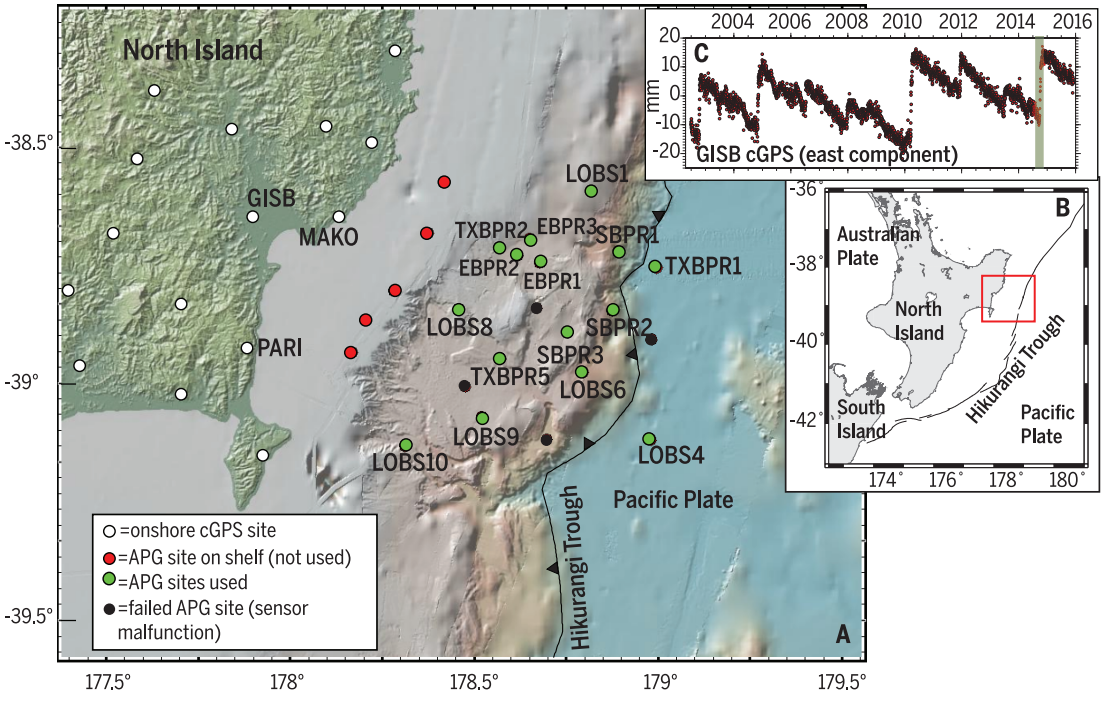


Fig. 1. Tectonic setting and HOBITSS network. (**A**) Tectonic setting of the northern Hikurangi margin and distribution of HOBITSS APG sites and the onshore continuous GPS network (www.geonet.org.nz). We used sites TXBPR1 and LOBS4 on the subducting Pacific Plate as references to remove oceanographic noise from the remaining network. The GPS sites we discuss in the text (GISB, MAKO, and PARI) are shown here, as are the APGs (Fig. 2). (**B**) Regional map of New Zealand. The red square indicates the location of (A). (**C**) East component of cGPS time series from GISB. Eastward (positive) jumps denote SSEs. The shaded green bar highlights the SSE from September and October 2014.

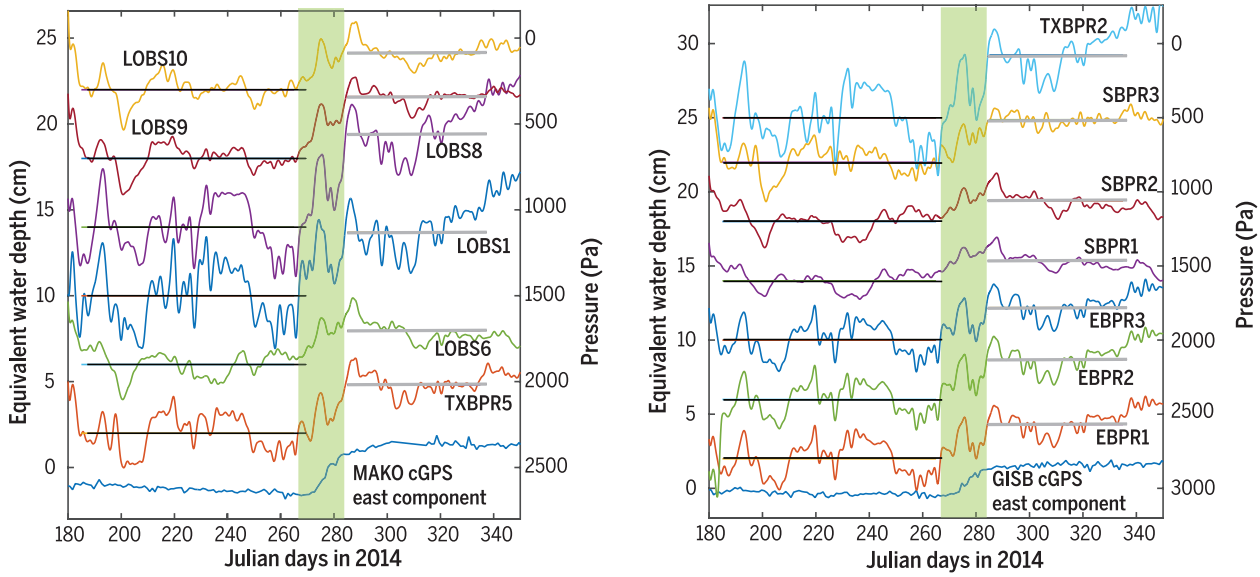


Fig. 2. cGPS (GISB and MAKO) and APG time series. The shaded green bar highlights the 2- to 3-week SSE that occurred in September and October 2014. We show APG time series in terms of pressure (Pascal) and equivalent water depth (centimeters). The values for each sensor are offset to separate each time series on the plot. We determined average seafloor pressure and equivalent water depth at each site for 3 months before the SSE (black lines) and 2 months after the SSE (gray lines). See Fig. 1 for site locations.

the Hikurangi Trough at 3 to 6 cm per year (*26*). SSEs at the northern Hikurangi margin occur offshore Gisborne, New Zealand, every 18 to 24 months (Fig. 1). These SSEs typically involve 1 to 3 cm of horizontal surface displacement at cGPS sites along the east coast over 1 to 2 weeks (*10*, *15*) and are expected to cause much larger displacements offshore. The frequent recurrence, short duration (<2 to 4 weeks), and large deformation signals make the offshore northern Hikurangi margin an ideal location to test the use of APGs to discern deformation of the seafloor during SSEs. To this end, the Hikurangi Ocean Bottom Investigation of Tremor and Slow Slip (HOBITSS) experiment began in May of 2014; this experiment involved deployment of 24 APGs and 15 ocean bottom seismometers directly above the shallow north Hikurangi SSEs. The instruments were in place

Downloaded from http://science.sciencemag.org/ on May 5, 2016

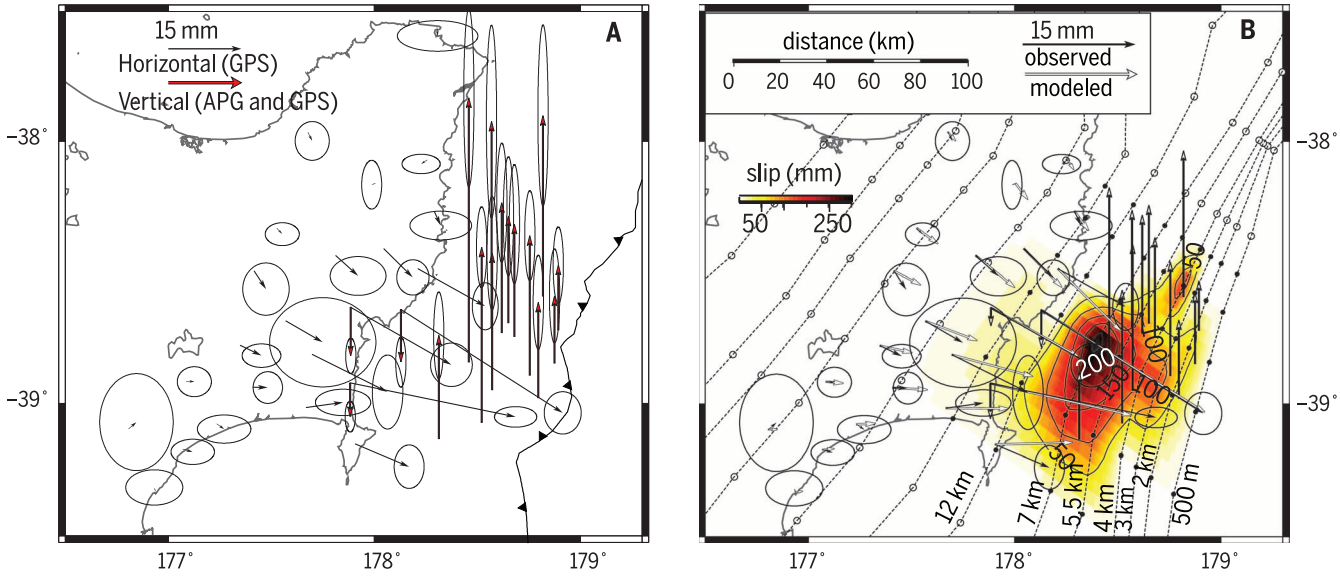


Fig. 3. Summary of surface displacements and slip inversion results for the SSE that occurred in September and October 2014. (**A**) Horizontal (black arrows; cGPS) and vertical displacements (red arrows; cGPS and offshore APGs) during the SSE of September and October 2014. The scale is the same for the horizontal and vertical displacements (scale bar in upper left). The deformation front is the same as in Fig. 1. (**B**) Inversion for slow slip from onshore and offshore surface displacements (*27*). The slip distribution on the interface is represented by a color gradient (see scale) and contours (labeled in millimeters). The dashed lines show the depth contours (kilometers) to the subduction interface. Note the slightly simplified deformation front used for modeling purposes.

for the duration of a large SSE that occurred beneath the HOBITSS network in September and October 2014 (Fig. 1); they were recovered in June 2015.

Seafloor pressure changes from oceanographic signals—particularly tides and eddies—are large. The largest (1 to 2 m) diurnal and semidiurnal tidal signals are easily removed by low-pass filtering the data. The eddies offshore of the Hikurangi coast produce pressure variations that vary over spatial scales of roughly 100 km (*27*) and thus produce pressure signals that are similar over most of the HOBITTS network. This enables the use of sites on the subducting plate (where vertical deformation during SSEs will be negligible) as reference sites to remove the oceanographic noise that is common across the array. Long-term instrumental drift of the pressure gauges can also be substantial (typically several centimeters per year) (*23*), although the short duration (<2 weeks) of the North Hikurangi SSEs makes instrument drift less problematic. Our processing of the APG data to remove oceanographic noise and instrument drift is relatively simple (*28*) and occurs in three stages: (i) We average the values from two reference sites (LOBS-4 and TXBPR-1) on the subducting plate and subtract this from the rest of the sites in the network. (ii) To remove instrument drift, we detrend the pressure time series using the 3-month period before the SSE. (iii) We apply a low-pass filter (2-day corner) to remove tidal and higher-frequency noise. Overall, we used pressure records from 13 of the 21 APG sites located on the upper plate to define the distribution of vertical deformation during the event. Five of the eight sites that we did not use were located in shallow water (less than 85 m depth), where

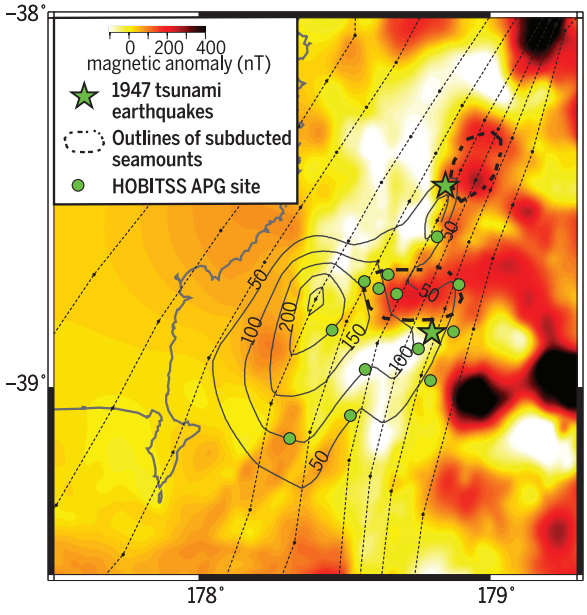


Fig. 4. Slow slip and magnetic anomalies. Magnetic anomalies (*38*) are shown overlain with the contours of the SSE from September and October 2014 (gray, labeled in millimeters) (Fig. 3B), the outlines of subducted seamounts (thick dashed lines), and the epicenters (green stars) of two tsunami earthquakes in March and May 1947 (*39*). The magnetic anomaly highs east of the trench coincide with known seamounts, whereas highs west of the trench are assumed to be subducted seamounts, which are also imaged in seismic reflection data (*29*).

near-coastal oceanographic signals made pressure records too noisy to reliably extract pressure changes due to a few centimeters of vertical deformation by using only deep water reference sites (green dots in Fig. 1). APGs at three of the upper-plate sites (black dots in Fig. 1) malfunctioned before the September SSE and thus did not produce usable data.

We observed a pressure decrease of 150 to 540 Pa (equivalent to a decrease in water depth of 1.5 to 5.4 cm) at all of the upper-plate HOBITSS APG sites during the large SSE observed on nearby cGPS sites in late September and early October 2014 (Fig. 2), reflecting uplift of the upper plate above the SSE source. The temporal evolution of the pressure changes in the offshore APG time series closely tracks that of the horizontal displacements observed in the cGPS time series at nearby sites GISB and MAKO, further confirming that the pressure changes we observe in the APG data are due to vertical displacement of the seafloor during the SSE (Fig. 2). The APG time series indicates the possibility that the seafloor pressure changes begin several days before large cGPS displacements, which suggests that the SSE may have begun on the shallow interface and propagated downdip with time. To calculate the vertical displacements during the SSE, we

Downloaded from http://science.sciencemag.org/ on May 5, 2016

calculated the difference between the average of the pressure data for the 3-month period before the SSE and the 2-month period after the SSE (Figs. 2 and 3). The uncertainties (Fig. 3A) are based on the root mean square error relative to the mean of the pressure data for the periods before and after the SSE. We chose the 3-month period before the SSE, as this was sufficiently outside the period of early rapid drift that occurs 1 to 2 months after APG deployment (*23*). To avoid disruption in the time series by a second SSE that occurred in December 2014, we used a 2-month period of data for the post-SSE averaging. The December SSE ruptured a patch of the interface just to the southwest of the region that ruptured in the September SSE. We find that APG sites just east (trenchward) of the shelf underwent the largest displacements (up to 5.4 cm), and the magnitude of uplift tapers toward the trench, with the sites 5 to 10 km from the trench (SBPR1, LOBS6, SBPR2) undergoing 1.5 to 2 cm of uplift. Uplift of these near-trench sites indicates that large SSE slip continues onto the shallowest portions of the subduction interface close to the trench, and possibly all the way to the trench itself. The site where we observe the largest uplift signal (LOBS8) is closest to the cGPS sites recording the largest horizontal SSE displacements (MAKO, GISB, PARI) (Fig. 1), and the offshore uplift signals taper both northeast and southwest along strike, in good agreement with the pattern of onshore cGPS displacements (Fig. 3A).

We inverted the onshore cGPS displacements and vertical displacements observed in the offshore APG network to determine the distribution of shallow slow slip on the subduction interface (*28*). Our best-fitting slip inversion (Fig. 3B) fits both the horizontal cGPS and the vertical APG displacements to within uncertainty, with a reduced χ^2 of 0.80 and 1.16 for the cGPS and APG data, respectively. The SSE in September and October 2014 has an equivalent moment magnitude of M_w 6.8.

Our best-fitting slip model (Fig. 3B) reveals the major locus of large slip (10 to 20 cm) focused between 7 and 4 km depth beneath the central portion of the HOBITSS network, with ~10 cm of slip penetrating updip as shallow as 3 km depth in some locations. Further northeast along strike, the observed large vertical displacement (3.7 cm) at LOBS1 is fit well by a small patch of shallow, large slip (~10 cm) occurring at ~4 km below the seafloor. Our results suggest that ~5 cm of slip penetrates to within 2 km of the seafloor beneath the HOBITSS network, and some slip (up to a few centimeters) might penetrate all the way to the trench. To determine the shallowest extent of slow slip required by our APG data, we conducted sensitivity tests for the updip limit of slip. These tests require a reasonable amount of slip (3 to 5 cm or more) to occur to within 2 km of the seafloor (*28*). An even denser network would be needed to resolve the slip distribution on the portion of the plate boundary between 2 km depth and the seafloor.

The shallow slow slip recorded by our APG network occurred on a portion of the plate interface that ruptured in a tsunami earthquake in March 1947 (*29*) (Fig. 4), which suggests that shallow SSE source areas are capable of hosting seismic rupture and tsunamigenesis. This observation has major implications for seismic and tsunami hazards at subduction zones worldwide. Tsunami earthquakes are defined as subduction thrust earthquakes located near the trench that produce a larger-than-expected tsunami for the earthquake's magnitude; they typically have long source durations and lack high-frequency energy. These characteristics are often attributed to similar transitional frictional conditions (*30*) thought to exist in shallow SSE source areas (*18*). Seismic reflection and magnetic data suggest the presence of a subducted seamount in the area of the March 1947 earthquake; rupture over this seamount is thought to have increased tsunami excitation (*29*). There is an apparent gap of large (>10-cm) slow slip in our best-fitting SSE model where the seamount collides with the subduction interface (Fig. 4), suggesting that the properties of the subduction interface in the region of seamount subduction may be less conducive to slow slip. If the seamount does act as a barrier to slow slip, two potential explanations are: (i) the region of the interface struck by the seamount may be interseismically locked (velocity weakening) and may host nucleation of earthquakes similar to the 1947 earthquake (*29*) or (ii) the portion of the fault affected by seamount subduction possesses velocity-strengthening behavior and creeps steadily. Answering this question remains at the heart of a debate over the role that subducting seamounts play in subduction interface seismogenesis (*31*–*33*).

The HOBITSS APG results provide the first detailed view of seafloor deformation during a shallow, offshore SSE and open a frontier for high-resolution, near-field investigations of shallow SSEs and other similarly sized transient deformation events at offshore plate boundaries. These data demonstrate that large SSEs can occur on the shallowest reaches of the subduction megathrust, where very low temperatures and pressures exist. Our result of slow slip near the trench suggests that conditionally stable or velocity-weakening frictional conditions exist on a portion of the interface traditionally thought to be dominated by steady creep (velocity strengthening). There is also evidence for shallow SSEs on continental faults (*34*, *35*). Similar physical mechanisms are probably behind shallow SSEs in continental versus subduction settings, but we expect that fluids may play a larger role in shallow SSEs at subduction zones. Our observations and those from Costa Rica (*25*, *36*) raise the likelihood that shallow SSEs observed at other subduction zones (*14*, *17*, *18*, *37*) may involve large slip to the trench. Seafloor geodetic investigations at these subduction zones and elsewhere are needed to discern the role that SSEs play globally in the accommodation of plate motion on the shallowest portion of the megathrust.

REFERENCES AND NOTES

1. G. Dragert, K. Wang, T. S. James, *Science* **292**, 1525–1528 (2001).
2. K. Obara, H. Hirose, F. Yamamizu, K. Kasahara, *Geophys. Res. Lett.* **31**, L23602 (2004).
3. S. Schwartz, J. Rokosky, *Rev. Geophys.* **45**, RG3004 (2007).
4. S. Ide, G. C. Beroza, D. R. Shelly, T. Uchide, *Nature* **447**, 76–79 (2007).
5. A. Kato *et al.*, *Science* **335**, 705–708 (2012).
6. Y. Ito *et al.*, *Tectonophysics* **600**, 14–26 (2013).
7. S. Ruiz *et al.*, *Science* **345**, 1165–1169 (2014).
8. S. Graham *et al.*, *Geophys. J. Int.* **197**, 1593–1607 (2014).
9. N. Uchida, T. Iinuma, R. M. Nadeau, R. Bürgmann, R. Hino, *Science* **351**, 488–492 (2016).
10. L. M. Wallace, J. Beavan, *J. Geophys. Res.* **115**, B12402 (2010).
11. N. M. Bartlow, S. Miyazaki, A. M. Bradley, P. Segall, *Geophys. Res. Lett.* **38**, L18309 (2011).
12. M. Radiguet *et al.*, *J. Geophys. Res.* **117**, B04305 (2012).
13. A. Douglas, J. Beavan, L. M. Wallace, J. Townend, *Geophys. Res. Lett.* **32**, L16305 (2005).
14. S. Ozawa, H. Suito, M. Tobita, *Earth Planets Space* **59**, 1241–1245 (2007).
15. L. M. Wallace, J. Beavan, S. Bannister, C. Williams, *J. Geophys. Res.* **117**, B11402 (2012).
16. T. H. Dixon *et al.*, *Proc. Natl. Acad. Sci. U.S.A.* **111**, 17039–17044 (2014).
17. M. Valée *et al.*, *J. Geophys. Res.* **118**, 2965–2981 (2013).
18. D. Saffer, L. M. Wallace, *Nat. Geosci.* **8**, 594–600 (2015).
19. Y. Yamashita *et al.*, *Science* **348**, 676–679 (2015).
20. R. Bürgmann, D. Chadwell, *Annu. Rev. Earth Planet. Sci.* **42**, 509–534 (2014).
21. T. Iinuma *et al.*, *J. Geophys. Res.* **117**, B07409 (2012).
22. S. Kodaira *et al.*, *Nat. Geosci.* **5**, 646–650 (2012).
23. A. Polster, M. Fabien, H. Villinger, *Geochem. Geophys. Geosyst.* **10**, Q08008 (2009).
24. W. Chadwick, S. Nooner, D. Butterfield, M. Lilley, *Nat. Geosci.* **5**, 474–477 (2012).
25. E. Davis, H. Villinger, T. Sun, *Earth Planet. Sci. Lett.* **410**, 117–127 (2015).
26. L. M. Wallace, J. Beavan, R. McCaffrey, D. Darby, *J. Geophys. Res.* **109**, B12406 (2004).
27. S. M. Chiswell, *N. Z. J. Mar. Freshw. Res.* **39**, 121–134 (2005).
28. Supplementary materials are available on *Science* Online.
29. R. Bell, C. Holden, W. Power, X. Wang, G. Downes, *Earth Planet. Sci. Lett.* **397**, 1–9 (2014).
30. S. Bilek, T. Lay, *Geophys. Res. Lett.* **29**, 1673 (2002).
31. C. Scholz, C. Small, *Geology* **25**, 487–490 (1997).
32. K. Mochizuki, T. Yamada, M. Shinohara, Y. Yamanaka, T. Kanazawa, *Science* **321**, 1194–1197 (2008).
33. K. Wang, S. Bilek, *Geology* **39**, 819–822 (2011).
34. J. R. Murray, P. Segall, *J. Geophys. Res.* **110**, B09407 (2005).
35. R. Jolivet *et al.*, *Earth Planet. Sci. Lett.* **377-378**, 23–33 (2013).
36. E. Davis, M. Heesemann, K. Wang, *Earth Planet. Sci. Lett.* **306**, 299–305 (2011).
37. T. Nishimura, *Prog. Earth Planet. Sci.* **1**, 22 (2014).
38. R. Sutherland, Geophysical Map 9: Magnetic anomalies in the New Zealand region (Institute of Geological and Nuclear Sciences, 1996).
39. D. I. Doser, T. H. Webb, *Geophys. J. Int.* **152**, 795–832 (2003).

ACKNOWLEDGMENTS

We acknowledge support from U.S. NSF grants OCE-1334654, 1333311, 1332875, and 1333025 to L.M.W., S.C.W., S.Y.S., and A.F.S. and Japan Society for the Promotion of Science grant KAKENHI-26257206 to Y.I. Raw data from the experiment are archived at the Incorporated Research Institutions for Seismology Data Management Center. Additional funding support came from Japan's Ministry of Education, Culture, Sports, Science and Technology; the University of Tokyo Earthquake Research Institute; and the International Research Institute of Disaster Science at Tohoku University. Support for ship time was provided by NSF, GNS Science, and Land Information New Zealand's Oceans 2020 program. We greatly appreciate the immense contribution to the success of this project from ocean bottom instrument engineering teams at LDEO, UTIG, University of Tokyo, and Tohoku University, as well as the captain and crew of the U.S. R/V *Roger Revelle* and New Zealand R/V *Tangaroa*.

SUPPLEMENTARY MATERIALS

www.sciencemag.org/content/352/6286/701/suppl/DC1
Materials and Methods
Supplementary Text
Figs. S1 to S4
Tables S1 and S2
References (*40*–*46*)

11 January 2016; accepted 25 March 2016
10.1126/science.aaf2349

Downloaded from http://science.sciencemag.org/ on May 5, 2016

GEOBIOLOGY

Mass-dependent and -independent signature of Fe isotopes in magnetotactic bacteria

Matthieu Amor,[1,2*] Vincent Busigny,[1*] Pascale Louvat,[1] Alexandre Gélabert,[1] Pierre Cartigny,[1] Mickaël Durand-Dubief,[3] Georges Ona-Nguema,[2] Edouard Alphandéry,[2,3] Imène Chebbi,[3] François Guyot[2]

Magnetotactic bacteria perform biomineralization of intracellular magnetite (Fe_3O_4) nanoparticles. Although they may be among the earliest microorganisms capable of biomineralization on Earth, identifying their activity in ancient sedimentary rocks remains challenging because of the lack of a reliable biosignature. We determined Fe isotope fractionations by the magnetotactic bacterium *Magnetospirillum magneticum* AMB-1. The AMB-1 strain produced magnetite strongly depleted in heavy Fe isotopes, by 1.5 to 2.5 per mil relative to the initial growth medium. Moreover, we observed mass-independent isotope fractionations in ^{57}Fe during magnetite biomineralization but not in even Fe isotopes (^{54}Fe, ^{56}Fe, and ^{58}Fe), highlighting a magnetic isotope effect. This Fe isotope anomaly provides a potential biosignature for the identification of magnetite produced by magnetotactic bacteria in the geological record.

Magnetotactic bacteria synthesize magnetite [$Fe(II)Fe(III)_2O_4$] nanoparticles under a genetically controlled pathway (*1*). They are morphologically, physiologically, and phylogenetically diverse (*2*, *3*). Nanoparticles of biogenic magnetite are produced in these cells in organelles called magnetosomes, consisting of a bilayered lipid membrane surrounding the magnetite crystal (*4*). Magnetosomes are assembled in chains inside the cell and provide it with a permanent magnetic dipole (*4*, *5*). Magnetotactic bacteria are markers of oxic/anoxic transition zones in sediments and aquatic systems (*1*). In addition, these bacteria have been proposed to represent some of the most ancient microorganisms capable of biomineralization (*6*, *7*), but the identification of their activity in the fossil record remains poorly resolved (*8*). Specifically, it is challenging to distinguish intracellular magnetite nanoparticles from abiotic or extracellular biogenic magnetites produced by Fe-metabolizing bacteria [i.e., Fe(III)-reducing and Fe(II)-oxidizing bacteria] (*5*, *6*, *8*, *9*). Moreover, magnetite nanoparticles can experience variable transformations during diagenetic and/or metamorphic processes and may thus have lost some of their original physical characteristics (*10*). Iron isotopes have been proposed as a tool to infer the presence of Fe(III)-reducing and Fe(II)-oxidizing bacteria in the Precambrian geological record (*11*–*13*). However, a previous study reported no fractionation of Fe isotopes (*14*) in magnetite produced by two strains of magnetotactic bacteria, *Magnetospirillum magnetotacticum* MS-1 and *Magnetovibrio blakmorei* MV-1 (*15*), and only oxygen isotope measurements showed a temperature-dependent fractionation between magnetite and water.

We measured the Fe isotope fractionation produced by another magnetotactic bacterium, *M. magneticum* strain AMB-1, which was cultured in batches with either Fe(III)-quinate or Fe(II)-ascorbate to investigate the effect of various Fe sources on the Fe isotopic signatures in magnetite (see the supplementary materials). A small fraction of the growth media was sampled before and after AMB-1 cultures for subsequent Fe isotope analyses. Magnetites were magnetically separated from bacterial lysates (i.e., plasmic membranes, periplasm, and cytoplasm) according to an optimized procedure, which ensured that the mineral was analyzed with no organic residue (*9*). Both organic and biomineralized fractions were analyzed for Fe isotope compositions.

Magnetite produced by AMB-1 was strongly depleted in the heavy Fe isotopes relative to the initial growth medium. Two replicates for each culture condition provided consistent results, with δ^{56}Fe values of −1.00 ± 0.08 per mil (‰) and −1.80 ± 0.13‰ for Fe(II)-ascorbate and Fe(III)-quinate experiments, respectively (Fig. 1 and table S1). Overall, the net Fe isotope fractionation between Fe sources and magnetite ranged between 1.5 and 2.5‰. Iron is usually assumed to reside either in magnetite or in the residual growth medium (*16*). Yet we found that bacterial lysates can represent up to 70% of cellular Fe (supplementary materials). In the two culture conditions of our experiments, bacterial lysate δ^{56}Fe values were enriched in the heavy isotopes by 0.3 to 0.8‰ relative to initial Fe sources. Although several studies reported heavy Fe(II) adsorbed on solid surfaces or ligated into organic complexes (*17*, *18*), Fe in the lysates is more likely to be present as Fe(III). This is consistent with the low δ^{56}Fe values of magnetite, which suggest partial reduction of

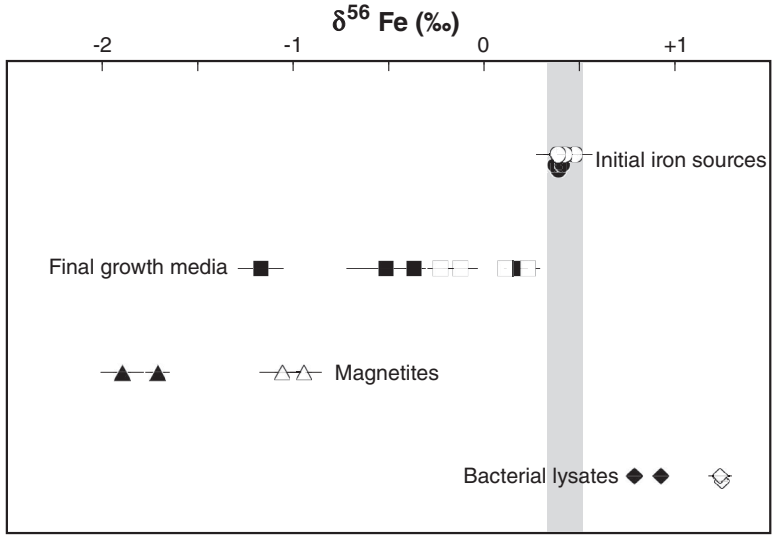


Fig. 1. Iron isotope compositions obtained from cultures of magnetotactic bacteria. δ^{56}Fe values (relative to international standard IRMM-014) of Fe sources (initial growth media, circles), growth media after AMB-1 cultures (squares), magnetite samples (triangles), and bacterial lysates (diamonds) in experiments using either Fe(III)-quinate (solid black symbols) or Fe(II)-ascorbate (open symbols) as Fe sources. The gray bar represents the range of Fe isotope compositions for initial growth media and can be regarded as a reference. Magnetite samples are enriched in light Fe isotopes relative to Fe sources, by ~1.5 to 2.5‰. Growth media are also enriched in light isotopes, with fractionation between 0.5 and 1.5‰. In contrast, bacterial lysates are enriched in heavy isotopes relative to Fe sources, by 0.5 to 0.75‰.

[1]Institut de Physique du Globe de Paris, Sorbonne Paris Cité, Université Paris Diderot, UMR 7154 CNRS, 75238 Paris, France. [2]Institut de Minéralogie, de Physique des Matériaux et de Cosmochimie, Sorbonne Universités, Université Pierre et Marie Curie, UMR 7590 CNRS, Institut de Recherche pour le Développement UMR 206, Museum National d'Histoire Naturelle, 75252 Paris Cedex 05, France. [3]Nanobactérie SARL, 36 Boulevard Flandrin, 75016 Paris, France.
***Corresponding author. Email: amor@ipgp.fr (M.A.); busigny@ipgp.fr (V.B.)**

Downloaded from http://science.sciencemag.org/ on May 5, 2016

Fe(III), whose residuals will be included in the lysates (*17*, *19*).

Based on our experimental results and previous models for magnetite precipitation in magnetotactic bacteria (*1*, *16*, *20*), we can propose a geochemical view of Fe cycling in AMB-1 cultures (Fig. 2). Iron initially present as Fe(II) or Fe(III) in the growth medium was incorporated into the cell and stored as Fe(III), possibly in the form of ferritine (*16*). Fe(III) was then partially reduced for trafficking to magnetosomes, where Fe(II) was precipitated as magnetite in processes involving cytochromes (*20*, *21*) or similar proteins. This geochemical model of magnetite precipitation in AMB-1 is in line with Fe isotope fractionations determined in Fe(III)-reducing bacteria and in abiotic magnetite precipitation (*17*, *19*, *22*). Bacterial Fe(III) reduction releases Fe(II) depleted in the heavy isotopes by ~3‰ (*17*). Then precipitation enriches magnetite in the heavy isotopes relative to Fe(II) by 0.8 to 1.5‰ (depending on kinetic or equilibrium control) in both abiotic and biotic systems (*19*, *22*). Overall, the net isotope fractionation between initial Fe(III) and magnetite would be 2.2 to 1.5‰. This range of values is consistent with our experimental results obtained for bacterial lysates and magnetite (Fig. 1).

We also observed that magnetite and bacterial lysates show distinct but homogeneous isotopic compositions whatever the initial source of Fe [Fe(II) or Fe(III)]. This contrasts with the prior observations of the absence of fractionation (*15*) and may result from differences between the strains and their culture conditions (supplementary materials). The presence of a large intracellular pool of Fe distinct from magnetite in our study may be important for explaining such differences. This extra Fe-bearing reservoir may have originated from the larger Fe concentrations in the initial growth media (150 μM versus 30 to 70 μM; supplementary materials)

Finally, we observed a statistically significant deviation from mass-dependent fractionation, expressed here as Δ^{57}Fe (*23*) (Fig. 3 and table S1). In Fe(III)-quinate experiments, both growth media after AMB-1 cultures and magnetite showed unambiguous deviations from mass-dependent fractionations, with Δ^{57}Fe values ranging between 0 and +0.23 ± 0.08‰ (2 SD). Each isotope mass balance lies within Δ^{57}Fe ~ 0.00 ± 0.04‰ for every experiment, confirming the isotope anomalies (supplementary materials). Moreover, a negative linear correlation between Δ^{57}Fe and δ^{56}Fe, with magnetite showing the largest deviation from mass-dependent fractionation line, reveals a mass-independent contribution referred to here as mass-independent fractionation (MIF) (Fig. 3). Such a linear correlation may represent a mixing between intracellular Fe with Δ^{57}Fe values different from zero and the pool of Fe in the growth medium.

We explored several possible mechanisms that could have produced this MIF signature. We first considered whether an apparent mass-independent isotope signal could be due to the mass conservation along mass-dependent isotope fractionations, similar to S isotope fractionation by sulfate-reducing bacteria (*24*). Indeed, mixing between two reservoirs with Δ^{57}Fe = 0 and contrasted isotopic compositions would produce an apparent MIF. Mixing between two Fe reservoirs in AMB-1 with extreme δ^{56}Fe values of –3 and +3‰, respectively, should result in variations of Δ^{57}Fe smaller than 0.003‰ from the mass-dependent line, which remains within error of our measurements (figs. S4 and S5). Such variations are therefore too small to account for Δ^{57}Fe values up to +0.23 ± 0.08‰ (Fig. 3).

Magnetic isotope effects (MIEs) can discriminate isotopes according to their nuclear spins and nuclear magnetic moments rather than by their masses and are affected by external magnetic fields (*25*). They are usually observed in reactions involving free radicals and paramagnetic species, and primarily affect odd as compared to even isotopes (*25*). Fe(II) (in high spin configuration) and Fe(III) ions are both paramagnetic. As a consequence, the isotope ^{57}Fe would behave differently from ^{54}Fe, ^{56}Fe, and ^{58}Fe. To test this hypothesis, we attempted to determine potential isotope anomalies on ^{58}Fe, expressed as Δ^{58}Fe (*23*) (fig. S10). No significant anomaly on Δ^{58}Fe is predicted with a MIE. Due to the very low abundance of ^{58}Fe (0.282% of the total Fe), only a few samples were measured with an acceptable precision better than ±1.5‰ (2 SD) on Δ^{58}Fe. These samples show Δ^{58}Fe ~ 0‰ within analytical uncertainties (fig. S10), suggesting that only ^{57}Fe is associated with a mass-independent signature and supporting a MIE as the process enriching magnetite in ^{57}Fe relative to ^{54}Fe, ^{56}Fe, and ^{58}Fe.

In contrast with the Fe(III)-quinate experiments, no detectable MIF was observed in Fe(II)-ascorbate experiments (Fig. 3 and table S1). The likely

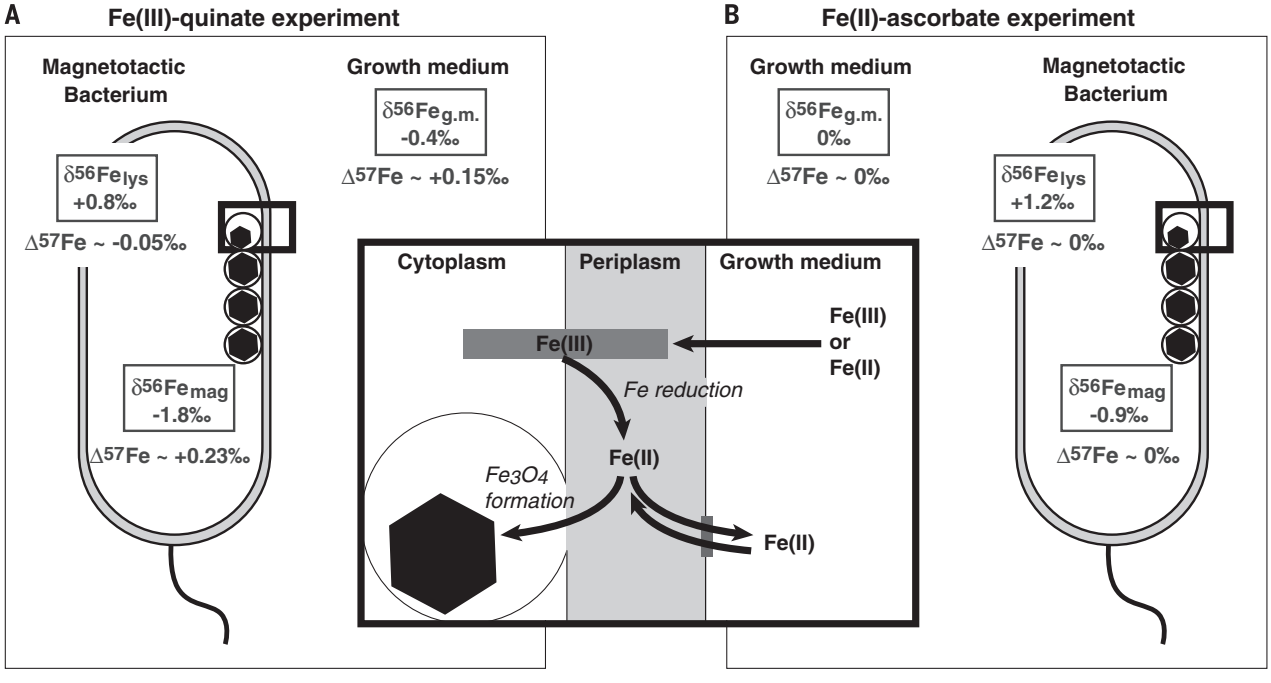


Fig. 2. Geochemical view of Fe cycling in AMB-1 showing the main Fe reservoirs and fluxes. Iron cycling in cultures with (**A**) Fe(III)-quinate and (**B**) Fe(II)-ascorbate. Fe(III) in the lysate fraction may be associated to ferritines either in the cytoplasm or periplasm for Fe storage in the cell (*16*). $\delta^{56}Fe_{lys}$, $\delta^{56}Fe_{g.m.}$, and $\delta^{56}Fe_{mag}$: mean δ^{56}Fe values of the lysate, growth medium after AMB-1 culture, and magnetite samples, respectively. Δ^{57}Fe: deviation from mass-dependent Fe isotope fractionation (*23*) in the growth medium, lysate, and magnetite samples. Starting Fe sources had Δ^{57}Fe = 0‰ within analytical uncertainties.

Downloaded from http://science.sciencemag.org/ on May 5, 2016

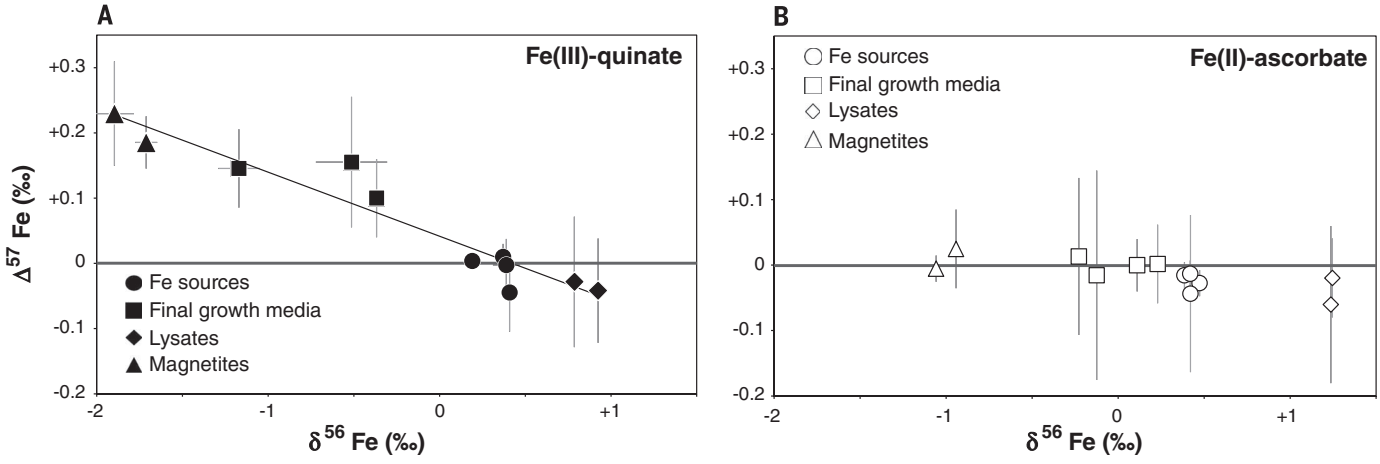


Fig. 3. MIF of odd Fe isotope in cultures. Plot of Δ^{57}Fe (*23*) versus δ^{56}Fe in growth media before (circles) and after (squares) AMB-1 cultures, bacterial lysates (diamonds), and magnetite samples (triangles). The gray horizontal lines correspond to Δ^{57}Fe = 0‰. (**A**) Experiments using Fe(III)-quinate as a Fe source (solid symbols). Δ^{57}Fe values of magnetite samples and growth media after AMB-1 cultures are significantly different from zero, even considering analytical uncertainties (2 SD). Data define a linear correlation between Δ^{57}Fe and δ^{56}Fe (correlation coefficient of 0.92). (**B**) Experiments using Fe(II)-ascorbate as a Fe source (open symbols). No MIF is observed.

explanation is that the pool of abundant extracellular Fe(II) can then diffuse toward the intracellular medium, mix with the small fraction of intracellular Fe(II), and dilute its MIF signature. This is compatible with the concept that in magnetotactic bacteria, the soluble Fe(II) species easily enter the cell by a diffusion like process, whereas Fe(III) species are actively (via proteins) incorporated into the cell (*26*). A dilution of the MIF signature by extracellular Fe(II) would suggest that only intracellular Fe(II) acquires the MIF signature. The mixing of intracellular Fe(II) having low δ^{56}Fe values produced by partial Fe(III) reduction (Fig. 2) with Fe(II) showing higher δ^{56}Fe values from the growth medium is also consistent with higher δ^{56}Fe values of magnetite formed in Fe(II)-ascorbate experiments relative to Fe(III)-quinate, as it is indeed observed (Figs. 1 and 3 and table S1). Finally, an outward diffusion of intracellular Fe(II) can also account for the evidence that the final growth media of the Fe(III)-quinate experiments also have positive Δ^{57}Fe values.

The MIF and MIE signatures observed in this study can be produced by a wide variety of mechanisms. MIEs are often produced by spin transitions (*25*), such as those observed during photochemical reactions of Hg isotopes (*27*). Here, AMB-1 was cultivated in the dark, preventing any photochemical MIE (supplementary materials). A likely explanation for MIEs in AMB-1 could be a shift from low-spin Fe in cytochromes (*28*) or similar proteins to high-spin Fe in magnetite (*29*). Cytochromes are redox proteins catalyzing Fe reduction or oxidation and are required for magnetite precipitation in magnetotactic bacteria (*20*, *21*). The MIE signature recorded in magnetite could have been produced during Fe(III) reduction or magnetite precipitation (Fig. 2); however, the absence of a MIF signature in magnetite formed under Fe(II)-ascorbate culture condition indicates that the MIE was more likely generated by spin transitions during Fe(III) reduction in cytochromes or similar proteins (*30*). The proximity of proteins involved in oxidation or reduction processes with the magnetite nanoparticles and their local magnetic field might provide adequate conditions for producing Fe-MIE specifically in magnetotactic bacteria. Iron isotope fractionations associated with spin configuration changes have already been proposed (*31*).

Mass-dependent and -independent fractionations of Fe isotopes may thus serve as potential biosignatures of magnetotactic bacteria in ancient environments, although it remains to be seen which environmental conditions result in Fe isotope fractionations and MIEs as reported here, and which do not. Second, identifying Fe-MIEs in natural samples remains difficult. Only few data report both δ^{56}Fe and δ^{57}Fe values of natural magnetites (*13*, *32*, *33*), and several samples display possible nonzero Δ^{57}Fe values, although with still too large errors on Δ^{57}Fe to be conclusive. High-precision Fe isotope studies of samples containing enough material to generate a signal may soon lead to the discovery of Fe-MIF biosignatures in the geological record.

REFERENCES AND NOTES

1. A. Komeili, *FEMS Microbiol. Rev.* **36**, 232–255 (2012).
2. D. Faivre, D. Schüler, *Chem. Rev.* **108**, 4875–4898 (2008).
3. C. T. Lefèvre, D. A. Bazylinski, *Microbiol. Mol. Biol. Rev.* **77**, 497–526 (2013).
4. D. A. Bazylinski, R. B. Frankel, *Nat. Rev.* **2**, 217 (2004).
5. J. Li, W. Wu, Q. Liu, Y. Pan, *Geochem. Geophys. Geosyst.* **13**, Q10Z51 (2012).
6. R. E. Kopp, J. L. Kirschvink, *Earth Sci. Rev.* **86**, 42–61 (2008).
7. C. T. Lefèvre *et al.*, *Environ. Microbiol.* **15**, 2267–2274 (2013).
8. C. Jimenez-Lopez, C. S. Romanek, D. A. Bazylinski, *J. Geophys. Res. Biogeosci.* **115**, G00G03 (2010)
9. M. Amor *et al.*, *Proc. Natl. Acad. Sci. U.S.A.* **112**, 1699–1703 (2015).
10. H. Vali, J. L. Kirschvink, *Nature* **339**, 203–206 (1989).
11. O. J. Rouxel, A. Bekker, K. J. Edwards, *Science* **307**, 1088–1091 (2005).
12. C. M. Johnson, B. L. Beard, C. Klein, N. J. Beukes, E. E. Roden, *Geochim. Cosmochim. Acta* **72**, 151–169 (2008).
13. P. R. Craddock, N. Dauphas, *Earth Planet. Sci. Lett.* **303**, 121–132 (2011).
14. Iron isotope data are reported using conventional delta notation relative to the international standard IRMM-014 and defined as $\delta^{xx}\mathrm{Fe}_{\mathrm{sample}} = \left(\frac{(^{xx}\mathrm{Fe}/^{54}\mathrm{Fe})_{\mathrm{sample}}}{(^{xx}\mathrm{Fe}/^{54}\mathrm{Fe})_{\mathrm{IRMM-014}}} - 1\right) \times 1000$ where *xx* is 56, 57, or 58.
15. K. W. Mandernack, D. A. Bazylinski, W. C. Shanks 3rd, T. D. Bullen, *Science* **285**, 1892–1896 (1999).
16. J. Baumgartner *et al.*, *Proc. Natl. Acad. Sci. U.S.A.* **110**, 14883–14888 (2013).
17. H. A. Crosby, C. M. Johnson, E. E. Roden, B. L. Beard, *Environ. Sci. Technol.* **39**, 6698–6704 (2005).
18. G. A. Icopini, A. D. Anbar, S. S. Ruebush, M. Tien, S. L. Brantley, *Geology* **32**, 205 (2004).
19. C. M. Johnson, E. E. Roden, S. A. Welch, B. L. Beard, *Geochim. Cosmochim. Acta* **69**, 963–993 (2005).
20. S. R. Jones *et al.*, *Proc. Natl. Acad. Sci. U.S.A.* **112**, 3904–3909 (2015).
21. M. I. Siponen *et al.*, *Nature* **502**, 681–684 (2013).
22. A. J. Frierdich, B. L. Beard, M. M. Scherer, C. M. Johnson, *Earth Planet. Sci. Lett.* **391**, 77–86 (2014).
23. Capital delta notation Δ^{xx}Fe illustrates the deviation of Fe isotope fractionation from single-step low-temperature equilibrium exchange reactions, as defined for S isotopes (*24*). In other words, Δ^{xx}Fe quantifies the deviation from mass-dependent fractionation and is expressed as $\Delta^{xx}\mathrm{Fe} = \delta^{xx}\mathrm{Fe} - 1000 \times [(1 + \frac{\delta^{56}\mathrm{Fe}}{1000})^{\beta} - 1]$ where *xx* is 57 or 58, and β corresponds to the variation of ^{57}Fe/^{54}Fe and ^{56}Fe/^{54}Fe mass ratios (i.e., 1.475) or ^{58}Fe/^{54}Fe and ^{56}Fe/^{54}Fe mass ratios (i.e., 1.932).
24. J. Farquhar, D. T. Johnston, B. A. Wing, *Geochim. Cosmochim. Acta* **71**, 5862–5875 (2007).
25. A. L. Buchachenko, *J. Phys. Chem. B* **117**, 2231–2238 (2013).
26. D. Schüler, E. Baeuerlein, *Arch. Microbiol.* **166**, 301–307 (1996).
27. B. A. Bergquist, J. D. Blum, *Science* **318**, 417–420 (2007).
28. R. Tsai *et al.*, *Proc. Natl. Acad. Sci. U.S.A.* **66**, 1157–1163 (1970).
29. A. Bengston, D. Morgan, U. Becker, *Phys. Rev. B* **87**, 10.1103/PhysRevB.87.155141 (2013).
30. M. L. Estevam *et al.*, *J. Biol. Chem.* **279**, 39214–39222 (2004).
31. R. Guilbaud, I. B. Butler, R. M. Ellam, *Science* **332**, 1548–1551 (2011).
32. G. Steinhoefel *et al.*, *Geochim. Cosmochim. Acta* **74**, 2677–2696 (2010).
33. A. D. Czaja *et al.*, *Earth Planet. Sci. Lett.* **363**, 192–203 (2013).

ACKNOWLEDGMENTS

We thank J. Moureau for analytical assistance on multi-collection–inductively coupled plasma–mass spectrometry measurements.

Downloaded from http://science.sciencemag.org/ on May 5, 2016

This work was funded by the programs InterrVie 2013 (V. B.) and 2015 (F. G.) of the Institut National des Sciences de l'Univers and the UnivEarths Labex program at Sorbonne Paris Cité (grants ANR-10-LABX-0023 and ANR-11-IDEX-0005-02). This is Institut de Physique du Globe de Paris contribution 3615. Parts of this work were supported by the Institut de Physique du Globe de Paris multidisciplinary program PARI, and by Region Ile-de-France SESAME grant no. 12015908.

We thank reviewers for their contributions to improvements of the manuscript. All data are available in the supplementary materials.

SUPPLEMENTARY MATERIALS

www.sciencemag.org/content/352/6286/705/suppl/DC1
Materials and Methods
Supplementary Text
Figs. S1 to S10
Table S1
References (*34*–*42*)

28 October 2015; accepted 28 March 2016
10.1126/science.aad7632

DEMOGRAPHY

Inequality in mortality decreased among the young while increasing for older adults, 1990–2010

J. Currie[1,2,3]* and H. Schwandt[3,4,5]

Many recent studies point to increasing inequality in mortality in the United States over the past 20 years. These studies often use mortality rates in middle and old age. We used poverty level rankings of groups of U.S. counties as a basis for analyzing inequality in mortality for all age groups in 1990, 2000, and 2010. Consistent with previous studies, we found increasing inequality in mortality at older ages. For children and young adults below age 20, however, we found strong mortality improvements that were most pronounced in poorer counties, implying a strong decrease in mortality inequality. These younger cohorts will form the future adult U.S. population, so this research suggests that inequality in old-age mortality is likely to decline.

Poorer people tend to have shorter lives and are more likely to die than richer people at all ages. Understanding the evolution of these inequalities in mortality is a central concern of economists, policy-makers, and the public. Not surprisingly, a great deal of highly publicized research has investigated changes in inequality in life expectancy and mortality in the United States over the past 20 years. A preponderance of the existing evidence points to alarming increases in inequality in mortality over this time period (*1*–*16*). Some studies investigating mortality trends across educational groups and geographic areas argue not only that inequality in life expectancy is widening, but that overall life expectancy is actually falling among the most disadvantaged groups (*11*–*13*).

However, much of the recent literature focuses on adults, and in particular on life expectancy at age 40 or 50, exploiting rich data sets that link individuals' career earnings to deaths at older ages (*1*–*8*). By construction, these analyses omit children, teens, and young adults. A second strand of research analyzes demographic subgroups defined by education, location, and/or race (*9*–*16*). These studies typically focus on overall life expectancy at birth.

Life expectancy at birth is a summary measure that collapses all of the age-specific mortality rates observed in a given year (and in a certain demographic subgroup) into a single number. It provides information about how long a cohort of newborns can expect to live, under the assumption that the age-specific mortality rates observed in that given year remain constant into the future. This assumption is unlikely to hold in the United States, given that mortality rates at all ages have been continuously changing (mostly improving) over the past century (*17*).

Changes in infant and childhood mortality have been shown to be important predictors of a cohort's health and mortality at later ages, and such data may therefore be more informative about the development of future death rates for the current young. Moreover, mortality at young ages is considered a sensitive indicator of social conditions because it responds relatively quickly to changes affecting the entire population, whereas old-age mortality is partly determined by conditions in the past. The infant mortality rate has been shown to be an important indicator of health for whole populations and one that is highly correlated with more complex measures such as disability-adjusted life expectancy (*18*).

Therefore, to study how inequality in mortality changes over time, it is important to understand age-specific mortality trends and in particular those at younger ages. Life expectancy at birth masks potential differences in age-specific trends, and the measure is also dominated by changes in old-age mortality because that is when most deaths occur. A recent study by Case and Deaton (*19*) highlights the relevance of examining age-specific mortality rates: They document increases in middle-age mortality for non-Hispanic whites, a striking development that would not be detectable in overall life expectancy at birth.

We followed an empirical approach, based on placing counties into groups, that allows us to analyze trends in age-specific mortality while taking into account population shifts across groups. We ranked all counties in 1990, 2000, and 2010 by their poverty level and then divided them into 20 groups, each representing roughly 5% of the overall U.S. population (fig. S1 and table S1). This enables us to compare, for example, the 5% of the population living in the poorest counties in 1990 with the 5% of the population living in the richest counties in 1990, and analyze how the mortality differences between these groups change over time. We refer to the county groups with the highest fractions of their populations in poverty as the poorest counties, and those with the lowest fractions of their populations in poverty as the richest counties.

Our approach reassigns county groups in 1990, 2000, and 2010 to adjust for changes in county ranking and population size. That is, we compare the poorest counties representing 5% of the population in 1990 with the poorest counties representing 5% of the population in 2010, even if they are not exactly the same counties. The advantages of this procedure and a comparison with other approaches are discussed below. Our county grouping approach is similar to that of Singh and Siahpush (*9*), who investigated life expectancy trends ranking U.S. counties by a deprivation index (comprising a set of county characteristics) up to 2001. Our approach differs from theirs in that they did not analyze age-specific mortality, analyzed data only up to 2001, and did not reorder county groups over time.

Mortality rates were constructed at the levels of county group, gender, and age by dividing death counts from the U.S. Vital Statistics by population counts from the decennial Census. We focused on 3-year mortality rates for Census years 1990, 2000, and 2010, based on a total of 21,175,011 deaths. Life expectancy was calculated by constructing a life table based on 19 age groups (see the supplement for additional details regarding the construction of mortality rates and life expectancy). Socioeconomic county characteristics, including poverty rate, median and per capita income, and percentage of high school

[1]Center for Health and Wellbeing, Princeton University, Princeton, NJ 08542, USA. [2]National Bureau of Economic Research, Cambridge, MA 02138, USA. [3]Institute for the Study of Labor (IZA), 53072 Bonn, Germany. [4]Department of Economics, University of Zurich, 8031 Zurich, Switzerland. [5]Center for Economic Performance, London School of Economics, London WC2A 2AE, UK.
*Corresponding author. Email: jcurrie@princeton.edu

Downloaded from http://science.sciencemag.org/ on May 5, 2016

dropouts, were taken from the Census in 1990 and 2000. For 2010 we used the 2008–2012 American Community Survey (ACS), which replaced the long form of the Census for 2010. Table S1 reports socioeconomic characteristics for the 20 county groups. The county group with the lowest fraction living in poverty had an average poverty rate of 3.75% and a median income (averaged across counties) of $62,445 in 1990. The comparable 2010 figures are 5.58% in poverty and a $62,752 median income. The county group with the highest fraction living in poverty had a 30.47% poverty rate and a median income of $23,595 in 1990. Comparable 2010 figures were 28.30% in poverty and a median income of $25,404.

We start with the analysis of overall life expectancy at birth, so as to make a better comparison with the strand of previous literature that has focused on this measure. Figure 1A plots male and female life expectancies at birth for the 20 county groups in 1990, 2000, and 2010 (see table S2 for numerical values and standard deviations). Standard deviations are within 0.1% of the estimates, and 95% confidence intervals (CIs) would be fully covered by the estimate markers if plotted in Fig. 1A. In addition to the plotted life expectancy values, we have drawn a linear regression line through the 20 dots representing each year (the line for 2000 omits symbols to reduce clutter). A steeper slope of the regression line indicates greater inequality in life expectancy. If there was no difference in life expectancy between richer and poorer county groups, then the line would be entirely flat.

Figure 1A shows that for men, there is a strong gradient in 1990, with those living in the richest counties enjoying 6.10 additional years of life expectancy relative to those living in the poorest counties (74.79 versus 68.70). For women, who have greater life expectancy overall, this gap is smaller at 3.01 years (80.20 versus 77.19). Between 1990 and 2010, life expectancy at birth increased across the entire poverty spectrum, both for men and for women. For men, the fitted lines in 1990 and 2010 are almost parallel, suggesting that life expectancy increased by similar amounts in rich and poor counties. In fact, residents of the poorest counties gained slightly more with 4.63 additional years, whereas those in the richest county group gained 4.35 years. For women, improvements were stronger for those in the richest county group (3.01 versus 2.06 years), and most of these improvements occurred between 2000 and 2010.

Figure 1B plots the changes in life expectancy between 1990 and 2010. For women, the fitted regression line is downward-sloping (P = 0.043), indicating increasing inequality in life expectancy over this period. For men, the slope of the regression line is positive but not significantly different from zero (P = 0.103), consistent with Fig. 1A's suggestion that decreases in mortality were equally distributed across men in rich and poor counties.

Turning to our key innovation—the analysis of age-specific mortality for all ages—Figs. 2 and 3 show that the evolution of overall life expectancy at birth masks considerable heterogeneity in trends in mortality rates at different ages. Similar to Fig. 1, each symbol in the figure represents the age-specific 3-year mortality rate in a bin representing 5% of the U.S. population, and the bins are ordered by county poverty rates. Mortality rates are plotted for 1990 and 2010 together with a linear regression line; only the line is shown for 2000. Regression lines are upward-sloping because mortality is higher in poorer counties, but, as in Fig. 1, a flattening of the line over time indicates a decrease in inequality. Tables S3 and S4 report standard errors for the mortality rates and tests for a change in the slope of the fitted regression lines.

The first panel in Fig. 2 shows the evolution of 3-year mortality rates for male newborns, which decreased by 4.2 per 1000 in the group of richest counties between 1990 and 2010, from 9.77 (95% CI, 9.10 to 10.44) to 5.53 (95% CI, 5.06 to 6.00). However, infant mortality in the group of poorest counties decreased by 8.49 deaths per 1000, which is more than twice as much over the same time period, from 18.28 (95% CI, 17.38 to 19.17) to 9.79 (95% CI, 9.22 to 10.37). These strong reductions in mortality in the poorer county groups are reflected in a considerable flattening of the regression line in 2010 relative to 1990. The slope of the regression line through the group values decreases by more than 50%, and this change is highly significant (P < 0.001, table S3). This flattening indicates a marked reduction in inequality in infant mortality.

A similar decline in mortality inequality can be observed up to age 20, although improvements for young children were greatest between 1990 and 2000. For older children, there were also large declines between 2000 and 2010. Looking at older ages, inequality decreased (i.e., the slope of the fitted regression line decreased significantly; see table S3 for P values) among males up to age 50. Between ages 50 and 75 there was no significant change in inequality in mortality, but after age 75, mortality inequality increased significantly among males. It is also striking that for adult men between 20 and 34, there was virtually no improvement in mortality rates between 2000 and 2010.

Figure 3 shows that the patterns are somewhat different for females. As it did for males, female mortality decreased strongly for age groups up to age 19, and these improvements were significantly stronger in the poorest counties, implying that inequality in mortality decreased sharply (see table S4 for P values of the differences in the slopes). However, although inequality decreased significantly for males until age 50, this trend is observed for females only up to age 30. For ages 30 to 45, there is no significant change in mortality inequality, whereas for all age groups over 45, inequality in mortality increases.

Turning to the mortality rates themselves, it is noteworthy that there was practically no improvement in mortality among women aged 30 to 45 between 1990 and 2010. This is a striking

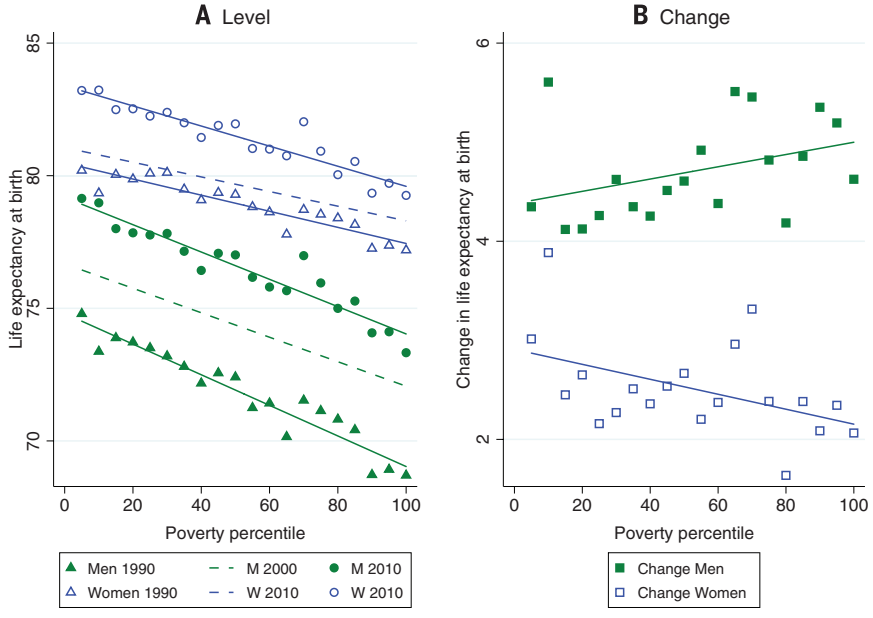


Fig. 1. Life expectancy at birth by poverty percentile and gender. (**A**) Average male and female life expectancy at birth by poverty percentile. Each bin represents a group of counties with about 5% of the overall population. The solid lines provide the fitted regression lines. Higher percentiles refer to higher poverty levels. A steeper slope implies greater inequality in life expectancy at birth. Magnitudes are reported in table S2. (**B**) Changes in average male and female life expectancy at birth by poverty percentile. The fitted regression line has a slope of 0.0062 (P = 0.103) for men and a slope of −0.0075 (P = 0.043) for women.

Downloaded from http://science.sciencemag.org/ on May 5, 2016

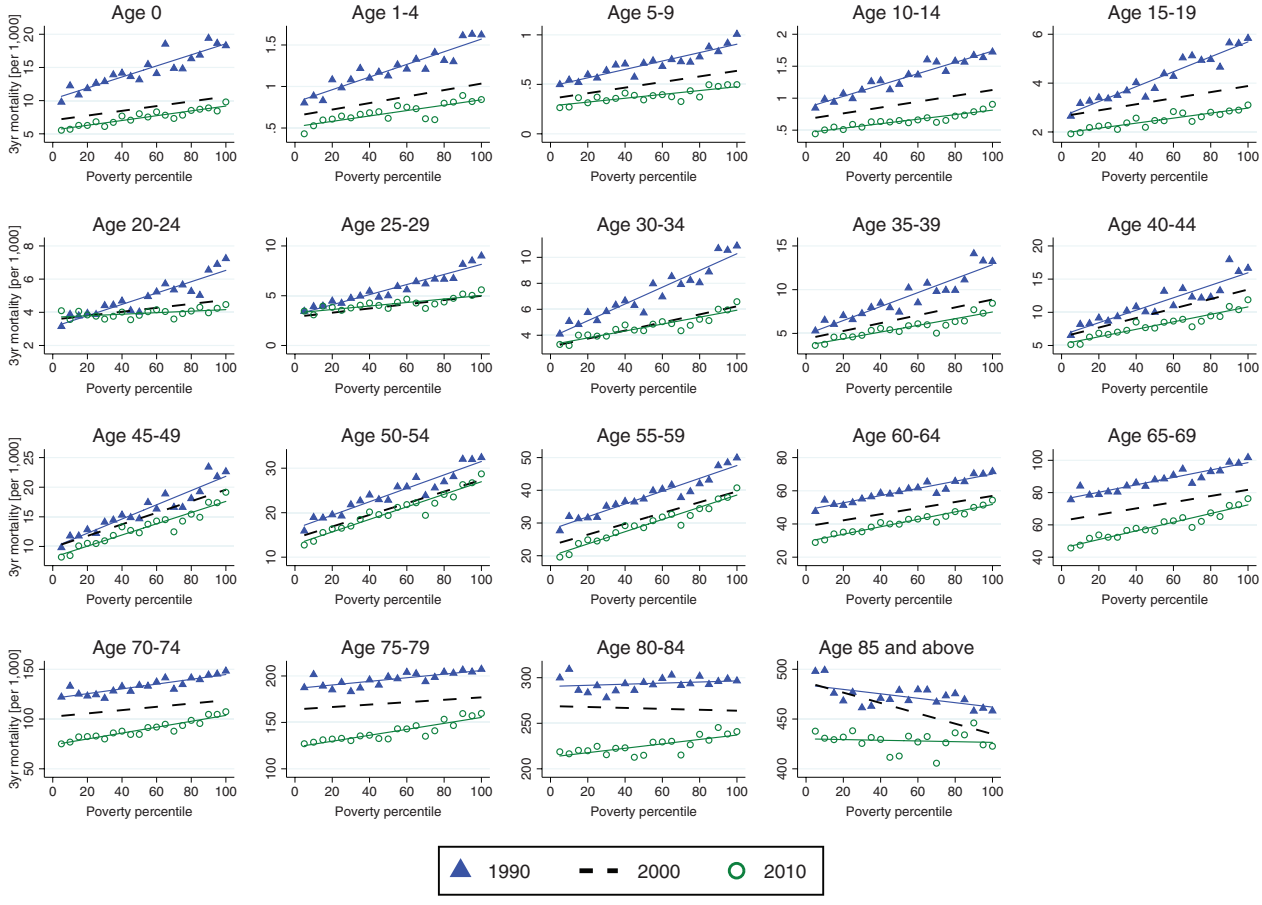


Fig. 2. Male 3-year mortality rates by poverty percentile across age groups. Average 3-year mortality rates are plotted across poverty rate percentiles. Each bin represents a group of counties with about 5% of the overall population in the respective year. Straight lines provide linear fits. Table S3 reports key magnitudes and standard errors.

development in light of the progress made in other age categories. A further remarkable fact is that mortality rates actually increased in some of the richest counties among females aged 20 to 29. After age 45, there are mortality declines, but they are larger in the richer county groups, driving the increase in mortality inequality noted above.

The results discussed so far are all based on ranking counties by poverty rates, which is arguably the most relevant measure if one is focusing on differences between the rich and poor. However, several additional measures of socioeconomic status are available at the county level. The age-specific trends in mortality are very similar when ranking counties by these alternative measures, including the share of high school dropouts, median income, and average life expectancy (figs. S2 to S4).

In contrast to many recent analyses of inequality in mortality that focus on life expectancy at middle age, we find overall improvements in life expectancy at birth both in counties with high poverty rates and counties with low poverty rates. However, we argue that life expectancy measures are not (despite their name) intended to be predictive of the number of future years of life that any particular cohort can expect to attain, and that it is more informative to examine age-specific mortality rates. Our analysis of these rates indicates that inequality in mortality between rich and poor counties has strongly declined among infants, children, and young adults up to age 30 of either gender, as well as among adult males up to age 50. Among older adults, mortality has continued to decline, although declines are generally greatest in the richest counties, indicating increasing inequality in mortality, which is in line with the literature that has focused on inequality trends at older ages (*1*–*8*).

Our focus on using county groups to examine inequality has advantages and disadvantages. Unlike subgroups defined by race and education or by individual counties, county groups are large enough to provide precise mortality estimates in age ranges with low mortality. Moreover, the county of residence is consistently reported both in the Vital Statistics and the Census data, which makes mortality rates by county group subject to less measurement error than using other demographic groups that can be constructed with these data sets. For example, education is often missing from death certificates, and education measures were switched from years of schooling to degrees for some states in the mortality files but not in the Census. Even race is not always consistently reported. For example, the Census introduced multiple race categories in 2000 while the Vital Statistics reports permit only single-race identification. These changes in the reporting of race and education introduce a fundamental bias because of their different impacts on the numerator and denominator of a given subgroup's mortality rate. And because these biases change over time, they confound the estimation of trends in inequality.

Changes in the composition of the analyzed demographic subgroups present another serious source of bias (*20*–*23*). For example, Olshansky *et al.* (*13*) documented decreasing life expectancy among non-Hispanic white women without a high school degree between 1990 and 2008. But the share of the population of white non-Hispanic females in this education category fell by about two-thirds between 1990 and 2010, which suggests that the average female high school dropout today is much more disadvantaged relative to her peers than the average female high school dropout in 1990. Bound *et al.* (*20*) argued that there is in fact no decrease in life expectancy

Downloaded from http://science.sciencemag.org/ on May 5, 2016

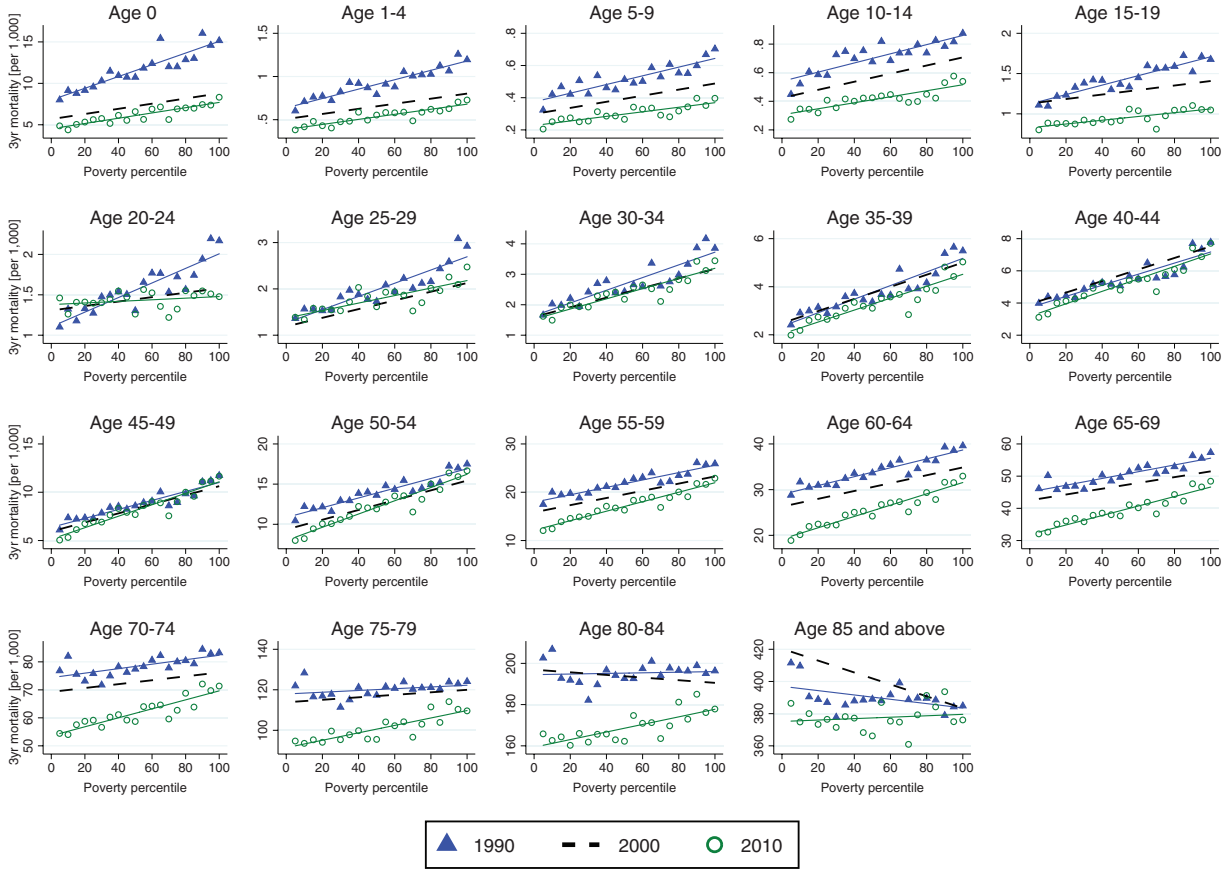


Fig. 3. Female 3-year mortality rates by poverty percentile across age groups. Data are displayed as in Fig. 2. Table S4 reports key magnitudes and standard errors.

for the least educated once these compositional changes are accounted for. Similarly, single counties that experienced declining life expectancy (*11*, *12*) tend to be poor places that have lost population over the past 20 years. If the healthiest people leave, then the ones who remain will be less healthy on average, biasing the estimated changes in mortality inequality. Our approach accounts for potential compositional changes by reordering county groups so that they represent constant shares of the population over time. In the context of county groups, however, such compositional changes do not seem to play a crucial role, as our results look very similar when we keep the county groups assigned in 1990 fixed and follow them up to 2010 (fig. S6).

One limitation of our approach is that it necessarily focuses on differences between groups of counties, whereas much of the increase in (for example) individual income inequality may be occurring within counties. However, by its nature, mortality must be calculated relative to some reference group. Using county groups as the reference allows one to cleanly answer questions about inequality between these groups in a way that may not be possible with respect to other reference groups, such as education.

What are potential causes for the different age-specific trends that we observe? Aizer and Currie (*24*) highlighted many possible reasons for large reductions in infant mortality among the poor, which have reduced inequality in mortality among infants. We are not aware of any research that has looked at the causes of reductions in mortality inequality among older children and young adult males. Some possibilities include expansions of public health insurance (*25*–*29*), other social safety net programs such as Head Start (*30*, *31*), and reductions in pollution, which tend to have disproportionate effects on the poor (*32*).

Among older adults, it is likely that at least some of the increasing disparities in mortality reflect differential patterns of both taking up and quitting smoking over their life cycles. For example, better-educated people stopped smoking much more quickly after the U.S. Surgeon General's 1964 report on the dangers of smoking (*33*, *34*). Improvements in medical care for conditions such as heart disease also tend to benefit the rich before they reach the poor. The outbreak of the opioid epidemic is another factor that may be driving increased mortality inequality and actual increases in mortality rates in middle age (*19*). As Case and Deaton (*19*) showed, it may be possible to get some insight into these questions by studying the causes of death in the Vital Statistics mortality data, although changes in measurement, measurement error, and missing data about causes mean that these data have to be interpreted cautiously.

Our results point to decreasing inequality in mortality, particularly among the younger cohorts who will form the future adult and elderly population of the United States. It is possible that survivors who would otherwise have died will be in poor health as they age and thus reduce the average level of health in the population. However, another possibility is that the declines in mortality at younger ages reflect improvements in the entire underlying distribution of health (*35*). In at least one important example—the case of expansions of public health insurance for poor infants and young children in the late 1980s and early 1990s—the reduced early death rates in these cohorts are associated with better health (*27*–*29*) and higher earnings (*25*) as these cohorts reach young adulthood. Thus, there appears good reason to hope that today's young will also be healthier when they reach old age, and that inequality in mortality will decrease among these elderly in the future.

REFERENCES AND NOTES

1. B. P. Bosworth, K. Burke, *Differential Mortality and Retirement Benefits in the Health and Retirement Study* (Brookings Institution, 2014).

Downloaded from http://science.sciencemag.org/ on May 5, 2016

2. B. Bosworth, K. Zhang, "Evidence of Increasing Differential Mortality: A Comparison of the HRS and SIPP," Center for Retirement Research at Boston College Working Paper 2015-13 (2015).
3. R. Chetty *et al.*, *JAMA* 10.1001/jama.2016.4226 (2016).
4. National Research Council, Committee on the Long-Run Macroeconomic Effects of the Aging U.S. Population, "The Growing Gap in Life Expectancy by Income: Implications for Federal Programs and Policy Responses" (2015).
5. J. Pijoan-Mas, J. V. Ríos-Rull, *Demography* **51**, 2075–2102 (2014).
6. H. Waldron, *Soc. Secur. Bull.* **67**, 1–28 (2007).
7. H. Waldron, *Soc. Secur. Bull.* **73**, 1–37 (2013).
8. J. Wilmoth, C. Boe, M. Barbieri, in *International Differences in Mortality at Older Ages: Dimensions and Sources*, E. M. Crimmins, S. H. Preston, B. Cohen, Eds. (National Academies Press, Washington, DC, 2011), pp. 337–372.
9. G. K. Singh, M. Siahpush, *Int. J. Epidemiol.* **35**, 969–979 (2006).
10. M. Ezzati, A. B. Friedman, S. C. Kulkarni, C. J. Murray, *PLOS Med.* **5**, e66 (2008).
11. C. J. Murray *et al.*, *PLOS Med.* **3**, e260 (2006).
12. H. Wang, A. E. Schumacher, C. E. Levitz, A. H. Mokdad, C. J. Murray, *Popul. Health Metr.* **11**, 8 (2013).
13. J. S. Olshansky *et al.*, *Health Aff.* **31**, 1803–1813 (2011).
14. E. R. Meara, S. Richards, D. M. Cutler, *Health Aff.* **27**, 350–360 (2008).
15. D. M. Cutler, F. Lange, E. Meara, S. Richards-Shubik, C. J. Ruhm, *J. Health Econ.* **30**, 1174–1187 (2011).
16. J. K. Montez, L. F. Berkman, *Am. J. Public Health* **104**, e82–e90 (2014).
17. Human Mortality Database; www.mortality.org.
18. D. D. Reidpath, P. Allotey, *J. Epidemiol. Community Health* **57**, 344–346 (2003).
19. A. Case, A. Deaton, *Proc. Natl. Acad. Sci. U.S.A.* **112**, 15078–15083 (2015).
20. J. Bound, A. Geronimus, J. Rodriguez, T. Waidman, "The Implications of Differential Trends in Mortality for Social Security Policy," University of Michigan Retirement Research Center Working Paper 2014-314 (2014).
21. J. B. Dowd, A. Hamoudi, *Int. J. Epidemiol.* **43**, 983–988 (2014).
22. T. Goldring, F. Lange, S. Richards-Shubik, "Testing for Changes in the SES-Mortality Gradient When the Distribution of Education Changes Too," National Bureau of Economic Research Working Paper 20993 (2015).
23. A. S. Hendi, *Int. J. Epidemiol.* **44**, 946–955 (2015).
24. A. Aizer, J. Currie, *Science* **344**, 856–861 (2014).
25. D. Brown, A. Kowalski, I. Lurie, "Medicaid as an Investment in Children: What Is the Long-Term Impact on Tax Receipts?" National Bureau of Economic Research Working Paper 20835 (2015).
26. S. Cahodes, S. Kleiner, M. F. Lovenhem, M. Grossman, "Effect of Child Health Insurance Access on Schooling," National Bureau of Economic Research Working Paper 20178 (2014).
27. S. Miller, L. R. Wherry, "The Long-Term Health Effects of Early Life Medicaid Coverage," Social Science Research Network Working Paper 2466691 (2015).
28. L. R. Wherry, B. Meyer, "Saving Teens: Using and Eligibility Discontinuity to Estimate the Effects of Medicaid Eligibility," National Bureau of Economic Research Working Paper 18309 (2013).
29. L. R. Wherry, S. Miller, R. Kaestner, B. D. Meyer, "Childhood Medicaid Coverage and Later Life Health Care Utilization," National Bureau of Economic Research Working Paper 20929 (2015).
30. J. Ludwig, D. L. Miller, *Q. J. Econ.* **122**, 159–208 (2007).
31. H. Hoynes, D. Whitmore-Schanzanbach, D. Almond, "Long Run Impacts of Childhood Access to the Safety Net," National Bureau of Economic Research Working Paper 18535 (2012).
32. A. Isen, M. Rossin-Slater, R. Walker, "Every Breath You Take Every Dollar You'll Make: The Long-Term Consequences of the Clean Air Act of 1970," National Bureau of Economic Research Working Paper 19858 (2014).
33. A. Fenelon, S. H. Preston, *Demography* **49**, 797–818 (2012).
34. D. de Walque, *J. Hum. Resour.* **45**, 682–717 (2010).
35. C. E. Finch, E. M. Crimmins, *Science* **305**, 1736–1739 (2004).

ACKNOWLEDGMENTS

We thank M. Barbieri, A. Case, A. Deaton, J. Goldstein, I. Kuziemko, R. Lee, and K. Wachter, as well as seminar participants at Berkeley, the Chicago Federal Reserve, Fundação Getúlio Vargas São Paulo, Bonn University, University of Munich, Princeton University, ETH Zurich, and the University of Zurich for comments. Supported by Princeton Center for Translational Research on Aging grant 2P30AG024928. Data and code are available at http://dx.doi.org/10.7910/DVN/C2VYNM.

SUPPLEMENTARY MATERIALS

www.sciencemag.org/content/352/6286/708/suppl/DC1
Materials and Methods
Figs. S1 to S8
Tables S1 to S4
References (*36*–*38*)

22 December 2015; accepted 17 March 2016
Published online 21 April 2016
10.1126/science.aaf1437

NEURODEVELOPMENT

Complement and microglia mediate early synapse loss in Alzheimer mouse models

Soyon Hong,[1] Victoria F. Beja-Glasser,[1]* Bianca M. Nfonoyim,[1]* Arnaud Frouin,[1] Shaomin Li,[2] Saranya Ramakrishnan,[1] Katherine M. Merry,[1] Qiaoqiao Shi,[2] Arnon Rosenthal,[3,4,5] Ben A. Barres,[6] Cynthia A. Lemere,[2] Dennis J. Selkoe,[2,7] Beth Stevens[1,8]†

Synapse loss in Alzheimer's disease (AD) correlates with cognitive decline. Involvement of microglia and complement in AD has been attributed to neuroinflammation, prominent late in disease. Here we show in mouse models that complement and microglia mediate synaptic loss early in AD. C1q, the initiating protein of the classical complement cascade, is increased and associated with synapses before overt plaque deposition. Inhibition of C1q, C3, or the microglial complement receptor CR3 reduces the number of phagocytic microglia, as well as the extent of early synapse loss. C1q is necessary for the toxic effects of soluble β-amyloid (Aβ) oligomers on synapses and hippocampal long-term potentiation. Finally, microglia in adult brains engulf synaptic material in a CR3-dependent process when exposed to soluble Aβ oligomers. Together, these findings suggest that the complement-dependent pathway and microglia that prune excess synapses in development are inappropriately activated and mediate synapse loss in AD.

Genome-wide association studies implicate microglia and complement-related pathways in Alzheimer's disease (AD) (*1*). Previous research has demonstrated both beneficial and detrimental roles of complement and microglia in plaque-related neuropathology (*2*, *3*); however, their roles in synapse loss, a major pathological correlate of cognitive decline in AD (*4*), remain to be identified. Emerging research implicates microglia and immune-related mechanisms in brain wiring in the healthy brain (*1*). During development, C1q and C3 localize to synapses and mediate synapse elimination by phagocytic microglia (*5*–*7*). We hypothesized that this normal developmental synaptic pruning pathway is activated early in the AD brain and mediates synapse loss.

The degree of region-specific synapse loss is a stronger correlate of cognitive decline in AD than counts of plaques, tangles, and neuronal loss (*8*, *9*). To determine how early synapse loss occurs, we used superresolution structured illumination microscopy (SIM) (*10*) to quantify synapse density in hippocampal CA1 stratum radiatum of familial AD-mutant human amyloid precursor protein (hAPP) ("J20") transgenic mice (*11*). Quantification of colocalized pre- and postsynaptic puncta [synaptophysin and postsynaptic density 95 (PSD95) (Fig. 1A); synaptotagmin and homer (fig. S1, A to D)] revealed a significant loss of synapses in J20 hippocampus at 3 to 4 months old (mo), an age that precedes plaque deposition (*11*, *12*). Synapse loss in preplaque J20 CA1 was confirmed by electron microscopy (fig. S1G). Confocal imaging also showed synapse loss in CA1, CA3, and dentate gyrus of 3 mo J20 hippocampus but not in striatum (fig. S1E). Synapse

[1]F.M. Kirby Neurobiology Center, Boston Children's Hospital (BCH) and Harvard Medical School (HMS), Boston, MA 02115, USA. [2]Ann Romney Center for Neurologic Diseases, Department of Neurology, Brigham and Women's Hospital (BWH) and HMS, Boston, MA 02115, USA. [3]Alector Inc., 953 Indiana Street, San Francisco, CA 94107, USA. [4]Annexon Biosciences, 280 Utah Avenue Suite 110, South San Francisco, CA 94080, USA. [5]Department of Anatomy, University of California San Francisco (UCSF), San Francisco, CA 94143, USA. [6]Department of Neurobiology, Stanford University School of Medicine, Palo Alto, CA 94305, USA. [7]Prothena Biosciences, Dublin, Ireland. [8]Stanley Center for Psychiatric Research, Broad Institute of MIT and Harvard, Cambridge, MA 02142, USA.
*These authors contributed equally to this work. †Corresponding author. Email: beth.stevens@childrens.harvard.edu

Downloaded from http://science.sciencemag.org/ on May 5, 2016

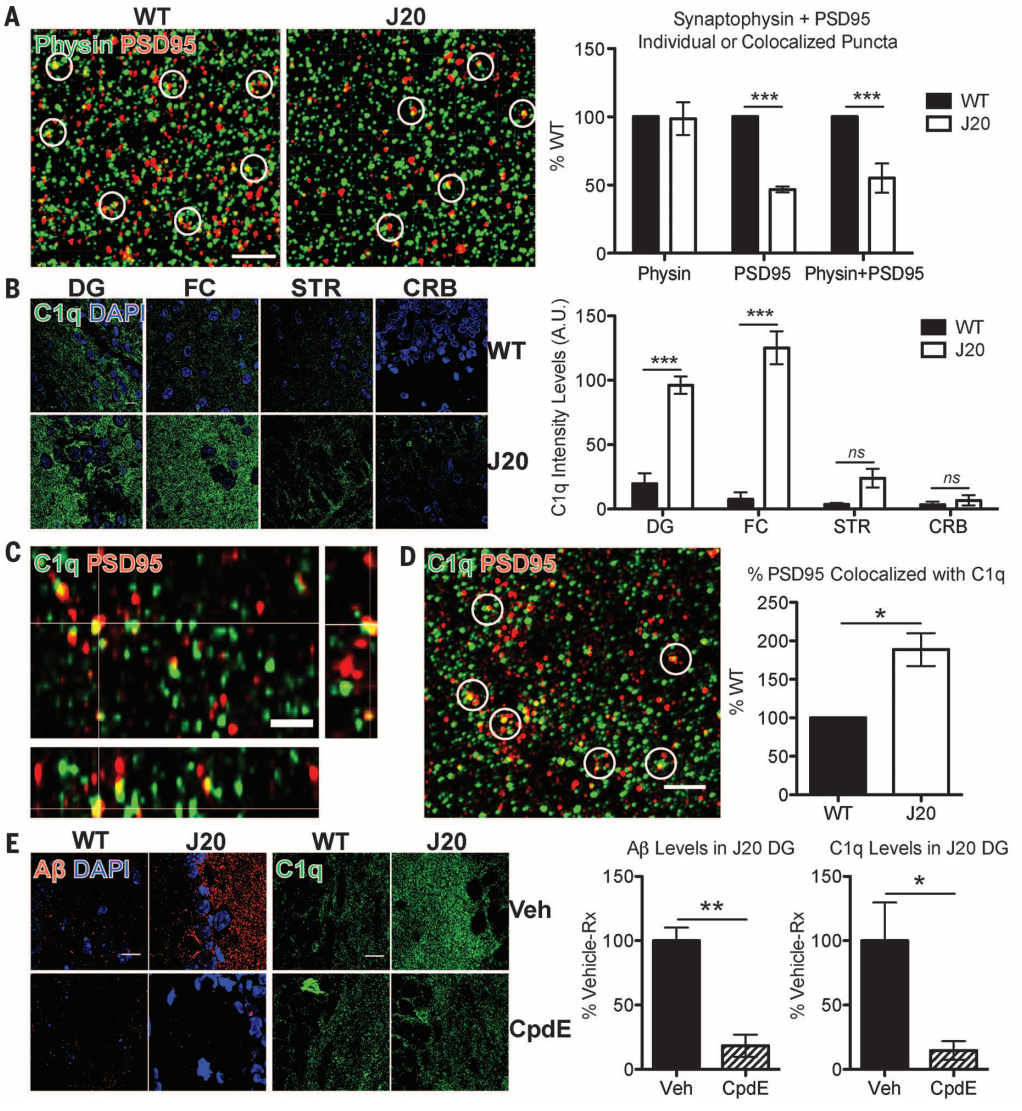


Fig. 1. C1q up-regulation and deposition onto synapses precede preplaque synapse loss in J20 mice. (**A**) Superresolution SIM images of synaptophysin (green)– and PSD95 (red)–immunoreactive puncta in stratum radiatum of 3 mo J20 or WT hippocampus (CA1). Quantification of synaptic puncta or their apposition using Imaris indicates selective loss of PSD95 in J20 hippocampus as compared to their WT littermate controls. See fig. S1. (**B**) Region-specific up-regulation of C1q (green) in 1 mo J20; DG, dentate gyrus; FC, frontal cortex; STR, striatum; CRB, cerebellum; DAPI, 4′,6-diamidino-2-phenylindole. See fig. S2. (**C**) Orthogonal view of SIM image showing colocalization of C1q (green) and PSD95 (red). (**D**) Higher percentage of PSD95 colocalized with C1q in 1 mo J20 dentate gyrus versus WT. (**E**) Compound E reduces deposited soluble Aβ (red) and C1q (green) in 1 mo J20 dentate gyrus, with minimal effect on C1q levels in WT mice. Scale bar, 2 μm (A, C, and D) or 10 μm (B and E). Means ± SEM; $n = 3$ or 4 mice per genotype or per treatment group per genotype. $^{*}P < 0.05$, $^{**}P < 0.01$, or $^{***}P < 0.001$ using two-way analysis of variance (ANOVA) followed by Bonferroni posttest (A and B), two-tailed one-sample t test (D), or two-tailed unpaired t test (E).

levels were not altered in 1 mo J20 brains versus wild-type (WT) littermates (fig. S1F), suggesting that the hippocampal synaptic loss at 3 mo is likely not a result of abnormal synaptic development.

We asked whether the classical complement cascade is up-regulated in preplaque brains when synapses are already vulnerable. C1q immunoreactivity (*13*) (antibody now available at Abcam) was elevated in J20 brains as early as 1 mo and preceding synapse loss (Fig. 1B and fig. S1). C1q elevation was region-specific, particularly in the hippocampus and frontal cortex, two regions vulnerable to synapse loss (*14*) (Fig. 1B and fig. S2A). C1q immunoreactivity was comparable between J20 and WT mice at postnatal day 21 (P21) (fig. S2B), suggesting that elevated levels at 1 mo are likely not a developmental artifact. C1q was also similarly increased in the hippocampus of another model of AD, the APP/PS1 (presenilin 1) mice (*15*) (fig. S2C). Notably, SIM demonstrated colocalization of C1q with PSD95-positive puncta in 1 mo J20 hippocampus (Fig. 1C). A higher percentage of PSD95 colocalized with C1q in the hippocampus of J20 mice than in that of WT littermates (Fig. 1D and fig. S3), suggesting that the C1q-associated synapses may be marked for elimination.

Punctate Aβ was found deposited in J20 hippocampus at 1 mo (fig. S4), long before Aβ plaques deposit (*11*, *12*), raising the question of whether C1q increase in these preplaque brains is dependent on soluble Aβ levels. To test this hypothesis, we injected the mice with compound E, a γ-secretase inhibitor that rapidly decreases Aβ production (*12*). Compound E markedly reduced soluble Aβ levels in J20 mice; there was a corresponding reduction of C1q deposition (Fig. 1E), suggesting that Aβ up-regulates C1q.

Downloaded from http://science.sciencemag.org/ on May 5, 2016

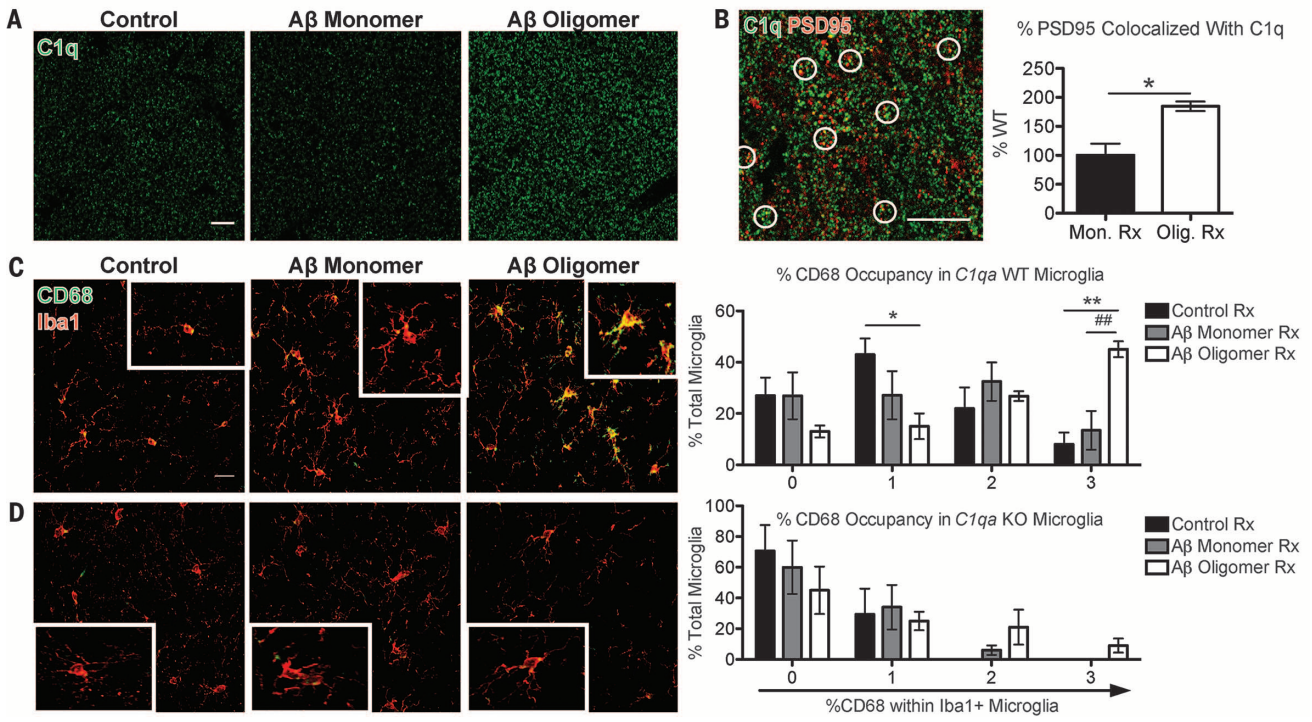
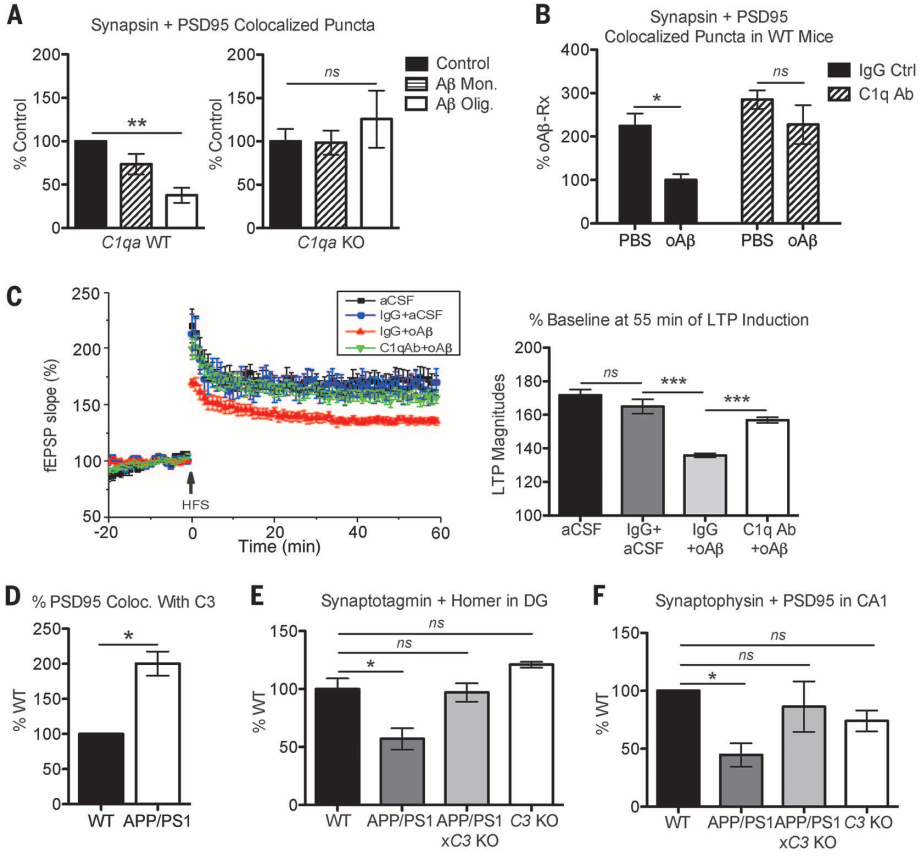


Fig. 2. Oligomeric Aβ increases C1q and microglial phagocytic activity. (**A** and **B**) Soluble Aβ oligomers in WT mice led to elevation of C1q (green) (A) and a higher percentage of PSD95 (red) colocalization with C1q versus monomers (B). (**C** and **D**) oAβ induced high levels of CD68 (green) immunoreactivity in Iba1-positive (red) microglia in WT mice (C), but not in those of *C1qa* KO mice (D). Both had negligible changes in morphology. See fig. S10. Scale bar, 10 μm (A), 5 μm (B), or 20 μm (C). Means ± SEM; n = 3 to 5 mice per treatment group per genotype. $^{*}P < 0.05$ using two-tailed t test (B) or $^{*}P < 0.05$, $^{**}P < 0.01$ versus control-treated or $^{\#\#}P < 0.01$ versus Aβ monomer–treated using two-way ANOVA followed by Bonferroni posttest (C).

Fig. 3. Complement is necessary for synapse loss and dysfunction in AD models. (**A**) Aβ oligomers induced loss of colocalized synapsin- and PSD95-immunoreactive puncta in the contralateral hippocampus of 3 mo WT mice (left panel); however, they failed to do so in *C1qa* KO mice (right panel). (**B**) Coinjection of Aβ oligomers with the function-blocking antibody against C1q, ANX-M1, but not with its IgG isotype control, prevented synapse loss in WT mice. (**C**) Pretreatment of hippocampal slices with the anti-C1q antibody, ANX-M1, prevented Aβ-mediated LTP inhibition (green) versus IgG (red). IgG alone had a minimal effect (blue) versus artificial cerebrospinal fluid (aCSF) vehicle (black). n = 6 to 11 slices per group. (**D**) Percentage of PSD95 co-localized with C3 is increased in APP/PS1 hippocampus versus that of WT mice. (**E** and **F**) Genetic deletion of *C3* prevents synapse loss in 4 mo APP/PS1 mice. Quantification of colocalized immunoreactive puncta for synaptotagmin and homer in dentate gyrus (E) or synaptophysin and PSD95 in CA1 stratum radiatum (F) of WT, APP/PS1, APP/PS1x*C3* KO, and *C3* KO hippocampi. Means ± SEM; n = 3 to 5 mice per genotype or per treatment group per genotype. $^{*}P < 0.05$, $^{**}P < 0.01$, or $^{***}P < 0.001$ using two-tailed one-sample t test (D), one-way (A, C, E, F) or two-way (B) ANOVA followed by Bonferroni posttest. ns, not significant.



Downloaded from http://science.sciencemag.org/ on May 5, 2016

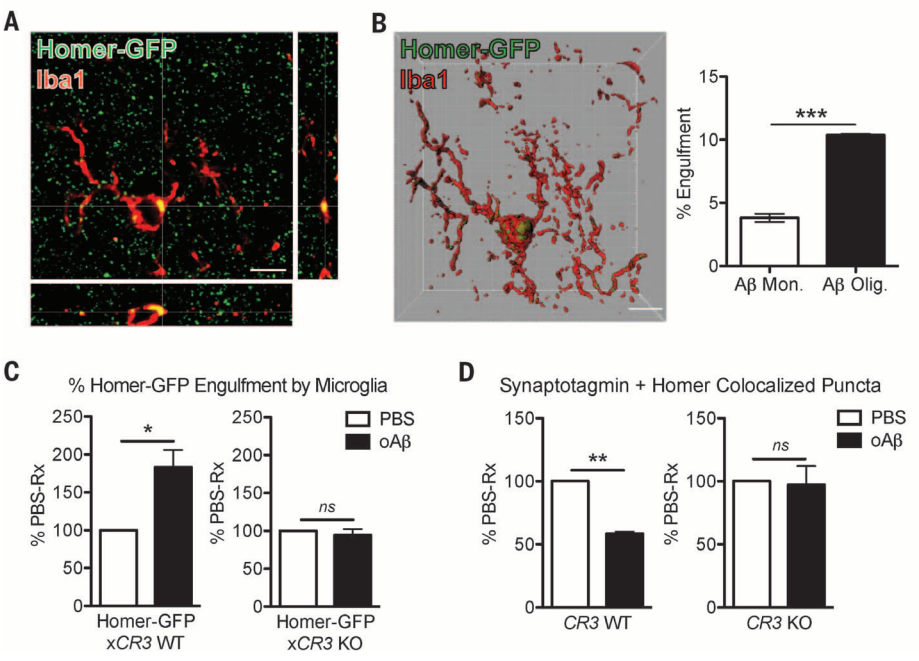


Fig. 4. Microglia engulf synapses via CR3 upon oligomeric Aβ challenge. (**A**) Orthogonal view of high-resolution confocal image shows colocalization of homer-GFP and Iba1 (red). (**B**) Three-dimensional reconstruction and surface rendering using Imaris demonstrate larger volumes of homer-GFP puncta inside microglia of oAβ-injected contralateral hippocampus versus those of monomer-injected. (**C**) Microglia of homer-GFPx*CR3* KO mice (right panel) show less engulfment of homer-GFP when challenged with oAβ versus those of homer-GFP mice (left panel). (**D**) Aβ oligomers failed to induce synapse loss in the contralateral hippocampus of *CR3* KO mice (right panel) as they did in WT mice (left panel). Scale bar, 5 μm (A and B). Means ± SEM; n = 3 mice per treatment group per genotype (n = 6 to 17 microglia analyzed per mouse). *P < 0.05, **P < 0.01, or ***P < 0.0001 using two-tailed t test (B) or two-tailed one-sample t test (C and D). ns, not significant.

To further address whether the increase of C1q is dependent on soluble Aβ, and if so, which species, we injected soluble Aβ oligomers or monomers into lateral ventricles of WT mice. Hippocampus contralateral to the injection site was examined to avoid any surgery-related effects. Oligomeric Aβ (oAβ), which is prefibrillar in nature and acts as a mediator of synapse loss and dysfunction in AD (*4*), but not the relatively innocuous monomeric Aβ or vehicle, induced C1q deposition (Fig. 2A and fig. S5). A higher percentage of PSD95 colocalized with C1q in oAβ-injected versus monomer-injected mice (Fig. 2B), in a manner similar to this colocalization in J20 mice. Together, these findings show an early and aberrant increase and synaptic localization of C1q in multiple AD model systems. Furthermore, fluorescent in situ hybridization (FISH) demonstrated up-regulated *C1qa* expression in microglia (fig. S6), implicating microglia as a major source of C1q in these preplaque brains.

To test whether C1q and oAβ act in a common pathway to eliminate synapses, we injected oAβ into lateral ventricles of *C1qa* knockout (KO) mice (*16*). Soluble oAβ induced a significant loss of colocalized synapsin- and PSD95-immunoreactive puncta in WT mice within 72 hours (Fig. 3A, left panel) (*17*). In contrast, oAβ failed to induce synapse loss in *C1qa* KO mice (Fig. 3A, right panel), suggesting that C1q is required for oAβ-induced synapse loss in vivo. To determine whether local, acute inhibition of C1 activation could similarly blunt the synaptotoxic effects of oAβ, we used an antibody against C1q (anti-C1q) (ANX-M1, Annexon Biosciences), which blocks the classical complement cascade (see fig. S7 and supplementary methods). Coadministration of the ANX-M1 anti-C1q antibody, but not its immunoglobulin G (IgG) isotype control, prevented oAβ from inducing synapse loss in WT mice (Fig. 3B). Thus, blocking C1 activation by either genetic or antibody-mediated means lessened oAβ's synaptotoxic effects.

To determine whether C1q is associated with synaptic dysfunction, we asked whether the established ability of oAβ to potently inhibit long-term potentiation (LTP) (*4*) was dependent on C1q. We tested the functional effects of the ANX-M1 anti-C1q antibody in acute hippocampal slices treated with oAβ. IgG alone had negligible effects on LTP induction in WT mouse hippocampal slices and on the ability of oAβ to inhibit LTP; however, pretreatment of hippocampal slices with the anti-C1q antibody significantly prevented the impairment of LTP by oAβ (Fig. 3C). Neither ANX-M1 nor its IgG control altered basal synaptic neurotransmission (fig. S8). Collectively, these results in hippocampal slices and in mice support C1q as a key mediator of oAβ-induced synaptic loss and dysfunction.

In the healthy developing brain, C1q promotes activation of C3, which opsonizes subsets of synapses for elimination, a process that is down-regulated in the mature brain (*5*, *6*). However, oAβ induced a significant C3 deposition in WT adult mice (fig. S7A, upper panel). This was significantly reduced in both the *C1qa* KO (fig. S7A, lower panel) and the ANX-M1 anti-C1q antibody–treated WT mice (fig. S7B), suggesting that the C3 deposition in this model is downstream of the classical complement cascade. Consistent with these findings, a higher percentage of PSD95 colocalized with C3 in J20 and APP/PS1 brains (Fig. 3D and fig. S9). To determine whether C3 is necessary for early synapse loss in AD genetic models, we crossed APP/PS1 mice, which, similar to the J20 mice, had a significant increase and localization of C1q and C3 onto hippocampal synapses (figs. S2C and S9), to *C3*-deficient mice (*18*). Quantification of colocalized pre- and postsynaptic puncta demonstrated synapse loss in 4 mo APP/PS1 hippocampus as compared to WT; however, APP/PS1x*C3* KO mice did not display this synapse loss (Fig. 3, E and F). Together, our data indicate that genetic deletion of *C3* ameliorates synapse loss in APP/PS1 mice, providing further evidence that the classical complement cascade mediates early synapse loss in AD mouse models.

Microglia express complement receptors and mediate synaptic pruning in the developing brain (*1*, *6*), raising the question of whether this normal developmental pruning pathway could be activated to mediate synapse loss in the preplaque AD brain. Consistent with this hypothesis, microglia had increased amounts of the lysosomal protein CD68 in J20 hippocampus compared to WT and less so in striatum, a less vulnerable region (figs. S1C and S10). Furthermore, in WT mice challenged with oAβ, microglia had significantly increased levels of CD68 immunoreactivity (Fig. 2C). However, in *C1qa* KO mice in which synapse loss was rescued, oAβ failed to induce such an increase (Fig. 2D), suggesting that microglia eliminate synapses through the complement pathway.

To directly test whether phagocytic microglia engulf synaptic elements, we adapted our in vivo synaptic engulfment assay (*19*) using intracerebroventricular injections of Aβ in homer-GFP (green fluorescent protein) mice (*20*) (Fig. 4A). oAβ induced a significantly higher volume of internalized homer-GFP in microglia than monomeric Aβ controls did at the contralateral hippocampus (Fig. 4B), indicating that microglia engulf synaptic elements when challenged with oAβ. Internalized homer-GFP often colocalized

Downloaded from http://science.sciencemag.org/ on May 5, 2016

with CD68 (fig. S11A), suggesting that the engulfed synapses are internalized into lysosomal compartments in a manner similar to that of developmental synaptic pruning (*6*). Notably, oAβ failed to increase synaptic engulfment in microglia lacking CR3 (*21*), a high-affinity receptor for C3 expressed on macrophages [homer-GFPx*CR3* KO versus homer-GFP mice, which received tail vein injections of phosphate-buffered saline (PBS) or oAβ (Fig. 4C)]. These data demonstrate that CR3 is necessary for oAβ-dependent engulfment of synapses by microglia.

To test whether inhibition in microglial engulfment leads to protection against oAβ-induced synapse loss, we performed tail vein injections of oAβ into WT and *CR3* KO mice. oAβ induced synapse loss in the hippocampus of WT mice but not in that of *CR3* KO mice (Fig. 4D). All CR3-positive microglia were P2RY12-positive (fig. S11), indicating that they are resident cells (*22*). Altogether, these results suggest that resident microglia engulf synaptic material when challenged by oAβ through a complement-dependent mechanism.

Synaptic deficits occur in early AD and mild cognitive impairment before onset of plaques and are some of the first signs of the neuronal degenerative process (*4*, *23*–*25*). Here we identify critical synaptotoxic roles of complement and microglia in AD models before plaque formation and neuroinflammation, in regions of the hippocampus undergoing synapse loss. Using multiple experimental approaches, we demonstrate a region-specific increase of phagocytic microglia and accumulation of C1q and C3 on synapses in preplaque brains. Microglia in the adult brain, when challenged with synaptotoxic, soluble Aβ oligomers, engulf synapses in the absence of plaque aggregates; deletion of CR3 blocks this process. Finally, inhibiting C1q, C3, or CR3 activity rescues synaptic loss and dysfunction.

Our data suggest a local activation of a developmental pruning pathway (*5*, *6*) as a key mechanism underlying oAβ-induced synapse loss in preplaque AD brain. C1q is aberrantly increased by diffusible oAβ in a region-specific manner and deposits onto synapses, triggering the activation of downstream classical complement pathway and phagocytic microglia. Blocking Aβ production in J20 mice significantly ameliorated C1q deposition in the hippocampus, and genetic or antibody-mediated inhibition of complement blocks oAβ from inducing microglial synaptic engulfment, synapse loss, and LTP inhibition. These complementary findings have direct therapeutic relevance.

We propose a model in which C1q and oAβ operate in a common pathway to activate the complement cascade and drive synapse elimination by microglia through CR3 (fig. S12). This could occur in multiple ways: Soluble oAβ associates with synaptic membranes and other synaptic markers (*4*, *26*); thus, oAβ bound to synapses may anchor C1q directly. Alternatively, oAβ binding to synapses may weaken the synapse (*4*) and expose a C1q receptor. Although specific receptors for C1q at synapses are not yet known, we have shown that C1q binds synapses in vulnerable regions undergoing synapse loss (*5*, *27*). It is also plausible that oAβ and C1q may work indirectly to mediate synapse loss through cytokines such as transforming growth factor–β (*7*), through microglial or astrocytic activation, or through other mechanisms, including major histocompatibility complex class I (MHCI)–PirB, another immune pathway critical for synapse elimination in development and AD (*28*–*30*).

Finally, our studies show that resident microglia in the adult central nervous system phagocytose synapses when challenged by synaptotoxic oAβ, implicating microglia as potential cellular mediators of synapse loss. Although microglia and complement activation are prominently involved in plaque maintenance and related periplaque neuropathology, their roles have heretofore been largely regarded as a secondary event related to neuroinflammation (*2*). Our studies directly challenge this view and suggest that microglia and immune-related pathways can act as early mediators of synapse loss and dysfunction that occur in AD models before plaques form. Although the complement pathway may not be involved in all pathological routes to AD, including plaque-associated synapse loss, the work reported here provides new insights into how synapses are lost in AD. It will be important in future studies to examine whether this microglia or the complement-dependent pathway also plays a role in plaque-associated synapse loss or in other synaptopathies, including tauopathies and Huntington's disease. If so, our findings may suggest complement and microglia as potential early therapeutic targets in AD and other neurodegenerative diseases involving synaptic dysfunction and memory decline.

REFERENCES AND NOTES

1. S. Hong, L. Dissing-Olesen, B. Stevens, *Curr. Opin. Neurobiol.* **36**, 128–134 (2016).
2. T. Wyss-Coray, J. Rogers, *Cold Spring Harb. Perspect. Med.* **2**, a006346 (2012).
3. M. E. Benoit *et al.*, *J. Biol. Chem.* **288**, 654–665 (2013).
4. L. Mucke, D. J. Selkoe, *Cold Spring Harb. Perspect. Med.* **2**, a006338 (2012).
5. B. Stevens *et al.*, *Cell* **131**, 1164–1178 (2007).
6. D. P. Schafer *et al.*, *Neuron* **74**, 691–705 (2012).
7. A. R. Bialas, B. Stevens, *Nat. Neurosci.* **16**, 1773–1782 (2013).
8. S. T. DeKosky, S. W. Scheff, *Ann. Neurol.* **27**, 457–464 (1990).
9. R. D. Terry *et al.*, *Ann. Neurol.* **30**, 572–580 (1991).
10. S. Hong, D. Wilton, B. Stevens, D. S. Richardson, Structured Illumination Microscopy for the investigation of synaptic structure and function. *Methods in Molecular Biology; Synapse Development: Methods and Protocols*.
11. L. Mucke *et al.*, *J. Neurosci.* **20**, 4050–4058 (2000).
12. S. Hong *et al.*, *J. Neurosci.* **31**, 15861–15869 (2011).
13. A. H. Stephan *et al.*, *J. Neurosci.* **33**, 13460–13474 (2013).
14. J. A. Harris *et al.*, *J. Neurosci.* **30**, 372–381 (2010).
15. J. L. Jankowsky *et al.*, *Hum. Mol. Genet.* **13**, 159–170 (2004).
16. M. Botto *et al.*, *Nat. Genet.* **19**, 56–59 (1998).
17. D. B. Freir *et al.*, *Neurobiol. Aging* **32**, 2211–2218 (2011).
18. M. R. Wessels *et al.*, *Proc. Natl. Acad. Sci. U.S.A.* **92**, 11490–11494 (1995).
19. D. P. Schafer, E. K. Lehrman, C. T. Heller, B. Stevens, *J. Vis. Exp.* **88**, 51482 (2014).
20. T. Ebihara, I. Kawabata, S. Usui, K. Sobue, S. Okabe, *J. Neurosci.* **23**, 2170–2181 (2003).
21. A. Coxon *et al.*, *Immunity* **5**, 653–666 (1996).
22. O. Butovsky *et al.*, *Nat. Neurosci.* **17**, 131–143 (2014).
23. D. J. Selkoe, *Science* **298**, 789–791 (2002).
24. S. W. Scheff, D. A. Price, F. A. Schmitt, E. J. Mufson, *Neurobiol. Aging* **27**, 1372–1384 (2006).
25. S. W. Scheff, D. A. Price, F. A. Schmitt, S. T. DeKosky, E. J. Mufson, *Neurology* **68**, 1501–1508 (2007).
26. S. Hong *et al.*, *Neuron* **82**, 308–319 (2014).
27. A. H. Stephan, B. A. Barres, B. Stevens, *Annu. Rev. Neurosci.* **35**, 369–389 (2012).
28. A. Datwani *et al.*, *Neuron* **64**, 463–470 (2009).
29. T. Kim *et al.*, *Science* **341**, 1399–1404 (2013).
30. H. Lee *et al.*, *Nature* **509**, 195–200 (2014).

ACKNOWLEDGMENTS

We thank B. Sabatini (HMS), T. Bartels (BWH), and members of the Stevens laboratory for critical reading of the manuscript; L. Dissing-Olesen (BCH) for help with the conceptual figure (fig. S12), M. Ericsson [HMS electron microscopy (EM) facility] for EM imaging, K. Kapur (BCH) for advice on statistics, D. M. Walsh (BWH) for Aβ oligomers (S26C), S. Okabe (University of Tokyo) for homer-GFP mice, and M. Leviten and T. Yednock (Annexon Biosciences) for characterization and advice on the ANX-M1 anti-C1q antibody; D. Richardson (Harvard Center for Biological Imaging), A. Hill BCH Intellectual and Developmental Disabilities Research Center Cellular Imaging Core NIH-P30-HD-18655, and H. Elliot and T. Xie (HMS Image and Data Analysis Core) for assistance with imaging and data analysis; and S. Kim (BWH), K. Colodner (BCH), and S. Matousek (BWH) for assistance with mice. The J20 mice, *C1qa* KO mice, P2RY12 antibody, and the ANX-M1 C1q function-blocking antibody are available from L. Mucke, M. Botto, O. Butovsky, and A. Rosenthal under material transfer agreements with UCSF Gladstone, Imperial College London, BWH, and Annexon Biosciences, respectively. A.R. is a cofounder, consultant, and chairman of the board of directors; B.A.B. is a cofounder and chairman of the scientific advisory board; and B.S. serves on the scientific advisory board of Annexon LLC. A.R., B.A.B., and B.S. are minor shareholders of Annexon LLC. All other authors declare no competing financial interests related to this project. The following patents related to this project have been granted or applied for: PCT/2015/010288 (S.H. and B.S.), US14/988387 and EP14822330 (S.H., A.R., and B.S.), and US8148330, US9149444, US20150368324, US20150368325, US20150368326, and US20120328601 (B.S. and B.A.B.). This work was funded by an Edward R. and Anne G. Lefler Fellowship (S.H.), Coins for Alzheimer's Research Trust (B.S.), Fidelity Biosciences Research Initiative (F-Prime) (B.S. and C.A.L.), JPB Foundation (B.A.B.), the National Institutes of Health AG000222 (S.H.), National Institute of Neurological Disorders and Stroke–NIH R01NS083845 (D.J.S.), National Institute on Aging–NIH 1RF1AG051496A (B.S.). Supplementary materials contain additional data, including materials and methods. S.H. and B.S. designed the study and wrote the manuscript, with help from all authors. S.H. performed most experiments and data analysis; V.F.B.-G. and B.M.N. performed microglial activation and engulfment experiments along with immunohistochemistry; S.R. and K.M.M. performed C1q immunohistochemistry; A.F. performed FISH; S.L. performed electrophysiology; Q.S. and C.A.L. assisted with design and collection of APP/PS1 tissue; A.R. and B.A.B. designed and characterized the ANX-M1 anti-C1q antibody; and D.J.S. contributed in the discussions and experimental design.

SUPPLEMENTARY MATERIALS

www.sciencemag.org/content/352/6286/712/suppl/DC1
Materials and Methods
Figs. S1 to S12

10 November 2015; accepted 18 March 2016
Published online 31 March 2016
10.1126/science.aad8373

Downloaded from http://science.sciencemag.org/ on May 5, 2016

EPIGENETICS

Single-molecule decoding of combinatorially modified nucleosomes

Efrat Shema,[1,2] Daniel Jones,[3] Noam Shoresh,[2] Laura Donohue,[1,2] Oren Ram,[1,2] Bradley E. Bernstein[1,2]*

Different combinations of histone modifications have been proposed to signal distinct gene regulatory functions, but this area is poorly addressed by existing technologies. We applied high-throughput single-molecule imaging to decode combinatorial modifications on millions of individual nucleosomes from pluripotent stem cells and lineage-committed cells. We identified definitively bivalent nucleosomes with concomitant repressive and activating marks, as well as other combinatorial modification states whose prevalence varies with developmental potency. We showed that genetic and chemical perturbations of chromatin enzymes preferentially affect nucleosomes harboring specific modification states. Last, we combined this proteomic platform with single-molecule DNA sequencing technology to simultaneously determine the modification states and genomic positions of individual nucleosomes. This single-molecule technology has the potential to address fundamental questions in chromatin biology and epigenetic regulation.

The activity of genes and regulatory elements is modulated by their cell type–specific chromatin organization. The fundamental building block of chromatin is the nucleosome. Nucleosomal histones are chemically modified at many amino acid positions (*1*, *2*), which has led to the hypothesis that combinatorial marks specify distinct regulatory outcomes (the "histone code") (*3*). However, our understanding of the histone code and other models (*4*) has been constrained by our limited ability to detect, quantify, and map combinatorially modified nucleosomes. Chromatin immunoprecipitation (ChIP), a prevalent method in chromatin biology, can identify the genomic location of a specific modification but cannot effectively distinguish whether coincident marks coexist on the same nucleosome or originate from different alleles or cells. Mass spectrometry can only compare marks if they are adjacent on the same histone peptide and does not address genomic location (*5*). Although alternative approaches (*6*), such as passing nucleosomes through nanochannels (*7*), show promise, they have limited throughput and/or do not provide genomic information.

We addressed these limitations by establishing a single molecule–based assay for investigating combinatorial histone modifications (Fig. 1A and figs. S1, S2, and S3). We began by isolating mononucleosomes from cells and ligating fluorescent biotinylated oligonucleotide adaptors to their free DNA ends. We captured the ligated nucleosomes in a spatially distributed manner on slides coated with polyethylene glycol (PEG) and streptavidin and incubated them with fluorescently labeled antibodies to histone modifications. We then used total internal reflection (TIRF) microscopy to record the position and modification state of each nucleosome. As proof of principle, we captured adaptor-ligated mononucleosomes from human embryonic kidney (HEK) 293 cells and incubated them with antibody to histone H3 lysine 9 acetylation (H3K9ac). We used a TIRF microscope to simultaneously detect nucleosomes by their fluorescent adaptors (Alexa555, green) and to distinguish the subset with H3K9ac by the antibody label (Alexa647, red) (Fig. 1B).

We imaged millions of nucleosomes and decoded their modification state. We found that although the nucleosome positions were fixed, the H3K9ac antibodies repeatedly bound and dissociated at a specific subset of these nucleosome positions in a dynamic pattern (fig. S2). Summation of individual binding events over time revealed that ~1% of the nucleosomes were marked by H3K9ac (Fig. 1C). In contrast, when we treated cells with histone deacetylase (HDAC) inhibitors, the fraction of acetylated nucleosomes increased to 7% (Fig. 1, C and D). When we repeated the analysis with recombinant unmodified nucleosomes, just 0.1% of nucleosomes scored (Fig. 1E and fig. S4). We also fluorescently labeled antibodies to histone H3 lysine 4 trimethylation (H3K4me3), lysine 27 trimethylation (H3K27me3), lysine 27 dimethylation (H3K27me2), and lysine 27 acetylation (H3K27ac); we confirmed their specificities by imaging unmodified recombinant nucleosomes and marked peptides and by probing arrays of modified peptides (Fig. 1, E and F, and figs. S4 and S5).

In embryonic stem cells (ESCs), developmental gene promoters appear to be concomitantly marked by repressive (H3K27me3) and activating (H3K4me3) histone modifications (*8*, *9*). This bivalent chromatin state has been suggested to poise these genes for alternate fates, but this remains controversial (*10*). Sequential ChIP and IP mass spectrometry have provided evidence for the coexistence of the opposing marks (*8*, *11*) but cannot definitely identify an individual bivalent nucleosome. We leveraged our single-molecule platform to quantify directly the coexistence of these key marks on nucleosomes derived from pluripotent ESCs, from ESCs differentiated to embryoid bodies (EBs), and from fully committed lung fibroblasts.

We captured nucleosomes and determined their positions as described above, chemically cleaved their fluorophores, and incubated them simultaneously with H3K4me3 (green) and H3K27me3 (red) antibodies (figs. S6 and S7). TIRF imaging revealed that ~6.5% of nucleosomes from ESCs carried H3K27me3 (Fig. 2A and figs. S8 and S9). This fraction was somewhat higher in EBs and lung fibroblasts, consistent with previous findings that this repressive mark expands during differentiation (*2*). The fraction of nucleosomes marked by H3K4me3 was relatively constant (ESCs, ~2%; EBs, ~1.6%; and lung, ~1.6%). Single-molecule counting revealed that 0.5% of nucleosomes in ESCs carried both marks and thus were truly bivalent (Fig. 2, A and D, and fig. S8). In contrast, in both EBs and fibroblasts, bivalent nucleosomes were much less prevalent and were depleted relative to random expectation (Fig. 2A).

A bivalent nucleosome could reflect either the symmetric co-occurrence of H3K4me3 and H3K27me3 on the same histone tail or asymmetric marking on opposite tails. To address this, we extracted individual histone molecules from ESCs, biotinylated them, spatially distributed them on our surface, and detected H3K4me3- and H3K27me3-modified tails (Fig. 2E). We found that 0.4% of H3K27me3-modified tails also carried H3K4me3. In comparison, just 0.04% of H3K27me3-modified tails scored for H3K27ac, a combination that is chemically prohibited (fig. S8). The 10-fold excess in the detection of bivalent H3 tails relative to the background suggests that symmetric bivalent nucleosomes do exist in ESCs. Nonetheless, we estimate that 94% of bivalent nucleosomes are asymmetric, whereas just 6% are modified on the same tail (fig. S8).

Genomic loci marked by bivalent chromatin in ESCs are frequently deregulated in cancer cells (*12*). Moreover, the Polycomb and trithorax complexes that catalyze H3K27me3 and H3K4me3 are often mutated in cancer (*12*). We therefore investigated these modifications in cancer cells (Fig. 2, B and C, and fig. S8). We detected bivalent nucleosomes in three cell lines that lack known Polycomb or trithorax mutations—T cell acute leukemia (DND-41), embryonic kidney (HEK293), and glioblastoma (GSC8)—at levels higher than in our differentiated models (EB and lung) but lower than in ESCs. When we examined a leukemia line (SKM-1) with a loss-of-function (LOF) mutation of the PRC2 subunit EZH2 (*13*), we observed very few H3K27me3-marked nucleosomes (~1%; Fig. 2C). We also examined a lymphoma cell line (Karpas422) with a gain-of-function (GOF) EZH2 mutation that increases its catalytic activity (*14*); we detected H3K27me3 on ~15% of nucleosomes. Bivalent nucleosomes were prevalent in the lymphoma cells, with roughly half

[1]Department of Pathology and Center for Cancer Research, Massachusetts General Hospital and Harvard Medical School, Boston, MA 02114, USA. [2]Broad Institute of MIT and Harvard, Cambridge, MA 02142, USA. [3]SeqLL, Woburn, MA 01801, USA.
*Corresponding author. Email: bernstein.bradley@mgh.harvard.edu

Downloaded from http://science.sciencemag.org/ on May 5, 2016

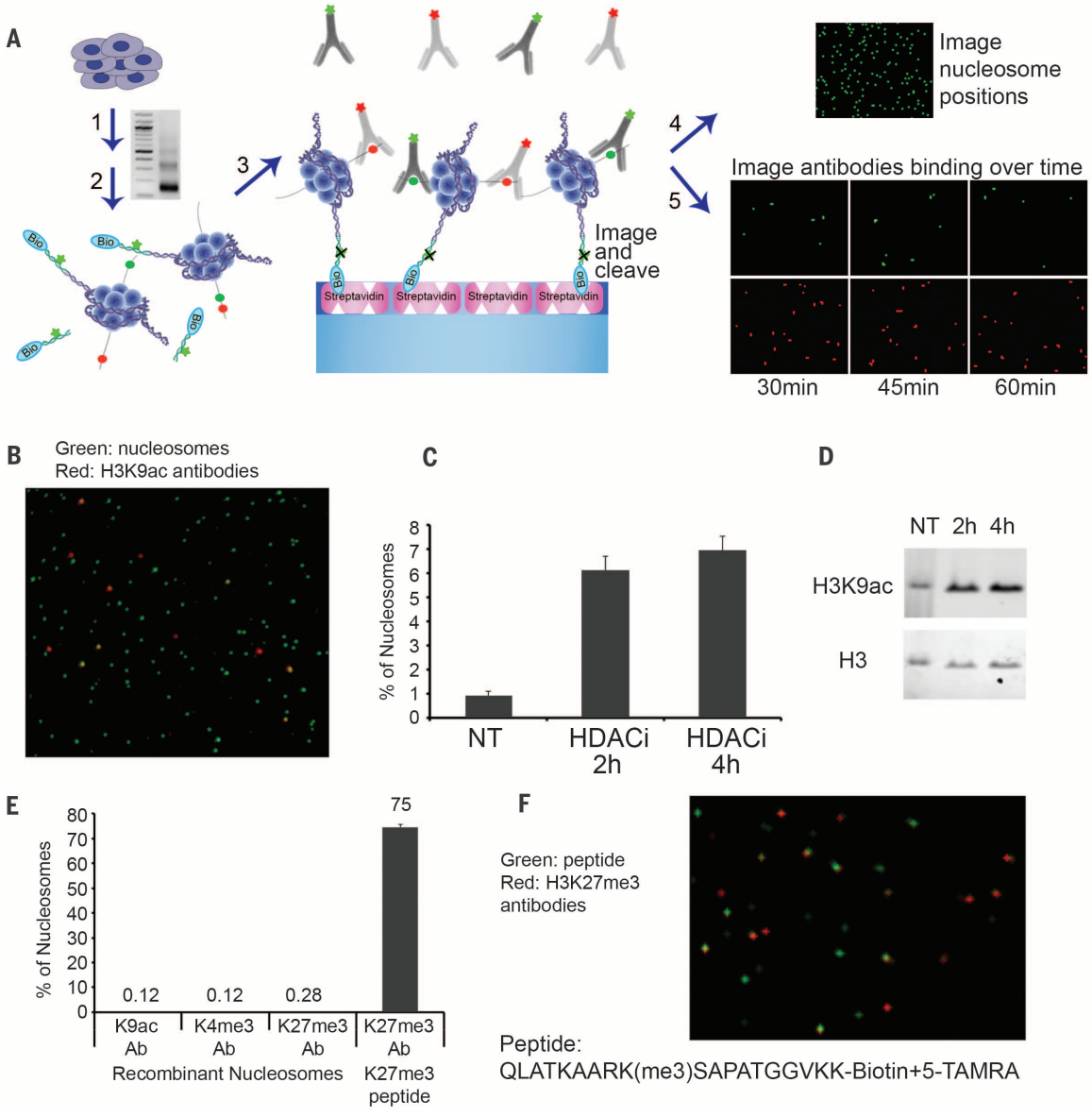


Fig. 1. Single-molecule detection of post-translational modifications on nucleosomes. (**A**) Experimental approach. Step 1: Nucleosomes from cells are prepared by micrococcal nuclease digestion. The gel shows nucleosomal DNA fragments of expected lengths. Step 2: Free DNA ends are ligated to fluorescent biotinylated oligonucleotide adaptors (Bio, biotin). Step 3: Adaptor-ligated mononucleosomes are purified on a glycerol gradient and captured on PEG-streptavidin–coated slides. Step 4: Nucleosome positions on the surface are imaged by TIRF microscopy, and the fluorophore is then cleaved from the adaptor. Step 5: Attached nucleosomes are incubated with fluorescently labeled antibodies to histone modifications. Time-lapse images detect repeated binding and dissociation events and are integrated to score modified nucleosomes. Throughout the diagram, red and green circles represent histone modifications, and the corresponding stars represent fluorophores conjugated to antibodies or oligonucleotide adaptors. In (B) to (D), HEK293 cells were treated with HDAC inhibitor (HDACi) (NT, nontreated; h, hours). (**B**) Single-molecule detection of labeled nucleosomes (Alexa555, green) bound by labeled H3K9ac antibodies (Alexa647, red). (**C**) The percentage of nucleosomes marked by H3K9ac under each condition was determined by single-molecule counting (error bars, SD). (**D**) Western blot confirms increased H3K9ac in treated cells. In (E) and (F), recombinant unmodified nucleosomes and H3K27me3-modified peptide were probed with the indicated antibodies (Ab). (**E**) The percentage of bound nucleosomes or peptides detected. (**F**) Single-molecule detection of labeled H3K27me3 peptide [TAMRA (5-carboxytetramethylrhodamine) green] with labeled H3K27me3 antibodies (Alexa647, red) at a single time point. Single-letter abbreviations for the amino acid residues are as follows: A, Ala; G, Gly; K, Lys; L, Leu; P, Pro; Q, Gln; R, Arg; S, Ser; T, Thr; and V, Val.

of all H3K4me3-marked nucleosomes carrying H3K27me3 (Fig. 2, C and F, and fig. S8). The proportion of bivalent nucleosomes is about four-fold greater than expected from random overlap, suggesting that the mutant EZH2 preferentially catalyzes H3K27me3 on nucleosomes that are marked by H3K4me3. This is consistent with the increased H3K27me3 over active promoters that has been observed in EZH2 GOF lymphomas (*15*). When we treated these lymphoma cells with an EZH2 inhibitor (*16*), H3K27me3 was preferentially lost from bivalent nucleosomes (Fig. 2G). This may reflect increased nucleosome turnover and/or preferential demethylation in such regions.

We next explored higher-order combinations of H3K27ac [which marks active enhancers (*2*)], H3K27me2 [which marks intergenic regions (*17*)], H3K4me3, and H3K27me3 (Fig. 3A and fig. S11). Monitoring of four or more histone modifications on single nucleosomes was carried out in successive steps of antibody incubation and imaging, which were separated by a wash step to remove antibodies. Single-molecule counting revealed that the proportions of nucleosomes marked by each of the four modifications were similar between ESCs and lung fibroblasts, with the exception that H3K27 methylations were modestly higher in the differentiated cells (Fig. 3A). When we considered these modifications in combination, however, we observed considerable differences between cell types (Fig. 3B and fig. S11).

ESC chromatin was enriched for the bivalent combination and for the pairwise combination of the two active marks, H3K4me3 and H3K27ac. The other pairwise combinations were present in roughly the same proportions as would be

Downloaded from http://science.sciencemag.org/ on May 5, 2016

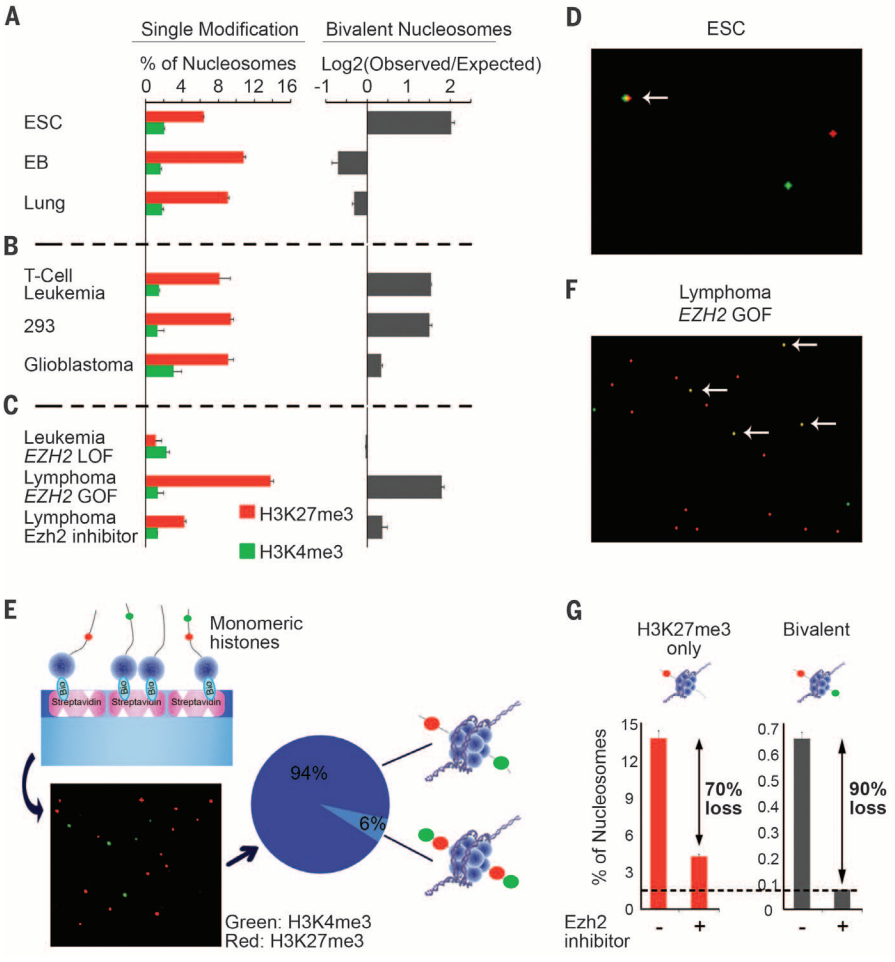


Fig. 2. Single-molecule imaging of symmetric and asymmetric bivalent nucleosomes. (**A**) We investigated modifications on nucleosomes from pluripotent ESCs, EBs, and lung fibroblasts. On the left, colored bars indicate percentages of nucleosomes with H3K27me3 (red) or H3K4me3 (green) (error bars, SD). On the right, black bars indicate relative over- or underrepresentation of bivalent nucleosomes. Results on the right are presented as the log2 ratio of the observed proportion of bivalent nucleosomes to the proportion of nucleosomes with these two marks that would be expected from random association (the latter is calculated as the fraction with H3K27me3 multiplied by the fraction with H3K4me3; fig. S10). (**B**) Nucleosomes from a T cell acute lymphoblastic leukemia line, from HEK293 cells, and from glioblastoma stem cells were decoded as in (A). (**C**) Nucleosomes from an acute leukemia line with an *EZH2* LOF mutation, a lymphoma line with an *EZH2* GOF mutation, and the lymphoma cells treated with EZH2 inhibitor GSK126. (**D**) A magnified TIRF image overlay reveals three nucleosomes, one with H3K27me3 (red), one with H3K4me3 (green), and one with concomitant bivalent modifications (arrow). (**E**) The diagram and image show H3K27me3 and H3K4me3 antibodies binding to individual histones isolated from ESCs. 94% of bivalent nucleosomes are asymmetric, whereas just 6% are modified on the same tail. In (F) and (G), the lymphoma cell line with the *EZH2* GOF mutation was treated with GSK126 for 3 days. (**F**) Nucleosomes were decoded for H3K27me3 and H3K4me3. The image shown is of pretreated samples, with arrows highlighting bivalent nucleosomes. (**G**) Plot showing the percentages of H3K4me3-negative (H3K27me3 only; left) and H3K4me3-positive (bivalent; right) nucleosomes carrying H3K27me3 (error bars, SD). Bivalent nucleosomes were more likely to lose H3K27me3 after treatment with GSK126.

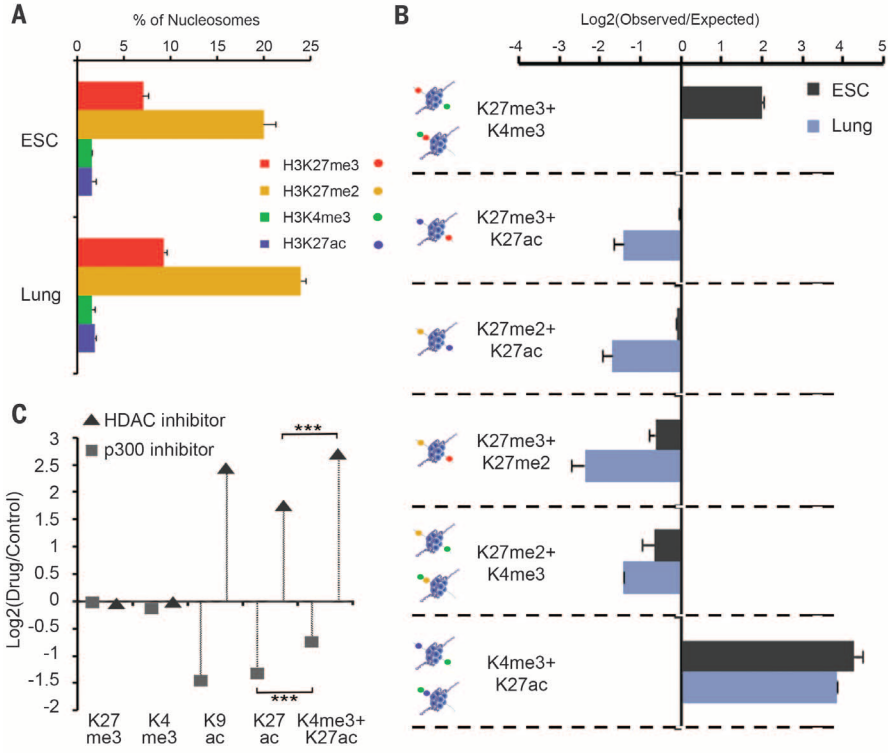


Fig. 3. Higher-order modification states across cellular states and inhibitor treatments. (**A**) Individual nucleosomes from ESCs and lung fibroblasts were decoded for H3K4me3, H3K27me3, H3K27me2, and H3K27ac, as described in Fig. 1. Bars depict the percentage of nucleosomes with the indicated modification (error bars, SD). (**B**) Bars indicate the relative over- or underrepresentation of each possible modification pair, relative to random expectation, as in Fig. 2A. Opposing modifications were relatively more likely to coexist in ESCs than in lung fibroblasts. (**C**) ESCs were treated with dimethyl sulfoxide (control), HDAC inhibitor (sodium butyrate), or p300 inhibitor (C646). Nucleosomes were isolated and decoded for H3K27me3, H3K4me3, H3K9ac, and H3K27ac. The plot shows the effects of the inhibitors on each single modification and on the combination of H3K27ac and H3K4me3. ***$P < 0.001$.

Downloaded from http://science.sciencemag.org/ on May 5, 2016

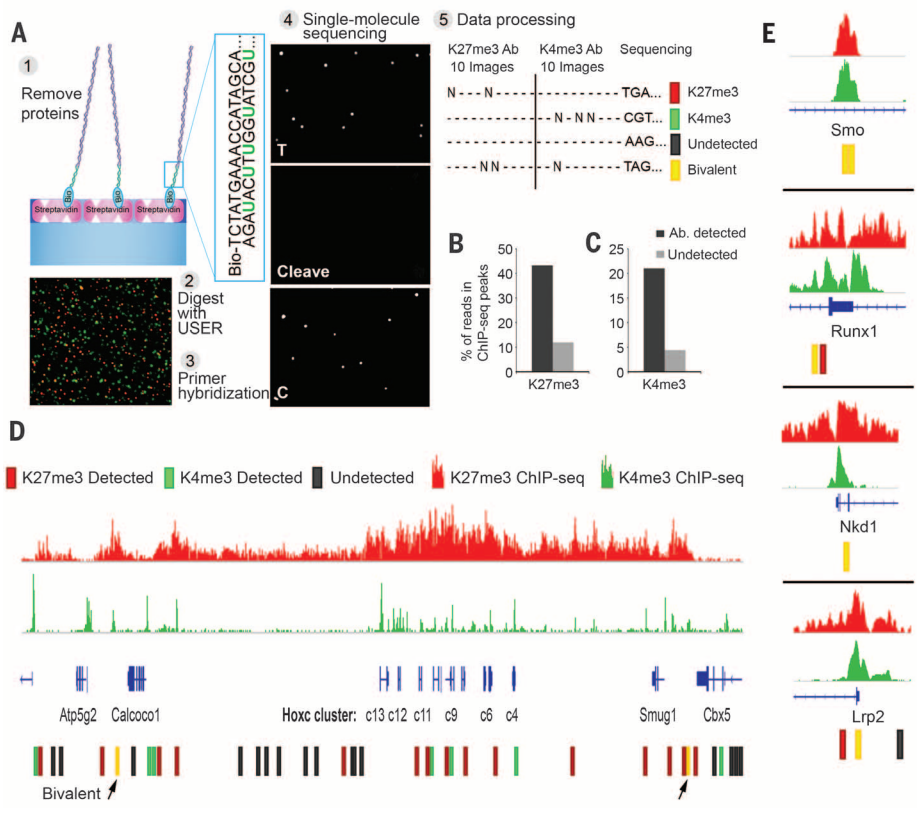


Fig. 4. Single-molecule sequencing determines genomic positions of modified nucleosomes. (**A**) Experimental approach. Step 1: Nucleosomes are captured and probed for their modification state, as in Fig. 1A. Histones are evicted by increasing salt concentration. Step 2: The enzyme USER (uracil-specific excision reagent) is applied to excise uracil bases incorporated into the nonbiotinylated adaptor strand and expose a known sequence. Step 3: Complementary primer is hybridized to the adaptor. The image shows single-molecule detection of nucleosomal DNA (Alexa647, red) and primer (Alexa555, green). Step 4: Direct single-molecule DNA sequencing-by-synthesis is performed (*22*). The images reflect two sequencing cycles, covering the incorporation of thymine, the cleavage of the fluorophore and terminator, and the incorporation of cytosine. Step 5: For each *x*,*y* coordinate on the surface, sequence data are analyzed and integrated with the initial images that scored the antibody binding and modification states of the corresponding nucleosomes. (**B**) Single-molecule reads were aligned to the genome. The plot shows percentages of H3K27me3-modified nucleosome reads (detected) or unmodified nucleosome reads (undetected) that aligned to H3K27me3-enriched regions per conventional ChIP-seq. (**C**) Percentages of H3K4me3-modified nucleosome reads that aligned to H3K4me3-enriched regions per conventional ChIP-seq. (**D**) Gene annotations (blue) for the *HOXC* gene cluster are shown with H3K27me3 and H3K4me3 ChIP-seq tracks. Single-molecule reads that aligned to these regions are indicated, along with the modification status of the corresponding nucleosome. (**E**) Analogous data for other developmental loci for which bivalent nucleosomes were definitively identified.

expected from chance overlap. The lung fibroblasts were enriched for the pairwise combination of active marks, like the ESCs, but not for the bivalent nucleosomes. However, the lung fibroblast chromatin was depleted for the other combinations (Fig. 3B), including the three pairwise states for H3K27 modifications, which are by definition asymmetric. These distinct combinatorial modification patterns probably relate to different chromatin environments in the respective cell types, particularly the hyperdynamic nature of ESC chromatin (fig. S12) (*18*).

We next examined how combinatorial chromatin states change upon treatment with a pan-HDAC inhibitor or with a p300 histone acetyltransferase inhibitor. HDAC inhibition significantly increased levels of H3K9ac and H3K27ac, whereas p300 inhibition had the opposite effect (Fig. 3D and fig. S11). Neither treatment altered H3K4me3 or H3K27me3. However, the changes in histone acetylation occurred preferentially on nucleosomes with specific markings. In the case of HDAC inhibition, increased acetylation preferentially affected H3K4me3-marked nucleosomes, consistent with the modulation of acetylation levels by HDACs at active promoters (*19*). In contrast, H3K4me3-marked nucleosomes were less affected by p300 inhibition, consistent with a role for this enzyme at enhancers (*20*).

Phosphorylation of the histone variant H2Ax (γH2Ax) is one of the earliest and best-studied marks of DNA damage. We therefore examined γH2Ax levels on individual nucleosomes extracted from ESCs. We found that ~2% of the nucleosomes contained γH2Ax at baseline (fig. S13). Combinatorial analysis revealed that γH2Ax was specifically enriched on nucleosomes with activating marks (H3K27ac and H3K4me3). Treatment with HDAC inhibitors led to concomitant increases in acetylation and γH2Ax levels, consistent with studies documenting high baseline levels of γH2Ax associated with decondensed chromatin in ESCs (*21*).

Last, we used single-molecule sequencing technology to read the DNA associated with each individual nucleosome (Fig. 4A and fig. S14). We captured adaptor-ligated nucleosomes from ESCs and queried their H3K27me3 and H3K4me3 status. We then displaced the histone octamers, leaving behind double-stranded nucleosomal DNA. We enzymatically cleaved the uracil bases that were incorporated into the nonbiotinylated strand of the adaptor, exposing a known sequence that was used as a priming site for single-molecule sequencing-by-synthesis (*22*). We used TIRF microscopy to detect repeated cycles of base addition, separated by chemical cleavage of the fluorescent label and terminator.

Integration of TIRF images for antibody-based detection of modifications with subsequent sequencing reaction data collected on the same flow cell allowed us to coordinately determine the modification state and DNA sequence of each nucleosome (Fig. 4). More than 80% of the ~300,000 reads aligned to the mouse genome. We then compared the genomic localization of individual nucleosomes with their modification states. Of the ~26,000 reads for which the corresponding nucleosomes scored positively for H3K27me3, 45% aligned to genomic regions within H3K27me3 ChIP sequencing (ChIP-seq) peaks (Fig. 4B). This is consistent with the 30 to 50% of reads that map to enriched intervals in a typical H3K27me3 ChIP-seq experiment. In comparison, just 12% of H3K27me3-negative nucleosomes aligned to H3K27me3 ChIP-seq peaks. In a subset of these experiments, we probed the sequenced nucleosomes for both H3K27me3 and H3K4me3, yielding ~1000 aligned reads for concomitantly marked molecules and thus providing the first definitive localization of individual bivalent nucleosomes (Fig. 4, D and E).

We have taken a critical step toward defining the nature and importance of combinatorial chromatin modifications. We used single-molecule technology to decode concurrent modifications on individual nucleosomes and sequence the associated DNA. We identified individual bivalent nucleosomes with concomitant repressive and activating marks and mapped their genomic locations. We also documented other combinatorial modification states whose proportions change during cellular specification or upon treatment with epigenetic inhibitors. The single-molecule assay that we describe here requires little starting material and is highly scalable, given that many millions or even billions of nucleosomes may be decoded and sequenced in an automated imaging run.

Downloaded from http://science.sciencemag.org/ on May 5, 2016

REFERENCES AND NOTES

1. C. M. Rivera, B. Ren, *Cell* **155**, 39–55 (2013).
2. A. J. Bannister, T. Kouzarides, *Cell Res.* **21**, 381–395 (2011).
3. T. Jenuwein, C. D. Allis, *Science* **293**, 1074–1080 (2001).
4. J. S. Lee, E. Smith, A. Shilatifard, *Cell* **142**, 682–685 (2010).
5. S. Sidoli, B. A. Garcia, *Proteomics* **15**, 2901–2902 (2015).
6. D. Gomez, L. S. Shankman, A. T. Nguyen, G. K. Owens, *Nat. Methods* **10**, 171–177 (2013).
7. P. J. Murphy *et al.*, *Proc. Natl. Acad. Sci. U.S.A.* **110**, 7772–7777 (2013).
8. B. E. Bernstein *et al.*, *Cell* **125**, 315–326 (2006).
9. V. Azuara *et al.*, *Nat. Cell Biol.* **8**, 532–538 (2006).
10. P. Voigt, W. W. Tee, D. Reinberg, *Genes Dev.* **27**, 1318–1338 (2013).
11. P. Voigt *et al.*, *Cell* **151**, 181–193 (2012).
12. S. B. Baylin, P. A. Jones, *Nat. Rev. Cancer* **11**, 726–734 (2011).
13. T. Ernst *et al.*, *Nat. Genet.* **42**, 722–726 (2010).
14. D. B. Yap *et al.*, *Blood* **117**, 2451–2459 (2011).
15. W. Béguelin *et al.*, *Cancer Cell* **23**, 677–692 (2013).
16. M. T. McCabe *et al.*, *Nature* **492**, 108–112 (2012).
17. K. J. Ferrari *et al.*, *Mol. Cell* **53**, 49–62 (2014).
18. E. Meshorer, T. Misteli, *Nat. Rev. Mol. Cell Biol.* **7**, 540–546 (2006).
19. O. Ram *et al.*, *Cell* **147**, 1628–1639 (2011).
20. N. D. Heintzman *et al.*, *Nat. Genet.* **39**, 311–318 (2007).
21. V. Turinetto, C. Giachino, *Nucleic Acids Res.* **43**, 2489–2498 (2015).
22. T. D. Harris *et al.*, *Science* **320**, 106–109 (2008).

ACKNOWLEDGMENTS

We thank I. Tirosh, P. Blainey, K. Xiong, and S. Elledge for constructive discussions; J. Reifenberger for help with imaging technology; M. Bray for help with image analysis; I.-S. Kim, K. Bouazoune, C. Epstein, and J. Kaur for their experimental contributions; and S. Deindl, B. Liau, and R. Ryan for valuable experimental advice. E.S. is supported by the Jane Coffin Childs Memorial Fund for Medical Research. D.J. is partially supported by National Human Genome Research Institute–Small Business Innovation Research grant R44HG005279. This research was supported by funds from the National Human Genome Research Institute, the Klarman Cell Observatory, and the Howard Hughes Medical Institute. Sequencing data are available in the supplementary materials (database S1). D.J. is a founder and the president of SeqLL, which contributed to the technologies described in this study. E.S., D.J., and B.E.B. have filed a provisional patent covering single-molecule methodologies described in the paper.

SUPPLEMENTARY MATERIALS

www.sciencemag.org/content/352/6286/717/suppl/DC1
Materials and Methods
Figs. S1 to S14
References (*23*–*28*)
Database S1

29 October 2015; accepted 6 April 2016
10.1126/science.aad7701

CELL BIOLOGY

Microtubule doublets are double-track railways for intraflagellar transport trains

Ludek Stepanek and Gaia Pigino*

The cilium is a large macromolecular machine that is vital for motility, signaling, and sensing in most eukaryotic cells. Its conserved core structure, the axoneme, contains nine microtubule doublets, each comprising a full A-microtubule and an incomplete B-microtubule. However, thus far, the function of this doublet geometry has not been understood. We developed a time-resolved correlative fluorescence and three-dimensional electron microscopy approach to investigate the dynamics of intraflagellar transport (IFT) trains, which carry ciliary building blocks along microtubules during the assembly and disassembly of the cilium. Using this method, we showed that each microtubule doublet is used as a bidirectional double-track railway: Anterograde IFT trains move along B-microtubules, and retrograde trains move along A-microtubules. Thus, the microtubule doublet geometry provides direction-specific rails to coordinate bidirectional transport of ciliary components.

The cilium is a conserved organelle that plays a fundamental role in signaling, sensing, and motility. Cilia have a complex microtubule-based structure that is not found in other cellular compartments. This structure includes nine peripheral microtubule doublets, each comprising a complete A-tubule and an incomplete B-tubule. However, the function of this distinctive conserved geometry has so far been unknown.

In addition to serving as platforms for periodically arranged axonemal proteins and protein complexes, ciliary microtubule doublets function as railways for intraflagellar transport (IFT), the process required for the assembly and disassembly of the cilium (*1*). Large protein complexes, known as IFT trains (*2*, *3*), rapidly traverse up and down the cilium to move ciliary building blocks between the cell body and the ciliary distal tip (*4*–*7*), where the assembly of the cilium takes place. Electron microscopy (EM) shows that IFT trains move along the doublets while keeping contact with the ciliary membrane (*2*, *3*, *8*). It has thus far been unclear, however, how the IFT machinery is organized to avoid collisions between anterograde and retrograde trains.

In trypanosome flagella, anterograde IFT trains move at different speeds and can approach each other and fuse, similar to trains shunting, suggesting that anterograde trains might travel on a restricted set of axonemal microtubule doublets (*9*). No such interactions are observed between retrograde trains, nor do trains moving in opposite directions collide. To further analyze the dynamics and potential interactions of IFT trains in cilia, we imaged green fluorescent protein (GFP)–tagged trains in *Chlamydomonas* cells by means of total internal reflection fluorescence (TIRF) microscopy (fig. S1 and movies S1, S2, and S3). As expected, we observed anterograde-anterograde and retrograde-retrograde train interactions. Typically, a faster train caught up with a slower one moving in the same direction and both would then progress together at the same speed (fig. S1 and movies S2 and S3). Thus, it appears that IFT trains moving in the same direction often share the same microtubule rail. We never observed collisions between trains that traveled in opposite directions (supplementary text). Because oppositely directed trains passed by each other without changes in the direction of motion (fig. S1), a mechanism must exist to prevent collisions.

Although it is possible that trains could switch to another microtubule when they encounter a train moving in the opposite direction, this would be predicted to cause deceleration, which was not evident in our kymographs (see also the supplementary text). In trypanosomes, IFT trains avoid microtubule doublets that contact the paraflagellar rod (*10*), raising the possibility that IFT trains can recognize specific microtubule doublets. This could allow anterograde and retrograde trains to use different axonemal microtubules. However, the resolution required to test this hypothesis cannot be achieved with TIRF microscopy. Only EM offers sufficient resolution to see detailed interactions between IFT trains and microtubules. Previous EM work, comparing IFT trains from flagella of wild-type cells and from those of mutant cells with defective IFT, has suggested that anterograde and retrograde trains can be distinguished on the basis of ultrastructure and size (*8*). Long and short IFT trains have been proposed to be associated with anterograde and retrograde transport, respectively (*8*). However, the lack of dynamic information has precluded a definitive interpretation of the directionality of IFT trains.

To overcome the technical limitations of static EM, we developed a correlative light and EM (CLEM) approach. Because the currently available CLEM techniques (*11*) do not provide sufficient spatiotemporal resolution to analyze IFT trains, which move at 2.5 to 4 μm/s, we developed a novel method that allows millisecond resolution in correlative TIRF and three-dimensional (3D) EM

Max Planck Institute of Molecular Cell Biology and Genetics (MPI-CBG), Pfotenhauerstraße 108, 01307 Dresden, Germany.
***Corresponding author. Email: pigino@mpi-cbg.de**

Downloaded from http://science.sciencemag.org/ on May 5, 2016

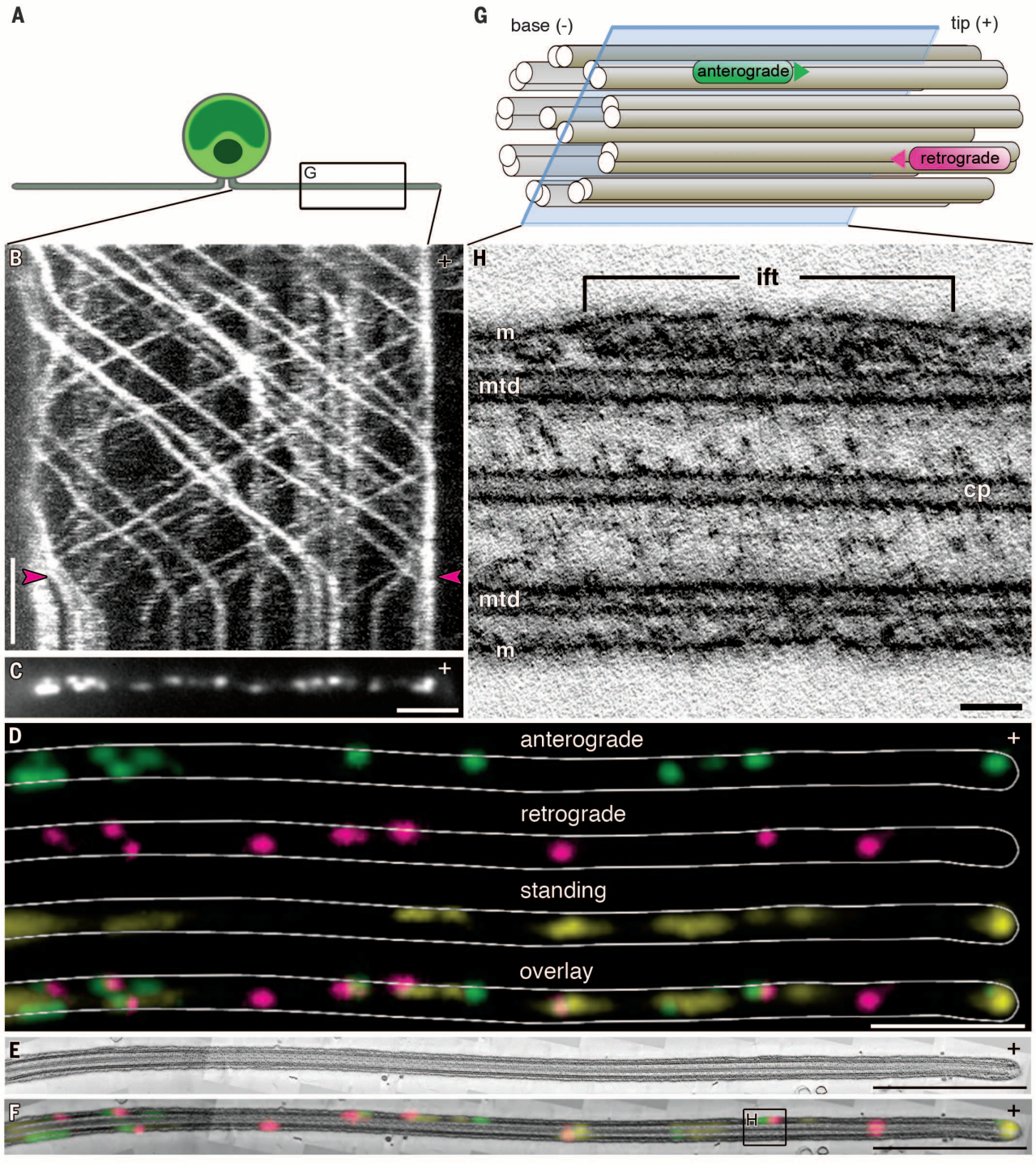


Fig. 1. Time-resolved CLEM of complete flagella. (**A**) Diagram of a *Chlamydomonas* cell with flagella in the gliding position. The area in the rectangle is enlarged in (G). (**B**) Kymograph showing fixation during live-cell imaging of *Chlamydomonas* (IFT27-GFP strain). Magenta arrowheads indicate the time point of glutaraldehyde addition. (**C**) TIRF microscopy image of the positions of IFT trains after fixation. (**D**) Each IFT train was color-coded according to the direction of movement: anterograde, green; retrograde, magenta; and standing, yellow. Intensity and contrast were adjusted separately for each fluorescent particle. (**E**) Longitudinal section through the cilium 3D reconstruction, assembled from 12 tomograms. (**F**) Overlay of fluorescence and EM images on the section shown in (E). The area in the rectangle is enlarged in (H). (**G**) Diagram of anterograde and retrograde trains traveling along microtubule doublets. The plane of the virtual slice in (H) is marked. (**H**) Virtual slice through the tomogram, containing an anterograde IFT train (m, membrane; mtd, microtubule doublet; cp, central pair microtubule; ift, IFT train). Throughout, plus signs indicate flagellar tips. EM virtual slice thickness, 7 nm; vertical scale bar, 2 s (B); horizontal scale bars, 2 μm [(B) to (F); the scale bar in (C) also applies to (B)] and 50 nm (H).

Downloaded from http://science.sciencemag.org/ on May 5, 2016

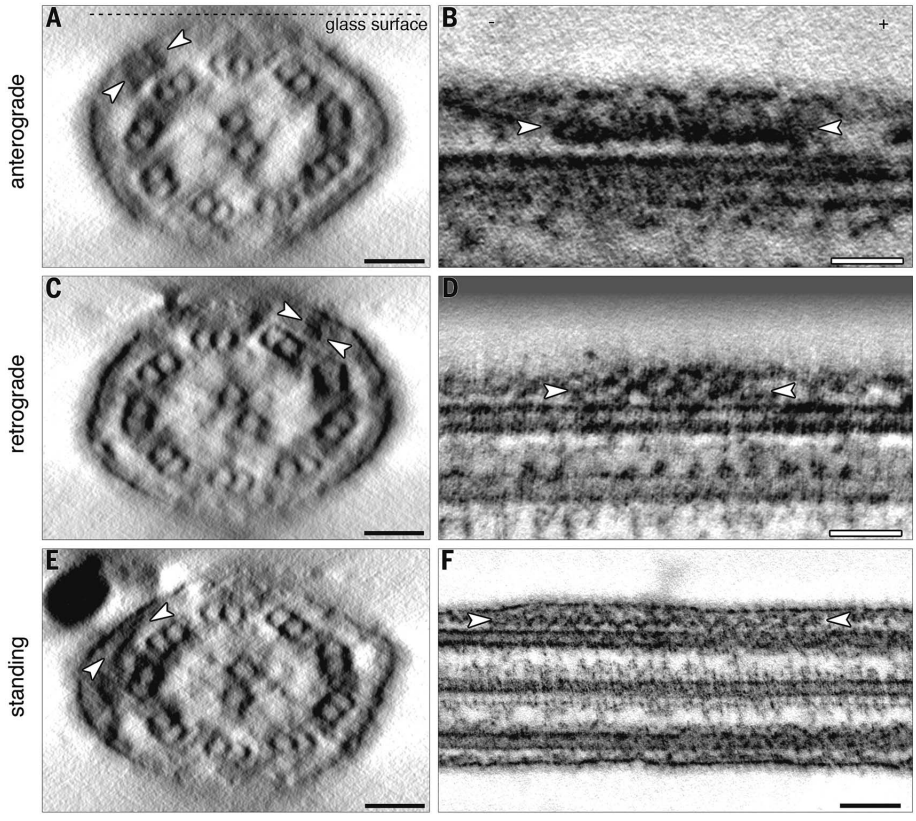


Fig. 2. Morphology of anterograde, retrograde, and standing trains. (**A**) Anterograde train in cross-sectional view and (**B**) longitudinal view. (**C**) Retrograde train in cross-sectional view and (**D**) longitudinal view. (**E**) Standing train in cross-sectional view and (**F**) longitudinal view. Arrowheads show the borders of IFT trains. Scale bars, 50 nm [(A) to (E)] and 100nm (F). Virtual slice thicknesses, 105 nm [(A), (C), and (E)], 70 nm [(B) and (D)], and 10 nm (F). Cross-sectional views [(A), (C), and (E)] are shown in proximal-to-distal orientation. Proximal (−) and distal (+) regions [(B), (D), and (F)] are indicated in (B). The position of the glass slide is indicated in (A).

(Fig. 1 and fig. S2). Briefly, a *Chlamydomonas* cell in gliding position was rapidly fixed with glutaraldehyde during time-lapse TIRF imaging of GFP-tagged IFT trains in the cilium (Fig. 1, B and C, and movie S4). In this way, the position of each fixed IFT train could be cross-referenced to its direction of movement just before fixation (Fig. 1D). In addition to anterograde trains (shown in green in Fig. 1D) and retrograde trains (shown in magenta in Fig. 1D), we also observed trains that did not move in the cilium during TIRF acquisition (shown in yellow in Fig. 1D). The same cell was then prepared for electron tomography, using a modification of the flat embedding protocol (*8*, *12*). A reconstruction of the 3D structure of the entire cilium was then obtained by stitching together several tomograms (Fig. 1E). This provided an overview of the complete cilium and offered sufficient spatial resolution to observe the structural details of each train and its interaction with microtubules. Last, correlation of light microscopy (LM) movies and electron tomograms (materials and methods and fig. S2) allowed us to identify anterograde and retrograde trains unambiguously in a complete flagellum (Fig. 1, F and H) and describe their ultrastructure.

In contrast to previous studies (*8*), our CLEM analysis revealed that anterograde and retrograde trains are of similar length (Fig. 2, B and D, and fig. S3, A to H). We measured a mean length of 233 nm (SD = 73 nm, n = 50) for anterograde trains and 209 nm (SD = 41 nm, n = 27) for retrograde trains (Fig. 2 and fig. S4). Nevertheless, anterograde and retrograde trains could be distinguished by their distinctive appearance (Fig. 2, A to D, and fig. S3, A to H). The morphology of the anterograde trains corresponded to that of those previously described as short trains (*8*) and has often been observed in electron micrographs of IFT trains (*2*, *13*). The anterograde trains appeared as compact electron-dense structures with clearly defined boundaries. In most of the 3D reconstructions of anterograde IFT trains, the main body of the train had repeating units, possibly IFT complexes, with a periodicity that ranged between 8 and 16 nm (Fig. 2B and fig. S3A). A characteristic feature of these trains was a straight plate-like structure at the interface between the train and the microtubule (Fig. 2, A and B; fig. S3, A to D; and movie S5). The structure of the retrograde trains appeared less condensed and less regular (Fig. 2, C and D; fig. S3, E to H; and movie S6), although in some tomograms, we observed repeating structures (fig. S3, E and F) with a similar periodicity to that previously reported for so-called long trains (*8*). The ultrastructure of these trains has not been reported in the literature, probably because it is not distinctive enough to be recognized as related to IFT without a CLEM approach.

We also identified another class of IFT train, which differed from anterograde and retrograde trains in both motility and morphology. These static trains appeared as bright standing particles along the cilium in TIRF microscopy (Fig. 1, B to D) and were 650 nm long in EM images (SD = 106 nm, n = 9) (fig. S4), with a regular 40-nm periodicity (Fig. 2F; fig. S3, I to K; and movie S7). Their ultrastructure and size clearly resembled the morphology of the long trains described previously (*8*). Our findings can thus be used to classify anterograde, retrograde, and standing IFT trains based on the correlation of ultrastructure and dynamics.

Next, we addressed the hypothesis that anterograde and retrograde trains avoid collisions by using different microtubule doublets. We first numbered the doublets (*14*) and then analyzed the positions of IFT trains in the flagellum. Anterograde and retrograde trains could share the same microtubule doublet (Fig. 3, A and I), leaving open the question of how collisions between trains that move in opposite directions are avoided. To answer this question, we carried out a more detailed analysis of the localization of the trains on the microtubule doublet. Only anterograde trains were associated with the B-microtubule (Fig. 3, A, B, D, E, F, and I, and fig. S5), and only retrograde trains were associated with the A-microtubule (Fig. 3, A, C, D, G, H, and I, and fig. S5). To confirm these observations and obtain more detailed 3D images of the connections between IFT trains and microtubules, we performed the same CLEM technique on cross sections of the cilium. With this approach, we observed clear connections (possibly representing the positions of the motors) between A-microtubules and retrograde trains and between B-microtubules and anterograde trains (Fig. 3, E to H). Thus, collisions between anterograde and retrograde IFT trains are prevented by direction-specific usage of the two microtubules in a doublet (fig. S6).

Downloaded from http://science.sciencemag.org/ on May 5, 2016

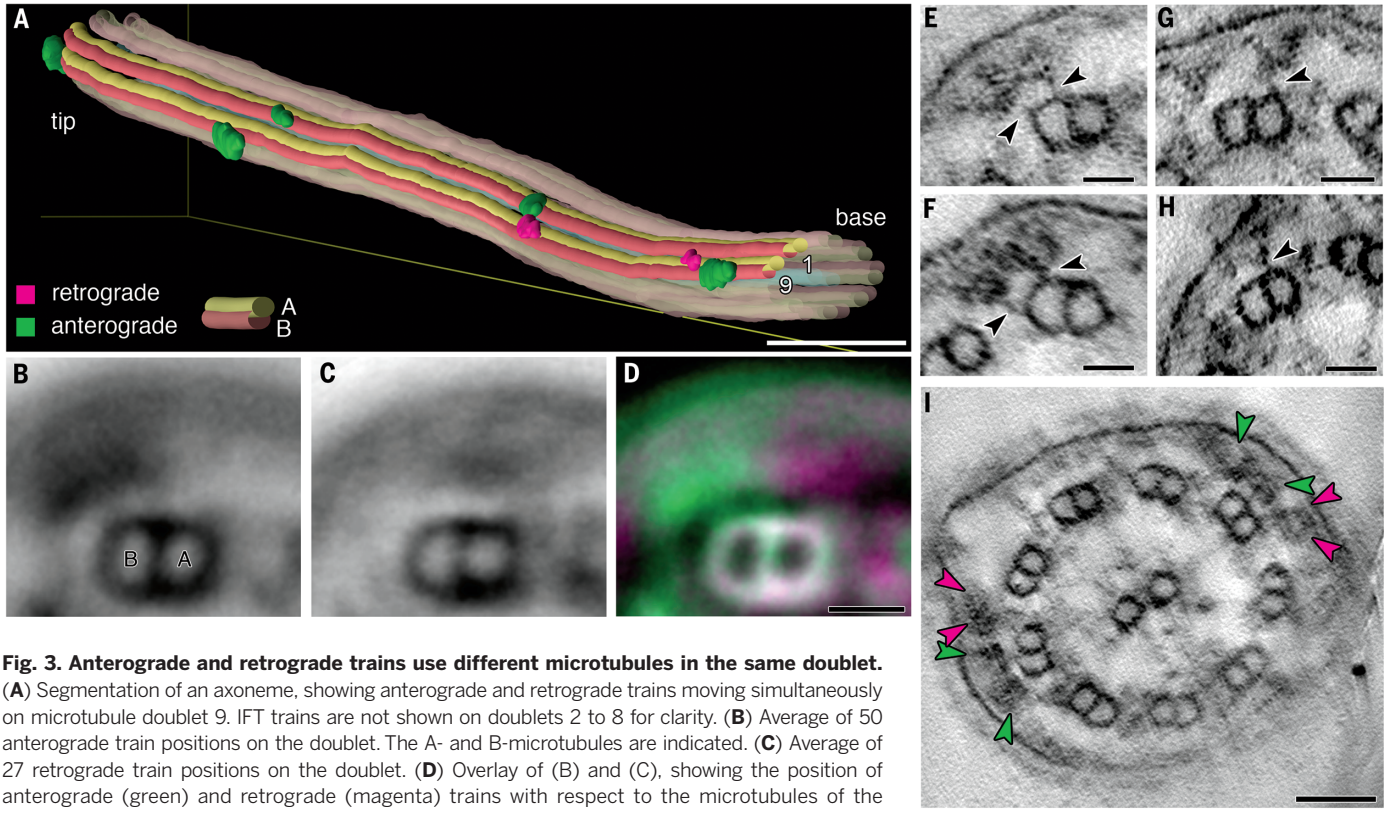


Fig. 3. Anterograde and retrograde trains use different microtubules in the same doublet. (**A**) Segmentation of an axoneme, showing anterograde and retrograde trains moving simultaneously on microtubule doublet 9. IFT trains are not shown on doublets 2 to 8 for clarity. (**B**) Average of 50 anterograde train positions on the doublet. The A- and B-microtubules are indicated. (**C**) Average of 27 retrograde train positions on the doublet. (**D**) Overlay of (B) and (C), showing the position of anterograde (green) and retrograde (magenta) trains with respect to the microtubules of the doublet. (**E** to **I**) Virtual slices through a cross-sectional tomogram, showing [(E) and (F)] anterograde trains (black arrowheads) connecting to the B-microtubule, [(G) and (H)] retrograde trains (black arrowheads) connecting to the A-microtubule, and (I) anterograde trains (green arrowheads) and retrograde trains (magenta arrowheads) stopped next to each other on the same doublet. Scale bars, 250 nm (A), 25 nm [(B) to (H)], and 50 nm (I). Virtual slice thickness, 7 nm. Cross-sectional views [(B) to (I)] are shown in proximal-to-distal orientation.

It is well known that anterograde and retrograde IFT trains use different molecular motors to move along microtubules. Whereas retrograde trains use dyneins, anterograde trains use kinesin-II motors (*3*, *15*, *16*). Our data therefore suggest that these specific motors must recognize A- and B-microtubules, respectively. One possibility could be that they recognize differences in the arrangement of α- and β-tubulin. However, this possibility seems to be ruled out by recent findings that A- and B-microtubules have the same tubulin arrangement, know as a B-lattice (*17*). An alternate possibility could be that IFT trains recognize specific posttranslational modifications on A- versus B-microtubules, similar to the mechanisms controlling the selective transport of cargos along axonal versus dendritic microtubules in mammalian axons (*18*). The human IFT anterograde motor kinesin-II has exhibited a differential response to posttranslational modifications of tubulin in a reconstituted in vitro system (*19*). Furthermore, differences have been reported in the posttranslational modification of A- and B-microtubules (*20*). This might contribute to the efficiency of IFT by providing optimized tracks for kinesin and dynein motors in addition to the IFT train segregation. Nevertheless, the effect of such modifications on the control of IFT in vivo remains unclear. Alternatively, a specific molecular machinery to direct trains to the correct microtubule could be present at the base and tip of the axoneme. More complex motor regulation could be necessary in the sensory cilia of *Caenorhabditis elegans*, where the B-microtubules do not extend beyond the middle segment of the flagellum. There, the kinesin-II moves only in the middle segment, and an additional motor, OSM-3, is required to bring cargo to the tip along the A-microtubules (*21*, *22*). Regardless of the mechanisms involved in the recognition of the microtubules by the motors, our work highlights the critical role played by microtubule doublets in the assembly of cilia.

REFERENCES AND NOTES

1. J. L. Rosenbaum, G. B. Witman, *Nat. Rev. Mol. Cell Biol.* **3**, 813–825 (2002).
2. K. G. Kozminski, K. A. Johnson, P. Forscher, J. L. Rosenbaum, *Proc. Natl. Acad. Sci. U.S.A.* **90**, 5519–5523 (1993).
3. K. G. Kozminski, P. L. Beech, J. L. Rosenbaum, *J. Cell Biol.* **131**, 1517–1527 (1995).
4. H. Qin, D. R. Diener, S. Geimer, D. G. Cole, J. L. Rosenbaum, *J. Cell Biol.* **164**, 255–266 (2004).
5. Y. Hou *et al.*, *J. Cell Biol.* **176**, 653–665 (2007).
6. S. Bhogaraju *et al.*, *Science* **341**, 1009–1012 (2013).
7. J. M. Craft, J. A. Harris, S. Hyman, P. Kner, K. F. Lechtreck, *J. Cell Biol.* **208**, 223–237 (2015).
8. G. Pigino *et al.*, *J. Cell Biol.* **187**, 135–148 (2009).
9. J. Buisson *et al.*, *J. Cell Sci.* **126**, 327–338 (2013).
10. S. Absalon *et al.*, *Mol. Biol. Cell* **19**, 929–944 (2008).
11. R. Rizzo, S. Parashuraman, A. Luini, *Histochem. Cell Biol.* **142**, 133–138 (2014).
12. M. Rogowski, D. Scholz, S. Geimer, *Methods Enzymol.* **524**, 243–263 (2013).
13. D. L. Ringo, *J. Cell Biol.* **33**, 543–571 (1967).
14. H. J. Hoops, G. B. Witman, *J. Cell Biol.* **97**, 902–908 (1983).
15. G. J. Pazour, C. G. Wilkerson, G. B. Witman, *J. Cell Biol.* **141**, 979–992 (1998).
16. M. E. Porter, R. Bower, J. A. Knott, P. Byrd, W. Dentler, *Mol. Biol. Cell* **10**, 693–712 (1999).
17. A. Maheshwari *et al.*, *Structure* **23**, 1584–1595 (2015).
18. Y. Konishi, M. Setou, *Nat. Neurosci.* **12**, 559–567 (2009).
19. M. Sirajuddin, L. M. Rice, R. D. Vale, *Nat. Cell Biol.* **16**, 335–344 (2014).
20. K. A. Johnson, *J. Cell Sci.* **111**, 313–320 (1998).
21. D. G. Cole *et al.*, *J. Cell Biol.* **141**, 993–1008 (1998).
22. J. J. Snow *et al.*, *Nat. Cell Biol.* **6**, 1109–1113 (2004).

ACKNOWLEDGMENTS

We thank J. Rosenbaum and D. Diener for providing the *Chlamydomonas* IFT27-GFP strain; P. Kiesel, the MPI-CBG EM facility, J. Meissner, the MPI-CBG LM facility, V. Geyer, and A. Kopach for technical support; I. Patten for comments and corrections to the manuscript; and J. Howard, S. Diez, J. Brugués, T. Hyman, M. Zerial, P. Tomancak, F. Jug, and I. Sbalzarini for fruitful discussion and comments. This work was supported by the Max Planck Society and a fellowship of the Dresden International Graduate School for Biomedicine and Bioengineering (GS97), granted by the German Research Foundation to L.S. Supporting data are provided in the supplementary materials.

SUPPLEMENTARY MATERIALS

www.sciencemag.org/content/352/6286/721/suppl/DC1
Materials and Methods
Supplementary Text
Figs. S1 to S6
References (*23*–*30*)
Movies S1 to S7

12 February 2016; resubmitted 2 March 2016
Accepted 14 April 2016
10.1126/science.aaf4594

Downloaded from http://science.sciencemag.org/ on May 5, 2016

PROTEIN STRUCTURE

Femtosecond structural dynamics drives the trans/cis isomerization in photoactive yellow protein

Kanupriya Pande,[1,2] Christopher D. M. Hutchison,[3] Gerrit Groenhof,[4] Andy Aquila,[5] Josef S. Robinson,[5] Jason Tenboer,[1] Shibom Basu,[6] Sébastien Boutet,[5] Daniel P. DePonte,[5] Mengning Liang,[5] Thomas A. White,[2] Nadia A. Zatsepin,[7] Oleksandr Yefanov,[2] Dmitry Morozov,[4] Dominik Oberthuer,[2] Cornelius Gati,[2] Ganesh Subramanian,[7] Daniel James,[7] Yun Zhao,[7] Jake Koralek,[5] Jennifer Brayshaw,[1] Christopher Kupitz,[1] Chelsie Conrad,[6] Shatabdi Roy-Chowdhury,[6] Jesse D. Coe,[6] Markus Metz,[2] Paulraj Lourdu Xavier,[2,8] Thomas D. Grant,[9] Jason E. Koglin,[5] Gihan Ketawala,[6] Raimund Fromme,[6] Vukica Šrajer,[10] Robert Henning,[10] John C. H. Spence,[7] Abbas Ourmazd,[1] Peter Schwander,[1] Uwe Weierstall,[7] Matthias Frank,[11] Petra Fromme,[6] Anton Barty,[2] Henry N. Chapman,[2,12] Keith Moffat,[10,13] Jasper J. van Thor,[3] Marius Schmidt[1]*

A variety of organisms have evolved mechanisms to detect and respond to light, in which the response is mediated by protein structural changes after photon absorption. The initial step is often the photoisomerization of a conjugated chromophore. Isomerization occurs on ultrafast time scales and is substantially influenced by the chromophore environment. Here we identify structural changes associated with the earliest steps in the trans-to-cis isomerization of the chromophore in photoactive yellow protein. Femtosecond hard x-ray pulses emitted by the Linac Coherent Light Source were used to conduct time-resolved serial femtosecond crystallography on photoactive yellow protein microcrystals over a time range from 100 femtoseconds to 3 picoseconds to determine the structural dynamics of the photoisomerization reaction.

Trans-to-cis isomerization constitutes a major class of chemical reactions of critical importance to biology, an example of which is the light-dependent isomerization of a retinal chromophore that underlies vision (*1*). Because isomerization occurs on the femtosecond to picosecond time scale, ultrafast time-resolved methods are necessary to follow the reaction in real time. The spectral response after photon absorption reveals the dynamics of the molecules involved (*2*–*5*) but does not directly observe the associated structural changes, which have to be inferred by computational approaches (*6*). Until recently, it has been impossible to directly determine the structure of molecules on ultrafast time scales. With the recent availability of hard x-ray pulses on the femtosecond time scale emitted by free electron laser (FEL) sources such as the Linac Coherent Light Source (LCLS), the ultrafast femtosecond-to-picosecond time scale has become experimentally accessible (*7*–*11*). Photochemical reactions (*12*) are initiated by photon absorption, which promotes electrons into the excited state. Thereafter, the nuclei experience and the structure evolves on the excited state potential energy surface (PES) (*13*, *14*). The shape of the surface controls the subsequent nuclear dynamics. After returning to the ground state PES, the reaction continues and is driven thermally. Although structures of longer-lived excited state intermediates have been characterized with ~100-ps time resolution at synchrotrons (*15*–*19*), the femtosecond structural dynamics of ultrafast photochemical reactions can only be investigated with an x-ray FEL (*11*). The photoactive yellow protein (PYP) is an ideal macromolecular system with which to investigate ultrafast trans-to-cis isomerization. Its chromophore, p-coumaric acid (pCA), can be photoexcited by absorbing a photon in the blue region of the spectrum. Upon photon absorption, PYP enters a reversible photocycle involving numerous intermediates (Fig. 1A). The primary photochemical event that controls entry into the photocycle is the isomerization of pCA about its C_2=C_3 double bond (see Fig. 1B for the pCA geometry). The pCA chromophore remains electronically excited for a few hundred femtoseconds (*3*, *5*, *20*). Excited state dynamics is thought to drive the configurational change from trans to cis (*3*, *21*). The chromophore pocket within the PYP protein is sufficiently flexible to allow certain relatively large atomic displacements, but also imposes structural constraints that may affect the pathway and dynamics of isomerization (*22*, *23*). In particular, the pCA chromophore is constrained by a covalent bond to the Cys^{69} side chain of PYP (Fig. 1B), by unusually short hydrogen bonds between its phenolate oxygen and nearby glutamate and tyrosine side chains (*24*), and by a hydrogen bond between the carbonyl oxygen of its tail and the main-chain amide of Cys^{69}.

Previously, we showed that time-resolved pump-probe serial femtosecond crystallography (TR-SFX) could be successfully carried out on PYP on the nanosecond-to-microsecond time scale. Difference electron density (DED) maps of very high quality, which compare the structures before (dark) and after (light) absorption of a photon (*25*), were obtained at near-atomic (1.6 Å) resolution. These experiments used a nanosecond laser pulse to initiate isomerization and subsequent structural changes. An overall reaction yield as high as 40% (*25*) could be reached. However, achieving femtosecond time resolution requires that a femtosecond pump laser pulse be used, which restricts the reaction yield to the much lower value of the primary quantum yield (around 10%) and correspondingly reduces the structural signal. The energy of femtosecond pulses (i.e., the number of photons per pulse) must also be limited to avoid damaging effects from their significantly higher peak power. Here, we present results of TR-SFX experiments covering the time range from 100 fs to 3 ps. We directly followed the trans-to-cis isomerization of the pCA chromophore and the concomitant structural changes in its protein environment in real time. Full details of the experiment and data analysis are provided in the supplementary materials (SM). Light-initiated structural changes in PYP were investigated at the Coherent X-ray Imaging (CXI) instrument of the LCLS (*26*). Electronic excitation was initiated in microcrystals of PYP by femtosecond pump laser pulses [wavelength (λ) = 450 nm]. Permanent bleaching of the chromophore was avoided by limiting the laser pulse energy to 0.8 mJ/mm^2 (5.7 GW/mm^2). Laser pulse duration, spectral distribution, and phase were characterized by second harmonic generation frequency-resolved optical gating (SHG-FROG) (*27*). The pulse duration was 140 ± 5 fs and had both positive group delay dispersion and third-order dispersion to maximize the conversion to the excited state (*28*). Offline spectroscopic experiments on thin crushed crystals of PYP had established that photoexcitation with femtosecond laser pulses under comparable conditions could be as high as 10% without inducing damage (SM). The structural changes induced by the laser pulse were probed with 40-fs x-ray FEL pulses at 9 keV (1.36 Å). Both the pump-probe and the reference x-ray diffraction data were collected at the full 120-Hz

[1]Department of Physics, University of Wisconsin–Milwaukee, Milwaukee, WI 53211, USA. [2]Center for Free Electron Laser Science, Deutsches Elektronen Synchrotron, Notkestrasse 85, 22607 Hamburg, Germany. [3]Faculty of Natural Sciences, Department of Life Sciences, Imperial College, London SW7 2AZ, UK. [4]Nanoscience Center and Department of Chemistry, University of Jyväskylä, Post Office Box 35, 40014 Jyväskylä, Finland. [5]Linac Coherent Light Source, SLAC National Accelerator Laboratory, Sand Hill Road, Menlo Park, CA 94025, USA. [6]School of Molecular Sciences and Biodesign Center for Applied Structural Discovery, Arizona State University, Tempe, AZ 85287, USA. [7]Department of Physics, Arizona State University, Tempe, AZ 85287, USA. [8]IMPRS-UFAST, Max Planck Institute for Structure and Dynamics of Matter, Luruper Chaussee 149, 22761 Hamburg, Germany. [9]Hauptman-Woodward Institute, State University of New York at Buffalo, 700 Ellicott Street, Buffalo, NY 14203, USA. [10]Center for Advanced Radiation Sources, University of Chicago, Chicago, IL 60637, USA. [11]Lawrence Livermore National Laboratory, Livermore, CA 94550, USA. [12]Center for Ultrafast Imaging, University of Hamburg, Luruper Chaussee 149, 22761 Hamburg, Germany. [13]Department of Biochemistry and Molecular Biology and Institute for Biophysical Dynamics, University of Chicago, Chicago, IL 60637, USA.
***Corresponding author. Email: m-schmidt@uwm.edu**

Downloaded from http://science.sciencemag.org/ on May 5, 2016

pulse repetition rate of the LCLS to a resolution of 1.6 and 1.5 Å, respectively. To address concerns that the detector response might be influenced by the stray light of the intense femtosecond laser pulse, the reference data were collected as a negative time delay, where the femtosecond laser pulse arrived 1 ps after the x-ray pulse.

To assess whether femtosecond laser pulses excited a sufficiently large number of molecules under these experimental conditions, we first performed a positive control experiment with a 200-ns pump-probe time delay, where large structural differences between the light and dark states have been well characterized (*25*, *29*). From the pump-probe TR-SFX data and the reference data, DED maps were calculated (SM). Figure 1C shows that the femtosecond laser pulses are able to initiate sufficient entry into the photocycle to produce strong, chemically meaningful features. The 200-ns DED map is essentially identical to maps determined earlier at both the LCLS (*25*) and at BioCARS (*29*) at a time delay of 1 μs, and can be interpreted with the same mixture of intermediates, pR_1 and pR_2. The extent of reaction initiation is 12.6% as determined by fitting a calculated "pR_1 + pR_2 minus pG" difference map to the 200-ns DED map, a value which agrees with the maximum extent of excitation determined spectroscopically (7 to 10%). The femtosecond time scale was explored by using nominal settings for the time delay of 300 and 600 fs. The timing jitter between the 140-fs laser pump and 40-fs x-ray probe pulses is ~280 fs (*8*). The jitter was measured for every x-ray pulse by a timing tool (*30*, *31*), which was combined with adjustments that take longer-term experimental drift into account (SM). Thus, each individual diffraction pattern was associated with a definite "time stamp." However, due to the drift, the time stamps were non-uniformly distributed in time (fig. S1). Because the quality of structure amplitudes and of the DED maps derived from them depends on the number of diffraction patterns, indexed time-stamped diffraction patterns were binned into eight different pump-probe delays with about the same number of patterns (40,000) in each bin, spanning the time range from 100 to 1000 fs (table S1B). A set of diffraction patterns at a time delay of 3 ps was also collected. Because the jitter and drift are much smaller than the delay, time stamping was not necessary for the 3-ps or 200-ns delays. The values of R-split (table S1) for all data sets are 7.5 to 9.9%, which indicates the high quality of the diffraction data and results in DED maps of comparable good quality for all delays. Maps at seven time delays are shown in Fig. 2. Visual inspection of these maps reveals an important qualitative result. The features in all maps at delays less than 500 fs are similar (compare Fig. 2, A to C), and features in all maps at delays greater than 700 fs are also similar (compare Fig. 2, D to G) but differ from those in the first set. Consequently, there must be a structural transition between the 455- and 799-fs time delays that gives rise to the two distinct sets of features.

To identify with more precision the time delay at which this transition occurs, the time-stamped diffraction patterns were re-binned into 16 narrower time bins with about 20,000 patterns in each bin (table S1A). The resultant time series of 16 DED maps in the femtosecond time range (together with the map for the 3-ps time delay) were subjected to singular value decomposition (SVD; fig. S2B) (*32*). The volume occupied by the pCA chromophore, the Cys^{69} sulfur, and the Glu^{46} carboxyl was included in the analysis. When a time series exhibits a change, a corresponding change should be even more readily recognizable in the right singular vectors (rSVs). This change is evident in the magnitude of both the first and second rSVs around 550 fs (red arrow in fig. S2B). The substantial increase in the magnitude of the first rSV after 155 fs (fig. S2B) shows the earliest (fastest) evolution of the structure after excitation. We tentatively associate the structural transition at around 550 fs, which is qualitatively evident from inspection of the DED maps and more quantitatively in their SVD analysis, with the trans–to-cis isomerization of the pCA chromophore. The transition occurs within ~180 fs (fig. S2B), but its exact duration needs to be further established. Rate kinetics would require that after a ~500-fs dwell time, the transition time would be stretched beyond the bandwidth-limited rate. Yet the observed transition time matches the experimental bandwidth of 3.15 THz. Therefore, the ensemble phase relation imparted by the optical pulse appears to be maintained for the duration of the dwell time, which may be supported by coherent motion. Although no oscillatory motion was detected in the TR-SFX data (they may be masked by the non-uniform data sampling), the time delay is, however, within the vibrational dephasing time of the PYP S_1 state (*3*) and ground state modes in proteins (*33*). We further propose that at ~550 fs, the system lies at or very close to a conical intersection (*20*) (fig. S8), a branch point from which molecules either continue toward the cis configuration and enter the photocycle, or revert to the trans configuration and return to the resting (dark) state.

To identify the isomerization, refined structures before and after the transition are required. Initially, data from bins with 40,000 indexed diffraction patterns each were used, and preliminary PYP structures were refined against these data. Refinement details are in the SM. The three bins with the shortest delays can be interpreted as having chromophores in a twisted trans configuration (Fig. 2, A to C). After 700 fs, the configuration is near cis (Fig. 2, D and E). The time course of the refined ϕ_{tail} torsional angles can be fit with a transition time identical to that observed in the second rSV (Fig. 3). We took advantage of the similarity of the DED maps for extended time ranges before and after the transition to further increase the accuracy of the refined structures. We combined the diffraction patterns into two bins: the fast time scale (100 to 400 fs, with 81,237 patterns) and a slower time scale (800 to 1200 fs, with 157,082 patterns) (table S1C). We refined the structure denoted PYP_{fast} against the 100- to 400-fs data, and that denoted PYP_{slow} against the 800- to 1200-fs data. The refinement statistics are presented in table S2. The DED maps are shown in insets in Fig. 3 (see also fig. S9, B and D), with the corresponding refined structures of PYP_{fast} and PYP_{slow} in pink and light green, respectively. The 3-ps DED map and the refined PYP_{3ps} structure are shown in Fig. 2G. We used as many diffraction patterns as possible to refine PYP_{slow} (fig. S12, B and D) and PYP_{3ps}, because at the transition, roughly 30% of the excited molecules return directly to the dark state, no longer contribute to the DED maps, and reduce the signal. We emphasize that the refinement of transient structures populated on an ultrafast time scale is challenging, because these structures are very far from equilibrium and likely to be highly strained. Restraints in standard libraries are derived from structures at equilibrium and are therefore not applicable. In order to provide restraints more appropriate for this refinement, we used excited state quantum mechanics/molecular mechanics (QM/MM) calculations on PYP (*20*, *34*) (SM). In addition, we used an iterative procedure, in which improved difference phases $\phi^{\Delta F,calc}$ were obtained and used with observed difference structure factor amplitudes during refinement (SM). The structural results of the refinement are summarized in Table 1. For the shortest time delays (up to about 450 fs), the PYP chromophore tail adopts a highly strained, twisted trans configuration, in which the C_1–C_2=C_3–$C_{1'}$ torsional angle ϕ_{tail} (shown by the

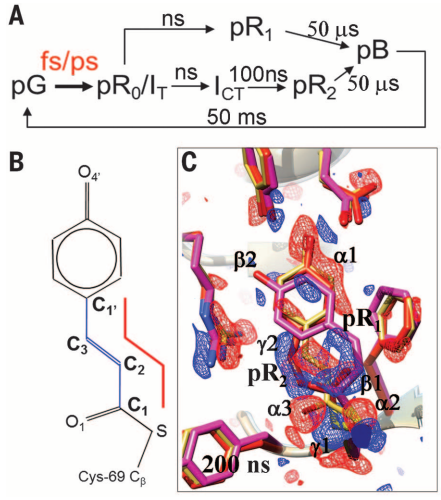


Fig. 1. Structural dynamics of PYP. (**A**) The PYP photocycle from the perspective of a time-resolved crystallographer. Approximate time scales are given. The femtosecond/picosecond time scale (in red) is structurally charted in this paper. (**B**) The chemical structure of the pCA chromophore. The red line marks the four atoms that define the torsional angle ϕ_{tail} about the C_2=C_3 bond. (**C**) Results of the positive control experiment at a 200-ns time delay. Reaction was initiated by femtosecond laser pulses. Negative (red) and positive (blue) DED features on the −3σ/3σ level. A mixture of the pR_1 (magenta) and pR_2 (red) structures is present. Main signature of pR_1: features β1 and β2. Main signature of pR_2: features γ1 and γ2. The structure of PYP_{ref} (dark) is in yellow.

Downloaded from http://science.sciencemag.org/ on May 5, 2016

red line spanning these four atoms in Fig. 1B) is ~140°. The position of the $C_2 = C_3$ double bond in PYP_{fast} is displaced by ~1 Å behind the chromophore plane (loosely defined by the Cys^{69} sulfur, the tail carbonyl oxygen, and the atoms of the phenyl ring; Fig. 2, A to C). Hydrogen bonds to Glu^{46} and Tyr^{42}, which are unusually short in the reference (dark) structure (*24*), are substantially elongated from 2.5 to 3.4 Å (Table 1). This structure is primed for the transition to cis. During the structural transition, substantial rotation about the double bond takes place. The head of the chromophore pivots about tail atom C_2 and thereby aligns the C_2C_3 bond along the tail axis. Simultaneously, the head rotates about the C_3 - $C_{1'}$ single bond. (The complex motions can be effectively illustrated by using an educator's stick model set, see fig. S3). The phenolate oxygen (Fig. 1B, $O_{4'}$) moves even further away (3.6 Å, Table 1) from Glu^{46} (Fig. 2, D to F, and fig. S9, C and D), thereby breaking the hydrogen bond. At time delays longer than about 700 fs, ϕ_{tail} has decreased to ~50° (PYP_{slow}, Fig. 3), which is characteristic of a cis configuration. PYP_{slow} relaxes further toward the 3-ps structure (PYP_{3ps}), in which the hydroxyl oxygen of the head reestablishes its hydrogen bond with Glu^{46} (Fig. 2G). ϕ_{tail} changes slightly to ~35°. The PYP_{3ps} structure is already very similar to the early structures derived with 100-ps time resolution by independent synchrotron-based approaches (Table 1; Protein Data Bank entries 4I38 and 4B90) (*22*, *23*) and has evolved only slightly from PYP_{slow} by establishing shorter hydrogen bonds to Tyr^{42} and Glu^{46}.

The structures derived from the refinements confirm that the transition at around 550 fs is indeed associated with a trans–to-cis isomerization. Theoretical considerations (*20*) (fig. S8) suggest that during isomerization, the PYP chromophore relaxes through a conical intersection between the electronically excited state PES and the ground state PES. Accordingly, structures between 100 and 400 fs can be identified as electronically excited, whereas the structures at time delays >700 fs can be identified with the electronic ground state. In both the excited and ground states, structural changes (i.e., translation of atoms) may also have occurred. Our experiments identified the ultrafast dynamics of both the excited state structures and the ground state structures (Figs. 2 and 3). Because we restricted our pump laser pulses to moderate power, we avoided damaging nonlinear effects (e.g., two-photon absorption), and most excited molecules populate the excited state surface S_1 (*5*). Part of the stored energy is used to rapidly displace the chromophore by about 0.7 Å within the crowded molecular environment in the interior of PYP (Fig. 2A and Table 1). If this initial displacement is complete after 250 fs, the chromophore must have experienced an acceleration of ~2×10^{15} m/s^2 and attains a final velocity of 500 m/s (SM). Figure 1B shows that nine carbon atoms, two oxygen atoms, and seven hydrogen atoms (molecular mass = 147 g/mol) are displaced. During the first few hundred femtoseconds, the force on the chromophore is ~500 pN, which is enormous compared to forces in single molecules at thermal equilibrium, which are usually only a few piconewtons (*35*). The origin of the force is due to the change of the potential energy surface when the chromophore is excited to the electronic excited state, which affects the intra- and intermolecular interactions of the chromophore as also inferred from ultrafast Raman spectroscopy (*3*). The energy required to displace the chromophore is ~0.2 eV, which is ~10% of the blue photon energy (2.76 eV) that starts the reaction. It appears that by rapidly evolving down the excited state PES, part of the photon energy is initially converted into kinetic energy, which is then released by collision of the chromophore atoms with the surrounding protein atoms that make up the chromophore pocket. The excited chromophore loses 0.12 eV of energy by intramolecular vibrational energy redistribution on the sub–100-fs time scale (*36*), which can be roughly estimated from the Stokes shift by comparing absorption and fluorescence spectra (*3*). Accordingly, ~85% of the photon energy remains stored as strain and electronic excitation in the chromophore before

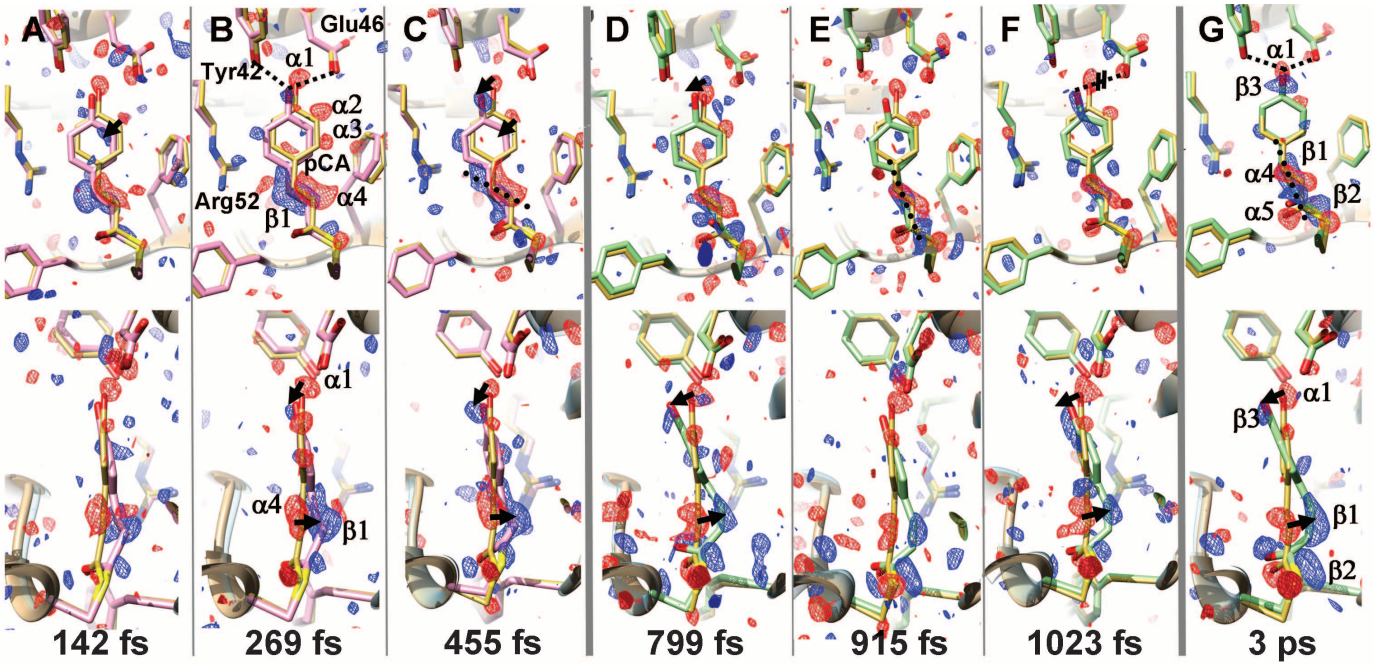


Fig. 2. Trans-to-cis isomerization in PYP. Weighted DED maps in red (−3σ) and blue (3σ); front (upper) and side view (lower). Each map is prepared from about the same number of diffraction patterns, except the 3-ps map (table S1, B and C). The reference dark structure is shown in yellow throughout; structures before the transition and still in the electronic excited state PES are shown in pink; structures after the transition and in the electronic ground state PES are shown in light green. Important negative difference density features are denoted as α and positive features as β in (B) and (G). Pronounced structural changes are marked by arrows. (**A** to **C**) Time delays before the transition. (A) Twisted trans at 142 fs, ϕ_{tail} 154°. (B) Twisted trans at 269 fs, ϕ_{tail} 140°, some important residues are marked; dotted lines: hydrogen bond of the ring hydroxyl to Glu^{46} and Tyr^{42}. (C) Twisted trans at 455 fs, ϕ_{tail} 144°; dotted line: direction of C_2=C_3 double bond. (**D** to **G**) Time delays and chromophore configuration after the transition. (D) Early cis at 799 fs, ϕ_{tail} 50°. (E) Early cis at 915 fs; dotted line: direction of $C_2 = C_3$ double bond. (F) Early cis at 1023 fs; for (E) and (F), ϕ_{tail} ~ 65°. (G) 3-ps delay; dashed line: direction of C_2=C_3 double bond, feature β1; ϕ_{tail} is 35°.

Downloaded from http://science.sciencemag.org/ on May 5, 2016

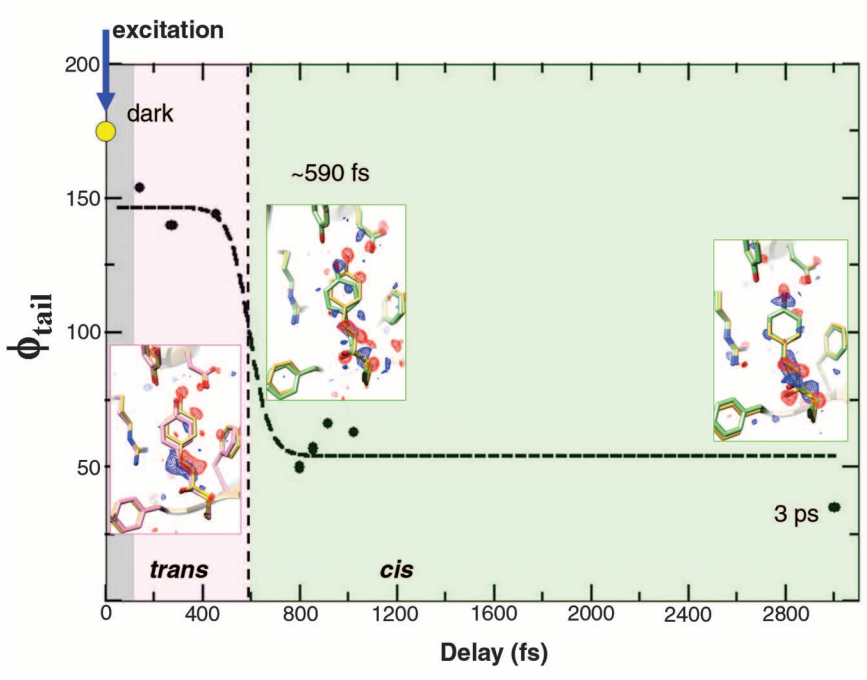


Fig. 3. Chromophore tail torsional angle dynamics. Pink: twisted trans on excited state PES; light green: cis on ground state PES. Torsional angle ϕ_{tail} (solid spheres) is from structural refinement at various delays (table S3). Gray region: not time-resolved. Dashed line: fit with eq. S2, with a transition time of about 590 fs (fig. S2). Insets: structures of PYP_{fast} (pink), PYP_{slow}, and PYP_{3ps} (light green), and dark-state structure PYP_{ref} in yellow. Difference electron density is shown in red (−3σ) and blue (3σ).

isomerization occurs. On passing through the conical intersection (*20*), the molecules either revert toward the initial dark state (30% of the excited molecules, Table 1 and table S3) or continue relaxing toward the cis isomer (70%), gradually releasing the excess energy as heat. Because the chromophore pocket tightly restricts the chromophore head displacements, further structural changes must be volume-conserving; i.e., they minimize the volume swept out by the atoms as they move. Accordingly, the chromophore performs the complex motions described above (fig. S3). Although the energy stored in the chromophore is sufficient to break the hydrogen bonds (~0.1 eV), the spatial constraints imposed by the chromophore pocket direct the reformation of the hydrogen bonding network at longer time delays (Table 1). This is a macromolecular cage effect reminiscent of the solvent cage effect in liquid chemical dynamics (*37*). The macromolecular cage in PYP, however, is soft enough to allow certain specific, relatively large (up to 1.3 Å, Table 1) structural changes. This contrasts with crystals of small molecules, where the stronger crystal lattice constraints usually do not allow such large displacements. Hence, biological macromolecular crystallography aimed at elucidating biological function may also provide insight into the reaction mechanisms of small molecules.

To assess global conformational changes of PYP on the femtosecond time scale, we calculated the radius of gyration R_g from each refined structure

Table 1. Geometry of PYP structures. The PYP_{fast} structure was refined using a data bin spanning 100 to 400 fs with 81,327 snapshots and the PYP_{slow} structure from a bin spanning 800 to 1200 fs with 157,082 snapshots (table S1B). Structures of I_T, pR_0, and pB_1 are from the Protein Data Bank, with the accession code in parentheses (*22*, *23*, *47*). Uncertainties of the torsional angles can be estimated to be ±20° by displacing the four atoms that define the angle with the coordinate error (0.2 Å). na, not applicable; nd, not determined.

	PYP_{ref} (dark)	PYP_{fast}	PYP_{slow}	PYP_{3ps}	PYP_{200ns} (fs laser) pR_1/pR_2	I_T (4I38)	pR_0 (4B90)	pB_1 (1TS0)
Time delay	0	100–400 fs	800–1200 fs	3 ps	200 ns	100 ps	100 ps	1 ms
				Torsional angles (°)				
C_1-C_2=C_3-$C_{1'}$ (ϕ_{tail})	172	136	53	35	3/–8	90	33	–27
O_1-C_1-C_2=C_3	–15	–21	28	30	12/–6	11	29	–10
CB-S-C_1-C_2	–185	–171	–164	–137	163/–165	–136	–123	180
				Hydrogen bonds (Å)				
pCA-$O_{4'}$-Glu^{46}-O_ε	2.50	3.40	3.60	2.94	4.97/2.88	2.73	2.73	8.03
pCA-$O_{4'}$-Tyr^{42}-O_η	2.54	2.92	2.63	2.88	2.97/2.66	2.57	2.59	5.19
pCA-O_1-Cys^{69}-N	2.77	3.11	2.50	3.12	3.37/4.29	3.04	3.05	2.88
				Others				
<pCA>* (Å)	0	0.66	0.78	0.60	1.55/0.81	0.67	0.68	2.39
<Global>† (Å)	0	0.20	0.19	0.24	0.13	0.13	0.19	0.17
Radius of gyration‡ (Å)	13.32	13.33	13.30	13.34	13.29	nd	nd	nd
Volume ($Å^3$)	17,831	17,856	17,833	17,838	17,672	17,830	17,683	17,807
ΔV to dark ($Å^3$)	0	25	2	7	–159	–1	–148	–24
Photoactivation yield (%)§	na	15.2	9.6	10.1	12.5‡	(5%)‖	(10%)‖	(10%)‖

*Mean displacement of equivalent chromophore atoms relative to dark (SM). †Mean displacement of equivalent c_α atoms relative to dark (SM). ‡See SM for the calculation. §Determined by fitting calculated DED maps to the experimental DED maps in the chromophore region. ‖Estimate.

Downloaded from http://science.sciencemag.org/ on May 5, 2016

(SM). R_g fluctuates by only 0.2% in all structures from 200 fs to 200 ns (Table 1). An increase of R_g by up to 1 Å, determined by others using x-ray scattering in solution upon photodissociation of CO from CO-myoglobin (*9*), was not observed in our PYP crystals. Concomitant systematic large volume changes were also not apparent in PYP crystals over the first 3 ps that our data span. Our data show no evidence for a protein quake (*9*, *10*, *38*), characterized by an ultrafast and large change in R_g that occurs significantly before a large volume change. The reason for this is unclear and will require further experiments.

Ultrafast fluorescence and transient absorption spectroscopy of PYP have shown that excited state decay is multi-phasic (*3*, *5*, *39*). The fast (subpicosecond) time constants are significantly more productive in creating the cis-like photoproduct than the slow (picosecond) time constants; the long-lived excited state population primarily decays back to the ground state (*5*, *36*). With excitation at 450 nm, at least 50% of the total isomerization yield is generated with a dominant ~600-fs time constant (*5*), which agrees with our observation of a transition at ~550 fs. It should be noted that a ground state intermediate with a 3- to 6-ps life time has been proposed by ultrafast spectroscopy (*36*). However, under the conditions used here, the peak concentration of this intermediate is expected to be small (*5*). In contrast to spectroscopic techniques that reported vibrational coherence with 50 cm^{-1} and 150 cm^{-1} frequency (*3*, *40*), we could not unambiguously detect oscillations in our data. Intense femtosecond optical pumping of PYP crystals generates both excited state and ground state vibrational coherences within the 3.15-THz experimental bandwidth (*41*). It will be an important goal of future experiments to structurally characterize these coherences using femtosecond TR-SFX. Nevertheless, our data show that before 400 fs, there are large distortions corresponding to a Franck-Condon (FC) excited state (*42*). The nuclear dynamics of the FC excited state at 100 to 200 fs agrees with the conclusions from ultrafast spectroscopy (*3*, *42*–*45*) that also suggest a distortion of the C_2=C_3 double bond on similar time scales, as in the PYP_{fast} structure. The isomerization at 550 fs through the conical intersection between the excited state and ground state PES is in reasonable agreement with the time scales for isomerization reported by others (*3*, *5*, *42*, *46*). After passing through the conical intersection, the chromophore is cis-like and still highly strained. The transiently broken hydrogen bond is reestablished quickly as the structure relaxes, exemplified by the PYP_{3ps} structure (Fig. 3). Further relaxation on the ground state PES completes the initial phase of the isomerization.

REFERENCES AND NOTES

1. G. Wald, *Science* **162**, 230–239 (1968).
2. Y. Mizutani, T. Kitagawa, *Science* **278**, 443–446 (1997).
3. R. Nakamura, N. Hamada, H. Ichida, F. Tokunaga, Y. Kanematsu, *J. Chem. Phys.* **127**, 215102 (2007).
4. P. M. Champion, *Science* **310**, 980–982 (2005).
5. C. N. Lincoln, A. E. Fitzpatrick, J. J. van Thor, *Phys. Chem. Chem. Phys.* **14**, 15752–15764 (2012).
6. A. Warshel, *Nature* **260**, 679–683 (1976).
7. M. P. Minitti *et al.*, *Phys. Rev. Lett.* **114**, 1–5 (2015).
8. J. M. Glownia *et al.*, *Opt. Express* **18**, 17620–17630 (2010).
9. M. Levantino *et al.*, *Nat. Commun.* **6**, 6772 (2015).
10. D. Arnlund *et al.*, *Nat. Methods* **11**, 923–926 (2014).
11. T. R. M. Barends *et al.*, *Science* **350**, 445–450 (2015).
12. P. Coppens, *Struct. Dyn.* **2**, 020901-1–020901-8 (2015).
13. A. H. Zewail, *Angew. Chem. Int. Ed. Engl.* **39**, 2586–2631 (2000).
14. M. Gao *et al.*, *Nature* **496**, 343–346 (2013).
15. S. Techert, F. Schotte, M. Wulff, *Phys. Rev. Lett.* **86**, 2030–2033 (2001).
16. C. D. Kim, S. Pillet, G. Wu, W. K. Fullagar, P. Coppens, *Acta Crystallogr. A* **58**, 133–137 (2002).
17. J. B. Benedict *et al.*, *Chem. Commun. (Camb.)* **47**, 1704–1706 (2011).
18. H. Ihee *et al.*, *Science* **309**, 1223–1227 (2005).
19. R. Neutze *et al.*, *Phys. Rev. Lett.* **87**, 195508 (2001).
20. G. Groenhof *et al.*, *J. Am. Chem. Soc.* **126**, 4228–4233 (2004).
21. D. S. Larsen *et al.*, *Biophys. J.* **86**, 2538–2550 (2004).
22. Y. O. Jung *et al.*, *Nat. Chem.* **5**, 212–220 (2013).
23. F. Schotte *et al.*, *Proc. Natl. Acad. Sci. U.S.A.* **109**, 19256–19261 (2012).
24. S. Anderson, S. Crosson, K. Moffat, *Acta Crystallogr. D Biol. Crystallogr.* **60**, 1008–1016 (2004).
25. J. Tenboer *et al.*, *Science* **346**, 1242–1246 (2014).
26. M. Liang *et al.*, *J. Synchrotron Radiat.* **22**, 514–519 (2015).
27. R. Trebino *et al.*, *Rev. Sci. Instrum.* **68**, 3277–3295 (1997).
28. C. J. Bardeen, Q. Wang, C. V. Shank, *Phys. Rev. Lett.* **75**, 3410–3413 (1995).
29. M. Schmidt *et al.*, *Acta Crystallogr. D Biol. Crystallogr.* **69**, 2534–2542 (2013).
30. N. Hartmann *et al.*, *Nat. Photonics* **8**, 706–709 (2014).
31. M. R. Bionta *et al.*, *Opt. Express* **19**, 21855–21865 (2011).
32. M. Schmidt, S. Rajagopal, Z. Ren, K. Moffat, *Biophys. J.* **84**, 2112–2129 (2003).
33. K. D. Rector, M. D. Fayer, *Laser Chem.* **19**, 19–34 (1999).
34. G. Groenhof, *Methods Mol. Biol.* **924**, 43–66 (2012).
35. M. Rief, H. Grubmüller, *ChemPhysChem* **3**, 255–261 (2002).
36. D. S. Larsen *et al.*, *Biophys. J.* **87**, 1858–1872 (2004).
37. F. Patron, S. A. Adelman, *Chem. Phys.* **152**, 121–131 (1991).
38. L. Genberg, L. Richard, G. McLendon, R. J. D. Miller, *Science* **251**, 1051–1054 (1991).
39. M. Vengris *et al.*, *Biophys. J.* **87**, 1848–1857 (2004).
40. N. Mataga *et al.*, *Chem. Phys. Lett.* **352**, 220–225 (2002).
41. A. T. N. Kumar, F. Rosca, A. Widom, P. M. Champion, *J. Chem. Phys.* **114**, 6795–6815 (2001).
42. M. Creelman, M. Kumauchi, W. D. Hoff, R. A. Mathies, *J. Phys. Chem. B* **118**, 659–667 (2014).
43. M. L. Groot *et al.*, *Biochemistry* **42**, 10054–10059 (2003).
44. K. Heyne *et al.*, *J. Am. Chem. Soc.* **127**, 18100–18106 (2005).
45. L. J. van Wilderen *et al.*, *Proc. Natl. Acad. Sci. U.S.A.* **103**, 15050–15055 (2006).
46. S. Devanathan *et al.*, *Biophys. J.* **77**, 1017–1023 (1999).
47. H. Ihee *et al.*, *Proc. Natl. Acad. Sci. U.S.A.* **102**, 7145–7150 (2005).

ACKNOWLEDGMENTS

This work is supported by the NSF Science and Technology Center BioXFEL (grant NSF-1231306); by NIH grants R01GM095583 (P.F.), R01EY024363 (K.M.), and R24GM111072 (V.S., R.H., and K.M.); Helmholtz Association Virtual Institute Dynamic Pathways (H.C.); and grant NSF-0952643 (M.S.). K.P. is partly supported by grant NSF-1158138 (to D. Saldin and M.S.) and Federal Ministry of Education and Research, Germany (BMBF) grant 05K14CHA (to H.C.). J.J.v.T. acknowledges support from the Engineering and Physical Sciences Research Council via grant agreement EP/M000192/1. G.G. and D.M. are supported by the Academy of Finland, D.O. by BMBF project 05K13GUK, and M.M. by the European Union through grant FP7-PEOPLE-2011-ITN NanoMem. Use of the LCLS, SLAC National Accelerator Laboratory, is supported by the U.S. Department of Energy, Office of Science, Office of Basic Energy Sciences, under contract DE-AC02-76SF00515. Part of this work was performed under the auspices of the U.S. Department of Energy by Lawrence Livermore National Laboratory (LLNL) under contract DE-AC52-07NA27344, and M.F. was supported by LLNL Lab-Directed Research and Development Project 012-ERD-031. C.G. thanks the PIER Helmholtz Graduate School for financial support. Parts of the sample injector used at LCLS for this research were funded by NIH grant P41GM103393, formerly P41RR001209. We thank the Moscow State University supercomputing center and the Finnish IT Center for Science (CSC-IT) Center for Science, Finland, for computing resources. We thank M. Hunter for valuable discussions, T. Graen for help with the computer simulations, and C. Li for assistance with injectors. The PYP_{ref}, PYP_{fast}, PYP_{slow}, PYP_{3ps}, and PYP_{200ns} structures are deposited in the Protein Data Bank together with their respective weighted difference structure factor amplitudes under accession codes 5HD3, 5HDC, 5HDD, 5HDS, and 5HD5, respectively. M.S. prepared the proposal with input from J.J.vT., K.M., V.S., J.C.H.S., H.N.C., A.O., and P.F.; A.A., S.B., M.L., J.S.R., and J.E.K. operated the CXI instrument, including the time tool and the femtosecond laser; and K.P., A.B., J.T., S.B., T.A.W., N.Z., O.Y., and T.D.G. analyzed the SFX data. C.D.M.H and J.J.vT. set up the FROG at the CXI instrument; G.G. and D.M. performed QM/MM calculations; J.T., J.B., D.O., P.L.X., C.G., C.K., and M.S. prepared protein and grew nano- and microcrystals; D.DeP., C.K., C.C., S.R.-C., J.D.C., M.M., G. K., and U.W. provided and operated the injector system; M.F., R.F., M.S., J.T., P.F., D.O., and C.G. wrote the electronic log; M.F., M.S, J.T., J.S.R., J.J.vT., and K.M. discussed femtosecond laser excitation; J.T., M.S, V.S, R.H, C.D.M.H., and J.J.vT. performed preliminary ultrafast experiments on crystals; M.S. calculated and analyzed the difference maps; and M.S., K.P., K.M., G.G., P.F., and J.J.vT. wrote the manuscript, with improvements from all authors.

SUPPLEMENTARY MATERIALS

www.sciencemag.org/content/352/6286/725/suppl/DC1
Materials and Methods
Supplementary Text
Figs. S1 to S12
Tables S1 to S5
References (*48*–*84*)

27 September 2015; accepted 5 April 2016
10.1126/science.aad5081

Downloaded from http://science.sciencemag.org/ on May 5, 2016

NEW ENGLAND BioLabs® Inc.

Migrate to Monarch®.

Environmentally-friendly Nucleic Acid Purification Kits from New England Biolabs

Want to feel good about your choice in DNA purification? With our fast and reliable Monarch Nucleic Acid Purification Kits, you can achieve optimal purification while creating less waste. Available for plasmid minipreps, DNA gel extraction and enzymatic cleanup (including PCR), our products use up to 44% less plastic and are packaged using responsibly-sourced, recyclable materials. Make the change and migrate to Monarch today.



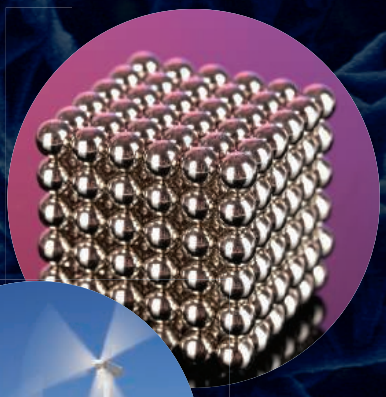
"These kits might be the best I have used for the price. The best part is that it uses less plastic for production!! Thank you for caring about our environmental impacts, NEB!!!"

– NEB customer

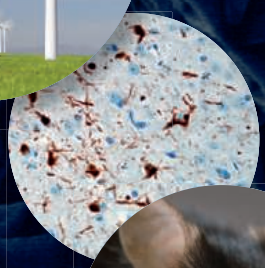
Request your free sample at **www.NEBMonarch.com**

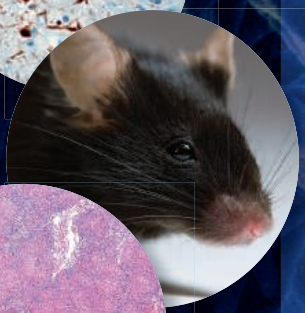
NEW ENGLAND BIOLABS®, NEB® and MONARCH® are registered trademarks of New England Biolabs, Inc.

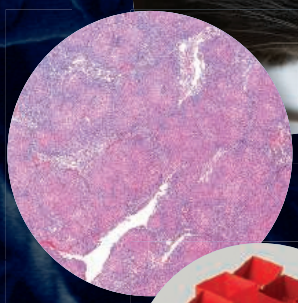
PNAS Congratulates 2015 Cozzarelli Prize Recipients













PNAS has selected six outstanding PNAS papers for the 2015 Cozzarelli Prize. The award was established in 2005 as the PNAS Paper of the Year Prize and renamed the Cozzarelli Prize in 2007 to honor late PNAS Editor-in-Chief Nicholas R. Cozzarelli. Papers receiving the Cozzarelli Prize were chosen from the more than 3,100 research articles published by PNAS in 2015 and represent the six broadly defined classes under which the National Academy of Sciences is organized.

CLASS I: PHYSICAL AND MATHEMATICAL SCIENCES

Mimicking the magnetic properties of rare earth elements using superatoms

Shi-Bo Cheng, Cuneyt Berkdemir, and A. W. Castleman Jr. 112(16):4941–4945

CLASS II: BIOLOGICAL SCIENCES

Maternal intestinal HIF-2α is necessary for sensing iron demands of lactation in mice

Sadeesh K. Ramakrishnan, Erik R. Anderson, Angelical Martin, Brook Centofanti, and Yatrik M. Shah 112(28):E3738–E3747

CLASS III: ENGINEERING AND APPLIED SCIENCES

Origami tubes assembled into stiff, yet reconfigurable structures and metamaterials

Evgueni T. Filipov, Tomohiro Tachi, and Glaucio H. Paulino 112(40):12321–12326

CLASS IV: BIOMEDICAL SCIENCES

Evidence for α-synuclein prions causing multiple system atrophy in humans with parkinsonism

Stanley B. Prusiner, Amanda L. Woerman, Daniel A. Mordes, Joel C. Watts, Ryan Rampersaud, David B. Berry, Smita Patel, Abby Oehler, Jennifer K. Lowe, Stephanie N. Kravitz, Daniel H. Geschwind, David V. Glidden, Glenda M. Halliday, Lefkos T. Middleton, Steve M. Gentleman, Lea T. Grinberg, and Kurt Giles 112(38):E5308–E5317

CLASS V: BEHAVIORAL AND SOCIAL SCIENCES

Rising morbidity and mortality in midlife among white non-Hispanic Americans in the 21st century

Anne Case and Angus Deaton 112(49):15078–15083

CLASS VI: APPLIED BIOLOGICAL, AGRICULTURAL, AND ENVIRONMENTAL SCIENCES

Low-cost solution to the grid reliability problem with 100% penetration of intermittent wind, water, and solar for all purposes.

Mark Z. Jacobson, Mark A. Delucchi, Mary A. Cameron, and Bethany A. Frew 112(49):15060–15065

PNAS

www.pnas.org

Podcast interviews with the authors will be available at:
pnas.org/site/misc/cozzarelliprize.xhtml

my science **SUBMIT**

American Heart Association®
life is why™

SCIENTIFIC SESSIONS 2016



Sessions: November 12–16
New Orleans, Lousiana

Expect **big** In **2016** Things

Opportunity for Publication:

Accepted abstracts are published in *Circulation*, an American Heart Association journal.

About *Circulation*:

Top-ranked for total cites, Impact Factor, 5-Year Impact Factor, *Article Influence® Score*, and *Eigenfactor®* Score (Thomson Reuters, 2015)

Global Reach:

2015 abstracts were featured in:

Associated Press
TIME Magazine
The New York Times
USA Today
NBC News
FOX News
BBC
MSNBC.com
Reuters Wire Service
U.S. News
World Report

Member Benefits:

More than $160,000 in council awards and travel grants available to professional members, early career investigators, trainees and students submitting abstracts to Scientific Sessions.

WORLD-RENOWNED SCIENCE
starts with an abstract

The American Heart Association is bringing the premier cardiovascular conference for **basic, translational, clinical, and population science** to New Orleans, Louisiana this November. Attracting nearly **18,000 professional** attendees from **more than 100 countries**, AHA's Scientific Sessions provides an elite forum for presentation of innovative research findings.

Abstract & Council Award Submissions:

Open | Wednesday, April 20, 2016
Close | Wednesday, June 8, 2016

Registration:

Open | Wednesday, June 15, 2016

Submit Your Science Now!
scientificsessions.org

©2016, American Heart Association

Automated Immunoassay Platform

A pioneer in miniaturizing and automating immunoassays at nanoliter scale has released the Gyrolab Affinity Software module, which is available on both the Gyrolab xP workstation and the recently launched single compact disc (CD) Gyrolab xPlore system. This new, intuitive software module enables users to easily set up and run in-solution affinity determinations of up to 14 interacting pairs in parallel in just one hour. Characterization of antibody-target binding is a critical element in the discovery and development of therapeutic antibodies. Gyros technology allows biotherapeutic developers to determine accurate equilibrium dissociation constants (K_D) of unmodified substances down to low-picomolar levels by measuring free interactants in equilibrated solutions. The flow-through affinity column format in Gyrolab CDs is ideal for in-solution affinity determination, as interaction times of only a few seconds avoid the equilibrium shifts inherent in assays requiring longer incubation times.

Gyros
For info: +46-(0)-18-56-63-00
www.gyros.com



FISH Hybridization System

A high-capacity system for performing fluorescence in situ hybridization (FISH) assays is now available. The system consists of one CytoBrite Slide Incubation System for performing rapid probe denaturation on batches of 12 FISH slides, and one CytoBrite Slide Oven for overnight hybridization of 60 slides. Removable slide trays streamline slide setup and transfers between instruments. The combined instruments are equivalent to six older-generation ThermoBrite instruments at a fraction of the bench space and cost.

SciGene
For info: 408-733-7337
www.scigene.com

Handheld Scanner

The HandHeld is a truly portable instrument for manual sample picking and effective use in the field. This intelligent device provides users with the ability to immediately identify tubes and track samples when away from the lab. This includes manual picking from repositories as well as effective recording when collecting samples in the field. The new Ziath HandHeld scanner can be operated using one hand, and incorporates a lightweight build and intuitive interface that is easy enough for anyone in the lab to use. Its portable nature is perfect for a number of underserved applications, such as generating multiple pick lists for accurate tube selection, vial checking to confirm sample labelling, and easily recording samples in the field at the point of collection. Because the scanner is battery operated, users have the option to effortlessly enter data about specific samples as soon as they are scanned.

Ziath
For info: +44-(0)-1223-655577
www.ziath.com

Oligonucleotide Conjugation Kit

Thunder-Link PLUS is a new and improved version of the original Thunder-Link kit, enabling even faster and more efficient oligonucleotide conjugation. The new kit offers all of the advantages of the original Thunder-Link technology, but now also works with antibody fragments and small proteins. Thunder-Link PLUS provides antibody and oligo activation in just 30 minutes, and oligo conjugation in only one hour, with no lengthy protocols. The kit enables excellent antibody and oligo recovery, with a robust and flexible cleanup procedure. Fast, easy, and efficient conjugation of oligonucleotides and antibodies has traditionally been a major obstacle when developing assays such as immuno-polymerase chain reaction (immuno-PCR), proximity extension assays, proximity ligation assays, and electrochemical proximity assays. Thunder-Link and now Thunder-Link PLUS are the easiest to use, fastest, most efficient, and most effective oligonucleotide conjugation kits of their kind on the market.

Innova Biosciences
For info: +44-(0)-1223-496170
www.innovabiosciences.com

Cell Growth Substrate

The substrate rigidity to which cells adhere can affect cell propagation, differentiation, lineage specification, gene expression, morphology, and migration. Grow cells in their native, in vivo softness with the new CytoSoft Discovery Kit. The kit contains seven plates with different elastic moduli (0.2, 0.5, 2, 8, 16, 32, and 64 kPa), covering a broad physiological range. On the bottom of each well, there is a thin layer of specially formulated biocompatible silicone, whose elastic modulus is carefully measured and certified. The surfaces of CytoSoft are functionalized to form covalent bonds with amines on proteins. Cells are given the opportunity to grow in the in vivo softness they enjoy.

Advanced BioMatrix
For info: 800-883-8220
www.advancedbiomatrix.com

SampleBank

The Mosaic SampleBank offers the benefits of sample management best practices gained from collaborating with big pharma companies in a cost-effective format that can be deployed quickly. SampleBank encapsulates key modules of Titian's industry-leading Mosaic software in a preconfigured format allowing simple, efficient startup. SampleBank users can now rapidly organize all their samples into a centralized, traceable resource. SampleBank's inventory tracking, workflow, and order-management functionality promotes quality-assured data gained from efficient manual or automated processes. Customers will benefit from Titian's integration with an extensive library of laboratory automation used in sample management workflows.

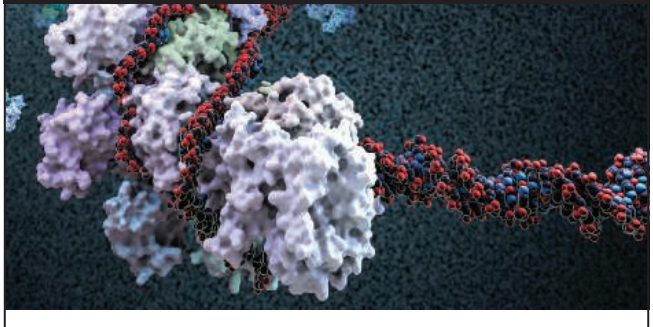
Titian
For info: +44-(0)-20-7367-6869
www.titian.co.uk

Electronically submit your new product description or product literature information! Go to www.sciencemag.org/about/new-products-section for more information.

Newly offered instrumentation, apparatus, and laboratory materials of interest to researchers in all disciplines in academic, industrial, and governmental organizations are featured in this space. Emphasis is given to purpose, chief characteristics, and availability of products and materials. Endorsement by *Science* or AAAS of any products or materials mentioned is not implied. Additional information may be obtained from the manufacturer or supplier.



Join our live webinar!



CRISPR/Cas9 in drug discovery

Applications in target discovery, hit identification, and lead optimization

To register, go to:
bit.ly/ScienceWebinarMay11

Wednesday, May 11, 2016
12 noon Eastern,
9 a.m. Pacific,
5 p.m. UK,
6 p.m. CEST

Science
AAAS

Sponsored by GE Healthcare

AAAS *Travels*

SOUTH AFRICA!
Wildlife & Spring Bloom
October 1-14, 2016



The southern-most point of the African continent is a riotous mix of picturesque mountains, tumbling rivers, fields of flowers, heathland, and an endless series of bays, lagoons, and headlands forming the stunning coastline. The Western Cape Flora is one of only six floral kingdoms of the world. Explore world famous gardens and national parks. See elephants and rhinos as you enjoy spring in South Africa. $4,995 + air.

For a detailed brochure, call (800) 252-4910
All prices are per person twin share + air

BETCHART EXPEDITIONS INC.
17050 Montebello Rd, Cupertino, CA 95014
Email: AAASInfo@betchartexpeditions.com
www.betchartexpeditions.com

R&D SYSTEMS
a bio-techne brand

What's in Your Sample?



Choose the right immunoassay to get your answers!

Learn more | rndsystems.com/immunoassays

bio-techne®
Global info@bio-techne.com bio-techne.com/find-us/distributors TEL +1 612 379 2956
North America TEL 800 343 7475 **Europe | Middle East | Africa** TEL +44 (0)1235 529449
China info.cn@bio-techne.com TEL +86 (21) 52380373
bio-techne.com



There's only one Science

Science Careers Advertising

For full advertising details, go to ScienceCareers.org and click For Employers, or call one of our representatives.

Tracy Holmes
Worldwide Associate Director
Science Careers
Phone: +44 (0) 1223 326525

THE AMERICAS

E-mail: advertise@sciencecareers.org
Fax: +1 (202) 289 6742

Tina Burks
Phone: +1 (202) 326 6577

Nancy Toema
Phone: +1 (202) 326 6578

Online Job Posting Questions
Phone: +1 (202) 312 6375

EUROPE / INDIA / AUSTRALIA / NEW ZEALAND / REST OF WORLD

E-mail: ads@science-int.co.uk
Fax: +44 (0) 1223 326532

Sarah Lelarge
Phone: +44 (0) 1223 326527

Kelly Grace
Phone: +44 (0) 1223 326528

Online Job Posting Questions
Phone: +44 (0) 1223 326528

JAPAN

Katsuyoshi Fukamizu (Tokyo)
E-mail: kfukamizu@aaas.org
Phone: +81 3 3219 5777

Hiroyuki Mashiki (Kyoto)
E-mail: hmashiki@aaas.org
Phone: +81 75 823 1109

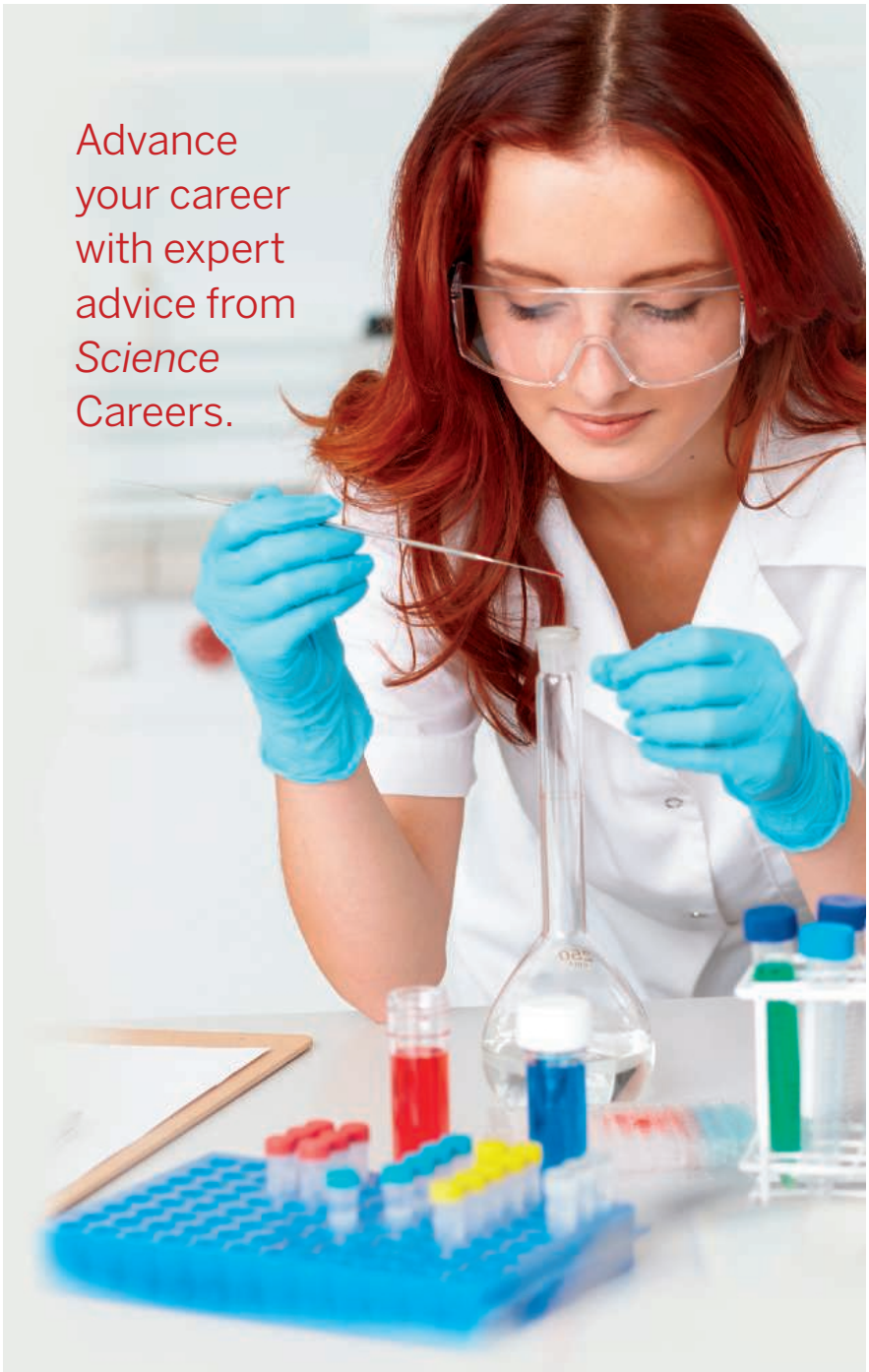
CHINA / KOREA / SINGAPORE / TAIWAN / THAILAND

Ruolei Wu
E-mail: rwu@aaas.org
Phone: +86 186 0082 9345

All ads submitted for publication must comply with applicable U.S. and non-U.S. laws. *Science* reserves the right to refuse any advertisement at its sole discretion for any reason, including without limitation for offensive language or inappropriate content, and all advertising is subject to publisher approval. *Science* encourages our readers to alert us to any ads that they feel may be discriminatory or offensive.

ScienceCareers
FROM THE JOURNAL SCIENCE AAAS

ScienceCareers.org



Download Free Career Advice Booklets!
ScienceCareers.org/booklets

Featured Topics:

- Networking
- Industry or Academia
- Job Searching
- Non-Bench Careers
- And More



ScienceCareers
FROM THE JOURNAL SCIENCE AAAS

ScienceCareers online @sciencecareers.org

Baylor College of Medicine

CHIEF SCIENTIFIC OFFICER

Baylor College of Medicine (BCM) is conducting a retained search for an energetic and visionary leader for the research collaboration between BCM and Baylor Scott & White Research Institute (BSWRI) in Dallas and Temple.

The Chief Scientific Officer will also serve as a Section Chief in the BCM Department of Medicine. The main focus of this executive will be to provide leadership, direction and strategic planning in the overall enhancement of research and development at BSWRI and will be instrumental in implementing and maximizing the value of the collaborative relationship between BSWRI and BCM. This dynamic leader serves as the liaison between the two institutions and as a resource to board and executive leadership on matters pertaining to research activities.

The successful candidate will have a minimum of five years of experience in research leadership and management within a research enterprise of significant scope and size and a distinguished record that merits national/international credibility in research and qualify for appointment at BCM at the rank of full professor. An active lab and grant portfolio in basic or translational research is desired. A PhD, MD, or MD/PhD is required.

Baylor College of Medicine (BCM): The only private health sciences university in the greater Southwest, BCM is an internationally respected medical and research institution that consistently ranks among the nation's top medical schools, with *U.S. News and World Report* placing BCM 20th among all medical schools in its latest annual survey for research. In fiscal year 2014, the College was ranked fifth by the National Science Foundation for total research expenditures in biological science, and 20th in National Institutes of Health (NIH) funding. Eight departments ranked among the top 20 for NIH funding, with Genetics and Cell Biology ranked #1. BCM is home to a number of centers of excellence, including the NCI-designated Dan L. Duncan Comprehensive Cancer Center and the Human Genome Sequencing Center.

Baylor Scott & White Research Institute (BSWRI): The result of the 2016 integration of the legacy research programs of Baylor Health Care System and Scott & White Healthcare, BSWH and its affiliates offer BSWH researchers unique access to one of the largest patient bases available for research in the US with a single institution. As the entity designated by the BSWH Board of Directors to administer all research across the BSWH system, BSWRI promotes and supports research to bring innovative treatments from the laboratory workbench to the patient bedside. Focusing on basic science, clinical trials, health care effectiveness and quality-of-care research, BSWRI is conducting more than 2,000 active research protocols with 750 research investigators, spanning more than 60 medical specialties.

About Baylor Scott & White Health
Formed from the 2013 merger between Baylor Health Care System and Scott & White Healthcare, the system referred to as Baylor Scott & White Health (BSWH) is the largest not-for-profit health care system in the state of Texas. With about $9 billion in total assets, BSWH has the vision and resources to provide its patients continued quality care while creating a model system for a dramatically changing health care environment. The system consists of 48 hospitals including Baylor University Medical Center at Dallas and Scott & White Memorial Hospital as the top ranked flagship facilities, more than 900 access points, 6,000 active physicians, and 40,000 employees, plus the Scott & White Health Plan, Baylor Scott & White Research Institute and Baylor Scott & White Quality Alliance — a network of clinical providers and facilities focused on improving quality, managing the health of patient populations, and reducing the overall cost of care.

Please submit nominations and/or curriculum vitae to the search consultant:
Jannah Hodges, Managing Partner, Hodges Partners
100 Highland Park Village, Suite 200, Dallas, TX 75205
Phone: 214.902.7901 E-mail: jannah@hodgespartners.com

JOB FOCUS: IMMUNOLOGY

TENURE-TRACK FACULTY POSITION IN IMMUNOLOGY MASSACHUSETTS GENERAL HOSPITAL HARVARD MEDICAL SCHOOL

The Center for Immunology and Inflammatory Diseases and the Division of Rheumatology, Allergy and Immunology at the MGH is seeking an outstanding scientist to develop a rigorous independent research program in immunology. Applicants whose programs address any area of basic experimental immunology or translational human immunology are encouraged to apply. Areas of particular interest include single cell genomics and bioinformatics, B cell biology, tolerance, autoimmunity and allergy. Laboratory space is within the MGH Center for Immunology and Inflammatory Diseases, a diverse interactive research center focused on basic immunology and mechanisms of immune-mediated diseases. Applicants may have an M.D., Ph.D. or M.D./Ph.D. degrees. Academic appointment at the Assistant or Associate Professor level will be on the tenure-track at Harvard Medical School and a generous start up package will be provided. Applicants should submit a CV, research plan and the names of three references to **Dr. Andrew Luster** c/o **CIIDsearch@mgh.harvard.edu**.

Women and minority applicants are particularly encouraged to apply.

Post Your Jobs
1.4 million candidates*
235,000 job applications*
Reach Scientists. Fill Positions.
ScienceCareers
employers.sciencecareers.org
*Jan–Dec 2015

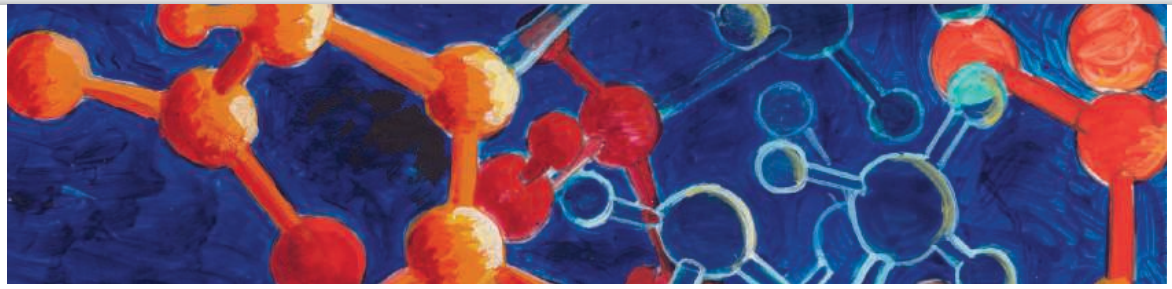


Don't hit the pavement for your job search.

Target your job search using relevant resources on **ScienceCcareers.org**.

ScienceCareers
FROM THE JOURNAL SCIENCE AAAS

Are you a million-dollar professor?



The Howard Hughes Medical Institute (HHMI) invites applications for the HHMI Professors Program competition from natural sciences faculty members who, through innovative teaching and mentoring, can convey the excitement and values of scientific research to undergraduate students. Through sustained investment in the Professors program, **HHMI aims to inspire research universities to value innovation in teaching as highly as innovation in research.** HHMI expects to appoint up to 15 professors, awarding each a five-year, non-renewable grant of $1 million.

ELIGIBILITY

- Affiliated with an institution classified as a Doctoral University, Highest Research Activity (R1) according to the 2015 Carnegie Classification of Institutions of Higher Education
- Tenured faculty member of a baccalaureate degree-granting natural sciences department
- Full-time faculty appointment in current home department for at least three consecutive years prior to application
- Assigned role in the development or implementation of undergraduate curriculum in home department as part of faculty appointment
- Principal investigator on one or more active, national peer-reviewed research award of at least three years duration

APPLICATION INFORMATION

http://www.hhmi.org/hhmiprofs2017

Deadline for Intent to Apply: July 1, 2016

Deadline to submit all electronic application materials: October 6, 2016

hhmi | Howard Hughes Medical Institute

Science Careers online @sciencecareers.org

FUNDING OPPORTUNITIES — U.S. Department of Defense

Defense Health Program

Peer Reviewed Medical Research Program

The Peer Reviewed Medical Research Program (PRMRP) funds exceptional research with the goal to improve the health and well-being of all military Service Members, Veterans, and their beneficiaries. The PRMRP received ***$278.7 million*** in fiscal year 2016 (FY16) and seeks grant applications in the following ***topic areas:***

Acute Lung Injury
Antimicrobial Resistance
Chronic Migraine and Post-Traumatic Headache
Congenital Heart Disease
Constrictive Bronchiolitis
Diabetes
Dystonia
Emerging Infectious Diseases
Focal Segmental Glomerulosclerosis
Fragile X Syndrome
Hepatitis B
Hereditary Angioedema
Hydrocephalus
Inflammatory Bowel Disease
Influenza
Integrative Medicine
Interstitial Cystitis
Lupus
Malaria
Metals Toxicology
Mitochondrial Disease
Nanomaterials for Bone Regeneration
Nonopioid Pain Management
Pancreatitis
Pathogen-Inactivated Dried Plasma
Polycystic Kidney Disease
Post-Traumatic Osteoarthritis
Psychotropic Medications
Pulmonary Fibrosis
Respiratory Health
Rett Syndrome
Rheumatoid Arthritis
Scleroderma
Sleep Disorders
Tinnitus
Tuberculosis
Vaccine Development for Infectious Disease
Vascular Malformations
Women's Heart Disease

Descriptions of the FY16 PRMRP Program Announcements and General Application Instructions are anticipated to be posted on Grants.gov by ***mid-March 2016:***

- Clinical Trial Award
- Discovery Award
- Focused Program Award
- Investigator-Initiated Research Award
- Technology/Therapeutic Development Award

All applications must conform to the Program Announcements and General Application Instructions that will be available for electronic downloading from the Grants.gov website (all viewable under CFDA number 12.420). Execution management support will be provided by the Congressionally Directed Medical Research Programs.

For more information, please visit: http://cdmrp.army.mil/funding/prmrp.shtml
http://cdmrp.army.mil

UCDAVIS

PRIMATE NEUROLOGIST

The University of California, Davis, Department of Neurology in collaboration with the California National Primate Research Center (CNPRC) seeks to fill a tenure-track or tenured position at the Associate/Full Professor level in the In-Residence or Ladder Rank Professor series with an emphasis on research in age-related cognitive decline in nonhuman primates. Preference will be given to candidates with a research program in an area of cognitive neuroscience with a focus on aging in nonhuman primates that compliments existing programs within the CNPRC, Department of Neurology, School of Medicine, and UC Davis.

The CNPRC at UC Davis is one of seven national centers established by the National Institutes of Health, Office of the Director (NIH/OD). The CNPRC is a national resource for collaborative and consultative expertise, biologic and genetic material, normative data, and specialized facilities and equipment to support nonhuman primate-related research. Members of the scientific staff (Core Scientists), represent a variety of disciplines including behavioral, cognitive neuroscience, cell and developmental biology, genetics, psychology, physiology, reproductive biology, virology, and immunology.

The level of appointment will be commensurate with credentials. Qualified applicants should upload a CV, names and contact information of three references online at **http://apptrkr.com/804870** .

EOE

POSITIONS OPEN

CRANIOFACIAL BONE PHYSIOLOGIST

The Dental and Craniofacial Research and Tissue Regeneration Directorate at the US Army Institute of Surgical Research at Fort Sam Houston, San Antonio, TX is seeking applications to fill a craniofacial bone physiologist position. The successful candidate should have experience in craniofacial bone healing research and will be expected to develop a strong competitive bone research program. For full details of the vacancy and how to apply, please visit website: **https://www.usajobs.gov/GetJob/ViewDetails/437296400**

Post your jobs
Fast and Easy



ScienceCareers
employers.sciencecareers.org

Join the Conversation!

Twitter is a great way to connect with AAAS members and staff about the issues that matter to you most. Be a part of the discussion while staying up-to-date on the latest news and information about your personal member benefits.

Follow us @AAASmember and join the conversation with #AAAS

AAAS MemberCentral
MemberCentral.aaas.org

西南交通大學 Southwest Jiaotong University

Southwest Jiaotong University, Chengdu, China Invites Applications for the Academic Positions

Southwest Jiaotong University (SWJTU), founded in 1896 and located in Chengdu, the capital of Sichuan province--China's dynamically growing West. SWJTU is an elite university with national key multidisciplinary "211" and "985 Feature" projects directly managed by the Ministry of Education.SWJTU is currently on the strategic "Developing and Strengthening the University by Introducing and Cultivating talents" campaign. Thus, you are cordially invited to apply for the following academic positions.

More information is available at http://www.swjtu.edu.cn/

Positions and Requirements

A. High-level Talented Leaders: Candidates should be qualified to be listed in national top talents programs such as Program of Global Experts, Top Talents of National Special Support Program, "Chang Jiang Scholars", China National Funds for Distinguished Young Scientists and National Award for Distinguished Teacher.

B. Young Leading Scholars: Candidates are preferable to be listed or qualified for the following programs: National Thousand Young Talents Program,The Top Young Talents of National Special Support Program (Program for Supporting Top Young Talents), Science Foundation for the Excellent Youth Scholars.

C. Excellent Young Academic Backbones

D. Excellent Doctors and Post Doctoral Fellows

Please contact Mr. Yu Wang, Ms. Ye Zeng, Ms.Qing Ya Wang
Telephone number: 186-28-66367238/ 66366202
Email: talent@swjtu.edu.cn
Address: Human Resources Department, SWJTU, Western Park of High-Tech Zone, Chengdu, Sichuan, China, 611756

大连海事大学 DALIAN MARITIME UNIVERSITY

Faculty Positions Available in Dalian Maritime University

Dalian Maritime University (DMU), established in 1909, is the key maritime institution under the Ministry of Transport, People's Republic of China. DMU enjoys a high reputation internationally as an excellent center of maritime education and training as recognized by the International Maritime Organization (IMO). DMU is also one of the member universities of "Project 211", a plan to build one hundred national-level universities in China. Subjects include engineering, science, management, economics, law, arts and philosophy, etc.

Complying with its goal to become a high-level university with distinctive characteristics in shipping, DMU welcomes talents, from home and abroad, to join us. (www.dlmu.edu.cn)

Recruitment Programs

■National Thousand Talents Program
Long-term or Short-term Research Program (Full Time/Part Time)
Young Talents (Full Time)
■Chang Jiang Scholars Program
Distinguished Professors(Full Time)
Chair Professors (Part Time)
Young Scholars(Full Time)
■Overseas Returned Scholars with PhD degree

Research Areas Required

Transportation Engineering, Naval Architecture and Ocean Engineering, Information and Communication Engineering, Control/Environmental/Management Science and Engineering, Computer Science and Technology, Logistics/Business/Public Administration, Law, Etc.

Support, Salary and benefits

Successful applicants will be offered highly competitive salary and benefits, research space, scientific research funds and extensive opportunities for promotion etc.

Contact Us

For more information, please visit http://www.dlmu.edu.cn/. If you're interested, please send your CV and relevant materials to zhaopin@dlmu.edu.cn or make telephone to +86-411-84727809, +86-411-84729228.

第三軍醫大學

Faculty Positions Available in the Third Military Medical University, Chongqing, China

The Third Military Medical University (TMMU) is seeking high-level medical talents from home and abroad. Applicants must have a nationality of China and a Ph.D. and/or M.D. degree. Competitive remuneration packages will be provided to successful applicants.

Located in Chongqing, the TMMU is a national key university, one of the military "2110 Project" key universities , and one of the first universities allowed to grant doctor's degree and to offer eight-year medical education program in China. Currently, the university has 3 academicians of Chinese Academy of Sciences and Chinese Academy of Engineering, over 200 high-level talents including distinguished professors entitled "Changjiang Scholar" and winners of "National Outstanding Youth Foundation," and over 900 staff members with senior professional titles. The TMMU has 25 national key disciplines, key state laboratories and national engineering centers, and three grade-A affiliated hospitals. It has harvested over 1700 scientific and technological achievements, including 7 first prizes of the National Science and Technology Progress Award.

Further information is available at www.edu.cn/tmmu

Please forward your CV and any other proof materials reflecting your teaching and research background to sydrcb@sina.com. Please call at +86-23-68752105 for any queries.

山东理工大学

Shandong University of Technology Is Seeking for High-level Talents at Home and Abroad

I. Recruiting subjects

Mechanical engineering, agricultural engineering, chemical engineering and technology, electrical engineering, computer science and technology, civil engineering, surveying and mapping science and technology, transportation engineering, biology, economics, ect..

II. Recruitment Scope

Professor, Associate Professor, Assistant Professor, Post doctor, doctor

III. Welfare and Benefits

(1) Annual salary for assistant professor or higher-level talents is RMB 400,000-1,200,000 with setting-in allowance of RMB 500,000-1,000,000;

(2) Annual salary for post doctor and doctor is RMB 300,000-400,000 and other relevant benefits.

IV. Talents who are eligible for the State's Thousand Talents Plan and Shandong Taishan Scholars as well as other talent projects enjoy corresponding policies and treatments after successfully recommended.

V. Contact information

Address: Recruitment Office of Shandong University of Technology, No. 266, Xincun West Road, Zhangdian District, Zibo City, Shandong Province
Zip code: 255049
Contact: Professor Zhang
E-mail: rshch@sdut.edu.cn

ScienceCareers online @sciencecareers.org



Special Job Focus:

Biotechnology

Issue date: May 27

Ads accepted until May 20
if space allows

For recruitment in science, there's only one *Science*.

What makes *Science* the best choice?

- Read and respected by 400,00 readers around the globe
- 75% of readers read *Science* more often than any other journal
- Your ad dollars support AAAS and its programs, which strengthens the global scientific community.

Why choose this Biotechnology Focus for your advertisement?

- Relevant ads lead off the career section with special biotechnology banner
- Bonus distributions:

  BIO, June 6–9, San Francisco, CA

  BIO Career Fair, June 9, San Francisco, CA.

Expand your exposure. Post your print ad online to benefit from:

- Link on the job board homepage directly to biotechnology jobs
- Dedicated landing page for jobs in biotechnology
- Additional marketing driving relevant job seekers to the job board.

Produced by the *Science*/AAAS Custom Publishing Office.

Deliver your message to a global audience of targeted, qualified scientists.

129,574
subscribers in print every week

48,366
unique active job seekers searching for **biotechnology** positions in 2015

27,111
applications submitted for **biotechnology** positions in 2015



SCIENCECAREERS.ORG

ScienceCareers
FROM THE JOURNAL SCIENCE AAAS

To book your ad: **advertise@sciencecareers.org**

The Americas
+202 326 6582
Japan
+81 3 3219 5777

Europe/RoW
+44(0)1223 326500
China/Korea/Singapore/Taiwan
+86 186 0082 9345

香 港 大 學
THE UNIVERSITY OF HONG KONG

Tenure-Track Associate Professor/Assistant Professor in the Department of Chemistry (2 posts)

Applications are invited for tenure-track appointments as Associate Professor/ Assistant Professor in Computational Chemistry [post (A) **(Ref.: 201600456)**] and Assistant Professor in Synthetic Chemistry [post (B) **(Ref.: 201600457)**] in the Department of Chemistry, to commence on January 1, 2017 or as soon as possible thereafter. These posts are tenure-track positions with consideration for tenure during the second three-year appointment.

For post (A) (Ref.: 201600456), applicants should have a Ph.D. degree with a strong background and research record in the computational chemistry with research interests in material science, catalysis, energy or drug design. **For post (B) (Ref.: 201600457)**, applicants should have a Ph.D. degree with a strong background and research record in synthetic chemistry with research interests in metal catalysis, materials synthesis, and/or x-ray crystallography. **For both posts**, the appointees are expected to develop original and independent research programs, and excel in both undergraduate and postgraduate teaching. A suitable start-up fund for research will be provided to the appointees. Information about the Department can be obtained at http://www.chemistry.hku.hk.

A globally competitive remuneration package commensurate with qualifications and experience will be offered. At current rates, salaries tax does not exceed 15% of gross income. The appointments will attract a contract-end gratuity and University contribution to a retirement benefits scheme, totalling up to 15% of basic salary, as well as annual leave, and medical benefits. Housing benefits will be provided as applicable.

Applicants should send a completed application form, together with an up-to-date C.V., a research proposal, and a statement on teaching philosophy by e-mail to scchem@hku.hk. They should indicate clearly the reference number and the level they wish to be considered for in the subject of the e-mail. Application forms (341/1111) can be downloaded at http://www.hku.hk/apptunit/form-ext.doc. Further particulars can be obtained at http://jobs.hku.hk/. **Closes May 31, 2016**.

The University thanks applicants for their interest, but advises that only candidates shortlisted for interviews will be notified of the application result.

The University is an equal opportunities employer and is committed to a No-Smoking Policy

TEXAS TECH UNIVERSITY
HEALTH SCIENCES CENTER
School of Medicine

Tenure-Track Faculty Positions

The Department of Cell Biology and Biochemistry at the Texas Tech University Health Sciences Center in Lubbock, TX invites applications for three tenure-track positions at the Assistant, Associate, or Professor level in any area of Biochemistry, Cellular, or Molecular Biology. The department (http://www.ttuhsc.edu/SOM/cbb/) currently has fourteen full-time faculty members and seeks accomplished scientists to complement existing research programs in cancer, reproductive biology, diabetes, membrane protein structure and function, development, and neurodegenerative diseases. Appointments will be in the School of Medicine and the Graduate School of Biomedical Sciences and come with a highly competitive start-up package and state-supported salary. Qualified candidates at the Professor level may be eligible for an endowed chair in Cancer Biology. Applicants should have a Ph.D., and/or M.D. degree, and will be expected to participate in the research and teaching missions of the department. Applicants with funded programs or strong evidence of funding potential will be given the strongest consideration. The Department of Cell Biology and Biochemistry is committed to diversity in education and employment, and strongly encourages applications from women and minorities.

Interested candidates must apply online (job **6733BR**, **6734BR**, or **6737BR**) at **http://www.ttuhsc.edu/som/cbb/positions.aspx**. Candidates should submit a single document in PDF format containing a cover letter describing their interest in the department (including possible collaborations with current faculty), a curriculum vitae, and a brief summary of their research interests. Candidates should also arrange to have three letters of recommendation sent in electronic format to cellbiology.biochemistry@ttuhsc.edu. Review of applications will continue until the positions are filled.

The TTUHSC is an Equal Opportunity /Affirmative Action/Veterans/ Disabilities Employer.

University of Missouri
School of Medicine

The University of Missouri (MU) School of Medicine in Columbia invites applications and nominations for the position of

SENIOR ASSOCIATE DEAN FOR RESEARCH

This position reports directly to the Dean of the School of Medicine.

MU has an outstanding research infrastructure in life sciences. MU has numerous distinctions including the largest and most powerful university-owned research reactor in the country; the only NIH-funded national swine resource and research center; one of 13 regional biocontainment laboratories in the nation; one of only four Mutant Mouse Regional Resource Centers; a Rat Resource and Research Center. Thus, MU is the only university in the nation to hold three major NIH national centers.

The Senior Associate Dean for Research will work with the Dean of the School of Medicine and campus research leaders to develop strategies that identify areas of research significance which will enable the School of Medicine to grow its research enterprise. The candidate will be expected to coordinate and lead extramural applications for research infrastructure and other large institutional awards; represent the School of Medicine to local, regional and national constituencies; and provide leadership in the area of clinical and translational research. The Senior Associate Dean will also oversee the graduate program in biomedical sciences, the research compliance programs, laboratory safety and the fiscal integrity of the research enterprise.

This individual will have an MD or PhD or equivalent degree, broad progressive administrative leadership experience in an academic health center environment; working knowledge of current national biomedical research interests with a history of sponsored funding; national recognition for achievement in research pursuits that would warrant appointment as a Full Professor. There should be a demonstrated record of promoting collaboration and cultivating both internal and external relations. The candidate must demonstrate the highest integrity and personal ethics and have a strong commitment to diversity.

Interested individuals should submit a letter of interest and a current CV to:
Barbara Montgomery,
staff for the search committee,
montgomeryb@health.missouri.edu or
MU School of Medicine, DC018.00
Columbia, MO 65212
telephone (573) 882-0003

For additional information, visit the following web sites:
http://medicine.missouri.edu/ and
http://missouri.edu/

The University of Missouri is fully committed to achieving the goal of a diverse and inclusive academic community of faculty, staff and students. We seek individuals who are committed to this goal and our core campus values of respect, responsibility, discovery and excellence.

An equal opportunity/Access/Affirmative Action/Pro Disabled & Veteran Employer

ScienceCareers online @sciencecareers.org

By **Peter M. Grace**

Learning the lessons of networking

When I was a young researcher, networking did not come naturally to me. I am a quiet person, and I preferred to engage with people I was already familiar with. However, I saw that many successful networkers also had successful careers with thriving, collaborative research programs and frequent speaking invitations. So, during my postdoc, I started making an effort to overcome my reclusive tendencies and build my professional network—and it has paid off. The network that I have built has championed my career advancement and contributed to my intellectual and professional development. Many of the opportunities that have come my way, including a tenure-track assistant professorship that I will begin next fall, have arisen from networking.

Because networking lacks direct or immediate outcomes, it is easy to ignore during academic training that focuses on quantifiable measures of success such as published articles and awarded grants and fellowships. It is also tempting to dismiss networking as a marketing ploy that distracts from scientific work that should speak for itself. As an initially hesitant networker, I have picked up some tips for those who want to develop a network without compromising their scientific or professional integrity but don't know where to start.



"As an initially hesitant networker, I have picked up some tips."

Attend conferences. With my mentor's approval, I prioritized conference attendance when I began my postdoc, even when it meant paying out of my own pocket. I chose three conferences to regularly attend each year. For me, this was the right number to reap the rewards of meeting people without disrupting my labwork; your optimal number might be different. Attending this variety of meetings, each with its unique but slightly overlapping profile of attendees, struck a balance between continually meeting new people from my broader field and strengthening the relationships with those in my niche discipline by seeing them multiple times a year.

Socialize. As an introvert, I usually want to retreat to my hotel room after a full day at a conference, but instead, I push myself to take advantage of the multiple formal and informal social events to further develop existing relationships and make new connections. Several of my collaborations have arisen from these conversations. Make the most of those opportunities by resisting the tendency to socialize exclusively with your friends.

Cold call. When I want to meet established researchers, I take the initiative to approach them directly, even if we don't have any connections. When I was a postdoc, for example, I asked a professor whether I could visit his lab and give a talk while visiting a friend in the same city. Another time, I asked a professor if we could meet for lunch or coffee during an upcoming conference. Afterward, I was able to call on this new contact for a letter of support. If you have the courage to ask for a meeting, you will be surprised by the success rate—and it could lead to future opportunities.

Give. The self-serving nature of networking can be repellant, but you can make up for it by being generous toward your trusted colleagues. Be willing to share ideas to help improve others' research, and be free with introductions among members of your network. The goodwill that follows will go a long way to help you become known not as a leech but as a good colleague and a knowledge hub.

Build your network before you need it. Developing a network during training, before you're actively looking to make your next career move, also helps minimize the feeling that networking is just self-serving. It avoids the awkwardness of starting a professional relationship with a request and allows you to sincerely build a network of peers and colleagues without ulterior motives. Remember that in the end, a strong network is based on its members' mutual respect for one another as scientists and friends. ■

Peter M. Grace is a research assistant professor in the Department of Psychology and Neuroscience at the University of Colorado, Boulder. *He thanks Andrew Gaudet for editorial advice. Send your story to SciCareerEditor@aaas.org.*

ILLUSTRATION: ROBERT NEUBECKER

Downloaded from http://science.sciencemag.org/ on May 5, 2016

Published by AAAS